Donor molecules and nuclear spins: a resource for quantum computing

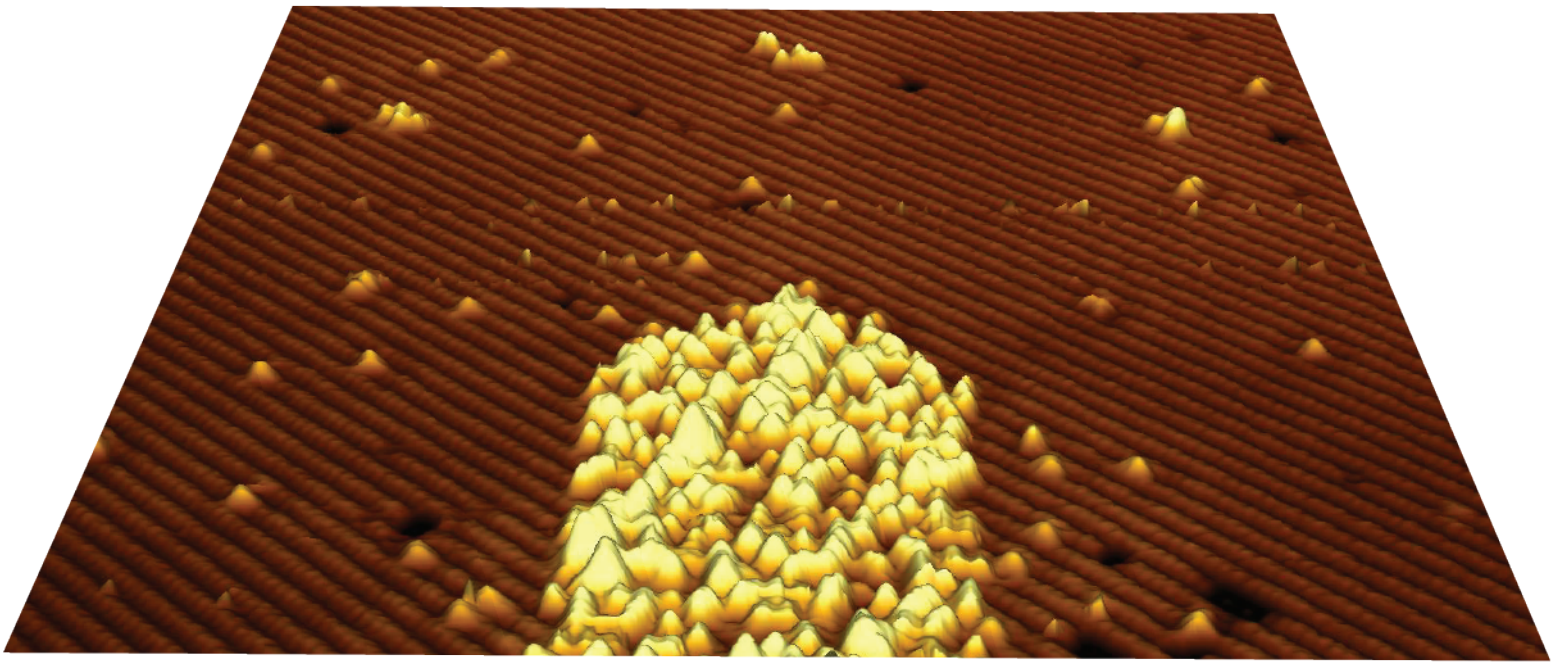

Felix Nicolas Krauth

A thesis submitted in fulfilment of the requirements for the degree of Doctor of Philosophy

UNSW

School of Physics

September 2021

ORIGINALITY STATEMENT

'I hereby declare that this submission is my own work and to the best of my knowledge it contains no materials previously published or written by another person, or substantial proportions of material which have been accepted for the award of any other degree or diploma at UNSW or any other educational institution, except where due acknowledgement is made in the thesis. Any contribution made to the research by others, with whom I have worked at UNSW or elsewhere, is explicitly acknowledged in the thesis. I also declare that the intellectual content of this thesis is the product of my own work, except to the extent that assistance from others in the project's design and conception or in style, presentation and linguistic expression is acknowledged.'

Signed:

Date: 16.06.2022

COPYRIGHT STATEMENT

Signed:

Date: 16.06.2022

AUTHENTICITY STATEMENT

‘I certify that the Library deposit digital copy is a direct equivalent of the final officially approved version of my thesis.’

Signed:

Date: 16.06.2022

INCLUSION OF PUBLICATIONS STATEMENT

UNSW is supportive of candidates publishing their research results during their candidature as detailed in the UNSW Thesis Examination Procedure.

Publications can be used in the candidate's thesis in lieu of a Chapter provided:

- The candidate contributed **greater than 50%** of the content in the publication and are the "primary author", i.e. they were responsible primarily for the planning, execution and preparation of the work for publication.
- The candidate has obtained approval to include the publication in their thesis in lieu of a Chapter from their Supervisor and Postgraduate Coordinator.
- The publication is not subject to any obligations or contractual agreements with a third party that would constrain its inclusion in the thesis.

The candidate has declared that **some of the work described in their thesis has been published and has been documented in the relevant Chapters with acknowledgement**.

A short statement on where this work appears in the thesis and how this work is acknowledged within chapter/s:
Chapter 3 and 4 are based on work that is part of an Australian provisional patent submission, has been published on the arXiv and is under review for publication. This is acknowledged in the introduction of each of the two chapters.

Signed:

Date: 16.06.2022

CANDIDATE'S DECLARATION

I declare that I have complied with the Thesis Examination Procedure.

Signed:

Date: 16.06.2022

Abstract

In this thesis we investigate donor molecules as a resource for scaling-up donor-based spin qubits in silicon towards error-corrected quantum computers. We first propose a novel donor-based qubit consisting of an electron spin spread across a single donor (1P) and a two-donor molecule (2P) that is electrically driven and coupled utilising the hyperfine interaction. This qubit belongs to a class of electron spin qubits called "flopping-mode" qubits, where the electron wave function is spread over two quantum dots. Using a complete error model, we first investigate how to minimise errors and the electrical driving power in the general class of qubits by optimising the magnetic gradients across the device. We then demonstrate how the magnetic gradient on the new qubit design can be atomically engineered using the hyperfine interaction within the donor molecules. In particular we show that by controlling the orientation of the nuclear spins in the qubit we can suppress the deleterious magnetic gradient originating from the hyperfine interaction within the two-donor molecule. We predict qubit errors well below 10^{-3} and show that the 1P-2P flopping-mode qubit can be strongly coupled to a superconducting cavity. Finally, we outline a way to scale the proposed qubits to a larger cavity-based architecture. Following this theoretical proposal we present experimental evidence that the required engineering of 2P donor-molecules is possible, using two atomic precision devices fabricated with hydrogen-resist STM lithography. We achieve high accuracy precision patterning of two-different devices that contain donor molecules to reveal the following results. First we show how to improve the fidelity of single shot electron spin readout from 83% to 94% using an optimised SET design. ESR spectra performed using adiabatic spin inversion yield precise measurements of the hyperfine interactions within the molecule. Using atomistic tight binding calculations in collaboration with the group of Professor Rahman we were able to perform metrology of the individual donor configurations within the dots. The metrology could be performed with a precision of $\pm 0.25\,\mathrm{nm}$ using measurements of the charging energies and improved to atomic precision using the hyperfine spectroscopy. The ESR spectra demonstrated the first

observation of a Stark shift in a tightly bound donor molecule. The magnitude of the shift observed was shown to depend on the molecular orientation within the crystal and offers future strategies for hyperfine engineering for optimal qubit operation. Finally, we demonstrate the first nuclear-spin readout of a tightly-bound donor molecule, with a fidelity of 88%, and show how we can track the nuclear spin states over time. Using a hidden Markov model we extracted the nuclear transition frequencies and uncover possible evidence of a dipolar coupling between the nuclear spins.

Aknowledgements

First of all I want to thank Professor Michelle Simmons for letting me be a part of her group and experience the wild adventure that was this PhD. I learned a tremendous amount in my years in her group and am very grateful for it.

I would like to thank Michael Jones and Dr. Yousun Chung for walking the road of the last few years together, as colleagues and friends, with all its ups and downs. Special thanks goes to my team of supervisors Dr. Yousun Chung and Dr. Samuel Gorman for their incredible level of support throughout my time in the group. Thanks go to Dr. Pascal Macha and Dr. Matthew House for some exciting times on the fridges, to Dr. Yu He who was always willing to help with a smile, to Dr. Joris Keizer and Dr. Matthias Koch who showed me the ropes on the STM, and to Dr. Jonathan Reiner for his kind friendship. A very special mention goes to Dr. Otte Homan who could be reliably counted on when problems occurred in the labs.

As to my fellow PhD students, Mark, Ludwik, Misha, Daniel; it was great to go through this adventure together. Among them I am very grateful to Prasanna Pakkiam for his support and many exciting discussions. To the admin staff: Esra and Sheree, thank you for keeping things running and being so friendly and kind.

Also, thanks to all the friends –in Australia and back home– who have supported me along the journey. Thank you Bayu, Brendan, Jakob, Eamonn, Eva, Nicola and Christian for making Australia a real home for me. Thank you Alexis, Killian and Pierre for keeping up our friendship despite our being at opposite ends of the world.

Thank you Yuki for coming all the way to the other end of the world with me, for all your support, your patience and many great moments together.

Finally, to my family, my dad, mom and brother: I couldn't have done this without your unwavering support.

Contents

Chapter 1

Introduction

The miniaturisation of transistors, the basic building block of classical computers, has fuelled incredible technological progress; and with it large societal changes. This downscaling that started in the 1970s and has so far been described by an exponential increase in the the transistor density ("Moore's Law"), will soon hit the limits set by the atomistic nature of matter [1]. While an increase in the computational power of computers is still possible by clever chip-designs, these advances will likely not be able to match the rate of progress seen in the last 50 years. A new computational paradigm called quantum computing, first proposed in the 1980s by Feynman and others [2] harnesses the strange laws of quantum physics and could sustain or even accelerate the rate of progress in computational power. In the 1990s quantum algorithms developed for these yet-to-be-constructed machines, promised significant computational speed-up for solving certain problems, when compared to available algorithms running on classical computers. Well known examples include Shor's prime factoring algorithm [3], that is set to break the commonly used RSA encryption scheme, and Grover's search algorithm [4]. Universal quantum computers store and manipulate information on two-level quantum-systems called qubits, in analogy to the bits of classical computing, and perform computations by using entangling interactions (quantum gates) between pairs of qubits.

Realisations of small quantum systems processors quantum algorithms were first demonstrated in the early 2000s. For example, in 2001, Shor's algorithm was used to factor the number 15 into its prime factors 3 and 5 using nuclear magnetic resonance on seven nuclear spins within molecules suspended in a liquid [5]. Since these proof-of-concept experiments, considerable progress has been made, leading to the demonstration in 2019 of a quantum computer solving a problem that a classical supercomputer could not solve in a practical amount of time [6]. Despite this

impressive demonstration of "quantum supremacy", on a superconducting quantum processor with 52 superconducting qubits, the problem solved has yet to demonstrate any commercial benefits. A quantum computer that can solve useful problems that are also intractable for a classical computer has not yet been demonstrated. The difficulty in building such a machine can in large part be attributed to the fragility of the quantum states within the quantum computer. A tremendous research effort in the last 20 years has lead to the realisation of qubits that are incredibly well protected from deleterious interaction with the environment and display very low errors. Nonetheless, these interactions cannot be fully eliminated and errors will invariably creep in for long computations. Various quantum error-correction schemes have been proposed to mitigate the fragility of quantum states in quantum computers [7, 8, 9, 10]. One particularly attractive candidate is the surface code, first proposed by Kitaev and coworkers [11, 12] in the late 1990s. The surface code allows for a relatively high qubit error rate of 0.1% during operation [13], a benchmark that has steered the field of quantum computing in the last 20 years. These benchmarks have now been achieved in various small scale physical systems (such as superconducting, ion-trap and nearly so in semiconductor-spin systems), making the prospect of practical error corrected quantum computation more realistic. However solving a useful problem on a quantum computer running the surface code in a reasonable amount of time will likely require at least tens of millions and possibly up to one billion physical qubits [13]. The leading quantum-computing platforms now face the daunting challenge of scaling up their quantum processors to these large sizes.

In this thesis we investigate how the challenge of scaling-up universal quantum computers can be met using atom based qubits in the semiconductor spin-qubit platform. The semiconductor spin-qubit platform can rely on the incredible materials technology development and know-how in the semiconductor industry, which now routinely manufactures billions of transistors –structures not unlike qubits– on a single chip [14]. One significant implementation of semiconductor spin-qubits is based on the electron spin trapped by a phosphorus impurity in silicon, and has demonstrated very long lifetimes and fault tolerant operation on a single-qubit [15, 16].

Chapter 2 lays out the incredible challenge that the semiconductor spin-qubit platform, and other platforms, face in scaling up such small devices to larger sizes. Electric operation of spin-qubits could meet this challenge, by allowing for faster operation and long distance coupling schemes using superconducting resonators. An overview is given of the fabrication method for the atomic-scale phosphorus spin-

qubit devices realised and measured in this thesis. Using a scanning tunnelling microscope (STM) under ultra-high vacuum conditions, we demonstrate atomic-scale lithography followed by phosphorus donor incorporation and silicon encapsulation. Additionally, details are provided on making electric contact to these atomic-scale devices, and integrating antennas on the devices that were used for controlling donor spin qubits. Finally, we discuss the fridge wiring and measurement set-up used to measure the atomic-scale phosphorus donor devices in this thesis.

Single electron spin qubits in silicon shown great promise for building a scalable quantum computer[17, 15, 18, 19]. However, despite the high-fidelity single qubit gates the operation time of the qubits remains to be orders of magnitude longer than those in superconducting qubits [20, 6]. These long gate times are due to the typically a weak interaction associated with magnetic control of electron spins [21, 22]. This weak interaction of single spins to magnetic fields also poses a challenge when performing long-range two-qubit gates mediated by microwave cavity photons where the experimentally realisable magnetic fields fall well below the strong-coupling regime (cavity-qubit coupling, g is larger than the decoherence rates of the qubit (γ) and cavity (κ)) [23]. To overcome the weak coupling of magnetic fields to spin qubits, other electrically driven spin qubits have been proposed using electric dipole spin resonance (EDSR) [24, 25, 26]. In **Chapter 3**, we discuss the implementation of a special type of electrically controlled spin qubits, known as "flopping-mode EDSR qubits" [26, 27, 28, 29, 30] when a single electron is delocalised across a double quantum in a gradient magnetic field. The flopping-mode qubit can be implemented in a variety of semiconductor systems involving quantum dots and phosphorus donors and offers fast single-qubit gate times comparable to superconducting qubits ($\sim$ nanoseconds). In addition, the qubit allows for long-distance qubit coupling through the large electric dipole associated with the double quantum dot system [27, 31, 32, 33]. We show how the two magnetic field gradients defining the qubit (perpendicular and longitudinal to the external magnetic field) give rise to a complex interplay of dephasing associated with the qubit driving and the qubit energy. Through a detailed theoretical analysis of dephasing, relaxation, and leakage errors we show how to optimise a flopping-mode qubit to achieve single-qubit gate errors below 10^{-3}—well below the 2D surface-code error threshold. In particular, we theoretically demonstrate that the previously proposed second-order charge noise sweet spot (where the second derivative of the qubit energy approaches zero) is detrimental to the overall qubit performance and the longitudinal magnetic field gradient should be minimised for high-fidelity qubit operations. Using the re-

sults presented in this chapter it will be possible to design a fast, high-fidelity qubit capable of long-distance qubit-qubit couplings mediated through superconducting microwave cavities in the strong coupling regime.

Building on the theoretical modelling detailed in the previous chapter, **Chapter 4** we theoretically propose and analyse a flopping-mode qubit based on phosphorus donor quantum dots in silicon. The all-epitaxial flopping-mode qubit will benefit from the ultra-low charge noise present in scanning tunnelling microscopy (STM) devices that are well separated from any interfaces [34]. We use the theoretical error model in the previous chapter to estimate the qubit performance while including additional leakage states due to the nuclear spin states of the phosphorus donors. The qubit is defined between a 2P quantum dot and a single donor (1P) where the hyperfine interaction is used to electrically drive flip-flop transitions between the electron and nuclear spin on the 1P. The longitudinal effective magnetic field gradient arises from the hyperfine interaction of the two donors on the 2P quantum dot and therefore can be minimised through electron shielding (operating with 2 closed shell electrons on the 2P) and initialising the nuclear spins into antiparallel nuclear spin states to cancel the total hyperfine interaction felt by the electron spin. By optimising the magnetic field gradients we demonstrate the qubit can be operated with an error rate of 2×10^{-4} at a magnetic field of ~ 0.2 T and maintains an error rate below 10^{-3} over a wide range of magnetic fields (0.1 - 0.6 T) and tunnel couplings ($\sim$ 1 - 20 GHz). We then show that the qubit can theoretically reach the strong-coupling regime to a superconducting microwave cavity with a cooperativity, $C = g^2/\gamma\kappa = 130 \gg 1$. Finally, using the excellent donor-based flopping-mode qubit we propose a 2D surface-code quantum computing architecture where the qubit can be coupled either via direct charge-dipoles or floating gates. The architecture utilises only 2 gates per qubit in nodes with qubit densities 28 μm^{-2} (0.25 μm^{-2}) for the dipole coupling (floating gate coupling). The outer qubits of each node are coupled via superconducting microwave cavities over the millimetre length-scale to allow for space for the classical control electronics required for measurement and control of the qubits. The high-fidelity donor-based flopping-mode qubit combined with the quantum computing architecture offers a direct route for scaling spin qubits defined on phosphorus donors in silicon.

In **Chapter 5**, we discuss the design considerations and simulations performed in order to design a device that can independently operate single qubit operations on three donor quantum dots, and perform two-qubit gates between two of the three pairs. The device is compatible with the long term goal of running a small fragment

of the surface-code error-correction algorithm. In order to achieve independent control, initialisation and readout of the three electron/nuclear spin qubits, as well as coupling of two of the electron spin qubit pairs using exchange-based gates, it is necessary to consider both the geometry of the device and the number of donors in each dot. By measuring in a dilution refrigerator, it was confirmed that the chosen geometry and donor numbers per dot fulfilled the original design requirements, which allowed for tunable independent electrostatic control of the charge state of three unpaired electron spins. The donor configurations was also estimated for each of the quantum dots by comparing measurements of the quantum dot charging energies to recently modelled tight binding simulations. The resulting donor configurations were found to be compatible with high quality STM images of the arrangement of phosphine species adsorbed in each quantum dot before incorporation. The tunnel rates of all three unpaired electrons on the left, middle and right dots were shown to fall within the ideal range for high fidelity spin readout. We demonstrated spin readout of the electron on the left 2P donor-quantum dot with 83% fidelity, which was limited by the on-off ratio of the SET and prevented electron spin readout on charge transitions with a faster tunnel rate ($> 15\,\mathrm{kHz}$). The sub-optimal on-off ratio of the SET was caused by variations in the SET dimensions caused by drift of the STM tip during patterning. Strategies to mitigate such variations are presented in Sect. 5.2.1, where advances in the design of the SET charge sensor yielded a significant improvement of the electron spin readout fidelity on a donor quantum dot, from 83% with the previous sensor, to 94.4% with the improved sensor. Electron spin resonance using adiabatic spin inversion was then demonstrated on the first electron of the right donor quantum dots of the device. Electron spin resonance spectra revealed four peaks which can be attributed to a 2P molecule with a hyperfine interaction of the first and second nucleus to the electron of $A_1 = 189 \pm 5\,\mathrm{MHz}$ and $A_2 = 83 \pm 5\,\mathrm{MHz}$, respectively. By matching the measured hyperfine interaction strengths to values obtained by tight binding simulations, we were able to determine the donor configuration in each quantum dot. The difference in the hyperfine interaction strengths is attributed to a linear Stark effect that was previously observed in ion-implanted single phosphorus donors but not in tightly bound donor molecules. Together, the total hyperfine value and the hyperfine difference identify $[1.5, 0.5, 0]a_0$ as the most probable donor configuration, where a_0 is the silicon lattice constant. We then perform nuclear spin readout on a tightly bound donor molecule, with a fidelity of 88%. The nuclear spin readout is used to track the nuclear spin states over times. Using a hidden Markov model, we extract the transition frequencies between

nuclear spin states and reconstruct the nuclear spin sequence during the tracking experiment. The extracted relaxation rates are in agreement with those observed on a single phosphorus donor [35]. The extracted nuclear excitation rates are attributed to the ionisation shock mechanism also observed on a single donor [35]. The hidden Markov model extracts a non-zero transition rate between the antiparallel nuclear spin states $\Downarrow\Uparrow\leftrightarrow\Uparrow\Downarrow$. This "flip-flop" transition rate could be due to the dipolar interaction between the nuclear spins, when the molecule is fully ionised. This dipolar interaction has not been observed within donor-molecules before and will be the focus of future work.

Finally, we summarise the results and give an outlook on future work in **Chapter 6**.

Bibliography

[1] Mitchell Waldrop. More than Moore. *Kyokai Joho Imeji Zasshi/Journal of the Institute of Image Information and Television Engineers*, 530:144–147, 2016.

[2] Richard P. Feynman. Simulating physics with computers. *International Journal of Theoretical Physics*, 21(6-7):467–488, 1982.

[3] Peter W. Shor. Polynomial-time algorithms for prime factorization and discrete logarithms on a quantum computer. *SIAM Journal on Computing*, 26(5):1484–1509, 1997.

[4] Lov K. Grover. Quantum Mechanics Helps in Searching for a Needle in a Haystack. *Physical Review Letters*, 79(2):325–328, jul 1997.

[5] Lieven M.K. Vandersypen, Matthias Steffen, Gregory Breyta, Costantino S. Yannoni, Mark H. Sherwood, and Isaac L. Chuang. Experimental realization of Shor's quantum factoring algorithm using nuclear magnetic resonance. *Nature*, 414:883–887, 2001.

[6] Frank Arute, Kunal Arya, Ryan Babbush, Dave Bacon, Joseph C. Bardin, Rami Barends, Rupak Biswas, Sergio Boixo, Fernando G.S.L. Brandao, David A. Buell, Brian Burkett, Yu Chen, Zijun Chen, Ben Chiaro, Roberto Collins, William Courtney, Andrew Dunsworth, Edward Farhi, Brooks Foxen, Austin Fowler, Craig Gidney, Marissa Giustina, Rob Graff, Keith Guerin, Steve Habegger, Matthew P. Harrigan, Michael J. Hartmann, Alan Ho, Markus Hoffmann, Trent Huang, Travis S. Humble, Sergei V. Isakov, Evan Jeffrey, Zhang Jiang, Dvir Kafri, Kostyantyn Kechedzhi, Julian Kelly, Paul V. Klimov, Sergey Knysh, Alexander Korotkov, Fedor Kostritsa, David Landhuis, Mike Lindmark, Erik Lucero, Dmitry Lyakh, Salvatore Mandrà, Jarrod R. McClean, Matthew McEwen, Anthony Megrant, Xiao Mi, Kristel Michielsen, Masoud Mohseni, Josh Mutus, Ofer Naaman, Matthew Neeley, Charles Neill, Murphy Yuezhen Niu, Eric Ostby, Andre Petukhov, John C. Platt, Chris Quintana, Eleanor G.

Rieffel, Pedram Roushan, Nicholas C. Rubin, Daniel Sank, Kevin J. Satzinger, Vadim Smelyanskiy, Kevin J. Sung, Matthew D. Trevithick, Amit Vainsencher, Benjamin Villalonga, Theodore White, Z. Jamie Yao, Ping Yeh, Adam Zalcman, Hartmut Neven, and John M. Martinis. Quantum supremacy using a programmable superconducting processor. *Nature*, 574(7779):505–510, 2019.

[7] Asher Peres. Reversible logic operations. *Physical Review A*, 32(6):3266–3276, 1985.

[8] Peter W. Shor. Scheme for reducing decoherence in quantum computer memory. *Physical Review A*, 52(4):2493–2496, 1995.

[9] Andrew Steane. M ultiple-particle interference and quantum error correction. *Proceedings of the Royal Society A*, 452:2551–2577, 1996.

[10] Daniel Gottesman. Class of QEC codes saturating Hamming bound. *Physical Review A*, 54(3):1862–1868, 1996.

[11] A. Yu Kitaev. Fault-tolerant quantum computation by anyons. *Annals of Physics*, 303(1):2–30, 2003.

[12] Eric Dennis, Alexei Kitaev, Andrew Landahl, and John Preskill. Topological quantum memory. *Journal of Mathematical Physics*, 43(9):4452–4505, 2002.

[13] Austin G. Fowler, Matteo Mariantoni, John M. Martinis, and Andrew N. Cleland. Surface codes: Towards practical large-scale quantum computation. *Physical Review A*, 86(3):032324, sep 2012.

[14] L. M. K. Vandersypen, H. Bluhm, J. S. Clarke, A. S. Dzurak, R. Ishihara, A. Morello, D. J. Reilly, L. R. Schreiber, and M. Veldhorst. Interfacing spin qubits in quantum dots and donorshot, dense, and coherent. *npj Quantum Information*, 3(1):1–10, 2017.

[15] Juha T. Muhonen, Juan P. Dehollain, Arne Laucht, Fay E. Hudson, Rachpon Kalra, Takeharu Sekiguchi, Kohei M. Itoh, David N. Jamieson, Jeffrey C. McCallum, Andrew S. Dzurak, and Andrea Morello. Storing quantum information for 30 seconds in a nanoelectronic device. *Nature Nanotechnology*, 9(12):986–991, 2014.

[16] J. T. Muhonen, A. Laucht, S. Simmons, J. P. Dehollain, R. Kalra, F. E. Hudson, S. Freer, K. M. Itoh, D. N. Jamieson, J. C. McCallum, A. S. Dzurak, and

A. Morello. Quantifying the quantum gate fidelity of single-atom spin qubits in silicon by randomized benchmarking. *Journal of Physics Condensed Matter*, 27(15), 2015.

[17] M. Veldhorst, J. C.C. Hwang, C. H. Yang, A. W. Leenstra, B. De Ronde, J. P. Dehollain, J. T. Muhonen, F. E. Hudson, K. M. Itoh, A. Morello, and A. S. Dzurak. An addressable quantum dot qubit with fault-tolerant control-fidelity. *Nature Nanotechnology*, 9(12):981–985, 2014.

[18] M Veldhorst, C H Yang, J C C Hwang, W Huang, J P Dehollain, J T Muhonen, S Simmons, A Laucht, F E Hudson, K M Itoh, A Morello, and A S Dzurak. A two-qubit logic gate in silicon. *Nature*, 526:410–414, 2015.

[19] C. H. Yang, K. W. Chan, R. Harper, W. Huang, T. Evans, J. C.C. Hwang, B. Hensen, A. Laucht, T. Tanttu, F. E. Hudson, S. T. Flammia, K. M. Itoh, A. Morello, S. D. Bartlett, and A. S. Dzurak. Silicon qubit fidelities approaching incoherent noise limits via pulse engineering. *Nature Electronics*, 2(4):151–158, 2019.

[20] R. Barends, J. Kelly, A. Megrant, A. Veitia, D. Sank, E. Jeffrey, T. C. White, J. Mutus, A. G. Fowler, B. Campbell, Y. Chen, Z. Chen, B. Chiaro, A. Dunsworth, C. Neill, P. O'Malley, P. Roushan, A. Vainsencher, J. Wenner, A. N. Korotkov, A. N. Cleland, and John M. Martinis. Superconducting quantum circuits at the surface code threshold for fault tolerance. *Nature*, 508(7497):500–503, 2014.

[21] F H Koppens, C Buizert, K J Tielrooij, I T Vink, K C Nowack, T Meunier, L P Kouwenhoven, and L M Vandersypen. Driven coherent oscillations of a single electron spin in a quantum dot. *Nature*, 442(7104):766–771, 2006.

[22] Jarryd J Pla, Kuan Y Tan, Juan P Dehollain, Wee H Lim, John J L Morton, David N Jamieson, Andrew S Dzurak, and Andrea Morello. A single-atom electron spin qubit in silicon. *Nature*, 489(7417):541–545, sep 2012.

[23] Eisuke Abe, Hua Wu, Arzhang Ardavan, and John J.L. Morton. Electron spin ensemble strongly coupled to a three-dimensional microwave cavity. *Applied Physics Letters*, 98(25), 2011.

[24] K C Nowack, F H L Koppens, Y V Nazarov, and L M K Vandersypen. Coherent Control of a Single Electron with Electric Fields. *Science*, 318:1430–1433, 2007.

[25] Jun Yoneda, Kenta Takeda, Tomohiro Otsuka, Takashi Nakajima, Matthieu R. Delbecq, Giles Allison, Takumu Honda, Tetsuo Kodera, Shunri Oda, Yusuke Hoshi, Noritaka Usami, Kohei M. Itoh, and Seigo Tarucha. A quantum-dot spin qubit with coherence limited by charge noise and fidelity higher than 99.9%. *Nature Nanotechnology*, 13(2):102–106, 2018.

[26] Xuedong Hu, Yu Xi Liu, and Franco Nori. Strong coupling of a spin qubit to a superconducting stripline cavity. *Physical Review B - Condensed Matter and Materials Physics*, 86(3):1–5, 2012.

[27] J. J. Viennot, M. C. Dartiailh, A. Cottet, and T. Kontos. Coherent coupling of a single spin to microwave cavity photons. *Science*, 349(6246):408–411, 2015.

[28] Félix Beaudoin, Dany Lachance-Quirion, W. A. Coish, and Michel Pioro-Ladrière. Coupling a single electron spin to a microwave resonator: Controlling transverse and longitudinal couplings. *Nanotechnology*, 27(46), 2016.

[29] Guilherme Tosi, Fahd A Mohiyaddin, Vivien Schmitt, Stefanie Tenberg, Rajib Rahman, Gerhard Klimeck, and Andrea Morello. Silicon quantum processor with robust long-distance qubit couplings. *Nature Communications*, 8(1):450, dec 2017.

[30] X. Croot, X. Mi, S. Putz, M. Benito, F. Borjans, G. Burkard, and J. R. Petta. Flopping-mode electric dipole spin resonance. 1:1–6, 2019.

[31] X. Mi, M. Benito, S. Putz, D. M. Zajac, J. M. Taylor, Guido Burkard, and J. R. Petta. A coherent spin-photon interface in silicon. *Nature*, 555(7698):599–603, 2018.

[32] N. Samkharadze, G. Zheng, N. Kalhor, D. Brousse, A. Sammak, U. C. Mendes, A. Blais, G. Scappucci, and L. M.K. Vandersypen. Strong spin-photon coupling in silicon. *Science*, 359(March):1123–1127, 2018.

[33] F. Borjans, X. G. Croot, X. Mi, M. J. Gullans, and J. R. Petta. Resonant microwave-mediated interactions between distant electron spins. *Nature*, 577(January):195–199, 2019.

[34] Ludwik Kranz, Samuel Keith Gorman, Brandur Thorgrimsson, Yu He, Daniel Keith, Joris Gerhard Keizer, and Michelle Yvonne Simmons. Exploiting a Single-Crystal Environment to Minimize the Charge Noise on Qubits in Silicon. *Advanced Materials*, 32(40):1–8, 2020.

[35] Jarryd J. Pla, Kuan Y. Tan, Juan P. Dehollain, Wee H. Lim, John J. L. Morton, Floris A. Zwanenburg, David N. Jamieson, Andrew S. Dzurak, and Andrea Morello. High-fidelity readout and control of a nuclear spin qubit in silicon. *Nature*, 496(7445):334–338, apr 2013.

Chapter 2

Background

This chapter sets the background to the following three results chapters. First the chapter reviews some of the challenges towards scalable quantum computation and then discusses some of advantages and disadvantages of the current major material platforms. We then focus on qubits based on the electron and nuclear spin on phosphorus donors in silicon that form the basis of devices proposed and measured in this thesis. The fabrication method for such donor-based devices is then detailed, before finally describing the measurement set-up.

2.1 The challenge of scaling up to error-corrected quantum computers

2.1.1 Error correction using the Surface Code

Parity measurement of 2 qubits: the stabilisers

Quantum error correction cannot be realised via a projective measurement of each qubit because direct measurement of a quantum states collapses the state that is being protected [1, 2]. To circumvent this measurement issue, the surface code, like other quantum error correction codes [1, 3], rely on measurements of an ancilla qubit that has been entangled with the qubit in question. Error correction in the surface code is based on stabiliser measurements, which are non-destructive projective measurements on the neighbouring data qubits involved in quantum computation. The X and Z-stabiliser correspond to simultaneous measurement $\hat{X} \otimes \hat{X}$ and $\hat{Z} \otimes \hat{Z}$ of the two qubits along the eigenbasis defined by the Pauli-x and -z operators $\hat{X}$, and $\hat{Z}$ respectively. It can be shown [2] that the two qubit parity operators $\hat{X} \otimes \hat{X}$ and

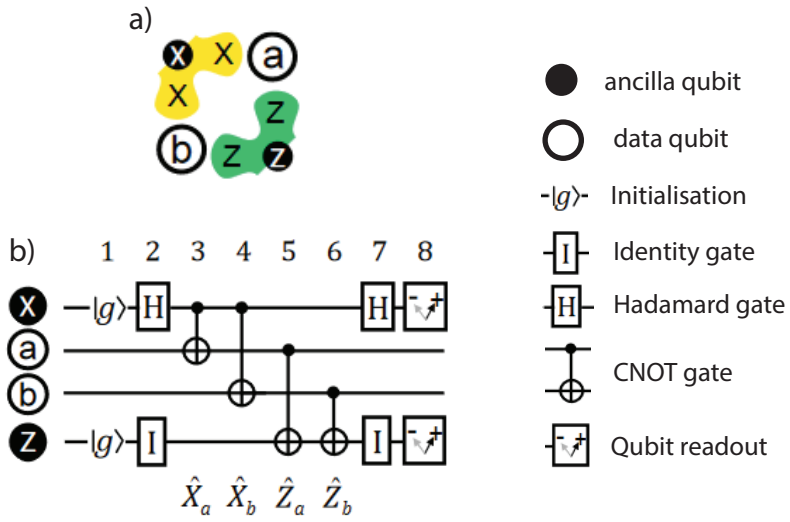

Figure 2.1: **Z- and X-stabilisers using ancilla qubits Z and X respectively on two data-qubits "a" and "b". a)** a fragment of the surface code square lattice containing the two ancilla qubits x (yellow) and z (green) and two data qubits a and b. **b)** Process diagram for executing a X and Z-stabiliser. Illustration reproduced from ref. [2]

$\hat{Z} \otimes \hat{Z}$ commutes, and thus share a common eigenbasis. The stabiliser measurement, projects the 2-qubit state into one of these eigenstates, and any subsequent measurement whether a Z- or a X-stabiliser, does not alter that state in the absence of errors on either qubits.

Implementing stabilisers via Ancilla qubits

The surface code implements the X- and Z- stabilisers non destructively, by using a second type of qubits, called X- and Z-ancilla qubits which are only involved in the error correction and do not hold any information appertaining to the quantum computation. Each Z and X-stabiliser measurement is achieved by initialising the ancilla qubit in the $\hat{X}$ and $\hat{Z}$ eigenbasis, entangling it with its neighbouring data qubits via 2-qubit gates, and reading out the ancilla in the $\hat{X}$ and $\hat{Z}$ eigenbasis. The initialisation and readout in the $\hat{X}$ eigenbasis are both performed via a Hadamard gate performed after and before the initialisation and readout in the $\hat{Z}$ eigenbasis. The circuit diagram in Fig. 2.1 shows an implementation of Z- and X- stabiliser on two data qubits a and b.

Error detection on 2 qubits

Most errors can be approximated by random occurrences of single qubit X, Y and Z operations [2], e.g. an X-error on a 2-qubit code, can be written as the operator $\hat{E}_x = \mathbb{I} \otimes \mathbb{I} + \epsilon \hat{X} \otimes \mathbb{I}$, where ϵ is directly related to the error rate of that specific error and $\mathbb{I}$ is the identity. In most cases, such an error will project the stabilised 2-qubit state ψ onto itself, but with a small probability ϵ it will project it onto another stabiliser eigenstate $\hat{E}_x \cdot \psi$, and the subsequent X-stabilisers will register a change in its measurement outcome, which is the basic principle of error detection in the surface code. Stabiliser measurements on two qubits do not allow determining which of the two qubit was subject to the error because different errors can lead to the same stabiliser measurement outcome. Therefore the error cannot be corrected with only two qubits. Furthermore, with two qubits only, the Z and X stabilises fully constrain the state of the two data qubits and thus they cannot be used to perform any computation.

Error correction on bigger arrays

The surface code therefore ultimately relies on large assemblies of data and ancilla qubits to accurately pinpoint which qubit was subject to the error and what the error type was (X or Z). To implement the surface code, the data qubits are thus arranged in a 2D square lattice interspersed with alternating X- and Z-ancilla qubits, each linked to its 4 nearest neighbour data qubits as depicted in Fig. 2.2. An isolated $X(Z)$ error on a given data qubit will produce a change in the $Z(X)$ stabiliser measured by the two neighbouring $Z(X)$ ancillas but not in the two other ancillas whereas a Y error is registered by all 4 neighbouring qubits since $\hat{Y} = \hat{Z}\hat{X}$. Errors in the measurement process are likely restricted to a single ancilla, and will not appear in the subsequent surface code cycle. Errors in the 2-qubit operations generate a distinct pattern of stabiliser-measurement changes and can also be localised and identified. The identification of the error type and location based on the stabiliser measurement outcome needs to be run synchronously by classical algorithms running on classical electronics. Once the error has been identified, it can also be corrected. The correction does not have to be applied to the qubits themselves, but can be kept track of by the classical control software that runs the qubits. For example, any single-qubit error can be corrected by multiplying the subsequent measurement by -1, and two subsequent errors will cancel out. The error detection above requires that the errors are rare. As the errors rate grows, errors will appear closer to each other and will reduce the fidelity with which the classical algorithms can pinpoint

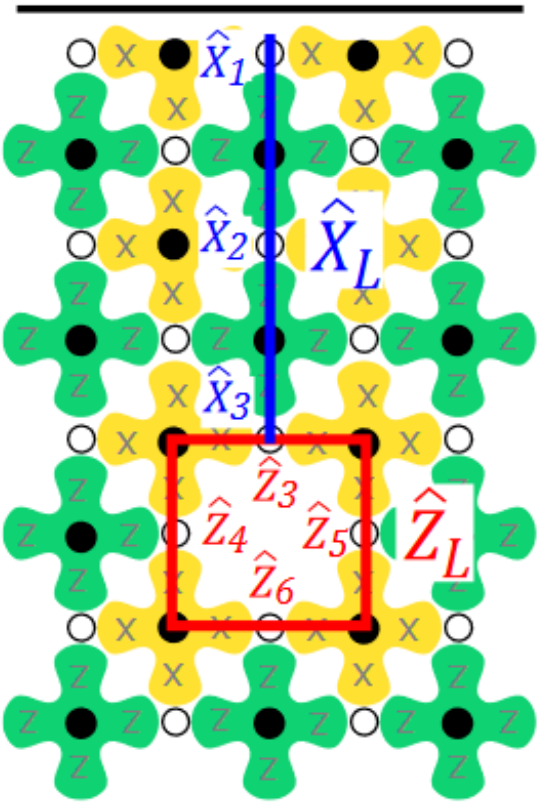

Figure 2.2: **A schematic of a logical qubit in the 2D surface code.** The logical qubit exists as two degrees of freedom in the state of the 20 data qubits in the grid displayed above (white dots) constrained by stabiliser measurements ("Z" and "X") performed by the 19 ancilla qubits (black dots). The two degrees of freedom are implemented by switching off one of the 20 ancillas in the grid, which is shown as a white "hole". A Z- and X- gate Z_L and X_L on the thus defined logical qubit is performed by performing a series of single qubit gates $\hat{Z}_i$ and $\hat{X}_i$ on chains of data qubits circling around the "hole" or connecting it to an outside edge of the surface code grid respectively. Illustration reproduced from ref. [2]

the type and location of the error. Above a certain error rate, errors cannot be accurately corrected. This is known as the error threshold for the code.

The logical qubit: a protected degree of freedom

To perform quantum computation, the surface code uses degrees of freedom within the grid of data qubits that are not constrained by the stabilisers. Two degrees of freedom can for example be produced by switching off one ancilla qubit. Indeed each data qubit adds two degrees of freedom to the surface code, while every ancilla qubit adds two constraints to it. Two degrees of freedom can thus be added by simply by removing one pair of constraints, that is by switching off one ancilla qubit

(see Fig. 2.2). Each pair of degrees of freedom in the surface code grid forms a logical qubit and consists in an error protected qubit. The logical qubits can be manipulated via chains of X and Z operators as pictured in Fig. 2.2. A logical qubit can be interpreted as a quantum state that is spread over many physical data qubits in the surface code array, and is thus protected from localised errors. An error-protected logical qubit can be used to perform fault tolerant quantum computation [2].

2.1.2 Successes and challenges of major quantum computing platforms

In the race for universal quantum computing, several major platforms have come to the fore, of which we will discuss three in this section. Qubits encoded in the electronic states of trapped ions have demonstrated long relaxation times of several hours [4], long coherence times of up to 50 seconds without any dynamic decoupling protocols and at room temperature [4], with high operation fidelities [5, 6, 4] (see Table 2.1). Errors of single-qubit and two-qubit operations as low as 10^{-6} and 10^{-3} respectively have indeed been demonstrated [5], with preparation and fast-readout errors below 10^{-4} [7, 8]. Compared to other systems, the very low errors reduces the number of physical qubits needed to encode an error corrected logical qubit in the surface code (see Fig. 2.3). However, coupling and operating a large number of trapped ions is challenging due to electric field noise and footprint constraints so that there remain significant technological hurdles to scaling up processors beyond 100 to 1000 qubits [9, 10], a number well below the expected size of a quantum error corrected processor [2], even for the high qubit fidelities displayed by trapped ion qubits.

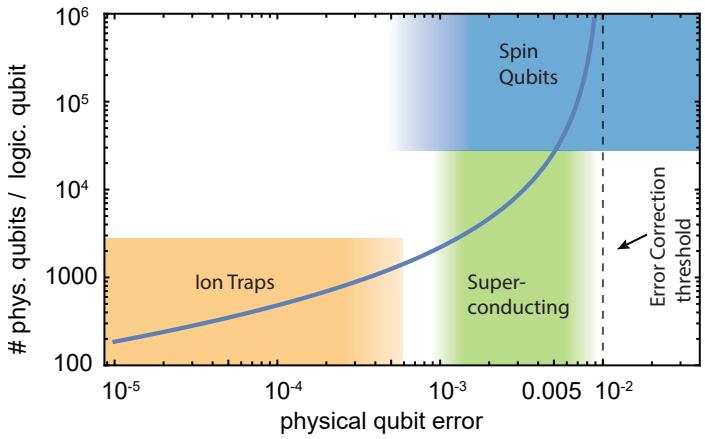

Figure 2.3: **Number of physical qubits needed for a computational logical qubit with error rate below 10^{-14}, as a function of physical qubit operation error.** The coloured regions indicate the range of values of state of the art operation error for three major quantum computing platforms.

		Ion traps	Superconducting	Semiconductor spin
lifetimes	T_1	hours [4]	90 μs [11]	6 s [12] (65 s [13])
	T_2	50 s(*) [4]	70 μs(echo) [11]	0.5s (30s) (CPMG)[12]
1-qubit gate	error (RB)	1×10^{-6} [4]	8×10^{-4} [14]	4.3×10^{-4}
	t_π	24 μs	16 ns	2 μs [15]
2-qubit gate	error (RB)	8×10^{-4} [5]	6×10^{-3} [14]	5.3×10^{-2} [16]
	time	30 μs	40 ns	1.4 μs
readout	error	$1(5^{(\dagger)}) \times 10^{-4}$ [7]	8×10^{-3} [17]	1.4×10^{-3}[18] (3×10^{-2} [19])
	time	145 ($10^{(\dagger)}$) μs	88 ns	65μ s (1.5 μs)

Table 2.1: **Best quoted values of qubit lifetimes, operation errors and gate times for three major quantum computing platforms.** The coherence times (T_2) for the ion qubit platform is a T_2^* time, as indicated by the asterisk, whereas the coherence times for the other two platform use a form of dynamical decoupling indicated in parenthesis (echo and CPMG for superconducting and semiconductor platform respectively). The value with (†) are theoretical predictions from ref. [7].

Another implementation, photonic qubits, also possesses the advantage of robust qubits at room temperature and naturally allows for high bandwidth and large distance quantum information transfer [20]. However, the lack of deterministic entangling gates and of a scalable platform present significant obstacles on the way to fault tolerant universal quantum computing using photonic qubits [21].

The two remaining quantum computing platforms that we consider here are both based on condensed matter systems. Qubits based on superconducting circuits have shown fast and high-fidelity operations (single-qubit gate fidelity of 99.92% and a two-qubit gate fidelity of up to 99.4%), with gates shorter than 100 ns demonstrating errors below the surface code error correction threshold of 1% [22] despite the relatively short qubit lifetime of only a few tens of microseconds (see Table 2.1).

The superconducting qubit platform is compatible with many of the fabrication techniques developed for the silicon semiconductor industry which can be harnessed for scaling up devices. In 2019, a device consisting of 52 nearest neighbour coupled superconducting qubits in a square lattice demonstrated quantum supremacy [23], with average single and two qubit operation errors of less than 0.2 and 1% respectively, and readout errors being slightly higher at 4%. While errors of operations in such state-of-the-art superconducting devices are below the 10^{-2} surface code error threshold [2] (see Table 2.1), they are about a factor 10 higher than what has been achieved in the ion trap platform (see Table 2.1). Due to the higher errors an error-protected computational logical qubit with acceptable levels of error (about 10^{-14} for Shor's algorithm [2]) requires 10 times more physical qubits (see Fig. 2.3). Fig. 2.3 shows a plot of the number of physical qubits needed per logical qubit as a function of physical qubit error or fidelity. Improving the errors of superconducting qubits further will require engineering of the qubit relaxation time T_1, since this currently limits the coherence time of their qubits. Indeed the superconducting transmon qubit dephasing times have been limited by relaxation times of at most $100\,\mu$s [24, 22]. Changes in the material used for the bulk of the device from aluminium to tantalum have recently been shown to increase the relaxation time to $\approx 300\,\mu$s [25]. Further advances in the device design and fabrication are required to allow for improvement in the qubit relaxation times, and thus reducing superconducting qubit errors [26, 27].

The last competitive platform in the race for universal quantum computing which we bring into focus now is that of semiconductor spin qubits. Semiconductor spin qubits combine the long coherence times of trapped ion qubits with the scope for scalability of superconducting qubits. Indeed, spin qubits in phosphorus donor atoms in silicon have shown relaxation times, T_1 of seconds [12] (minutes [13]) for electron (nuclear) spins on a donor in silicon respectively, as well as dephasing times of several seconds [12] (see Table 2.1). Errors for single-qubit gates and qubit readout below those of state-of-the-art superconducting devices have been demonstrated in semiconductor spin qubits, and two-qubit gate errors are expected to follow this trend [16]. At the same time, silicon has become the material system of choice to host semiconductor spin qubits, making such qubits compatible with the CMOS processes used by the semiconductor industry, and therefore offering promising prospects for scalability.

In summary, we have introduced three quantum-computing platforms that have demonstrated error rates near or below the error threshold of the surface code error-

correction scheme, making the prospect of error-corrected quantum computing realistic. However, quantum processors based on these platforms will likely require a large number of physical qubits, so that the fabrication and operation of such processors remain a daunting challenge. Section 2.1.3 describes major challenges that all three platforms face in scaling up the processors and highlights some advantages of the semiconductor computing platform in this regard.

2.1.3 The scale-up challenge of universal quantum computing

The trapped-ion, superconducting and semiconductor QC platforms have all three demonstrated qubits at or near the surface code fault-tolerant threshold. In this section we first show that an error-corrected universal quantum computer will require millions of physical qubits. Then we identify the challenges and uniques advantages that each platform possesses to scale-up the number of qubits. In particular, the challenges identified here for the semiconductor spin qubits motivate the development of a qubit that can be driven electrically instead of magnetically. The electrical driving results in faster gates and allows coupling of the qubits over long distances. The proposed qubit is the focus in the following chapters.

The challenge of scaling up quantum processors can be illustrated by estimating the size of a universal quantum computer needed to efficiently run an algorithm that solves a useful problem using the surface code error correction scheme. A problem that is often used for this purpose in the literature [2] is the prime factoring of large numbers, which is computationally very expensive when using a classical computer but has been shown to be exponentially faster when using a quantum computer running an algorithm proposed by Shor [28] in 1994. Using Shor's algorithm, a N-bit number can be factored into primes using a number of operations scaling polynomially with N. No classical algorithm has been found that can perform this problem with similar polynomial scaling. The prime factoring problem has practical implications in cryptography, because the difficulty of factoring large numbers into its prime numbers is at the heart of the RSA cryptography scheme [29], widely used for secure data transmission.

Using a particular implementation of Shor's algorithm [2, 30], the prime factoring of a commonly used 1024-bit RSA key would necessitate about 2000 computational logical qubits [2], and potentially 10 times more for an error correction specific process called magic state distillation [2]. Each logical qubit is encoded using a number of physical qubits that depends on the error rates of the operations on the

	Ion traps	Superconducting	Semiconductor spin
⟨error⟩	3×10^{-4}	5×10^{-3}	$9 \times 10^{-4\,(*)}$
# comput. phys. qubits	1.8×10^{6}	5×10^{7}	$4 \times 10^{6\,(*)}$
approx. # tot. phys. qubits	2×10^{7}	5×10^{8}	$4 \times 10^{7\,(*)}$
t_M	$145\,(10^{(\dagger)})\,\mu$s	88 ns	65μ s $(1.5\,\mu$s)
tot. comput. time	$216\,(14^{(\dagger)})$ days	3 hours	97 (2) days

Table 2.2: **Comparison of size and speed of ion trap, superconducting and semiconductor spin qubits to factorise 1024 bit number.** Estimation of the quantum computer size and computation time needed to factorise a 1024 bit number using Shor's algorithm, for the state-of-the-art error rates of each quantum computing platform. Note that the accurate estimation of the total number of qubits (including qubits needed for magic state distillation) is quite involved [2], so that we simplistically assume that about 10 times more qubits are needed for distillation than for computation (as is found for the two example in appendix M of ref. [2]). The specific algorithm is optimised for a low number of physical qubits at the cost of longer execution time, as outlined in ref. [31, 30, 32]. For the semiconductor platform, we assumed that a below threshold value of 10^{-3} for the two-qubit gate error is achievable [16]. The according number are marked with $(*)$. Numbers with $(\dagger)$ refer to theoretical estimates from ref. [7].

physical qubits. Larger physical qubit error rates translate into a larger number of necessary physical qubits required to encode an error protected logical qubit with a fixed error rate (see Fig. 2.3). Using the current state of the art error rates for the three platforms displayed in Table 2.1, one would require 10 million to hundred millions of physical qubits to perform the error corrected prime factoring on the ion trap and condensed matter platforms respectively.

The computation time t_C needed to execute the chosen implementation of Shor's algorithm can also be estimated (see ref. [2]) and can be related to the RSA key size N and the time t_M taken to read out a physical qubit: $t_C \approx 120N^3 t_M$. Using state of the art readout times of qubits for the three major quantum computing platforms, we estimate that running the algorithm on an ion trap based quantum computer would take about ten to two hundred days[1], only three hours on a superconducting quantum computer and about two days on a semiconductor spin quantum computer [19]. The estimated quantum computer sizes and executions times are summarised in Table 2.2. The calculation to arrive at these execution times follow ref.[2], and are outlined in more detail in the Appendix A.1. The numbers are based on one of many implementation of Shor's algorithm (as outlined in reference [2]). The particular implementation we chose requires fewer logical qubits at the expense of more computer clock cycles. Such an implementation of the algorithm is well suited for physical qubits with fast gates but large error rates (e.g. condensed matter qubits).

[1] 14 days assuming a theoretical projection of readout times [7].

Indeed, encoding a logical qubit with error-prone physical qubits requires many such physical qubits, making it advantageous to keep the number of logical qubits low. Furthermore the fast gate times of such qubits translate into fast code execution despite the many clock cycles required. Other algorithms exist that need more logical qubits but require less clock cycles [2]. These could be better suited for platforms with low physical-qubit errors (and thus less physical qubit required to encode each logical qubit) but slower gates, such as the ion-trap platform.

Each of the three quantum computing platforms that we focused on, faces unique challenges in scaling up to such large quantum processors that can solve useful problems in reasonable amounts of time. We now describe these challenges in broad terms for each of the three platforms and reference to solutions that have been put forward.

The trapped ion platform displays undeniable advantages compared to the superconducting and semiconductor spin qubits. In particular, Ion trap qubits have demonstrated exceptionally low error rates (see Table 2.2) and can be operated at room temperature. Room temperature operation eliminates a lot of the scaling challenges associated with cryogenic operation, which is required for the superconducting and semiconductor spin qubits. However, it faces other sizeable challenges in terms of scaling up.

Trapped ions qubits have been traditionally implemented using large single electromagnetic traps using macroscopic, mechanically-assembled three-dimensional electrodes in ultra-high vacuum chambers, with the electrodes forming a single pseudo-potential minimum, that can contain up to a few hundred qubits [10]. The number of ions that can be contained in a single trap being limited [10], it is unavoidable that the ion qubits platform will require the coupling of many ions originating from different traps, either by shuttling them into the same trap or coupling them while held in separate traps.

Ion-trap based processors with qubits hosted in separate traps will require systems in which the ions are shuttled for readout, manipulation and coupling. This has been realised [33] and is the basis of several large-scale architecture proposals [34, 35]. In such architectures, shuttling allows bringing two distant ions from separate traps into the same trap, where they can be coupled using well know techniques using optical [36, 37] or radio-frequency radiation [38]. Alternate architectures rely on coupling ions held in separate traps, using Coulomb coupling [39, 40], or photonic interconnects [41] .[2] While these two approaches to couple ions from separate traps

[2]gate time of photonic interconnects are slow, at about 200 ms [42].

show promise, they have yet to be demonstrated on devices containing more than a few qubits.

Another challenge in scaling-up ion traps is the physical size of large scale quantum processors based on the ion-trap system. For example, running Shor's algorithm on a 1024-bit number, could require up to 10 million physical qubits (see Sect. 2.1.3). This many ions would require hundred thousand separate traps, assuming every trap contains hundreds of qubits. The resulting footprint of the quantum processor can then be estimated to $50 \times 50\text{m}^2$ assuming a traditional three dimensional mechanically assembled single trap with a footprint of $5 \times 5\,\text{cm}^2$, and not taking into account the large area needed to accommodate the Ultra High Vacuum (UHV) systems, and lasers. Building such large systems while unpractical, is not unfeasible [35]. In order to reduce the footprint of ion-trap processors, advances have been made to fabricate two-dimensional chips using micro-fabrication methods developed for Microelectromechanical Systems (MEMS) [43]. The proposal by Lekitsch et. al. [35] harnesses these technological advances, but still predicts a surface area of about $100 \times 100\,\text{m}^2$ to accommodate for 2 billion ions in order to perform Shor's algorithm on a 1024-bit number in about 110 days (albeit assuming a less than optimal error rate of about 10^{-3}). Despite the large footprint and execution time, such a processor would be a formidable and useful proof-of-concept.

Another challenge that the ion trap platform is facing in terms of scaling up, is that the hardware for qubit control and readout typically consists of lasers pointed at the trap from outside of the vacuum chamber. This is in stark contrast to the condensed matter platforms where most of the control and readout architecture is co-fabricated with the qubits. Advances in co-fabricating the photonics hardware with the traps have been made and will help solve this challenge [44, 45, 46]. The architecture proposal by Lekitsch *et al.*. [35] bypasses the complexity of using individual lasers by using magnetic spatial gradients to allow for microwave mediated qubit operations. However, these microwave-mediated gates are much slower than photon-mediated gates (a few milliseconds [47] instead of a few microseconds [5]), and would therefore translate into orders of magnitude slower quantum computers.

In general, the time of qubit operations on trapped ion qubits is one to three orders of magnitude larger when compared to the other platforms. This translates into longer computing times when using the same implementation of the algorithm (see Table 2.2), and could become a significant drawback for the platform.

However, if the proposed innovations in scaling up the size of the ion trap processors can be implemented while conserving their exceptionally low error rates, the

lower number of physical qubits needed to encode each logical qubit could motivate the use of algorithms requiring more logical qubits but decreasing execution time.

In the context of scaling up, the condensed matter quantum-computing platforms and in particular the semiconductor-spin platform have the major advantage compared to the trapped-ion platform that they can fully harness the technological know-how of the classical computing semiconductor industry, which now routinely produces computer chips containing more than one billion transistors [48]. Indeed most processes needed to fabricate the condensed matter devices that are cited in the Table 2.1 use materials and processes compatible with the techniques and tools used in the semiconductor industry, making large scale manufacturing of large condensed matter based quantum computing processors a realistic prospect.

As described for the ion-trap platform, the speed of the qubit operations is also linked to scalability insofar that fast gates allow the use of algorithms with less logical qubits while keeping execution time low. This gives condensed matter platforms an advantage with respect to the ion-trap platform because gates are one and three orders of magnitude faster Table 2.1, for the semiconductor ($2\,\mu$s) and superconducting (16 ns) platforms respectively. Indeed, Section 3.1 of this thesis outlines how electrical control of semiconductor spin qubits could bring the operation times closer to those of superconducting ones.

Another advantage of the condensed matter platforms is that a good part of the readout and control electronics is routinely co-fabricated with the chip. This means that advances in scaling up the number of qubits can be leveraged to scale up the supporting electronics as well.

However, only part of this supporting electronics is currently manufactured on-chip (charge sensors, resonators, electrostatic gates, flux control loops etc.., mainly because condensed matter qubits need to be operated at cryogenic temperatures (below 200 mK for most platforms). The rest of the electronics hardware is typically placed off-chip, within the cryostat (amplifiers, filters, circulators) or at room temperature (microwave and waveform generators, IQ demodulators, Digital to Analog Converters (DAC) and Analog to Digital Converters(ADC)). The fact that a lot of the electronic hardware is still located outside of the cryostat poses a significant hurdle for scaling up the processors.

Indeed, the surface code requires that each physical qubit be initialised, read out and controlled independently. In most superconducting and semiconductor spin architectures, each qubit (at cryogenic temperatures) is coupled to the readout and control electronics (mostly at room temperature) with two to three electrical wires.

Having several millions to billions of wires running from deep in the cryostat to room temperature is challenging, due to the significant amount of heat and noise that would be transferred into the cryostat as well as the cross-section of such a cable. This problem can be solved by placing some of the control and readout electronics inside the cryostat, either on the same chip as the qubits or on a higher temperature stage of the cryostat (200mK or 1K stage). However this solution remains challenging due to the limited cooling power of cryostats ($\approx 20\,\mu$W at 20 mK).

Furthermore, interfacing the qubits with the readout and control electronics, whether placed inside or outside the cryostat remains a difficult problem as described in detail in ref. [48]. The first challenge of interfacing a quantum processor is simply to manufacture leads that reach each of the qubits for control and readout. Indeed, wiring up a monolithic block of N qubits using CMOS technology with only a single lead per qubit would require a number $n_{\text{lith. layers}} \approx \frac{\sqrt{N}}{2n_L+3}$ of separate lithographic layers, where n_L is the number of leads that can be routed between two adjacent qubits in the surface code square grid (see Sect. 4.5.3). Assuming only a single lead can be fed through between two adjacent qubits ($n_L = 1$), a monolithic quantum computer of a billion physical qubits would require about six thousand lithographic layers, a number that is two orders of magnitude larger than currently used in state-of-the-art semiconductor BEOL (Back-end-of-line) processes, that use at most 15 layers [49]. This makes a monolithic approach highly challenging. The challenge of interfacing with a large number of qubits could be addressed by spatial and frequency multiplexing schemes, reminiscent of those used in the Dynamic Random Access Memory (DRAM) devices Such schemes would reduce the number of leads required per qubit [48]. However, multiplexing comes with the drawback that it reduces the clock-cycle of the surface code because qubits have to be addressed sequentially within one surface code cycle. This slowdown not only increases the execution time of an algorithm but also the impact of dephasing and relaxation errors. Several proposals suggest that such an approach is nonetheless possible [50, 51], notably the proposal of Hill *et al.*. in ref. [50], which harnesses the uniformity and long lifetimes of donor qubits in silicon to implement a spatial multiplexing scheme to interface the quantum and classical layers of the qubits.

The challenge of interfacing the quantum and classical hardware will likely be solved by using a modular quantum computer architecture, in which some of the classical electronics is placed in-between blocks of qubits. Such a modular computer architecture has been proposed for various platforms [41, 48, 52, 53] and consists of

nodes hosting many qubits that are coupled over distances up to a few micrometers. The nodes are coupled to each other via longer distance interconnects (micrometers to millimetres). In a modular architecture the qubits within each node can be interfaced with classical control and readout electronics using a realistic number of lithographic layers. Also, the physical space between nodes can be used to house the classical electronics or to route control lines off from the chip [48]. Pushed to its extreme, the modular architecture consists of nodes of single qubits [54]. In that case the qubits are spaced far enough that a large part of the electronics required for control and readout of the qubit (memory, RF signal generation, DC bias generation) is placed adjacent to it. Geck *et al.* estimated in ref. [54] that such classical electronics would necessitate a footprint of about $20 \times 20\,\mu\text{m}^2$ per qubit using state-of-the-art industrial fabrication techniques, putting a lower bound of about $20\,\mu$m on the spacing between qubits for this architecture.

To solve the challenge of interfacing the classical electronics with the qubits, it will most certainly be necessary to place some of the classical electronics inside the cryostat. This comes with its own challenges because some of the electronic hardware dissipates heat, and the cooling power of dilution refrigerators is limited [48, 54]. Geck *et al.* estimate in ref. [54] that a few thousand qubits could be controlled by classical electronics on-chip at sub-Kelvin temperatures, assuming progress is made in low-power transistors and using a standard dilution refrigerator. Scaling such a system to a larger number of qubits will likely require the control electronics to be placed off-chip at a higher temperature stage of the cryostat, as well as further advances in low power cryogenic classical electronics or even larger cryostats with much larger cooling powers. An exciting alternative could be the use of qubits operating at temperatures above 1 K [55], where cryostats have much larger cooling power.

In summary, we have investigated the challenges that the ion trap and condensed matter platforms face to scale up processors to a point where they can solve useful problems in a reasonable time using quantum-error correction. Using the example of Shor's algorithm, the physical-qubit error rate was shown to be instrumental in determining the number of physical qubits needed to define an error-protected logical qubit, and therefore has important repercussion on the processor's size. Furthermore the qubit operation speed was identified as another important parameter, with faster gates enabling faster code execution and allowing the use of algorithms requiring less qubits.

The advantages and challenges of each platform with regards to scaling up were

	Ion traps	Superconducting	Semiconductor spin
T_2	50 s(*) [4]	70 μs(echo) [11]	0.5s (30s) (CPMG)[12]
avg. gate error (1&2 qubit)	$10^{-6} - 10^{-3}$ [4, 5]	$\approx 10^{-3}$ [14]	$10^{-4} - 10^{-2}$ [15, 16]
gate speeds	$10 - 100\,\mu$s [4, 5]	$10 - 100$ ns [14]	$1 - 2\,\mu$s [15, 16]
qubit footprint	$\approx 50 \times 50\,\text{cm}^2$ [35]	$\approx 1 \times 1\,\text{mm}^2$ [14]	$\approx 100 \times 100\,\text{nm}^2$ [15, 16]
Silicon μ-fab. compatibility	limited (MEMS approach [43])	compatible	fully compatible
co-fab. of control structures	limited (laser optics)	yes	yes

Table 2.3: **Scaling-up advantages and disadvantages for three major QC platforms.**

then described (in terms of footprint and execution time). They are summarised in Table 2.3.

Ion-trap quantum processors based on optical operations will likely face challenges in scaling up the optical control systems. This problem is circumvented by ion-trap processors based on microwave-mediated operations which however display very slow two qubit operations [35]. Both optical and microwave-mediated ion-trap qubit operations are quite slow compared to condensed matter operation, translating into a lower clock-frequency of the quantum processors. The implementation of the classical to quantum interfacing is expected to be less of a problem for ion trap when compared to condensed matter systems, due to the relatively large size of the ion trap quantum processors[3] leaving enough space for large semiconductor chips in-between. Likewise, heating due to the classical electronics is expected not be as big of an issue because ion-traps can be operated at room temperature, or at liquid-nitrogen temperature [35].

For condensed-matter platforms one of the major scale-up challenges consists in interfacing the quantum and classical hardware [48]. Due to the cryogenic operation of most condensed-matter qubits, such interfacing will likely require some or most of the classical electronics to be located inside the cryostat hosting the qubits. The interfacing can be facilitated by spacing the qubits apart to leave space for some classical hardware, using long-distance qubit interconnects. The compatibility of the condensed matter platforms with industrial semiconductor manufacturing techniques, makes them a prime candidate to solve this interfacing challenge. Another advantage of condensed matter platforms compared to the ion trap platform is the faster qubit operations that translate into high processor clock frequencies. Operations in state-of-the-art semiconductor systems are an order of magnitude faster than in state-of-the-art ion-trap systems, but still two orders of magnitude away from operations in superconducting systems.

In the remainder of this thesis we focus on the semiconductor spin-qubit platform.

[3] units cells are at least tens of micrometers [56, 57], but more likely a few millimetres [35]

In particular, Sect. 3.1 demonstrates that scaling up semiconductor spin qubits can be facilitated by all electrical control and coupling of the qubits. Advances in this regard are the focus of this thesis. Chapter 3 investigates electrical driving and coupling of a spin qubit in a general semiconductor platform, while the remaining chapters investigated devices based on phosphorus donor placed by STM-lithography in silicon.

2.2 Donor spin qubits in silicon

2.2.1 Electrons in the silicon crystal

Silicon crystal structure and surface reconstruction

The silicon crystal structure consists of two intertwined face centred cubic (fcc) lattices separated by a quarter of the width a of the unit cell in each dimension ($a = 0.54\,\text{nm}$). Each silicon atom in the crystal is covalently bonded to four equidistant neighbours in a tetrahedral arrangement (see Fig. 5.9 a). Positions in the fcc cubic lattice are described by lattice vectors $\boldsymbol{R}$, and can be mapped into a reciprocal-lattice defined through lattice vectors $\boldsymbol{G}$ such that $\boldsymbol{G} \cdot \boldsymbol{R} \equiv 0 \pmod{2\pi}$.[4] Any position $\boldsymbol{K}$ in reciprocal space can be described by the sum of a vector $\boldsymbol{k}$ closer to the origin than any point in the reciprocal lattice and a reciprocal lattice vector $\boldsymbol{G}$. The points described by all such vectors k defines the first Brillouin zone of the direct lattice (see Fig. 5.9 b).

The atomically flat surface of the silicon crystal, described by the normal vector (001) is used in this thesis for patterning of devices using scanning tunnelling microscope (STM) hydrogen lithography (more details on STM hydrogen lithography in Sect. 2.3). Each silicon atom at the surface is covalently bonded to two neighbours, one lattice plane below the surface, and therefore possesses two unused bonds (dangling bonds, see Fig. 2.5 a). The energy of the (001)-surface can be reduced by a 2×1 surface reconstruction in which every atom on the surface forms a σ-bond with a neighbour to form a pair called a silicon dimer (see Fig. 2.5 b). Each atom on the slicon(100) surface retains one dangling bond, and forms a π-bond together with the other dangling bond on the dimer.

[4] the reciprocal lattice of a fcc lattice is body centred cubic (bcc).

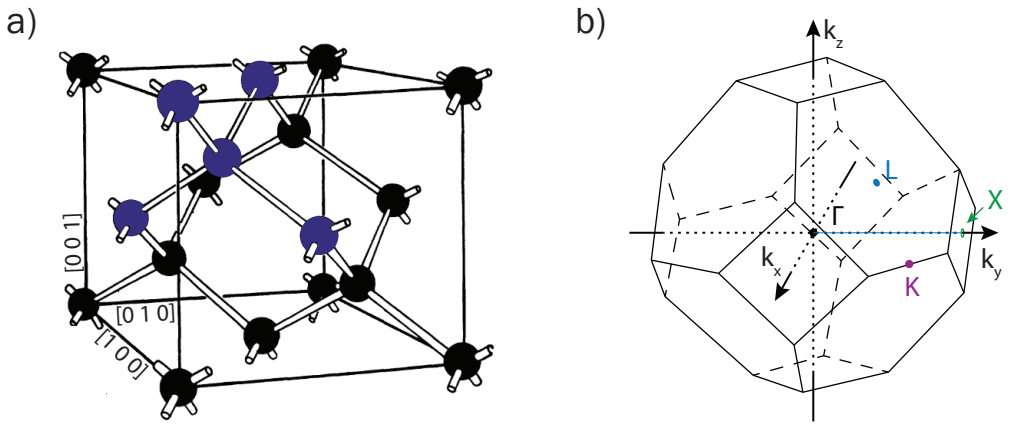

Figure 2.4: **The silicon fcc lattice and its reciprocal lattice a)** Unit cell of the silicon diamond lattice consisting of two fcc lattices shifted by (1/4,1/4,1/4). Each atom is linked to four neighbours via four covalent bonds forming a tetrahedron (see 5 atoms highlighted in blue). **b)** First Brillouin zone of the fcc lattice. Symmetry points are labeled by latin and greek letters. **a** is reproduced from [58] and [59].

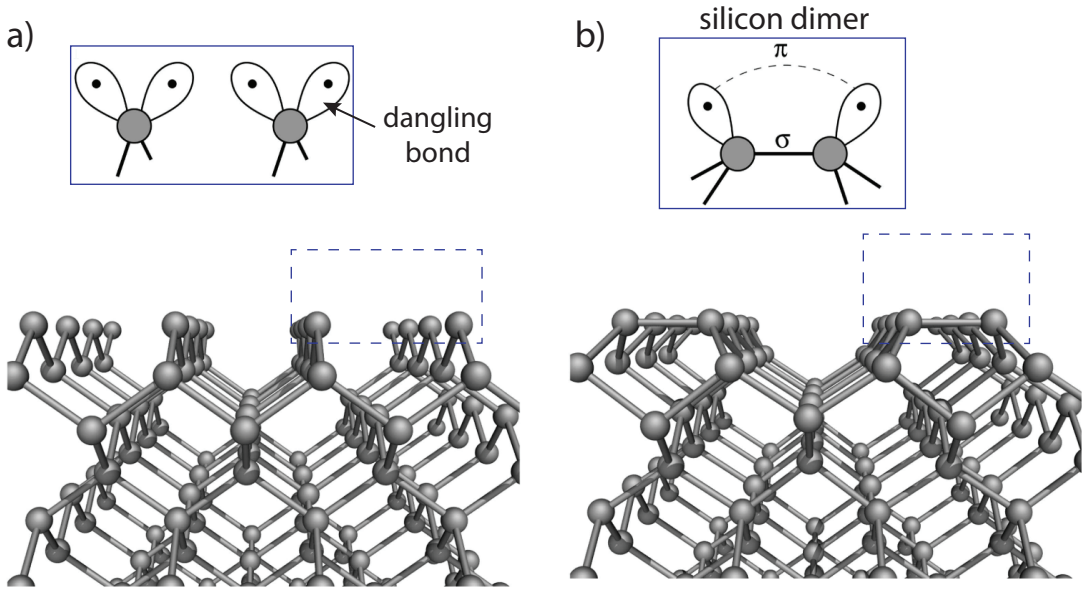

Figure 2.5: **Silicon(001) 2x1 surface reconstruction**. **a)** Non reconstructed silicon surface. Each silicon atom at the surface forms two covalent bonds with silicon atoms below it. The two remaining covalent bonds form dangling bonds at the surface (see inset). **b)** 2×1 reconstructed silicon surface. A σ-bond is formed between neighbouring pairs of silicon atoms on the surface called dimers, and lowers the energy of the lattice. Atoms in the reconstructed surface remains with one dangling bond. The overlap between the dangling bonds across dimers forms a π-bond. Adapted from [59].

Silicon band structure and effective-mass theory

Electrons serve as the building block for most of the quantum information processing performed in this thesis. In particular, the spin of electrons is used to encode information and individual electron hopping on and off atom-based quantum dots are used for spin readout. The physics of electrons in the silicon crystal can be well captured by the so-called effective mass approximation, in which the influence of electrostatic potentials (from gates or donors) is treated as a perturbation to the physics of non-interacting electrons in the lattice (described by the band structure). The basic framework of the effective mass theory, which is summarised in the following section, highlights how silicon nano-structures can be used to shape the electrostatic potentials experienced by electrons down to the atomic level.

Non-interacting electrons within the periodic potential defined by the nuclei in the lattice can be described in the basis of the Bloch functions Ψ consisting of a plane wave with wave vector $\boldsymbol{K}$ and a lattice periodic function $u_{\boldsymbol{K}}(\boldsymbol{r})$: $\Psi = e^{\imath \boldsymbol{K}\cdot\boldsymbol{r}} u_{\boldsymbol{K}}(\boldsymbol{r})$. The wave vector $\boldsymbol{K}$ can take any value, and is usually decomposed into a sum $\boldsymbol{k}+n\boldsymbol{G}$, where $\boldsymbol{k}$ is a vector within the first Brillouin zone, $\boldsymbol{G}$ is a unit vector in the reciprocal crystal lattice and the integer n is called the band index. This decomposition yields the Bloch functions:

$$\Psi_{n,k} = e^{\imath \boldsymbol{k}\cdot\boldsymbol{r}} u_{n,\boldsymbol{k}}(\boldsymbol{r}). \tag{2.2.1}$$

Without the influence of the crystal, the Bloch functions yield a series of dispersion relations for a free electron in the crystal [60]:

$$E_{n,\boldsymbol{K}} = \frac{\hbar^2}{2m_e}(\boldsymbol{k} - n\boldsymbol{G})^2. \tag{2.2.2}$$

Each integer n, yields one dispersion relation within the first Brillouin zone called an energy band, and the multiple dispersions therefore describe the band structure of the lattice (within the free-electron model).

The interaction of the electrons with the nuclei in the silicon lattice modifies this free-electron band structure and introduces an energy gap, within which no electron state is available (see Fig. 2.6 b). In silicon the energy gap appears between the fourth and the fifth band. The fourth band is called the valence band and has a maximum E_{vb} at the origin Γ of the first Brillouin zone, while the fifth band is called the conduction band and has 6 equivalent minima E_{cb} near the X point of the first Brillouin zone (and equivalent positions). The first four bands describe electrons participating in the covalent bonds between nuclei (each silicon atom forms four covalent bonds). In a pure silicon crystal no additional electron can freely

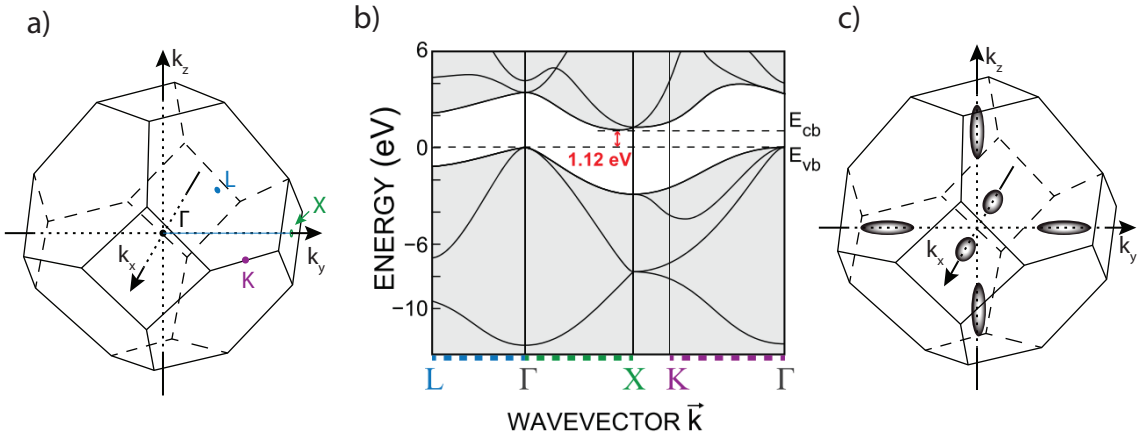

Figure 2.6: **Silicon band structure. a)** First Brillouin zone of the silicon crystal lattice (fcc). Significant symmetry points are labelled. **b)** Band structure of silicon along significant symmetry lines of the first Brillouin zone. A band gap of about 1.1 eV is opened between the valence band maximum at Γ and the conduction band minima (near X). **c)** The energy of an electron near any of the six equivalent conduction band minima can be represented by equipotential surfaces in the shape of ellipsoids. Each of theses surface represents one of the six valleys in the band structure of silicon. Reproduced and adapted from [62, 63].

circulate through the crystal and the four first bands are fully occupied (disregarding thermal occupation). Electrons that are introduced to the crystal with a chemical potential at or above the conduction band edge (through thermal activation, doping, electrostatic gating) are not involved in the covalent bonds of the crystal and can therefore participate in electric conduction.

The 6 potential wells at the conduction band minimum are called valleys and are centred around the symmetric positions $\pm k_0 \hat{\boldsymbol{k}}_i \, i = x, y, z$ (see Fig. 2.6 c) which can be approximated by a parabolic dispersion. For the k_x valley for example, the dispersion can be approximated by [61]:

$$E = E_{\mathrm{cb}} + \frac{\hbar^2}{2m_{\mathrm{L}}}(k_x - k_0)^2 + \frac{\hbar^2}{2m_{\mathrm{T}}}(k_y^2 + k_z^2), \tag{2.2.3}$$

where the coefficient $m_{\mathrm{L}} \approx 0.98 m_e$ and $m_{\mathrm{T}} \approx 0.19 m_e$ are called the longitudinal and transverse effective mass of the electron. The same dispersion relation holds for the other valleys (with the appropriate change in indices and sign of k_0). This dispersion relation of Eq. 2.2.3 is that of the free electron, with modified masses along the principe axes of each valley.

In silicon nano-structures, the description of the electron motion (and dispersion) is more complicated because the electron is subjected to electric and magnetic fields. Nonetheless, the electron's wavefunction can be expressed as a wave packet of Bloch

functions $\Psi_{n,\boldsymbol{k}}$. For weak enough electric and magnetic fields this wave packet can be approximated near each of the 6 conduction-band minima ($n = n_c$, $\boldsymbol{k} = \boldsymbol{k}^{(i)}$, $i = 1, \ldots, 6$) by the lattice periodic Bloch function u at the band minimum and an envelope function F:

$$\Psi^{(i)}(\boldsymbol{r}) = F^{(i)}(\boldsymbol{r}) u_{n_c,k^{(i)}}(\boldsymbol{r}). \tag{2.2.4}$$

In crystals with a single valley at the Γ-point (such as GaAs and InAs), the envelope function for a conduction electron at the conduction band minimum is well described by the Schrödinger equation describing an electron in free space, with the effect of the lattice only being captured by the electron effective mass and effective g-factor at the band minimum. This is called the effective mass approximation [60].

In crystals with multiple valleys (e.g. Silicon and Germanium), the electron's wavefunction has to be approximated by a superposition of Bloch functions at the different valleys and the effective mass approximation is more complex. The perturbation introduced by a donor in the lattice can still be described by a simple effective mass approximation analogous to that for a single minimum at Γ. Indeed, the 6 envelope functions $F^{(i)}(\boldsymbol{r})$ satisfy a Schrödinger equation where the effect of the lattice is simply captured by the effective masses m_{T} and m_{L} [61].

The effective mass approximation is so useful and powerful that the lattice-periodic part of the electron wavefunction in semiconductor nano-structures is often neglected for convenience, and the envelope function F is referred to as the electron wave function. We will use this convention in the following sections and chapters, unless explicitly specified.

The sophisticated manufacturing technology of the semiconductor industry allows tailoring of the electric potential felt by the electron's envelope function over the scales of nanometers.The effective mass approximation allows treating an electron within these potentials as if it were in vacuum, with only a change of the electron's mass. Technologies that produce electric potentials in free space, for example in ion or atom traps, have not nearly reached the degree of control and miniaturisation of semiconductor nano-structures. In the new "2 nm" transistor generation from IBM for example, the conduction channel of the field effect transistors consists in 3 "nano-sheets", 12 nm long, 5 nm high, and 40 nm wide, entirely surrounded by metallic gates (see Fig. 2.7 a). Producing such small potential wells in free space would be excruciatingly difficult. On even smaller length scales, the precision placement of donors through STM hydrogen lithography allows the formation of a three dimensional electric potential that confines the electron wavefunction over a radius of only a few nanometers (the Bohr radii vary from 0.5 to a few nm depending on

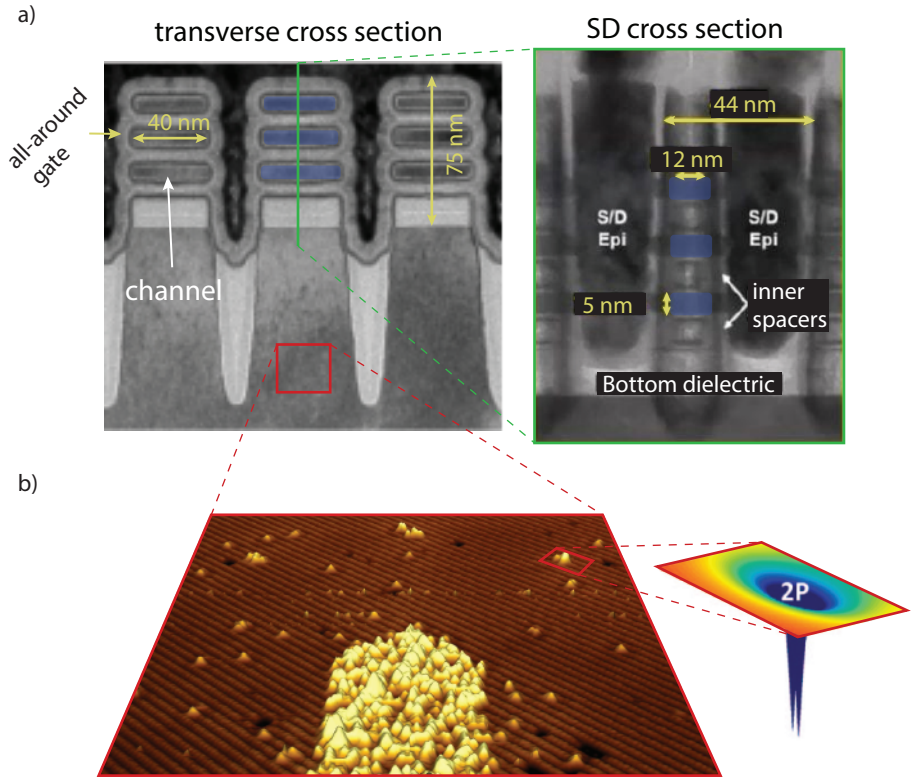

Figure 2.7: **A comparison of state-of-the-art silicon nano-fabrication with IBM 2nm FinFETs and precision donors patterned by STM a)** "2 nm"-node field effect transistor from IBM manufactured using extreme ultraviolet lithography. The conduction channel consists in three silicon "nano-sheets" (in blue). All-around metallic gates allow a high degree of control of the electric potential within the channels, and an efficient pinch-off of the conduction channel through gate voltages. The inset shows the source and drain contacts of the transistor and channel length of 12 nm. Adapted from newsroom.IBM.com. **b)** A three-qubit device manufactured using precision placement of donors through STM lithography, and measured in this thesis. The bright yellow regions correspond to regions where phosphorus donors are placed. The inset shows the tight confinement potential in the right-most qubit defined by two phosphorus donors (2P). Inset reproduced from [64].

the donor number and electron shell filling [65]) (see Fig. 2.7 b). In the following section, the electron and nuclear spin in donors are introduced as a very attractive platform for quantum computation.

2.2.2 Atomically precise donor devices

Phosphorus donors in silicon provide an attractive platform for hosting qubits. When a silicon atom in the lattice is replaced by a phosphorus atom containing on additional proton, it produces a Coulomb potential that can host a single electron in a very tightly confined hydrogen-like wavefunction with a Bohr radius of 2nm.[5] The spin of such a donor-confined electron encodes a very robust two level system, and has demonstrated lifetimes of up to 50 min at 0.32 T and temperatures of 1.25 K as early as 1959 in electron nuclear double resonance (ENDOR) experiments by Feher and coworkers [68]. In the same experiment, the nuclear spin 1/2 of the phosphorus dopant in silicon was found to be even longer-lived with relaxation times longer than 10 h under similar conditions. These experiments were performed in macroscopic silicon samples uniformly doped with phosphorus donors (bulk doping), with electron and nuclear spin resonance performed on a large ensemble of theses donors using macroscopic microwave cavities and radio-frequency coils (bulk ESR and bulk NMR).

With the conceptual emergence of the quantum computer in the 1980s [69], followed in the 1990 by the discovery of algorithms with a quantum advantage [28, 70], and of quantum error correction algorithms [1, 3, 71, 72, 73], the long relaxation time of the electron and nuclear spins of phosphorus donors in silicon made them as very attractive candidate for long-lived solid-state qubits [74].

The electron and nuclear spin on phosphorus donors in silicon was further confirmed as a frontrunner for a solid state qubit when bulk-ESR and NMR measurements revealed long spin coherence times in isotopically purified ^{28}Si [75, 76, 77, 78]. Isotopically purified ^{28}Si contains almost none of the magnetic isotope ^{29}Si (I = 1/2), which is known to produce fluctuating magnetic fields [79] and promotes spin decoherence [80]. The experiments demonstrated coherence times $T_2 = 10\,\mathrm{s}$ and 180 s for the electron [77] and nuclear [78] spin on phosphorus donors, at a temperature of 1.8 K and magnetic fields of 350 mT and 85 mT respectively.[6]

The lifetimes and coherence times of the electron and nuclear spin on a single

[5] This is according taking a geometric average [66] of the transverse and longitudinal Bohr radii in [67]

[6] The electron spin coherence times are measured in [77] using a spin echo sequence, and the nuclear spin coherence time in [78] using a 16-pulse dynamical decoupling sequence.

donor were not measured until the early 2010s [80, 13], due to the formidable challenge of manufacturing a device with a single donor and the infrastructure to control it and read it out. Measurement on single donor devices yielded electron(nuclear) relaxation times of 6 (65) s and coherence times of 0.5 (30)s[12, 13],[7] approaching that of the lifetimes and coherence times of trapped ion qubits in vacuum.

The manufacturing of single phosphorus donor devices can be split into a "top-down" and a "bottom-up" approach. The top-down approach relies on the implantation of phosphorus donors using beams of high-energy (15keV) phosphorus ions that implant into the crystal and scatter within it. A short thermal anneal is used to activate the donor and repair the damage made to the crystal. However, this can lead to deactivation of the donor as it likes to travel back up the implant pathway to the Si-SiO_2 interface. As a consequence a low area implant is prepared with 100s of donors to prevent this pathway and end up with some activated donors within the active region of the device. Aluminium gates are then lithographically patterned on the surface by electron beam lithography (EBL) [81, 82]. At cryogenic temperatures the gates can electrostatically induce an electron gas at the interface between the silicon and a high quality thermal oxide. The entire process is compatible with processes developed by the semiconductor industry, and the materials are strictly CMOS compatible. However, the scattering process of the ion during implantation is non-deterministic and leads to an uncertainty of 10 nm in its lateral position when implanted at a depth of 20 nm (14 keV ions) [83, 84]. This uncertainty makes the reliable manufacturing of exchange-coupled donors challenging using ion-implantation because the exchange interaction is very sensitive to displacement of only few nanometers [85, 86]. With a state-of-the-art lateral uncertainty of 10 nm, the probability of reaching a large enough coupling between a ion-implanted donor pair ($t_c > 0.1$ meV) has been estimated to be only 20% [87]. The non-deterministic manufacturing of exchange-coupled donors is a significant drawback for the top-down approach because the exchange coupling is the principle way in which two-qubit gates have been proposed and realised [88, 89, 90, 85]. Methods of coupling ion-implanted donor qubits that do not rely on the exchange interaction have recently been proposed [91]. If this coupling can be achieved without destroying qubit coherence then the top-down approach remains a competitive platform for large-scale quantum computation.

The bottom-up approach relies on the atomically precise placement of phosphorus donor within the silicon lattice. This is currently achieved using a scanning

[7] All but the nuclear spin lifetime were measured in isotopically purified silicon (800ppm ^{29}Si)[12].

tunnelling microscope (STM) to perform lithography on a silicon surface passivated with a hydrogen mask. With STM lithography, a single donor placement accuracy of ± 1 lattice site (± 0.38 nm) has been achieved [92], allowing for less than one order of magnitude variations in the exchange interaction between two donors just placed 12 nm apart [86]. The reliable manufacturing of exchange coupled donor-pairs is therefore considered realistic using the bottom-up approach but not so using the top-down one [93, 87]. The atomically precise patterning method enabled the first demonstration of an exchange mediated two-qubit SWAP gate between two electron spins in phosphorus donor quantum dots [85].

STM-hydrogen lithography has been used to fabricate a variety of high precision atomic-scale devices ranging from 0D structures such as single-donor quantum dots [92, 94, 95, 96] and multi-donor donor quantum dots [97, 94, 98, 96], 1D structures such as atomically thin wires [99], 2D structures such as single electron transistors used to perform high fidelity spin-readout [94, 19] and even three dimensional all-epitaxial structures such as a 3D single electron transistor [100].

The possibility of patterning donor molecules with more than one donor is an important feature of the bottom-up approach using STM-hydrogen lithography. Multi-donor quantum dots allow for increased electron spin relaxation times [65, 101], increased electrostatic tunability of the exchange coupling [64], and addressability of the donor quantum dots in electron spin resonance (ESR) experiments [95, 97]. Further advantages of engineering the number of donors in multi-donor quantum dots are at the heart of this thesis, such as the ability to reduce decoherence in an electrically driven donor-based qubit proposed in Chapter 4, and the increased electrostatic tunability of multi-quantum dot charge states in Chapter 5.

2.3 Atomic-scale device manufacturing

The devices investigated in this thesis are fabricated by performing hydrogen lithography with a scanning tunnelling microscope (STM-HL). The technique allows the placement of substitutional phosphorus dopants at the silicon surface with a precision of ± 1 lattice sites (± 0.38 nm) [92]. The technique can also be used for patterning larger two-dimensional highly-doped structures such as charge sensors, electrostatic gates, and leads.

The scanning tunnelling microscope (STM) was invented by Binning and Rohrer at IBM in 1982 [102, 103], and is traditionally used to capture images of surfaces with atomic precision. The microscope relies on an atomically sharp and conductive

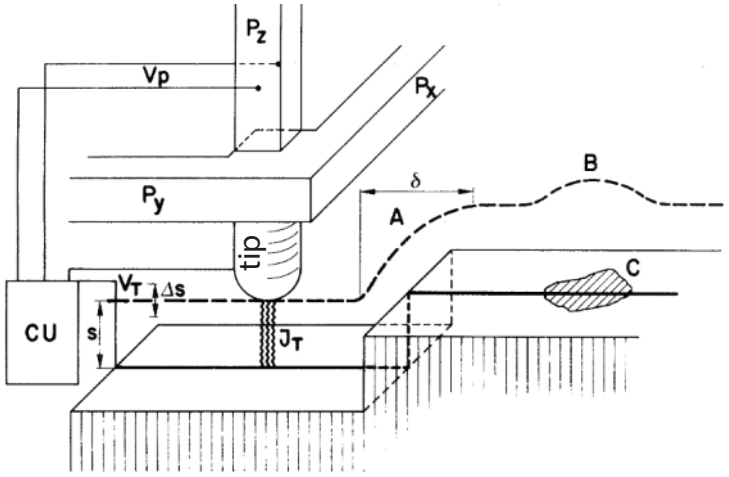

Figure 2.8: **Scanning tunnelling microscope.** A schematic of the STM showing the piezodrive P_X and P_Y that allows the metal tip to scan across the surface. The control unit (CU) detects the current J_T and applies a voltage V_P, which in turn controls the z-axis piezodrive P_Z in a feedback loop that ensures a constant tunnel current J_T is maintained at constant tunnel voltage V_T. The topography of the surface can be inferred directly from the applied voltages to P_X, P_Y, and P_Z for constant work function. Alternatively, the work function can be measured by modulating the tunnel distance s by Δs. The broken line illustrates the z-axis displacement of the tip as it scans over a surface step (A) and a contamination spot (B,C), which is a region with lower work function. Reproduced from [102].

tip being brought in such close proximity with a surface that electrons can tunnel across the vacuum barrier between the two, when they are held at a non-zero voltage bias. The tunnelling current is fixed by controlling the distance between the tip and the surface using piezoelectric actuators. The displacement of the tip when scanned across the surface is then used to construct a topographic map of the surface (see Fig. 2.8). The STM was soon used not only to image surfaces, but also to interact with them [104, 105, 106]. Eigler and coworkers notably demonstrated the manipulation of single atoms [104] or molecules [105] to form atomically precise patterns on surfaces. STM hydrogen lithography was first demonstrated by Lyding *et al.* to perform the atomically precise oxidation of a 2×1-reconstructed Si(100) surface [106]. The silicon surface, held in ultra high vacuum (UHV), was first passivated with a monoatomic layer of hydrogen. The hydrogen acts as a mask that protects the surface from interacting with molecules in the vacuum. The STM tip was then used to selectively desorb the hydrogen along lines of 1 nm width using voltage pulses. The bare areas of silicon were then oxidised by introducing oxygen into the vacuum chamber.

By introducing phosphine gas(PH_3) instead of oxygen, and performing a thermal annealing step at 350°C, the technique of hydrogen lithography was later used to

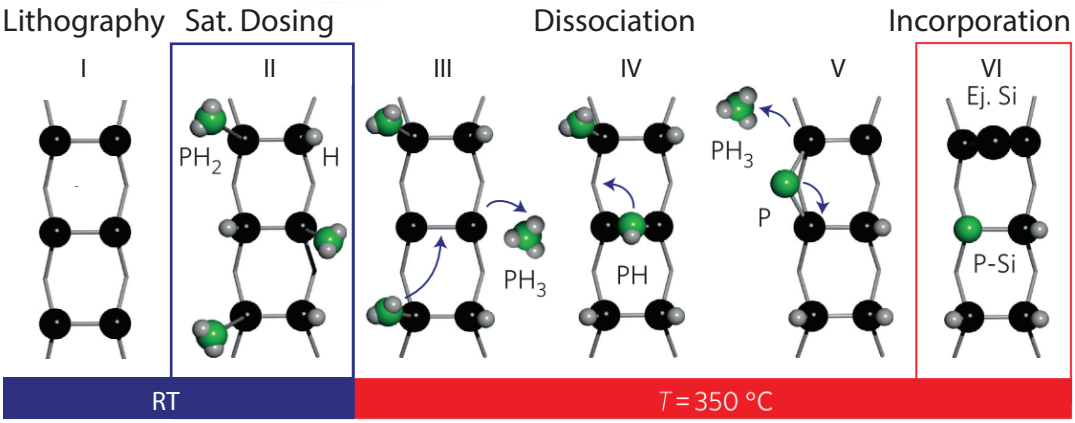

Figure 2.9: **Placement of a single phosphorus dopant into the silicon lattice with atomic precision.** Three dimers on the silicon surface have been desorbed of hydrogen using the STM tip (I). Phosphine (PH_3) is introduced to the vacuum chamber and a PH_3 molecule adsorbs to each dimer. It forms a PH_2 adsorbate by transferring one of its hydrogen atoms across the dimer (II). The sample is then heated to 350°C, triggering a series of chemical reactions on the surface (III-VI). First, a PH_2 adsorbate transfers to the central dimer where it forms a PH species bonded to both silicon atoms of the dimer (IV). A hydrogen atom is left over at its prior position and a phosphine molecule is released to the vacuum. The central PH molecule then transfers one of its two bonds to the upper dimer, leaving another hydrogen atom on the dimer and releasing another phosphine molecule to the vacuum (V). Finally, the phosphorus atom incorporates into the surface. The phosphorus atom substitutes with a silicon atom on the central dimer, which is ejected onto the surface (Ej. Si). Adapted from [92].

selectively place phosphorus dopants into the silicon lattice [107]. By desorbing only three silicon dimers (area of $0.38 \times 0.77\text{nm}^2$), Schofield demonstrated the ability to place single phosphorus dopants into the silicon surface, with a lateral precision well below 1 nm. After introducing phosphine to the chamber, phosphine molecules (PH_3) attach to the bare silicon atoms in the desorbed dimers in the form of PH_2 adsorbates. Saturation dosing allows every bare dimer to be covered with a PH_2 molecule and a hydrogen atom. When heating the sample at 350°C (incorporation step), the PH_2 molecules attached to the surface undergo further dissociation, first into PH, then P and finally the phosphorus atom switches place with a silicon atom in the surface. This series of chemical reactions is depicted in Fig. 2.9 for a set of three bare silicon dimers that have had their hydrogen mask removed. For such a lithographic patch size it was shown that only a single phosphorus donor can incorporate into the lattice. The temperature during incorporation is low enough ($<$ 350°C) that the hydrogen mask stays in place, allowing for further lithographic steps to be performed. When areas larger than three dimers are desorbed of their hydrogen mask, additional donors can be incorporated to form multi-donor quantum dots, electrostatic control gates and even large conductive leads. Electrical measurement

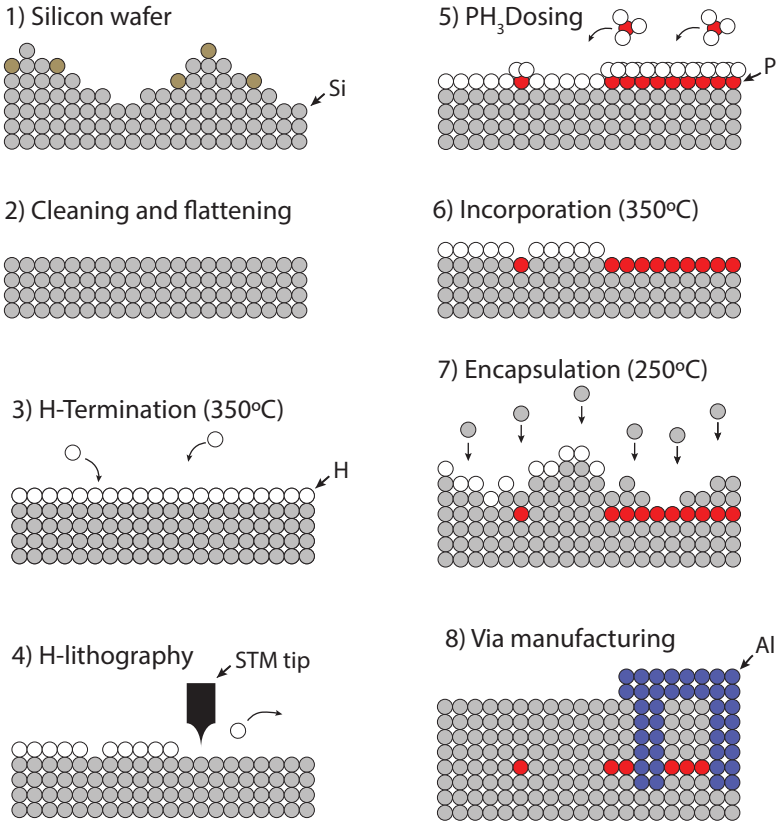

Figure 2.10: **Device fabrication using STM-hydrogen lithography.** The device fabrication steps are described as follows, (1) silicon wafer, (2) cleaning and flattening of the silicon surface, (3) the hydrogen termination of the surface, (4) hydrogen lithography, (5) Phosphine dosing, (6) incorporation, (7) silicon encapsulation, and (8) post processing by electrical contacting of the buried dopants. Adapted from [109].

of the electron densities in such large areas have shown that one in every four atoms on the surface is replaced by a phosphorus dopant after saturation doping and incorporation at 350°C [108].

Hydrogen lithography and incorporation is only one of the steps in the atomic-scale fabrication of devices using STM hydrogen lithography. The device fabrication notably involves cleaning and flattening of the silicon surface, the hydrogen termination of the surface, hydrogen lithography and incorporation as just discussed, followed by silicon encapsulation, and finally by electrical contacting of the buried dopants. These steps are summarised in Fig. 2.10, and will be discussed in more details in the following sections.

2.3.1 Surface preparation

The fabrication of donor-based devices using STM hydrogen lithography starts with a 2" lightly boron-doped silicon wafer grown through the Czochralski method. The wafer has a resistivity of less than 10 Ω cm and is cut along the (100) plane with a thickness of 300 µm. The doping ensures the sample is conductive at room temperature to allow operation of the STM. The doping density is low enough that it is unlikely for the device to be patterned near a boron acceptor.[8]

Registration marker fabrication

First, registration markers are patterned on the silicon surface. The markers are required to locate the device after STM lithography, and need to be UHV compatible as well as resistant to the high temperature (up to 1100 °C) required for the surface preparation. Registration markers are therefore wet-etched into the surface using a solution of tetra methyl ammonium hydroxide (TMAH) and a mask of furnace grown silicon dioxide (grown in-house). The silicon oxide mask is defined using a standard electron beam lithography (EBL) protocol[9] and etched using buffered hydrofluoric acid (BHF). The fabrication process for the STM registration markers is outlined below (see Fig. 2.11):

- The oxidised wafer is cleaved into 20 mm × 10 mm squares using a diamond-tip scribing tool. This yields 8 samples of 2.5 mm × 10 mm.
- A 200 nm layer of PMMA resist is spun and baked onto the sample, and the marker pattern is written onto the resist using an EBL tool, and developed using MIBK (methyl isobutyl ketone) (see Fig. 2.11 1)).
- The furnace-grown oxide mask is etched away in the developed areas using buffered hydrofluoric acid (see Fig. 2.11 2)) and rinsed in de-ionised (DI) water.[10]
- The PMMA is removed from the sample, using an acetone bath, and is followed by anisopropyl alcohol (IPA) rinse. Remaining organic contaminants are removed using a standard SP solution (3:1 Sulphuric acid:Hydrogen peroxide), and rinsed in DI water.

[8] A resistivity of 5-10 Ω cm corresponds to a boron density of 1.8×10^{15} cm^3, yielding a 2% chance only to find a Boron dopant tunnel-coupled to a donor within a sphere of 20 nm radius.

[9] Spinning of the polymethyl methacrylate resist (PMMA), baking on a hotplate, electron beam exposure using a scanning electron microscope and developing.

[10] DI water of resistivity larger than 18 MΩ.

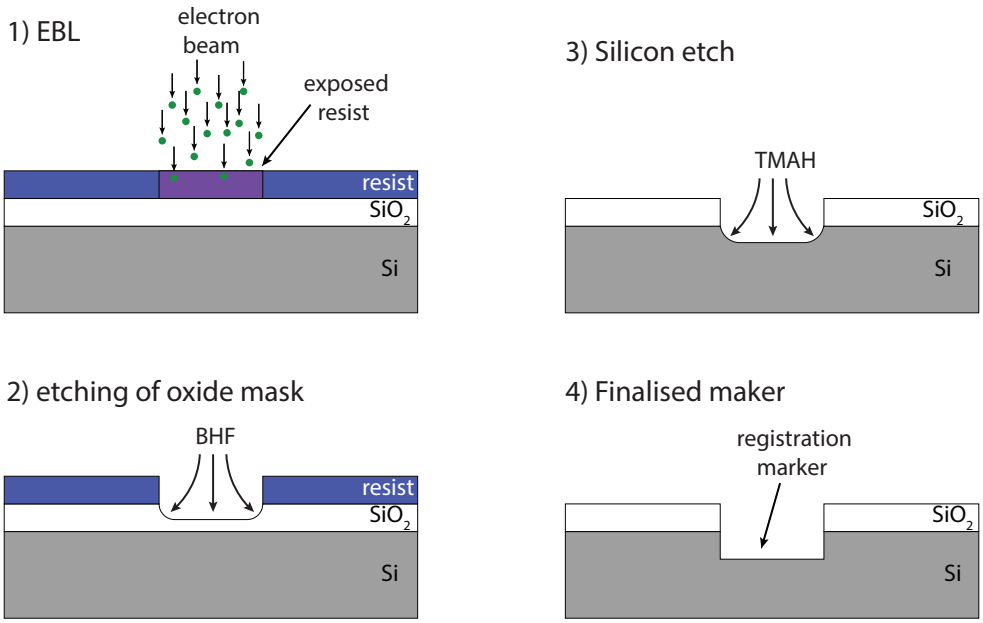

Figure 2.11: **STM registration marker fabrication**. A silicon dioxide mask is fabricated using EBL on PMMA resist (1), and wet etching the oxide using buffered hydrofluoric acid (BHF) in (2). The resist is then removed and the TMAH is used to selectively etch the silicon, and not the silicon dioxide mask (3).

- The thin layer of native silicon oxide that has grown within the trenches etched in the furnace-grown oxide is removed using a short 10 s hydrofluoric acid etch (10% concentration).

- Immediately after, the silicon markers are etched for 60 min in the TMAH solution (25%), yielding an etch depth of about 300 nm (see Fig. 2.11 3) and 4)). The sample is then rinsed in DI water and blow-dried with nitrogen.

- Finally the sample is cleaved into 8 samples of 2.5 mm × 10 mm, that are compatible with the sample holders used to load sample into the STM.

Silicon full-clean

Once the markers have been etched into the silicon, the samples are thoroughly cleaned to remove any contaminants. This is essential because contaminants can disrupt many of the following UHV fabrication processes (including surface reconstruction, lithography and silicon overgrowth). The silicon full clean used in this thesis is a standard process for semiconductor manufacturing. The steps are outlined below:

- First the furnace-grown oxide remaining from the marker fabrication is etched away using a 20% diluted buffered hydrofluoric acid etch. The etch is complete when the surface turns hydrophobic. The sample is then rinsed in DI water (3 min overflow rinse).

- Organic contaminants are removed by plunging the sample in a solution of SP (3 parts sulphuric acid,1 part hydrogen peroxide) for 8 min.

- The sample is thoroughly rinsed in DI water (8 min overflow rinse).

- The native oxide grown during the SP clean is removed by dipping the sample in an ultra clean hydrofluoric acid solution (10% diluted). The sample is then rinsed for 5 minutes in DI water (overflow rinse).

- Metallic contaminants are removed from the sample by immersing it in a RCA-2 solution (6 parts DI water, 1 part hydrochloric acid, 1 part hydrogen peroxide) held at 80 °C on a hot plate for 8 minutes.

- The sample is rinsed in DI water for 5 minutes (overflow rinse)

- Finally the sample is blow-dried with high purity nitrogen and carefully loaded in the STM sample holders.

- The sample, held in the sample holder is promptly transported within a nitrogen environment to the STM load-lock (to prevent oxidation and contamination), and the load lock is immediately pumped down to prevent excessive sample oxidation.

UHV surface preparation

After being loaded into the UHV system with base pressure below 1×10^{-11} mbar, the sample and the sample holder are outgassed at 350 °C using a resistive heater to remove contaminants such as water (for about 12 hours). The sample is then outgassed further by heating it for two hours at 480 °C using a direct current passing through the sample. The temperature is monitored from outside the UHV chamber using a Impac 8 Pro Series pyrometer, inferring the temperature from the characteristic infrared radiation emitted by the sample. Finally, the sample undergoes a series of high temperature annealing steps that remove any native oxide that has grown on the surface after the full-clean, sublimate remaining contaminants on the surface and flatten the surface. The procedure consists in three 20 s anneals at 1120 °C,

separated by 2 min at which the sample is allowed to cool down to 400 °C. A final 6 s anneal at 1120 °C is followed by a hold at 800 °C, and followed by a controlled cool-down of the sample at a rate of about 4.7 °C s^{-1} (280 °C min^{-1}) until the sample reaches 350 °C. The final anneal and the controlled cool-down produces a low-defect 2×1 surface reconstruction of the silicon (100) surface. Immediately after the anneals, the surface is terminated with a monolayer of monoatomic hydrogen that will serve as the mask for the STM lithography. To achieve this, a collimated beam of monoatomic hydrogen is directed towards the silicon surface held at 350 °C. The hydrogen atoms adsorb to the surface and thanks to the thermal energy provided by the heating, they rearrange to from a full coverage. The beam of monoatomic hydrogen gas is produced by a cracker in which di-hydrogen molecules are thermally dissociated into hydrogen atoms using a filament resistively heated to 1350 °C. After 5 minutes at a chamber pressure of 5×10^{-7} mbar, the hydrogen supply is closed off, the cracker filament is cooled-down, and the sample is finally left to cool down to room temperature.

After the hydrogen termination the surface is inspected for defects in the STM. A high-speed scan over areas of 15 µm × 15 µm is taken near the registration markers to verify the absence of large contaminants, pinning the formation of silicon step edges. The surface is then imaged more closely 50 nm × 50 nm, to verify a successful surface reconstruction with a low amount of vacancy defects (missing silicon atoms and dimers at the surface) and a successful hydrogen termination with a low amount of dangling bonds. Our surface preparation reliably yield vacancy densities below 5 per 25 nm × 25 nm and dangling bond densities below 2 per 25 nm × 25 nm.

2.3.2 Hydrogen lithography and encapsulation

After surface preparation, the device is patterned using voltage pulses on the STM tip that locally desorb the hydrogen mask. The hydrogen desorption can occur in two different regimes [110, 111]. For high voltages applied between the tip and the surface (6-7 V), electrons can be field-emitted from the tip and have enough energy to break silicon-hydrogen bonds where they impinge on the surface. Typical current set-points of $4-8$ nA desorb areas of several tens of nanometers at once, with the STM tip being held a few nanometers form the surface. This allows reliable, high-speed desorption of large structures, with STM tip speeds exceeding 3 µm s^{-1} and area desorption at a speed of 0.2 $µm^2$/min. A second regime of desorption at lower voltages ($2.5 - 3.5$ V) and higher current set-points ($10 - 20$ nA) allows desorption of only a few dangling bonds at a time. In that regime, electrons that

tunnel between the tip and the surface can excite vibrational modes of the silicon-hydrogen bond. If the tunnelling current is high enough, the energy that is injected to the bond within the lifetime of the vibration may overcome the energy barrier to desorption (3 eV [110]). The long lifetime of the vibration in silicon (10 ns in silicon (100)) as opposed to metals ($\approx$ 1 ps) [110], allows for desorption to occur with high probability for currents as low as a few nA. Atomic precision desorption in this vibrational regime is only possible for atomically-sharp STM tips.

Extensive work goes into preparing and conditioning atomically-sharp STM tip. For the devices presented in this thesis, the tips are etched out of $\approx$ 500 µm-thick tungsten wires using electrolysis in a potassium hydroxide solution (0.1 g of KOH per mL). The tungsten filament is held in the solution, and a voltage of about 7 V is applied between the tip and a platinum/iridium electrode. The etch-rate is fastest near the meniscus formed at interface of the tungsten filament and the surface of the solution because products of the electrolysis fall down the side of the filament, reducing the etch rate below the meniscus. After a few minutes, the part of the wire near the meniscus is thin enough that it tears under the weight of the immersed part of the filament. This event is detected from a sudden drop in the electrolysis current, upon which the process is stopped. Under the right conditions, this procedure yields atomically sharp tips. These tips are loaded into the UHV system using dedicated holders, and are also thermally outgassed before being used in the STM. In most cases the tip needs to be conditioned further within the STM, to remove oxide layers and sharpen it using voltage pulses ($3.5 - 7$ V at $10 - 20$ nA set point). In some cases, the tip is further conditioned using controlled collisions with the surface synchronised with voltage pulses.

Once the tip is conditioned so that it can desorb hydrogen bonds with atomic precision (in the vibrational mode), the inner-most part of the device containing the single or multi-donor quantum dots is patterned (see Fig. 2.12 a). Once the desired desorption pattern has been written, phosphine is introduced to the UHV system at to reach a steady chamber pressure of 2×10^{-7} mbar for 2 minutes. The arrangement of phosphine adsorbates species (PH_x) within the lithographic patches is then imaged to verify that the quantum dot will host the desired number of phosphorus donors after the incorporation anneal with high probability (see Fig. 2.12 b), more details in [112]). If this is the case, the charge sensor and gate structures are patterned (still in vibrational lithography mode), the dimensions of the charge sensor are verified to be up to standard, and if so, the sample is saturation dosed with phosphine dose again using the same procedure.

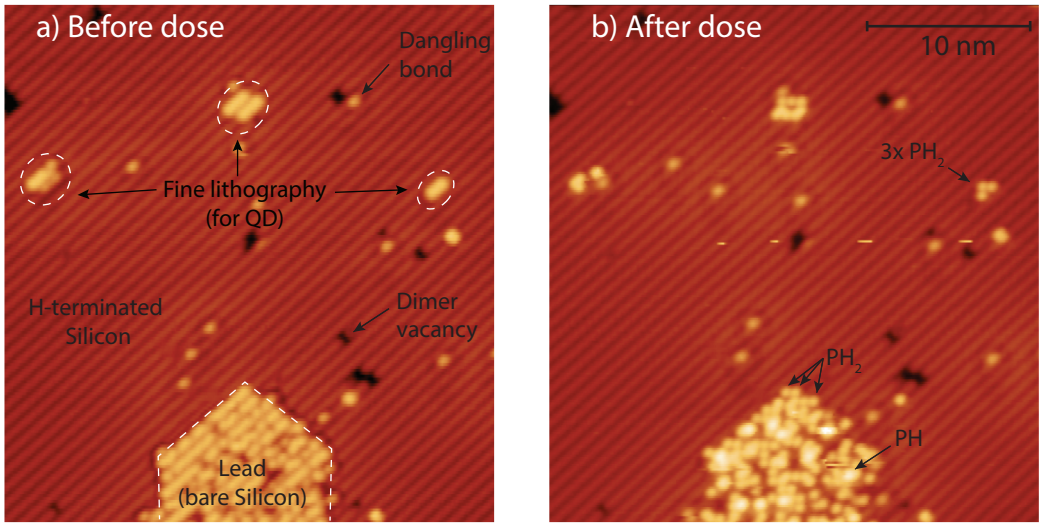

Figure 2.12: **Atomic scale STM hydrogen lithography and phosphine dosing**. **a)** STM image of the hydrogen terminated silicon (100) surface after desorption of three small patches that will host donor quantum dots (QD) and an electron reservoir (lead) at the bottom. The terminated surface appears dark orange while the areas where the hydrogen mask has been desorbed appear yellow. Dangling bonds therefore also appear yellow, while silicon dimer vacancies appear black. **b)** After phosphine dosing, phosphine species have adsorbed to the bare silicon inside the lithographic areas (dangling bonds do not absorb any phosphine species). PH_2 species are visible as asymmetric features on the silicon dimer which are wider and brighter than dangling bonds, while PH species appear brighter than any other feature and are centred across the silicon atoms of the dimer. We observe that the right hand dot hosts exactly three PH_2 species in a zig-zag pattern designed to host a single donor after the incorporation anneal.

In the final step of hydrogen lithography, long leads and contacts pads ($0.8 \times 1\,\mu m^2$) are patterned using field-emission mode lithography and the sample is saturation dosed a final time (same procedure as above). The pads will be contacted electrically using metallic vias in a later step.

Once the lithography is finalised, the phosphine species that have adsorbed within the desorbed silicon areas are incorporated into the silicon surface using a 1 minute anneal at 335 °C. The anneal is performed using direct sample heating and the temperature is monitored using the pyrometer. After a minute the sample temperature is adjusted to 250 °C and the surface is encapsulated with at least 40 nm of silicon at a growth rate of 0.14 nm/ min (about one silicon monolaye (ML) per minute). The growth rate and temperature have been optimised to produce a defect free epitaxial growth for at least 20 nm[113], and full electrical activation of the dopants [114]. The full activation of dopants was inferred from measured phosphorus sheet densities matching the measured electron sheet densities [108, 114]. The silicon source used for the growth process is an MBE Komponenten silicon sublimation source, that heats a solid filament of silicon to temperatures above 1000 °C at which silicon atoms sublimate from the surface. The silicon encapsulation is the final step of the UHV processing steps. The remaining fabrication steps used standard cleanroom processing tools to make electrical contact with the buried dopant layer.

Note that the all UHV components that are heated in the fabrication process are outgassed several hours in advance, in the absence of the sample, to minimise contamination of the sample in the later stages (this includes manipulators, the hydrogen cracker and the silicon sublimation source).

2.3.3 Clean-room processing

Manufacturing of electrical vias

Electrical measurement of the sample is reliant on making contact to the dopant, buried 40-50 nm below the silicon surface, using metallic vias. These vias are fabricated by first etching circular pits of 150 nm diameter to a depth of 60-70 nm, exceeding the depth of the dopant layer. Aluminium is then deposited onto the surface to form leads that fill the pits and contact the dopants on its circumference. This part of the fabrication process is performed in a cleanroom environment to prevent contamination of the surfaces.

The cleanroom processing starts by determining the precise position of the buried

dopants using the registration markers etched into the silicon before the STM lithography stage. The sample is then coated with 350 nm of PMMA resist, and circular openings of 150 nm diameter are written into it using electron beam lithography at the position of the buried phosphorus contact pads (see Fig. 2.13 a) 1)). The pattern is developed in MIBK, rinsed in IPA, and a short 2 minute oxygen plasma ash (50 W, 340 mTorr) is performed in a Denton plasma asher in order to remove any residual resist within the developed areas. Then, the holes are etched in a Oxford reactive ion etching (RIE) tool, using a CHF_3 : CF_4 plasma at a power of 150 W and a pressure of 100 mTorr (see Fig. 2.13 b) 2)). The PMMA is then removed in an ultrasonic acetone bath. To remove any possible contaminants within the holes that could prevent a good electrical contact with the metal to be evaporated, the sample is further cleaned using a oxygen plasma ash (same procedure as above), and a silicon SP-clean (see Sect. 2.3.1).

Immediately after, the fabrication of the electrical contacts starts. The lead pattern that connects the holes to large bond pads is written into a PMMA mask using EBL lithography (as described above). Before metallisation, a short oxygen ash is performed to remove residual resist, and the sample is dipped in buffered hydrofluoric acid (1:15) to remove any native oxide that has grown inside the holes and could prevent electrical contact between the metal and the dopants. Immediately after, a 100 nm thick layer of aluminium is evaporated into the sample using a Lesker electron-beam evaporator, with a deposition rate of 10 $\text{Å}\,\text{s}^{-1}$ (see Fig. 2.13 a) 3)). Lift-off of the metal evaporated on top of the PMMA mask is performed by immersing the sample into a solution of n-methyl-pyrrolidone (NMP) heated to 80 °C for one hour, This is followed by short ultrasonic bath in acetone, and a rinse in IPA. This concludes the fabrication of the electrical contacts (see Fig. 2.13 a) 4)).

A cross-sectional SEM image of the metallised holes reveals the slope in the side-walls which allows good adhesion of the metal near the phosphorus delta-layer (see Fig. 2.13 b)).

Alignment of a surface ESR antenna

The antenna, used for electron spin resonance experiments, is fabricated with aluminium in a process similar to that used for the patterning of the metallic leads. Aluminium markers patterned together with the leads in the previous step serve as alignment markers. They allow the placement of the antenna with respect to the quantum dots with a precision of ≈ 300 nm. The antenna pattern is written into a PMMA mask using EBL and developed using MIBK. A short oxygen plasma ash re-

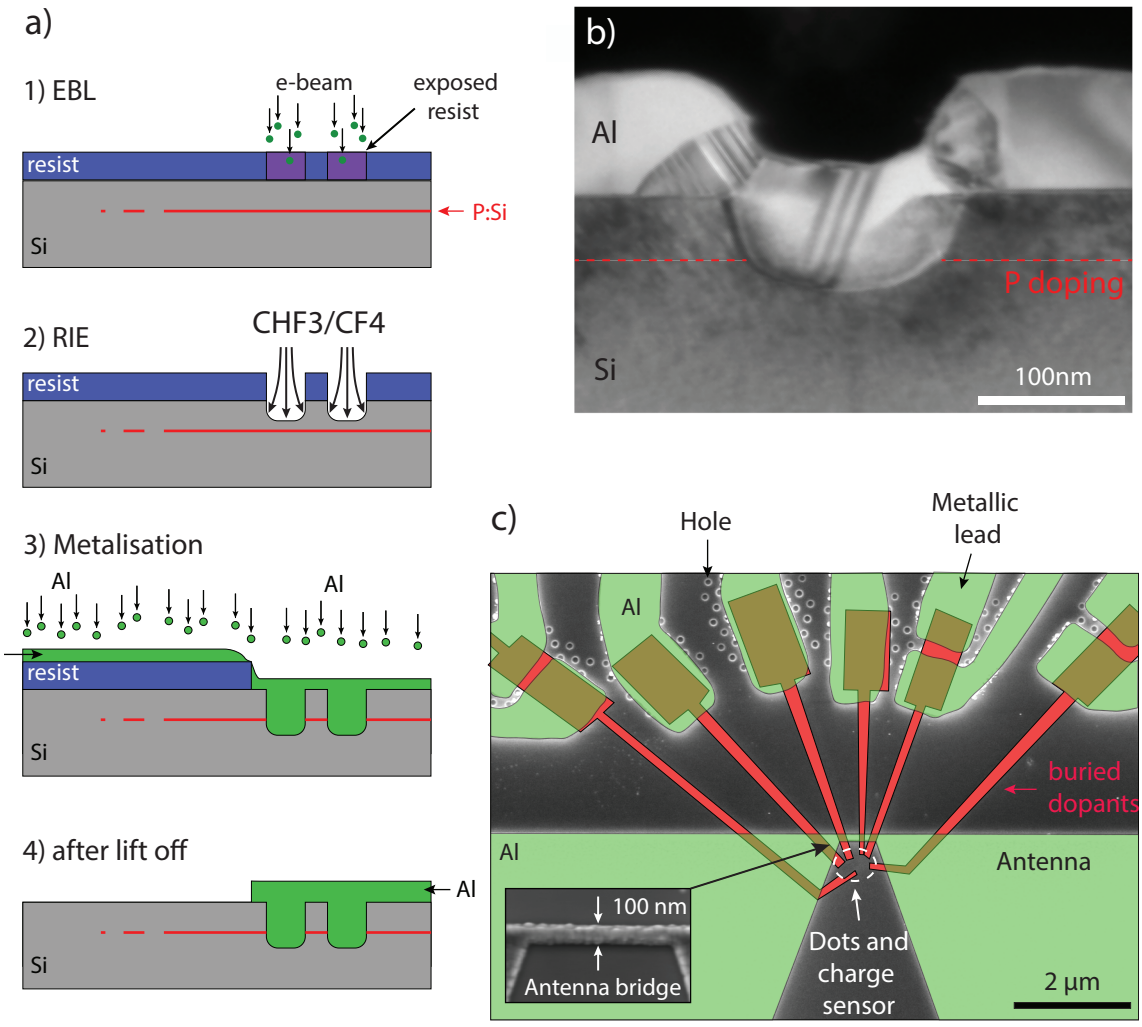

Figure 2.13: **Device fabrication of electrical contact and antenna**. **a)** Process flow for the fabrication of electrical vias. (1) Electron beam lithography (EBL): circular openings are defined within PMMA resist using an electron beam. After developing in MIBK, the sample is subjected to a CHF_3/CF_4 plasma inside an reactive ion etching (RIE) machine (2). The plasma etches the silicon within the exposed areas. A further EBL step (similar to (1)) defines a PMMA mask for the metallic contacts. Then the sample is metallised with aluminium (3) inside an electron-beam evaporator. Finally the metallic areas on top of the resist are removed (lift-off), and the metallic contact fabrication is finalised. **b)** Cross-sectional SEM image of one hole after the process in a) is finalised. The hole profile is smooth and sloped. It allows good contact between the phosphorus doped δ-layer (indicated in red) and the aluminium (light areas). **c)** SEM image of the inner part of a device. The buried phosphorus-doped areas are depicted in red. The inner part of the device (quantum dots, gates and charge sensor) are positioned at the centre of the image (white circle). Long phosphorus-doped leads extend to the phosphorus-doped contact pads. Holes (circles) have been etched below the buried contact pads, and aluminium leads have been defined above using EBL (green areas). Finally an aluminium antenna has been precisely positioned near the device (bottom green areas). The antenna bridge is 100 nm wide (see inset), and produces oscillating magnetic fields to the drive the electron spins on the donor quantum dots.

moves the remaining resist and contaminants in the developed areas and the metal is evaporated using the Lesker electron-beam evaporator to a thickness of 100 nm and at a rate of $2\,\text{Å}\,\text{s}^{-1}$. The lift-off is then performed in NMP in a similar manner to the metallic leads. The sample is then diced into a size of approximately $2.5\,\text{mm} \times 5\,\text{mm}$, leaving a clearance of only 150 µm at the edge of the antenna waveguide to reduce the length of the bonds to the antenna and improve microwave transmission. The final step in the processing involves gluing the sample onto our custom printed circuit board (PCB) and bonding it using an aluminium wedge bonder.

Figure 2.13 c)) displays a SEM image of the inner part of the device, showing the entire buried phosphorus areas, the holes etched through RIE, the metallic leads used for electrostatic control and measurement, and the antenna used for manipulation of the electron spin on the phosphorus donor quantum dots.

2.4 Cryogenic measurements

Devices are first tested at a temperature of 4.2 K by immersing them in liquid helium. This measurement step is used to screen devices before measurement at lower temperatures in a dilution refrigerator. The screening step in liquid helium tests the electrical contacts, measures the sheet density of phosphorus doped regions and verifies the functionality of the charge sensor and the presence of quantum dot transitions. If a device passes this screening at 4.2 K, it is then transferred to a dilution refrigerator whose base temperatures of about 50 mK allows the investigation of spin-physics. Dilution refrigerators rely on a mixture of ^{3}He and ^{4}He isotope that separate into a ^{3}He-rich and a ^{3}He-poor phase below 1 K, mostly comprised of ^{4}He. The mixture absorbs heat when ^{3}He isotopes cross from ^{3}He-rich to the ^{3}He-poor phase. The dilution refrigerator uses an elaborate circuit that provides continuous cooling power at temperatures below 50 mK by extracting gaseous ^{3}He from the ^{3}He-poor phase and supplying it in liquid form to the ^{3}He-rich phase. This complex circuit is mostly held below liquid helium temperature, either through immersion in liquid ^{4}He (wet-fridge) or through a pulse tube cooler that can operate without cryogenic liquids (dry fridge). The data presented in Chapter 5 was measured in two different ^{3}He/^{4}He dilution refrigerator, an Oxford Kelvinox K100 wet fridge and a Leiden dry fridge. In the following, the measurement setup used in both experiments is presented (small variations in the setups are omitted).

The single electron transistor (SET) that acts as a charge sensor is operated using either direct currents (DC) and radio frequency (RF) voltages (time-resolved

experiments are mostly performed using RF operation, due to the larger measurement bandwidth). The combined setup is presented in Fig. 2.14. For both DC and RF readout, a voltage is applied to the source contact of the SET using a battery powered Stanford Research Systems (SRS) SIM928 module. The voltage creates a current that traverses the SET from source to drain. Right after the voltage source, the voltage is reduced using a 50:1 voltage divider to increase the voltage resolution and reduce the electrical noise transmitted from the instrument to the device. The electrical current then enters the fridge and reaches the low temperature stages using twisted pairs of copper wires (loom wire). A custom[11] two- stage RC filter and a π-filter then attenuate high frequency noise originating from the higher temperature parts of the circuit with a cutoff of 300 kHz and 80 MHz respectively. Finally gold meanders[12] on sapphire thermalise the wire to the mixing chamber temperature before it reaches the device. The DC current originating from the SET drain contact then passes a resonant circuit used for the RF readout and is split from RF signals using a bias tee with a cutoff of 66 kHz. After the bias tee, the signal traverse the same thermalisation and filter setup just described, exits the fridge and is amplified using a Femto-amp DLPCA-200 trans-impedance amplifier, with a variable gain and bandwidth (typical gains are 10^8 V/A). The voltage originating from the trans-impedance amplifier is passed through a SRS SIM910 JFET pre-amp (with unit gain, simply to cut ground loops) and is further filtered using a SRS SIM965 8 stage Bessel filter with a variable cutoff (adapted for each readout). Finally the signal reaches an analogue to digital converter (ADC), a Nidaq USB-6363 from National Instruments (NI). The digital output of the ADC is processed and stored in real time using a computer running a custom python code[13].

The RF readout uses a resonant tank circuit connected to the drain of the SET. The resonance frequency of the tank circuit shifts slightly when the SET changes from its coulomb blockaded state to its conductive state. The changes in the resonance frequency of the tank circuit can be detected as a change in the amplitude and phase of the RF signals reflected from the tank circuit. Using this setup, the state of the SET can be monitored from reflected RF signals alone [115, 19]. The LC tank circuit, is located on the PCB holding the device, and formed by a surface mounted commercial 1.2 µH inductor and the parasitic capacitance to ground (typically about 1 pF). These typical values of inductance and capacitance yield a resonant frequency

[11] made by Michael Jones and Andrey Timofeev

[12] made by Michael Jones and Andrey Timofeev

[13] effort lead by Matthew House, Samuel Hile, Matthew McEwan, Prasanna Pakkiam and many others

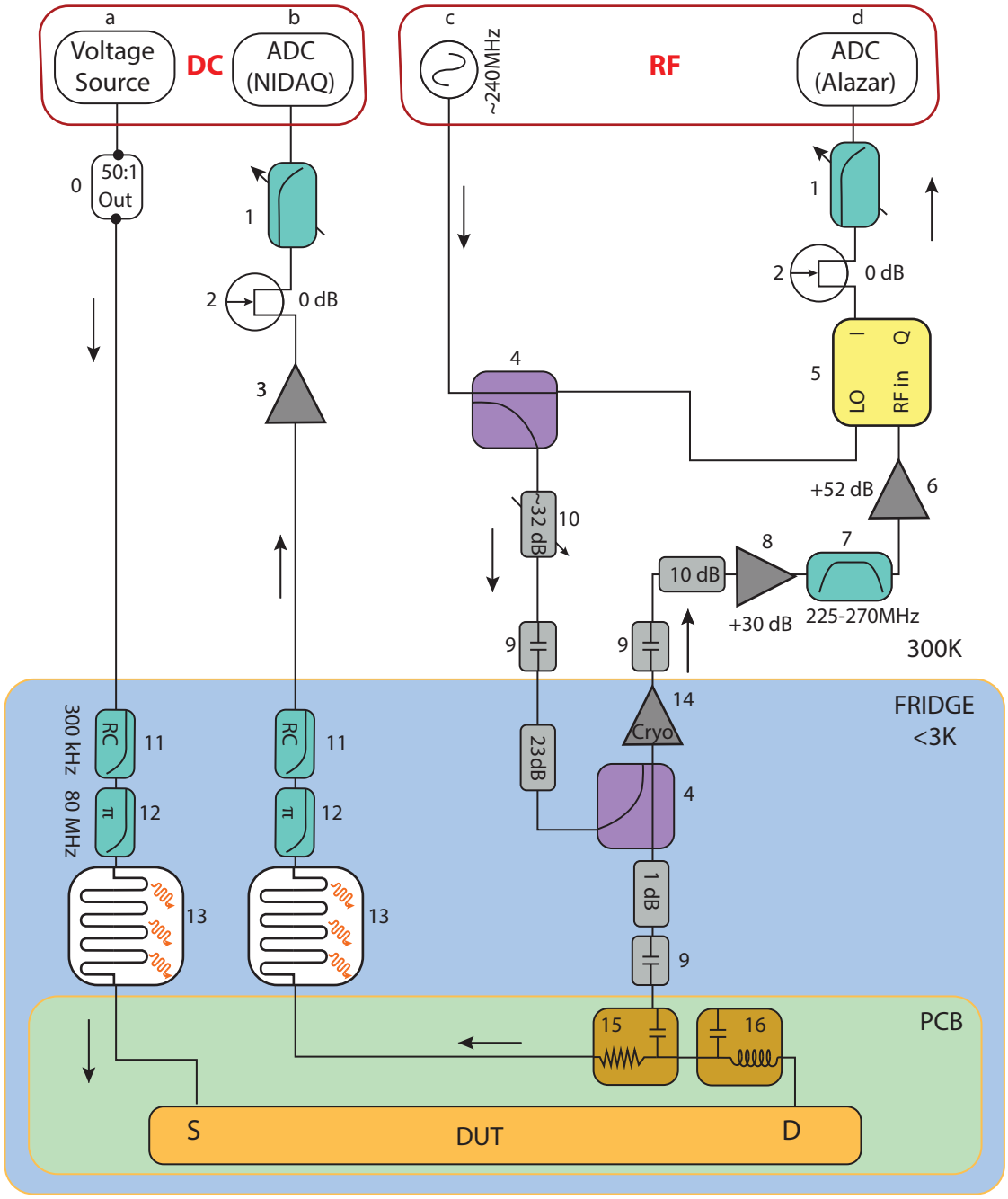

Commercial components

a) SRS SIM928
b) NI USB-6363
c) RF Source: SRS SG386
d) Alazar ATS9440
1) SRS SIM965
2) SRS SIM910 JFET preamp
3) Femto DLPCA-200
4) Direc. Coupl. ZFDC-20-4L
5) IQ demod. AD0105B
6) RF amp. PE15A1013
7) minicircuit bp (225-270 MHZ)
8) RF amp. PE15A1012
9) DC block Pasternack PE8212
10) RF step attenuator PE7398
14) Cryo. amp. CITLF2

Custom components

0) Voltage divide (50:1)
11) RC low-pass filter (300 kHz cutoff)
12) Pi-filter (80 MHz cutoff)
13) Saphire thermalizer
15) Bias Tee (66 kHz cutoff0
16) Resonator ~235MHz
(1.2 μH, parasitic cap)

Figure 2.14: **Measurement set-up for readout of donor devices.**

of about $220 - 250\,\mathrm{MHz}$. The sinusoidal RF signal is produced by an SRS SG286 source, and the reflected signal is demodulated into I and Q quadratures using the AD0105B IQ demodulator from Polyphase microwave (see Fig. 2.14). The signal is fully transferred into one of the quadratures by adjusting the RF frequency by about 1 MHz close to the resonance, and the quadrature voltage holding the signal is then digitised using the high-bandwidth Alazar ATS9440 card within the measurement computer. The RF power reaching the device (typically $-90\,\mathrm{dBm}$) is adjusted using a Pasternack PE8212 step attenuator placed after the RF source. The RF signal entering the fridge is thermalised at the various temperature stages of the refrigerator, with typical total attenuation of $\approx 10\,\mathrm{dB}$ and a further $\approx 3\,\mathrm{dB}$ from the copper/nickel coaxial cables. The input RF signal is then transferred to the drain using a ZFDC-20-4L directional coupler from Minicircuits, before it reaches the custom made bias tee (cutoff 66 kHz used to separate DC and RF signals) and finally the resonant circuit. The signal reflected from the resonant circuit traverses the directional coupler with less than 0.3 dB attenuation (IN to OUT), is then amplified using a CITLF2 cryogenic amplifier from Cosmic Microwave Technology Inc. with an amplification of about 30 dB and a noise floor of about 3 K. After the signal exits the fridge, it passes a bandpass filter centred around the resonant frequency and is further amplified by about 70 dB using a PE15A1012 and PE15A1013 room temperature amplifier from Pasternack before it finally reaches the IQ demodulator. After the demodulator, the quadrature voltage is passed through a SRS SIM910 JFET pre-amp (with unit gain simply to cut ground loops) and filtered using a SRS SIM965 8 stage Bessel filter with adjustable frequency cutoff. Additional passive components not mentioned here (mostly DC blocks and attenuators) are displayed in Fig. 2.14.

Fast independent control over the quantum dot chemical potential, necessary for spin readout, is provided by pulsed and DC voltage sources connected to the electrostatic gates of the device. The typical setup for one of the electrostatic gates is displayed in Fig. 2.15. Typically this setup is reproduced on two or three gates in total, with some minor variations. We use two voltage sources to provide a constant voltage at the gate ("slow" voltages, and an AWG to provide fast time-resolved voltage pulses for spin readout ("fast" voltages). The "slow" voltages are added to the "fast" voltages using a bias tee on the device PCB, with a cutoff of 70 Hz. The low cutoff is chosen so that most of the high frequency components used for spin readout fall on the fast side of the setup, where they reach the PCB on copper/nickel coaxial cable with low attenuation and low parasitic capacitance to the other lines.

The "slow" voltage is provided by two separate voltage sources. First, a stable electrostatic working point is provided by the battery powered SRS SIM928 voltage source. The instrument is very reliable, has low noise characteristics and is therefore only attenuated by a factor 5 before reaching the fridge. The low attenuation allows for large voltages to be applied to the device. This allows flexibility in tuning the charge configuration of the quantum dots. Furthermore this "coarse" voltage provides a stable working point, resistant to power failure or instrument malfunction. Additionally to the coarse voltages, the National Instruments NIDAQ USB-6363 ADC provides a finer voltage resolution. The voltage is attenuated by a factor 50 to increase the voltage resolution and reduce the electrical noise transmitted to the device. This "fine" voltage source is used to precisely adjust the working point for a given experiment, or to take "gate-gate" maps that map out the voltage configurations at which electrons are loaded onto the quantum dots. Finally an arbitrary waveform generator (AWG), the Tektronik 5208 (or 5014C), provides fast voltage pulses for spin readout with a 16 bit voltage resolution and at a time resolution of up to 5 GS/s. The same pulse shape is generated on both the "slow" and "fast" side of the bias tee on the device PCB, to avoid pulse offsets and distortions of the frequency components of the pulse that are close to the bias tee cutoff. Both slow and fast lines are attenuated by about 30 dB in total, to thermalise the wires and increase the voltage resolution (more details in Fig. 2.15).

On the slow side, the AWG compensation pulse is attenuated by 20 dB and added to the coarse voltage using an SRS SIM980 voltage adder (zero gain), the output of which is fed into the voltage divider with a 5:1 ratio, where it is added to the fine voltage. At that point the three voltages on the slow side have been combined and enter the fridge. The voltages descend through the fridge using twisted pairs of copper cable (loom wire), are thermalised at the different temperature stage, until they reach the mixing chamber. At the mixing chamber stage, the signal is filtered using the same setup as for the DC readout (RC filter, π-filter, and sapphire thermalisation). Finally the "slow" line reaches the device PCB on the cold finger, where it is added to the "fast" AWG signal at the bias tee.

For the observation of spin physics, the sample is placed in a constant magnetic field that provides the spin Zeeman splitting. The magnetic field is produced by a superconducting coil placed inside the fridge, and powered by a dedicated current source (AMI 4Q06125PS and controller 4Q06125PS-430 for the Leiden fridge). Finally for the electron spin resonance experiments, the microwave signals are produced by a Keysight E8267D microwave source. Low frequency components of the

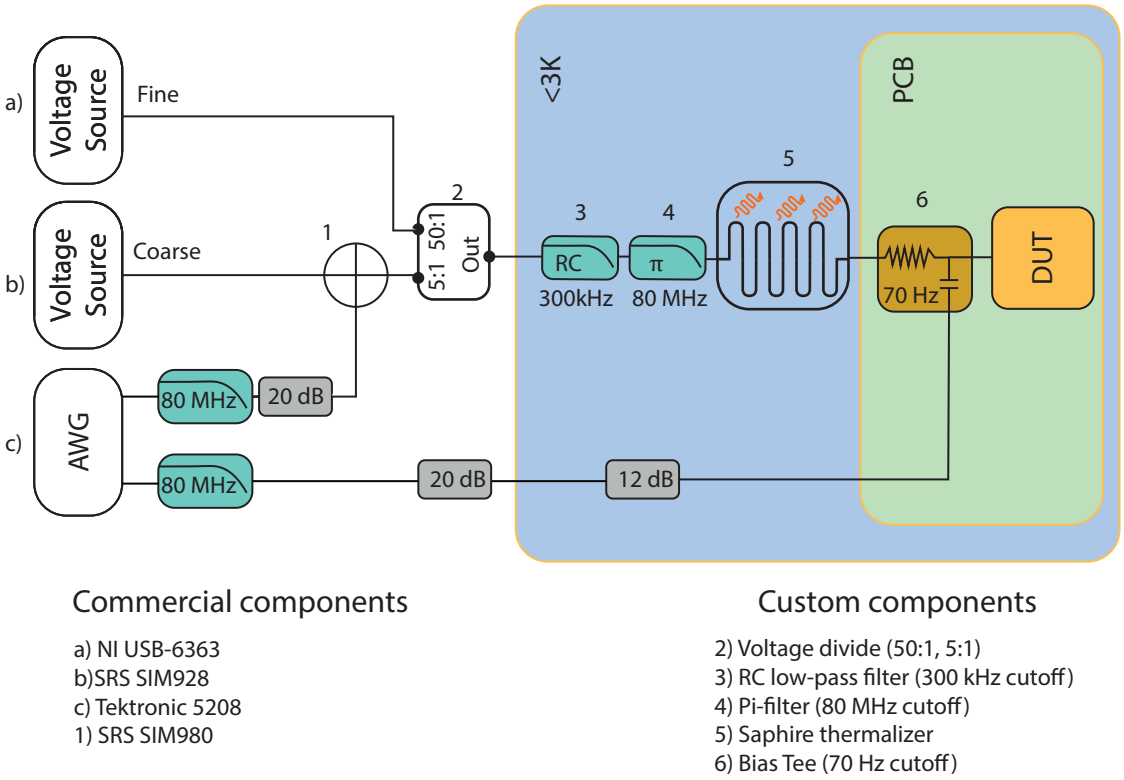

Figure 2.15: **Measurement set-up for fast pulsing**.

microwave signal are filtered using a DC block and a 26 GHz high-pass filter before being fed into the fridge. Within the fridge, the signal is routed within copper/nickel coaxial cables, (with high frequency SK connectors between temperature stages). The coaxial cable is thermalised using 12 dB attenuation on the lower temperature stages before it finally reaches the device PCB. On the PCB, a tapered coplanar waveguide routes the signal to contact pads close to the silicon chip. Finally bond wires connect the coplanar waveguide on the PCB to aluminium the antenna.

All the instruments are synchronised by using the AWG as the "master". Trigger signals are routed from the AWG to the NIDAQ ADC for DC readout, to the ALAZAR ADC for RF readout, and to the microwave source for precise timing of the ESR pulses.

2.5 Summary

This chapter has set the background to the information needed for the following three results chapters. First, a review of the state of the quantum computing field highlighted the challenges facing the various physical platforms on the road to error corrected universal quantum computation. The scaling-up of the processors is un-

deniably the major challenge on all hardware platforms. The compatibility of the silicon spin qubit platform with the materials and processes of the semiconductor industry was identified as a major advantage to solve this challenge. However the difficulty of coupling spin qubits over long distances was highlighted as a possible hurdle. This is the subject of Chapter 3 and Chapter 4. The long relaxation and coherence times of silicon spin qubits was identified as another advantage for the platform on the road to scaling up. Phosphorus donors were especially identified as a promising host for silicon spin qubits. Such donor-based qubits were then introduced in a second section, together with the two leading manufacturing methods used to fabricate them. The third section of this chapter detailed one of these fabrication method, based on STM hydrogen lithography. This technique is at the basis of devices proposed or measured in Chapter 4 and Chapter 5. Finally, the measurement setup used for the results of Chapter 5 was detailed in a fourth section.

Bibliography

[1] Peter W. Shor. Scheme for reducing decoherence in quantum computer memory. *Physical Review A*, 52(4):2493–2496, 1995.

[2] Austin G. Fowler, Matteo Mariantoni, John M. Martinis, and Andrew N. Cleland. Surface codes: Towards practical large-scale quantum computation. *Physical Review A*, 86(3):032324, sep 2012.

[3] Daniel Gottesman. Class of QEC codes saturating Hamming bound. *Physical Review A*, 54(3):1862–1868, 1996.

[4] T. P. Harty, D. T.C. Allcock, C. J. Ballance, L. Guidoni, H. A. Janacek, N. M. Linke, D. N. Stacey, and D. M. Lucas. High-fidelity preparation, gates, memory, and readout of a trapped-ion quantum bit. *Physical Review Letters*, 113(22):2–6, 2014.

[5] J. P. Gaebler, T. R. Tan, Y. Lin, Y. Wan, R. Bowler, A. C. Keith, S. Glancy, K. Coakley, E. Knill, D. Leibfried, and D. J. Wineland. High-Fidelity Universal Gate Set for Be 9 + Ion Qubits. *Physical Review Letters*, 117(6):1–5, 2016.

[6] C. J. Ballance, T. P. Harty, N. M. Linke, M. A. Sepiol, and D. M. Lucas. High-Fidelity Quantum Logic Gates Using Trapped-Ion Hyperfine Qubits. *Physical Review Letters*, 117(6):1–6, 2016.

[7] A. H. Myerson, D. J. Szwer, S. C. Webster, D. T.C. Allcock, M. J. Curtis, G. Imreh, J. A. Sherman, D. N. Stacey, A. M. Steane, and D. M. Lucas. High-fidelity readout of trapped-ion qubits. *Physical Review Letters*, 100(20):2–5, 2008.

[8] C. L. Edmunds, T. R. Tan, A. R. Milne, A. Singh, M. J. Biercuk, and C. Hempel. Scalable hyperfine qubit state detection via electron shelving in the 2D5/2 and 2F7/2 manifolds in 171Yb+. *ArXiv*, pages 1–12, 2021.

[9] C. Monroe and J. Kim. Scaling the ion trap quantum processor. *Science*, 339(6124):1164–1169, 2013.

[10] Colin D. Bruzewicz, John Chiaverini, Robert McConnell, and Jeremy M. Sage. Trapped-ion quantum computing: Progress and challenges. *Applied Physics Reviews*, 6(2), 2019.

[11] Hanhee Paik, A. Mezzacapo, Martin Sandberg, D. T. McClure, B. Abdo, A. D. Córcoles, O. Dial, D. F. Bogorin, B. L.T. Plourde, M. Steffen, A. W. Cross, J. M. Gambetta, and Jerry M. Chow. Experimental Demonstration of a Resonator-Induced Phase Gate in a Multiqubit Circuit-QED System. *Physical Review Letters*, 117(25):1–5, 2016.

[12] Juha T. Muhonen, Juan P. Dehollain, Arne Laucht, Fay E. Hudson, Rachpon Kalra, Takeharu Sekiguchi, Kohei M. Itoh, David N. Jamieson, Jeffrey C. McCallum, Andrew S. Dzurak, and Andrea Morello. Storing quantum information for 30 seconds in a nanoelectronic device. *Nature Nanotechnology*, 9(12):986–991, 2014.

[13] Jarryd J. Pla, Kuan Y. Tan, Juan P. Dehollain, Wee H. Lim, John J. L. Morton, Floris A. Zwanenburg, David N. Jamieson, Andrew S. Dzurak, and Andrea Morello. High-fidelity readout and control of a nuclear spin qubit in silicon. *Nature*, 496(7445):334–338, apr 2013.

[14] R. Barends, J. Kelly, A. Megrant, A. Veitia, D. Sank, E. Jeffrey, T. C. White, J. Mutus, A. G. Fowler, B. Campbell, Y. Chen, Z. Chen, B. Chiaro, A. Dunsworth, C. Neill, P. O'Malley, P. Roushan, A. Vainsencher, J. Wenner, A. N. Korotkov, A. N. Cleland, and John M. Martinis. Superconducting quantum circuits at the surface code threshold for fault tolerance. *Nature*, 508(7497):500–503, 2014.

[15] C. H. Yang, K. W. Chan, R. Harper, W. Huang, T. Evans, J. C.C. Hwang, B. Hensen, A. Laucht, T. Tanttu, F. E. Hudson, S. T. Flammia, K. M. Itoh, A. Morello, S. D. Bartlett, and A. S. Dzurak. Silicon qubit fidelities approaching incoherent noise limits via pulse engineering. *Nature Electronics*, 2(4):151–158, 2019.

[16] W. Huang, C. H. Yang, K. W. Chan, T. Tanttu, B. Hensen, R. C.C. Leon, M. A. Fogarty, J. C.C. Hwang, F. E. Hudson, K. M. Itoh, A. Morello,

A. Laucht, and A. S. Dzurak. Fidelity benchmarks for two-qubit gates in silicon. *Nature*, 569(7757):532–536, 2019.

[17] T. Walter, P. Kurpiers, S. Gasparinetti, P. Magnard, A. Potočnik, Y. Salathé, M. Pechal, M. Mondal, M. Oppliger, C. Eichler, and A. Wallraff. Rapid High-Fidelity Single-Shot Dispersive Readout of Superconducting Qubits. *Physical Review Applied*, 7(5):1–11, 2017.

[18] Patrick Harvey-Collard, Benjamin D'Anjou, Martin Rudolph, N. Tobias Jacobson, Jason Dominguez, Gregory A.Ten Eyck, Joel R. Wendt, Tammy Pluym, Michael P. Lilly, William A. Coish, Michel Pioro-Ladrière, and Malcolm S. Carroll. High-Fidelity Single-Shot Readout for a Spin Qubit via an Enhanced Latching Mechanism. *Physical Review X*, 8(2):1–11, 2018.

[19] D. Keith, M. G. House, M. B. Donnelly, T. F. Watson, B. Weber, and M. Y. Simmons. Single-Shot Spin Readout in Semiconductors Near the Shot-Noise Sensitivity Limit. *Physical Review X*, 9(4):41003, 2019.

[20] Jeremy L. O'Brien, Akira Furusawa, and Jelena Vučković. Photonic quantum technologies. *Nature Photonics*, 3(12):687–695, 2009.

[21] S. Takeda and A. Furusawa. Toward large-scale fault-tolerant universal photonic quantum computing. *APL Photonics*, 4(6), 2019.

[22] G. Wendin. Quantum information processing with superconducting circuits: A review. *Reports on Progress in Physics*, 80(10), 2017.

[23] Frank Arute, Kunal Arya, Ryan Babbush, Dave Bacon, Joseph C. Bardin, Rami Barends, Rupak Biswas, Sergio Boixo, Fernando G.S.L. Brandao, David A. Buell, Brian Burkett, Yu Chen, Zijun Chen, Ben Chiaro, Roberto Collins, William Courtney, Andrew Dunsworth, Edward Farhi, Brooks Foxen, Austin Fowler, Craig Gidney, Marissa Giustina, Rob Graff, Keith Guerin, Steve Habegger, Matthew P. Harrigan, Michael J. Hartmann, Alan Ho, Markus Hoffmann, Trent Huang, Travis S. Humble, Sergei V. Isakov, Evan Jeffrey, Zhang Jiang, Dvir Kafri, Kostyantyn Kechedzhi, Julian Kelly, Paul V. Klimov, Sergey Knysh, Alexander Korotkov, Fedor Kostritsa, David Landhuis, Mike Lindmark, Erik Lucero, Dmitry Lyakh, Salvatore Mandrà, Jarrod R. McClean, Matthew McEwen, Anthony Megrant, Xiao Mi, Kristel Michielsen, Masoud Mohseni, Josh Mutus, Ofer Naaman, Matthew Neeley, Charles Neill,

Murphy Yuezhen Niu, Eric Ostby, Andre Petukhov, John C. Platt, Chris Quintana, Eleanor G. Rieffel, Pedram Roushan, Nicholas C. Rubin, Daniel Sank, Kevin J. Satzinger, Vadim Smelyanskiy, Kevin J. Sung, Matthew D. Trevithick, Amit Vainsencher, Benjamin Villalonga, Theodore White, Z. Jamie Yao, Ping Yeh, Adam Zalcman, Hartmut Neven, and John M. Martinis. Quantum supremacy using a programmable superconducting processor. *Nature*, 574(7779):505–510, 2019.

[24] R. Barends, J. Kelly, A. Megrant, D. Sank, E. Jeffrey, Y. Chen, Y. Yin, B. Chiaro, J. Mutus, C. Neill, P. O'Malley, P. Roushan, J. Wenner, T. C. White, A. N. Cleland, and John M. Martinis. Coherent josephson qubit suitable for scalable quantum integrated circuits. *Physical Review Letters*, 111(8):1–5, 2013.

[25] Alexander P.M. Place, Lila V.H. Rodgers, Pranav Mundada, Basil M. Smitham, Mattias Fitzpatrick, Zhaoqi Leng, Anjali Premkumar, Jacob Bryon, Andrei Vrajitoarea, Sara Sussman, Guangming Cheng, Trisha Madhavan, Harshvardhan K. Babla, Xuan Hoang Le, Youqi Gang, Berthold Jäck, András Gyenis, Nan Yao, Robert J. Cava, Nathalie P. de Leon, and Andrew A. Houck. New material platform for superconducting transmon qubits with coherence times exceeding 0.3 milliseconds. *Nature Communications*, 12(1), 2021.

[26] Yaniv J. Rosen, Matthew A. Horsley, Sara E. Harrison, Eric T. Holland, Allan S. Chang, Tiziana Bond, and Jonathan L. Dubois. Protecting superconducting qubits from phonon mediated decay. *Applied Physics Letters*, 114(20), 2019.

[27] Chenlu Wang, Xuegang Li, Huikai Xu, Zhiyuan Li, Junhua Wang, Zhen Yang, Zhenyu Mi, Tang Su, Chuhong Yang, Guangyue Wang, Wenyan Wang, Yongchao Li, and Mo Chen. Transmon qubit with relaxation time exceeding 0.5 milliseconds Chenlu. *arXiv preprint arXiv:2105.09890*, 2021.

[28] Peter W. Shor. Polynomial-time algorithms for prime factorization and discrete logarithms on a quantum computer. *SIAM Journal on Computing*, 26(5):1484–1509, 1997.

[29] A. Shamir L. Adelman R. Rivest. CRYPTOGRAPHIC COMMUNICATIONS SYSTEM AND METHOD Patent 4405829, 1983.

[30] Stephane Beauregard. Circuit for Shor's algorithm using 2n+3 qubits. *Quantum Information and Computation*, 3(2):175–185, 2003.

[31] Steven A. Cuccaro, Thomas G. Draper, Samuel A. Kutin, and David Petrie Moulton. A new quantum ripple-carry addition circuit. *ArXiv*, pages 1–9, 2008.

[32] Pijush Kumar Koley and Srimanta Pal. Comments on "Quantum networks for elementary arithmetic operations". *Neural, Parallel and Scientific Computations*, 20(1):11–16, 2012.

[33] Jonathan P Home, David Hanneke, John D Jost, Jason M Amini, Dietrich Leibfried, and David J Wineland. Complete Methods Set for Scalable Ion Trap Quantum Information Processing. *Science*, 325(September):2–6, 2009.

[34] D. Kielpinski, C. Monroe, and D. J. Wineland. Architecture for a large-scale ion-trap quantum computer. *Nature*, 417(6890):709–711, 2002.

[35] Bjoern Lekitsch, Sebastian Weidt, Austin G. Fowler, Klaus Mølmer, Simon J. Devitt, Christof Wunderlich, and Winfried K. Hensinger. Blueprint for a microwave trapped ion quantum computer. *Science Advances*, 3(2):1–12, 2017.

[36] J. I. Cirac and P. Zoller. Quantum computations with cold trapped ions. *Physical Review Letters*, 74(20):4091–4094, 1995.

[37] Anders Sørensen and Klaus Mølmer. Quantum computation with ions in thermal motion. *Physical Review Letters*, 82(9):1971–1974, 1999.

[38] Florian Mintert and Christof Wunderlich. Ion-trap quantum logic using long-wavelength radiation. *Physical Review Letters*, 87(25):257904–1–257904–4, 2001.

[39] J. I. Cirac and P. Zoller. A scalable quantum computer with ions in an array of microtraps. *Nature*, 404(6778):579–581, 2000.

[40] A. C. Wilson, Y. Colombe, K. R. Brown, E. Knill, D. Leibfried, and D. J. Wineland. Tunable spin-spin interactions and entanglement of ions in separate potential wells. *Nature*, 512(1):57–60, 2014.

[41] C. Monroe, R. Raussendorf, A. Ruthven, K. R. Brown, P. Maunz, L. M. Duan, and J. Kim. Large-scale modular quantum-computer architecture with atomic

memory and photonic interconnects. *Physical Review A - Atomic, Molecular, and Optical Physics*, 89(2):1–16, 2014.

[42] D. Hucul, I. V. Inlek, G. Vittorini, C. Crocker, S. Debnath, S. M. Clark, and C. Monroe. Modular entanglement of atomic qubits using photons and phonons. *Nature Physics*, 11(1):37–42, 2015.

[43] Dong Il Dan Cho, Seokjun Hong, Minjae Lee, and Taehyun Kim. A review of silicon microfabricated ion traps for quantum information processing. *Micro and Nano Systems Letters*, 3(1):31–34, 2015.

[44] J. True Merrill, Curtis Volin, David Landgren, Jason M. Amini, Kenneth Wright, S. Charles Doret, C. S. Pai, Harley Hayden, Tyler Killian, Daniel Faircloth, Kenneth R. Brown, Alexa W. Harter, and Richart E. Slusher. Demonstration of integrated microscale optics in surface-electrode ion traps. *New Journal of Physics*, 13, 2011.

[45] Amira M. Eltony, Shannon X. Wang, Gleb M. Akselrod, Peter F. Herskind, and Isaac L. Chuang. Transparent ion trap with integrated photodetector. *Applied Physics Letters*, 102(5), 2013.

[46] A. P. Vandevender, Y. Colombe, J. Amini, D. Leibfried, and D. J. Wineland. Efficient fiber optic detection of trapped ion fluorescence. *Physical Review Letters*, 105(2):1–4, 2010.

[47] S. Weidt, J. Randall, S. C. Webster, K. Lake, A. E. Webb, I. Cohen, T. Navickas, B. Lekitsch, A. Retzker, and W. K. Hensinger. Trapped-Ion Quantum Logic with Global Radiation Fields. *Physical Review Letters*, 117(22):1–6, 2016.

[48] L. M. K. Vandersypen, H. Bluhm, J. S. Clarke, A. S. Dzurak, R. Ishihara, A. Morello, D. J. Reilly, L. R. Schreiber, and M. Veldhorst. Interfacing spin qubits in quantum dots and donorshot, dense, and coherent. *npj Quantum Information*, 3(1):1–10, 2017.

[49] Zsolt Tokei. Scaling the BEOL a toolbox filled with new processes, boosters and conductors, 2019.

[50] C. D. Hill, E. Peretz, S. J. Hile, M. G. House, M. Fuechsle, S. Rogge, M. Y. Simmons, and L. C. L. Hollenberg. A surface code quantum computer in silicon. *Science Advances*, 1(9):e1500707–e1500707, oct 2015.

[51] M. Veldhorst, H. G.J. Eenink, C. H. Yang, and A. S. Dzurak. Silicon CMOS architecture for a spin-based quantum computer. *Nature Communications*, 8(1), 2017.

[52] Guilherme Tosi, Fahd A. Mohiyaddin, Stefanie Tenberg, Arne Laucht, and Andrea Morello. Robust electric dipole transition at microwave frequencies for nuclear spin qubits in silicon. *arXiv*, jun 2017.

[53] Kenneth R. Brown, Jungsang Kim, and Christopher Monroe. Co-designing a scalable quantum computer with trapped atomic ions. *npj Quantum Information*, 2(1):1–10, 2016.

[54] Lotte Geck, Andre Kruth, Hendrik Bluhm, Stefan van Waasen, and Stefan Heinen. Control electronics for semiconductor spin qubits. *Quantum Sci. Technol.*, 5(015004), 2020.

[55] Chih Hwan Yang, R. C.C. Leon, J. C.C. Hwang, A. Saraiva, T. Tanttu, W. Huang, J. Camirand Lemyre, K. W. Chan, K. Y. Tan, F. E. Hudson, K. M. Itoh, A. Morello, M. Pioro-Ladrière, A. Laucht, and A. S. Dzurak. Silicon quantum processor unit cell operation above one Kelvin. *arXiv*, 580(April), 2019.

[56] Roman Schmied, Janus H. Wesenberg, and Dietrich Leibfried. Optimal surface-electrode trap lattices for quantum simulation with trapped ions. *Physical Review Letters*, 102(23):2–5, 2009.

[57] F N Krauth, J Alonso, and J P Home. Optimal electrode geometries for 2-dimensional ion arrays with bi-layer ion traps. *Journal of Physics B-Atomic Molecular and Optical Physics*, 48(1):15001, 2015.

[58] Frank Herman. The Electronic Energy Band Structure of Silicon and Germanium. *Proceedings of the IRE*, 43(12):1703–1732, 1955.

[59] Steven R Schofield. *Atomic-scale placement of individual phosphorus atoms in silicon (001)*. Phd. thesis, University of New South Wales, 2004.

[60] Thomas Ihn. *Semiconductor nanostructures*. Oxford University Press, 2010.

[61] W. Kohn and J. M. Luttinger. Theory of donor states in silicon. *Physical Review*, 98(4):915–922, 1955.

[62] Samuel James Hile. *Spin Control and Coherence in Scalable Phosphorus Donor Qubits by*. Phd. thesis, University of New South Wales, 2017.

[63] James R. Chelikowsky and Marvin L. Cohen. Electronic structure of silicon. *Physical Review B*, 10(12):5095–5107, 1974.

[64] Yu Wang, Archana Tankasala, Lloyd C L Hollenberg, Gerhard Klimeck, Michelle Y Simmons, and Rajib Rahman. Highly tunable exchange in donor qubits in silicon. *npj Quantum Information*, 2(1):16008, nov 2016.

[65] Yu Ling Hsueh, Holger Büch, Yaohua Tan, Yu Wang, Lloyd C.L. Hollenberg, Gerhard Klimeck, Michelle Y. Simmons, and Rajib Rahman. Spin-lattice relaxation times of single donors and donor clusters in silicon. *Physical Review Letters*, 113(24):1–5, 2014.

[66] J. S. Smith, A. Budi, M. C. Per, N. Vogt, D. W. Drumm, L. C.L. Hollenberg, J. H. Cole, and S. P. Russo. Ab initio calculation of energy levels for phosphorus donors in silicon. *Scientific Reports*, 7(1):1–11, 2017.

[67] Belita Koiller, Xuedong Hu, and S. Das Sarma. Exchange in Silicon-Based Quantum Computer Architecture. *Physical Review Letters*, 88(2):027903, dec 2001.

[68] G. Feher and E. A. Gere. Electron spin resonance experiments on donors in silicon. II. Electron spin relaxation effects. *Physical Review*, 114(5):1245–1256, 1959.

[69] Richard P. Feynman. Simulating physics with computers. *International Journal of Theoretical Physics*, 21(6-7):467–488, 1982.

[70] Lov K. Grover. Quantum Mechanics Helps in Searching for a Needle in a Haystack. *Physical Review Letters*, 79(2):325–328, jul 1997.

[71] Andrew Steane. M ultiple-particle interference and quantum error correction. *Proceedings of the Royal Society A*, 452:2551–2577, 1996.

[72] Asher Peres. Reversible logic operations. *Physical Review A*, 32(6):3266–3276, 1985.

[73] A. Yu Kitaev. Fault-tolerant quantum computation by anyons. *Annals of Physics*, 303(1):2–30, 2003.

[74] B. E. Kane. A silicon-based nuclear spin quantum computer. *Nature*, 393(6681):133–137, may 1998.

[75] M. Tyryshkin, A. Lyon, V. Astashkin, and M. Raitsimring. Electron spin relaxation times of phosphorus donors in silicon. *Physical Review B - Condensed Matter and Materials Physics*, 68(19):12–15, 2003.

[76] John J. L. Morton, Alexei M. Tyryshkin, Richard M. Brown, Shyam Shankar, Brendon W. Lovett, Arzhang Ardavan, Thomas Schenkel, Eugene E. Haller, Joel W. Ager, and S. A. Lyon. Solid-state quantum memory using the 31P nuclear spin. *Nature*, 455(7216):1085–1088, oct 2008.

[77] Alexei M. Tyryshkin, Shinichi Tojo, John J. L. Morton, Helge Riemann, Nikolai V. Abrosimov, Peter Becker, Hans-Joachim Pohl, Thomas Schenkel, Michael L. W. Thewalt, Kohei M. Itoh, and S. A. Lyon. Electron spin coherence exceeding seconds in high-purity silicon. *Nature Materials*, 11(2):143–147, dec 2011.

[78] M Steger, K. Saeedi, M. L. W. Thewalt, J. J. L. Morton, H. Riemann, N. V. Abrosimov, P. Becker, and H.-J. Pohl. Quantum Information Storage for over 180 s Using Donor Spins in a 28Si "Semiconductor Vacuum". *Science*, 336(6086):1280–1283, jun 2012.

[79] G. Feher. Electron spin resonance experiments on donors in silicon. I. Electronic structure of donors by the electron nuclear double resonance technique. *Physical Review*, 114(5):1219–1244, 1959.

[80] Jarryd J Pla, Kuan Y Tan, Juan P Dehollain, Wee H Lim, John J L Morton, David N Jamieson, Andrew S Dzurak, and Andrea Morello. A single-atom electron spin qubit in silicon. *Nature*, 489(7417):541–545, sep 2012.

[81] Kuan Yen Tan, Kok Wai Chan, Mikko Möttönen, Andrea Morello, Changyi Yang, Jessica Van Donkelaar, Andrew Alves, Juha Matti Pirkkalainen, David N. Jamieson, Robert G. Clark, and Andrew S. Dzurak. Transport Spectroscopy of single phosphorus donors in a silicon nanoscale transistor. *Nano Letters*, 10(1):11–15, 2010.

[82] Mateusz Tomasz Madzik. *Two-qubit gates with ion-implanted phosphorus donors in silicon*. Phd. thesis, University of New South Wales, 2020.

[83] Jessica Van Donkelaar, C. Yang, A. D.C. Alves, J. C. McCallum, C. Hougaard, B. C. Johnson, F. E. Hudson, A. S. Dzurak, A. Morello, D. Spemann, and D. N. Jamieson. Single atom devices by ion implantation. *Journal of Physics Condensed Matter*, 27(15), 2015.

[84] Andrea Morello, Jarryd J. Pla, Patrice Bertet, and David N. Jamieson. Donor Spins in Silicon for Quantum Technologies. *Advanced Quantum Technologies*, 3(11):2000005, 2020.

[85] Y. He, S. K. Gorman, D. Keith, L. Kranz, J. G. Keizer, and M. Y. Simmons. A two-qubit gate between phosphorus donor electrons in silicon. *Nature*, 571(7765):371–375, 2019.

[86] B. Voisin, J. Bocquel, A. Tankasala, M. Usman, J. Salfi, R. Rahman, M. Y. Simmons, L. C.L. Hollenberg, and S. Rogge. Valley interference and spin exchange at the atomic scale in silicon. *Nature Communications*, 11(1):1–11, 2020.

[87] John King Gamble, N. Tobias Jacobson, Erik Nielsen, Andrew D. Baczewski, Jonathan E. Moussa, Inès Montaño, and Richard P. Muller. Multivalley effective mass theory simulation of donors in silicon. *Physical Review B - Condensed Matter and Materials Physics*, 91(23):1–9, 2015.

[88] Daniel Loss and David P. DiVincenzo. Quantum Computation with Quantum Dots. *Physical Review A*, 57(1):12, 1998.

[89] J R Petta, a C Johnson, J M Taylor, E a Laird, A Yacoby, M D Lukin, C M Marcus, M P Hanson, and a C Gossard. Coherent Manipulation of Coupled Electron Spins in Semiconductor Quantum Dots. *Science*, 309(September):2180–2184, 2005.

[90] M Veldhorst, C H Yang, J C C Hwang, W Huang, J P Dehollain, J T Muhonen, S Simmons, A Laucht, F E Hudson, K M Itoh, A Morello, and A S Dzurak. A two-qubit logic gate in silicon. *Nature*, 526:410–414, 2015.

[91] Guilherme Tosi, Fahd A Mohiyaddin, Vivien Schmitt, Stefanie Tenberg, Rajib Rahman, Gerhard Klimeck, and Andrea Morello. Silicon quantum processor with robust long-distance qubit couplings. *Nature Communications*, 8(1):450, dec 2017.

[92] Martin Fuechsle, Jill A Miwa, Suddhasatta Mahapatra, Hoon Ryu, Sunhee Lee, Oliver Warschkow, Lloyd C L Hollenberg, Gerhard Klimeck, and Michelle Y Simmons. A single-atom transistor. *Nature nanotechnology*, 7(4):242–246, 2012.

[93] Jessica A. Van Donkelaar, Andrew D. Greentree, Andrew D C Alves, Lenneke M. Jong, Lloyd C L Hollenberg, and David N. Jamieson. Top-down pathways to devices with few and single atoms placed to high precision. *New Journal of Physics*, 12(6):065016, jun 2010.

[94] T. F. Watson, B. Weber, M. G. House, H. Büch, and M. Y. Simmons. High-Fidelity Rapid Initialization and Read-Out of an Electron Spin via the Single Donor D Charge State T. *Physical Review Letters*, 115(16):166806, oct 2015.

[95] Samuel J. Hile, Lukas Fricke, Matthew G. House, Eldad Peretz, Chin Yi Chen, Yu Wang, Matthew Broome, Samuel K. Gorman, Joris G. Keizer, Rajib Rahman, and Michelle Y. Simmons. Addressable electron spin resonance using donors and donor molecules in silicon. *Science Advances*, 4(7):eaaq1459, jul 2018.

[96] Lukas Fricke, Samuel James Hile, Prasanna Pakkiam, and Michelle Y. Simmons. To be published. 2021.

[97] H. Büch, S. Mahapatra, R. Rahman, A. Morello, and M. Y. Simmons. Spin readout and addressability of phosphorus-donor clusters in silicon. *Nature Communications*, 4:ncomms3017, jun 2013.

[98] M. A. Broome, T. F. Watson, D. Keith, S. K. Gorman, M. G. House, J. G. Keizer, S. J. Hile, W. Baker, and M. Y. Simmons. High-Fidelity Single-Shot Singlet-Triplet Readout of Precision-Placed Donors in Silicon. *Physical Review Letters*, 119(4):046802, jul 2017.

[99] B. Weber, S. Mahapatra, H. Ryu, S. Lee, A. Fuhrer, T. C. G. Reusch, D. L. Thompson, W. C. T. Lee, G. Klimeck, L. C. L. Hollenberg, and M. Y. Simmons. Ohm's Law Survives to the Atomic Scale. *Science*, 335(6064):64–67, jan 2012.

[100] Matthias Koch, Joris G. Keizer, Prasanna Pakkiam, Daniel Keith, Matthew G. House, Eldad Peretz, and Michelle Y. Simmons. Spin read-out in atomic qubits in an all-epitaxial three-dimensional transistor. *Nature Nanotechnology*, page 1, jan 2019.

[101] Thomas F. Watson, Bent Weber, Yu Ling Hsueh, Lloyd C.L. Hollenberg, Rajib Rahman, and Michelle Y. Simmons. Atomically engineered electron spin lifetimes of 30 s in silicon. *Science Advances*, 3(3):1–7, 2017.

[102] G. Binnig, H Rohrer, Ch Gerber, and E Weibel. Surface Studies by Scanning Tunneling Microscopy. *Physical Review Letters*, 49(1):57–61, jul 1982.

[103] G. Binnig, H. Rohrer, Ch Gerber, and E. Weibel. Tunneling through a controllable vacuum gap. *Applied Physics Letters*, 40(2):178–180, 1982.

[104] D. M. Eigler and E. K. Schweizer. Positioning single atoms with a scanning tunnelling microscope. *Nature*, 344(6266):524–526, apr 1990.

[105] J. A. Stroscio and D. M. Eigler. Atomic and Molecular Manipulation with the Scanning Tunneling Microscope. *Science*, 254(5036):1319–1326, nov 1991.

[106] J. W. Lyding, T. C. Shen, J. S. Hubacek, J. R. Tucker, and G. C. Abeln. Nanoscale patterning and oxidation of H-passivated Si(100)-21 surfaces with an ultrahigh vacuum scanning tunneling microscope. *Applied Physics Letters*, 64(15):2010–2012, 1994.

[107] S. R. Schofield, N. J. Curson, M. Y. Simmons, F. J. Rueß, T. Hallam, L. Oberbeck, and R. G. Clark. Atomically precise placement of single dopants in Si. *Physical Review Letters*, 91(13):2–5, 2003.

[108] K. E.J. Goh, L. Oberbeck, M. Y. Simmons, A. R. Hamilton, and M. J. Butcher. Influence of doping density on electronic transport in degenerate Si:P δ -doped layers. *Physical Review B - Condensed Matter and Materials Physics*, 73(3):1–6, 2006.

[109] L. Oberbeck, N.J. Curson, T. Hallam, M.Y. Simmons, and R.G. Clark. STM imaging of buried P atoms in hydrogen-terminated Si for the fabrication of a Si:P quantum computer. *Thin Solid Films*, 464-465:23–27, oct 2004.

[110] T. C. Shen, C Wang, G. C. Abeln, J R Tucker, J W Lyding, Ph Avouris, and R E Walkup. Atomic-Scale Desorption Through Electronic and Vibrational Excitation Mechanisms. *Science*, 268(5217):1590–1592, jun 1995.

[111] M. Rudolph, S. M. Carr, G. Subramania, G. Ten Eyck, J. Dominguez, T. Pluym, M. P. Lilly, M. S. Carroll, and E. Bussmann. Probing the limits of Si:P δ-doped devices patterned by a scanning tunneling microscope in a field-emission mode. *Applied Physics Letters*, 105(16), 2014.

[112] Martin Fuechsle. *Precision Few-Electron Silicon Quantum Dots*. PhD thesis, UNSW, 2011.

[113] Xiao Deng, Pradeep Namboodiri, Kai Li, Xiqiao Wang, Gheorghe Stan, Alline F. Myers, Xinbin Cheng, Tongbao Li, and Richard M. Silver. Silicon epitaxy on H-terminated Si (100) surfaces at 250C. *Applied Surface Science*, 378:301–307, 2016.

[114] Sarah R. McKibbin, Warrick R. Clarke, and Michelle Y. Simmons. Investigating the surface quality and confinement of Si:P δ -layers at different growth temperatures. *Physica E: Low-Dimensional Systems and Nanostructures*, 42(4):1180–1183, 2010.

[115] M. G. House, T. Kobayashi, B. Weber, S. J. Hile, T. F. Watson, J. van der Heijden, S. Rogge, and M. Y. Simmons. Radio frequency measurements of tunnel couplings and singlettriplet spin states in Si:P quantum dots. *Nature Communications*, 6:8848, nov 2015.

Chapter 3

Flopping-mode qubits: the need for magnetic-gradient engineering

Semiconductor spin qubits together with superconducting qubits and ion-trap qubits offer a promising platform for building a large-scale universal quantum computer. As described in Chapter 2, all three platforms face varying challenges for scaling up processors to a size that allows solving useful problems in a reasonable time. For semiconductor spin qubits, the two major challenges that we focus on in this thesis are the need for fast ($\sim$ ns) gates and the need for long range qubit coupling mechanisms. A variety of different spin-qubit implementations offer possible solutions to those challenges, with qubits based on single electron spins as well as multiple ones (singlet/triplet as well as exchange only/resonant exchange qubits). We argue that qubits based on a single electron spin are one of the most promising qubit implementations to meet these challenges.

Single-spin qubits can be manipulated by high-frequency magnetic fields in a process called electron-spin resonance (ESR). They have demonstrated high-fidelity single-qubit and two-qubit gates in silicon [1, 2]. However, to date single-qubit and two-qubit gate times have been limited to a few microseconds, about two orders of magnitude slower than superconducting qubit gates. This slower gate speed arises from the use of magnetic control directly translates into the universal quantum processor being about two orders of magnitude slower when using the spin qubit platform as opposed to the superconducting one.[1] The macroscopic antenna needed to produce the high-frequency magnetic fields that drive the spin have a large ($\sim$ mm^2) footprint. This is a significant challenge when scaling up the number of qubits.

[1] provided the single-qubit and two-qubit gates are the time-limiting operation. This is not strictly the case as measurements are still the limiting operation.

Whilst, long-distance qubit coupling of such single spins has not been demonstrated alternative architectures based on global magnetic control have been proposed [3] but limit fabrication tolerances.

In parallel, there has been a growing interest in EDSR to control single-spin qubits with local electric fields. Electric-dipole spin resonance is achieved by coupling the spin to the charge degree-of-freedom [4]. This spin–charge coupling can be created by a number of different mechanisms such as the use of large-spin–orbit-coupling materials [5, 6, 7], gradient magnetic fields from micromagnets [8, 9, 10, 11], and the hyperfine interaction between the electrons and surrounding nuclear spins [12, 13, 14]. Electric driving only necessitates a single gate to generate the driving electric field, as opposed to a macroscopic antenna for magnetic driving, and is generally an order of magnitude faster, thanks to the strong coupling of electric fields to the charge of the electron.

Recent proposals for EDSR using single electron spins have focused on the creation of large dipole moments so that the qubits can not only be driven faster than conventional EDSR but can also be coupled to a superconducting microwave cavity for circuit-quantum electrodynamics (cQED) [15, 16], allowing for qubit coupling over millimetres. The large dipole moment is formed by a superposition of charge states between two QDs [17] or by QD/donor hybrid [12] systems, in what is called flopping-mode operation. The additional charge degree of freedom of the flopping-mode qubit results in the formation of dephasing sweet spots — device tuning parameters for which the qubit is protected from noise fluctuations, because the derivative of Hamiltonian parameters through which the noise couples, vanishes to a given number, called the order of the sweet spot. At one particular electric tuning of the flopping-mode qubit, the qubit is protected from charge noise fluctuations up to second order, and represents an attractive option for operation of the qubit [12, 18]. This operation point is called a second order sweet spot.

In this chapter we will introduce three different qubit implementations that are operated in flopping-mode. One of them is the proposal developed in this thesis and will be studied in more detail in Chapter 4. We first describe the mechanism behind the appearance of a spin electric dipole moment, and demonstrate how this not only allows for fast electric driving but also how this makes the qubit vulnerable to charge noise. To investigate if the benefit of the faster driving can outweigh the vulnerability to charge noise we then build a qubit-error model that captures not only charge- and magnetic-dephasing errors, but also relaxation and leakage errors. Finally, we will numerically optimise the error of a generic flopping-mode qubit, and show that

engineering a low longitudinal energy gradient is instrumental in protecting the qubit from charge noise while still allowing strong electrical driving. This longitudinal gradient corresponds to the change of the qubit energy with electric field and has a different physical origin in each of the three different physical implementations of the flopping mode qubit. Using the same error model we show that operation of the qubit at the second-order charge dephasing sweet spot is actually detrimental to the qubit total error when performing a x- or y- gate, contrary to previous suggestions in the literature [12, 18].

The work for this chapter was performed by this author, with help from Dr.Yu He, and supervision by Dr. Samuel Gorman. Some of the work presented here is the object of provisional Australian patent application 2021900702, and is under review for publication [19].

3.1 Advances in electrical control and coupling of semiconductor spin qubits

Spin qubits in semiconductors offer a very promising pathway for universal quantum computing (see Sect. 2.1.3). A fully isolated spin qubit can be controlled through an oscillating magnetic field coupling to the spin's magnetic moment. Coherent single spin control was first demonstrated in a quantum dot (QD) in 2006 by Koppens *et al.* [20] in a QD defined in a GaAs/AlGaAs heterostructure using electrostatic gates to locally deplete a two dimensional electron gas (2DEG), and a microwave titanium/gold strip line antenna (see Fig. 3.1 a). In this initial device, the spin coherence was of a comparable magnitude to the oscillation period so that only a few oscillations were observed before dephasing occurred. Since this time, magnetic single spin control in QD qubits has been perfected to a point that magnetically controlled single spin qubit display the best control fidelities of any semiconductor qubit, outperforming even superconducting single qubit gates. Indeed, Yang *et al.* recently demonstrated an averaged π-gate error of 4.3×10^{-4} in $2\,\mu$s [21] (see Fig. 3.1 b) using a QD defined by electrostatic gates at a silicon metal-oxide-semiconductor (SiMOS) interface. In this work the oscillating magnetic field was also applied using a microwave strip line this time made from aluminium compared to the titanium/gold antenna used by Koppens in the original experiment. Similar errors and gate times were demonstrated on electron spins confined to a single phosphorus donor in silicon by Muhonen *et al.*, with an average π-gate error of 10×10^{-4} in $3\,\mu$s in Ref. [22] (see Fig. 3.1 c), using a similar antenna design. In the same device, even higher control

fidelities where achieved on the phosphorus donor nuclear spin, with a π-gate error of 1×10^{-4}, but a slower π-gate time of $\sim 150\,\mu$s. While state-of-the-art magnetic electron spin control outperforms the superconducting single qubit gates by a factor 2 (see Table 2.1), currently the gate times in these gate-defined devices are almost two orders of magnitude longer. Faster control would help bring control errors down to levels achieved in ion trap qubits and nitrogen vacancy centres in diamonds in which errors in the 10^{-5} range have been reported [21]. The capability to perform long distance coupling of magnetically controlled spins in semiconductors [23] provides an important technological advance that has not yet been demonstrated.

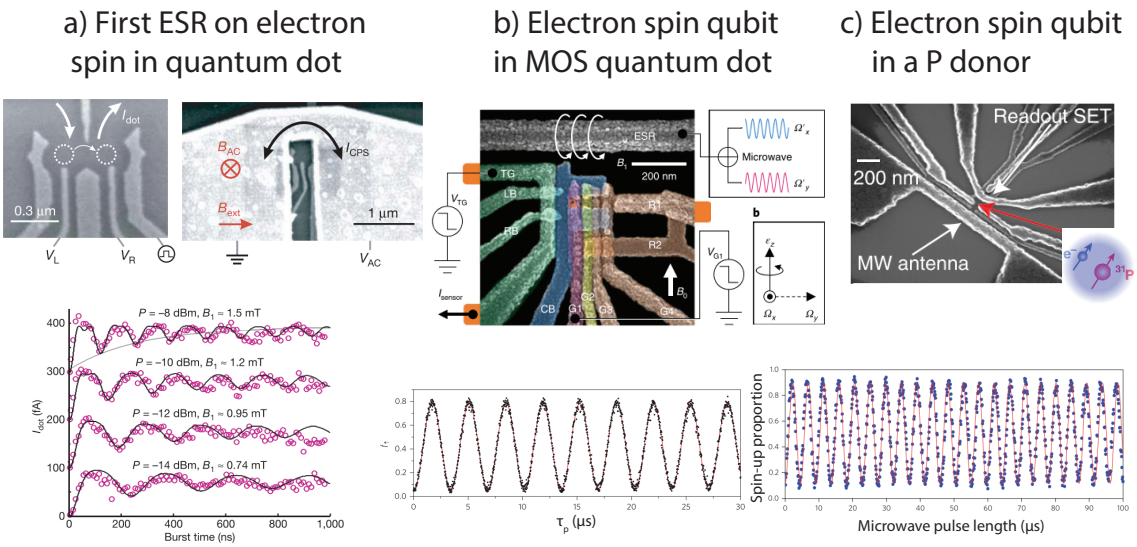

Figure 3.1: **Magnetic control of electron spin qubits by electron spin resonance (ESR). a)** First demonstration of ESR in GaAs/AlGaAs QDs by Koppens *et al.* [20]. **b)** State-of-the-art ESR in gate defined QDs demonstrating a $2\,\mu$s π gate with 4.3×10^{-4} error in a MOS QD [21] (Rabis oscillation from a similar device from ref. [24]). **c)** State-of-the-art ESR of an electron spin on a single phosphorus donor in silicon, demonstrating a $3\,\mu$s π gate with 5×10^{-4} error [22] (Rabi oscillations of same device from ref. [1]).

3.1.1 Charge qubits

The charge qubit is the system of choice for fast control and coupling of a condensed matter qubits. Indeed, as early as 1999, almost a decade before the first coherent single spin control, Nakamura *et al.* demonstrated the first electrically controlled qubit in a solid state device [25], where the two qubit levels are defined by two charge states on a superconducting island called a Cooper pair box (CPB). These qubits are connected to each other via tunnelling of an electron pair quasiparticle called a Cooper pair from a superconducting reservoir through a Josephson tunnel junction.

While the coherence time of this charge qubit was quite short (not measured, but estimated at about 1 ns), very fast Rabi frequencies of about 10 GHz were demonstrated. Five year later, Wallraff *et al.* demonstrated strong coupling of such a CPB qubit to a superconducting cavity [15], with a coupling strength larger than either the coherence time of the qubit or the relaxation time of a cavity photon. This result paved the way for long distance coupling of superconducting charge qubits. Combined these two experiments have demonstrated that charge qubits can be used to achieve very fast (nanoseconds) driving strength using only electric fields.

From this time it was another four years until the charge qubit was first implemented in semiconductor QDs by Hayashi *et al.* in 2003 using a double quantum dot (DQD) defined by electrostatic gates on top of a GaAs/AlGaAs heterostructure [26] (see Fig. 3.2 a). Hayashi et. al demonstrated fast coherent control, with Rabi frequencies about 2.3 GHz. However, the coherence time, T_2^* of this system was only ~ 1 ns, translating into a Q-factor, $Q = f_R T_2^* \sim 2$ (see Fig. 3.2 b). Using the simplest error model (see Eq. B.4.17 in Appendix Sect. B.4), a Q factor of ~ 30 (~ 100) is needed for 1%(0.1%) error rates. Since this first experiment by Hayashi *et al.*, many subsequent implementations of a charge qubit have been demonstrated in gate defined QDs in GaAs/AlGaAs and SiGe heterostructure [27, 28, 29, 30], with coherence times T_2^* ranging from 1 to 7 ns, and Rabi frequencies from 1 to 3 GHz corresponding to Q factors between 1 and 10. The implementation by Gorman *et al.* [28] using silicon-on-insulator QDs falls outside of this with much longer coherence times $T_2^* \approx 220$ ns but slower Rabi frequencies of about 62 MHz corresponding to a Q factor of 14. In this experiment, the charge dephasing time was increased by a factor 30 compared to similar experiments by Petersson *et al.* [29], by using a device where the DQD and control leads were are etched out of the Si/SiO_2 two-dimensional electron gas instead of being electrostatically defined by surface electrodes (see Fig. 3.2 c)). In this design the electrons in the QDs are not surrounded by interfaces where charge traps can form. An alternative explanation for the increased dephasing time in the etched device was that the qubit was measured using a charge sensor that was not tunnel coupled to the DQD. Strong tunnel coupling to electron reservoirs can lead to unwanted tunnelling of electrons into the QDs meaning that the coherent electrons are lost to the reservoir resulting in control errors.

Further experiments were focused on coupling the charge qubit to a superconducting cavity [32, 33, 34] giving rise to an order of magnitude improvement in the coherence times of gate defined charge qubits. The coherence time can estimated

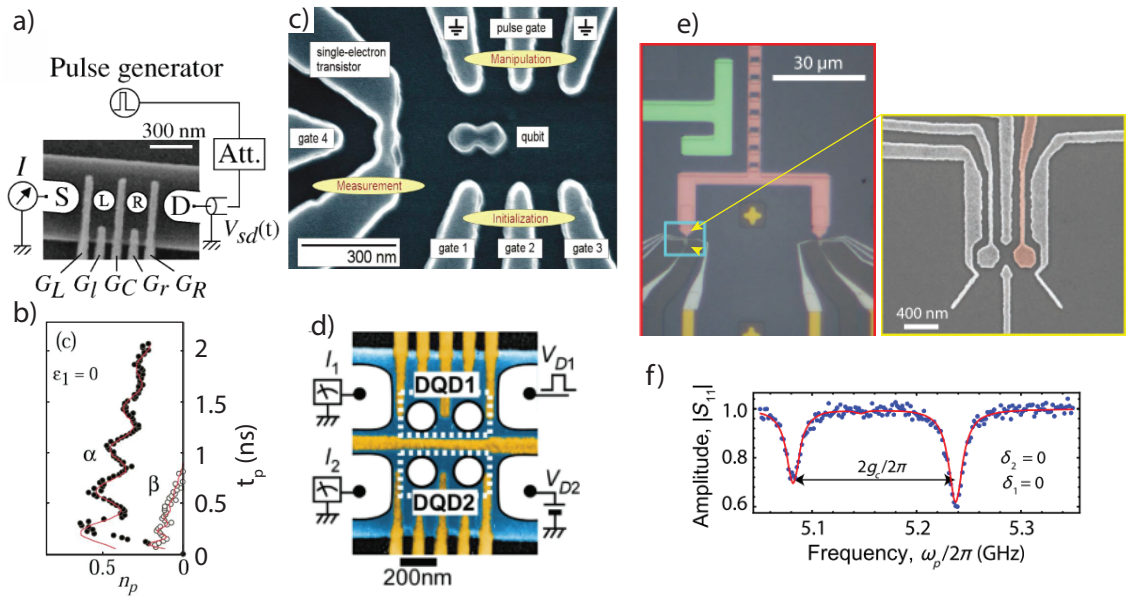

Figure 3.2: **Advances in electrical control and coupling of semiconductor charge qubits. a) and b)** The first electrically controlled charge qubit demonstrated in a GaAs DQD by Hayashi *et al.* (reproduced from Ref. [26]). The Rabi oscillations in b) demonstrated fast qubit control (~ 400 ps) with similarly short coherence times. **c)** Increases in the charge qubit coherence time to ~ 220 ns could be achieved by Gorman *et al.* using an etched heterostructure to reduce charge noise (image reproduced from Ref.[28]). **d)** Demonstration of capacitive coupling of two charge qubits by Shinkai (device image reproduced from ref. [31]). **e) and f)** Demonstration of coherent coupling of two DQD charge qubits in GaAs using a superconducting cavity (red in e). The reflection spectrum in f) shows the two coupled charge qubit bright states separated by the two-qubit coupling rate $g_c/2\pi = 77\,\mathrm{MHz}$.

in these cavity coupled qubits by measuring of the qubit linewidth when readout by the cavity and was shown to be 3 MHz (4.5 MHz) corresponding to $T_2^* \approx 50$ ns ($T_2^* \approx 35$ ns) in a GaAs/AlGaAs heterostructure in ref. [33] and ref. [34], respectively. Finally, Mi *et al.* have demonstrated linewidths of 2.5 MHz ($T_2^* \approx 64$ ns) [32]. In these three experiments coherent control was not demonstrated, however assuming the Rabi frequencies previously reported of ~ 1 GHz [26], the measured linewidths would translate into $Q \sim 100$. Such a Q-factor could reach the 1% error threshold using realistic noise models, but is orders of magnitude smaller than the Q factors demonstrated by ion-trap qubits where $Q \approx 10^6$ has been observed [35]). One charge qubit implementation by Kim *et al.* in 2015 [30] came close to fault tolerance ($< 1\%$ error rate) with single gate fidelities of 86% achieved using pure microwave electrical control of the charge qubit. Due to limits in the coherence times and Q-factors mainly arising from the presence of charge noise it remains uncertain as to whether charge qubits will reach error levels acceptable for universal quantum computation. However, as we will see, the fast electrical driving strengths of charge qubit has informed improvements in the driving strengths of spin based qubits. Before we address this, we first highlight how the study of charge qubits also provided a roadmap for long distance coupling of semiconductor spin qubits, a crucial milestone for scaling up universal quantum computers. Advances towards long distance coupling of two charge qubits in semiconductors have ranged from the initial demonstration of capacitive coupling between two charge qubits in 2009 ([31, 36]), using two DQDs in GaAs/AlGaAs (coupling distance of about 300 nm, see Fig. 3.2 d). Beyond this has been the demonstration of photon mediated interaction in a GaAs/AlGaAs heterostructure between two charge qubits over $\sim 50\,\mu$m (see Fig. 3.2 e and f) to over $\sim 300\,\mu$m between a charge qubit and a transmon qubit using a microwave cavity by Woerkom *et al.* in 2018 [37] and Scarlino *et al.* in 2019 [38], respectively. An important milestone on the road to demonstrating such photon mediated long distance coupling between qubits is the demonstration of strong coupling of the qubit to a cavity. The strong coupling regime is achieved when the coupling of the qubit to the cavity, g is larger than the decoherence rate, γ and photon decay rate of the cavity, κ. That is, $g^2/\gamma\kappa > 1$. Strong coupling was first demonstrated by Petersson *et al.* in 2012 [16] in a DQD defined using metallic gates deposited on an Indium Arsenide (InAs) nanowire. The strong coupling regime has since been demonstrated in gate-defined QDs in a GaAs/AlGaAs heterostructure in 2017 by Stockklauser [39] and by Mi *et al.* [32] in Si/SiGe.

To conclude we have shown that charge qubits have pioneered key advances in

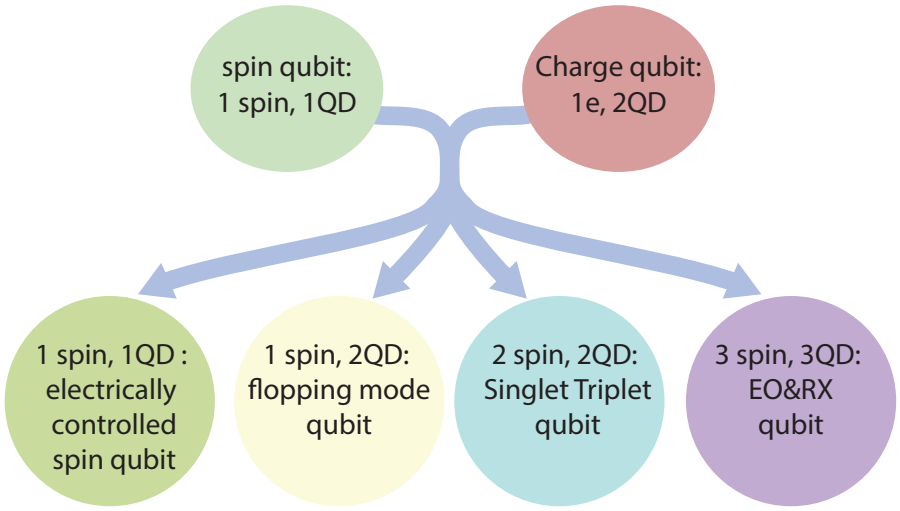

Figure 3.3: **A schematic showing how hybrid qubits can evolve from single spin and single charge qubits.** The pure spin qubit can be combined with the principle of the charge qubit into a multitude of spin-charge hybrids that hybridise a particle's (electron or hole) spin to its charge degree of freedom in either one (1 QD), two (2QDs) or three (3 QDs) to allow electrical control of the spin.

fast driving and long distance coupling of semiconductor qubits. However, due to the strong vulnerability of charge qubits to noise arising from electric field fluctuations, the errors of charge qubits have remained below the error threshold for quantum error correction using the surface code. This is a crucial reason as to why, shortly after the first demonstration of a semiconductor charge qubit in semiconductors in 2003, the semiconductor community has turned its focus to spin qubits due to the remarkably long coherence times already demonstrated in bulk ESR experiments [40]. The charge qubit has however, highlighted that electrical control could offer a way towards very fast qubit control, and has since served as a testbed for long distance coupling of qubits in semiconductors using microwave cavities.

Whilst charge qubits have demonstrated fast driving with short coherence times magnetically-driven single spin qubits have demonstrated weak driving strengths but promising long coherence times in isotopically purified materials. In the past 20 years, a multitude of hybrid qubit implementation in semiconductors have been proposed to best combine the advantages of each implementation without suffering from their respective drawbacks. Such "hybrid" spin-charge qubits range from the singlet triplet qubit where two spins are shared between two QDs [41, 42] to the exchange-only (EO) qubit [43] and resonant exchange (RX) qubit [44, 45] (three spins across three QDs), to the flopping-mode qubit [18, 46] (one spin hosted on two QDs) and the electrically driven spin qubit in a single QD [47, 48] (see Fig. 3.3).

In the following we will review how successfully each of these four spin-charge

hybrid implementations has been in bringing together the advantages of the charge and spin qubits over the past 15 years. The ultimate goal of these hybrid systems is to demonstrate a fast ($\sim$ ns) electrically driven qubit with low error ($< 1\%$) that can be coupled over long distances (> 10 μm) using microwave cavities.

3.1.2 Electric driving and coupling of a single spin in a single quantum dot

We first review the progress of electrical control and coupling of single spins in single QDs. In such implementations, the coupling of the spin to the charge degree of freedom has been achieved through various mechanisms which we consider here including the asymmetric g-factor modulation, hyperfine coupling, spin-orbit interaction and a micromagnet induced magnetic gradient.

Electric spin manipulation through g-factor modulation was first demonstrated by Kato *et al.* in 2003 in a parabolic quantum well within a GaAs/AlGaAs heterostructure hosting many electrons [49]. The effect relies on the electric field dependence of an asymmetric g-tensor, that translates into a Zeeman term transverse to the static magnetic field. An oscillating electric field at the frequency defined by the longitudinal Zeeman splitting, then creates a transverse oscillating term that can drive Rabi oscillations between the spin down and up states.

A second mechanism to couple the spin and charge (or orbital) degree of freedom is the intrinsic spin-orbit (SO) coupling present materials such as GaAs and InAs heterostructures. Here, the intrinsic SO coupling in a GaAs QD served as a basis for electric driving of spins as early as 2003 [50, 51] resulting in the first demonstration of electrical driving of a single electron spin in semiconductor QDs by Nowack *et al.*. in 2007 [48]. In Nowack's experiment, performed only a year after the first demonstration of magnetically driven spin resonance by Koppens *et al.*, Rabi frequencies of ~ 4 MHz were attained limited by the strength of the SO interaction (spin-orbit length, $l_{SO} \approx 30$ μm which is inversely proportional to the Rabi frequency) in GaAs (see Fig. 3.4 a). Later implementations in InAs nanowires attained Rabi frequencies around 50 MHz [16, 52] due to an enhanced spin-orbit interaction ($l_{SO} \approx 150$ nm). However, the qubits suffered from relatively short coherence time ($T_2^* \approx 8$ ns and $T_2^{\text{Hahn}} \approx 8$ ns in Ref. [52]) due to the coupling of the qubit to charge noise. This illustrates a common issue shared by many electrically driven spin qubits, namely that coupling the spin to electric fields for electric driving also increases the coupling of the spin to charge noise. We will show that more complex spin-charge hybrid qubits have been engineered to reap the benefits of faster qubit driving without

proportionally increasing the susceptibility to charge noise.

Electrical driving of spins trough the spin-orbit effect was also demonstrated on hole spins as early as 2013 by Pribiag *et al.* [53] in an InSb nanowire. Hole spins have also been confined in gate defined QDs within a Ge/SiGe heterostructure by Hendrickx *et al.* in 2020 [54]. Hendrickx *et al.* demonstrated large Rabi frequencies up to 57 MHz with coherence times of 100 to 400 ns (compared to $T_2^* \approx 8$ ns electron spin qubits [52]). While these qubit characteristics correspond to Q factors of $\sim$ 23, well below those shown by state-of-the-art electron spin qubits, improvements in the coherence times can be achieved through engineering sweet spots at which the susceptibility of the spin to electric field is minimised [55], with Wang *et al.*. predicting Q factors as large as 10^5. If achievable, such improvements would make this platform a viable candidate for large scale quantum computing.

Spin transitions can also be driven electrically by utilising a micromagnet. The micromagnet can produce a magnetic gradient over the location of the QD. Moving the electron within that magnetic gradient using an oscillating electric field can then be used to drive spin transitions. This concept was first proposed and formalised in 2006 in Ref. [47], in which Tokura *et al.* described the oscillatory motion of the electron as an electric-field dependent hybridisation of the symmetric ground state QD orbital, with the first excited state antisymmetric orbital (see Fig. 3.4 b for an electric field pointing to the left). This mechanism was then first demonstrated in 2008 [56] by measuring the spectra from the spins in two separate QDs (in a GaAs/AlGaAs heterostructure) driven electrically within a magnetic gradient induced by a cobalt micromagnet (Fig. 3.4 c). Improved micromagnet designs [57] have since yielded coherent two-axis electrical control in a Si/SiGe heterostructure in 2014 with a Rabi frequency of 5 MHz [58] and a Rabi frequency of up to 127 MHz with 96% control fidelity in a GaAs/AlGaAs QD [59].

The control fidelity of such electrically driven spins within a single QD using a micromagnet induced magnetic field gradient has been further improved by manufacturing the QDs in isotopically purified Si/SiGe heterostructures. This strategy was employed in 2018 by Yoneda *et al.* in a landmark experiment [8] that demonstrated the first spin control fidelities above 99.9% in semiconductor qubits. The coherence time $T_2^* \approx 20\mu s$ of the spin qubit was shown to be limited by charge noise and not by magnetic noise, as had been the case with previous spin qubits (see Fig. 3.4 d). The high fidelities were achieved at Rabi frequencies of ~ 4 MHz. Such driving speeds are an order of magnitude faster than that of state-of-the-art magnetic driving of single electron spins [21] ($\sim$ 0.5 MHz with fidelities above

99.9% also), but still an order of magnitude below driving speeds of state-of-the-art superconducting qubits [60] ($\sim$ 60 MHz with fidelities above 99.9%).

In the same experiment Yoneda *et al.* could reach driving speeds comparable to those of superconducting qubits, with Rabi frequencies up to 30 MHz ($t_\pi \approx 33$ ns). However at driving speeds much faster than the optimal one of 4 MHz, the fidelity of the gates decreased starkly. This is reflected in a drop in the Rabi oscillation Q factor from 444 to 14 when driving at 20 MHz instead of the optimal 4 MHz. The decrease in the Q factor at higher Rabi frequencies is attributed to heating and/or population leakage. A similar decrease in the quality factor of the Rabi oscillation was observed in a different device by Takeda *et al.* [61]. As pointed out by Takeda and coworkers, heating and leakage can be reduced without decreasing the speed of operation, by increasing the magnetic field produced by the micromagnet or by increasing the electric coupling of the driving gate to the electron. Both can be achieved by manufacturing the micromagnet or the gate closer to the quantum dot.

In summary, the experiment of Yoneda *et al.* shows that electrically driven spins can maintain the very high fidelities of magnetically driven spin qubits while achieving driving speeds one order of magnitude faster [21, 22]. An additional order of magnitude improvement in the gate speed was also demonstrated, albeit with a decrease in the qubit control fidelity. This decrease in the control fidelity might be avoided by improvements in the device design. With such improvements, single qubits gates in spin qubits would reach the speeds and fidelities of superconducting devices.

Before moving to long distance coupling of single spins in single QDs, an alternative way of coupling the spin and charge degrees of freedom is using the hyperfine interaction of the electron with its surrounding nuclear spins. The hyperfine interaction of an electron in a GaAs/AlGaAs QD qubit with the nuclei host material was harnessed by Laird *et al.* in 2007 [62] to drive spin transitions electrically. Coherent driving was however, not achieved due to the averaging of the transverse hyperfine term over long time scales [51]. The electrically controlled hyperfine spin transitions could nonetheless be used to induce sizeable nuclear spin polarisation within the QD, generating magnetic fields up to 840 mT. While this spin-charge coupling was not pursued further for single spin EDSR in single QDs, it is crucial for magnetic field engineering of singlet triplet qubits and also forms the basis of the flopping-mode qubit proposals presented in this thesis in Chapter 4.

Despite the promising demonstrations of electrical control of single spins in single QDs reviewed above, a single spin has not yet been coupled to a cavity within a

single QD to-date despite being proposed as early as 2008 [63]. The failure to demonstrate long distance coupling using single spins in single QDs can be related to the fact that the electric fields required to couple the spin in a single QD to the cavity are much larger than those produced by today's state-of-the-art cavities, which can produce voltage fluctuation of the order of $0.5\,\mu$V as demonstrated in the double QD experiments by Samkharadze *et al.* from the Delft [64, 65] and Mi *et al.* from Princeton [32] that will be the focus of the next section. The microwave powers applied in the 2018 experiment by Yoneda to drive a spin on a single QD (displaying 99.9% fidelity) are not quoted in Ref. [8], but a prior publication [59] quotes powers of -32 to -11 dBm at the sample to achieve Rabi frequencies of 29 to 126 MHz. The voltage amplitudes associated with these driving powers are 6 and 63 mV, more than three orders of magnitude larger than the values associated with state-of-the-art cavities [64]. This disparity hinders the ability to achieve strong coupling of a spin qubit in a single QD to a cavity.

For coupling spin qubits to cavities, the community has turned towards more complex spin-charge hybrid qubits utilising several electrons spins and/or several quantum dots. These hybrid qubits offer a stronger coupling of the electric field to the charge and potentially protect those qubits from electrical noise by operation at certain qubit energies that are insensitive to electrical fluctuations, known as charge-noise sweet spots. The hybrid qubits are formed by various combination of spin and charge, such as two spins on two quantum dots (singlet triplet qubits [41, 66, 67]) or three spins on three quantum dots (the Exchange Only (EO) qubit [44, 68] and Resonant Exchange Only (RX) qubit [69, 70, 71]). This chapter and the following one will focus on the hybrid spin qubits consisting of one electrons shared by two quantum dots and which will be referred to as the flopping mode qubit.

3.1.3 Single spins in a double quantum dot: the flopping mode qubit

This section focuses on the flopping mode qubit, which is defined by a single electron in a DQD. The orbital degree of freedom (charge in left/right QD) and spin degree of freedom (spin up/down) can define both a traditional charge qubit as described earlier and a simple spin qubit. Under the right conditions, and in the presence of a magnetic field gradient, the spin and charge qubits can hybridise with each other, allowing for the spin qubit to acquire properties of the charge qubit, including an electric dipole moment, but also susceptibility to electric field noise. As with EDSR in a single QD in a magnetic field gradient, the electric driving of the spin

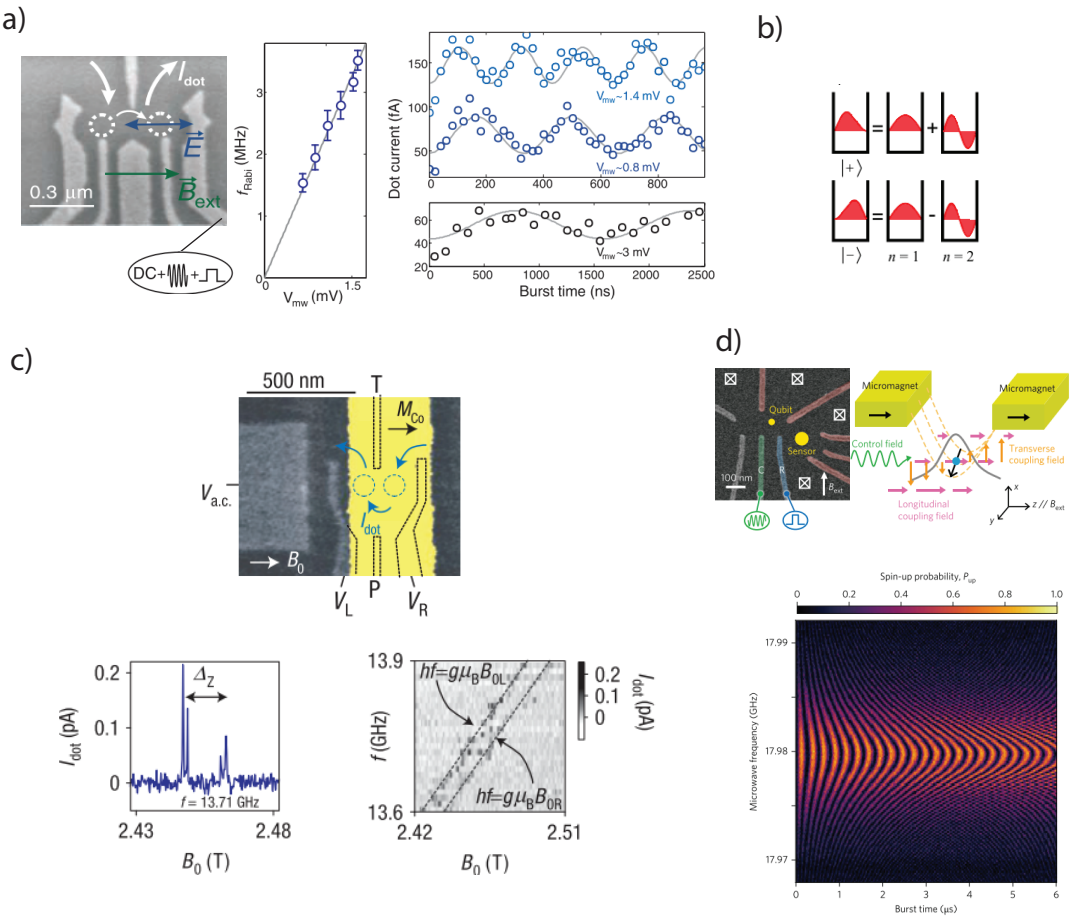

Figure 3.4: **Electrically driven resonance of a single spin in a SQD. a)** First demonstration of coherent EDSR on a spin confined to one of the QDs of a DQD in a GaAs/AlGaAs heterostructure (see SEM picture of the device on the left). Rabi oscillations are presented below, with the oscillation frequency f_{Rabi} linearly dependent on the microwave drive amplitude V_{mw} (top right). **b)** In the presence of an electric field the ground (excited) state electron wavefunction is shifted to the right(left), through hybridisation of the QD's symmetrical ground state orbital (without electric fields) to higher asymmetric QD orbitals (illustration reproduced from ref. [47]). **c)** First demonstration of selective EDSR of electron spins trapped in two separate dots of a DQD device using an integrated surface micromagnet (yellow stripe) to induce spin-orbit coupling. The EDSR spectra shows to sets of resonant peaks corresponding to the resonant flipping of electron spins in the two respective QDs (bottom left), with both peaks depending linearly on the homogeneous magnetic field B_0 (figures reproduced from ref. [56]). **d)** State-of-the-art EDSR of a single spin in a single QD using a micromagnet to induce the magnetic field gradient. The extremely clean chevron pattern on the bottom is a consequence of the high control fidelity of 99.9% (reproduced from ref. [8]).

in the DQD can be explained by the effective oscillating transverse magnetic field experienced by the spin as it is moved by an oscillating electric field between the two QDs. The motion of a spin in the single QD emerges from the electric field dependent hybridisation within excited orbitals of the same QD. The flopping mode qubit can be described in a similar manner, with orbitals of each QD needed to describe the system. The benefit of flopping-mode operation of single QD EDSR is that the coupling of the two QD orbitals can be fully engineered using realistic electric fields in a DQD. This allows for full control over the DQD charge qubits characteristics, and thus full control over the degree of spin-charge hybridisation. A second large advantage of the flopping mode qubit is that both the strength of the charge qubit electric dipole moment and the amplitude of the transverse magnetic field experienced by the spin is proportional to the distance between the QD orbitals. By separating the charge in two separate QDs typically $\sim$ 100 nm apart [26, 32] we can improve both the electric dipole moment and transverse magnetic field. This is because when the electron is equally shared between both QDs, a small electric field $\sim$ 1 kV/m can fully move the electron from one QD to the other whereas an electron confined tn a single QD would move much less under the same electric field due to the tight confinement potential.

The basic mechanism of the flopping mode qubit was first proposed by Hu *et al.* in 2012 for gate defined QD in a magnetic gradient (see Fig. 3.5 a) and explained using second-order perturbation theory [73]. Hu *et al.* proposed coupling a flopping mode qubit to a superconducting cavity where it was predicted that a two order of magnitude improvement could be achieved in the coupling strength to the superconducting cavity photon. This contrast in achievable coupling compared to single QD EDSR is due to the increased charge dipole and magnetic coupling related to the larger separation of dot orbitals as discussed above. The paper by Hu *et al.* introduced an estimation of the relaxation rate of the spin due to the magnetic field gradient ($\sim$ 1 kHz) [73], but did not provide a detailed analysis of the achievable qubit error that would include charge noise induced dephasing and relaxation as well as leakage errors.

In a subsequent publication in 2016, Beaudoin *et al.* [72] quantified the error of a quantum state transfer from a flopping mode qubit to a superconducting cavity ($\sim$ 10 %). Here, the considered dephasing errors due to electric noise coupling through the longitudinal magnetic gradient, relaxation errors due to qubit and cavity phonon relaxation as well as due to cavity decay. The dephasing errors arising from perturbations in the qubit Zeeman splitting induced by electric field noise

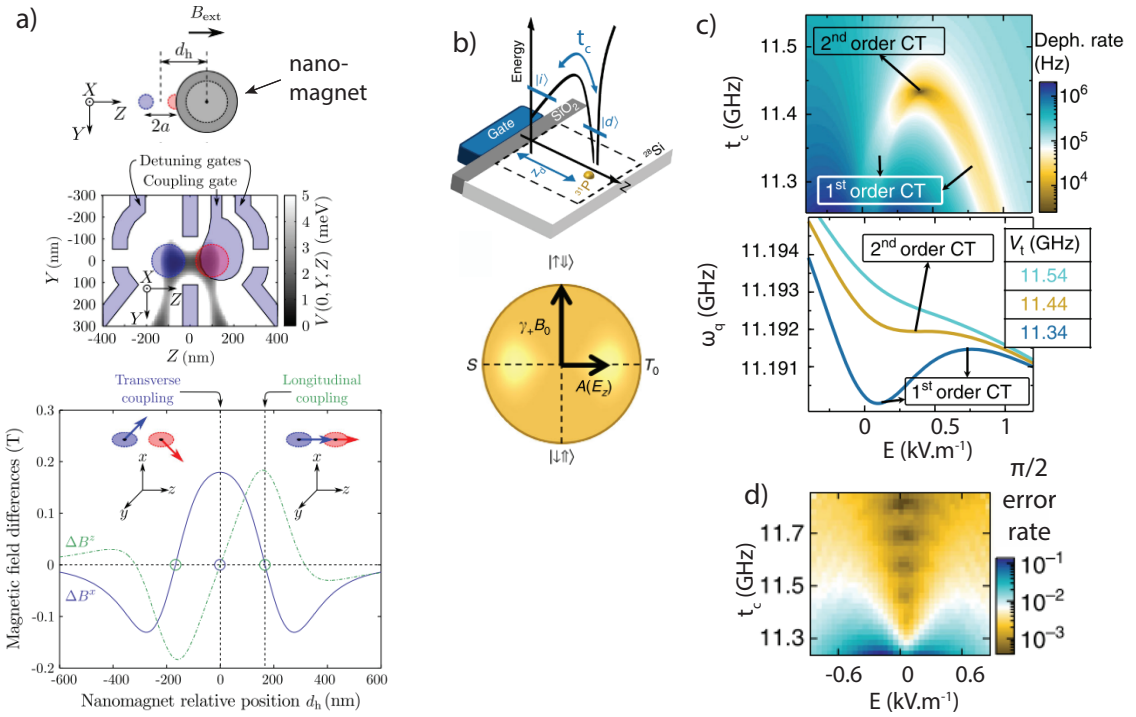

Figure 3.5: **The flopping mode qubit: a single spin in a double quantum dot.** The flopping mode qubit is defined by a single spin with a wavefunction extending to the two sites of a double quantum dot (DQD) in blue and red in **a)**. An artificial spin-orbit coupling is created by fabrication of a nano-magnet on top of the DQD (top **a)**). Careful placement of the micromagnet allows control of the transverse and longitudinal magnetic field differences ΔB^x and ΔB^z respectively. Placement at $d_h = 0$ allows maximising ΔB^x while $\Delta B^x \approx 0$, and has important repercussions on the qubit's susceptibility to charge noise. **b)** An alternative implementation of the flopping mode qubit called the flip-flop qubit that uses a phosphorus donor (P in yellow) to define the one QD and a electrostatic gate to define another QD near the Si/SiO_2 interface. The magnetic gradient is provided by the hyperfine interaction of the electron spin with the nuclear spin of the phosphorus donor. **c):** Tosi *et al.* demonstrated the presence of a second-order sweet spot (a second-order clock transition) with respect to the electric field detuning E at a particular tunnel coupling value $2t_c = 11.44\,\text{GHz}$. Here, the qubit energy splitting ω_q is insensitive to electric field fluctuations. **d)** The full error of a $\pi/2$ X-gate shows a sweet spot at zero detuning ($E = 0$) but does not exhibit a second-order sweet spot, due to presence of charge noise induced fluctuations of the Rabi frequency and leakage for a chosen drive amplitude. Images in a) and b)- d) are reproduced from references [72] and [12], respectively.

which shifts the electrons position within the stray longitudinal gradient produced by the micromagnet (parallel to the spin quantisation axis). This error is estimated analytically to second-order to be proportional to the ratio squared of the longitudinal magnetic differences Δb^z over the transverse magnetic field difference Δb^x. Additional dependences on driving strength are found in equation (14) of ref. [72]):

$$1 - F \propto \left(\frac{\Delta b^z}{\Delta b^x}\right)^2 .$$

The authors estimated through numerical simulation of the device that by careful placement of the nanomagnet above the DQD, the transverse magnetic difference could be maximised while the longitudinal difference vanishes (see a plot of both magnetic differences in Fig. 3.5 a) taken from ref. [72]. They estimated however; that a 10 nm error in the nanomagnet position is likely, yielding dephasing errors of about 0.8%, assuming a realistic cavity voltage amplitude of 0.2 μeV (50 MHz) and a noise amplitude 2.3 GHz. Neither dephasing errors due to electric field noise induced fluctuations in the dipole coupling or leakage errors were considered in this work.

In a later proposal by Tosi *et al.* in 2017 [12], a new qubit called a flip-flop qubit was proposed that consists of an electron trapped on a DQD consisting of a first QD formed by a phosphorus impurity implanted 10 nm below the silicon-silicon dioxide interface, and by a second metal-oxide-semiconductor (MOS) QD defined at that interface by electrostatic gates (see Fig. 3.5 b). The transverse magnetic field gradient is provided by the hyperfine interaction of the electron spin with the nuclear spin 1/2 of the phosphorus donor. In the following section we will show that this proposal is fundamentally equivalent to the flopping mode qubit proposed by Hu *et al.* [73]. Tosi *et al.* were the first to discuss the presence of a second-order sweet spot protecting the qubit from longitudinal dephasing errors induced by electric field noise. This second-order sweet spot appears at one particular value of the spin and charge qubit detuning, and static electric field E detuning the two dot levels. The spin and charge detuning is engineered using the electric field E, the static homogeneous magnetic field B and the tunnel coupling t_c between the two dots. The longitudinal dephasing rate is displayed as a function of E and t_c for a magnetic field 0.4 T in Fig. 3.5 c) (taken from ref. [12]) and displays the second-order sweet spot at one particular value of tunnel coupling and electric field indicated in the figure. Tosi *et al.* additionally presented a complete error model for electrically driven gates, including leakage, relaxation and dephasing errors related both to charge

noise induced variations in the qubit energy splitting (longitudinal dephasing) as well as variations in the driving amplitude (transverse dephasing). As reproduced from Fig. 3.5 d), the error experienced by the qubit during $\pi/2$ X-rotation displays a minimum when the electric field detuning vanishes. It is interesting to note that this does not occur at the location of the second-order sweet spot expected for the longitudinal dephasing error, indicating that for the particular parameters chosen here (drive amplitude and magnetic field especially), other errors were dominant with the second-order longitudinal error sweet spot not being relevant to the total error. Fig. 3.5 d indicates that gate errors below 10^{-3} are possible for this type of flopping mode qubit when driven at zero electric detuning and for a range of tunnel couplings of at least 0.5 GHz.

In 2019, Benito *et al.* [74] also disclosed the presence of a second-order sweet spot for the longitudinal dephasing of a flopping mode qubit defined using a gated defined DQD using the magnetic gradient of micromagnet. As we will study in more detail in the next sections, due to the mathematical equivalence of the flip-flop qubit [75] and the flopping mode qubit [74], the second-order sweet spot presented in both publications is related to the same physical mechanism.

The first experimental realisation of a flopping mode qubit dates back to 2015 with an implementation by Viennot *et al.* in a DQD defined in a carbon nanotube [76] (see the atomic force microscopy (AFM) image of the device in Fig. 3.6 a) using ferromagnetic PdNi leads to engineer a magnetic gradient (see magnetic force microscopy (MFM) image Fig. 3.6 b). Strong coupling of the spin to a Nb superconducting cavity was demonstrated as shown in the cavity transmission spectrum of Fig. 3.6 c), showing the cavity resonance being shifted by a spin at positive and negative magnetic fields.

The same experiment was reproduced in silicon in 2018 by both Mi *et al.* [17] and Samkharadze *et al.* [65] demonstrating strong coupling of a flopping mode spin qubit defined in Si/SiGe gate-defined DQD to superconducting microwave cavities. In both cases this represented the first demonstration of strong coupling of a spin (hybrid) qubit to a superconducting cavity in silicon, representing an important milestone for the semiconductor quantum computing community. In addition to the strong coupling (cooperativity, $C = g^2/\kappa\gamma = 5.5^2/1.8 \times 2.4 \approx 7$ of the qubit to the cavity, Mi *et al.* [17] also demonstrated readout of the flopping mode qubit through the cavity (with a measurement time of 20 μs to allow for qubit initialisation through relaxation) as well as electric driving of the spin when confined to a single QD with a frequency of 6 MHz. Importantly, by varying the degree of spin-charge hybridisation

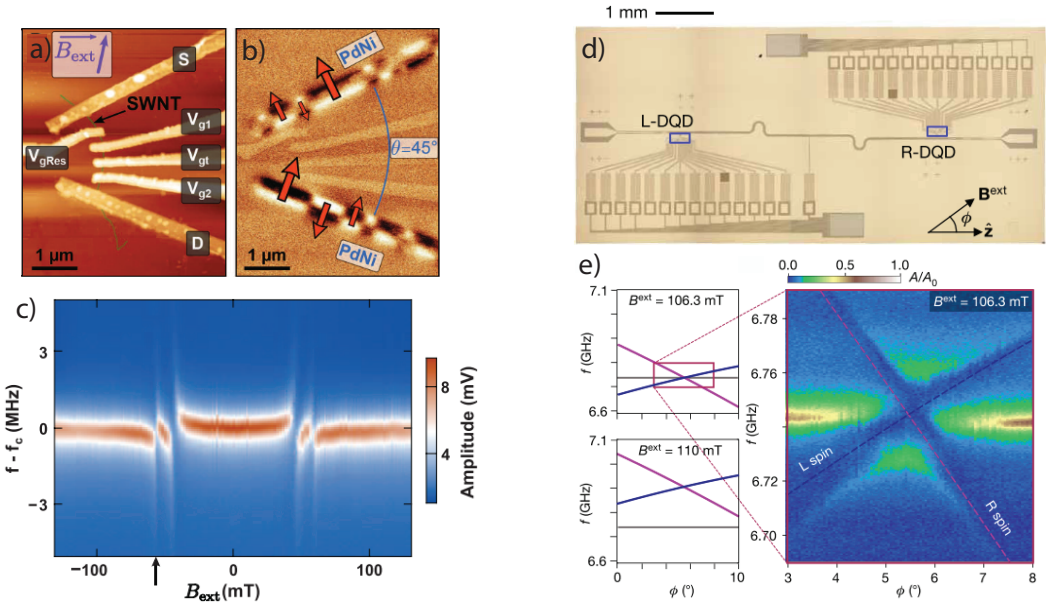

Figure 3.6: **Coupling of s flopping mode qubit to a superconducting cavity.** Strong coupling of a flopping mode qubit to a cavity was demonstrated as early as 2015 by Viennot [76] in a DQD defined within a single walled Carbon Nanotube (SWNT) visible in green in **a)**. The magnetic gradient was produced by the source and drain (S/D) leads using ferromagnetic PdNi contacts, as shown by the magnetic Force Microscopy (MFM) image of the device in b). Strong coupling of the spins to the cavity was evidenced by the transmission spectrum in c) showing the cavity resonance anti-crossing with the two valleys at positive and negative magnetic fields. **d), e)** Landmark experiment by Borjans *et al.* [77] demonstrating coherent coupling of two flopping mode spin qubits over 5 mm using a superconducting cavity (device picture in d) . Control over both the angle ϕ and magnitude B^{ext} of the external magnetic field brings both qubit transition energies in resonance with the cavity as evidenced by the avoided crossing of the three transitions visible in the transmission spectrum in **e)**. Figure a)-c) and d)-e) are reproduced from ref. [76] and [77], respectively.

using the electric field detuning parameter ϵ, Mi *et al.* demonstrated control over the spin-photon coupling by two orders of magnitude. This large controllability in the spin-photon coupling was achieved by tuning the flopping mode qubit from the two dot regime, where the wavefunction is equally shared between the two QDs with up to 1 nm displacement of the electron wavefunction by the electric driving field, to the single dot regime where the wavefunction is confined to a single QD and is only moved by an estimated 3 pm by the same electric field drive amplitude.

Coherent coupling of two flopping mode qubits via a microwave cavity was demonstrated a year later by Borjans *et al.* [77]. This also represented another landmark for semiconductor spin qubits, demonstrating the feasibility of long distance spin coupling. One important reason why coupling of two flopping mode qubit could not be performed in the earlier experiment was that the two qubit energies differed by about 40 MHz (1.5 mT) due to differences in the longitudinal magnetic field induced by the respective micromagnets deposited on each of DQD. This meant that the effective coupling was reduced due to the detuning between the two flopping mode qubits. As opposed to the EO and RX qubits, it is important to note that the flopping mode qubit splitting is mainly determined by the longitudinal static magnetic field experienced by the spin. As such, it was not possible to tune the local electric field without operating away from decoherence sweet spot and the dephasing time of the qubits was significantly reduced. Whilst electric tuning of the qubit splitting is possible through control of the tunnel coupling, the effect is a second-order process that is quite weak. Local magnetic tuning of the qubits was also not possible in that experiment since this would require additional hardware for magnetic control such as the presence of magnetic flux loops. In the 2018 experiment [17], coupling of the two qubit was therefore not possible due to the lack of local tunability in the different resonant frequencies of the two qubits but also by the fact that this difference was 8 times larger than the coupling of the individual qubits to the cavity.

In the follow-up experiment by Borjans *et al.* [77], the lack of electric tunability was counteracted by intentionally patterning the distant DQDs hosting the flopping mode qubits at an angle to each other in such a way that the DQD separation axes were not parallel to each other (30 degrees difference). In this way the difference in the two distant spins Zeeman splitting, largely defined by the projection of the large homogeneous magnetic field permeating the sample is made dependent on the angle of the DQD axis to the magnetic field. Together with control of the magnitude of the magnetic field, this gave two degrees of freedom to bring both qubit transition

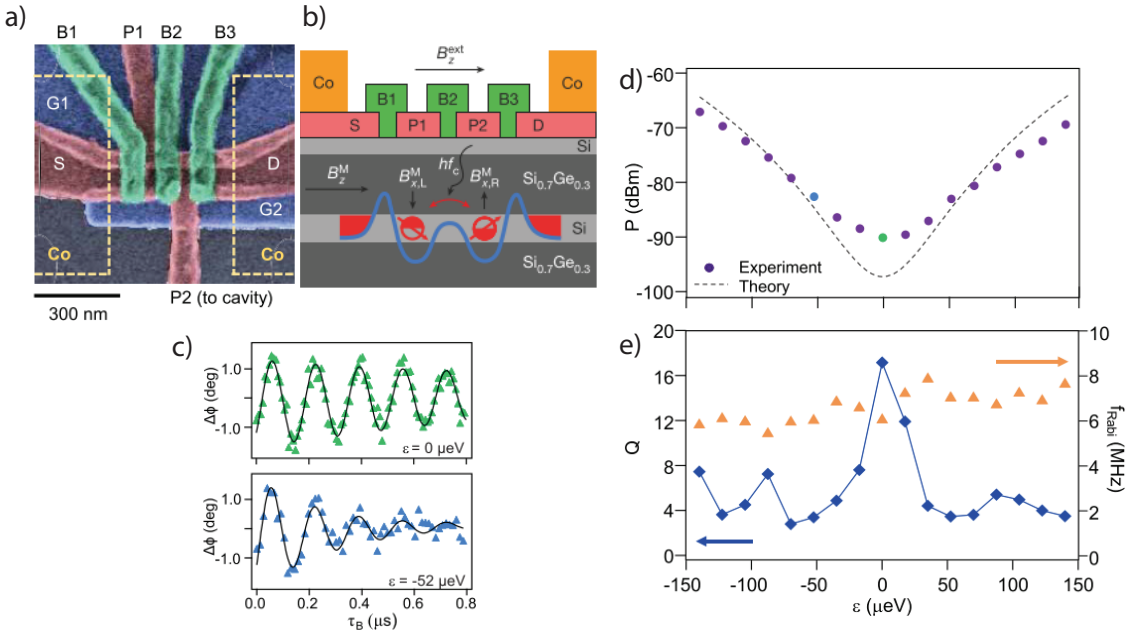

Figure 3.7: **Coherent operation of the flopping mode qubit in a Si/SiGe double quantum dot.** Here, a Si/SiGe gate defined DQD [46], is placed in a magnetic field gradient induced by a cobalt micromagnet (see SEM image of the device in a) along with an illustration of the different layers used in the device in b reproduced from Ref. [46]). Coherent oscillations of the qubit were demonstrated via cavity readout. The Q-factor (blue squares) of the Rabi oscillations for a fixed Rabi frequency (orange triangles) shows a clear maximum at zero detuning $\epsilon = 0$, demonstrating the presence of a second-order sweet spot in e). The microwave power needed to maintain a constant Rabi frequency is plotted in d) with a clear minimum at zero detuning, demonstrating that the electric drive is most efficient when the electron wave-function is shared between the two QDs. All images taken from [46] but b) which is taken from [17].

frequencies in resonance with the cavity's frequency as displayed in the magnetic field angle dependence of the cavity resonance spectrum (Fig. 3.6 e) at a magnetic field amplitude of 106.3 mT. Using this technique Borjans *et al.* demonstrated a clear resonant interaction between the two flopping mode spin qubits separated by ~ 5 mm. Whilst this proof-of-concept experiment can be used to generate long-range two-qubit gates between spatially distant spins, it is not scalable to more qubits. This is because in order to operate the flopping mode qubits at the noise sweet spots since adjusting the charge qubit splitting will move the qubit away from the sweet spot. Therefore, for true scalability of the flopping mode qubit it is likely that local magnetic field control will have to be implemented. Ultimately, if this can be achieved then it opens up the possibility of modular quantum computer architectures using long-range interconnects.

Coherent control of the flopping mode qubit (in the DQD regime) was not demon-

strated until 2020, in an experiment by Croot *et al.* [46] using a DQD device defined by electrostatic gates on a natural Si/SiGe heterostructure, using a cobalt micromagnet and a superconducting niobium superconducting cavity (see Fig. 3.7 a and b). Croot *et al.* confirmed the existence of a sweet spot at zero electric detuning $\epsilon = 0$ between the two QDs, where the qubit is insensitive to first order to electric field fluctuations. Indeed Rabi oscillations taken at $\epsilon = 0\,\mu$eV (green spot in Fig. 3.6 c) were seen to decay less than oscillations taken for the same operational parameters but away from the sweet spot, at $\epsilon = -52\,\mu$eV (blue spot, $12.57\,\text{GHz} \approx 2t_c/h$) and at higher power (to achieve the same Rabi frequency). The presence of the sweet spot in coherence is demonstrated even more clearly by measuring the Q-factor of the Rabi oscillations achieved for a range of electric detuning values $\epsilon = \pm 3 \times 2t_c/h$ in Fig. 3.6 e (blue squares). Here, they tuned the microwave power P to keep the Rabi frequency constant (the Rabi frequency is displayed as orange triangles). The Q-factor is seen to reach a clear maximum of $Q \approx 17$ at the sweet spot compared to $Q \approx 4$ detuned from the sweet spot. The power required to maintain the same Rabi frequency of approximately 7 MHz, is displayed in Fig. 3.6 d), and shows a clear minimum at the coherence sweet spot, with -90 dBm power needed at the device compared to -67 dBm at $\epsilon = -3 \times 2t_c/h$. This corresponds to a 200-fold decrease in driving power necessary to reach the same Rabi frequency, demonstrating the advantage of driving the spin at the sweet spot. At the we are in the delocalised regime where the wave function responds most strongly to the electric field drive but is protected to first-order from electric field fluctuations since the qubit energy does not change to first-order in detuning.

Note that fault tolerant operation of the flopping mode qubit has not yet been demonstrated, but the $Q \sim 17$ for both qubit control axes has been demonstrated by Croot *et al.* [46]. This value of Q corresponds to an approximate error of 3% using the simplified error formula in Eq. B.4.17 in Appendix Sect. B.4 and are promising values at this stage of development with $Q \sim 100$ typically required for fault-tolerant quantum computation.

3.1.4 Summary

In summary we have shown that hybridisation of spin qubits with their charge degree of freedom has allowed an order of magnitude speedup in the single qubit gate times, with less than an order of magnitude increase of qubit error for electrically driven single spins (see Table of qubit characteristics Table 3.1). Much faster gates ($\sim$ nanoseconds) are possible when the qubit is purely of charge character but is

accompanied by a dramatic decrease in fidelity (the best error demonstrated by a charge qubit is 14% [28]), due to increased susceptibility to charge noise. To reach strong coupling of the qubits to a superconducting cavity the electric dipole moment of the spin qubits has to be increased beyond what is possible within a single dot. It is likely that the singlet/triplet qubit in which two electrons are hosted by two QDs will be able to reach the strong coupling regime in the near future, with stronger hybridisation of the qubit to excited charge states (as seen in Ref. [78]).

To date, no spin based qubit has demonstrated both fast ($\sim$ ns) fault tolerant electric operation as well as long distance coupling to a cavity. However, the flopping-mode qubit has demonstrated Q-factors indicating that fault tolerance is within reach. Singlet/triplet qubits have shown large Q-factor qubits [79] and after the demonstration of strong coupling of a singlet/triplet qubit to a cavity would satisfy the scaling requirements for a quantum computer. The feasibility of fault tolerant operation of the RX qubit is not easy to estimate as the qubit has not widely been implemented and has benefited less from technological transfer from other platforms. Both the RX and EO qubit are the only demonstrated spin-based qubit that are fully electrically tunable and therefore these also remain strong candidates for large scale quantum computation using semiconductor qubits. If a qubit implementation can demonstrate fault tolerant single qubit gates with strong coupling to a cavity, the next milestone will be the demonstration of fault tolerant cavity mediated 2-qubit gates.

Qubit type	1-qubit gate error	t_π	T_2^*	Cap. coupl.	Strong coupl. to cav.	Qubit-cavity-qubit	Full electric tunability
magnetically-driven (1spin, 1QD)	4.3×10^{-4} [21]	2 μs [21]	3.3 μs [21]	x	x	x	x
Charge qubit (1charge, 2QD)	0.14 [30]	$\approx$ 0.5 ns [30, 29]	50 ns [33]	✓ [31]	✓ [32]	✓ [37]	✓
Electrically-driven (1spin, 1QD)	1×10^{-3} [8]	125 ns [8]	20 μs [8]	x	x	x	x
Singlet/Triplet (2spin, 2QD)	4×10^{-3} [80]	125 ns [80]	1.3 μs [80]	✓ [81]	x	x	x
RX qubit (3spin, 3QD)	N/A	5 ns [44]	16 ns [70]	x	✓ [70]	x	✓
Flopping mode (1spin, 2QD)	N/A	83 ns [46]	1.4 μs [46]	x	✓ [17]	✓ [77]	x

Table 3.1: **A summary of electrically-driven single-qubit gate metrics.** The table shows the single-qubit gate error, the time for a π-rotation (t_π), T_2^*, demonstration of capacitive inter-qubit coupling, and values related to cavity coupling; strong coupling regime, qubit-qubit coupling mediated by a cavity and finally whether the qubit can be controlled by pure electrical means.

3.2 Flopping-mode qubits

In this section we will first demonstrate that the flopping-mode Hamiltonian describes a variety of proposed qubits including one that will be the subject of this thesis (see Chapter 4). Using perturbation theory we illustrate how the emergence of the qubit's electrical dipole moment is linked to the hybridisation of the electron spin to its orbital degree of freedom. We will show that for weak hybridisation, the electric driving appears classically as the motion of an electron spin in a magnetic gradient. Finally, an analysis of charge dephasing will reveal the presence of n^{th}-order dephasing sweet spots where the qubit energy is insensitive to n^{th}-order to charge noise and error rate of the qubit will be reduced. In Sect. 3.3 we will present the error model used in this chapter and Chapter 4, to describe not only dephasing errors, but also other errors, due to relaxation and leakage.

Flopping-mode qubits are based on an electron spin localised on two tunnel-coupled QDs. The electric field E can be tuned such that the electron wave function is either fully localised on one of the QDs, or shared between them. In the first case, the qubit states are purely the electron spin states populating the orbital state associated with the QD, yielding long coherence ($\sim \mu$s) and relaxation times ($\sim$ s).

In the second case, the qubit states consists of the electron spin states in a superposition of two QD orbitals, yielding shorter coherence and relaxation times, but enabling coupling to electric fields. Transitions between the two electron spin states is achieved by engineering an artificial spin–orbit coupling, enabling electric control over the electron spin state. This spin–orbit coupling results from a transverse magnetic coupling has different values for each orbital occupation: by controlling the electric field, the orbital occupation and thus the transverse coupling can be varied in time. By modulating the strength of that coupling at a frequency that matches the energy separation of the two spin states, the transition can be addressed and driven electrically. This transverse coupling may arise due to a transverse magnetic field or a hyperfine coupling to nuclear spins. Whilst the current chapter studies the flopping-mode qubit in a way that is agnostic to the physical origin of the transverse coupling mechanism, Chapter 4 focuses on a transverse coupling produced by the hyperfine interaction with donor nuclear spins. In that chapter we show that the nuclear spins produce stable effective magnetic gradients, that are not affected by the electric driving. Later, in Chapter 5 we show experimentally that the nuclear spins in a 2P donor molecule –such as the one used in the qubit proposal of Chapter 4– flip spontaneously, but at a rate low enough that it would not affect operation of the proposed qubit.

Contrary to classical electric dipole spin resonance (EDSR), where a single orbital is shifted by oscillating electric field within a spatially varying transverse field, for the flopping-mode qubit, two distinct, spatially separated orbitals are used to increase the charge dipole moment of the electron. A positive consequence of this is that the orbital part of the electron wavefunction is very sensitive to electric fields around the "zero-detuning" point where the wavefunction is equally split between both QDs. The sensitivity is here proportional to $\frac{1}{t_c^2}$, where t_c is the tunnel coupling between the two-QD orbitals. The response of the electron to an oscillating electric field can then be classically interpreted as an oscillating motion of the spin in a magnetic field gradient and can lead to electron spin rotations, with driving strengths limited to a few MHz only. The second advantage of using two spatially separated orbitals compared to one is that the strength of the spin-charge coupling can be further enhanced by tuning the orbital part of the qubit such that the electron spin-up orbital state acquires some excited orbital character leading to faster qubit control. As a consequence a strong electric-dipole coupling emerges between the two qubit states, the strength of which is proportional to the admixture of excited orbital state which allows for the fast electric driving. The disadvantage of coupling the qubit

to electric fields, is that this allows for charge-noise and phonons to couple to the qubit increasing the dephasing and relaxation mechanisms respectively.

In this section we will show that three separate proposals for EDSR qubits can be related to the same flopping-mode Hamiltonian in the basis consisting of a pseudo-spin and the two orbital-states $\{\tilde{\uparrow},\tilde{\downarrow}\}\otimes\{L,R\}$:

$$H(\tilde{\epsilon}) = \Omega_z\sigma_z/2\otimes\mathbb{1} + \mathbb{1}\otimes\{\tilde{\epsilon}\sigma_z + t_c\sigma_x\} + \{\frac{\Delta\Omega_z}{4}\sigma_z + \frac{\Delta\Omega_x}{4}\sigma_x\}\otimes\sigma_z, \tag{3.2.1}$$

where Ω_z is the bare spin qubit splitting, $\tilde{\epsilon}$ is related to the electrostatic energy detuning $\epsilon = eEd/\hbar$ between the two dots, t_c is the tunnel coupling between the two orbital states, and $\Delta\Omega_{z/x}$ is the longitudinal/transverse energy difference between the two dots. The infinite-dimensional orbital Hilbert space $\mathscr{H} = L^2(\mathbb{R}^3)$ has been reduced to a discrete Hilbert space $\mathscr{H}_c = \text{Span}\left(\{|L\rangle,|R\rangle\}\right)$ consisting of the two only orbitals L and R. The validity of this simplification has been confirmed by tight binding simulations [12].

First we will cover the "flopping-mode" implementation proposed by Hu *et al.* [73] and refined by Beaudoin [72] and Benito et. al. [74] where both QDs are gate-defined, and both energy gradients result from a micromagnet deposited on the surface of the device. Following this, we cover the flip-flop implementation proposed by Tosi *et al.* [12], where one QD is defined at the silicon/silicon–dioxide interface, while the other QD is defined by a phosphorus donor implanted $\sim 10\,\text{nm}$ below the interface. The third "all epitaxial flopping-mode qubit" implementation is the proposal described in this thesis. Here, each QD is defined by a multi-donor phosphorus QD embedded in silicon $\sim 50\,\text{nm}$ below the surface.

3.2.1 Flopping-mode qubit Hamiltonian

In the case of the flopping-mode Hamiltonian, with a magnetic field $B_z^{L/R}\hat{z} + B_x^{L/R}\hat{x}$ on the left/right dot respectively, the transformation to the Hamiltonian of Equ. 3.2.1 is straightforward. The pseudo-spin basis $\{\tilde{\uparrow},\tilde{\downarrow}\}$ is equivalent to the electron-spin basis $\{\uparrow,\downarrow\}$, and the different variables in the Hamiltonian are:

$$\Omega_z = \gamma_e B_z,\ \Delta\Omega_z = \gamma_e\Delta B_z,\ \Delta\Omega_x = \gamma_e\Delta B_x,\ \text{and}\ \tilde{\epsilon} = \epsilon,$$

with $B_z = \frac{B_z^L + B_z^R}{2}, \Delta B_{z/x} = B_{z/x}^L - B_{z/x}^R$, and $\gamma_e \approx 28\,\text{GHz/T}$ is the electron gyromagnetic ratio.

In the remainder of this chapter we will investigate the general flopping-mode

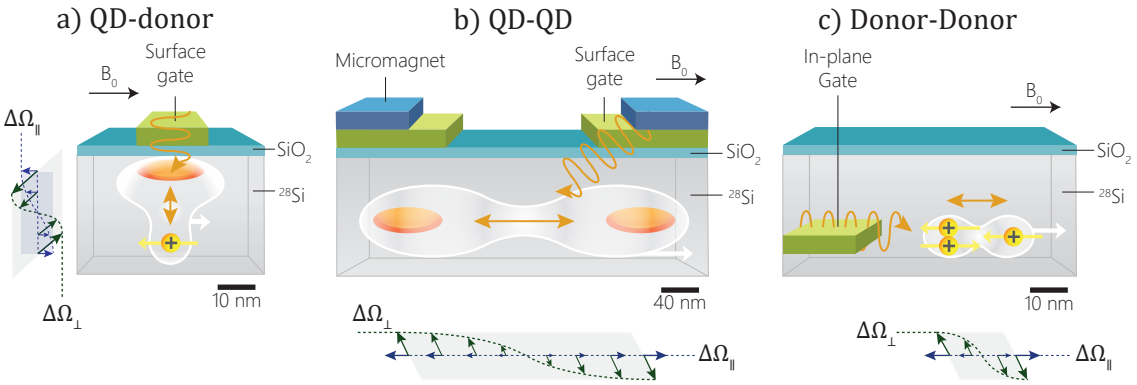

Figure 3.8: **Comparison of flopping-mode electric-dipole spin resonance systems.** Three different flopping-mode EDSR systems implemented using a) QD-donor, b) QD-QD, and c) donor-donor sites. The QD-donor and donor-donor implementations both use the hyperfine interaction from the electron-nuclear system naturally present in donor systems to generate a spin-orbit coupling. The QD-QD system utilises a micromagnet to create a spatially-varying magnetic field that can be used to induce an artificial spin-orbit coupling.

Hamiltonian of Eq. 3.2.1 that describes all three systems. In this section we describe how the electron spin can acquire an electric dipole moment through careful electric tuning. In Sect. 3.3 we then describe how the emergence of an electric dipole moment translates into a vulnerability of the spin to charge noise resulting into dephasing. The optimal tradeoff between both effects, will then be investigated in subsequent in Sect. 3.4.

For the donor–donor implementation, leakage out of the four-dimensional subspace can occur through an undesired flip-flop of the electron spin with a different nuclear spin than the one intended. This is the only error not described by the general flopping-mode Hamiltonian of Eq. 3.2.1, and will be investigated in detail in Chapter 4.

3.2.2 Engineering a pseudo-spin with an electric dipole moment

A coupled system of spin and charge qubits

We have shown in Sect. C.1 how a variety of Hamiltonians can be reduced to a general flopping-mode Hamiltonian, $H(\tilde{\epsilon})$ (Eq. 3.2.1).

When electrically driving the flopping-mode qubit using microwave pulses, the electric field changes periodically with time corresponding to an oscillating value of the electric detuning parameter ϵ. Indeed, an electric field $E(t) = E_d \cos(\omega_d t)$, oscillating with frequency ω_d along the two dots separated by a distance d results

in a time-dependent detuning parameter in the flopping-mode Hamiltonian:

$$\tilde{\epsilon}(t) = \epsilon + \epsilon_d(t),$$

where $\epsilon_d(t) = \frac{eE_d d}{2\hbar}\cos(\omega_d t)$ is the detuning drive and ϵ is the static detuning. The other parameters in Equ. 3.2.1 are unaffected by the oscillating electric field.

The electric-field burst can be written as a time-dependent detuning parameter in the flopping-mode Hamiltonian:

$$\tilde{\epsilon}(t) = \epsilon + \epsilon_d(t),$$

where $\epsilon_d(t) := \frac{eE_d d}{2\hbar} g(t)\cos(\omega_d t)$ is the detuning drive, ϵ is the static detuning and d is the distance between the two QDs.

We can now write out the full Hamiltonian in the presence of the oscillating electric field to be:

$$H_f(t) = H(\epsilon) + H_d(t), \tag{3.2.2}$$

$$H_d(t) = \mathbb{1} \otimes \epsilon_d(t)\sigma_z. \tag{3.2.3}$$

$H(\epsilon)$ is the flopping-mode Hamiltonian of Eq. 3.2.1 with a static detuning parameter ϵ instead of the time-dependent $\tilde{\epsilon}(t)$. The driving Hamiltonian is essentially the dipole moment operator : $H_d = \boldsymbol{d}E_d$, where $\boldsymbol{d} = \frac{ed}{\hbar}\mathbb{1} \otimes \sigma_z$. Any off-diagonal matrix elements of the dipole-moment operator connecting the two basis states, allows for electrical driving between the latter. In the current basis, the dipole moment operator is diagonal, and thus no electrical transition between the chosen basis states is allowed. We will see however that in the eigen-basis of $H(\epsilon)$, off-diagonal dipole coupling elements appear. The Hamiltonian in Equ. 3.2.2 can be partially diagonalised by diagonalising the non-coupled charge Hamiltonian $\mathbb{1} \otimes (\epsilon\sigma_z + t\sigma_x)$.

The charge qubit:

The charge Hamiltonian describing the charge qubit can be diagonalised to $\Omega_c\sigma_z$ in the Eigenbasis $(|\tilde{+}\rangle, |\tilde{-}\rangle)$ outlined below, where $\Omega_c = \sqrt{\epsilon^2 + t^2}$ is half the charge qubit splitting:

$$|\tilde{\mp}\rangle\,(\epsilon, t) = \left(a(\pm\epsilon)|L\rangle \mp \mathrm{sign}(t)a(\mp\epsilon)|R\rangle\right). \tag{3.2.4}$$

where $a(\pm\epsilon)) = \frac{1}{\sqrt{2}}\sqrt{1 \pm \frac{\epsilon}{\Omega_c}}$, which describes the shifting of the orbital population with detuning. It describes the Stark shift of the contact hyperfine interaction to a nuclear spin on a left/right dot: $A(\epsilon) = A\,|a(\pm\epsilon)|^2$.

The energy spectrum of the charge Hamiltonian is represented in Fig. 3.9 as a function of the electric detuning parameter ϵ. The spectrum displays two curved branches, the lower/higher one corresponding to the ground and excited charge states, denoted by the bare eigenstates $|\tilde{\mp}(\epsilon)\rangle$ respectively. The two branches result from an avoided crossing of the uncoupled left and right dot orbital energies, which vary linearly with the electric detuning amplitude ϵ. At far negative/positive detuning ($\epsilon \ll 0$ and $\epsilon \gg 0$ respectively), the electronic wave function is pushed towards the left/right dot, and the ground state is accordingly the left/right QD orbital $|L/R\rangle$. The excited charge state corresponds to the energetically unfavourable configuration where the orbital which is higher in energy is occupied. At zero detuning, both orbitals have the same energy, and the ground/excited state is an antisymmetric/ symmetric combination of the two. The width of the detuning range within which the left and right orbitals hybridise is proportional to the tunnel coupling, t_c. The splitting between the ground and excited branches is given by the bare charge qubit splitting $\Omega = 2\Omega_c = 2\sqrt{\epsilon^2 + t_c^2}$, which is equal to twice the tunnel coupling t_c at $\epsilon = 0$. The Pauli operators transform as follows under this change of basis:

$$\sigma_z \mapsto \frac{\epsilon}{\Omega_c}\sigma_z + \frac{|t|}{\Omega_c}\sigma_x \tag{3.2.5}$$

$$\sigma_x \mapsto \frac{t}{\Omega_c}\sigma_z - \frac{\epsilon}{\Omega_c}\mathrm{sign}(t)\sigma_x. \tag{3.2.6}$$

The transformation of Eq. 3.2.5 describes the emergence of an electric dipole moment between the ground and excited charge states described above.

A time-dependent electric detuning $\epsilon_0 + \epsilon_d(t)$ results in a time-dependent drive Hamiltonian $\epsilon_d(t)\sigma_z$ (in the orbital basis) acting purely on the charge subspace. Under the above transformation of the σ_z matrix, this drive Hamiltonian acquires an off-diagonal element $\epsilon_d(t)\frac{t_c}{\sqrt{\epsilon^2+t_c^2}}$ that describes the driving strength of the charge qubit. This driving strength displays a strong peak at $\epsilon = 0$ where it is equal to ϵ_d, but asymptotically vanishes away from zero detuning. The driving strength at zero detuning can be interpreted as the product of the geometric charge dipole of the electron charge $D^c = ed$ multiplied by the electric-field driving strength. Indeed, $\epsilon_d = \frac{eE_d d}{2\hbar} = \frac{D^c E_d}{2\hbar}$. The geometric charge dipole D^c describes the maximal dipole moment the charge qubit can have when the electron is equally shared between both dots. At zero detuning the charge qubit can now be described by the simple two-level Hamiltonian, in the charge eigenbasis:

$$H^c = \Omega_c\sigma_z + \epsilon_d(t)\sigma_x\,. \tag{3.2.7}$$

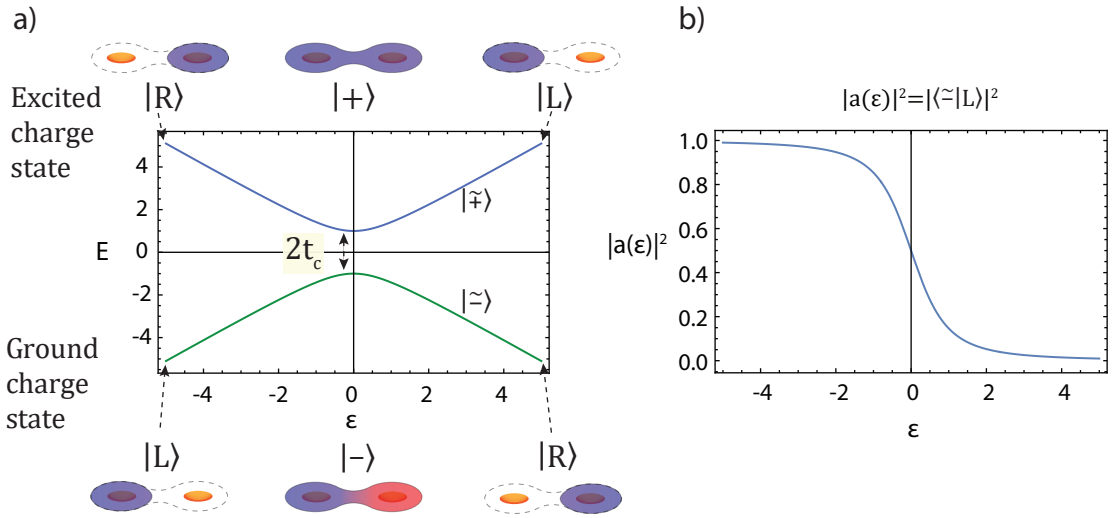

[H]

Figure 3.9: **Charge qubit ground and excited states**. **a)** The charge qubit wavefunction is a combination of the two QD orbitals that change with the electrostatic detuning ϵ. For negative electric detuning, the ground state wavefunction is pushed by the electric field to the left dot, whereas for positive detuning it is pushed to the right. The charge excited states display the opposite behaviour. At zero detuning, the ground state wave function is an equal but antisymmetric combination of the two QD orbitals ($|-\rangle$), whereas for the excited state it is a symmetric superposition of the two QD orbitals ($|+\rangle$). **b)** The probability of the electron being in the left quantum dot L as a function of detuning between the two QDs.

When driving the electric detuning at the frequency corresponding to the charge qubit splitting $2\Omega_c$, in a frame rotating with that same frequency, the qubit is well approximated by $H^c = 1/2\epsilon_d(t)\sigma_x$, enabling coherent rotations between the charge qubit states, with Rabi frequency $1/2\epsilon_d(t)$.

The near-diagonal flopping-mode Hamiltonian:

We can apply the charge diagonalisation transformation Eqs. 3.2.5 and 3.2.6 to the general Hamiltonian of Eq. 3.2.2, and obtain a near-diagonal Hamiltonian:

$$H_f = H_b + H' + H_d. \tag{3.2.8}$$

The bare qubit Hamiltonian H_b is diagonal, and describes the non-coupled spin and charge qubits, H' represents the coupling Hamiltonian between the two qubits, and H_d is the electric-drive Hamiltonian:

$$H_b = \Omega_z\sigma_z/2 \otimes \mathbb{1} + \mathbb{1} \otimes \Omega_c\sigma_z \tag{3.2.9}$$

$$H' = \left(\frac{\Delta\Omega_z}{4}\sigma_z + \frac{\Delta\Omega_x}{4}\sigma_x\right) \otimes \left(\frac{\epsilon}{\Omega_c}\sigma_z + \frac{t}{\Omega_c}\sigma_x\right) \tag{3.2.10}$$

$$H_d = \mathbb{1} \otimes \epsilon_d(t)\left(\frac{\epsilon}{\Omega_c}\sigma_z + \frac{t}{\Omega_c}\sigma_x\right). \tag{3.2.11}$$

The static Hamiltonian $H_b + H'$ determines the eigenstates and energies of the system which define the qubit. The first term in H_b describes a spin-like state (or spin qubit) whose energy is defined by a Zeeman-like term, and the second term in H_b describes a charge state (or charge qubit) whose energy is defined by electrostatic detuning and tunnel coupling. The second term H' describes the coupling term between those spin and charge qubits. The drive Hamiltonian, H_d describes the electrical drive of the system related to σ_x and σ_z.

The energy spectrum for a general implementation of the device is displayed in figure 3.10 b) as a function of the static detuning parameter ϵ. Each of the charge ground and excited states branches that we described in Fig. 3.9 is now split into two branches corresponding to the spin configuration $|\downarrow / \uparrow\rangle$, and separated by the Zeeman energy $\gamma_e B$, where γ_e (in frequency units) is the electron gyromagnetic ratio. When the Zeeman splitting is smaller than the charge qubit energy, the four branches do not overlap, and the spectrum is split into four distinct branches labelled by the electron's spin and charge states: $|\downarrow \tilde{-}\rangle$, $|\uparrow \tilde{-}\rangle$,$|\downarrow \tilde{+}\rangle$ and$|\uparrow \tilde{+}\rangle$, from bottom to top in ascending energy.

If the coupling Hamiltonian is zero (for vanishing energy gradients $\Delta\Omega_{x/z}$), the

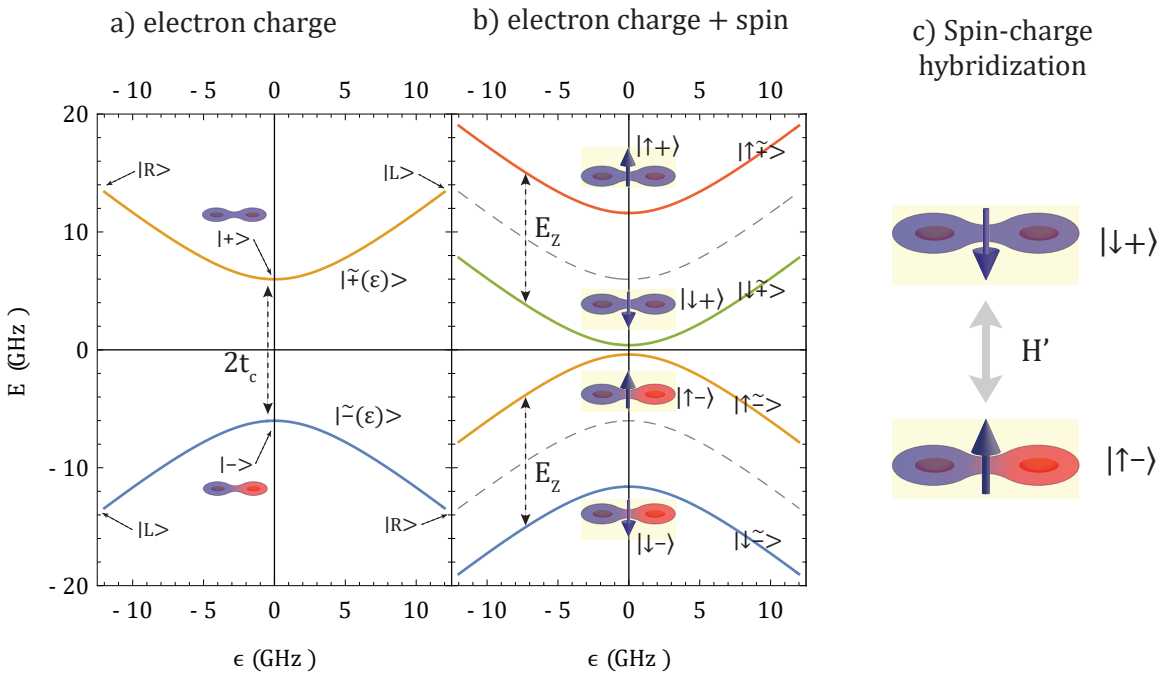

[H]

Figure 3.10: **Flopping-mode energy spectrum and spin–charge hybridisation**. Each branch of the charge spectrum in **a)** splits into two branches corresponding to the two possible electron-spin orientations in **b)**. When the charge and qubit energies are similar, the two inner branches are close in energy around $\epsilon = 0$ ($|\uparrow -\rangle$ and $|\downarrow +\rangle$) in b), and hybridise due to the coupling Hamiltonian H'.

static Hamiltonian reduces to H_b which is already diagonal, the spin and charge basis states are the energy eigenstates and the drive Hamiltonian can be seen to only allow transitions between the charge qubit states. This qubit is however extremely sensitive to charge noise, which is why the flopping-mode qubit is based on the spin qubit. We thus see that without the coupling Hamiltonian H', the spin qubit cannot be addressed electrically.

For a non-vanishing coupling Hamiltonian H', the eigenstates result from a hybridisation of the spin and charge states of the uncoupled system. As we will see next in an analytical treatment, this hybridisation is especially strong when the charge and spin qubit energies are similar (the charge and spin qubits are in resonance). Hybridisation can be interpreted as a rotation of the uncoupled spin and charge product states, which when applied to H_d will result in dipole-coupling elements between the hybridised spin qubit states.

Analytical estimation of spin–charge hybridisation

The coupling Hamiltonian H' is a small perturbation of the diagonal matrix $H^0 = H_b + H_d$, as it is proportional in magnitude to the gradients $\Delta\Omega_{x/z}$, which will be at least one order of magnitude smaller than the bare spin qubit splitting Ω_s. Within perturbation theory, the coupling matrix affects the qubit eigenstates and results in a hybridisation of the spin and charge eigenstates. Perturbation theory also generates an effective Hamiltonian restricted to the qubit subspace

Hybridisation of spin and charge eigenstates To estimate the degree of spin–charge hybridisation, we employ first-order perturbation theory on the spin- charge eigenstates $|\downarrow \tilde{-}\rangle$, $|\uparrow \tilde{-}\rangle$,$|\downarrow \tilde{+}\rangle$ and$|\uparrow \tilde{+}\rangle$. The main contribution arises from the eigenstates $|\uparrow \tilde{-}\rangle$ and $|\downarrow \tilde{+}\rangle$ that are close in energy for small spin–charge detuning $\Delta = \Omega - \Omega_s$ is small. This results in perturbed eigenstates $|\widetilde{\uparrow -}\rangle$ and $|\widetilde{\downarrow +}\rangle$ where the unperturbed states have hybridised. To first order in the gradients $\Delta\Omega_{z/x}$, we find[2] :

$$\langle\widetilde{\uparrow -}|\downarrow \tilde{+}\rangle = -h \tag{3.2.12}$$

$$\langle\widetilde{\downarrow +}|\uparrow \tilde{-}\rangle = +h \tag{3.2.13}$$

$$\text{with } h = \frac{t\Delta\Omega_x}{2\Omega\Delta}. \tag{3.2.14}$$

[2]We use first-order perturbation of the unperturbed eigenstate $|n\rangle$ through interaction with the other unperturbed eigenstate $|m\rangle$ resulting in the perturbed eigenstate $|\widetilde{n}\rangle$: $\langle m|\widetilde{n}\rangle \approx \frac{\langle m|H'|n\rangle}{E_n - E_m}$.

The degree of spin–charge hybridisation[3] h is inversely proportional to the spin–charge detuning Δ and proportional to the transverse energy difference $\Delta\Omega_x$, so that when the spin–charge detuning becomes comparable in magnitude to the transverse energy gradient, the spin will hybridise to charge. We expect that this will coincide with the emergence of an electric dipole moment for the hybridised spin qubit. This effect can be treated analytically by performing perturbation theory on the Hamiltonian instead of the eigenvectors.

An effective qubit Hamiltonian The perturbative effect of the coupling Hamiltonian H' on the uncoupled (diagonal) spin–charge Hamiltonian H^0 is given by the following effective Schrieffer–Wolff transform, which gives the following approximation of the full Hamiltonian $H_f = H^0 + H'$, to zeroth, first and second-order:

$$H^{(0)}_{mm'} = H^0_{mm'}, \tag{3.2.15}$$

$$H^{(1)}_{mm'} = H'_{mm'}, \tag{3.2.16}$$

$$H^{(2)}_{mm'} = \frac{1}{2}\sum_l H'_{ml}H'_{lm'}\left(\frac{1}{H^0_{mm} - H^0_{ll}} + \frac{1}{H^0_{m'm'} - H^0_{ll}}\right). \tag{3.2.17}$$

Applying this transformation, and subtracting global energy shifts, yields the following approximation of the qubit Hamiltonian, to second-order in the gradients $\Delta\Omega_{z/x}$:

$$H_r = \frac{\tilde{\Omega}_s}{2}\sigma_z + \Omega_r\sigma_x, \tag{3.2.18}$$

in the spin–charge hybridised eigenbasis: $\left\{\widetilde{|\uparrow -\rangle}, \widetilde{|\downarrow -\rangle}\right\}$. The perturbed qubit splitting and dipole coupling element are given by:

$$\tilde{\Omega}_s = \Omega_s \overbrace{-\frac{\epsilon\Delta\Omega_z}{\Omega}}^{\tilde{\Omega}_s^{(1)}} \overbrace{-\frac{\Omega_s^2 - (2\epsilon)^2}{2\Omega_s\left(\Omega^2 - \Omega_s^2\right)}\left(\frac{\Delta\Omega_x}{2}\right)^2}^{\tilde{\Omega}_s^{(2)}}, \tag{3.2.19}$$

$$\Omega_r = -\frac{t^2\Delta\Omega_x\left(2\Omega^2 - \Omega_s^2\right)}{\Omega^3\left(\Omega^2 - \Omega_s^2\right)}\epsilon_d, \tag{3.2.20}$$

and we have defined the charge qubit energy spacing $\Omega = 2\Omega_c$.

The qubit energy $\tilde{\Omega}_s$ is given to zeroth order by the bare spin qubit energy Ω_s, reflecting the fact that the qubit is based on the spin qubit that is slightly hybridised to charge. The Rabi frequency $\tilde{\Omega}_r$, which vanishes to zeroth order, becomes finite to

[3] At zero electric detuning, the degree of hybridisation simplifies to the ratio of the two quantities: $h(\epsilon = 0) = \frac{1}{4}\frac{\Delta\Omega_x}{\Delta}$.

first order in $\Delta\Omega_x$, for finite charge qubit splitting Ω and describes the emergence of an electric dipole moment. It is proportional to the electric detuning drive amplitude ϵ_d and to the magnitude of the transverse gradient $\Delta\Omega_x$. This transverse term $\tilde{\Omega}_r$ allows full electrical control of the flopping-mode qubit through an electric field oscillating at a microwave frequency corresponding to the qubit splitting $\tilde{\Omega}_s$ and is at the heart of how the qubit operates.

The equations above that describe the qubit energy and Rabi frequency highlight the existence of two regimes of operation of the flopping-mode qubit: the first regime where the spin–charge hybridisation dominates the qubit energy and the spin–charge detuning Δ is small ($\Delta \lesssim \Omega_s$), and the second regime where the spin and charge qubits are weakly hybridised ($\Delta \gtrsim \Omega_s$) and the qubit energy and Rabi frequency can be understood classically as the motion of a spin in a magnetic gradient. Depending on which regime the qubit is in the different dephasing mechanisms will dominate the qubit error.

Qubit energy and coupling in the hybridised regime The modification of the qubit energy due to the hybridisation of the spin qubit to the charge qubit is described by the second-order term $\tilde{\Omega}_s^{(2)}$ in Eq. 3.2.19 (proportional to $\Delta\Omega_x^2$), the magnitude of which can be substantial when the term $(\Omega^2 - \Omega_s^2)$ in the denominator approaches zero, i.e. when the bare charge and spin qubit splitting are comparable. Indeed, the second-order energy term is proportional to the degree h of spin–charge hybridisation of Eq. 3.2.14, and simplifies for low spin–charge detuning ($\Omega_s \simeq \Omega$):

$$\tilde{\Omega}_s^{(2)} = -h \cdot \frac{\Delta\Omega_x \Omega(\Omega_s^2 - 4\epsilon^2)}{4t_c\Omega_s(\Omega + \Omega_s)} \xrightarrow[\Omega_s \to \Omega]{} -\frac{h}{2}\frac{2t_c}{\Omega} \cdot \frac{\Delta\Omega_x}{2}. \tag{3.2.21}$$

The expression for the Rabi frequency Ω_r in Eq. 3.2.20 is proportional to the degree of spin–charge hybridisation h:

$$\Omega_r = -h\frac{2t_c}{\Omega}\frac{2\Omega^2 - \Omega_s^2}{\Omega(\Omega + \Omega_s)}\epsilon_d \xrightarrow[\Omega_s \to \Omega]{} -\frac{h}{2}\frac{2t_c}{\Omega} \cdot \epsilon_d = \frac{h}{2}\Omega_r^{\text{charge}}. \tag{3.2.22}$$

For small spin–charge detuning Δ, the qubit Rabi frequency reduces to the charge qubit Rabi frequency multiplied by the degree of spin–charge hybridisation, where $\Omega_r^{\text{charge}} = \frac{2t_c}{\Omega}\epsilon_d$ is the charge qubit Rabi frequency. This highlights that for small spin–charge detuning, the spin hybridises to charge and acquires some of the charge qubit's electric dipole moment.

In next section, we derive the expressions for the qubit splitting and Rabi frequency in the weak spin-charge coupling regime where the qubit operation can be

interpreted classically as the motion of an electron spin in longitudinal and transverse magnetic gradient.

Qubit energy and coupling in the classical regime. For large spin–charge detuning $\Delta = \Omega - \Omega_s >> 0$, the perturbative contribution of the second-order energy term $\tilde{\Omega}_s^{(2)}$ becomes negligible compared to that of the first-order term $\tilde{\Omega}_s^{(1)} = -\frac{\epsilon}{\Omega_c}\Delta\Omega_z/2$ and can be written in terms of a gradient function $G(\epsilon) = -\frac{\epsilon}{\Omega_c}$:

$$\tilde{\Omega}_s^{(1)} = G(\epsilon)\frac{\Delta\Omega_z}{2}\,. \tag{3.2.23}$$

Importantly we find that in the far-detuned regime $\Omega \gg \Omega_s$, the Rabi frequency of Eq. 3.2.20 is also related to $G(\epsilon)$:

$$\Omega_r = -\frac{t^2\Delta\Omega_x\left(2\Omega^2-\Omega_s^2\right)}{\Omega^3\left(\Omega^2-\Omega_s^2\right)}\epsilon_d \xrightarrow[\Omega_s\to\Omega]{} -\frac{2t^2}{\Omega^3}\Delta\Omega_x\epsilon_d = \frac{1}{2}\frac{\partial}{\partial\epsilon}\left(G(\epsilon)\frac{\Delta\Omega_x}{2}\right)\epsilon_d\,. \tag{3.2.24}$$

We now show that $G(\epsilon)$ describes the response of the electron's wavefunction to the electric field, and can be interpreted as a spatial gradient experienced by a classical point-like spin displaced by an electric field. Indeed, the electron occupies the left/right QD orbital with probability $p^{\mathrm{L/R}}(\epsilon) = |a(\pm\epsilon)|^2 = \frac{1}{2}\left(1 - \frac{\pm\epsilon}{\Omega_c}\right)$, where the coefficient $a(\pm\epsilon)$, describes the hybridisation of the left and right orbitals forming the charge eigenbasis (see Eq. 3.2.4). If the electron has an energy $E^{L/R} = \pm E$ when fully centred on the left and right dot respectively, the energy of the electron when its wave function is spread over the two QD can be estimated by the sum $E_{\mathrm{avg}}(\epsilon)$ of the left and right dot energies $E_{L/R}$, weighted by the probability of occupation of the left and right orbitals respectively. This yields the function G:

$$\begin{aligned} E^{\mathrm{avg}}(\epsilon) &:= p^L(\epsilon)\,E^{\mathrm{L}} + p^R(\epsilon)\,E^{\mathrm{R}} = \left(|a(\epsilon)|^2 - |a(-\epsilon)|^2\right)E && (3.2.25)\\ &= -\frac{\epsilon}{\Omega_c}E && (3.2.26)\\ &= G(\epsilon)E. && (3.2.27) \end{aligned}$$

The approximation E_{avg} was validated by tight binding calculations by Tosi *et al.* [12]. The function $G(\epsilon)$ is plotted in Fig. 3.11 b). It asymptotically tends towards ± 1 at large negative/positive electric detunings, where the wave function is confined to a single QD and shows a sharp negative slope at $\epsilon = 0$, where the wave

function rapidly swaps from the left to the right QD within a width proportional[4] to the value of the tunnel coupling t_c.

For the qubit first-order energy term $\tilde{\Omega}_s^{(1)} = G(\epsilon)\frac{\Delta\Omega_z}{2}$, the energy term $E = \frac{\Delta\Omega_z}{2}$ is the longitudinal energy term, and $\tilde{\Omega}_s^{(1)}$ describes the averaged longitudinal energy experienced by the electron spin. Similarly, the transverse coupling element $E = \Delta\Omega_x/2$ produces an electric detuning dependent Hamiltonian transverse coupling element $E_x(\epsilon) = G(\epsilon)\frac{\Delta\Omega_x}{2}$ experienced on average by the electron spin.

We now consider driving the electric detuning with a sine wave of amplitude ϵ_d centred around the static detuning value ϵ_0 where the slope of G is maximal, as described in Fig. 3.11 b). The transverse coupling experienced by the electron then follows a sine wave of amplitude $\Omega_r^{\text{clas.}}$ proportional to the derivative of the gradient $E^x(\epsilon)$ at ϵ_0 (to first order in ϵ). This allows driving of the qubit:

$$\Omega_r^{\text{clas.}} = \frac{\partial}{\partial\epsilon}E_x(\epsilon_0)\epsilon_d = \frac{\partial}{\partial\epsilon}\left(G(\epsilon)\frac{\Delta\Omega_x}{2}\right)\epsilon_d. \tag{3.2.28}$$

This oscillating transverse coupling $\Omega_r^{\text{clas.}}$ equals half the asymptotic limit of the perturbative expression for the Rabi frequency :$\Omega_r^{\text{clas.}} = \Omega_r/2$, and shows that the classical interpretation is valid. This classical interpretation is only valid if the electron is driven adiabatically so that its wave function responds to the electric drive and thus experiences the instantaneous value of E_x at each given time. This is the case when the charge-qubit splitting is much larger than the spin-qubit splitting, so that it is unlikely for the electron to leak into the excited charge-state, and the electron wave function responds to electric drive.

The first-order approximation of the Rabi frequency $\Omega_r^{(1)}/2$ is plotted in green Fig. 3.11 a against the relative spin–charge detuning Δ/Ω_s for $\epsilon_d = 1$. As expected, the model fits the numerical data (blue markers) very well for detunings larger than 1, corresponding to the point where the charge qubit splitting is twice the qubit splitting. For smaller detuning $\Delta < 1$, this first-order approximation underestimates the electric driving strength, because it does not capture the spin–charge hybridisation that scales like $1/\Delta$. The full analytical model for the Rabi frequency in Eq. 3.2.20, that captures both regimes is displayed in red in Fig. 3.11 a) and fits the numerical data well.

Summary In summary, we have seen that the qubit's energy and dipole coupling strengths can be split into two regimes. At low spin–charge detunings $\Delta \approx 0$,

[4] $G = \pm 0.5$ at $\epsilon = \mp 0.58\, t_c$

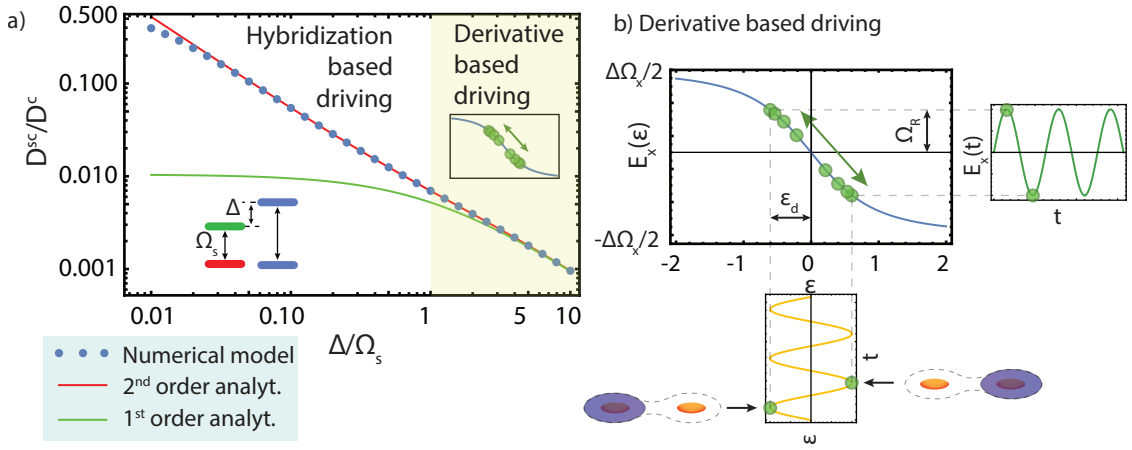

Figure 3.11: **Hybridisation- and derivative-based driving. a)** normalised qubit electric-dipole moment versus the relative spin–charge detuning Δ/Ω_s. The numerical simulations (blue dots), that are well reproduced by the second-order perturbative approximation $\Omega_r(\epsilon = 0)$ (red). The classical model $\Omega_r^{\text{clas.}}$ (green line) reproduces the numerical data well for large spin–charge detunings, where the driving becomes adiabatic wrt. charge and the drive can be interpreted as originating from the motion of the electron in a transverse magnetic-field gradient as illustrated in **b)**.

the spin qubit is strongly hybridised and both the energy and the electric coupling strength of the qubit are proportional to the degree of spin–charge hybridisation. On the other hand, at large spin–charge detunings $\Delta >> 0$, at which the spin is only weakly hybridised to charge, the qubit energy and driving strength can be interpreted by the classical model of a point-like electron spin moving in a longitudinal and transverse magnetic gradient, as a response to a static and microwave electric field respectively. Therefore, depending on the spin-charge hybridisation we need to consider the full qubit Hamiltonian up to higher-orders which can lead to faster qubit driving. In the following section, we will introduce the concept of charge dephasing and show how charge dephasing can be reduced at particular qubit energies called sweet spots, and highlight that the sweet spots are affected by the interplay of the different order derivatives in the perturbative approximations for the energy and Rabi terms that we studied in this section.

Appendix B.1 contains the derivation of the full 4 dimensional flopping-mode effective Hamiltonian using a second-order Schrieffer–Wolff transform (including the two excited charge states).

3.2.3 Charge dephasing, and dephasing sweet spots in the flopping-mode qubit

Stable operation of a qubit relies on the qubit phase precession speed, given by the qubit's energy splitting $\tilde{\Omega}_s = 2z$ staying stable in time. Variations in the qubit energy due to environmental noise will translate into variations in the speed of the phase precession, resulting in an uncertainty in the qubit's phase. This process is called dephasing and can be quantified by the dephasing rate σ_z.

In the case of the flopping-mode qubits, charge noise translates into variations in the electric detuning ϵ that can be modelled by a random variable ϵ described by probability distribution function (PDF) $P(\epsilon)$ with a standard deviation σ_ϵ (the noise amplitude[5]). In the case of the flopping-mode qubit, the qubit splitting $2z(\epsilon)$ is dependent on ϵ, so that variations in the electric detuning translate into variation in the qubit energy. The dephasing rate of the qubit is then defined as standard deviation $2\sigma_z$ of the dependent random variable $2z(\epsilon)$. Charge noise will not only lead to variations in the qubit energy but also in the qubit's Rabi frequency $\Omega_r = 2x(\epsilon)$, translating into uncertainty in the qubit's precession angle when it is driven. This process can also be interpreted as dephasing, and is captured by a x-dephasing rate $2\sigma_x$.

Section 3.3.3 shows that the random variable ϵ can be well described by a Gaussian PDF, centred around the static value of ϵ and with a standard deviation σ_ϵ, so that the dependent random variables $z(\epsilon)$ and $x(\epsilon)$ can also be described by a Gaussian PDF with standard deviation given to first and second-order by:

$$\sigma_{z/x} \approx \frac{\partial z/x(\epsilon)}{\partial \epsilon}\sigma_\epsilon + \frac{\partial^2 z/x(\epsilon)}{\partial \epsilon^2}\frac{\sigma_\epsilon^2}{2}. \tag{3.2.29}$$

At particular values of detuning which we denote as ϵ_{ss}, the derivatives of the dependent variable z or x vanish to n^{th} order and the corresponding terms in the expansion of $\sigma_{z/x}$ vanish to the same order n resulting in a lower dephasing rate. These positions ϵ_{ss} are called n-th order (z/x)-dephasing sweet spots[12, 74] and are important for low-error operation of the qubit. The parameters $\sigma_{z(x)}$ can be readily estimated by using the analytical models for two Hamiltonian parameters $\tilde{\Omega}_s$ and Ω_r derived in Sect. 3.2.2.

A first-order sweet spot results in a first-order protection of the qubit energy to noise. The first-order energy term (proportional to $\Delta\Omega_z$) is a monotonous function of the detuning variable, and thus does not display a sweet spot. We will now see,

[5]For details on the charge dephasing modelling, see Sect. 3.3.3.

how for the qubit energy model, which is the sum of the zeroth, first and second-order terms, the relative strength of the longitudinal and transverse energy gradient determines the presence and position of the detuning sweet spots.

Figure 3.12 shows the analytical qubit splitting and the qubit coupling (Eqs. 3.2.19 and 3.2.20) for two of the flopping-mode implementations discussed in Sects. C.1. The figure illustrates the differences in the energy spectrum for devices with small and large energy gradients.

The first and second-order qubit energies are plotted in Figs. 3.12 a) and d) for a small and large longitudinal energy gradient respectively, for three values of spin–charge detuning Δ/Ω_s (green to orange), corresponding to decreasing spin–charge hybridisation. The first-order term is displayed in blue and does not change appreciably with the spin charge detuning (only a single curve is plotted), while the second-order term (in green to orange) significantly changes with the spin–charge detuning. The first-order term (in blue) is a monotonous function of the detuning, and thus does not display any sweet spot. The second-order term however displays a clear sweet spot at $\epsilon = 0$, where the spin and charge qubit energies are closest, and the spin–charge hybridisation is thus maximal. While the first-order term is nearly flat for the small longitudinal gradient, it changes appreciably for the larger-gradient device, over a range comparable to the second-order term.

The full analytical model for the qubit energy in Eq. 3.2.19, including the bare spin-qubit energy (a constant w.r.t. ϵ), the first and the second-order term is described by the solid lines in Fig. 3.12 b) and e). The corresponding full numerical simulation is displayed by solid markers, showing that in both cases, the analytical model fits the numerical simulation very well. For the device with smaller longitudinal gradient, the energy is mainly determined by the second-order term and thus by the degree of spin–charge hybridisation. Consequently, the z-dephasing sweet spot remains at $\epsilon = 0$ for all three chosen spin–charge detuning values. For the device with larger longitudinal gradient however the gradient of the first-order term shifts the location of the first order z-dephasing sweet spot towards negative electric detunings. For increasing spin -charge detunings (bottom to top), the magnitude of the second-order term decreases so that longitudinal gradient becomes dominant and the first order sweet spot disappears (for a detuning of 6%). Just before the first order sweet spot disappears, at the intermediate spin–charge detuning value of 4.5%, the qubit energy becomes flat at about $\epsilon = 0.5$GHz. This points corresponds to a second-order sweet spot, where the derivatives of the energy with respect to detuning disappear up to second-order, i.e. when the second derivatives of the first and

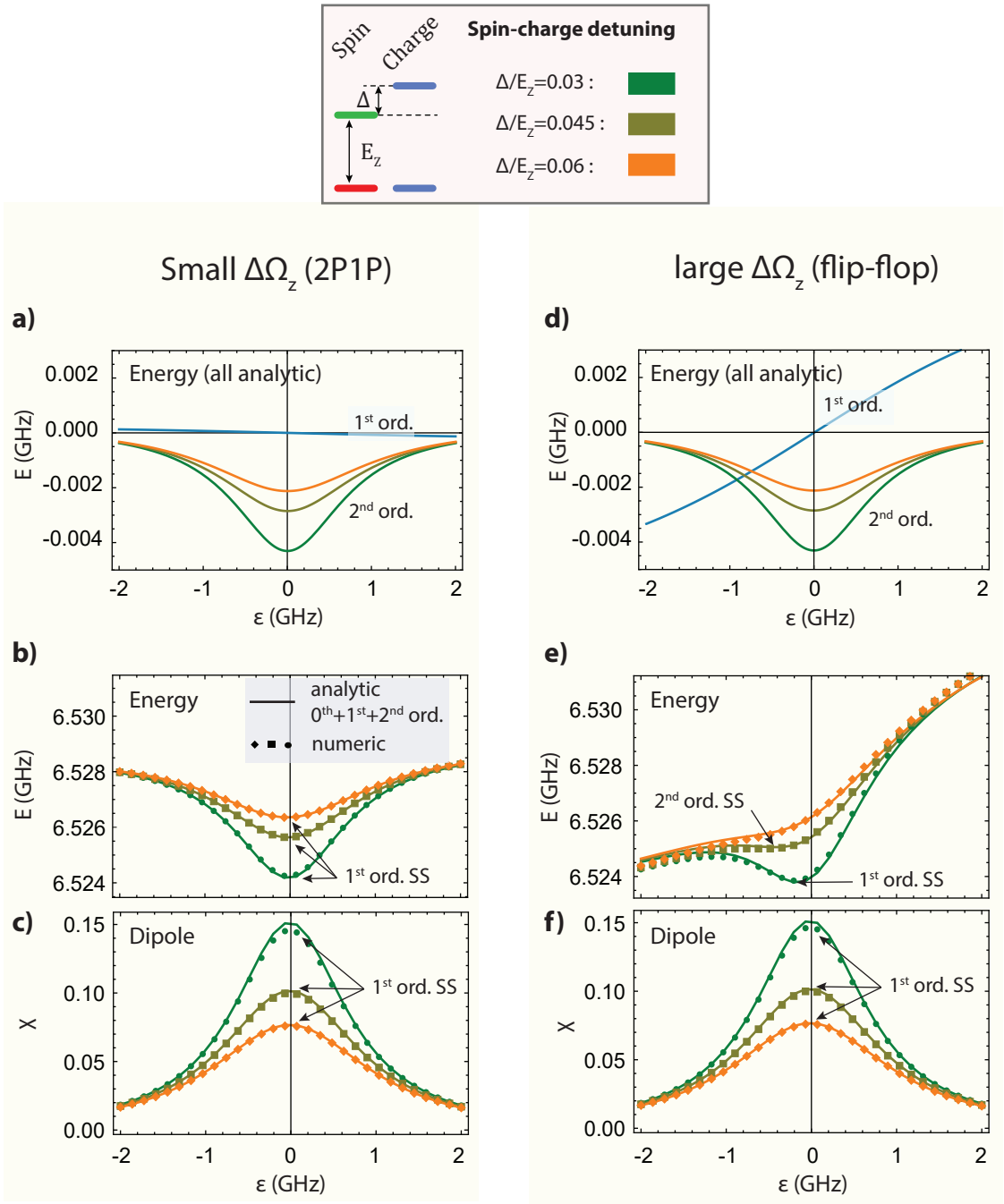

Figure 3.12: **Effect of the longitudinal magnetic field gradient on the qubit energy. a)** The first and second derivative (1^{st} order and 2^{nd} order) of the qubit energy for small longitudinal magnetic field gradient, $\Delta Omega_z$. The 1^{st} order is relatively flat over the investigated detuning region minimising charge noise and the 2^{nd} order plot (for different spin-charge detunings, Δ as shown in the legend at the top of the figure) shows a minimum near $\epsilon = 0$. **b)** The qubit energy up to second order as a function of detuning showing first-order sweet spots near $\epsilon = 0$. **c)** The qubit dipole transition moment, X (proportional to the Rabi frequency) over the same detuning range showing first-order sweet spots near at the same detuning positions as for the qubit energy. **d)** The same first and second derivatives as in a) but for large longitudinal magnetic field gradients. Here, the 1^{st} order energy changes significantly as a function of detuning due to the large $\Delta Omega_z$. **e)** The qubit energy as a function of detuning up to second-order showing a first and second order sweet spot away from $\epsilon = 0$. **f)** The dipole transition moment still shows first-order sweet spots at $\epsilon = 0$ which means that the optimal detuning position is different for x and z-dephasing leading to lower overall qubit fidelity for larger $\Delta Omega_z$ values.

second-order term cancel each other. The detuning value Δ at which this happens is determined by the relative magnitude of first and second-order terms that are themselves determined by the magnitude of the longitudinal and transverse gradients $\Delta\Omega_{z/x}$ respectively. This second-order sweet spot is at the heart of the flip-flop and flopping-mode proposals, because by itself, it offers an increased protection with respect to detuning noise. Note however that this second-order z-dephasing sweet spot is never at zero detuning, as opposed to the x-dephasing sweet spot. In Sect. 3.4.2 it will be shown that for realistic devices and optimal drive amplitude, the x-dephasing errors (linked to charge-noise induced variations in the Rabi frequency) is dominant over the z-dephasing error (linked to charge-noise induced variations in the qubit energy). Driving at the second order SS z-dephasing sweet spot is therefore rarely optimal.

In Fig. 3.12 c) and f), we compare the analytical model for the qubit Rabi frequency from Eq. 3.2.20 to different strengths of the longitudinal magnetic field gradient. Again, the model fits the numerical data very well. The Rabi frequency at unit drive amplitude $\epsilon_d = 1$ corresponds to the ratio D^{sc}/D^c of the flopping-mode qubit dipole moment over the geometric charge dipole moment ed. As for the charge-qubit dipole moment, the flopping-mode qubit dipole moment show a peak at $\epsilon = 0$ and vanishes asymptotically away from zero. The peak increases for decreasing spin–charge detuning, reaching up to 15% of the geometric-charge-qubit dipole moment at a relative spin–charge detuning $\Delta/\tilde{\Omega}_s = 3\%$. The peak in the Rabi frequency at $\epsilon = 0$ corresponds to a first order x-dephasing sweet spot for both devices, irrespective of the spin–charge detuning, and offering resilience to electric-detuning noise coupling via the Rabi frequency.

Numerical calculations of the z- and x-dephasing rate are displayed in Fig. 3.13 a) and b) respectively as a function of spin–charge detuning Δ and the electric detuning ϵ, and display the sweet spots discussed with the help of the analytical expression for the qubit energy and Rabi frequency discussed above. In the plots in a) and b) three horizontal coloured dotted lines indicate illustrative values of spin–charge detuning in three different regimes, the highly hybridised regime (grey square marker) at $\Delta = 0.1$, the weakly hybridised regime (red triangular marker) at $\Delta = 2$, and the intermediate regime at $\Delta \approx 0.3$ (green star). The qubit energy and normalised dipole coupling strength is plotted in Fig. 3.13 c) and d) for these three linecuts. The first order z- and x- sweet spot are indicated by black dotted lines in Fig. 3.13 a) and b). While the x-dephasing first-order sweet spot stays at $\epsilon = 0$ for any value of the spin–charge detuning Δ, the z-dephasing first-order sweet spot describes an arc

originating at $\epsilon = 0$ and bending to the right.

At low spin–charge detunings the qubit energy has two extrema indicated by grey triangles at which the first-order derivative with respect to electric detuning disappears (see grey curve in Fig. 3.13 c). The minimum at $\epsilon = 0$ corresponds to the minimum in the second-order energy term $\Omega_s^{(2)}$ that dominates at low spin–charge detunings, while the maximum at larger detuning values results from a competition between the second-order and first-order terms. These two extrema correspond to the two z-dephasing sweet spot indicated in the colour plot above by the same markers. At large spin–charge detunings (e.g. red triangular markers) the qubit energy (red curve in Fig. 3.13 c) is monotonous. Accordingly no dephasing sweet spot can be found in a). At the particular spin–charge detuning indicated by the green star in Fig. 3.13 a), the first and second derivatives of the first-order and second-order energy terms $\Omega_s^{(1)}$ and $\Omega_s^{(2)}$ cancel out at one particular position of electric detuning corresponding to a saddle point (grey circle). This corresponds to a single second-order z-dephasing sweet spot indicated by a white circle in Fig. 3.13 a).

In Fig. 3.13 e) we show how these sweet spots make the qubits insensitive to dephasing noise. The origin of dephasing noise is due to fluctuations in the qubit energy relative to some external source, either electrical or magnetic. The coupling of charge noise to the qubit energy is through the detuning parameter between the two QDs. The order of the sweet spots (n) corresponds to the n^{th} derivative of the qubit energy along the detuning axis. The qubit energy, E shown in Fig. 3.13 e) shows a first-order sweet spot at $\epsilon = 0$, that is, $dE/d\epsilon|_{\epsilon=0} = 0$. As a result any fluctuations when the qubit is centred around $\epsilon = 0$ will have a negligible effect on the qubit energy (see right side of Fig. 3.13 e)). If the qubit is detuned such that $\epsilon \neq 0$, then $dE/d\epsilon|_{\epsilon\neq 0} \neq 0$ and for the same noise distribution (see bottom inset of Fig. 3.13 e)) the qubit will experience larger dephasing (see left side of Fig. 3.13 e)). This can be extended to second-order sweet spots where the second-derivative of the qubit energy goes to zero at some value of ϵ.

In summary, with Fig. 3.13 we have shown that the while the x-dephasing rate exhibits a single first-order dephasing sweet spot at zero electric detuning, the z-dephasing sweet spot results from a competition between the first-order energy term that describes the longitudinal gradient and does not have any sweet spot and the second-order energy term that has a first-order sweet spot at $\epsilon = 0$. This first order z-sweet spot survives as long as the second-order term dominates the longitudinal gradient. This competition results in the first-order z-dephasing sweet spot describing an arc in the $\epsilon - \Delta$ plane. A second-order z-dephasing sweet spot exist at the

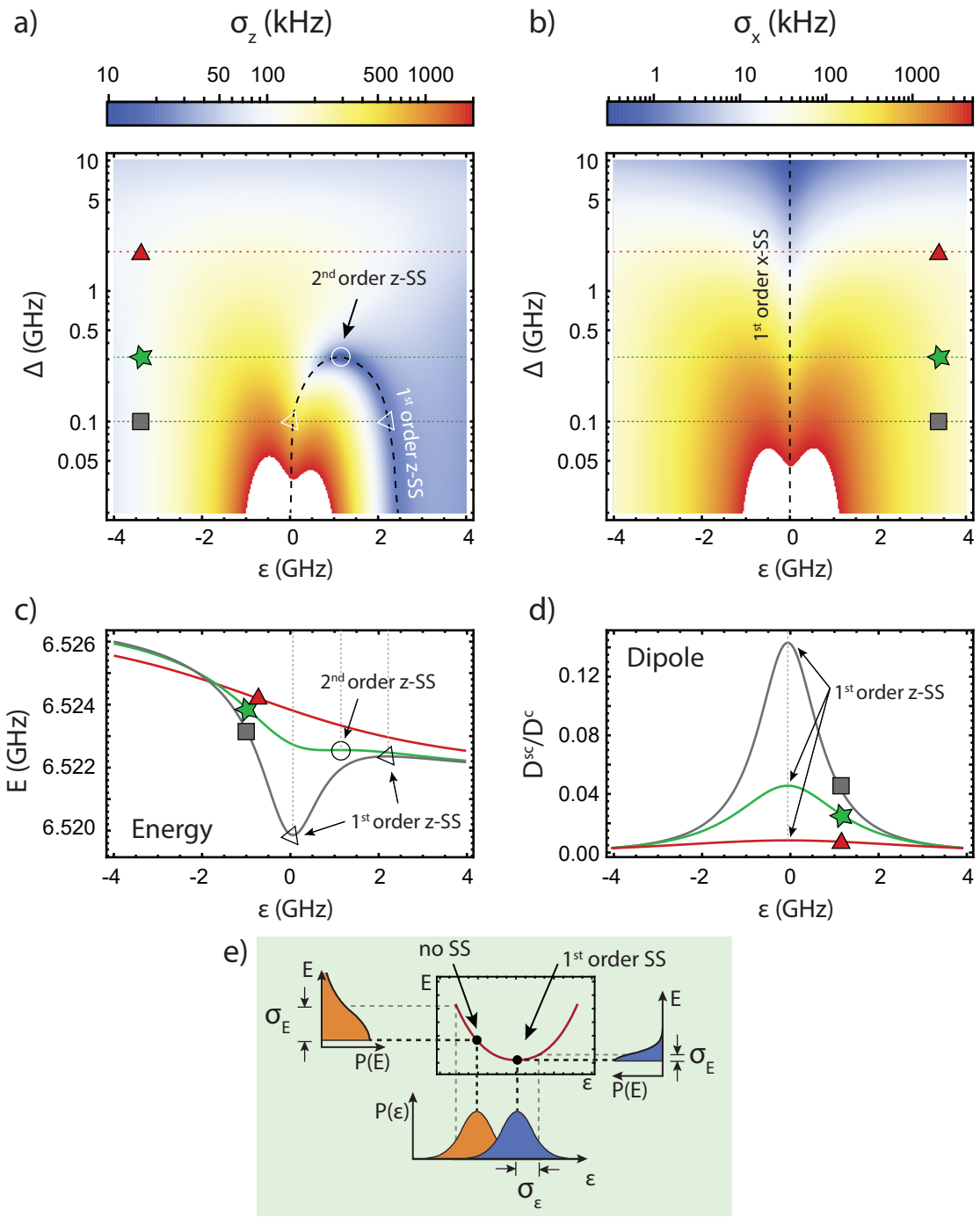

Figure 3.13: **Locations of the dephasing sweet spots in the flopping-mode qubit.** The z- and x- charge dephasing rates σ_z and σ_x are depicted in **a)** and **b)** respectively, and correspond to variations in the qubit energy and Rabi frequency (respectively). The black dotted lines indicate the location of the first order z(x)-dephasing sweet spots (z-sweet spot and x-sweet spot), at which the first derivative of the qubit energy(dipole) moment w.r.t. electric detuning ϵ vanishes. At one specific location, the z-sweet spot is protected to second-order and corresponds to a second-order sweet spot (white circle). **c)** and **d)** show line cuts of the qubit energy and normalised dipole moments indicated by horizontal lines in the plots in **a)** and **b)** respectively the plots above. **e)** Illustration of the first order sweet spot mechanism. All data are simulated for $B = 0.2\,\mathrm{T}$, $\Delta\Omega_z = 5\,\mathrm{MHz}$ and a charge noise amplitude $\sigma_\epsilon = 0.3\mathrm{GHz}$.

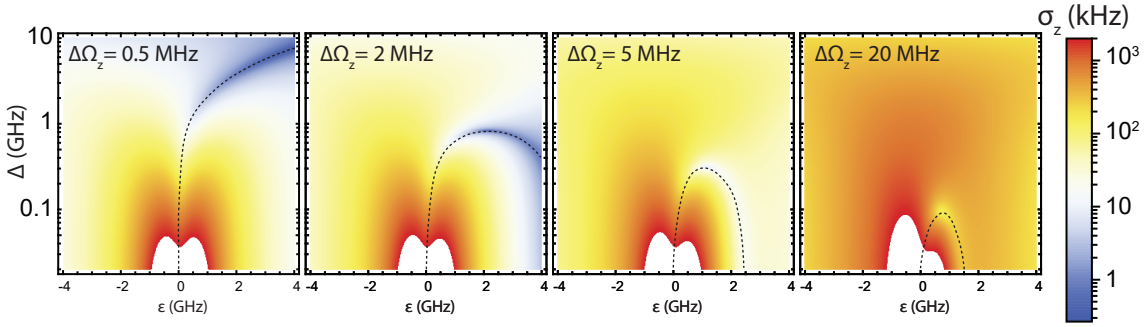

Figure 3.14: **Demonstration of the change in the z-dephasing sweet spot of the flopping-mode qubit with longitudinal gradient $\Delta\Omega_z$,** at a magnetic field $B = 0.2\,\mathrm{T}$. The plots depict the z-dephasing rate σ_z corresponding to variations in the qubit energy due to charge noise, for increasing magnitudes of longitudinal gradients $\Delta\Omega_z$ from left to right. The first order sweet spot (z-sweet spot) is indicated by the dashed black line. The dephasing rate, σ_z is seen to increase over the whole parameter space with increasing longitudinal magnetic field gradient, $\Delta\Omega_z$. The arc described by the first order z-sweet spot is seen to become smaller with increasing longitudinal gradient $\Delta\Omega_z$.

apex of that arc, and corresponds to one specific value of the spin–charge detuning and the electric detuning where the first and second-order derivatives of the first and second-order terms are similar in magnitude and cancel out. At this position, the energy is insensitive to second-order to electric field fluctuations and the z-dephasing rate is as low as $\sim 10\,\mathrm{kHz}$.

Because the presence of the first-order z-dephasing sweet spot depends on the second-order energy term dominating the longitudinal energy gradient, the survival of the first-order z-sweet spot can be extended to larger spin–charge detunings by decreasing the longitudinal difference $\Delta\Omega_z$ that determines the magnitude of the longitudinal-energy gradient. The persistence of the first-order z-dephasing sweet spot to large spin–charge detuning values is important because the x-dephasing rate decreases strongly with increasing spin–charge detuning and is quite large for low detuning values (see Fig. 3.13 b)). The x-dephasing rate is proportional to the drive amplitude ϵ_d, (arbitrarily set to 0.1 GHz in the figure), so that finding the optimal operation point of the qubit which minimises both z- and x-dephasing errors (and other errors as well) necessitates a multi-dimensionsal optimisation (see Sect. 3.4).

The dependence of the z-dephasing sweet spot on the magnitude of the longitudinal gradient is illustrated in Fig. 3.14, in which the z-dephasing rate is plotted for four increasing values of the longitudinal difference $\Delta\Omega_z$, from a value of 0.5 MHz expected for the 2P1P3e flopping-mode implementation (see Chapter 4) to a value of 20 MHz that is close to the 13 MHz expected for the flip-flop qubit [12].

The arc described by the first-order z-dephasing sweet spot is large at a low longitudinal-energy gradient. The dephasing rate at the first and second-order sweet spot also increases with the gradient from well below 1 kHz at low $\Delta\Omega_z = 0.5\,\mathrm{MHz}$ to about 100 kHz at the second-order z-sweet spot at $\Delta\Omega_z = 20\,\mathrm{MHz}$. Notably, the dephasing rate in the regime where the longitudinal gradient is dominating (above the arc) also increases with the magnitude of the longitudinal energy gradient. This is because the first order term of the qubit energy is proportional to $\Delta\Omega_z$.

3.2.4 Summary

In summary, we have shown in Sect. 3.2 that the flopping-mode Hamiltonian describes three proposed DQD qubits. Using perturbation theory we illustrated how the emergence of an electrical dipole moment for the electron spin is linked to the hybridisation of the spin to the charge qubit defined by the electron charge and the two QDs. We saw that for weak hybridisation, the electric driving can be understood classically as the motion of an electron spin in a magnetic gradient. Finally, a simple analysis of charge dephasing reveals the presence of different dephasing sweet spots in the qubit systems, where we expect the error rate of the qubit to be low.

3.3 Modelling errors during driving of the flopping-mode qubits

In Sect. 3.2 we have reduced the general flopping-mode qubit Hamiltonian to a coupled four level system, and shown the emergence of a dipole-coupling element between the resulting charge-hybridised spin-eigenstates, which define a qubit. This dipole coupling allows electrical driving between the qubit states. The viability of such an electrically driven qubit, as part of a universal quantum computer for example, can now be assessed by estimating the error of the single-qubit gates used for qubit control.

3.3.1 Errors for the driven flopping-mode qubit

Imperfect control of the physical system impacts the evolution of the system and generates errors. This cannot be avoided because the qubit, rather than being isolated, is interacting with it's environment, for example during measurement and manipulation. The interaction with the coupled system may be described as an interaction with a leakage state, which can be modelled by a unitary evolution of

the system that includes the leakage state. It may not be possible to avoid this interaction due to imperfect control over the system. In some cases, the interaction with the coupled system is so complex that it cannot be described by a unitary operation and thus needs to be approximated statistically. Dephasing and relaxation which we will consider in the present chapter belong to this category. Leakage, dephasing and relaxation are the three general mechanisms leading to errors that we will consider.

Leakage is the mechanism by which the qubit wave function spreads out of the qubit subspace. For the flopping-mode qubit, the qubit states are indeed coupled to excited charge states, and strong non-adiabatic manipulation of the qubit leads to leakage. Dephasing, the second mechanism we consider, results from the interaction of the system with a noisy environment. It consists of unpredictable variations in the unitary evolution of the system which lead to control errors. The dominant noise source for the flopping-mode qubit is charge noise (see Sect. 3.3.3) and is induced by electric fluctuators near the qubit. We will also consider dephasing caused by magnetic fluctuators near the qubit. Finally, relaxation is the thermodynamic process by which a system reaches its ground energy state. For the flopping-mode qubit the dominant relaxation mechanism is charge T_1-relaxation (see Sect. 3.3.4). It consists of the excited charge state emitting its energy as a phonon and relaxing to its ground state [82].

We will combine the charge dephasing error e_ϵ, the magnetic dephasing error e_B, the T_1 relaxation error e_{T_1} and the leakage error $\mathrm{e}_{\mathrm{leak}}$ into one total error metric e_{tot}, assuming that they all originate from independent random processes:

$$\mathrm{e}_{\mathrm{tot}} = 1 - (1 - \mathrm{e}_\epsilon)(1 - \mathrm{e}_B)(1 - \mathrm{e}_{T_1})(1 - \mathrm{e}_{\mathrm{leak}}). \tag{3.3.1}$$

Independence is assumed in this because magnetic and charge dephasing errors as well as T_1-relaxation errors originate from different physical mechanisms linked to charge fluctuators, magnetic nuclear spin isotopes and phonons, respectively [73, 72]. Leakage and T_1 processes can be combined into a separate error, which will be covered in the T_1 error estimation e_{T_1}.

To obtain a representative error metric,one needs to average the total gate error over all possible initial states of the qubit. This is crucial, because some errors can vary by more than one order of magnitude. In polar coordinates the initial state can be written as $\Psi_i = \cos\theta/2|0\rangle + \sin\theta/2e^{\imath\phi}|1\rangle$, where θ and ϕ are the longitudinal and azimuthal angles of the state on the Bloch sphere and the qubit ground/excited states are $|0\rangle$ and $|1\rangle$ respectively. Averaging of an error $e(\Psi_i)$ over the Bloch sphere

$\mathscr{B}$ can then be performed as an integration over the unit sphere :

$$\langle e(\Psi_i)\rangle_{\mathscr{B}} := \frac{1}{4\pi}\int_0^{2\pi}\int_0^{\pi} \mathrm{e}\left(\Psi_i(\theta,\phi)\right)\sin\theta \mathrm{d}\theta\mathrm{d}\phi. \tag{3.3.2}$$

The final error is given by:

$$\begin{aligned} \mathrm{e} &= \langle \mathrm{e}_{\mathrm{tot}}(\theta,\phi)\rangle_{\mathscr{B}} && (3.3.3)\\ &\approx \langle 1-\mathrm{e}_{\epsilon}\rangle_{\mathscr{B}}\langle 1-\mathrm{e}_{B}\rangle_{\mathscr{B}}\langle 1-\mathrm{e}_{T_1}\rangle_{\mathscr{B}}\langle 1-\mathrm{e}_{\mathrm{leak}}\rangle_{\mathscr{B}}. && (3.3.4)\end{aligned}$$

In the last step we approximate the angle integrals of the total error by the product of the integrals of the different error components. This approximation allows for the integrations to be performed analytically. At the same time it reproduces the exact results obtained by numerical integration. We will also see that some errors do not depend on the qubit start-state in which case the approximation is exact.

In the following three subsections we will introduce separate Bloch sphere averaged error models for each error type. Then, in Sect. 3.3.2 we consider leakage errors to fully model the error pathways in flopping-mode qubits.

3.3.2 Leakage modelling of flopping-mode qubits

Leakage consists in a spread of the wave function outside of the qubit subspace due to external couplings. Leakage can thus be described using a Hamiltonian including all leakage state. In the case of the flopping-mode qubit the qubit states are the hybridised spin states $\left\{|0\rangle = |\widetilde{\uparrow -}\rangle, |1\rangle = |\widetilde{\downarrow -}\rangle\right\}$ in the charge ground state $|-\rangle$ and the leakage states correspond to the states where the charge has been excited: $\left\{|2\rangle = |\widetilde{\uparrow +}\rangle, |3\rangle = |\widetilde{\downarrow +}\rangle\right\}$. In appendix Sect. B.1, we show using second-order perturbation theory that the full flopping-mode Hamiltonian can be reduced to the following form in the systems eigenbasis $\left\{|0\rangle = |\widetilde{\uparrow -}\rangle, |1\rangle = |\widetilde{\downarrow -}\rangle, |2\rangle = |\widetilde{\uparrow +}\rangle, |3\rangle = |\widetilde{\downarrow +}\rangle\right\}$, when operated close to zero electric detuning ($\epsilon = 0$):

$$H_{\mathrm{fm}} = \begin{pmatrix} 0 & \Omega_r & \Omega_l & 0 \\ \Omega_r & \tilde{\Omega}_s & 0 & \Omega_l \\ \Omega_l & 0 & \tilde{\Omega} & \Omega_r \\ 0 & \Omega_l & \Omega_r & \tilde{\Omega}+\tilde{\Omega}_s \end{pmatrix}. \tag{3.3.5}$$

The Hamiltonian H_{fm} describes an electron spin with an energy splitting $\tilde{\Omega}_s$ and an electric coupling strength Ω_r, that can be in either the charge ground state, or in

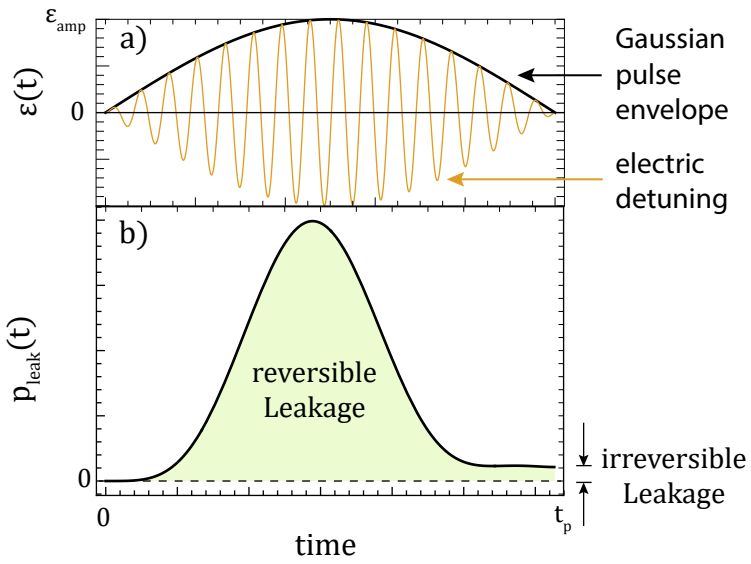

Figure 3.15: **Reversible and irreversible leakage population during an adiabatic Gaussian pulse.** The electric detuning pulse is plotted in **a)** as a function of time, with the Gaussian pulse envelope indicated in black. The leakage population during such an adiabatic pulse is shown below in **b)** (in black). The population that is de-excited during the second half of the pulse (in green) corresponds to reversible leakage, while the population leakage popolution at the end of the pulse corresponds to irreversible leakage

the charge excited state. Direct charge excitation of the spin states is described by the matrix element $\Omega_l \approx \frac{t_c}{\Omega}$, that describe the charge–qubit electric dipole moment.

In order to drive only the qubit transition, we will gradually increase and then decrease the drive electric-field amplitude in time using a symmetric Gaussian pulse shape (see Fig. 3.15 a). The time dependent electric drive leads to a time dependent occupation of the leakage states. Using the Gaussian pulse, the occupation proportion of the leakage states first increases when the pulse amplitude increases and then decreases when the pulse amplitude decreases. A symmetric continuous pulse shape starting and ending at zero allows for most of the leakage state population to be de-excited in the second half of the pulse [83], for low enough drive amplitudes (see Fig. 3.15 b).

Irreversible leakage leads to errors with a finite probability, proportional to the leakage state occupation at the end of the pulse, for the qubit to collapse into one of the leakage states upon measurement. The irreversible leakage error is thus given by the occupation probability of the leakage states at the end of the pulse.

Reversible leakage leads to errors if the state into which the system temporarily occupies is itself prone to errors. The two main errors we will discuss in relation to this are dephasing and relaxation via the excited charge states. Section 3.3.3 will show that charge dephasing via the excited charge-states is negligible, but T_1

relaxation of the excited charge states can lead to significant errors. Indeed, the excited charge states are temporarily occupied during pulsing, leading to a finite probability for the states to relax back to the ground state. In Section 3.3.4 we relate this error to the time integrated excited charge state proportion during the pulse. We estimate this integral in the present section before deriving a model for the irreversible leakage error.

In our simulations the electric-field burst $E(t)$ lasting a time t_p is shaped using a Gaussian pulse envelope $g(t, t_p)$ plotted in Fig. 3.15 a): $E(t) = E_d \cdot g(t, t_p)\cos(\omega_d t)$, where ω_d is the drive frequency.

$$g(t, t_p) = \frac{1 - \exp\left(\frac{2t(t_p - t)}{t_p^2}\right)}{1 - e^{1/2}}. \tag{3.3.6}$$

The time evolution of the flopping-mode Hamiltonian H_{fm} of Eq. 3.3.5 is simulated in the rotating frame (RF) that is locked to the phase precession of the qubit. When driving the microwave electric field $E(t)$ at the frequency corresponding to the qubit splitting $\tilde{\Omega}_s$ the rotating wave approximation (RWA) yields the following Hamiltonian in the rotating frame (more details on the RWA in Appendix B.2):

$$H_{\text{fm}}^{RF} = \begin{pmatrix} 0 & \Omega_r/2 & \Omega_l/2 & 0 \\ \Omega_r/2 & 0 & 0 & \Omega_l/2 \\ \Omega_l/2 & 0 & \Delta_{ql} & \Omega_r/2 \\ 0 & \Omega_l/2 & \Omega_r/2 & \Delta_{ql} \end{pmatrix}, \tag{3.3.7}$$

where $\Delta_{ql} = \tilde{\Omega} - \tilde{\Omega}_s$ is the spin–charge detuning that describes the energy gap between the second and third states in the energy spectrum $|\widetilde{\downarrow -}\rangle$ and $|\widetilde{\uparrow +}\rangle$. This Hamiltonian describes the errors related to reversible and irreversible leakage into the excited charge states.

The reversible leakage can be characterised by the time integrated overlap I_d of the qubit state with the two leakage states, during the $\pi/2$ Gaussian pulse of duration $t_{\pi/2}$,

$$I_d := \int_0^{t_{\pi/2}} \sum_{i=2}^{3} |\langle \Psi(t')|i\rangle|^2 \, \mathrm{d}t'. \tag{3.3.8}$$

The overlap integral, I_d can be estimated by assuming a non-noisy unitary time evolution of an initial state on the Bloch sphere. We find that the integral is inde-

pendent of the start state and can be well approximated to second-order in $\frac{\Omega_l}{\Delta_{ql}}$):

$$I_d \approx \alpha_d \frac{1}{\Omega_r} \frac{\Omega_l^2}{\Delta_{ql}^2}. \tag{3.3.9}$$

The coefficient α_d is related to the Gaussian pulse shape used to drive the qubit and equals 0.046 for the pulse shape of Eq. 3.3.6. The integral is independent of the qubit initial state because the coupling strengths Ω_l of the two qubit state to their respective leakage states are equal, so that any superposition of the qubit states is equally likely to leak out of the qubit subspace. The integrated leakage population is inversely proportional to the coupling Ω_r between the qubit states and is thus proportional to the gate time $t_{\pi/2} = \pi/(2\bar{g}\Omega_r)$ reflecting the fact that shorter pulses lead to a smaller time integral. The integral is finally dependent on the squared ratio of the leakage coupling over the energy gap, highlighting that higher leakage couplings and smaller gaps lead to more leakage.

We now turn to the irreversible leakage error, it is given by the probability of occupation of the leakage states $|2\rangle$ and $|3\rangle$ at the end of the $\pi/2$ pulse:

$$e_{\text{leak}} = p_{\text{leak}} = \sum_{i=2}^{3} \left| \langle \Psi(t_{\pi/2}) | i \rangle \right|^2 \tag{3.3.10}$$

For the flopping-mode qubit, the leakage coupling strength Ω_l is approximatively equal to the bare charge qubit coupling $\Omega_l \approx \Omega_r^{\text{charge}}$ (see more details in Appendix B.1). In contrast, the qubit Rabi frequency reduces to a proportion of that bare charge qubit coupling given by half the hybridisation proportion h:

$$\Omega_r = \frac{h}{2} \Omega_r^{\text{charge}}.$$

For the flopping-mode qubit, the ratio $\lambda = \Omega_l/\Omega_r$ of the leakage and qubit coupling strengths, is thus given by $\lambda \approx \frac{2}{h}$ and is much larger than unity as the hybridisation proportion is usually limited to at most a few percent in order to limit dephasing errors (see Sect. 3.4). The ratio λ is an important parameter to describe leakage, and is widely used for superconducting qubits [83]

In Fig. 3.16 we simulate the leakage population at the end of a $\pi/2$-pulse for the generic flopping-mode qubit as a function of the qubit Rabi frequency Ω_r, for a typical value of $\lambda = 21$, for Gaussian and square pulse shapes

For qubit drive amplitudes Ω_r that are much smaller than the energy gap to the nearest leakage state Δ_{ql} ("weak driving regime"), the leakage population grows

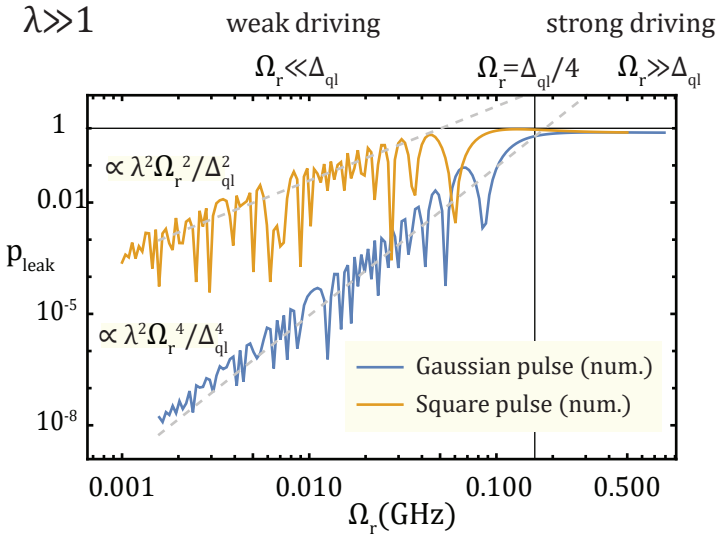

Figure 3.16: **Calculation of the population p_{leak} in the leakage states at the end of a $\pi/2$ X-gate,** for Gaussian and square pulse shapes, and as a function of qubit drive amplitude, Ω_r. We simulate the case where the coupling to the leakage state is larger than the coupling between qubit state, i.e. $\lambda := \Omega_l/\Omega_r >> 1$. The solid lines display the leakage population for a Gaussian and a square pulse shape, in blue and orange respectively, while the dotted grey lines indicate the asymptotic trends. We chose $\lambda = 21$, and $\Delta = 0.65\,\text{GHz}$ which corresponds to typical spin-charge detuning and coupling for a flopping-mode qubit.

polynomially with the qubit drive-amplitude Ω_r as the drive become less adiabatic. The population leakage associated with the Gaussian pulse shape grows slower than the square pulse because it adiabatically increases and decreases the drive amplitude. In that weak-driving regime, the leakage population linked to the Gaussian pulse shape is well approximated by:

$$p_{\text{leak}} \approx \alpha_{\text{leak}} \frac{\Omega_r^2 \Omega_l^2}{\Delta_{ql}^4} = \alpha_{\text{leak}} \lambda^2 \frac{\Omega_r^4}{\Delta_{ql}^4}, \tag{3.3.11}$$

where $\alpha_{\text{leak}} = 0.37$ is a constant related to the Gaussian pulse shape of the drive amplitude and is estimated by a fit to the numerical simulations. For a square pulse-shape, the leakage population follows a trend of lower polynomial order ($e_{\text{leak}} \propto \Omega_l^2/\Delta_{ql}^2 = \alpha_{\text{leak}} \lambda^2 \frac{\Omega_r^2}{\Delta_{ql}^2}$) which also depends on λ^2 but grows as the square of the ratio $\frac{\Omega_r}{\Delta_{ql}}$ of the qubit drive amplitude and the energy gap to the nearest leakage state. The leakage population associated with the Gaussian pulse shape instead depends on the fourth power of this ratio. For driving strengths much smaller than the energy gap, this results in a significant advantage of the Gaussian pulse over the square pulse in terms of minimising leakage errors.

When qubit-driving strengths get larger or comparable to the energy gap to

the leakage state $\Omega_r > \Delta$ ("strong driving regime"), the leakage populations for both pulse shapes asymptotically approach a constant (horizontal line in Fig. 4.5), that only depends on $\lambda = \Omega_l/\Omega_r$, the ratio of the leakage state and qubit state couplings. At such high drive amplitudes, the power-broadened qubit-transition-line width overlaps with the leakage transition, and both transitions are addressed. If the coupling strength to the leakage states is larger than the coupling between qubit states ($\lambda > 1$), the wave function tends to swap over from the qubit state to the leakage states and the leakage error approaches unity (see Fig. 4.5). When the coupling to the leakage state is smaller than the coupling between the qubit states ($\lambda < 1$ as displayed in Fig. 4.5), the qubit wave function only slightly evolves towards the leakage states, and the leakage population asymptotically approaches:

$$p_{\text{leak}} \to \sin\left(\frac{\pi}{4}\lambda\right)^2 \approx \left(\frac{\pi}{4}\right)^2 \lambda^2. \tag{3.3.12}$$

Leakage due to the Gaussian pulse shape is well described by Eq. 3.3.11 because it falls within the weak-driving regime for realistic driving amplitudes. Indeed the Rabi frequency of the qubit (at most a few tens of MHz) is much smaller than any realistic energy gaps to the excited charge state (a few hundreds of MHz at least). The leakage error e_{leak} of the flopping-mode qubit is therefore estimated using Eq. 3.3.11 with numerically calculated parameters that we examine together with the other leakage channels. The irreversible leakage error for the flopping-mode qubit is independent of the initial state of the qubit because of the symmetric coupling amplitudes. No averaging over the Bloch sphere is therefore necessary.

3.3.3 Modelling qubit dephasing

Sources of dephasing

Dephasing of the flopping-mode qubit results from its interaction with a noisy environment. The principal pathway for noise to couple to the flopping-mode qubit is electromagnetic. Charge fluctuators in the silicon lattice produce noisy electric fields that couple to the charge state of the qubit via the detuning parameter ϵ, whereas magnetic fluctuators couple to the spin state of the qubit via the magnetic field B. The following paragraphs briefly describe the microscopic origins and the characteristics of both magnetic and charge noise. Experimental data from the literature cited below shows that both kinds of electromagnetic noise at the sample are well described by Gaussian probability distribution functions (PDFs), with a standard deviation that will depend on the noise amplitude and on the sampling

frequency [84]. Charge and magnetic noise in semiconductors typically do not have a flat spectrum, and contain more energy at lower frequencies [85, 86]. When the noise is sampled over longer times, these low-frequency components increase the variations in the sampled noise amplitudes and result in a wider PDF [84]. The distribution of the noise power over the frequency spectrum is described by the power spectral density (PSD) $P(\nu)$ of the noise, that describes the noise power $P(\nu)\mathrm{d}\nu$ contained in an infinitesimal frequency interval $\mathrm{d}\nu$ [87]. The Gaussian shape of the PDFs hint at the fact that the magnetic and charge noise mostly originate from large ensembles of independent fluctuators (as stated by the central limit theorem). In reality a few fluctuators close to the qubit can have a larger effect than the remaining fluctuators of the ensemble [84], but the probability distribution functions observed experimentally remain Gaussian (see for example the measurement described by this author in Fig. 5.16 c). We now briefly describe the origins and characteristics of magnetic and charge noise and motivate the use of the quasi-static approximation that models the noise variable during each Hamiltonian time evolution, as a static noise variable sampled from the noise PDF.

Non-zero nuclear spin isotopes within the semiconductor material have been identified as the principle source of magnetic noise in semiconductor qubits. Natural silicon, for example consists of about 4.7% of ^{29}Si [88], which is the only of the three stable silicon isotopes (^{28}Si, ^{29}Si, and ^{30}Si) with a half-integer nuclear spin (1/2). Natural silicon can be isotopically purified into a fully non-magnetic material, drastically reducing the magnetic noise amplitude in the material [1]. As a comparison, GaAs/AlGaAs structures cannot be isotopically purified because all stable isotopes of Ga and As have a non-zero nuclear spin. This is the principle reason for the semiconductor-spin-qubit community changing its material system of choice from GaAs/AlGaAs to silicon in the 2010s. The magnetic noise in semiconductor devices that arise due to the nuclear spin baths has been attributed to magnetic and hyperfine mediated spin diffusion [85, 89]. The PDF of the magnetic-field noise is well approximated by a Gaussian distribution [90], with a standard deviation $\sigma_B = 0.1\,\mathrm{mT}$ in natural silicon [90] and $0.03\,\mu\mathrm{T}$ isotopically purified silicon (800ppm) [1] respectively for measurements typically lasting one hour. Such magnetic field variations correspond to standard deviations of $\sigma_E/h \approx 3\,\mathrm{MHz}$ and $1\,\mathrm{kHz}$ in the Zeeman energy, and thus also the phase precession rate of a pure electron spin-qubit.[6] This magnetic noise will also lead to magnetic dephasing in the flopping-mode qubit, because its dependence on the magnetic field is dominated by

[6] Assuming a gyromagnetic ratio of $28\,\mathrm{GHz/T}$.

the electron Zeeman term up to first order (see Eq. 3.2.19). The magnetic noise PSD has been shown to follow a $f^{-\alpha}$ with $0.5 \leq \alpha \leq 2$ behaviour [85, 89] in both silicon and gallium-arsenide semiconductor devices due to the distribution of two-level fluctuators in the material.

The origin of charge noise depends on the material system used, the device fabrication processes, and is still relatively poorly understood. Potential charge fluctuators cited in the literature are defects and impurities in the silicon lattice [84], defects at the silicon/native oxide interface [86], defects at the silicon/metal interfaces [86, 91]. In magnetically pure materials such as ^{28}Si charge noise is the dominant error source [8]. In our silicon devices (as in most other silicon devices in the community), the PSD of charge noise follows a frequency-distribution of the form $f^{-\alpha}$, where $0.5 \leq \alpha \leq 2$, and the PDF of the electric field noise is well described by a Gaussian with standard deviation describing the noise amplitude in the device [84]. For all our simulations we use a realistic electric field noise standard deviation of about 250 V/m, similar to that used in the other flopping-mode proposals [12, 92], corresponding to a standard deviation in the static detuning parameter of $\sigma_\epsilon = 0.3\,\text{GHz}$[7]. As we discussed in Sect. 3.2.3, this electric-field noise couples into both the flopping-mode qubit energy and Rabi frequency, z- and x-dephasing, respectively. The magnitude of both dephasing rate varies over many orders of magnitude depending on the presence of the electric tuning parameters, the magnetic-gradients and more even the electric driving strength for the x-noise. A flopping-mode device with a realistic longitudinal gradient between 0.5 to 20 MHz will experience a z-dephasing rate from $\sim$ 10 kHz to $\sim$ 1 MHz for operation at $\epsilon = 0$. This is one to several orders of magnitude higher than the dephasing rate expected from magnetic noise in isotopically purified silicon and will therefore be the dominating dephasing mechanism for the flopping mode qubit.

Both magnetic and charge noise display PSDs of the form $f^{-\alpha}$ ($0.5 < \alpha \leq 2$). Low-frequency noise therefore represents the overwhelming noise contribution during a measurement. However, this low frequency noise allows us to use the "quasistatic" approximation to describe the effect of charge or magnetic noise during an experiment which is repeated many times to build statistics of the quantum operation. The quasistatic approximation models the time-dependent noise as a random variable changing between each shot, but staying constant (thus the "static" in quasistatic) during the shot. It accurately describes a variety of qubit evolutions for magnetic noise [90] and for charge noise [8]. As mentioned above, a Gaussian

[7] Assuming a distance of 10 nm between the two dot locations, as is the case for the flip-flop and epitaxial flopping-mode qubit.

PDF accurately fits experimental sampling of the magnetic and charge noise PDFs. The variance of the noise over the duration of an experiment can be related to an integral over the PSD of the noise for the time duration of the measurement (see Appendix B.3).

Dephasing-error formula

We define the charge dephasing error of the unitary evolution associated with the $\pi/2$ gate to be the deviation of the expectation value of the noisy unitary evolution projected onto the ideal unitary evolution U_{id} of the initial state $\Psi_{i,\delta\epsilon}$ [75], averaged over the charge noise detuning PDF $P(\delta\epsilon)$:

$$\mathrm{e}_\epsilon = 1 - E\left(\left|\langle\Psi_{i,\delta\epsilon}|U_{\delta\epsilon}^\dagger U_{\mathrm{id}}|\Psi_{i,\delta\epsilon}\rangle\right|^2\right). \tag{3.3.13}$$

Analytical dephasing-error model

An analytical model of the state overlap $O(\delta\epsilon, \Psi_{i,\delta\epsilon}) := \left|\langle\Psi_{i,\delta\epsilon}|U_{\delta\epsilon}^\dagger U_{\mathrm{id}}|\Psi_{i,\delta\epsilon}\rangle\right|^2$, while approximate, accelerates the error computation, and renders feasible the averaging of the error over all possible initial states $\Psi_{i,\delta\epsilon}$ of the Bloch sphere. The latter is important because the gate error can vary by up to an order of magnitude depending on the initial qubit state. The average over the charge noise random variable $\delta\epsilon$ is then performed numerically.

Charge noise couples into the noisy unitary time evolution $U_{\delta\epsilon}$ through the perturbation of the parameters in the flopping-mode Hamiltonian (see Eq. 3.2.8), each corresponding to a separate error channel. Provided the system is driven adiabatically, the system dynamics is mostly confined to the qubit subspace, in which the qubit is well described by the two-level Hamiltonian: $\Omega_s/2\sigma_z + \Omega_r\sigma_x$, where Ω_s is the qubit energy splitting and Ω_r the qubit Rabi frequency (when driven). Both Ω_s and Ω_r are dependent on ϵ and thus offer a distinct pathway for charge noise to couple into the time evolution, which we term the z-/x- noise channel respectively. For a given detuning perturbation $\delta\epsilon$ we write $\tilde{\Omega}_s(\epsilon+\delta\epsilon)/2 = \tilde{\Omega}_s(\epsilon)/2 + \delta z$ and $\Omega_r(\epsilon+\delta\epsilon)/2 = \Omega_r(\epsilon)/2 + \delta x =: x + \delta x$. In the rotating frame, when driving the system resonantly, the reduced Hamiltonian becomes:

$$H_r(\delta z, \delta x) = \delta z\,\sigma_z + (x+\delta x)\,\sigma_x. \tag{3.3.14}$$

The time evolution associated with this Hamiltonian, can be modelled analytically

by approximating the Gaussian pulse $\epsilon_d\, g(t)$ by a constant pulse $\epsilon_d\, \bar{g}$, where $\bar{g} = 0.633$ is the average value of the pulse-shape $g(t)$ in time.

With the simplified 2-level Hamiltonian, and pulse-shape, the state overlap $O(\delta\epsilon, \Psi_{i,\delta\epsilon})$ in Eq. 3.3.13 for a initial state $\Psi_i = \cos(\theta/2)|0\rangle + \sin(\theta/2)e^{\imath\phi}|1\rangle$ is approximated by:

$$O(\delta\epsilon, \Psi_{i,\delta\epsilon}) \approx \left|\langle\Psi_i|U(H_r(0,0), t_{\pi/2})^\dagger \cdot U(H_r(\delta z, \delta x), t_{\pi/2})|\Psi_i\rangle\right|^2. \tag{3.3.15}$$

Here we estimate the $\pi/2$ gate time to be $t_{\pi/2} = \pi/(4\bar{g}x)$, we neglected the initial state perturbation due to $\delta\epsilon$ ($\Psi_i := \Psi_{i,0}$), and the unitary time evolution U of the Hamiltonian H is expressed as the matrix exponential $U(H, t_g) = \exp(-\imath H t_g)$ (in frequency units). The above expression can be evaluated analytically in Eq. 3.3.16 for the explicit expression, simplified by averaging over the Bloch Sphere. Figure 3.17, compares the fully numerical error (square markers) with the analytical error model (solid line) for a range of initial states on the Bloch sphere. The numeric calculation computes the overlap in Eq. 3.3.13, without any approximations, while the analytical model uses the analytical expression corresponding to Eq. 3.3.15. In black we include all the noise channels present in the flopping-mode Hamiltonian, whereas in red and blue we only include the x-/z-noise channels. Figure 3.17 highlights how specific initial qubit states for which the dynamics are protected against one of those noise channels (either x or z).

In Fig. 3.17 a), the z-error goes to zero for start points on the Bloch sphere described by angles $\phi = \pi/2$ and $\theta = \pi/4$. This initial state is singular because it corresponds to a time evolution passing through the north pole of the Bloch sphere halfway through the pulse. Any phase accumulation due to δz in the first half of the pulse is cancelled out in the second half. Two other singular initial states are captured in Fig. 3.17 b), where the x-error goes to zero at $\theta = \pi/2$ and $\phi = 0 \,(\mathrm{mod}\, \pi)$. These angles correspond to the two initial states for which the x-axis intercepts the Bloch sphere. These two states have a stationary time evolution and are thus not affected by x-noise since the x-rotation gate does not cause any rotations for this initial qubit state.

When including errors that couple through both the x and z error-channel, singular points in one noise channel are smoothed out by non-vanishing errors in the other (see black line in Fig. 3.17). This is due to the fact that in Fig. 3.17, we chose system settings for which both noise channels are equally important and visible. Whenever one of the error channel dominates, its variations essentially yield those of the total error.

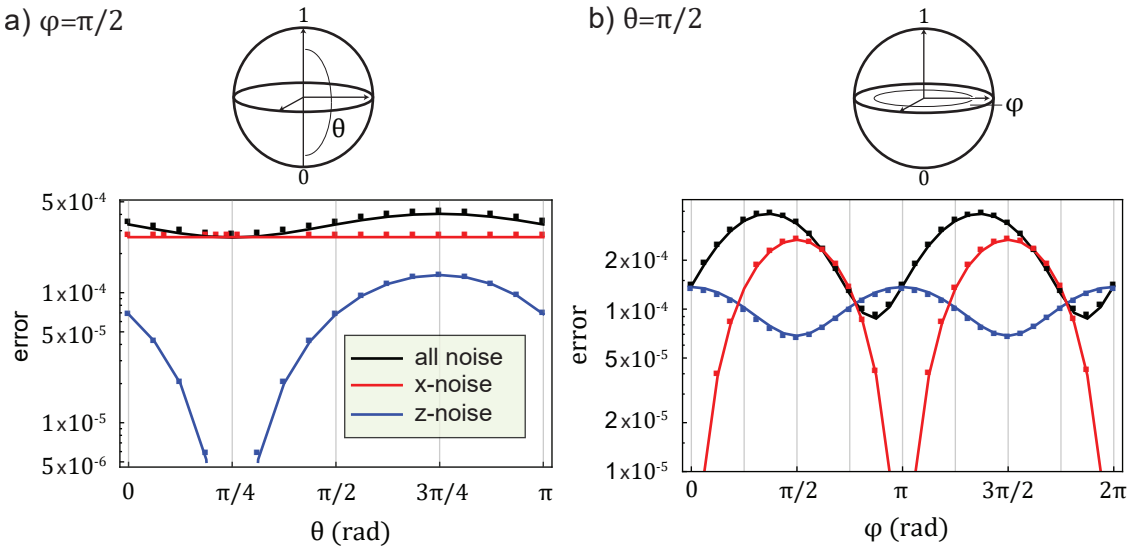

Figure 3.17: **Determination of the lowest error rates due to charge noise.** Both **a)** and **b)** show the angle dependence of the dephasing charge noise for $\phi = \pi/2$ and $\theta = \pi/2$ as a function of the longitudinal and azimuthal angles θ and ϕ respectively. The dark line displays the error when considering all channels through which charge noise can couple into the system. The red/blue lines only consider the x-/z- charge noise channels. The analytical model (lines) accurately fits the numerical calculation (square markers). In a), the z-error goes to zero at $\theta = \pi/4$ because variations δz are echoed out when passing the pole. In b), the x-error goes to zero at $\phi = 0\,(\mathrm{mod}\,\pi)$, because the start state is on the x-axis of the Bloch sphere. We used a magnetic field of 0.3 T at $\epsilon = 0$ and $t_c = 4.5\,\mathrm{GHz}$, for a drive amplitude $\epsilon_d = 0.2\,\mathrm{GHz}$ optimised based on balancing all of the noise sources and driving strengths in the system as these are close to realistically optimal qubit parameters.

We find that the model is accurate for driving amplitudes well above 1GHz, where reversible leakage becomes substantial and dephasing can couple via the leakage channels. Dephasing through the reversible excited-state proportion is suppressed to third order because the perturbations linked to each of the leakage states cancel. This is only the case when the coupling strengths Ω_l, to the two leakage states are identical, that is in the strong spin-charge hybridisation regime. Otherwise, this effect would need to be accounted for by appropriate pulse shaping. When the qubit error is dominated by leakage then the dephasing model breaks down, but leakage and relaxation are the main source of errors so that the total-error is still accurate since dephasing only contributes a small amount to the overall error.

The analytical model of Eq. 3.3.15 allows analytical evaluation of the integrals when averaging over different initial states on the Bloch sphere. This is important since various algorithms require different initial states and also since multiple gates will be run in a sequence meaning the gate operation could be performed on any qubit state. For a given charge noise induced detuning perturbation $\delta\epsilon$, coupling into the z- and x- components of the system Hamiltonian via variations δz and δx respectively, we find that the overlap between the perturbed and non-perturbed time evolution is given by:

$$\begin{aligned} O_{\mathscr{B}}(\delta z, \delta x) := \langle O(\delta z, \delta x, \Psi_{i,\delta\epsilon})\rangle_{\mathscr{B}} = \frac{1}{6\Omega_{2L}^2}\Bigg[& 4(x+\delta x)^2 + 3\delta z^2 \\ & + \delta z^2 \cos\left(\frac{\pi}{2}\frac{\Omega_{2L}}{x}\right) + 2(x+\delta x)\Omega_{2L}\sin\left(\frac{\pi}{2}\frac{\Omega_{2L}}{x}\right)\Bigg], \end{aligned} \tag{3.3.16}$$

with the driven qubit splitting $\Omega_{2L} = \sqrt{\delta z^2 + (x+\delta x)^2}$. The expression evaluates to 1 for $\delta z = 0$ and $\delta x = 0$, as the noisy time evolution is equal to the ideal time evolution. Both x and z noise perturbations δz and δx depend on the electric-detuning noise $\delta\epsilon$. To get the final averaged analytical charge dephasing error one has to average $1 - O_{\mathscr{B}}(\delta z(\delta\epsilon), \delta x(\delta\epsilon))$ over the electric detuning noise variable $\delta\epsilon$ (note that we will calculate this average over the Gaussian distributed random variable $\delta\epsilon$ numerically, unless indicated otherwise):

$$\langle \mathrm{e}_\epsilon\rangle_{\mathscr{B}} = 1 - \langle O_{\mathscr{B}}(\delta z(\delta\epsilon), \delta x(\delta\epsilon))\rangle_{\delta\epsilon}\,. \tag{3.3.17}$$

The dephasing error in Eq. 3.3.17 can however be estimated analytically by assuming both variables δz and δx to be independent Gaussian distributed variables. This is not strictly valid in our case because both variables are dependent on the

electric detuning noise $\delta\epsilon$ and thus not independent. Expanding Eq. 3.3.16 to second-order in δz and δx, and then taking the expectation value using the Gaussian PDF $\frac{1}{\sqrt{2\pi\sigma^2}}\exp\left(-\frac{\delta^2}{2\sigma^2}\right)$, we find to third order in $1/x$:

$$\langle \mathrm{e}_\epsilon \rangle_{\mathscr{B}} \approx \frac{\pi^2}{24}\left(\frac{\sigma_x}{x}\right)^2 + \frac{1}{3}\left(\frac{\sigma_z}{x}\right)^2 \tag{3.3.18}$$

$$\approx 0.41\left(\frac{\sigma_x}{x}\right)^2 + 0.33\left(\frac{\sigma_z}{x}\right)^2 . \tag{3.3.19}$$

Equation 3.3.18 highlights that the influence of the z-noise since the pre-factors are comparable (0.41 for x and 0.33 for z), which acts perpendicular to the rotation axis is comparable to x-noise acting directly on the rotation axis when the error is averaged over all initial qubit states.

Modelling magnetic dephasing

Modelling dephasing errors linked to magnetic fluctuations would in principle require integration of the charge noised averaged error of Eq. 3.3.17 over magnetic fluctuations:

$$\langle \mathrm{e}_{\epsilon,B} \rangle_{\mathscr{B}} = 1 - \langle O_{\mathscr{B}}(\delta z(\delta\epsilon, \delta B), \delta x(\delta\epsilon)) \rangle_{\delta\epsilon,\delta B} . \tag{3.3.20}$$

To evaluate the above equation, we could average over $\delta\epsilon$ numerically using a Gaussian PDF, and expand this to a double integration over δB. However this would make the error analysis significantly more computationally expensive which is not warranted since the magnetic dephasing rates in isotopically purified silicon devices are orders of magnitude smaller than the charge dephasing rates (see Sect. 3.3.3). As such magnetic-dephasing errors are expected to be negligible. Magnetic dephasing is therefore often neglected when considering silicon systems [72, 12].At some non-ideal parameters, such as when the spin and the charge are far detuned so that the spin-charge hybridisation is weak, the coupling of the qubit to charge will become negligible and magnetic dephasing can become dominant. We therefore use a simplified error model by which we calculate the magnetic dephasing error separately from the charge dephasing error: $\langle \mathrm{e}_{\epsilon,B} \rangle_{\mathscr{B}} \approx 1 - (1 - \langle \mathrm{e}_\epsilon \rangle_{\mathscr{B}})(1 - \langle \mathrm{e}_B \rangle_{\mathscr{B}})$. This approximation captures the total error accurately except for the situation where both charge and magnetic dephasing are of similar magnitude.

Similar to the charge-dephasing error, the magnetic dephasing error $\langle \mathrm{e}_B \rangle_{\mathscr{B}}$ can also be computed using the Bloch-sphere-averaged overlap $O_{\mathscr{B}}$ [90] in Eq. 3.3.16, that describes the overlap between an ideal and noisy qubit $\pi/2$ gate, and using the fact that the magnetic noise only couples weakly to the qubit Rabi frequency:

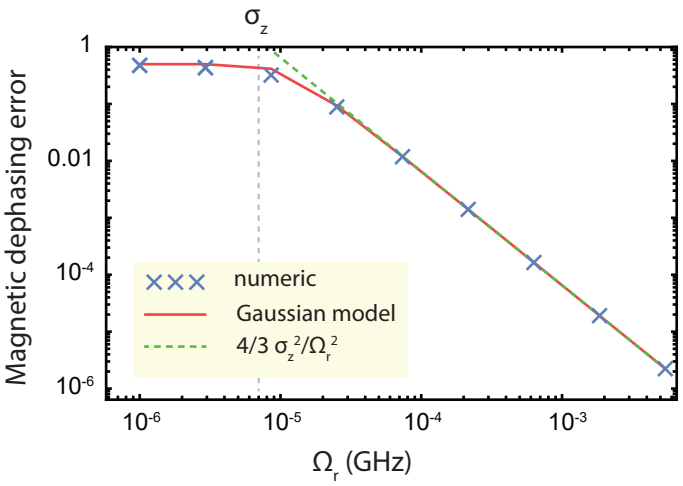

Figure 3.18: **Determination of the magnetic dephasing error as a function of the Rabi frequency.** A second-order magnetic dephasing error model (dotted green line) accurately fits the numerically calculated value (blue crosses) for Rabi frequencies larger than the magnetic noise amplitude $\Omega_r \gtrsim 10\sigma_z$. The Gaussian model (in red) is seen to fit the numerical data well for all Rabi frequencies

$$\begin{aligned} \langle \mathrm{e}_B \rangle_{\mathscr{B}} &= 1 - \langle O_{\mathscr{B}}(\delta z(\delta B), \delta x(\delta B)) \rangle_{\delta B} \\ &\approx 1 - \langle O_{\mathscr{B}}(\delta z(\delta B), 0) \rangle_{\delta B} \end{aligned}. \tag{3.3.21}$$

The dependence of the flopping-mode qubit energy, $2z$ on the magnetic field is mainly described by the Zeeman splitting $\gamma_e B$. The integration over the Gaussian distributed variable δB, approximated to lowest order gives:

$$\langle \mathrm{e}_B \rangle_{\mathscr{B}} \approx \frac{4}{3}\frac{\sigma_z^2}{\Omega_r^2}, \tag{3.3.22}$$

where Ω_r is the qubit Rabi frequency and $\sigma_z = \gamma_e \sigma_B/2$. This expansion Eq. 3.3.22 to second-order in σ_z (green dotted line in Fig. 3.18) overestimates the error when it approaches unity for example when the Rabi frequency is small and gate times are large. We find that Gaussian noise distribution also expands to $\frac{4}{3}\frac{\sigma_z^2}{\Omega_r}$ and captures this regime and matches numerical integration (red line in in Fig. 3.18):

$$\langle \mathrm{e}_B \rangle_{\mathscr{B}} \approx \frac{1}{2}\left(1 - \mathrm{Exp}\left(-\frac{8}{3}\frac{\sigma_z^2}{\Omega_r^2}\right)\right). \tag{3.3.23}$$

Equation 3.3.23 is used to estimate the magnetic dephasing error in the full qubit error model.

3.3.4 Charge T_1 relaxation modeling

The flopping-mode qubit can relax via the electron spin or the charge. Indeed, the electron spin state is hybridised to the excited charge state to allow electric driving of the electron spin. Any relaxation of the electron spin or the excited charge state translates into relaxation of the qubit. These spin or charge relaxation mechanism take place on a wide range of characteristic timescales ($\sim$ 10s of nanoseconds for charge [26, 28] and up to 30s for spin relaxation [93]).

The relaxation time of electron spins on phosphorus-donor QDs are on the order of seconds [94, 95, 96] at magnetic fields of about 1 T. The relaxation time of a charge qubit defined by the symmetric and antisymmetric superposition of two tunnel-coupled quantum-dot orbitals however has been measured to be on the order of only a few nanosecond in GaAs QDs [27] and in silicon/silicon-germanium QDs [30]. The charge-relaxation rate $1/T_1^c$ in silicon-donor QDs has not been measured, but has been theoretically modelled for a charge qubit defined by a phosphorus-donor QD and an interface QD [82]. Boross et al. [82] predict this relaxation rate is proportional to the charge qubit energy splitting and to the square of the tunnel coupling $2t_c$ between the two dots:

$$1/T_1^c \approx \Theta \left(2\sqrt{\epsilon^2 + t_c^2}\right) \cdot (2t_c)^2 \text{ (GHz)}, \tag{3.3.24}$$

where the coefficient $\Theta \approx 2.37 \times 10^{-6}$ (ns^2) is a silicon-specific constant [12, 82]. At zero detuning, which is the default operating point of the qubit, the charge-relaxation rate is therefore proportional to t_c^3. As an example, this yields a relaxation time of about 300 ns at a charge-qubit splitting of 11 GHz corresponding to a magnetic field of 0.4 T for an electron spin qubit. Therefore, the charge relaxation process will dominate the spin relaxation and as a result we can neglect the spin relaxation for the error calculations.

The probability of the excited charge state to decay from its higher energy state is described by $1-\exp(-t/T_1^c)$ and the corresponding error by $\frac{1}{2}(1-\exp(-t/T_1^c))$. The flopping-mode qubit states only partially overlap with the excited charge state, which makes it less probable for the qubit to decay in a given time. The exponential decay of the flopping-mode qubit therefore needs to include the time-integrated overlap of the qubit wave function with the excited charge state. The qubit relaxation error

can accordingly by expressed using the formula from Tosi *et al.* [12]:

$$\mathrm{e}_{T_1} = \frac{1}{2}\left[1 - \exp\left(-\int_0^{t_{\pi/2}} \sum_k \left|\langle\Psi(t')|\Psi_k^+\rangle\right|^2 \frac{1}{T_1}\mathrm{d}t'\right)\right], \tag{3.3.25}$$

where Ψ_k^+ are the product-basis states that contain the excited charge state $|+\rangle$. The qubit-relaxation error therefore grows exponentially with the gate time $t_{\pi/2}$ and with the overlap $\sum_k \left|\langle\Psi(t)|\Psi_k^+\rangle\right|^2$ of the qubit wave function with the excited charge state, integrated over the time of the gate.

There are two ways by which the qubit wave function can overlap with the excited charge state during a $\pi/2$ - X-gate. First, even when the qubit is not driven the qubit wave function overlaps with the excited charge state. Indeed, while the qubit ground state $|0\rangle$ does not overlap at all with the excited charge state (due to the large energy gap), the qubit excited state $|1\rangle$ is engineered by controlling the spin and charge qubit detunings to have a small excited charge state overlap $p_{1,+} = \sum_k \left|\langle 1|\Psi_k^+\rangle\right|^2$. This is a result of the hybridisation of the spin qubit with the charge qubit that allows electric driving of the flopping-mode qubit. The overlap of the qubit wave function with the excited charge state can thus be calculated as the product of the time-dependent overlap $O_i(t) = |\langle\Psi(t)|1\rangle|^2$ of the qubit wave function with the $|1\rangle$ state, and the overlap $p_{1,+}$ of the excited charge state with the qubit $|1\rangle$ state. The second way by which the qubit wave function can overlap with the excited charge state is by leakage into the two excited state branches during electric driving (see Sect. 3.3.2). We have described how the time dependent overlap $O_d(t) = \sum_{i=2}^{3} |\langle\Psi(t)|i\rangle|^2$ of the qubit wave function is dependent on the pulse shape, and the various drive parameters. The overlap of the qubit wave function with the excited charge state can thus be written as:

$$\sum_k \left|\langle\Psi(t)|\Psi_k^+\rangle\right|^2 \approx |\langle\Psi(t)|1\rangle|^2 \sum_k \left|\langle 1|\Psi_k^+\rangle\right|^2 \tag{3.3.26}$$

$$+ \sum_{i=2}^{3} |\langle\Psi(t)|i\rangle|^2 \tag{3.3.27}$$

$$= O_i(t) \cdot p_{1,+} + O_d(t), \tag{3.3.28}$$

As described in Eq. 3.3.25, the relaxation error is related to the integral of this

overlap over the duration of the pulse, yielding:

$$\int_0^{t_{\pi/2}} \sum_k \left|\langle\Psi(t')|\Psi_k^+\rangle\right|^2 \mathrm{d}t' = I_i \cdot p_{1,+} + I_d, \tag{3.3.29}$$

where $I_{i/d} := \int_0^{t_{\pi/2}} O_{i/d}(t')\mathrm{d}t$.

The integral $I_d \approx \alpha_d \frac{1}{\Omega_r}\frac{\Omega_l^2}{\Delta^2}$ is given by Eq. 3.3.9. It describes the integrated excited-charge leakage population and depends on the Rabi-frequency Ω_r, the coupling strength to the excited state Ω_l and the energy gap Δ between the qubit states and the nearest excited charge state. I_d is independent of the initial state of the qubit.

The integral I_i of the $|1\rangle$-state overlap can be estimated from the noiseless time evolution of a qubit initial state $\Psi_i = \cos\theta/2|0\rangle + \sin\theta/2 e^{\imath\phi}|1\rangle$ during a $\pi/2$ X-gate:

$$I_i(\theta,\phi) \approx \frac{1}{\Omega_r}\frac{1}{4}\left(\pi - 2\cos\theta - 2\sin\theta\sin\phi\right). \tag{3.3.30}$$

The time-integrated $|1\rangle$-state proportion I_i is maximal (minimal) when the time evolution passes the South(North)-pole of the Bloch-Sphere halfway through the gate, i.e. when the start of time evolution is given by the spherical angles $(\theta,\phi) = (3\pi/4, -\pi/2)$ ($(\theta,\phi) = (\pi/4, \pi/2)$). The full relaxation error in Eq. 3.3.25 for a given initial state can now be written as:

$$\mathrm{e}_{T_1}(\theta,\phi) = \frac{1}{2}\left(1 - e^{-I_i(\theta,\phi)O_{1,+}/T_1} e^{-I_d/T_1}\right). \tag{3.3.31}$$

Finally, the relaxation error averaged over the Bloch sphere is given by:

$$\langle \mathrm{e}_{T_1}\rangle_{\mathscr{B}} = \frac{1}{2}\left(1 - \left\langle e^{-I_i(\theta,\phi)O_{1,+}/T_1}\right\rangle_{\mathscr{B}} e^{-I_d/T_1}\right). \tag{3.3.32}$$

The Bloch-sphere average of $e^{-I_i(\theta,\phi)O_{1,+}/T_1}$ can be approximated analytically. Indeed, integration over ϕ gives a term with a Bessel function which can be approximated to third order in $\beta = \frac{O_{1,+}}{\Omega_r T_1}$. We obtain:

$$\left\langle e^{-I_i(\theta,\phi)O_{1,+}/T_1}\right\rangle_{\mathscr{B}} \approx e^{\frac{1}{4}(2+\pi)\beta}\frac{\beta - 2 + e^{\beta}(\beta+2)}{4\beta}. \tag{3.3.33}$$

The relaxation error of the qubit is calculated using Eq. 3.3.32 and Eq. 3.3.33, and the parameters entering the equation are calculated numerically. By combining all of these error sources in the next section we now have a complete description of the flopping-mode qubit and its error sources.

3.3.5 Summary

We have introduced the methodologies for calculating three different error types that affect the flopping-mode qubit

1. Leakage errors corresponding to the spread of the qubit wave function out of the qubit subspace due to non-adiabatic driving of the qubit. For all flopping-mode qubits this involves accidental charge excitation.

2. Dephasing errors linked to electric and magnetic noise coupling to the qubit, including qubit energy fluctuations z-dephasing and driving frequency fluctuations x-dephasing.

3. Relaxation errors during qubit driving (dT_1 errors) and idling (iT_1 errors) which correspond to the system evolving towards its ground state through loss of energy to the environment.

Leakage errors for the flopping-mode qubit are strongly linked to excitation of the qubit charge state. This excitation can be reduced through adiabatic pulse shapes (Gaussian in our case) that slowly increase the microwave electric field envelope, and then decrease it in a symmetric manner. The adiabatic pulse shape allows for large driving strengths, that result in some temporary leakage during the pulse ("reversible leakage") that is mostly reversed. The excited charge state proportion that is not reversed (de-excited) at the end of the pulse is responsible for the "irreversible" leakage error. The reversibly excited state proportion only leads to errors if it is prone to other errors itself. This is indeed the case because the reversibly excited charge proportion can relax due to T_1 charge relaxation. The overall dephasing error is caused by charge and magnetic noise with corresponding errors e_ϵ and e_B, respectively. To speedup the dephasing error computation, we simulate the qubit's unitary evolution within the qubit subspace analytically. This is exact when the coupling to the leakage state vanishes, and captures the exact unitary evolution very well. This analytical unitary evolution allows exact analytical integration of the dephasing error over all qubit start states on the Bloch sphere, and manifests in a significant speedup of calculations. The remaining integration over noise is performed numerically for charge noise, and approximated analytically for magnetic noise which is generally much smaller. The resulting errors e_ϵ and e_B match the numerically calculated errors well. The relaxation error of the flopping-mode qubit is principally linked to relaxation of the excited charge state. The excited charge state can be populated by non-adiabatic driving of the qubit ("drive- T_1" relaxation

error), but also due to the engineered hybridisation of the spin and charge qubit that allows electric driving.

Finally, we combine the charge and magnetic dephasing errors e_ϵ and e_B with the two types of T_1 errors e_{T_1} and the irreversible leakage errors $\mathrm{e}_{\mathrm{leak}}$:

$$\mathrm{e}_{\mathrm{tot}}(\theta,\phi) = 1 - (1-\mathrm{e}_\epsilon(\theta,\phi))(1-\mathrm{e}_B(\theta,\phi))(1-\mathrm{e}_{T_1}(\theta,\phi)(1-\mathrm{e}_{\mathrm{leak}}). \tag{3.3.34}$$

The final error is averaged error over all qubit initial state (on the Bloch sphere $\mathscr{B}$):

$$\mathrm{e} = \langle \mathrm{e}_{\mathrm{tot}}(\theta,\phi)\rangle_{\mathscr{B}} \tag{3.3.35}$$

$$\approx \langle 1-\mathrm{e}_\epsilon\rangle_{\mathscr{B}} \langle 1-\mathrm{e}_B\rangle_{\mathscr{B}} \langle 1-\mathrm{e}_{T_1}\rangle_{\mathscr{B}} (1-\mathrm{e}_{\mathrm{leak}}). \tag{3.3.36}$$

This equation is used to compute the error rates in the next section of this thesis, where we investigate the flopping-mode qubit performance for a range of experimental parameters.

3.4 Optimal driving/operation of a generic flopping-mode qubit

3.4.1 The longitudinal gradient in the flopping-mode qubit

In the previous sections we have seen that the flopping-mode qubit allows electric manipulation of the spin via its hybridisation with the charge degree of freedom. While offering the possibility to electrically drive the qubit and couple it to superconducting cavities, the charge hybridisation also opens the way for electric-field fluctuations naturally present in semiconductor devices to couple to the qubit in the form of dephasing errors and for the charge to relax as a result of the finite qubit lifetime (T_1 errors). The presence of the additional excited-charge states coupled to the qubit subspace can lead to errors through permanent leakage of the wavefunction out of the qubit subspace (leakage error), or through charge relaxation of that population during reversible charge excitation ("drive T_1 error"). Even after isotopic purification of the device host material, residual magnetic noise can still affect the spin qubit operation and lead to dephasing error ("Overhauser error"). In order to find out if fault-tolerant electric operation of the flopping-mode qubit is possible, it is necessary to find a parameter regime where all the above errors can be minimised. In Sect. 3.3 we have seen that a multitude of parameters determine the (approximate) error. The magnetic and electric noise amplitude σ_B and σ_ϵ respectively are good

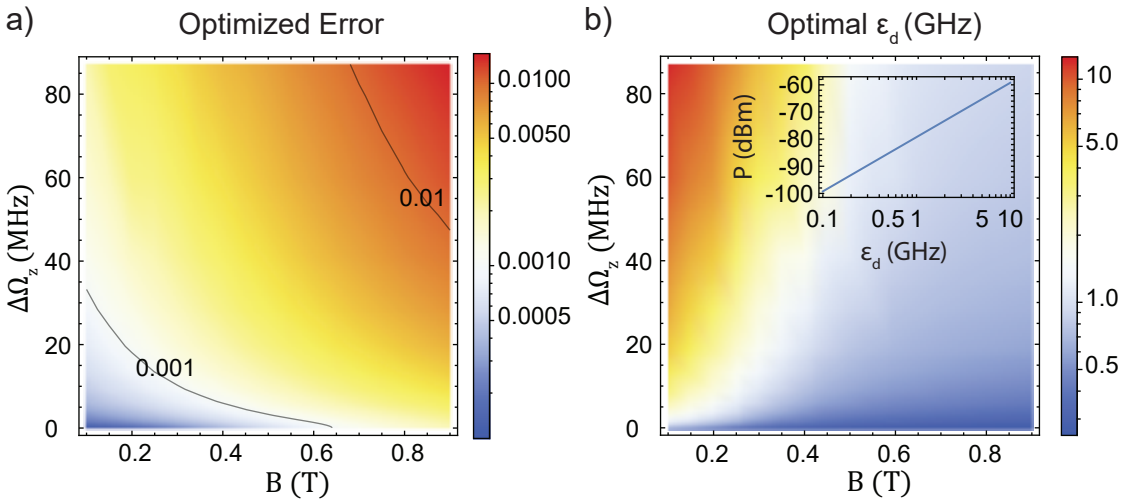

Figure 3.19: **Optimal $\pi/2$ X-gate error in the flopping-mode qubit.** Panel **a)** displays the error optimised for ϵ, t_c and ϵ_d, as a function of B and $\Delta\Omega_z$, for a fixed transverse energy difference $\Delta\Omega_x = 117\,\text{MHz}$, and electric/magnetic noise amplitudes $\sigma_\epsilon = 0.3\,\text{GHz}$ and $\sigma_B = 7\,\text{kHz}$ respectively. **b):** Optimal value ϵ_d used to minimise the error in a). Conversion from drive amplitude ϵ_d in GHz to microwave power at the gate (in dBm) or a typical flopping-mode qubit as in [46] is provided in the inset.

measures of the amount of noise present in a given device. We will keep these two parameters fixed during the optimisation and set them to state-of-the-art values in isotopically purified silicon ($\sigma_B = 7\,\text{kHz}$ and $\sigma_\epsilon = 0.3\,\text{GHz}$ [1]). This leaves us with 6 additional parameters to optimise: three magnetic parameters (the two gradients $\Delta\Omega_{z/x}$) and the static magnetic field B) and three electrically tuned ones (tunnel coupling t_c, static electric detuning ϵ, and electric drive amplitude ϵ_d). We choose a transverse gradient of 117 MHz [12, 97] typical for the donor-based flopping-mode qubit and now optimise the remaining five parameters.

The $\pi/2$ X-gate total error optimised with respect to the three electrically tunable parameters (ϵ, t_c and ϵ_d) is plotted in Fig. 3.19a) as a function of the two remaining magnetic parameters (B and $\Delta\Omega_z$). The total error includes all the errors discussed above (Charge and magnetic dephasing errors as well as relaxation and leakage errors). Due to the large impact of the drive amplitude on the qubit operation, we display the optimal drive amplitude ϵ_d found for each point in Fig. 3.19b.

At magnetic fields below 0.5 T, both the optimal error and drive amplitude, ϵ_d strongly depend on the longitudinal magnetic field gradient, $\Delta\Omega_z$. At a magnetic field of 0.1 T, a reduction of the longitudinal gradient from 80 MHz ($\Delta\Omega_z/\Delta\Omega_x = 70\%$) to 0.5 MHz ($\Delta\Omega_z/\Delta\Omega_x = 0.4\%$), results in a 15-fold decrease of the error, and a 21-fold decrease in the minimal optimal drive amplitude, corresponding to a 440-fold reduction in drive power. In general, Fig. 3.19 a) shows that in order to

reach errors below 10^{-3} with the flopping-mode qubit, a likely necessity for realistic scalable fault tolerant computation (as discussed in Chapter 2), longitudinal gradients below 30 MHz ($\Delta\Omega_z/\Delta\Omega_x = 26\%$) will be necessary. Operation at longitudinal gradients below 30 MHz will allow low-power operation of the qubit at drive amplitudes below 7 GHz (-62 dBm at the device) and as low as 0.25 GHz (−91 dBm)[8]. These driving powers are one to four orders of magnitude lower than the driving power used for Yoneda *et al.* single dot EDSR [8] (−50 dBm at the device to reach a 4 MHz Rabi frequency and an error of 10^{-3})[9], and two to five orders of magnitude lower than state of the art ESR (10^{-3} π gate error demonstrated by Muhonen *et al.* [1] with 0.16 MHz Rabi frequency at −40 dBm power). These low-power, high-fidelity qubit operations will be crucial for scaling up to many qubits required for a large-scale quantum computer. At magnetic fields larger than 0.5 T in Fig. 3.19, the error as well as the drive amplitude depend less strongly on the longitudinal magnetic field gradient, due to T_1 relaxation errors –that do not depend on the longitudinal gradient– becoming the dominant source of errors. Therefore, this region should be avoided when optimising the flopping-mode qubit. The T_1 relaxation error becomes dominant over dephasing errors at large magnetic field due to the cubic dependance of the bare charge relaxation rate on the tunnel coupling. The larger the magnetic field, the larger the tunnel coupling required to keep the charge qubit energy above the spin qubit energy. An increase in the magnetic field therefore results in a significant increase of the T_1 relaxation rate.

In Fig. 3.19, we perform the qubit optimisation with respect to ϵ_d and t_c numerically (using a custom two-dimensional Newton minimum search algorithm), while the parameter $\epsilon = 0$ is kept at the first-order sweet spot, that is optimal for the parameter space investigated. The behaviour of the qubit error in the two dimensional space spanned by the drive amplitude and the tunnel coupling numerically optimised is shown in Fig. 3.20, at four positions in the optimised Fig. 3.19 reproduced in the inset (high/low magnetic field and high/low longitudinal gradient). For clarity, we convert the tunnel coupling to the spin charge detuning $\Delta = 2t_c - E_Z$ in the figure.

The dark orange regions in Fig. 3.20 indicate where the error is above the 1% surface-code error-correction threshold, while lighter colours indicate that fault tol-

[8] For the conversion from voltage amplitude (ϵ_d in GHz) to power (in Watt), we assume a differential lever-arm of the driving gate of $\alpha = 6\%$ as measured by Croot in [46], and a $Z_0 = 50\,\Omega$ impedance transmission line: $P_{\mathrm{AC}}^{\mathrm{gate}} = \frac{1}{Z_0}\left(\frac{h\epsilon_d/e}{2\sqrt{2}\alpha}\right)^2$.

[9] The drive power to reach a Rabi frequency of 4 MHz as in ref. [8] is extrapolated from an estimated power of −32 dBm needed to reach a Rabi frequency of 29 MHz in a similar device measured by the same author [59].

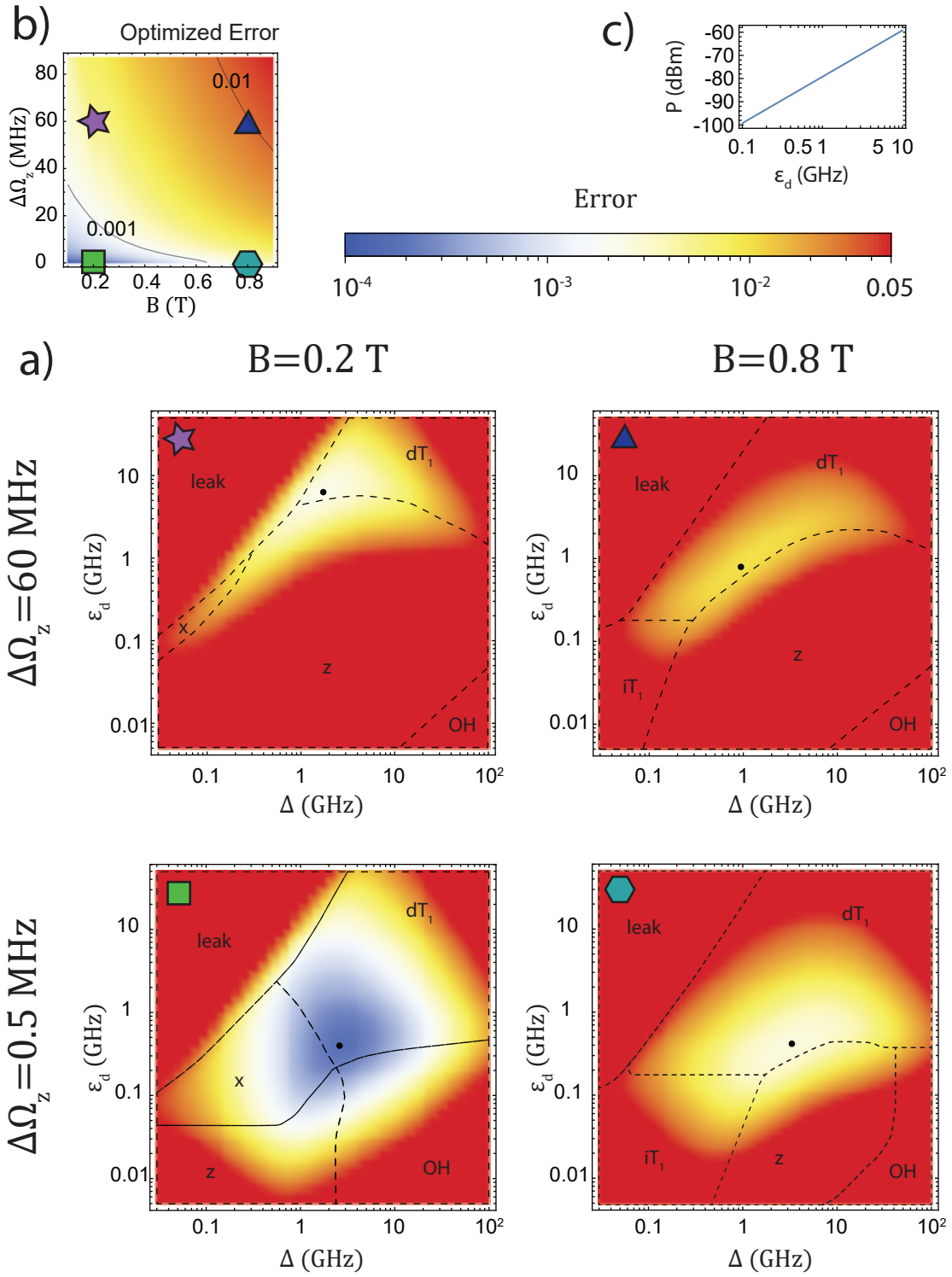

Figure 3.20: **Error optimisation of the $\pi/2$ X-gate in the flopping-mode qubit.** Panel **a)** displays the 4 panels of the error as a function of ϵ_d, $\Delta = 2t_c - \Omega_s$ at four positions indicated by markers in the **b)** corresponding to the four combinations of small/large magnetic field and longitudinal magnetic field gradients. The different error channels are leakage (leak), x-dephasing (x), z-dephasing (z), drive-T_1 (dT_1), idle-T_1 (iT_1), and Overhauser noise (OH). $\Delta\Omega_x = 117\,\text{MHz}$, $\sigma_\epsilon = 0.3\,\text{GHz}$, $\sigma_B = 7\,\text{kHz}$ and two different magnetic fields, $B = 0.2$ and 0.8 T. **c)** Conversion from drive amplitude ϵ_d in GHz to microwave power at the gate (in dBm) for a typical flopping-mode qubit as in [46].

erance is reached. The limiting error source at each point in each subfigure of Fig. 3.20a is indicated by the labelled regions, whereas the optimal operating point is indicated by a black dot. In general, errors are high for drive amplitudes and detuning significantly away from 1 GHz, which is the energy scale set by the charge noise amplitude[10] and the qubit energy [11]. Leakage errors are dominant at high drive amplitudes, due to the drive amplitude becoming comparable or larger than the energy gap to the leakage states. This situation is especially true for for small spin–charge detuning energies Δ, which results in dominating irreversible leakage errors (labelled "leak" in the figure), corresponding to irreversible excitation of the qubit wavefunction out of the qubit subspace. At high drive amplitudes and large spin–charge detuning Δ, the energy gap is sufficient to allow for most of the leaked-state proportion to be de-excited by the Gaussian pulse, but the increased charge-relaxation rate (higher Δ translates into higher t_c) makes the temporary excited charge-state proportion more prone to relaxation (drive T_1 error: "dT_1").

At small drive amplitudes (lower half of Fig. 3.20) errors are large because gates are slow and dephasing sources have more time to couple into the error. Electric field fluctuations lead to variations in the qubit energy (z-dephasing error :"z" in the figure), as well as variations in the qubit's dipole moment and thus Rabi frequency (x-dephasing error:"x" in the figure). Finally, magnetic field fluctuation linked to remaining non spin-less silicon nuclear isotopes produce an additional z-dephasing error (labelled "OH" for Overhauser in the figure). This error becomes dominant when the spin–charge detuning Δ is large, and the flopping-mode qubit is so weakly hybridised to charge that it is essentially a spin qubit that is mostly sensitive to magnetic-field fluctuations. While the lower half of all four plots is generally dominated by dephasing errors ("z","x","OH"), at higher magnetic fields the T_1 relaxation rate increases (due to operation at larger tunnel coupling), so that at small spin–charge detunings Δ and small drive amplitudes ϵ_d at which the spin becomes more hybridised to charge and the gate time is long. The probability of charge relaxation increases, even in the absence of electrical driving which corresponds to the idle T_1 relaxation error described in Sect. 3.3.4 and labelled "iT_1" in Fig. 3.20.

We have described the different parameter-space regions in which the various error sources become dominant and limit the achievable error. Turning now to the regions of low errors (yellow to blue regions), it becomes clear at first sight that the magnitude of the longitudinal gradients has a significant influence on the size of

[10] 0.3 GHz

[11] about 5.6 GHz at 0.2T and 22 GHz at 0.8T.

these regions. For a small longitudinal magnetic field gradient and small magnetic field (lower left figure), errors below 10^{-3} can be achieved for drive amplitudes and spin–charge detuning varying by more than one order of magnitude, while such low errors cannot be achieved at higher drive amplitudes or magnetic fields. Besides the significantly lower error, the resilience of the qubit error to variations in the tuning parameters Δ and ϵ_d is an important advantage for operation at low magnetic field longitudinal gradients ($\lesssim 10$ MHz). The dramatic difference in the size of the below-threshold regions between the different points in Fig. 3.20b can be mainly attributed to the influence of the z-dephasing error. By reducing the longitudinal magnetic field gradient the qubit dephasing is significantly reduced allowing for high-fidelity qubit operations. The regions in which the z-dephasing error become limiting (labelled by "z") grows significantly with increasing longitudinal magnetic field gradient, pushing the optimal operation point to higher drive amplitudes.

The behaviour of the dephasing errors, that are dominant for much of the parameter space accessible in experiments, can be well understood by making use of the lowest-order approximation of the Hamiltonian of Eq. 3.2.18 and the error model in Eq. 3.3.17. The Bloch sphere averaged z(x)- dephasing errors for Gaussian noise with amplitude $\sigma_z(x)$ along the z(x) axis of the Hamiltonian, for a Rabi frequency x along the x-axis is proportional to $(\sigma_{z(x)}/x)^2$ (to third order in σ/x, see Eq. 3.3.18)

The parameters $\sigma_{z(x)}$ that feed into the dephasing error model describe variations $\delta z = \delta\tilde{\Omega}_s/2$ in the qubit energy and $\delta x = \delta\Omega_r/2$ in the Rabi frequency, and can be estimated by using the analytical models for two Hamiltonian parameters $\tilde{\Omega}_s$ and Ω_r derived in Sect. 3.2.2. In that section we derived that both parameters the flopping-mode qubit energy and Rabi frequency can be related to the function $G(\epsilon)$ that describes the response of the wave function to the electric field (see Eq. 3.4.1). We found that for sufficiently large spin–charge detuning $\Delta > \Omega_s$, both the qubit splitting and Rabi frequency are very well described by the gradient G:

$$\begin{aligned} \tilde{\Omega}_s(\epsilon) =: 2z \quad &\approx \Omega_s + G(\epsilon)\frac{\Delta\Omega_z}{2} \\ \Omega_r(\epsilon) =: 2x \quad &\approx \frac{1}{2}\frac{\partial}{\partial\epsilon}\left(G(\epsilon)\frac{\Delta\Omega_x}{2}\right)\epsilon_d. \end{aligned} \tag{3.4.1}$$

The term $G(\epsilon)\frac{\Delta\Omega_{z/x}}{2}$ was simply interpreted as the longitudinal/transverse Zeeman terms experienced by the spin for a particular value of electric detuning (averaged over the probability density given by the wave function for this particular value of detuning).

We can now use these expressions to estimate the dephasing rate to lowest order

in ϵ. At $\epsilon = 0$ at which we will mostly operate the qubit, the curvature of G with respect to ϵ vanishes $\frac{\partial^2 G(0)}{\partial \epsilon^2} = 0$ so that the expansion of x has to be taken to second-order. Applying this to $\tilde{\Omega}_s(\epsilon)$ and $\Omega_r(\epsilon)$ we find:

$$\begin{aligned} \sigma_z &\approx \frac{\partial z(\epsilon)}{\partial \epsilon}\sigma_\epsilon &&= \frac{1}{2}\frac{\partial G(0)}{\partial \epsilon}\frac{\Delta\Omega_z}{2}\sigma_\epsilon \\ \sigma_x &\approx \frac{\partial^2 x(\epsilon)}{\partial \epsilon^2}\frac{\sigma_\epsilon^2}{2} &&= \frac{1}{4}\frac{\partial^3 G(0)}{\partial \epsilon^3}\frac{\Delta\Omega_x}{2}\epsilon_d\frac{\sigma_\epsilon^2}{2}. \end{aligned} \tag{3.4.2}$$

Based on the z- and x-dephasing rates above, the x and z errors can now be estimated analytically to lowest order in ϵ_d at $\epsilon = 0$:

$$\begin{aligned} e_z &\propto \left(\frac{\sigma_z}{x}\right)^2 &&\approx 4\left(\frac{\sigma_\epsilon}{\epsilon_d}\right)^2\left(\frac{\Delta\Omega_z}{\Delta\Omega_x}\right)^2 \\ e_x(\epsilon=0) &\propto \left(\frac{\sigma_x}{x}\right)^2 &&\approx \left(\frac{\partial^3 G(0)/\partial\epsilon^3}{\partial G(0)/\partial\epsilon}\sigma_\epsilon^2/2\right)^2 = \left(\frac{3}{2t_c^2}\sigma_\epsilon^2\right)^2, \end{aligned} \tag{3.4.3}$$

where for the z-error the spatial-gradient derivative $\frac{\partial G(\epsilon)}{\partial \epsilon}$ cancels out, and for the x-error, the drive amplitude ϵ_d and the transverse energy difference $\Delta\Omega_x$ does. We will now see that the cancellation of these terms is instrumental in explaining the dephasing behaviour described with Fig. 3.20.

The importance of the longitudinal magnetic field gradient can be traced back to the magnitude of the z-dephasing error being proportional to the squared ratio of the energy gradients: $e_z \propto \left(\frac{\Delta\Omega_z}{\Delta\Omega_x}\right)^2$ as seen in Eq. 3.4.3. The remaining dependencies captured by the equations explain where in the parameter space this term becomes dominant. The dominating influence of the z-dephasing error for much of the experimentally attainable parameter space in Fig. 3.20 can be linked to the dependency of both the x and z error on ϵ_d and t_c.

First, Eq. 3.4.3 highlights that the z-dephasing error is inversely proportional to the squared drive amplitude: $e_z \propto 1/\epsilon_d^2$, whereas the x-error is independent of the drive amplitude. The z-dephasing error dominates for small drive amplitude until it reaches the constant value set by the x-dephasing error (see Fig. 3.21 a). This is related to the fact that, on the one hand the z-dephasing rate is independent of the drive amplitude, meaning that stronger drive and thus faster gate operation leads to fewer errors, on the other hand the x-dephasing rate is proportional to the drive amplitude, meaning that reductions in the error related to faster gates are counterbalanced by an increase in the dephasing rate. From Eq. 3.4.3, we can derive the value of the drive amplitude ϵ_d at which the x- and z- dephasing error are equal. This crossing point describes the optimal drive amplitude (when dephasing

errors are dominating), and is seen to be proportional to the ratio of the magnetic gradients : $\epsilon_d^{\text{opt}} \propto \frac{\Delta\Omega_z}{\Delta\Omega_x}$. This explains the growing influence of the z-dephasing error for increasing longitudinal magnetic field gradient.

Second, to lowest order[12] the z-dephasing error is seen to be independent of the charge qubit parameters ϵ and t_c, while the x-dephasing error is inversely proportional to t_c^4. This explains why the x-error is only dominant at small t_c and thus small spin–charge detunings Δ in Fig. 3.20. This behaviour is depicted in Fig. 3.21 b), and can be physically explained by the dependencies of both errors on the spatial gradient $G(\epsilon, t_c)$. Indeed both the z-dephasing rate σ_z and the Rabi frequency x are proportional to the derivative of this gradient[13], so that the dependences on ϵ and t_c cancel in the ratio σ_z/x. However, the x-dephasing rate σ_x is proportional to the derivative of the Rabi frequency itself, and thus the dependency on ϵ and t_c do not cancel in the ratio σ_x/x.

The error in Eq. 3.4.3 can be slightly refined by using the full second-order approximations of the Hamiltonian in Eq. 3.2.18 to estimate the noise amplitude, and inputing those into the full analytical error model of Eq. 3.3.17. We find that to third-order in the electric detuning noise amplitude σ_ϵ, the x- and z-dephasing error are given by:

$$\begin{aligned} e_z &\approx \frac{4}{3}\left(\frac{\sigma_\epsilon}{\epsilon_d}\right)^2\left(\frac{\Delta\Omega_z}{\Delta\Omega_x}\right)^2\left(1-\left(\frac{\Omega_s}{\Omega_0}\right)^2\right)^2 \\ e_x &\approx \frac{\pi^2}{8}\left(\frac{\sigma_\epsilon^2}{2t_c^2}\right)^2\left(1+\frac{2\Omega_0}{\Omega_0^2-\Omega_s^2}\right)^2, \end{aligned} \tag{3.4.4}$$

where $\Omega_0 = \Omega(\epsilon = 0)$ is the charge-qubit splitting at zero electric detuning. These expression extend the simplified equations Eq. 3.4.3 to a lower spin–charge detuning regime. Importantly the final factor that suppresses the z-dephasing error for vanishing spin–charge detunings ($\frac{\Omega_s}{\Omega_0} \to 0$), describes the appearance of a first order sweet spot in the qubit energy-splitting at low spin–charge detunings, and reflects the hybridisation of the spin and charge qubit energies (see Sect. 3.2.2)[14]. This error model describes the numerical[15] error well, as can be seen from the solid lines in Fig. 3.21 a) and b).

[12] valid at large t_c and thus Δ

[13] in the regime $\Omega_s \lesssim \Delta$

[14] At such small spin–charge detunings, a higher order expansion of the dephasing rate σ_z would be necessary. However this is not necessary for the total error estimation as in the low-Δ regime, the x-dephasing error dominates

[15] Using the numerical noise integrals but using an analytical approximation for the unitary time evolutions, as described in Sect. 3.3.

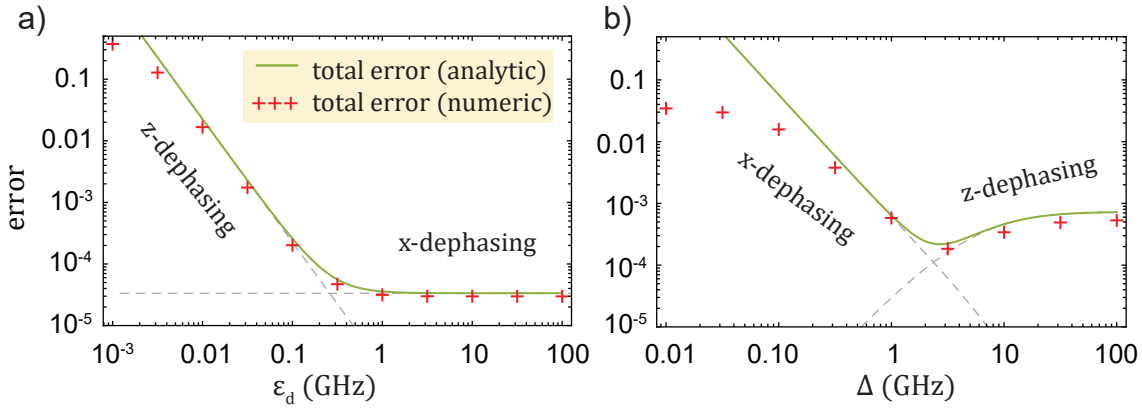

Figure 3.21: **Analytical dephasing error model, vs numerical model** at $B = 0.3\,\mathrm{T}$, for $\sigma_\epsilon = 0.3\,\mathrm{GHz}$. **a)** As a function of drive amplitude, for $\Delta = 4.2\,\mathrm{GHz}$. **b)** As a function of spin–charge detuning energy, for $\epsilon_d = 0.1\,\mathrm{GHz}$.

The expression for the z-dephasing error in Eq. 3.4.4 reproduces the dephasing error of a flopping-mode qubit within the electric field of a superconducting cavity by Beaudoin in ref. [72] (with a 40% difference in the prefactor)[16]. The x-dephasing error has not been considered in much of the literature ([74, 46]). It was alluded to very briefly by Tosi *et al.* in ref. [12] proposing the flip-flop qubit.

The extended error equation in Eq. 3.4.4 can be used to also estimate the optimal drive amplitude $\epsilon_d^{\mathrm{opt}}$ for dephasing limited noise. We find that $e_z = e_x$ (that is, when neither x or z errors are limiting the qubit performance) is solved by:

$$\epsilon_d^{\mathrm{opt}} \approx \frac{4}{\pi}\sqrt{\frac{2}{3}}\frac{1}{\sigma_\epsilon}\frac{\Delta\Omega_z}{\Delta\Omega_x}\frac{\left(\Omega_0^2-\Omega_s^2\right)^2}{3\Omega_0^2-\Omega_s^2}. \tag{3.4.5}$$

In summary, by conducting an optimisation of the flopping-mode qubit over a large parameter space, we found that the $\pi/2$ x-gate error decreases with both the longitudinal magnetic field gradients and the magnetic field. This reduction is directly related to decreases in the z-dephasing rate and the charge T_1 relaxation rate, respectively. For magnetic fields below $\sim$0.5 T the optimal electric drive amplitude also decreases strongly with the magnitude of the longitudinal magnetic field gradient between the two QDs. We derived a simplified description of the system relating the qubit-energy splitting to the spatial gradient G and the Rabi frequency to the first derivative of that gradient, allowing a good quantitative estimate of the dephasing errors. We found that for dephasing-limited errors, the optimal drive power and the z-dephasing error are proportional to the squared ratio of the longitudinal over transverse magnetic field gradients: $\frac{\Delta\Omega_z}{\Delta\Omega_x}$. Using this optimisation procedure we can

[16] Beaudoin's pre-factor is estimated at $2(12+\pi^2)/24 \approx 1.82$ (including a factor $1/\sqrt{2}$ belonging to the RMS of the cavity field), while our pre-factor is $4/3 \approx 1.33$.

now design an optimal flopping-mode qubit implemented using phosphorus-doped silicon devices.

3.4.2 Flopping-mode qubit at the first and second-order sweet spots

In this final section, we investigate the benefit of operating the flopping mode qubit at the first order x-dephasing sweet spot, compared to operating it at the second-order z-dephasing error sweet spot. To do so we compare numerical simulations of the total error at the location both sweet spots. The total error includes all the charge and magnetic dephasing errors, as well as relaxation and leakage errors.

Before turning to the full numerical simulations including all errors, let us briefly discuss the topology of the sweet spots in the parameter space. For that purpose, we first investigate numerical simulations of the x- and z-dephasing errors separately. The topology of the z- and x- dephasing sweet spots differ significantly as can be seen in the Fig. 3.22 a) displaying the z-dephasing error (x-dephasing error in the inset), for low and high magnetic-field operation at $B = 0.2\,\mathrm{T}$ and $B = 0.8\,\mathrm{T}$ respectively. For both magnetic field values, the x-dephasing error displays a clear first order sweet spot at the symmetric electric detuning position $\epsilon = 0$ extending for all values of spin–charge detuning $\Delta = \Omega - \Omega_s$. The first order z-dephasing sweet spot however describes a curve (black dotted line), and only overlaps with the x-dephasing sweet spot for small values of Δ, where both errors are large and qubit operation is therefore undesirable. As a consequence, one cannot operate the qubit on both the x- and z- sweet spot simultaneously. One potentially attractive operation point as detailed in Tosi *et al.* [12] for minimising the z-dephasing is the second-order z- dephasing sweet spot indicated by a black circle in Fig. 3.22a and corresponds to a particular value of spin charge detuning Δ and electric detuning ϵ where the z-dephasing error is especially low. The x-dephasing error is however quite large at that position, not only because that position is off the x-sweet spot but also because the x-error is large at small value of spin–charge detuning.[17] We therefore expect that the second-order sweet spot is *not* a suitable operation point when electrically driving rotations of the flopping-mode qubit.

The optimal operation point that minimises the sum of x- and z-dephasing errors (and other errors), will not only depend on the position of the sweet spots but would also depend on drive amplitude, as the z-dephasing error falls quickly with the drive

[17] Small values of spin–charge detuning correspond to small values of tunnel-coupling, especially for low magnetic field. This translates into large x-errors because $e_x \propto 1/t_c^4$, see Eq. 3.4.4.

amplitude. In Fig. 3.22 b, we plot numerical simulations of the total qubit error as a function of spin–charge detuning and electric-drive amplitude ϵ_d, for two values of the static detuning ϵ is indicated with coloured markers present in both Fig. 3.22 a and Fig. 3.22 b. In the top row of Fig. 3.22 b), the error is calculated at the electric detuning value corresponding to the second-order z-dephasing sweet spot, while in the bottom row the total error is calculated on the x-dephasing sweet spot ($\epsilon = 0$). While all of the parameter space in the bottom plots sits on the x-dephasing sweet spot, in the top plot only one value of Δ (vertical dotted line) corresponds to operation on the second-order z-dephasing sweet spot. In all four plots in b) the limiting error source is indicated by regions with dotted boundaries and labelled according to the dominant error, and the optimal operation point is indicated by a black dot.

At high magnetic field values near $B = 0.8\,\mathrm{T}$ (right hand side plots), the qubit error is hardly affected by which of the x- or z-sweet spot is favoured, because, T_1 related errors are dominant.[18] At the low magnetic field of $B = 0.2\,\mathrm{T}$ (left hand side plots) the influence of the electric detuning operation point can be split into two regimes around values of spin–charge detunings large ($\Delta \gtrsim 1$) and small ($\Delta \lesssim 1$). These two regimes correspond to the two z-dephasing regimes (strong and weak spin–charge hybridisation) identified in Sect. 3.2.3. In the detuned regime $\Delta \gtrsim 1$ in Fig. 3.22 b) the total qubit error does not change noticeably between operation off or on the x-dephasing sweet spot (top and bottom respectively) at large spin charge detuning values. This negligible change in error is related to the fact that at detuning values Δ beyond the second-order sweet spot, the z-dephasing error is dominated by the first order term describing the longitudinal magnetic field gradient, and the z-dephasing error does not depend on any static electric tuning parameter (e_z in Eq. 3.4.3). The x-dephasing error however does depend on ϵ, and thus operation at the x-dephasing sweet spot reduces the total error. At lower spin charge detuning values $\Delta \lesssim 1$, the z-dephasing sweet spot becomes relevant and the total error plots in b) differ appreciably. In general, operation at $\epsilon = 0$ is beneficial in this regime because the z- and x-dephasing sweet spots start to overlap, as can be seen from the low error region (blue region) in the lower plot extending to spin–charge detuning values as small as 100 MHz. Operation at non-zero electric detuning only has a slight advantage, when operating exactly on the second-order z-sweet spot (at $\Delta \approx 0.3$), and at low electric drive amplitude, as is indicated by the blue arrow in the top panel. Errors in this non-zero detuned regimes are however quite large (1%) and

[18] The operation at the second-order sweet spot (top plot, grey line) can however be seen by the x-dephasing error appearing as a limiting error source.

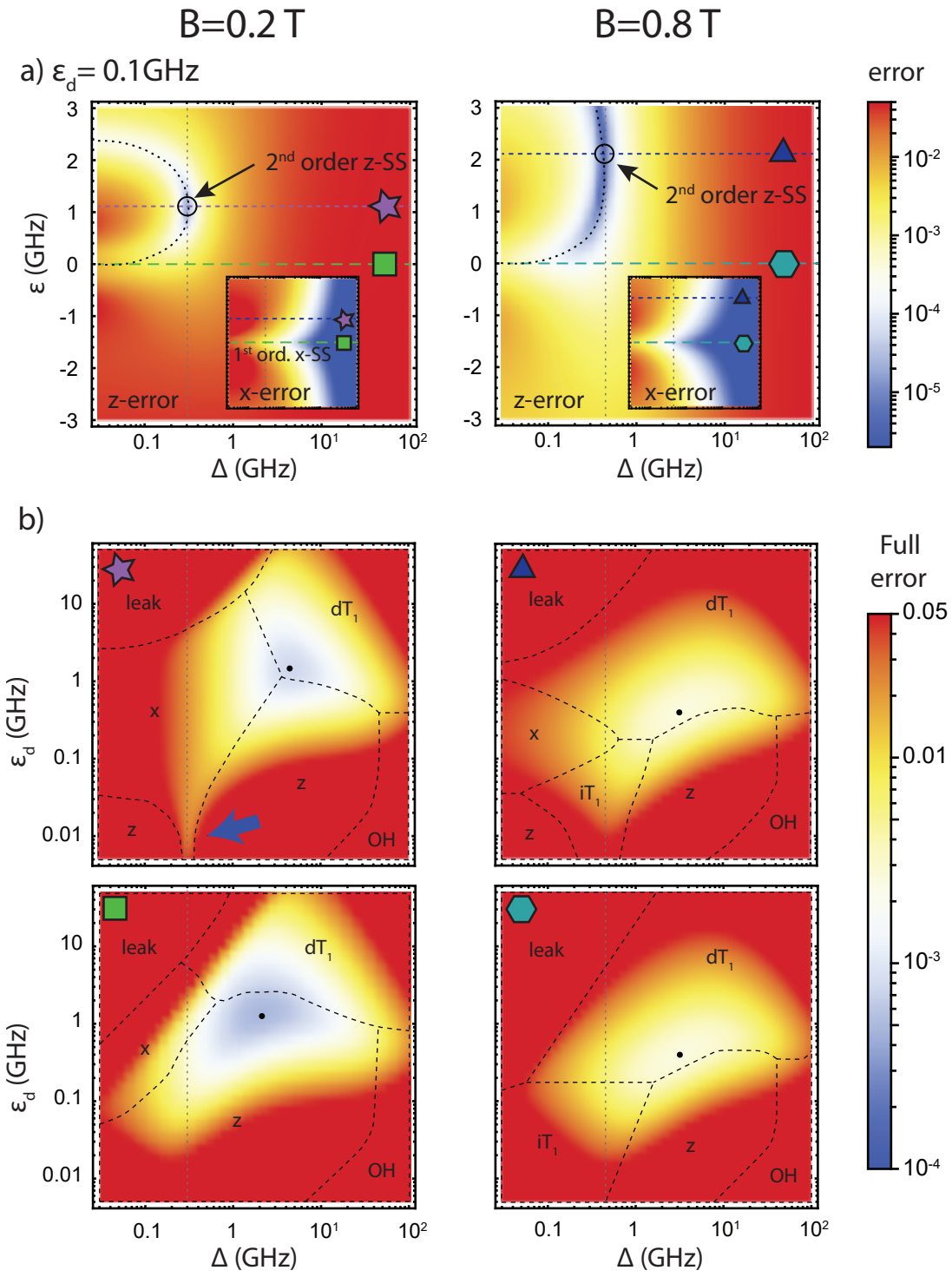

Figure 3.22: **Optimal $\pi/2$ X-gate operation on the flopping-mode qubit at the x- and z-dephasing sweet spots.** The left (right) column displays error simulation at magnetic fields of 0.2 (0.8) T, we chose magnetic field gradients $\Delta\Omega_{z/x} = 5\,(117)$ MHz typical for flopping mode qubits. Row **a)** displays the z-dephasing error (x-dephasing error in the inset) for an arbitrary fixed drive amplitude of $\epsilon_d = 0.1$ GHz as a function of detuning amplitude ϵ and Δ. **b)** Displays the full error when the electric detuning ϵ is tuned to the second-order sweet spot $\epsilon_{z\text{-sweet spot}}$ (top row), and at the first order x-dephasing sweet spot (x-sweet spot) at $\epsilon = 0$. Operation at the second-order sweet spot is only advantageous at low fields and for very small drive amplitudes (blue arrow on top left panel) since the errors associated with variation in the Rabi frequency are minimised. The different error channels are leakage (leak), x-dephasing (x), z-dephasing (z), drive-T_1 (dT_1), idle-T_1 (iT_1), and Overhauser noise (OH).

are far from the optimal.

The optimal operation point for the flopping-mode qubit is positioned at a spin charge detuning position in between the two regimes ($\Delta \approx 2 - 4\,\mathrm{GHz}$) indicated by the black dots. These optimal detuning positions corresponds to a regime where spin–charge hybridisation is relatively low, and where the qubit response to the electrical drive can be explained classically. In that intermediate regime, the influence of the electric-detuning position is observable. Indeed we find that the error at the optimal point (black dots) 50% higher when the qubit is operated at the non-zero electric detuning value (top plot) when compared to operation at the x-dephasing sweet spot (at $\epsilon = 0$). the optimal error is 4.8×10^{-4} at $\epsilon = 0$ in the bottom plot and 7.5×10^{-4} at $\epsilon = 1.1\,\mathrm{GHz}$ in the top plot.

In summary, we have shown that operation of the flopping-mode qubit at the second-order z-dephasing sweet spot is disadvantageous compared to operating the qubit on the x-dephasing sweet spot at the symmetric electric detuning point. This is because the x-dephasing is typically the dominant error source for large driving amplitudes. Operation at the second-order sweet spot is only beneficial below $\epsilon_d \approx 0.03\,\mathrm{GHz}$ corresponding driving powers being restricted below -100 dBm at the gate. This is well below drive powers of up to -60 dBm demonstrated experimentally by Croot *et al.* in ref. [46].

3.5 Conclusion

In this chapter we have shown that the flopping-mode qubit first proposed by Hu *et al.* [73], based on a single electron spin shared by two QDs is an attractive platform for quantum computation. It features low error ($\sim 10^{-4}$) and fast electric driving of the spin (tens of MHz), and ultimately, also long-range coupling via superconducting microwave cavities over the millimetre length-scale [77].

The flopping-mode qubit can be implemented in various physical systems. Engineering of the longitudinal magnetic field gradient either through micromagnet design or by controlling the hyperfine interaction that describes the change in the qubit energy when subjected to a static electric field is crucial in protecting the qubit from electric field noise. We find that minimising the longitudinal magnetic field gradient allows the qubit to reach low errors ($\sim 10^{-3}$) for significantly lower electric drive powers (-100 dBm). The engineered resilience of the qubit to electric field noise is related to the presence of dephasing sweet spots, at which the qubit energy is insensitive to different orders in the qubit energy electric-field fluctuations.

We show the second-order sweet spot for the qubit energy arising from the longitudinal magnetic field gradient, identified in ref. [12, 74], is not the optimal operation point when driving the qubit in the majority of device implementations. The optimal operation point in most cases is the symmetric electric detuning position, at which the qubit electric dipole is maximised, and the qubit's Rabi frequency as well as its energy can be protected from electric field fluctuation. This is especially the case for low longitudinal magnetic field gradients. Finally, our error model, allows fast optimisation and feedback for experimentalists to implement or optimise a flopping-mode qubit by providing optimal magnetic fields, detunings, drive powers and magnetic field gradients required to achieve high-fidelity qubit operations.

Bibliography

[1] Juha T. Muhonen, Juan P. Dehollain, Arne Laucht, Fay E. Hudson, Rachpon Kalra, Takeharu Sekiguchi, Kohei M. Itoh, David N. Jamieson, Jeffrey C. McCallum, Andrew S. Dzurak, and Andrea Morello. Storing quantum information for 30 seconds in a nanoelectronic device. *Nature Nanotechnology*, 9(12):986–991, 2014.

[2] W. Huang, C. H. Yang, K. W. Chan, T. Tanttu, B. Hensen, R. C.C. Leon, M. A. Fogarty, J. C.C. Hwang, F. E. Hudson, K. M. Itoh, A. Morello, A. Laucht, and A. S. Dzurak. Fidelity benchmarks for two-qubit gates in silicon. *Nature*, 569(7757):532–536, 2019.

[3] Ensar Vahapoglu, J. P. Slack-Smith, R. C.C. Leon, W. H. Lim, F. E. Hudson, T. Day, T. Tanttu, C. H. Yang, A. Laucht, A. S. Dzurak, and J. J. Pla. Single-electron spin resonance in a nanoelectronic device using a global field. *arXiv*, 2020.

[4] Emmanuel I. Rashba. Theory of electric dipole spin resonance in quantum dots: Mean field theory with gaussian fluctuations and beyond. *Phys. Rev. B*, 78:195302, 2008.

[5] L. S. Levitov and E. I. Rashba. Dynamical spin-electric coupling in a quantum dot. *Phys. Rev. B*, 67:115324, 2003.

[6] K. C. Nowack, F. H. L. Koppens, Yu. V. Nazarov, and L. M. K. Vandersypen. Coherent control of a single electron spin with electric fields. *Science*, 318(5855):1430–1433, 2007.

[7] S. Nadj-Perge, S. M. Frolov, E. P. A. M. Bakkers, and L. P. Kouwenhoven. Spin-orbit qubit in a semiconductor nanowire. *Nature*, 468(7327):1084–1087, 2010.

[8] Jun Yoneda, Kenta Takeda, Tomohiro Otsuka, Takashi Nakajima, Matthieu R. Delbecq, Giles Allison, Takumu Honda, Tetsuo Kodera, Shunri Oda, Yusuke Hoshi, Noritaka Usami, Kohei M. Itoh, and Seigo Tarucha. A quantum-dot spin qubit with coherence limited by charge noise and fidelity higher than 99.9%. *Nature Nanotechnology*, 13(2):102–106, 2018.

[9] M. Pioro-Ladrire, Y. Tokura, T. Obata, T. Kubo, and S. Tarucha. Micromagnets for coherent control of spin-charge qubit in lateral quantum dots. *Appl. Phys. Lett.*, 90(2):024105, 2007.

[10] Yasuhiro Tokura, Wilfred G. van der Wiel, Toshiaki Obata, and Seigo Tarucha. Coherent single electron spin control in a slanting zeeman field. *Phys. Rev. Lett.*, 96:047202, 2006.

[11] X. Croot, X. Mi, S. Putz, M. Benito, F. Borjans, G. Burkard, and J. R. Petta. Flopping-mode electric dipole spin resonance. *Phys. Rev. Research*, 2:012006, Jan 2020.

[12] Guilherme Tosi, Fahd A Mohiyaddin, Vivien Schmitt, Stefanie Tenberg, Rajib Rahman, Gerhard Klimeck, and Andrea Morello. Silicon quantum processor with robust long-distance qubit couplings. *Nature Communications*, 8(1):450, dec 2017.

[13] E. A. Laird, C. Barthel, E. I. Rashba, C. M. Marcus, M. P. Hanson, and A. C. Gossard. Hyperfine-mediated gate-driven electron spin resonance. *Phys. Rev. Lett.*, 99:246601, 2007.

[14] M. Shafiei, K. C. Nowack, C. Reichl, W. Wegscheider, and L. M. K. Vandersypen. Resolving spin-orbit- and hyperfine-mediated electric dipole spin resonance in a quantum dot. *Phys. Rev. Lett.*, 110:107601, Mar 2013.

[15] A. Wallraff, D. I. Schuster, A. Blais, L. Frunzio, R. S. Huang, J. Majer, S. Kumar, S. M. Girvin, and R. J. Schoelkopf. Strong coupling of a single photon to a superconducting qubit using circuit quantum electrodynamics. *Nature*, 431(7005):162–167, 2004.

[16] K. D. Petersson, L. W. McFaul, M. D. Schroer, M. Jung, J. M. Taylor, A. A. Houck, and J. R. Petta. Circuit quantum electrodynamics with a spin qubit. *Nature*, 490(7420):380–383, 2012.

[17] X. Mi, M. Benito, S. Putz, D. M. Zajac, J. M. Taylor, Guido Burkard, and J. R. Petta. A coherent spin-photon interface in silicon. *Nature*, 555(7698):599–603, 2018.

[18] M. Benito, X. Croot, C. Adelsberger, S. Putz, X. Mi, J. R. Petta, and Guido Burkard. Electric-field control and noise protection of the flopping-mode spin qubit. *Physical Review B*, 100(12):1–10, 2019.

[19] F. N. Krauth, S. K. Gorman, Y. He, M. T. Jones, P. Macha, S. Kocsis, C. Chua, B. Voisin, S. Rogge, R. Rahman, Y. Chung, and M. Y. Simmons. Flopping-mode electric dipole spin resonance in phosphorus donor qubits in silicon. may 2021.

[20] F H Koppens, C Buizert, K J Tielrooij, I T Vink, K C Nowack, T Meunier, L P Kouwenhoven, and L M Vandersypen. Driven coherent oscillations of a single electron spin in a quantum dot. *Nature*, 442(7104):766–771, 2006.

[21] C. H. Yang, K. W. Chan, R. Harper, W. Huang, T. Evans, J. C.C. Hwang, B. Hensen, A. Laucht, T. Tanttu, F. E. Hudson, S. T. Flammia, K. M. Itoh, A. Morello, S. D. Bartlett, and A. S. Dzurak. Silicon qubit fidelities approaching incoherent noise limits via pulse engineering. *Nature Electronics*, 2(4):151–158, 2019.

[22] J. T. Muhonen, A. Laucht, S. Simmons, J. P. Dehollain, R. Kalra, F. E. Hudson, S. Freer, K. M. Itoh, D. N. Jamieson, J. C. McCallum, A. S. Dzurak, and A. Morello. Quantifying the quantum gate fidelity of single-atom spin qubits in silicon by randomized benchmarking. *Journal of Physics Condensed Matter*, 27(15), 2015.

[23] C. D. Hill, E. Peretz, S. J. Hile, M. G. House, M. Fuechsle, S. Rogge, M. Y. Simmons, and L. C. L. Hollenberg. A surface code quantum computer in silicon. *Science Advances*, 1(9):e1500707–e1500707, oct 2015.

[24] M. Veldhorst, J. C.C. Hwang, C. H. Yang, A. W. Leenstra, B. De Ronde, J. P. Dehollain, J. T. Muhonen, F. E. Hudson, K. M. Itoh, A. Morello, and A. S. Dzurak. An addressable quantum dot qubit with fault-tolerant control-fidelity. *Nature Nanotechnology*, 9(12):981–985, 2014.

[25] Y Nakamura, Y.˜A. Pashkin, and J.˜S. Tsai. Coherent control of macroscopic-quantumstates in a single-Cooper-pair box. *Nature*, 398(April):786–788, 1999.

[26] T. Hayashi, T. Fujisawa, H. D. Cheong, Y. H. Jeong, and Y. Hirayama. Coherent manipulation of electronic states in a double quantum dot. *Physical Review Letters*, 91(22):1–4, 2003.

[27] J. R. Petta, A. C. Johnson, C. M. Marcus, M. P. Hanson, and A. C. Gossard. Manipulation of a single charge in a double quantum dot. *Physical Review Letters*, 93(18):1–4, 2004.

[28] J. Gorman, D. G. Hasko, and D. A. Williams. Charge-qubit operation of an isolated double quantum dot. *Physical Review Letters*, 95(9):1–4, 2005.

[29] K. D. Petersson, J. R. Petta, H. Lu, and A. C. Gossard. Quantum coherence in a one-electron semiconductor charge qubit. *Physical Review Letters*, 105(24):1–4, 2010.

[30] Dohun Kim, D. R. Ward, C. B. Simmons, John King Gamble, Robin Blume-Kohout, Erik Nielsen, D. E. Savage, M. G. Lagally, Mark Friesen, S. N. Coppersmith, and M. A. Eriksson. Microwave-driven coherent operation of a semiconductor quantum dot charge qubit. *Nature Nanotechnology*, 10(3):243–247, 2015.

[31] Gou Shinkai, Toshiaki Hayashi, Takeshi Ota, and Toshimasa Fujisawa. Correlated coherent oscillations in coupled semiconductor charge qubits. *Physical Review Letters*, 103(5):1–4, 2009.

[32] X. Mi, J. V. Cady, D. M. Zajac, P. W. Deelman, and J. R. Petta. Strong coupling of a single electron in silicon to a microwave photon. *Science*, 355(6321):156–158, 2017.

[33] P. Scarlino, D. J. Van Woerkom, A. Stockklauser, J. V. Koski, M. C. Collodo, S. Gasparinetti, C. Reichl, W. Wegscheider, T. Ihn, K. Ensslin, and A. Wallraff. All-Microwave Control and Dispersive Readout of Gate-Defined Quantum Dot Qubits in Circuit Quantum Electrodynamics. *Physical Review Letters*, 122(20):206802, 2019.

[34] P. Scarlino, J. H. Ungerer, D. J. van Woerkom, M. Mancini, P. Stano, C. Muller, A. J. Landig, J. V. Koski, C. Reichl, W. Wegscheider, T. Ihn, K. Ensslin, and A. Wallraff. In-situ Tuning of the Electric Dipole Strength of a Double Dot Charge Qubit: Charge Noise Protection and Ultra Strong Coupling. pages 1–24, 2021.

[35] T. P. Harty, D. T.C. Allcock, C. J. Ballance, L. Guidoni, H. A. Janacek, N. M. Linke, D. N. Stacey, and D. M. Lucas. High-fidelity preparation, gates, memory, and readout of a trapped-ion quantum bit. *Physical Review Letters*, 113(22):2–6, 2014.

[36] K. D. Petersson, C. G. Smith, D. Anderson, P. Atkinson, G. A C Jones, and D. A. Ritchie. Microwave-driven transitions in two coupled semiconductor charge qubits. *Physical Review Letters*, 103(1):1–4, 2009.

[37] D. J. Van Woerkom, P. Scarlino, J. H. Ungerer, C. Müller, J. V. Koski, A. J. Landig, C. Reichl, W. Wegscheider, T. Ihn, K. Ensslin, and A. Wallraff. Microwave Photon-Mediated Interactions between Semiconductor Qubits. *Physical Review X*, 8(4):41018, 2018.

[38] P. Scarlino, D. J. van Woerkom, U. C. Mendes, J. V. Koski, A. J. Landig, C. K. Andersen, S. Gasparinetti, C. Reichl, W. Wegscheider, K. Ensslin, T. Ihn, A. Blais, and A. Wallraff. Coherent microwave-photon-mediated coupling between a semiconductor and a superconducting qubit. *Nature Communications*, 10(1), 2019.

[39] A. Stockklauser, P. Scarlino, J. V. Koski, S. Gasparinetti, C. K. Andersen, C. Reichl, W. Wegscheider, T. Ihn, K. Ensslin, and A. Wallraff. Strong coupling cavity QED with gate-defined double quantum dots enabled by a high impedance resonator. *Physical Review X*, 7(1):1–6, 2017.

[40] Philipp Ross, Brendon C. Rose, Cheuk C. Lo, Mike L.W. Thewalt, Alexei M. Tyryshkin, Stephen A. Lyon, and John J.L. Morton. Electron Spin Resonance of P Donors in Isotopically Purified Si Detected by Contactless Photoconductivity. *Physical Review Applied*, 11(5):1, 2019.

[41] J R Petta, a C Johnson, J M Taylor, E a Laird, A Yacoby, M D Lukin, C M Marcus, M P Hanson, and a C Gossard. Coherent Manipulation of Coupled Electron Spins in Semiconductor Quantum Dots. *Science*, 309(September):2180–2184, 2005.

[42] B. M. Maune, M. G. Borselli, B. Huang, T. D. Ladd, P. W. Deelman, K. S. Holabird, A. A. Kiselev, I. Alvarado-Rodriguez, R. S. Ross, A. E. Schmitz, M. Sokolich, C. A. Watson, M. F. Gyure, and A. T. Hunter. Coherent singlet-triplet oscillations in a silicon-based double quantum dot. *Nature*, 481(7381):344–347, 2012.

[43] E. A. Laird, J. M. Taylor, D. P. DiVincenzo, C. M. Marcus, M. P. Hanson, and A. C. Gossard. Coherent spin manipulation in an exchange-only qubit. *Physical Review B*, 82(7):075403, aug 2010.

[44] J. Medford, J. Beil, J. M. Taylor, S. D. Bartlett, A. C. Doherty, E. I. Rashba, D. P. Divincenzo, H. Lu, A. C. Gossard, and C. M. Marcus. Self-consistent measurement and state tomography of an exchange-only spin qubit. *Nature Nanotechnology*, 8(9):654–659, 2013.

[45] Matthew P. Wardrop and Andrew C. Doherty. Characterization of an exchange-based two-qubit gate for resonant exchange qubits. *Physical Review B*, 93(7):1–10, 2016.

[46] X. Croot, X. Mi, S. Putz, M. Benito, F. Borjans, G. Burkard, and J. R. Petta. Flopping-mode electric dipole spin resonance. *Physical Review Research*, 012006:1–6, 2020.

[47] Yasuhiro Tokura, Wilfred G. Van Der Wiel, Toshiaki Obata, and Seigo Tarucha. Coherent single electron spin control in a slanting zeeman field. *Physical Review Letters*, 96(4):1–4, 2006.

[48] K C Nowack, F H L Koppens, Y V Nazarov, and L M K Vandersypen. Coherent Control of a Single Electron with Electric Fields. *Science*, 318:1430–1433, 2007.

[49] Y Kato, R C Myers, D C Driscoll, A C Gossard, J Levy, and D D Awschalom. Gigahertz Electron Spin Manipulation Using Voltage-Controlled g-Tensor Modulation. *Science*, 299(february):1181–1185, 2003.

[50] L. S. Levitov and E. I. Rashba. Dynamical spin-electric coupling in a quantum dot. *Physical Review B - Condensed Matter and Materials Physics*, 67(115324):5, 2003.

[51] Emmanuel I. Rashba. Theory of electric dipole spin resonance in quantum dots: Mean field theory with Gaussian fluctuations and beyond. *Physical Review B - Condensed Matter and Materials Physics*, 78(19):7–9, 2008.

[52] S. Nadj-Perge, S. M. Frolov, E. P.A.M. Bakkers, and L. P. Kouwenhoven. Spin-orbit qubit in a semiconductor nanowire. *Nature*, 468(7327):1084–1087, 2010.

[53] V. S. Pribiag, S. Nadj-Perge, S. M. Frolov, J. W.G. Van Den Berg, I. Van Weperen, S. R. Plissard, E. P.A.M. Bakkers, and L. P. Kouwenhoven. Electrical

control of single hole spins in nanowire quantum dots. *Nature Nanotechnology*, 8(3):170–174, 2013.

[54] N. W. Hendrickx, W. I.L. Lawrie, L. Petit, A. Sammak, G. Scappucci, and M. Veldhorst. A single-hole spin qubit. *Nature Communications*, 11(1), 2020.

[55] Zhanning Wang, Elizabeth Marcellina, Alex R. Hamilton, James H. Cullen, Sven Rogge, Joe Salfi, and Dimitrie Culcer. Optimal operation points for ultrafast, highly coherent Ge hole spin-orbit qubits. *npj Quantum Information*, 7(1), 2021.

[56] M. Pioro-Ladrière, T. Obata, Y. Tokura, Y.-S. Shin, T. Kubo, K. Yoshida, T. Taniyama, and S. Tarucha. Electrically driven single-electron spin resonance in a slanting Zeeman field. *Nature Physics*, 4(10):776–779, 2008.

[57] M. Pioro-Ladrière, Y. Tokura, T. Obata, T. Kubo, and S. Tarucha. Micromagnets for coherent control of spin-charge qubit in lateral quantum dots. *Applied Physics Letters*, 90(2), 2007.

[58] E. Kawakami, P. Scarlino, D. R. Ward, F. R. Braakman, D. E. Savage, M. G. Lagally, Mark Friesen, S. N. Coppersmith, M. A. Eriksson, and L. M.K. Vandersypen. Electrical control of a long-lived spin qubit in a Si/SiGe quantum dot. *Nature Nanotechnology*, 9(9):666–670, 2014.

[59] J. Yoneda, T. Otsuka, T. Nakajima, T. Takakura, T. Obata, M. Pioro-Ladrière, H. Lu, C. J. Palmstrøm, A. C. Gossard, and S. Z. Tarucha. Fast electrical control of single electron spins in Quantum dots with vanishing influence from nuclear spins. *Physical Review Letters*, 113(26):1–5, 2014.

[60] R. Barends, J. Kelly, A. Megrant, A. Veitia, D. Sank, E. Jeffrey, T. C. White, J. Mutus, A. G. Fowler, B. Campbell, Y. Chen, Z. Chen, B. Chiaro, A. Dunsworth, C. Neill, P. O'Malley, P. Roushan, A. Vainsencher, J. Wenner, A. N. Korotkov, A. N. Cleland, and John M. Martinis. Superconducting quantum circuits at the surface code threshold for fault tolerance. *Nature*, 508(7497):500–503, 2014.

[61] Kenta Takeda, Jun Kamioka, Tomohiro Otsuka, Jun Yoneda, Takashi Nakajima, Matthieu R. Delbecq, Shinichi Amaha, Giles Allison, Tetsuo Kodera, Shunri Oda, and Seigo Tarucha. A fault-tolerant addressable spin qubit in a natural silicon quantum dot. *Science Advances*, 2(8):1–6, 2016.

[62] E. A. Laird, C. Barthel, E. I. Rashba, C. M. Marcus, M. P. Hanson, and A. C. Gossard. Hyperfine-mediated gate-driven electron spin resonance. *Physical Review Letters*, 99(24):1–4, 2007.

[63] Mircea Trif, Vitaly N. Golovach, and Daniel Loss. Spin dynamics in InAs nanowire quantum dots coupled to a transmission line. *Physical Review B - Condensed Matter and Materials Physics*, 77(4):1–14, 2008.

[64] N. Samkharadze, A. Bruno, P. Scarlino, G. Zheng, D. P. DiVincenzo, L. DiCarlo, and L. M. K. Vandersypen. High-kinetic-inductance superconducting nanowire resonators for circuit qed in a magnetic field. *Phys. Rev. Applied*, 5:044004, 2016.

[65] N. Samkharadze, G. Zheng, N. Kalhor, D. Brousse, A. Sammak, U. C. Mendes, A. Blais, G. Scappucci, and L. M.K. Vandersypen. Strong spin-photon coupling in silicon. *Science*, 359(March):1123–1127, 2018.

[66] Filip K. Malinowski, Frederico Martins, Peter D. Nissen, Edwin Barnes, Łukasz Cywiński, Mark S. Rudner, Saeed Fallahi, Geoffrey C. Gardner, Michael J. Manfra, Charles M. Marcus, and Ferdinand Kuemmeth. Notch filtering the nuclear environment of a spin qubit. *Nature Nanotechnology*, 12(1):16–20, 2016.

[67] Frederico Martins, Filip K Malinowski, Peter D Nissen, Edwin Barnes, Saeed Fallahi, Geoffrey C Gardner, Michael J Manfra, Charles M Marcus, and Ferdinand Kuemmeth. Noise Suppression Using Symmetric Exchange Gates in Spin Qubits. *Physical Review Letters*, 116801(March):1–5, 2016.

[68] Maximilian Russ, Florian Ginzel, and Guido Burkard. Coupling of three-spin qubits to their electric environment. *Physical Review B*, 94(16):1–17, 2016.

[69] J. M. Taylor, V. Srinivasa, and J. Medford. Electrically protected resonant exchange qubits in triple quantum dots. *Physical Review Letters*, 111(5):1–5, 2013.

[70] A. J. Landig, J. V. Koski, P. Scarlino, U. C. Mendes, A. Blais, C. Reichl, W. Wegscheider, A. Wallraff, K. Ensslin, and T. Ihn. Coherent spinphoton coupling using a resonant exchange qubit. *Nature*, 560(7717):179–184, 2018.

[71] A. J. Landig, J. V. Koski, P. Scarlino, C. Müller, J. C. Abadillo-Uriel, B. Kratochwil, C. Reichl, W. Wegscheider, S. N. Coppersmith, Mark Friesen, A. Wall-

raff, T. Ihn, and K. Ensslin. Virtual-photon-mediated spin-qubittransmon coupling. *Nature Communications*, 10:1–7, 2019.

[72] Félix Beaudoin, Dany Lachance-Quirion, W. A. Coish, and Michel Pioro-Ladrière. Coupling a single electron spin to a microwave resonator: Controlling transverse and longitudinal couplings. *Nanotechnology*, 27(46), 2016.

[73] Xuedong Hu, Yu Xi Liu, and Franco Nori. Strong coupling of a spin qubit to a superconducting stripline cavity. *Physical Review B - Condensed Matter and Materials Physics*, 86(3):1–5, 2012.

[74] Monica Benito, Xanthe Croot, Christoph Adelsberger, Stefan Putz, Xiao Mi, Jason R. Petta, and Guido Burkard. Electrical control and decoherence of the flopping-mode spin qubit. pages 28–32, 2019.

[75] Guilherme Tosi, Fahd A. Mohiyaddin, Stefanie Tenberg, Arne Laucht, and Andrea Morello. Robust electric dipole transition at microwave frequencies for nuclear spin qubits in silicon. *arXiv*, jun 2017.

[76] J. J. Viennot, M. C. Dartiailh, A. Cottet, and T. Kontos. Coherent coupling of a single spin to microwave cavity photons. *Science*, 349(6246):408–411, 2015.

[77] F. Borjans, X. G. Croot, X. Mi, M. J. Gullans, and J. R. Petta. Resonant microwave-mediated interactions between distant electron spins. *Nature*, 577(January):195–199, 2019.

[78] J. C. Abadillo-Uriel, M. A. Eriksson, S. N. Coppersmith, and Mark Friesen. Enhancing the dipolar coupling of a S-T0 qubit with a transverse sweet spot. *Nature Communications*, 10(1), 2019.

[79] Pascal Cerfontaine, Tim Botzem, Julian Ritzmann, Simon Sebastian Humpohl, Arne Ludwig, Dieter Schuh, Dominique Bougeard, Andreas D. Wieck, and Hendrik Bluhm. Closed-loop control of a GaAs-based singlet-triplet spin qubit with 99.5% gate fidelity and low leakage. *Nature Communications*, 11(1):5–10, 2020.

[80] K. Takeda, A. Noiri, J. Yoneda, T. Nakajima, and S. Tarucha. Resonantly Driven Singlet-Triplet Spin Qubit in Silicon. *Physical Review Letters*, 124(11):117701, 2020.

[81] John M. Nichol, Lucas A. Orona, Shannon P. Harvey, Saeed Fallahi, Geoffrey C. Gardner, Michael J. Manfra, and Amir Yacoby. High-fidelity entangling gate for double-quantum-dot spin qubits. *npj Quantum Information*, 3(1):3, dec 2017.

[82] Gábor Széchenyi Peter Boross and András Pályi. Valley-enhanced fast relaxation of gate- controlled donor qubits in silicon. *IOP Nanotechnology*, 27(1), 2016.

[83] F. Motzoi, J. M. Gambetta, P. Rebentrost, and F. K. Wilhelm. Simple Pulses for Elimination of Leakage in Weakly Nonlinear Qubits. *Physical Review Letters*, 103(11):1–4, 2009.

[84] Ludwik Kranz, Samuel Keith Gorman, Brandur Thorgrimsson, Yu He, Daniel Keith, Joris Gerhard Keizer, and Michelle Yvonne Simmons. Exploiting a Single-Crystal Environment to Minimize the Charge Noise on Qubits in Silicon. *Advanced Materials*, 32(40):1–8, 2020.

[85] Filip K. Malinowski, Frederico Martins, Łukasz Cywiński, Mark S. Rudner, Peter D. Nissen, Saeed Fallahi, Geoffrey C. Gardner, Michael J. Manfra, Charles M. Marcus, and Ferdinand Kuemmeth. Spectrum of the Nuclear Environment for GaAs Spin Qubits. *Physical Review Letters*, 118(17):1–6, 2017.

[86] Blake M. Freeman, Joshua S. Schoenfield, and HongWen Jiang. Comparison of low frequency charge noise in identically patterned Si/SiO ₂ and Si/SiGe quantum dots. *Applied Physics Letters*, 108(25):253108, jun 2016.

[87] P. Dutta and P. M. Horn. Low-frequency fluctuations in solids: 1f noise. *Reviews of Modern Physics*, 53(3):497–516, 1981.

[88] Alexei M. Tyryshkin, Shinichi Tojo, John J. L. Morton, Helge Riemann, Nikolai V. Abrosimov, Peter Becker, Hans-Joachim Pohl, Thomas Schenkel, Michael L. W. Thewalt, Kohei M. Itoh, and S. A. Lyon. Electron spin coherence exceeding seconds in high-purity silicon. *Nature Materials*, 11(2):143–147, dec 2011.

[89] Mateusz T. Madzik, Thaddeus D. Ladd, Fay E. Hudson, Kohei M. Itoh, Alexander M. Jakob, Brett C. Johnson, David N. Jamieson, Jeffrey C. McCallum, Andrew S. Dzurak, Arne Laucht, and Andrea Morello. Controllable freezing of the nuclear spin bath in a single-atom spin qubit. *Science Advances*, pages 1–12, 2019.

[90] Jarryd J Pla, Kuan Y Tan, Juan P Dehollain, Wee H Lim, John J L Morton, David N Jamieson, Andrew S Dzurak, and Andrea Morello. A single-atom electron spin qubit in silicon. *Nature*, 489(7417):541–545, sep 2012.

[91] O. E. Dial, M. D. Shulman, S. P. Harvey, H. Bluhm, V. Umansky, and A. Yacoby. Charge noise spectroscopy using coherent exchange oscillations in a singlet-triplet qubit. *Physical Review Letters*, 110(14):1–5, 2013.

[92] M. Benito, X. Croot, C. Adelsberger, S. Putz, X. Mi, J. R. Petta, and Guido Burkard. Electric-field control and noise protection of the flopping-mode spin qubit. *Phys. Rev. B*, 100:125430, 2019.

[93] Thomas F. Watson, Bent Weber, Yu Ling Hsueh, Lloyd C.L. Hollenberg, Rajib Rahman, and Michelle Y. Simmons. Atomically engineered electron spin lifetimes of 30 s in silicon. *Science Advances*, 3(3):1–7, 2017.

[94] G. Feher and E. A. Gere. Electron spin resonance experiments on donors in silicon. II. Electron spin relaxation effects. *Physical Review*, 114(5):1245–1256, 1959.

[95] H. Büch, S. Mahapatra, R. Rahman, A. Morello, and M. Y. Simmons. Spin readout and addressability of phosphorus-donor clusters in silicon. *Nature Communications*, 4(1):2017, dec 2013.

[96] T. F. Watson, B. Weber, M. G. House, H. Büch, and M. Y. Simmons. High-Fidelity Rapid Initialization and Read-Out of an Electron Spin via the Single Donor D Charge State T. *Physical Review Letters*, 115(16):166806, oct 2015.

[97] Lukas Fricke, Samuel James Hile, Prasanna Pakkiam, and Michelle Y. Simmons. To be published. 2021.

Chapter 4

An all-epitaxial flopping-mode qubit and quantum-computing architecture

The previous chapter introduced the concept of flopping mode qubits and how they have been realised in different physical systems. In particular, this chapter dealt with the importance of engineering magnetic field gradients in these devices and the different sweet spots in the qubit energy landscape where it was shown that by reducing the longitudinal magnetic field gradient (to remove second-order sweet spots) the qubit dephasing time could be maximised. With this knowledge, we then introduced a new error model to describe the optimal operation point of the qubit. In this chapter we will explicitly address how to engineer an all-epitaxial flopping mode qubit and how it can be scaled up into a large-scale quantum computing architecture.

The work for this chapter was performed by this author, with help from Dr.Yu He, and supervision by Dr. Samuel Gorman. The work presented here is the object of provisional Australian patent application 2021900702, and is under review for publication [1].

4.1 Introduction

Donor-based spin-qubits have demonstrated some of the longest coherence and relaxation times [2] in solid-state quantum devices together with single-qubit gate fidelities of 10^{-3} [3], well below the error threshold of the leading quantum error correction code (the surface code). This makes donor-based spin-qubits an attractive candi-

date for large-scale universal quantum computation. Traditionally, spin qubits have been driven by bulky microwave antennas producing oscillating magnetic field from high-powered microwave voltages using electron spin resonance (ESR). State-of-the-art ESR has demonstrated high fidelity ($> 99\%$) single qubit gates. However, the gates are two orders of magnitude slower than single-qubit gates in superconducting qubits for comparable fidelities due to the difficulty in applying large high-frequency magnetic fields. In donor spin-qubits, a π-gate was demonstrated with 10^{-3} error in about $3\,\mu$s in ref. [3]. In superconducting qubits a π gate was demonstrated with 8×10^{-4} error in about 16 ns in ref. [4].

Both the bulky, heat dissipating ESR antennas and the relatively slow gates make it challenging to scale-up quantum processors based on the magnetic control of donor spin-qubits. We note the recent appearance of a paper where a global ESR magnetic field can be used as a scalable architecture [5]; however, it is not clear how such a system would deal with variations in the electron spin resonance frequencies in a large-scale device [6]. Furthermore, long-distance qubit coupling schemes will likely be indispensable to the scaling-up of quantum computers to large sizes, due to the need for classical control electronics to be interfaced with the qubits, typically requiring cryogenic temperatures (see Sect. 2.1.3). In silicon, the low spin–orbit interaction renders current long-distance coupling schemes difficult to use via the established technological platform based on superconducting resonator due to the weak coupling of spins to the magnetic field of the cavity.

As a consequence there has been recent growing interest in electric dipole spin resonance (EDSR) as means to couple single-electron spins over a large (mm scale) distance [7]. This technique electrically controls spin qubits through local electric fields and couples qubits via their charge dipole moment. Electric-dipole spin resonance is therefore achieved by coupling the spin of an electron to its charge degree of freedom. This allows the spin state to be controlled by moving the electron using electric fields [8]. As discussed in the previous chapter, spin–charge coupling can be created by a number of different physical mechanisms such as the use of large spin–orbit coupling materials [9, 10, 11], magnetic-field gradients from micromagnets [12, 13, 14, 15], and the hyperfine interaction between the electron and the surrounding nuclear spins [16, 17, 18].

Depending on the nature of the different physical mechanism that couples the spin and charge degree of freedom, EDSR can be used in different ways to drive qubit operations. The use of materials with intrinsic spin–orbit coupling such as III-V semiconductor materials [9, 10, 11, 19] allows for EDSR without any addi-

tional control structures [12]. For material systems with low intrinsic spin–orbit coupling however such as electrons in silicon it is difficult to operate a qubit using EDSR without creating spin–orbit coupling using extrinsic mechanisms. To generate a synthetic spin–orbit coupling, micromagnets were therefore introduced to create a gradient magnetic field near the spin qubits [12]. However, these micromagnets require further device processing steps and complicated device architectures. Micromagnets have also been shown to introduce additional charge noise originating from stray magnetic fields [20]. Typically when an electron is moved back-and-forth within the magnetic-field gradient perpendicular to the static magnetic field, B_0, it experiences an effective oscillating magnetic field with a corresponding energy, $\Delta\Omega_\perp$ which can be used to drive spin rotations [14]. However, any stray magnetic-field gradient parallel to B_0 with a corresponding energy, $\Delta\Omega_\parallel$ can lead to charge noise induced dephasing as discussed in the previous chapter.

In this chapter, we specifically consider flopping-mode EDSR where a single electron is shuttled between two donor-based quantum dots (QDs) [15, 21, 22] rather than shaking an electron within a single QD [10]. The proposed qubit is theoretically shown to be able to achieve long coherence times by minimising the longitudinal-magnetic-field gradient while maintaining a large ~ 100 MHz transverse-magnetic-field gradient for fast gate operations. Additionally, we will show that these flopping-mode qubits can be measured via dispersive charge readout [15] or by direct single-shot spin readout [23], and can be coupled over long distances using a superconducting cavity [7]. This makes the flopping mode EDSR qubit a promising candidate for scaling up quantum processors based on electron spins important to realise error-corrected quantum computation using the surface code.

In Fig. 4.1a)-c) we describe three different flopping-mode qubits in silicon. The two magnetic-field gradients, $\Delta\Omega_\perp$ (single-qubit gate speed) and $\Delta\Omega_\parallel$ (qubit dephasing) — present in each design—arise from different physical mechanisms. Figure 4.1a) shows the donor–QD hybrid qubit (flip-flop qubit) [18]. Here, the spin–charge coupling arises from the hyperfine interaction of the electron spin with the nuclear spin of a single phosphorus used to generate electron-nuclear spin donor–QD transitions [24]. The flopping-mode operation EDSR is performed by positioning the electron in a superposition of charge states between the donor nuclei and an interface QD created using electrostatic gates. In this charge-superposition state the hyperfine interaction is known to change from $A \approx 117$ MHz on the donor to $A \approx 0$ MHz on the QD [18]. The qubit states are $|0\rangle \equiv |\Uparrow\downarrow\rangle$ and $|1\rangle \equiv |\Downarrow\uparrow\rangle$ ($|$nuclear spin, electron spin$\rangle$). The transverse-magnetic-field gradient, $\Delta\Omega_\perp$ (green)

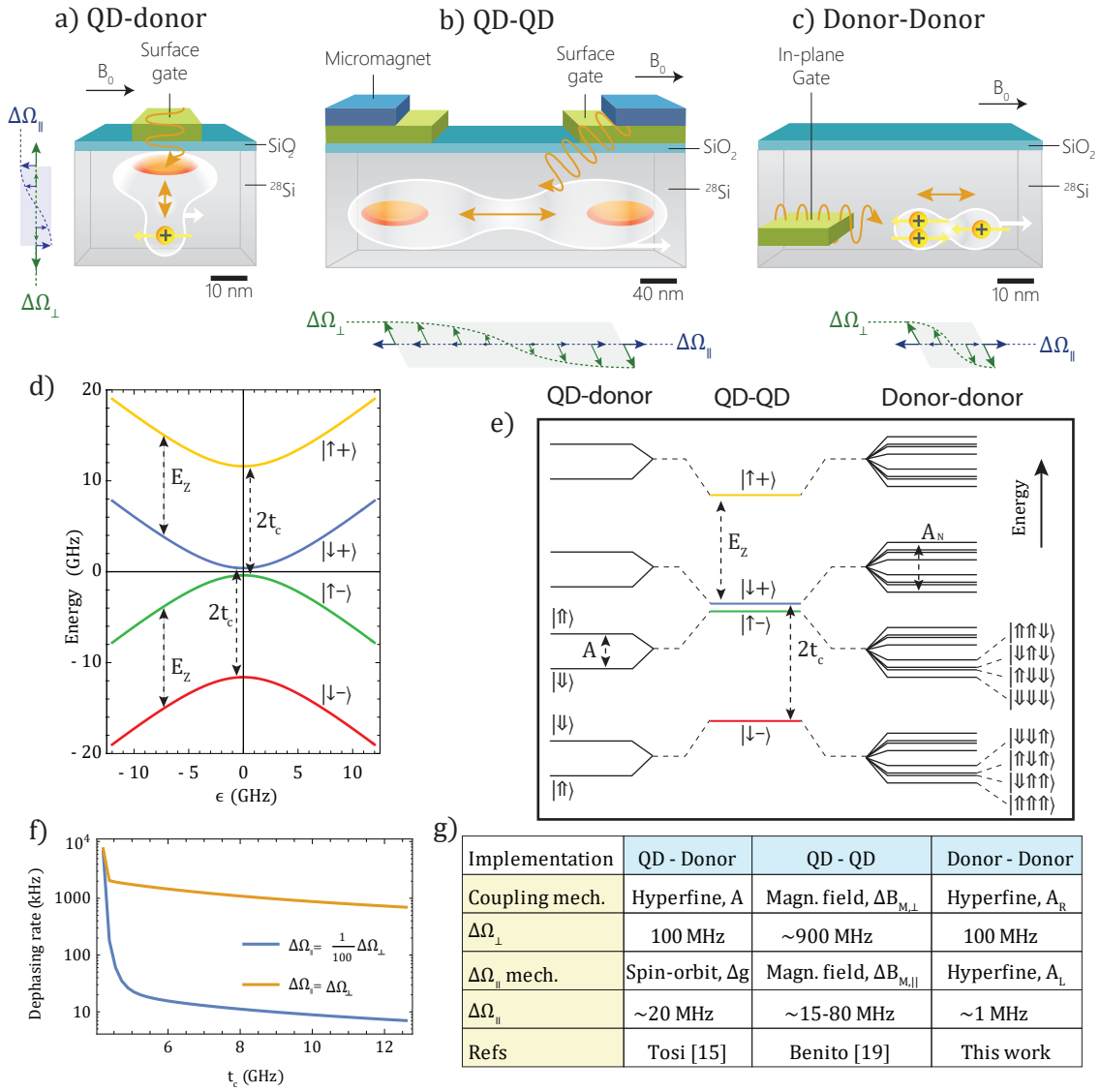

Implementation	QD - Donor	QD - QD	Donor - Donor
Coupling mech.	Hyperfine, A	Magn. field, $\Delta B_{M,\perp}$	Hyperfine, A_R
$\Delta\Omega_\perp$	100 MHz	~900 MHz	100 MHz
$\Delta\Omega_\parallel$ mech.	Spin-orbit, Δg	Magn. field, $\Delta B_{M,\parallel}$	Hyperfine, A_L
$\Delta\Omega_\parallel$	~20 MHz	~15-80 MHz	~1 MHz
Refs	Tosi [15]	Benito [19]	This work

Figure 4.1: **A comparison of different flopping-mode electric-dipole spin-resonance qubits.** Three different flopping-mode EDSR qubits that can be implemented using a) donor–QD, b) QD–QD, and c) donor–donor sites. The longitudinal (blue) and transverse (green) magnetic-field gradients, $\Delta\Omega_\parallel$ and $\Delta\Omega_\perp$ are shown next to the different implementations. The donor–QD and donor–donor implementations both use the hyperfine interaction from the electron-nuclear spins that are naturally present in donor systems to generate a spin–orbit coupling. The QD–QD system requires an additional micromagnet to create a spatially-varying magnetic field to induce an artificial spin–orbit coupling. The electron wave function is shown as the white cloud with a spin orientated parallel to the external magnetic field, B_0. The donor nuclei are shown as yellow positive charges. d) The energy spectrum for a single electron in a magnetic field ($E_z = \gamma_e B_0$) near the charge degeneracy between two different charge states with tunnel coupling, t_c. The energy spectrum at $\epsilon = 0$ for e) donor–QD, QD–QD, and donor–donor implementations show the additional nuclear-spin states ($\Uparrow$ and $\Downarrow$) present in donor systems. f) The qubit dephasing rate for different longitudinal-magnetic-field gradients, $\Delta\Omega_\parallel = \Delta\Omega_\perp$ (yellow) and $\Delta\Omega_\parallel = \Delta\Omega_\perp/100$ (blue) with $\Delta\Omega_\perp = 117\,\text{MHz}$. Here, the smaller the longitudinal-magnetic-field gradient the more gradual the change in qubit energy, which results in lower errors over a larger detuning range. g) Summary of the effective magnetic-field gradients found in the different flopping-mode EDSR qubits.

arises from the changing hyperfine interaction as the electron is moved away from the donor nucleus. This voltage-dependent hyperfine can then be used to resonantly drive the qubit states by applying an oscillating electric field. The longitudinal-magnetic-field gradient, $\Delta\Omega_{\parallel}$ (blue) is created by the difference in the electron g-factor between the QD and donor such that the qubit energy differs whether the electron resides on the QD or the donor.

The second flopping-mode-qubit implementation in Fig. 4.1b) is the QD–QD system [25]. Here the qubit states are the pure spin states of the electron in the ground charge state of the double-quantum-dot system, $|0\rangle \equiv |\downarrow\rangle$ or $|1\rangle \equiv |\uparrow\rangle$. The transverse-magnetic-field gradient, $\Delta\Omega_{\perp}$, required to drive qubit rotations is generated by an additional micromagnet ($\sim$ 300 nm away) designed to create a large magnetic-field gradient ($\sim$ 10 mT) across the two QDs [26]. As previously discussed the flopping-mode EDSR is performed by biasing a single electron to a superposition between two charge states of different QDs and applying an oscillating electric field on resonance with the qubit energy. The stray field of the micromagnet is known to create a magnetic-field gradient parallel to the external magnetic field corresponding to $\Delta\Omega_{\parallel}$ which leads to dephasing of the qubit.

In this chapter we focus on the details of a flopping-mode qubit based on two donor-based QDs with an asymmetric number of donors in each QD as shown in Fig. 4.1c). In this implementation the qubit utilises the hyperfine interaction of the electron spin on one QD with a nuclear spin to create a flip-flop transition on only one of the QDs. The other nuclear spins on the second QD are used to reduce the dephasing rate of the qubit by minimising the longitudinal magnetic field gradient. This builds on a previous proposal [27] where the electron spin could be electrically controlled by simultaneously flip-flopping with all nuclear spins across two donor-based QDs. In principle, each donor QD can be defined by any number of nuclear spins. Whilst a 1P-1P configuration is possible [28] we show that this configuration leads to significant dephasing, as such we consider an asymmetric donor system to reduce the dephasing anticipated from this longitudinal-magnetic-field gradient. Typically, as the number of donors comprising the QD is increased, the hyperfine strength of the first electron on that QD becomes larger [29]. This donor-based control of the hyperfine interaction is useful for increasing the transverse-magnetic-field gradient required for qubit driving such that the hyperfine interaction can be made significantly different between the QDs to address particular flip-flop transitions. However, the larger hyperfine interaction on the secondary QD also makes the longitudinal-magnetic-field gradient larger leading to reduced coherence times.

To reduce this effect, we propose filling one of the QDs with more electrons in order to shield the outer electron from the inner core donor nuclear spins. This results in a reduced hyperfine coupling [29] and therefore a lower dephasing rate.

We choose to implement the two aforementioned strategies to optimise the hyperfine interactions within the qubit (inactive nuclear spins and inner-shell electron shielding) on the specific case of a single donor coupled to a 2P QD (2P-1P) at the (2,1)↔(3,0) charge transition. This particular charge transition corresponds to an unpaired electron being shared by the two QDs (as is required for flopping mode operation), while two inner electrons on the 2P (left) QD lower the hyperfine interaction of the outermost electron. Furthermore, nuclear-spin control of the in active donors in the 2P QD allows us to engineer the total hyperfine coupling experienced by the electron. As we will show later, this reduces the longitudinal-magnetic-field gradient, $\Delta\Omega_{\parallel}$ and leads to increased coherence times. The qubit states are $|0\rangle \approx |\Downarrow\Uparrow\Uparrow\downarrow\rangle$ and $|1\rangle \approx |\Downarrow\Uparrow\Downarrow\uparrow\rangle$ which are coupled via a flip-flop transition of the electron with the 1P (right) nuclear spin. Such a donor–donor implementation therefore also utilises the hyperfine interaction from the electron–nuclear-spin system to drive qubit transitions as with the flip-flop qubit in Fig. 4.1a). The key difference is that the magnetic-field gradient can be engineered during fabrication by controlling the number of donors in each QD and the number of electrons on these QDs. Since the hyperfine interaction is known to change considerably for multi-donor QDs we can make $\Delta\Omega_{\perp}$ up to ~ 300 MHz and $\Delta\Omega_{\parallel}$ less than a few MHz [30], see Fig. 4.1g). This is in contrast to the flip-flop qubit where $\Delta\Omega_{\parallel}$ is primarily determined by the difference in the electron g-factor on the donor atom and the QD, the latter being known to vary due to atomic steps at the interface where the QD is formed [31].

In this chapter we show that the additional nuclei in these multi-donor QDs can be used to minimise the dephasing rate of the qubit. This is because it is the strength of the hyperfine interaction of the electron spin with the nuclear spins that are not flipping during electric driving that largely determines the dephasing rate. By engineering the hyperfine strength on the multi-donor QDs, we can therefore maximise the coherence time of the EDSR qubit. By directly controlling the nuclear-spin states and the number of electrons on the double-donor flopping-mode EDSR qubit, we can also operate over a wide range of magnetic fields and tunnel couplings. Most importantly, the qubit shows low errors, $< 10^{-3}$, below the error threshold for surface-code error correction, with realistic noise levels achieved in isotopically purified silicon-28 [2, 32]. The robustness of the qubit to variations in the magnetic field and to variable tunnel couplings is particularly useful for scaling

to large qubit arrays where inevitable imperfections in fabrication and measurement control can reduce qubit quality. Moreover, we show that the low error rate and the spin–charge coupling predicted for the qubit will allow for strong-coupling to superconducting microwave cavities. This spin–cavity coupling has been systematically studied by Osika *et al.* [28] who consider the specific case of a 1P-1P double donor system. They show that the use of a symmetric hyperfine coupling in a 1P-1P or the recently discovered electrically induced spin–orbit coupling [33], allows for strong coupling of a phosphorus-doped silicon qubit to a superconducting cavity (simulated using finite-element modelling). This chapter, together with the work on spin cavity coupling by Osika *et al.*, highlights multiple routes for achieving two-qubit couplings between Si:P qubits via superconducting microwave resonators. Furthermore, we show that a fully electrical initialisation and readout of the all-epitaxial qubit is possible, including a pathway for initialisation of the nuclear spin without the need for nuclear magnetic resonance. In summary, we show in this chapter that the proposed donor-based EDSR qubit allows fast and high fidelity qubit driving, as well as long-distance electrical coupling via superconducting cavities, with scalable all-electrical initialisation. These properties make the qubit an attractive candidate for large-scale universal quantum computation. In a final section of this chapter, we propose a large-scale quantum-computing architecture based on the described qubit that will be compatible with the surface-code-error correction algorithm.

4.2 Donor-based flopping-mode qubits

A generic energy-level spectrum for all flopping-mode EDSR qubits is shown in Fig. 4.1d). The spectrum describes a single electron near the degeneracy point of two different charge states as a function of the detuning between them, ϵ (at $\epsilon = 0$ the charge states are equal in energy). The charge states have a tunnel coupling, t_c and the electron-spin states are split by the Zeeman interaction, $E_z = \gamma_e B_0$ in a static magnetic field, B_0, where γ_e is the electron gyromagnetic ratio. The system is described by the spin of the single electron and the bonding/anti-bonding charge states ($|+\rangle = (|L\rangle + |R\rangle)/\sqrt{2}$ and $|-\rangle = (|L\rangle - |R\rangle)/\sqrt{2}$ where $|L\rangle$ and $|R\rangle$ are the left and right QD orbitals, respectively) resulting in a set of four basis states $\{|\downarrow -\rangle, |\uparrow -\rangle, |\downarrow +\rangle, |\uparrow +\rangle\}$ corresponding to the red, green, blue, and yellow states in Fig. 4.1d). The spin–charge coupling is maximised when the charge ground state $|\uparrow -\rangle$ (green) hybridises with the charge excited state $|\downarrow +\rangle$ (blue), which at $\epsilon = 0$ occurs when $E_z \approx 2t_c$ where the spin and charge qubits are effectively

degenerate (see Fig. 4.1d)). In donor-based systems these electron spin states are split due to the hyperfine interaction of the electron with the quantised nuclear-spin states. Fig. 4.1e) compares the energy levels involved for the donor–QD, QD–QD and donor–donor implementations at $\epsilon = 0$. The QD–QD system is comprised of only charge and electron spin states which is the simplest implementation of the flopping mode qubit. The presence of nuclear spins in donor systems increases the number of states by a factor of 2^n where n is the number donors (the donor–QD flopping-mode qubit has 8 combined electron, nuclear and charge states and our proposal for a 2P-1P system has 32 such states, see Fig. 4.1e)). For operation of the donor-based EDSR qubit the electron and nuclear spins must be anti-parallel, $|\Uparrow\downarrow\rangle$ or $|\Downarrow\uparrow\rangle$ to allow for the flip-flop transition. The presence of the hyperfine interaction of the electron with the nuclear spins in the donor-based EDSR proposal means that the qubit does not require any additional micromagnets to generate a spin–charge coupling. This is a significant positive since it can reduce the qubit footprint and also because the longitudinal magnetic gradient produced by micromagnets can allow charge noise to couple to the qubit and generate errors [20]. However, it is important to now manage any unwanted nuclear-spin flip-flop transitions to avoid leakage out of the computational basis. We will show that the added leakage pathways from the nuclear spins can be largely controlled through Gaussian pulse shaping, and error rates on the order of 10^{-4} can be reached. In the long term this can probably be improved further by using pulse-shaping techniques such as derivative reduction by adiabatic gates (DRAG [34]).

Minimising the longitudinal magnetic-field gradient $\Delta\Omega_\parallel$ parallel to B_0 reduces the chance of dephasing the qubit. The longitudinal-magnetic-field gradient arises from either the stray field of the micromagnet [20, 35] or from the hyperfine interaction between the electron and nuclear spins [29]. The hyperfine interaction takes the form $A(s_x i_x + s_y i_y + s_z i_z)$ in the Hamiltonian, where s_i (i_i) is the electron (nuclear) spin operator. The hyperfine interaction is isotropic, and therefore —irrespective of the magnetic field orientation— there will always be some hyperfine component parallel to the external magnetic field resulting in an energy gradient $\Delta\Omega_\parallel$ (with respect to detuning). Since charge noise couples to the qubit via charge detuning, the smaller this gradient, the flatter the qubit energy as a function of detuning, and the lower the charge-noise-induced dephasing during qubit operation.

Figure 4.1 f) shows the resultant qubit dephasing rate calculated using the model in the previous chapter as a function of tunnel coupling at $\epsilon = 0$ (where the qubit drive is performed) for two values of $\Delta\Omega_\parallel = \Delta\Omega_\perp/100$ MHz (small $\Delta\Omega_\parallel$)

and $\Delta\Omega_{\parallel} = \Delta\Omega_{\perp}$ MHz (large $\Delta\Omega_{\parallel}$). We can see the qubit dephasing rate remains smaller over a wider range of tunnel couplings for small $\Delta\Omega_{\parallel}$ compared to large $\Delta\Omega_{\parallel}$ indicating that the qubit performs better when $\Delta\Omega_{\parallel}$ is minimised. In general, flopping-mode qubits favour large $\Delta\Omega_{\perp}$ (qubit driving) and small $\Delta\Omega_{\parallel}$ (qubit dephasing). Figure 4.1g) finally compares the physical parameters that would be expected for the three different flopping-mode EDSR qubit implementations. The QD–QD implementation obtains $\Delta\Omega_{\perp}$ of the order of 900 MHz allowing for fast qubit operations; however, $\Delta\Omega_{\parallel} \sim 15 - 80$ MHz is also relatively high leading to faster qubit dephasing. The donor–QD and donor–donor qubits both have similar $\Delta\Omega_{\perp} \sim 100$ MHz values due to the similar hyperfine interaction strengths from the phosphorus donor. However, by minimising the hyperfine interaction on the multi-donor QD instead of the difference in g-factors, we can achieve $\Delta\Omega_{\parallel} \sim 0$ MHz for the donor–donor EDSR qubit, smaller than other flopping-mode qubits. At the same time the donor–donor implementation operates away from interfaces that lead to charge noise and do not require additional micromagnets which can also induce charge noise [20]. In the next sections we theoretically investigate the fidelity of single-qubit gates and microwave cavity coupling for two-qubit gates. In particular, we focus on the benefits of using two different size donor QDs (2P-1P) for flopping-mode EDSR to maximise $\Delta\Omega_{\perp}$ and minimise $\Delta\Omega_{\parallel}$ by controlling the nuclear spins and the electron shell filling on both donor-based QDs.

4.2.1 Nuclear spin states in the 2P1P all-epitaxial flopping-mode qubit

The qubit proposed here utilises flopping-mode EDSR to electrically drive the electron–nuclear flip-flop transition where the two charge sites are defined by donor-based QDs. The Hamiltonian for a single electron shared by two tunnel-coupled donor-based QDs spaced approximately 10 - 15 nm apart with N_L donors in the left QD and N_R donors in the right QD is given by,

$$H = H_{\text{Zeeman}} + H_{\text{Charge}} + H_{\text{Hyperfine}}. \tag{4.2.1}$$

The first term $H_{\text{Zeeman}} = \gamma_e B_0 s_z + \gamma_n B_0 \sum i_z$ in Eq. 4.2.1 is the Zeeman term for both the electron ($\gamma_e \approx 27.97$ GHz, the electron gyromagnetic ratio) and nuclear spins ($\gamma_n \approx -17.41$ MHz, the nuclear gyromagnetic ratio). The second term in Eq. 4.2.1 H_{Charge} describes the tunnel coupling, t_c and detuning, ϵ between the charge states of the donors that have an excess electron on one of the QDs $(2n_l, 2n_r + 1) \leftrightarrow$

$(2n_l+1, 2n_r)$. Finally $H_{\text{Hyperfine}}$ in Eq. 4.2.1 represents the detuning dependent contact hyperfine interaction (A_L and A_R for the left and right QDs) of the outermost electron spin to each of the $N_L + N_R$ phosphorus nuclear spins. The Hamiltonian Eq. 4.2.1 is a model Hamiltonian that is agnostic to the shape of the electron wavefunction which depends on the exact donor configuration and the electric fields within the device [29]. The effect of the donor configuration and the electric field is captured by the free model parameters ϵ, t_c, A_L, A_R, γ_e and γ_n. The model of Eq. 4.2.1 has been shown by Tosi *et al.* to reproduce atomistic tight binding simulations which precisely model the electron wavefunction on the donor [18].

In principle, each QD can be formed by any number of phosphorus donors. Here we investigate the specific case $N_L = 2$ and $N_R = 1$, that is, the 2P-1P system (see Fig. 4.2a) for the energy level diagram at $\epsilon = 0$). The qubit states are defined as $|0\rangle \approx |\Downarrow\Uparrow\Uparrow\downarrow -\rangle$ and $|1\rangle \approx |\Downarrow\Uparrow\Downarrow\uparrow -\rangle$ and a transition between the two states corresponds to a flip-flop of the electron spin with the nuclear spin on the right donor QD. The nuclear spin states on the left donor QD remain unchanged during the transition. The charge state $|-\rangle$ is defined by the two quantum-dot orbitals associated with the $(3,0) \leftrightarrow (2,1)$ charge transition.

The two quantum-dot orbital $|-\rangle$ is expected to be well defined and non-degenerate. Indeed the $|-\rangle$ state is the bonding state of the 1P1e orbital in the right donor QD, that is known to be non-degenerate [37], and the 2P3e orbital in the left donor QD, that is not expected to be degenerate either due to the large extent of the wavefunction. In particular the T_2 state degeneracy that can be present for the 2P1e orbital does not necessarily carry over to the 2P3e case, because the wavefunction is spread much more broadly [29], so that the 2P3e wavefunction cannot be described by a combination of the 2P1e orbitals that can be degenerate, but needs to be described as a linear combination of many $1s$, $2s$, $3s$, $4s$ ... orbitals, which in general should be non-degenerate [1].

To compare the donor–donor flopping-mode qubit to the QD–QD and donor–QD implementations, we approximate the Hamiltonian of Eq. 4.2.1 using a Schrieffer–Wolff transformation to a general flopping-mode Hamiltonian in terms of the transverse ($\Delta\Omega_\perp$) and longitudinal ($\Delta\Omega_\parallel$) gradients (see Sect. C.1.2),

$$H = \frac{\Omega_z}{2}\sigma_z + \epsilon\tau_z + t_c\tau_x + \Big(\frac{\Delta\Omega_\parallel}{4}\sigma_z + \frac{\Delta\Omega_\perp}{4}\sigma_x\Big)\tau_z. \tag{4.2.2}$$

Here σ_i (τ_i) are the Pauli-operators for the combined electron-nuclear spin (charge)

[1] Private communication with Prof. Rajib Rahman

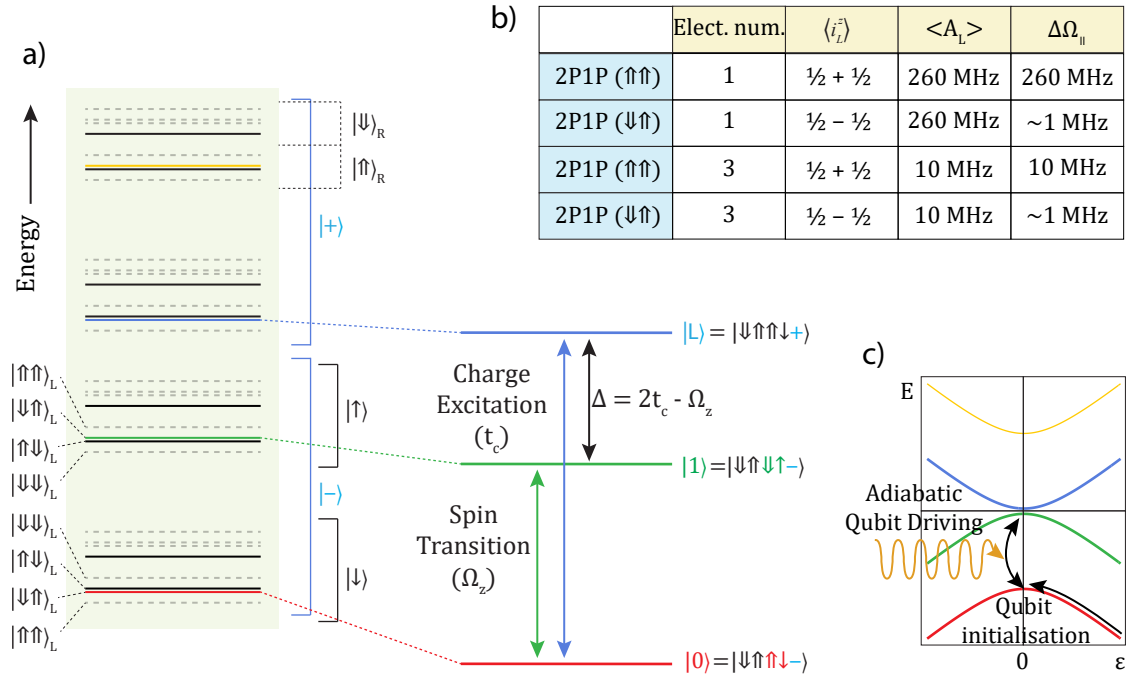

	Elect. num.	$\langle i_L^z \rangle$	$<A_L>$	$\Delta\Omega_{\|\|}$
2P1P (⇑⇑)	1	½ + ½	260 MHz	260 MHz
2P1P (⇓⇑)	1	½ − ½	260 MHz	~1 MHz
2P1P (⇑⇑)	3	½ + ½	10 MHz	10 MHz
2P1P (⇓⇑)	3	½ − ½	10 MHz	~1 MHz

Figure 4.2: **Operation of the donor–donor flopping-mode qubit.** Due to spin conservation, only a subset of the nuclear spin states in the hyperfine manifold in **a)** need to be considered for qubit operation. For a 2P-1P donor–donor device, the qubit states are displayed in red and green, the lowest (highest) excited charge state in blue (yellow), the nuclear spin leakage states where the total spin of the system is conserved are shown in black. The leakage probability of the nuclear-spin states can be minimised through pulse design. The states not involved in the qubit operation (other nuclear spin states with no leakage pathway) are shown as dashed grey lines. **b)** Control of the electron number using electrostatic gates and nuclear-spin orientation ($\langle i_L^z \rangle$) using NMR allows us to tune the hyperfine coupling, $\langle A_L \rangle$ and longitudinal-magnetic-field gradient $\Delta\Omega_{\|}$. The value $\langle A_L \rangle \approx 260\,\text{MHz}$ with one electron are based on experimental measurements [36] while that with a three-electron occupation ($\langle A_L \rangle \approx 10\,\text{MHz}$) is based on numerical tight binding simulations by Wang *et al.* [29]. **c)** Leakage out of the qubit subspace needs to be considered both when initialising the qubit for control and when driving the qubit at $\epsilon = 0$.

degree of freedom. The first term, Ω_z is the energy of the combined electron-nuclear spin state (which depends on the exact value of the left and right donor hyperfine interaction, A_L and A_R),

$$\Omega_z = \sqrt{\Omega_s^2 + A_R^2/4}, \tag{4.2.3}$$

where $\Omega_s = (\gamma_e + \gamma_n)B_0 + \sum_k^{N_L} A_{L,k} \left\langle i_{L,k}^z \right\rangle /2$ is the Zeeman energy with a correction due to the hyperfine interaction of the electron with the nuclear spins in the left QD and $\left\langle i_{L,k}^z \right\rangle$ is the expectation value of the z-projection of the k-th nuclear spin on the left QD. The charge part of the Hamiltonian is described by the second (detuning, ϵ) and third (tunnel coupling, t_c) terms of Eq. 4.2.2. The rightmost term in Eq. 4.2.2 corresponds to the charge-dependent hyperfine interaction:

$$\Delta\Omega_{\parallel} = \sum_k^{N_L} A_{L,k} \left\langle i_{L,k}^z \right\rangle \cos\theta - A_R \sin\theta, \tag{4.2.4}$$

$$\Delta\Omega_{\perp} = A_R \cos\theta - \sum_k^{N_L} A_{L,k} \left\langle i_{L,k}^z \right\rangle \sin\theta, \tag{4.2.5}$$

where $\tan\theta = A_R/(2\Omega_s)$. Since Ω_s is typically optimised to be > 5 GHz, is generally much greater than $A_R \approx 100$ MHz [38, 29], $\sin\theta \approx 0$ and $\cos\theta \approx 1$ then $\Delta\Omega_{\parallel} \approx \sum_k^{N_L} A_{L,k} \left\langle i_{L,k}^z \right\rangle$ and $\Delta\Omega_{\perp} \approx A_R$. The value of A_R is that of the well-known hyperfine interaction on a single phosphorus donor and has been experimentally measured to be ≈ 100 MHz [38, 36]. Numerical tight binding simulations used for the 2P hyperfine values A_L reproduce this value [29]. We can control $\Delta\Omega_{\parallel}$ during the fabrication stage by engineering the number of the donor atoms in each QD. Additionally, during qubit operation $\Delta\Omega_{\parallel}$ can be optimised by controlling the nuclear spins on the left QD using nuclear magnetic resonance (NMR) [39], or by dynamic nuclear polarisation [40], and additionally by controlling the electron-shell filling in the left QD. Figure 4.2b) shows a Table of different nuclear and electron spin configurations determining the magnitude of the hyperfine-coupling strengths $A_{L,k}$ and their effect on the value of $\Delta\Omega_{\parallel}$. The values are based on experimental measurement of the 2P hyperfine interactions with a single electron [36] and numerical tight binding simulation of the 2P hyperfine interaction with one and three electrons by Wang *et al.* [29]. Wang *et al.* have predicted that the larger the QD, the larger $\sum A_{L,k}$ since the phosphorus donors create a stronger confinement potential for the electron which increases the contact hyperfine strength. This is confirmed by recent experimental measurements of the hyperfine interactions on 2P QDs (see ref. [36] as well the measurements by this author in Chapter 5). Wang *et al.* predicted that

the hyperfine interaction strength can in turn be lowered on multi-donor QDs by adding inactive pairs of electron spins to the QD. In our proposal this is achieved by increasing the total electron number on the left quantum dot from 1 to 3. The two innermost electrons then form an inactive singlet state that screens the outermost electron defining the qubit from the nuclear potential of the donors. This shielding was confirmed by tight binding simulations for the specific case of the 2P QD by Wang *et al.* [29] which predict a decrease in the hyperfine interaction to 10 MHz with three electrons [2] . This decrease in $\sum A_{L,k}$ will result in longer dephasing times for the proposed qubit. Furthermore, the presence of more than one donor in the left QD allows another reduction of the longitudinal gradient $\Delta\Omega_{\|}$ by controlling the nuclear spin states. From Fig. 4.2b) it follows that by using antiparallel nuclear-spin states ($\langle i^z_{L,1}\rangle = 1/2$ and $\langle i^z_{L,2}\rangle = -1/2$) on a 2P QD the value of $\Delta\Omega_{\|}$ can be lowered to almost zero. This ability to control the number of electrons and nuclear spin states on the left QD motivates the operation of the qubit using $|0\rangle \approx |\Downarrow\Uparrow\Uparrow\downarrow -\rangle$ and $|1\rangle \approx |\Downarrow\Uparrow\Downarrow\uparrow -\rangle$ at the $(3,0) \leftrightarrow (2,1)$ transition. Note that the nuclear-spin states $|\Uparrow\Downarrow\rangle$ and $|\Downarrow\Downarrow\rangle$ for the 2P are equivalent to $|\Downarrow\Uparrow\rangle$ and $|\Uparrow\Uparrow\rangle$, respectively and so are absent from Fig. 4.2b).

Additional nuclear spin states can potentially however create more leakage pathways out of the computational basis. Here we show that these additional nuclear spin states can act as a resource and are not a limiting factor for the qubit operation. In particular, there are two crucial steps in the qubit operation where leakage from the computational basis can occur: during initialisation of the qubit and during driving of single-qubit gates (see Fig. 4.2c)). In the following section, we will first describe the model used to estimate qubit errors during electrical driving, and then investigate the effect of the nuclear spin states during initialisation and electrical driving.

4.3 Modelling errors during driving of the flopping-mode qubit

During electric driving of the qubit, errors in the operation of the qubit are introduced by dephasing, T_1 relaxation and state leakage. Our error model detailed in the previous chapter, includes dephasing of the qubit due to electric field noise due to electrostatic gates and charge defects, magnetic-field noise from spinful nuclear

[2]The wave function of the third electron on a 2P dot is calculated using a Hartree self-consistent field solution by Wang *et al.* and depicted in fig. 5 a) of ref. [29]

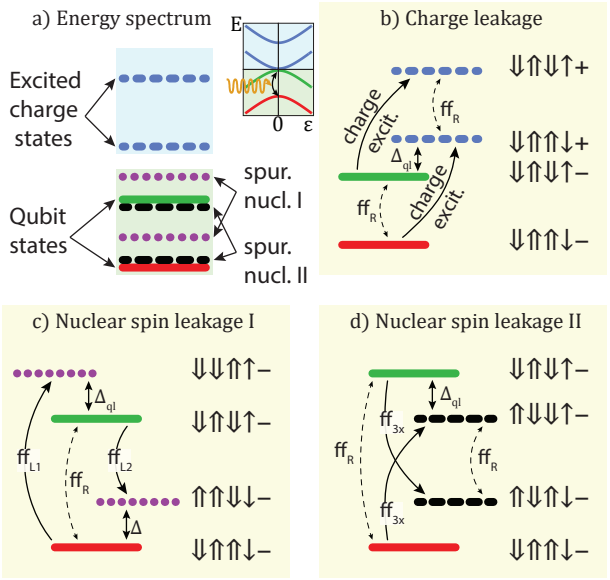

Figure 4.3: **Dominant leakage pathways for the 2P1P (3e ⇓⇑) system. a)** Energy level diagram at $\epsilon = 0$ for a 2P1P donor-based flopping mode qubit. The blue region corresponds to excited charge (leakage) states. The dotted and dashed black lines in the green (qubit subspace) correspond to different nuclear spin states that can also be occupied during qubit operation which leads to errors. **b)** The possible charge leakage pathways of the qubit into the excited charge state of the double QD system with ff_R corresponding to the qubit frequency and Δ_{ql} the detuning between the qubit and leakage states. **c)** Nuclear spin leakage I occurs when the one of the nuclear spins undergoes an unwanted flip-flop transition with ff_{L1} (ff_{L2}) corresponding to a flip **b)** of the first (second) nuclear spin on the left QD. **d)** Nuclear spin leakage II occurs when there is a simultaneous flip-flop of the electron spin with all three nuclear spins in the system ($ff_{3\times}$). The coupling of these state to the qubit states are low but are close in energy resulting in a possible leakage pathway.

isotopes, T_1 relaxation of the charge qubit, and leakage out of the computational basis of the qubit via nuclear spin transitions. Pure spin relaxation is not included as the spin-relaxation rates are orders of magnitude lower than the charge-related error sources [2] ($\sim 1\,\mathrm{Hz}$). Of all the error sources, only nuclear-spin-leakage error was not covered in the previous chapter. In Sect. 4.3.1 we describe the model developed to capture such nuclear spin leakage errors. A detailed description of the model used to capture the other error sources is contained in Sect. 3.3 of the Chapter 3.

4.3.1 Modelling leakage during electric driving of the spin

For the 2P1P qubit, the qubit states can potentially leak to the other states of the same magnetisation is shown schematically in Fig. 4.3. Leakage into any of the excited-charge-state branches (light blue square in Fig. 4.3 a) and in the inset) is dominated by the direct charge transition. That is, the transitions connect the

qubit states $|S_{0/1}-\rangle$ (in red and green in Fig. 4.3) to the excited charge states $|S_{0/1}+\rangle$ (blue dotted lines in Fig. 4.3), where $S_{0/1}$ is the electron and nuclear spin configuration of the qubit ground and excited states respectively that are unchanged by the transition. All other transitions to the excited-charge branches (blue dotted lines) involve not only charge but also spin transitions and are only possible through hybridisation with the charge qubit. The four level systems composed by these four states $|S_{0/1}-/+\rangle$ is displayed in Fig. 4.3 b). In the following we refer to leakage within this four level system as the "charge leakage pathway".

The EDSR qubit can leak into other spin states in the ground-charge-state branch (light green square in Fig. 4.3 a) and in the inset), depicted by black dotted and dashed lines in Fig. 4.3. These spin leakage states can be broken into two more pathways that we will refer to as: "nuclear spin leakage pathways". The first nuclear spin leakage pathway corresponds to a flip-flop of the electron with one of the nuclear spin of the left QD instead of the right dot (see Fig. 4.3 c) and the dotted purple lines). The ground (excited) qubit state $|\Downarrow\Uparrow\Uparrow\downarrow -\rangle$ ($|\Downarrow\Uparrow\Downarrow\uparrow -\rangle$) can leak to the spin state $|\Downarrow\Downarrow\Uparrow\uparrow -\rangle$ ($|\Uparrow\Uparrow\Downarrow\downarrow -\rangle$) via a flip-flop transition, ff_{L2} (ff_{L1}) with the second (first) nuclear spin on the left QD. This leakage pathway will be referred to as "type I nuclear spin leakage". The second nuclear spin leakage pathway in the 2P1P donor–donor qubit corresponds to leakage from the qubit states into the near degenerate levels $|\Uparrow\Downarrow\Downarrow\uparrow -\rangle$ and $|\Uparrow\Downarrow\Uparrow\downarrow -\rangle$ via three simultaneous electron–nuclear flip-flop transitions with all the nuclear spins in the system ($\mathrm{ff}_{3\times}$). The coupling term corresponding to the combined nuclear spin flips is very weak as it is a higher-order process. However, the states are almost degenerate with the qubit state so the effective coupling can be quite strong and needs to be considered as a potential source of error. This second pathway, the "type II nuclear spin leakage" pathway is displayed in figure 4.3 d) with the leakage states corresponding to the black dashed lines. We model leakage within each of these three pathways as a different four-level Hamiltonian containing the qubit states as well as the two corresponding leakage states accessible from the qubit $|0\rangle$ and $|1\rangle$ states. The three different leakage pathways can be considered independently of each other, allowing for the dynamics to be modelled separately by a four-level Hamiltonian and the total leakage error can be combined afterwards. This approximation is motivated by the fact that one leakage pathway generally dominates all others by several orders of magnitude at any given qubit parameter region.

To model the leakage pathways into the leakage charge and nuclear spin states we use the model described in Sect. 3.3.2. Here, Δ_{ql} corresponds to the different

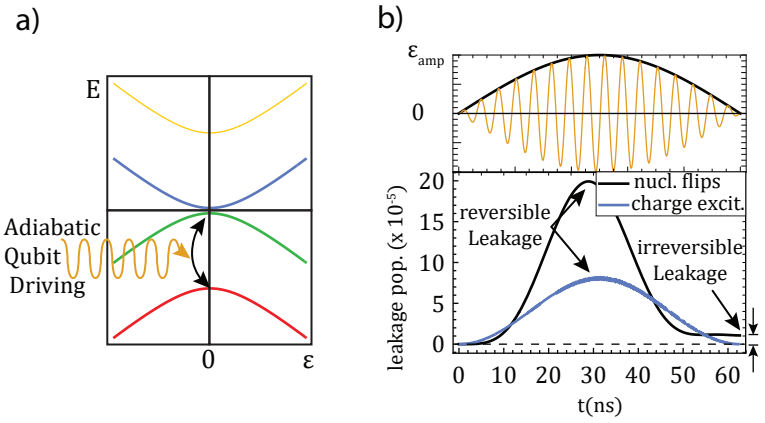

Figure 4.4: **Adiabatic electric driving of the flopping-mode qubit. a)** Leakage out of the qubit subspace needs to be considered when driving the qubit at $\epsilon = 0$. **b):** Driving of the qubit states using microwave pulses allows full control of the qubit states. Gaussian pulse shaping allows for the reversal of state leakage during the qubit operation (top). We show the charge (blue) and nuclear spin (black) leakage probabilities during the $\pi/2-X$ Gaussian pulse for the donor–donor qubit using the optimised parameters for this device (see Fig. 4.7), drive amplitude of $\epsilon_{\text{amp}} = 0.9\,\text{GHz}$ at $B = 0.23\,\text{T}$, and $t_c = 5.6\,\text{GHz}$ (bottom). The irreversible leakage for the the nuclear spin states is $\sim 1 \times 10^{-5}$ well below the 1% error required for fault tolerance due to the adiabatic drive pulse.

energy separations between the qubit and leakage states and Ω_l (Ω_r) is the coupling between the qubit-leakage (qubit-qubit) states. The nuclear leakage error, e_{leak} is captured by the probability of occupation of the two nuclear leakage states $|2\rangle$ and $|3\rangle$, p_{leak} within each leakage channel at the end of the $\pi/2$ pulse:

$$e_{\text{leak}} = p_{\text{leak}} = \alpha_{\text{leak}} \lambda^2 \frac{\Omega_r^4}{\Delta_{ql}^4}. \tag{4.3.1}$$

The magnitude of the leakage error is well described by the ratio $\lambda := \Omega_l/\Omega_r$ of the leakage and qubit-coupling strengths, and by the ratio Ω_r/Δ_{ql} of the qubit-coupling strength over the energy gap to the nearest leakage state.

For a small ratio $\lambda = 1/100$ realistic for both the charge and nuclear spin leakage pathways of the donor-based flopping mode qubit since the other transitions will be detuned significantly from the qubit transition (that is, the nuclear spins will have different hyperfine interaction strengths with the electron spin), the leakage error is smaller than 10^{-4}, even for strong driving of the qubit (see Fig. 4.5).

For the nuclear-leakage pathways, the energy gap to the leakage states is typically between 1 MHz to a few hundred MHz, depending on the system and thus comparable to the Rabi frequency. Leakage to these other nuclear spin states can therefore take place in both the weak and the strong driving regime. The coupling

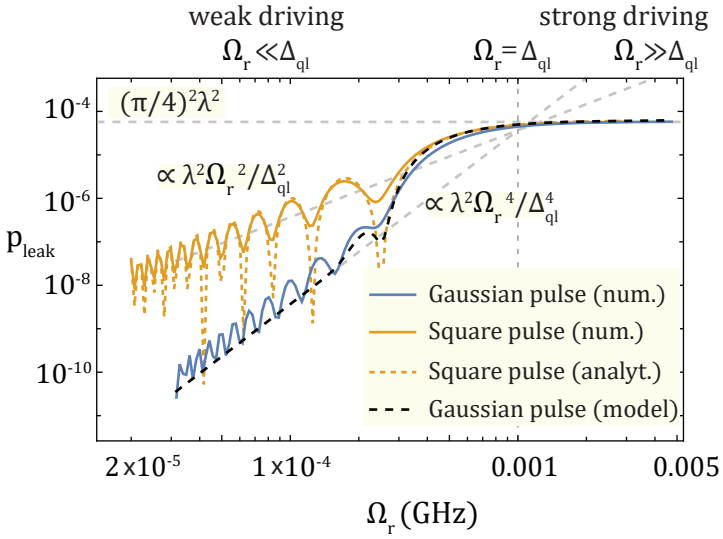

Figure 4.5: **Population p_{leak} in the leakage states at the end of a $\pi/2$ X-gate,** for different pulse shapes, and as a function of qubit drive amplitude and $\lambda = \Omega_l/\Omega_r << 1$. The solid curves in a) and b) display the leakage population for a Gaussian and a square pulse shape, in blue and orange respectively. The black dotted line displays an analytical model for the leakage population of the Gaussian pulse shape. We used typical values for a 2P1P flopping mode qubit with $\lambda = 1/100$ and $\Delta_{ql} = 1\,\mathrm{MHz}$.

to the nuclear-leakage states can be engineered to be much weaker than the qubit-coupling (regime $\lambda \ll 1$). As a consequence the errors can be negligible even in the strong driving regime, as described by Eq. 3.3.12 (see also Sect. 4.4.3).

The analytical model based on Eq. 3.3.12 captures the leakage behaviour in both the weak and strong-driving regime fits the numerically simulated leakage population for the Gaussian-pulse shape very well (black dotted line in figure 4.5). The model combines the power-law trend of the Gaussian-pulse shape at low drive powers (Eq. 3.3.11) and the analytical formula for the square-pulse shape at high power (orange dotted line in Fig. 4.5). For this purpose, we use two fermi distributions $f(x,T) = 1/(1+\exp(-x/T))$ with opposite polarities that switches between the asymptotic trend $p^0_{\mathrm{leak}} = \alpha_{\mathrm{leak}}\lambda^2\frac{\Omega_r^4}{\Delta_{ql}^4}$ at low powers to the exact analytical leakage behaviour of the square pulse at high powers $p^1_{\mathrm{leak}} = \lambda^2\frac{\Omega_r^2}{\Delta_{ql}^2+\lambda^2\Omega_r^2}\sin\left(\frac{\pi\sqrt{\Delta^2+\lambda^2\Omega_r^2}}{4\Omega_r}\right)^2$. The final leakage model is then:

$$f(\Delta - y, T)p^0_{\mathrm{leak}} + f(-(\Delta - y), T)p^1_{\mathrm{leak}}, \tag{4.3.2}$$

were the transition point between the two regimes is estimated at $y = \Omega_r\sqrt{14-\lambda^2}$, and the heuristic width of $T = y/50$ is used for the Fermi distributions.

All leakage errors discussed so far are independent of the initial qubit state,

due to the naturally symmetric coupling elements of the qubit states to the leakage states, so that no averaging of the leakage error over all possible qubit start-sates is necessary.

In summary, in this section we have described the three pathways that can lead to leakage errors for the 2P1P all-epitaxial flopping-mode qubit. The Leakage probability can be described by a four-level Hamiltonian and determined by the ratio of leakage to qubit coupling as well as the ratio of qubit coupling to the energy gap to the leakage state. The first leakage pathway corresponds to direct excitation of the charge state found in all flopping-mode qubits. It can lead to leakage error due to the non-reversed excitation of the charge (that is, non-adiabatic transitions) as well as through relaxation of the temporary excited-charge-state proportion to the ground qubit state. The remaining two nuclear spin leakage pathways correspond to undesired flip-flops of the electron spin with the nuclear spins in the QD not used for the qubit transitions. The charge leakage errors can be minimised by using a Gaussian pulse shape that allows reversing most of the leakage population excited during the pulse.

4.4 A scalable, electrically controlled spin-qubit with low errors

Scaling up universal quantum processors to larger sizes can be facilitated by using all-electrical high-fidelity qubits that can be coupled over large distances (see Chapter 2). In this section we will show that the all-epitaxial flopping-mode qubit can fulfil these requirements by reaching low dephasing and leakage errors and strong coupling to a superconducting cavity through hyperfine engineering. This hyperfine engineering relies on the control of inner-shell electrons on the donor QDs and the control of the nuclear-spin states within the QDs. Carefully engineered, these possibly near-degenerate nuclear-spin states are neither limiting the speed nor increasing the error of qubit operations, be it during initialisation or electrical driving[3].

[3]During optimised qubit operation, the nuclear spins in the left quantum dot remain stationary and can therefore be considered as being part of the qubit's environment. The engineering of the nuclear spins and electron filling on the left quantum dot can therefore be seen as manipulations of the qubit's environment.

4.4.1 Fast high-fidelity orbital-state transfer

First, we will describe and examine the initialisation process for potential charge and nuclear spin state leakage. Leakage to the excited charge states is present in all flopping-mode qubits due to the hybridisation of charge and spin. For $|\epsilon| \gg t_c$ there is no charge-like component of the qubit and the ground state can be initialised simply by loading a $|\downarrow\rangle$ electron from a nearby electron reservoir [23]. The nuclear spins can also be initialised via NMR [39], dynamic nuclear polarisation [41], or even using EDSR (see Sect. 4.4.5) to place the nuclear spin into the $|\Uparrow\rangle$ state. Next, the detuning is ramped to $\epsilon = 0$ to initialise the $|0\rangle$ qubit state, see Fig. 4.6 b). During the ramp, the qubit can leak out of the computational basis via charge excitation into the excited charge state or through unwanted nuclear spin flips. In Fig. 4.6 b) we show the simulated leakage probability of a donor-based flopping-mode qubit for both leakage pathways during the initialisation ramp as a function of ramp time with $t_c = 5.6$ GHz, $\Delta A_L = |A_{L,1} - A_{L,2}| = 1$ MHz and $B_0 = 0.23$ T chosen as realistic values obtainable in a donor-based flopping mode qubit. Regardless of the initialisation pulse time, t_{pulse} the leakage into the excited charge states (blue line in Fig. 4.6 b)) is the dominant pathway compared to the nuclear-spin leakage (black line in Fig. 4.6 b)). The nuclear-spin leakage is much lower than charge leakage because the probability of a flip-flop transition away from $\epsilon = 0$ is small. This is because the hyperfine strength changes very slowly with detuning compared to the charge states and the nuclear-spin leakage states are only weakly coupled to the qubit states since the hyperfine coupling terms are small for the other nuclear spin transitions. The charge-leakage mechanism exists for all flopping-mode EDSR based qubits due to the non-adiabaticity of the initialisation pulse. By ramping slowly enough using electrostatic gates however, we can initialise the qubit at $\epsilon = 0$ with a leakage error of 10^{-3} for a $t_{\text{pulse}} = 4\,\text{ns}$ ramp. The nuclear spin leakage does not depend heavily on the pulse time and remains well below the charge leakage with an error of $\sim 2 \times 10^{-5}$ obtained via numerical simulations. Therefore, the nuclear-spin-state leakage is not a limiting factor in the initialisation of the qubit.

The adiabatic orbital state transfer displayed in Fig. 4.6 b) is calculated numerically for a 2P-1P device operated at the (2,1) $\leftrightarrow$ (3,0) electron state with the nuclear spins on the left QD initialised in antiparallel spin states at a magnetic field of $B = 0.3\,\text{T}$ and a tunnel coupling of $t_c = 5.9\,\text{GHz}$. We chose a difference in the hyperfine coupling to the two nuclei in the left dot of $\Delta A_L = 1\,\text{MHz}$ based on the measured couplings from a 2P QD where there was no measurable difference between the hyperfine values of each nuclear spin [30]. We start the adiabatic ramp

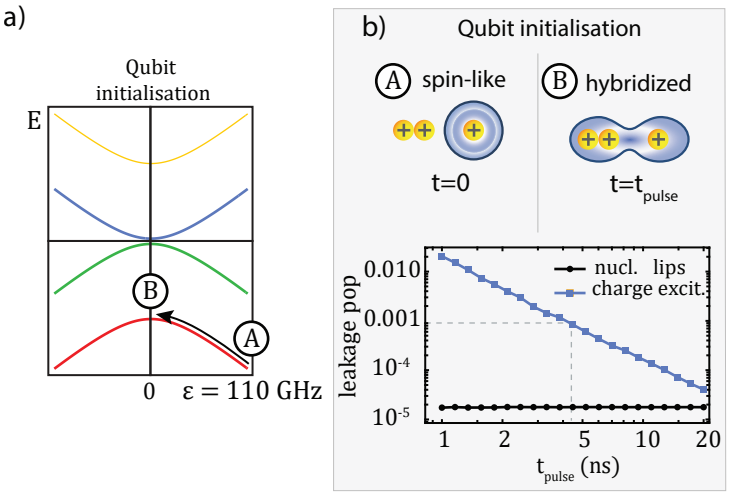

Figure 4.6: **Orbital state transfer of the flopping-mode qubit**. **a)** Qubit initialisation pulse scheme. The qubit detuning is adiabatically ramped to $\epsilon = 0$ from some positive detuning where the qubit is spin-like with long coherence times. **b)** Initialisation of the qubit ground state for a 2P-1P donor–donor qubit at the (3,0) $\leftrightarrow$ (2,1) electron configuration from the localised electron state (at $\epsilon = 110\,\mathrm{GHz}$) to the hybridised state (at $\epsilon = 0$), using a variable pulse time t_{pulse}, for $B = 0.3\,\mathrm{T}$, $t_c = 5.9\,\mathrm{GHz}$. The qubit population that leaks into the excited charge states (blue line) and other nuclear-spin states (black lines) at the end of the transfer are displayed as a function of the pulse time.

at $\epsilon(t = 0) = 110\,\mathrm{GHz}$ (point A in Fig. 4.6a)) away from the charge-degeneracy point ($\epsilon = 0$) where the spin-like state only has a 0.1% of charge component and qubit coherence times are approximately those of a single-electron spin. At this position A, we initialise the qubit into an even superposition of the two qubit states, $|0\rangle \equiv |\Downarrow\Uparrow\Uparrow\downarrow -\rangle$ and $|1\rangle \equiv |\Downarrow\Uparrow\Downarrow\uparrow -\rangle$. We then perform a numerical time evolution of that state under the influence of a linear detuning pulse ending at $\epsilon = 0$ where the qubit can be driven electrically. At the end of the pulse of duration t_p, some of the qubit population (blue line in Fig. 4.6 b)) has leaked out of the qubit subspace. The leakage probability into the excited-charge states is calculated by summing the final-state population in the excited-charge states $|+\rangle$, whereas the leakage probability due to nuclear-spin flips (black line in Fig. 4.6 b)) in the left QD is estimated by summing the final-state population in the nuclear-spin states in the ground charge states $|-\rangle$ (excluding the qubit states). A time- and state-resolved analysis of the orbital state transfer can be found in Sect. C.5. In particular, we show that direct charge excitation is the dominant charge-leakage pathway, and that, as expected, nuclear-spin leakage is dominated by transitions between the near degenerate states separated by the engineered hyperfine difference $\Delta A_L = 1\,\mathrm{MHz}$ through a nuclear spin leakage II process.

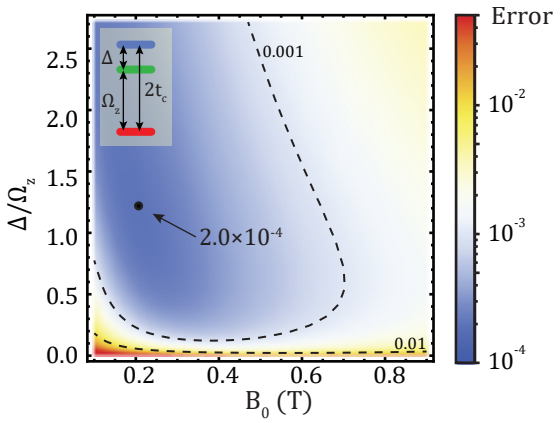

Figure 4.7: $\pi/2$**-gate error of the all-epitaxial flopping-mode EDSR donor-based qubit.** Qubit error with $\Delta A_L = |A_{L,1} - A_{L,2}| = 1$ MHz as a function of the external magnetic fields B_0 and spin–charge detuning $\frac{\Delta}{\Omega_z} = \frac{2t_c - \Omega_z}{\Omega_z}$ at $\epsilon = 0$. The gate error remains below 10^{-3} over a magnetic field range of 0.4 T and for Δ/Ω_z values from 0.5 to more than 2.5. The optimal operating point with a minimum error of 2×10^{-4} is shown at the black dot. The inset shows the three-level energy diagram for the qubit with energy, Ω_z, tunnel coupling, t_c and spin–charge detuning, $\Delta = 2t_c - \Omega_z$ (which determines the effective spin–charge coupling strength).

4.4.2 Low-error and robust electric driving of the epitaxial flopping-mode qubit

We now investigate the qubit performance during electrical driving. Figure 4.7 displays the qubit error for a $\pi/2-X$ gate as a function of magnetic field and tunnel coupling including dephasing, relaxation and leakage errors (see Sect. 4.3). The gate error remains low ($< 10^{-3}$) over a wide range of magnetic fields ($\sim 0.1 - 0.5$ T) and for relative changes in the tunnel couplings of more than 300%, corresponding to a tolerance of more than 8 (17) GHz at $B = 0.2\,(0.4)$ T. To-date other flopping-mode qubits have been optimised over a much smaller parameter space, confined to the location of so-called error sweet spots, that restrict the range of magnetic fields and of tunnel couplings that the qubit can be operated at [18, 42]. The wide range of operation in donor-based flopping mode qubits is crucial in a large-scale architecture with a fixed magnetic field where small uncertainties in the tunnel coupling can lead to variation in the qubit performance. The large range of tunnel couplings where the donor–donor qubit can operate means that these small uncertainties will not be detrimental to the overall quantum-computer performance. By optimising the magnetic field and tunnel coupling during fabrication we can achieve a minimum gate error of 2.0×10^{-4} well below the fault-tolerant threshold of the surface code.

Both the low errors and the wide operational parameter space achieved can largely be attributed to the low value of the longitudinal gradient $\Delta\Omega_{\|}$, attainable

using hyperfine engineering. Indeed, the qubit dephasing error is proportional to $\left(\frac{\Delta\Omega_{\parallel}}{\Delta\Omega_{\perp}}\right)^2$ the longitudinal over the transverse energy gradient (see Eq. 3.4.4). By minimising the longitudinal energy gradient $\Delta\Omega_{\parallel} \approx \sum_k^{N_L} A_{L,k} \left\langle i_{L,k}^z \right\rangle = \Delta A_L/2$ using nuclear-spin control, the dephasing error can be reduced. This is important as we do not have to compensate by driving faster rotations, which in turn could increase other types of error, such as the leakage error. In the following section, we will discuss how such nuclear-spin leakage errors can be avoided.

4.4.3 Drive-leakage errors of the flopping-mode qubit

The three nuclear spin in the 2P1P all-epitaxial flopping-mode qubit introduce 28 additional states compared to the implementation without donors. These states can bring about additional leakage pathways and errors. We will now show that using hyperfine-engineering, these additional nuclear-spin leakage errors can largely be minimised, and safely neglected at the optimal qubit operation point. Three types of leakage errors can occur during electric driving of the qubit. The first corresponds to direct charge excitations and is present for all flopping-mode implementations, while the other two are due to the presence of the nuclear spin states in the 2P-1P donor system.

The qubit error is limited by nuclear spin leakage (unwanted nuclear spin flips of the other nuclear spin states not used for qubit transitions) at low spin–charge detunings, $\Delta = 2t_c - \Omega_z$, where dephasing errors are also generally large due strong spin-charge coupling causing charge dephasing (see Fig. 4.8).The optimal operation point of the qubit is situated at large spin–charge detuning (black dot in Fig. 4.7, at $B \approx 0.2\,\mathrm{t}$ and $\Delta/\Omega_z \approx 1.2$) where charge dephasing is limiting the error and excited state charge-relaxation errors are significant (see "charge dephasing (T_1 limited) errors" in Fig. 4.8) and nuclear-spin leakage is negligible. Next, we describe how nuclear spin leakage errors are kept negligible by hyperfine engineering.

Leakage errors are well described by the $\lambda = \Omega_l/\Omega_r$ of the leakage and qubit coupling, and by the ratio Ω_r/Δ of the qubit coupling over the energy gap to the nearest leakage state (see Sect. 4.3.1). The leakage error is not only linked to these two quantities λ and Ω_r/Δ, but also to the microwave pulse envelope $g(t, t_p)$. In superconducting devices, the leakage error was often minimised by adiabatic pulse shapes for example, such as the Gaussian shape considered in the previous section [43]. All $\pi/2$ X-gate simulations used in this chapter use the Gaussian pulse shape described in Eq. 3.3.6 and shown in Fig. 4.4 b). For this Gaussian pulse shape,

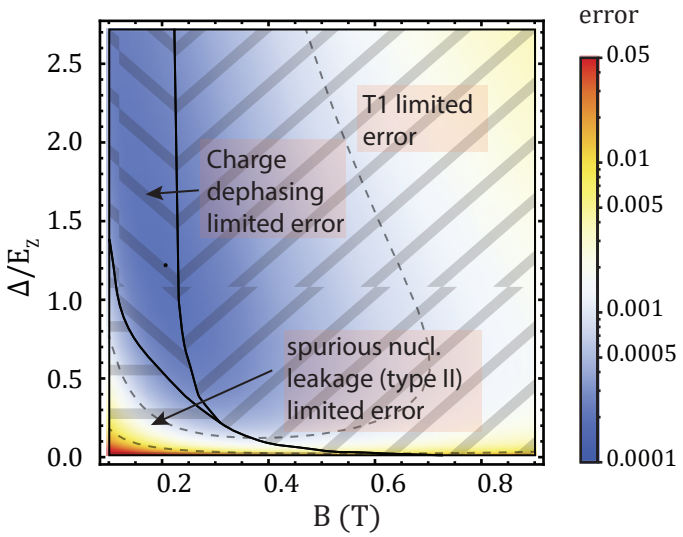

Figure 4.8: **Limiting error sources for the 2P-1P qubit at the (2,1)↔(3,0) transition with an optimised $\Delta A_L = 1\,\mathbf{MHz}$.** Overlaid over the error plot from Fig. 4.7, we show the three regions where different errors sources dominate the total error at the optimal drive amplitude. For high spin–charge detuning Δ/E_z and high magnetic field (top right of the plot), the T_1 error limits the total error. For low magnetic fields ($\lesssim 0.3$ T), charge dephasing mostly dominates the error. Leakage errors are only significant (> 0.001) for small spin–charge detuning ($\lesssim 0.5E_z$) and small magnetic fields ($\lesssim 0.3$ T). In that region, only leakage to the near-degenerate nuclear-spin states is significant.

the leakage error is proportional to $\lambda^2 \left(\frac{\Omega_r}{\Delta}\right)^4$ (see Eq. 3.3.11).[4] To minimise the leakage error, it is critical to minimise the ratio of leakage coupling and qubit coupling (λ) as well as the ratio of qubit coupling and the energy gap (Ω_r/Δ). In the 2P-1P system, the energy gaps and coupling strengths can be tuned by the configuration of the nuclear spins in the respective QDs and by the number of electrons on the QDs, allowing control over the leakage errors.

One straightforward strategy to reduce charge leakage errors is to minimise the electric drive amplitude ϵ_d used to drive qubit rotations. Leakage and dephasing errors display opposite dependences on the drive amplitude. While the leakage errors grow with increasing drive amplitudes, dephasing errors decrease. The leakage error is extremely sensitive to the drive amplitude, as it is proportional to the fourth power of the drive amplitude ($e_{\text{leak}} \propto \epsilon_d^4$ for a Gaussian pulse, see Eq. 3.3.11), so that even small reduction in the electric drive amplitude can result in a large reduction in the leakage error.[5] The flopping-mode qubit charge dephasing error is proportional to ϵ_d^{-2} (see e_z in Eq. 3.4.4), while the error related to charge-noise-induced variations of the Rabi frequency is constant with respect to the electric-drive amplitude (see e_x in Eq. 3.4.4) and sets the lower bound to the charge-noise-induced error. The Rabi frequency noise error bound is reached for a drive amplitude that is proportional to $\frac{\Delta\Omega_\parallel}{\Delta\Omega_\perp}$, the ratio of the energy gradients (see Eq. 3.4.5) up to second-order in charge noise. In general, reducing the longitudinal energy gradient $\Delta\Omega_\parallel$ therefore allows the dephasing errors to reach their minimum before leakage errors become dominant. For the 2P1P flopping-mode qubit, the longitudinal gradient is reduced from a value of 125 MHz to about 0.5 MHz, by initialising the two nuclear spins in the 2P donor QD in opposite directions $\Uparrow/\Downarrow$ and then using the two inner-shell electrons to shield the hyperfine interaction of the third electron spin to the nuclei. By exploiting this we can reduce the leakage error at the optimal dephasing operation point by nine orders of magnitude.

The remaining strategies to reduce leakage error in a 2P1P EDSR qubits relies on minimising the ratios $\lambda = \Omega_l/\Omega_r$ and Ω_r/Δ by engineering the qubit and leakage couplings Ω_r and Ω_l, as well as energy gap Δ within each leakage pathway. Minimising these ratios can be achieved by optimising the magnetic field and spin–charge coupling in the device. We will now briefly introduce how the remaining strategies of minimising λ and maximising the energy gaps can be implemented in the 2P1P device to decrease leakage errors for the two nuclear leakage pathways.

[4] neglecting the Landau–Zenner-type oscillations in the error.

[5] In the weak driving regime, $e_{\text{leak}} \propto \left(\frac{\Omega_r}{\Delta}\right)^4 \propto \epsilon_d^4$, see Eq. 3.3.11.

The first leakage pathway in the proposed donor–donor qubit corresponds to direct charge excitation of the qubit to the excited charge states and can be a source of significant error due to the large electric dipole ($\sim$ GHz) of the direct charge excitation. The EDSR qubit transition only possesses a fraction of this electric-dipole strength, given by half the spin–charge hybridisation proportion $h \ll 1$ (see Eq. 3.2.22). The corresponding charge-leakage error is proportional to $\lambda^2 = 4/h^2 \gg 1$ and can only be limited by ensuring that the energy gap to the leakage state is much larger than the qubit Rabi frequency. Thanks to the Gaussian pulse, the leakage error is indeed proportional to $\left(\Omega_r/\Delta\right)^4$ of Rabi frequency over the leakage state energy gap and this quantity can compensate for the large leakage coupling. [6] For a near-optimal spin–charge hybridisation of 1%, and a qubit Rabi frequency of 10 MHz, the leakage error stays below 0.1% for energy gaps larger than 0.5 GHz which are readily achievable for donor-based device. The nuclear-spin-leakage errors only become critical, that is, they begin limiting the qubit performance for nearly degenerate nuclear-spin hyperfine values because the coupling to the leakage state is generally weaker than the qubit transition. These small energy separations are obtained when the hyperfine couplings are similar, for example when $A_{L,k} \approx A_R$ or $A_{L,1} \approx A_{L,2}$.

The first nuclear-spin-leakage error (see Fig. 4.3c)) in the 2P-1P donor-based flopping-mode qubits is due to an unwanted electron–nuclear flip-flop transition with the nuclear spins in the left QD such as the transition $|\Downarrow\Uparrow\Uparrow\downarrow -\rangle \rightarrow |\Downarrow\Downarrow\Uparrow\uparrow -\rangle$. Here, $\lambda \approx A_{L,k}/A_R$ and therefore we must minimise the relative hyperfine interaction between the left and right nuclear spins with the electron. The energy gap to the leakage state is related to the difference in the hyperfine coupling to the right and left nuclei, $\Delta_{ql} \approx (A_R - A_L)/4$. Minimising λ and maximising Δ_{ql}, can be achieved my minimising A_L and maximising A_R. On the 2P1P system, the hyperfine coupling A_L to the 2P QD can be lowered significantly by shielding the unpaired electron defining our qubit with two inner-shell electrons bound to the 2P QD, reducing the hyperfine coupling from about 250 MHz to about 10 MHz [29]. The hyperfine coupling A_R to the 1P donor QD cannot be increased in this fashion because the QD has no deeper shell electrons. A possible future strategy to increase A_R further would be to increase the number of nuclei in the right dot; however, we will not consider this in this thesis. For the 2P1P implementation with two inner-shell electrons on the 2P donor QD, the ratio $\lambda \approx A_{L,k}/A_R$ can be estimated from the tight binding numerical estimation $A_L = 10$ MHz [29], and the well known value of the single

[6] For a simple square pulse shape, the error is proportional to the second power of the ratio $\Omega_r/Delta$.

donor hyperfine value $A_R \approx 117\,\mathrm{MHz}$ [38, 36, 29]. We obtain $\lambda = A_L/A_R \approx 0.08$ which puts an upper bound of $\left(\frac{\pi}{4}\right)^2 \lambda^2 = 4 \times 10^{-3} = 0.4\%$ to the possible leakage error. The energy gap is equal to $\Delta_{ql} = (A_R - A_L)/4 = 27\,\mathrm{MHz}$ is larger than the optimal Rabi frequencies on most of the parameter space placing the system in the weak-driving regime, so that nuclear spin leakage error is much lower than the upper bound of 0.4% set by λ (see Fig. 4.5). In summary, leakage through unwanted flip-flops of the electron spin with the nuclear spins in the left dot, is expected to be small for the 2P1P flopping-mode qubit, through optimisation of the hyperfine couplings through electron-shell filling.

The second nuclear-spin leakage process (see Fig. 4.3d)) involves an unlikely simultaneous electron–nuclear flip-flop with all three nuclear spins (for example, $|\Downarrow\Uparrow\Uparrow\downarrow -\rangle \rightarrow |\Uparrow\Downarrow\Downarrow\uparrow -\rangle$). This leakage process may be large because the energy gap to the leakage state equals one half of the longitudinal-energy gradient $\Delta_{ql} = \Delta A_L/4 = \Delta\Omega_{\parallel}/2$, which is engineered to be small in order to minimise z-dephasing. In other words, the longitudinal gradient (and thus the energy gap to the leakage state), can only be as small as the leakage error permits. The energy gap $\Delta A_L/4$ between the qubit states is unlikely to vanish completely due to the presence of static electric fields in a device that slightly Stark shifts the hyperfine couplings to nuclei in the 2P donor QD. In the total-qubit-error calculations in Fig. 4.7 a realistic value of $\Delta A_L = 1\,\mathrm{MHz}$ [36], yields a gap of $\Delta_{ql} = 500\,\mathrm{kHz}$ that is smaller than the optimal Rabi frequency Ω_r. In this "strong driving regime", the nuclear spin II leakage error does not depend on the ratio Ω_r/Δ and is only proportional to the ratio λ^2 (see Eq. 3.3.12). This ratio is below 1% on most of the parameter space and the corresponding upper bound for the leakage error is very small: $\left(\frac{\pi}{4}\right)^2 \lambda^2 \approx 6 \times 10^{-5}$. The ratio λ is so small, because the coupling to the leakage state results from a higher-order process involving three virtual nuclear-spin flip-flop transitions ff_{3x} (see Fig. 4.3 d)) whose electric-dipole moment is much smaller than the one associated with a single spin flip-flop transition.

4.4.4 Strong coupling of the epitaxial flopping-mode qubit to a superconducting cavity

Finally, we examine the suitability of the proposed flopping-mode qubit for two-qubit couplings. Due to the charge-like character, the flopping-mode qubit can be coupled directly via the charge-dipole interaction [18]. The range of the dipole interaction can be extended using floating-gate structures [44] or by coupling two qubits to a superconducting microwave resonator [45]. Indeed, spin–charge coupling

is particularly attractive because it allows for coupling of single spins to microwave cavities which can be used for two-qubit gates between distant qubits [46, 47]. Spin–cavity coupling is achieved by designing the cavity frequency, f_c to be on resonance with the qubit frequency, that is, $2t_c \approx \gamma_e B_0 \approx f_c$. Recent high-kinetic-inductance cavities have demonstrated large zero-point voltage fluctuations on the order of 20 μV with photon loss rates on the order of $\kappa = 1$ MHz [47, 48]. Following the detailed work in Osika *et al.* [28] where a specific implementation of the 1P-1P qubit is discussed we assume that the charge-cavity coupling is on the order of 100 MHz. However, in Ref [28] the kinetic inductance of the superconductor was neglected, and therefore the 100 MHz is only a lower bound for the charge–cavity coupling.

Figure 4.9a) represents the expected ratio of the spin–cavity coupling g_{sc}, to the qubit-dephasing rate γ, for an optimised 2P-1P qubit with $\Delta\Omega_{\|} = 0.5$ MHz by initialising the nuclear spins in antiparallel states and using the 3 electron regime. The dephasing rate γ is calculated by converting the error probability into a coherence time based on the $\pi/2$ gate time for each value of t_c and B_0 (see Appendix C.6). The qubit dephasing rate itself is smaller than g_{sc} for all values of t_c and B_0 shown indicating that the qubit coherence is not the limiting factor in achieving the strong-coupling regime. To achieve strong qubit–cavity coupling, g_{sc} also needs to be faster than the decay rate of the cavity such that the cooperativity is larger than one: $C = g_{sc}^2/\gamma\kappa > 1$. In Fig. 4.9b), we show the estimated coupling parameters for the different flopping-mode qubit implementations discussed in this work [18, 49, 42]. Theoretical analysis of the EDSR protocol yields $T_2^* = 17.6\mu$s for the 2P-1P configuration (see Sect. C.6). Taking this coherence time as a reasonable estimate of the spin dephasing rate for qubit–cavity coupling suggests that it would allow the strong-coupling limit to be reached, with $g_{sc}/\gamma = 48$. The cooperativity of the 2P-1P qubit is comparable to that of other flopping-mode EDSR systems, indicating that donor-based flopping mode qubit can also coupled to superconducting resonators for two-qubit gates. Indeed, all of the proposed flopping-mode qubit implementations can reach the strong-coupling regime with $C > 1$ allowing for two-qubit interactions using superconducting cavities, see Fig. 4.9b).

4.4.5 Readout and initialisation of the epitaxial flopping-mode qubit

For scalable operation of the all-epitaxial flopping-mode qubit within a quantum-computing architecture, initialisation and readout of the qubit state has to be possible with high fidelity but also using as little hardware as possible. In the following

a)

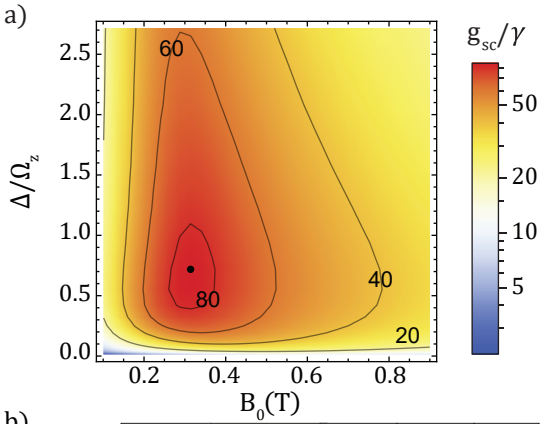

b)

	T_2^* (μs)	g_{sc} (MHz)	g_{sc}/γ	g_{sc}/κ	C
2P1P	17.6	2.7	48	2.7	130
QD-D	3.0	1.8	5.4	1.8	9.7
QD-QD [34] ([11])	0.7 (1.8)	16.8 (18.5)	12 (20)	17 (18)	204 (370)

Figure 4.9: **Strong coupling of the proposed all-epitaxial flopping-mode qubit to a superconducting cavity resonators. a)** For the 2P-1P with the 2P nuclear spins in $|\Downarrow\Uparrow\rangle$ at the (2,1) $\leftrightarrow$ (3,0) charge transition, the ratio of the spin–cavity coupling strength, g_{sc} to the qubit decoherence rate, γ as a function of the spin–charge relative detuning Δ/Ω_z and the external magnetic field, B_0. We assume charge coupling of the qubit to cavity to be 100 MHz. **b)** Table of the main qubit-cavity coupling characteristic values for different flopping-mode implementations outlined in Fig. 4.1. The cooperativity, C is defined as the product of g_{sc}/γ and g_{sc}/κ. For each implementation, all values are calculated at the tunnel coupling t_c and magnetic field B_0 value where C is a maximum under the condition that the qubit drive error is below 0.1% (not necessarily where g_{sc}/γ is the largest). This is therefore lower than the maximum achievable coupling of $g_{sc}/\gamma = 85$ in a) at the cost of higher g_{sc}/κ such that the Cooperativity is the largest. For the QD-D qubit [18], $\Delta\Omega_{\parallel} = 117\,\mathrm{MHz}$, and $\Delta\gamma = -0.2\%$ corresponding to $\Delta\Omega_{\parallel} = 11\,\mathrm{MHz}$ at $B = 0.2\,\mathrm{T}$. For the QD-QD qubit gradient values cited in [15] and [42] respectively. In Benito *et al/* ([42]), $\Delta\Omega_{\perp} = 0.96\,\mathrm{GHz}$ (corresponding to $2b_x = 4\,\mu\mathrm{eV}$) and $\Delta\Omega_{\parallel} = 78\,\mathrm{MHz}$ (corresponding to $2b_z = 0.32\,\mu\mathrm{eV}$). In Croot *et al.* ([15]), $\Delta\Omega_{\perp} = 0.84\,\mathrm{GHz}$ (corresponding to $2b_x = 30\,\mathrm{mT}$) and $\Delta\Omega_{\parallel} = 15\,\mathrm{MHz}$ (corresponding to $2b_z \approx 0.5\,\mathrm{mT}$)

we describe how both the initialisation and the readout of the qubit states can be performed all electrically without any additional infrastructure on the qubit chip, using demonstrated techniques of spin and charge readout and initialisation.

Initialising the qubit in its ground state is possible through a combination of voltage pulses. First we initialise the nuclear spins on both QD as well as the electron spin through spin-selective tunnelling of an electron down-spin from the nearby reservoir that initialises the electron's spin in the $|\downarrow\rangle$ state and its charge in the ground-state orbital. Electron-spin initialisation is required during nuclear-spin initialisation, and will therefore be treated first.

Electron spin initialisation

The electron spin can be initialised into the spin ground state $|\downarrow\rangle$ by first emptying the QD of the unpaired electron forming the qubit, and by subsequent spin-selective tunnelling of another electron from the reservoir [23]. By adjusting the reservoir Fermi level in between the Zeeman-split empty spin states, electrons spin-down states in the reservoir have sufficient energy to populate the empty quantum-dot state, while spin-up states do not.

Electron-spin readout

The electron-spin state of the flopping-mode qubit can be read out using conventional methods when the electron wavefunction is centred on one of the two QDs defining the flopping-mode qubit. Alternatively, the hybridisation of the electron-spin-up states to the excited charge state as discussed in Chapter 3 can also be used to measure the spin state when the electron wave function is shared between both QDs.

Conventional electron-spin readout can be performed for example through spin-selective tunnelling to a nearby reservoir [23]. This destructive measurement technique requires a charge sensitive device to capture the electron tunnelling. Alternatively, the electron spin can be read out via singlet–triplet readout methods by deterministically loading a spin down on a second tunnel-coupled QD.[7] This can be done destructively using the Pauli spin-blockade [50, 51], or non-destructively using dispersive singlet–triplet readout [52, 53, 54].

A more advantageous method of spin readout in the flopping-mode qubit is based on measuring its spin state by dispersively sensing its charge state. Indeed, the electron spin-up state is slightly hybridised to the excited charge state when the

[7] Either the other QD used to host the flopping-mode qubit, or a third dedicated QD.

electron wave function is shared between both dots. A resonant circuit capacitively connected to the electron via a nearby gate can then be used to sense the response of the electron charge to an oscillating electric pulse [19]. This response is different if the electron is hybridised to the excited charge state, and manifests itself as a change in the phase and/or amplitude of the probing signal. Such dispersive readout via the charge state has been implemented using a superconducting resonator coupled to a flopping-mode qubit hosted in two gate-defined QDs in a SiGe heterostructure [55, 56] and is anticipated to be possible in our all epitaxial implementation. As a readout technique it can be performed by any of the two gates necessary to control the qubit, and therefore reduces the overall qubit footprint.

Nuclear-spin readout

Nuclear-spin readout of donor devices in silicon has traditionally been implemented by using microwave pulses to test different electron-spin transitions (ESR) that have been split by the hyperfine interaction of the electron with the nuclear spins [39]. Indeed, it is difficult to otherwise couple the nuclear spin to a charge degree of freedom that can be read out by the charge sensors. Here, we propose a nuclear-spin readout protocol similar to that used in ref [39], but using EDSR instead of ESR.

In our proposed physical setup, nuclear-spin readout relies on probing the different EDSR transition frequencies of the electron spin, as the latter are dependent on the nuclear-spin states through the hyperfine interaction. Thus the nuclear-spin readout needs to be performed in the two-dot regime so that the electric dipole is large enough to allow EDSR. This has the additional benefit that the nuclear spins of both QDs can then be read out simultaneously as the electron is coupled to the nuclear spins in both QDs in the hybridised regime.

First, an EDSR spectrum has to be measured in order to identify all possible flip-flop transitions and their transitions frequencies. It has been shown [39] that the phosphorus nuclear spins randomise over long periods of time (minutes), so that, provided the EDSR spectrum is acquired over longer time scales, all possible nuclear-spin states are likely to be populated during the experiment, and all possible EDSR transition should become visible. In general, the spectrum is expected to be non-degenerate, each peak in the EDSR spectrum corresponding to a flip-flop of the electron spin (loaded in a spin-down state) with one specific nuclear spin, for one particular configuration of the other nuclear spin. If necessary, degenerate transitions can be split by slightly changing the static electric-field bias. If the

degeneracy originates from nuclear spin on different dots, the respective electron-hyperfine coupling strength will vary strongly with electric field. In the unlikely occurrence that both nuclear spin originate from the same donor QD, a stark effect should be sufficient to suppress the degeneracy.

Unless the nuclear spin are fully polarised into the $|\Downarrow\rangle$ state, the nuclear-spin configuration can be probed by repeatedly loading spin-down electrons and testing all possible EDSR transitions, a successful spin flip then identifies the nuclear-spin configuration.[8] The following protocol is adopted: a spin-down electron is loaded into the right dot (into the $|R\rangle$ charge state). This charge and spin state is then adiabatically transferred to the chosen region in the hybridised regime.[9] Once the state has been transferred to the hybridised regime, an EDSR burst probes the first of the possible EDSR transitions. One then reads out the qubit state through either spin or charge readout, depending on the chosen device setup). If it is in the electron spin-up branch (with some excited charge state proportion if the readout is performed in the hybridised regime), the nuclear-spins are indeed in the configuration that was probed, and the nuclear-spin readout is complete. If the qubit state however is not in the spin up branch, the nuclear spins are not in the probed configuration, and one needs to probe another of the untested EDSR transitions. This process is repeated until the electron spin has been successfully flipped. In practice, the EDSR burst will likely be performed by adiabatic inversion, as opposed to a coherent π-pulse, the former being more robust against variations in the driving strengths of different transitions.

Nuclear-spin initialisation

Once the state of the nuclear spins has been established by nuclear-spin readout one can initialise the nuclear spins in the desired state by flipping the wrongly oriented nuclear-spin. The nuclear spins can be flipped by the traditional method of nuclear magnetic resonance (NMR). With NMR, an antenna couples to the nuclear magnetic moment with radio-frequency magnetic fields. Whilst this method is challenging to scale to a large number of qubits as each antenna can only produce one RF pulse at time it can be resolved within a modular quantum computing architecture where nodes of closely-coupled qubits are well separated using superconducting resonators (see Sect. 4.5). In such a modular architecture, an antenna can be manufactured on

[8] including the nuclear spin that flip-flopped with the electron.

[9] Note that this transfer needs not be adiabatic with respect to nuclear spins, but only reversible in that respect. In almost all cases this is of no concern as the adiabaticity with respect to charge automatically guarantees adiabaticity with respect to both nuclear and electron spin.

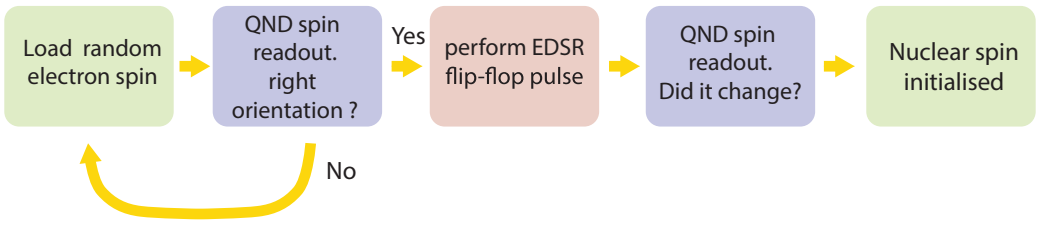

Figure 4.10: **Flowchart for EDSR based nuclear spin control.** Protocol to control and initialise nuclear spin states into the qubit ground state using EDSR. A random electron spin is first onto one of the QDs where quantum non-demolition (QND) readout is performed using a reflectometry circuit. If the qubit is able to be driven then it is in one of the qubit states and then can be reinitialised by performing a qubit pi-pulse. If the qubit was not measured properly then the nuclear spin state was wrong then another random electron spin is loaded to attempt to repeat the process. The whole process is then checked to confirm the pi-pulse was accurate and if it succeeded the nuclear spin state is then properly intialised.

top of each node, and each antenna only needs to address nuclear spin within the node.

Due to the challenges associated with NMR nuclear-spin control, we propose an alternative procedure based on EDSR, that is local, and thus mode scalable. The procedure relies on electrically driving a flip-flop of that electron spin with the target nuclear spin. For the flip-flop to occur the electron spin needs to be initialised in the opposite orientation to the target nuclear spin. The electron spin can be deterministically loaded in the spin-down $\downarrow$ configuration through spin-selective tunnelling, but not in the more energetic spin-up state. Initialisation in that spin-up state may however be performed via repeated randomised loading of the electron. Indeed, if the qubit spin state can be read out using quantum non demolition readout (QND, see Sect. 5.1.5), the electron can be initialised in the spin-up state by repeatedly loading a random spin, and reading it out non-destructively. There is 50% probability of the spin being in the up configuration for each attempt. The procedure is repeated until the spin was read out in the up state. The EDSR pulse can then be performed in order to flip the nuclear spin from down to up.

Qubit readout

Once the nuclear spin states of the qubit is known, the state of the flopping-mode qubit is determined by the electron spin orientations, provided the charge qubit is not fully excited. Because the nuclear spin states are stable in time [39], qubit readout can thus be simply performed via spin readout.

4.4.6 Summary

In summary, we have proposed the implementation of a flopping-mode qubit using two donor-based QDs and performed detailed calculations of the error sources. The nuclear spins not directly involved in the flip-flop transition defining the qubit can be used to minimise the longitudinal-magnetic-field gradient to increase the qubit coherence time. We have shown that the qubit can achieve error rates below the 1% necessary for fault-tolerant quantum computation and can be operated over a wide range of magnetic fields (0.4 T) and for relative variations in the tunnel coupling above 300% ($\sim 5 - 20$ GHz). Fast, high-fidelity single-qubit gates with errors on the order of 10^{-4} are theoretically predicted, comparable to that found in other semiconductor qubits with full electrical control [14, 57]. We then examined the possibility of coupling this qubit to a superconducting cavity and showed that strong coupling is achievable with a cooperativity, $C \sim 130$ for optimised qubit parameters with $\Omega_{\parallel} = 1$ MHz. Finally, we showed that the qubit, including its nuclear spin states, can be initialised and read out through electrical pulses, without the need for additional on-chip structures such as dedicated charge sensors, ESR or NMR antennas. Based on the low qubit-error rate, small qubit footprint, versatility in two-qubit coupling, and robustness to fabrication errors we have shown that flopping-mode EDSR based on two donor-quantum-dots provides an attractive route for scaling in donor-based silicon computing.

4.5 Consideration of a quantum-computing architecture for the all-epitaxial flopping-mode qubit

Solving a useful problem in a reasonable amount of time on a quantum computer running the surface code will likely require more than 100 million qubits (see Sect. 2.1.3), posing a multitude of engineering challenges.

The donor-based flopping-mode-qubit proposal, by promising fast and low-error electrical qubit operation and by enabling long distance qubit coupling is a promising solution to solve these challenges. In this section we consider the formation of a large-scale universal quantum-computing architecture based on the all-epitaxial flopping-mode qubit proposed in Sect. 4.2. The proposed architecture is compatible with the surface-code error-correction algorithm, a leading solution to alleviate the effect of qubit errors.

4.5.1 Two-qubit coupling schemes for a large scale architecture

The all-epitaxial flopping-mode qubits can be coupled to one-another using three different coupling-schemes outlined below. These allow flexibility in the design of the architecture.

Dipole–dipole coupling

A fully-realised surface-code algorithm requires two-qubit entangling gates between neighbouring qubits. The electric-dipole interaction from the charge character of the proposed qubit allows for fast, high-fidelity two-qubit gates over medium distances and long-distance gates via superconducting cavity resonators. The electric dipole of an electron moving between two QDs separated by a distance d is given by

$$\mu = ed. \tag{4.5.1}$$

The dipole–dipole coupling, H_{dd} between at a distance r is given by

$$H_{dd} = V(\sigma_{z,1}\sigma_{z,2} + \sigma_{z,1} + \sigma_{z,2}), \tag{4.5.2}$$

where σ_z, i is the Pauli-z operator for qubit i and

$$V = \Gamma\frac{-2\mu_1\mu_2}{4\pi h\epsilon_0\epsilon_r r^3}. \tag{4.5.3}$$

The geometric correction Γ depends on the orientation of the dipoles relative to each other. It equals 1/4 for the planar geometry and 1 for the vertical qubits. Finally, μ_i is the dipole moment of qubit i, h is Plank's constant, ϵ_0 is the permittivity of free space, and $\epsilon_r = 11.7$ is the relative permittivity of silicon.

The charge qubit coupling, g_{2c} is given by,

$$g_{2c} = V\frac{t_1 t_2}{\Omega_1\Omega_2}. \tag{4.5.4}$$

where t_i and Ω_i are the tunnel coupling and charge qubit energy of qubit i. This dipolar coupling, g_{2c} can reach a few GHz for small qubit separations. The relative strength of the qubit-qubit coupling can be controlled by varying the charge character of the EDSR qubit, that is, by controlling the spin–charge detuning, Δ. Therefore, qubit separations of a few 100 nm are possible.

Floating-gate coupling

The dipolar coupling can be significantly increased by using a floating-gate electrode between the two qubits [44], allowing for qubit separations on the order of a few micrometers. These floating gates operate by increasing the capacitive coupling between the two qubits for a given separation.

Superconducting Coupling

Superconducting cavities can significantly extend the coupling distance of the two qubits. In this scenario, both qubits must be coupled to the cavity with a frequency, ν with a coupling strength given by

$$g_{sc} = \frac{eE_{rms}d}{4h}\frac{t}{\Omega}, \tag{4.5.5}$$

where E_{rms} is the rms electric-field fluctuations of the cavity. For the interaction of the qubits to occur with low error, the coupling of each qubit to the superconducting cavity must be larger than the error rate affecting of the qubit. The superconducting cavity allows qubit couplings over length scales of a few millimetres and allows space for classical electronics and wiring within a quantum-computing architecture.

4.5.2 Large-scale architecture

The proposed scalable EDSR qubit architecture consists of a two-dimensional square-lattice arrangements of the 2P1P flopping mode qubits, nearest-neighbour-coupled via either dipole couplings (direct or mediated by floating gates) or superconducting resonators Fig. 4.11. Qubits concentrated in square sub grids which we call nodes are coupled only via the shorter-range interaction (dipole or floating-gate coupling). The edge qubits of each node are coupled to edge qubits of the nearest nodes via superconducting resonators, in a square super grid of nodes. The empty spaces between nodes contains readout resonators, access for qubit-driving lines and DC control lines.

An example of a large-scale architecture is sketched out in Fig. 4.11. Each qubit (circles) is coupled to four nearest-neighbour qubits in a square lattice. The coupling between qubits within each node is not shown in this figure and is considered in more detail in the following section. The qubits on the perimeter of each node have one or two nearest neighbour qubits in a different node if there are on the edge or on the corner of the perimeter respectively. They are connected to this distant nearest

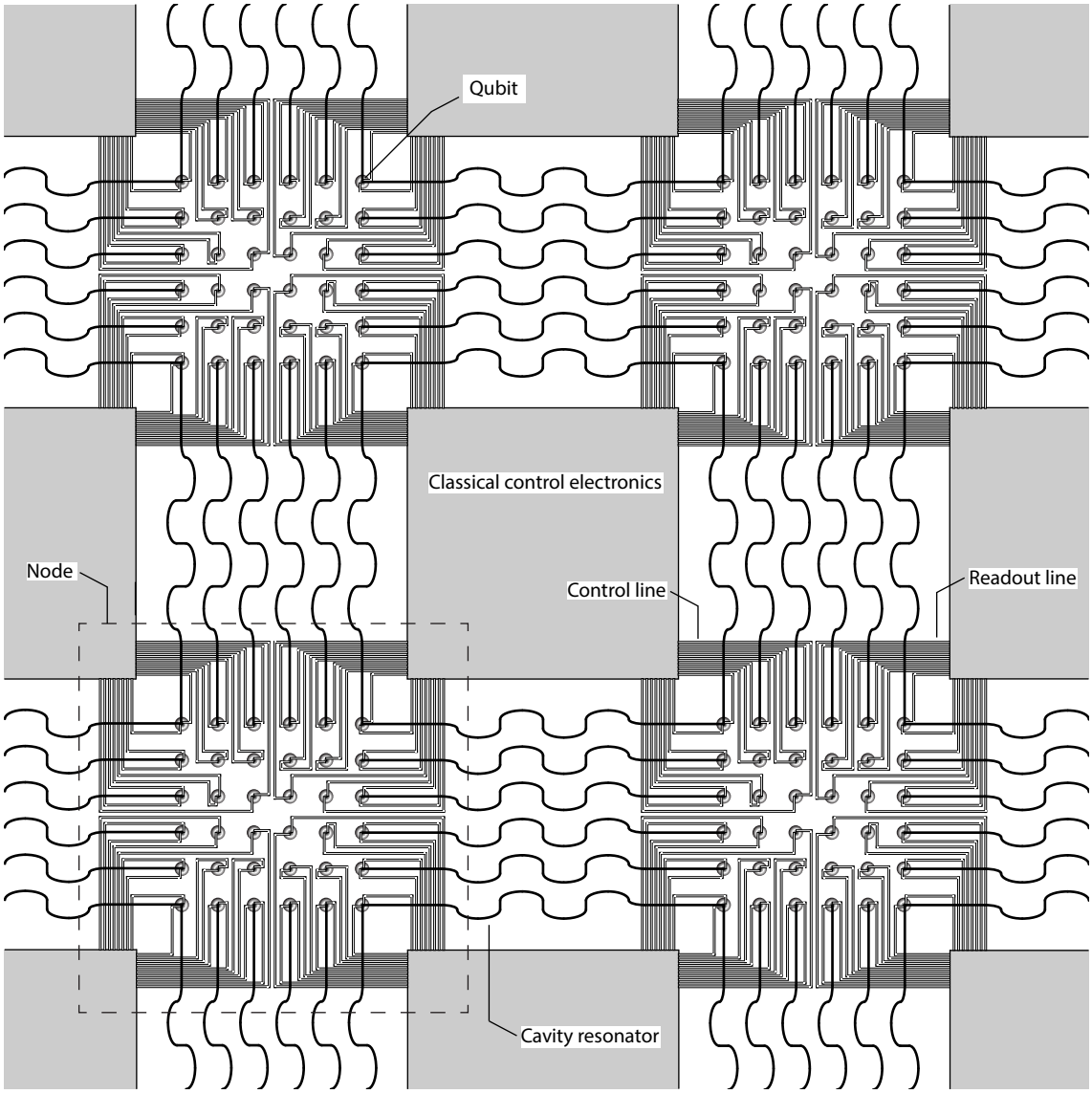

Figure 4.11: **Large scale implementation of a quantum computing architecture.** A top-down schematic view of the proposed quantum computing architecture based on the donor flopping mode qubit. The qubits are separated into nodes of $N \times N$ qubits ($N = 6$ is shown here). Control and readout (classical) electronics are situated between the qubit nodes (grey squares) to allow for sufficient space on the silicon substrate. The white lines are drive and readout lines used to address the individual qubits in the nodes. The squiggle lines represent superconducting microwave cavities used to connect the outer qubits of each node to their nearest neighbour to build a continuous 2-dimensional array for the surface code.

neighbour via superconducting cavities (black undulating lines). The qubit control and readout is performed via metallic gates that connect the greyed out interstitial space between nodes to each qubit (two gates per qubit in this particular case). The interstitial space contains some of the classical control and readout electronics, and interconnects to off-chip electronics (for example with the "flip-chip" technique, or using bond wires).

One could envisage that the readout signals would be multiplexed so that only a few RF lines are needed in each interstitial space, and resonators of non-overlapping frequencies (superconducting or not) patterned within that space allow addressability of each qubit. The electric microwave signals as well as DC control signals would also be routed to their respective qubit within this space. DC control signals could be multiplexed using DRAM-like technologies, allowing for a number of DC lines running from the cold finger of the dilution fridge refrigerator to each interstitial node. This would allow for a much less control lines to be needed per qubit. Indeed, a number N^2 of qubits per node, would require $2N$ bit and word lines to address every qubit individually. The control and readout of the bit and word lines can be either done off-chip (would require $2N$ DC lines routed to each node) or on-chip using binary multiplexing (would require $\log_2(2N)$ lines routed to each node). For high heat output of the binary multiplexing circuits, it might not be possible to place it on chip, and would need to be placed at a different stage of the dilution refrigerator, providing more cooling power [58]. The low refresh rate needed for the slow DC biasing might however be compatible with on-chip operation.

The DC, readout (RF or MW) and Drive (MW) signals would be routed to the respective qubit control lines using bias tees. In the case that each qubit is addressed by two gates, one would separate the readout from the drive signal in order to avoid additional complexity.

4.5.3 Gate routing and qubit density

The complexity of routing the control lines from the interstitial nodes to the qubits within the nodes depends on the number of qubits within the nodes and on the spacing between neighbouring qubits. The spacing between qubits, and the available pitch of the lithographic method used informs the number n_L of leads one can route between existing qubits. With existing lithographic techniques a 40 nm pitch for 10 nm leads is achievable. On the microwave lines, the pitch might be increased due to the need to design a coplanar waveguide to improve the transmission of the signals. The distance between qubits could be of the order of 200 nm for dipole

coupled qubits, whereas it could be of the order of $\approx 2\,\mu$m for the floating gate coupling mechanism. This would allow about $n_L \approx 4$ for dipole coupled qubits, and $n_L \approx 50$ for floating gate coupled qubits.

For a small number (N^2) of qubits, and a high number n_L of possible feedthroughs between qubits, one can route a gate to every qubit using a single lithographic plane. Such a single-layer routing is shown in Fig. 4.11 for 36 qubits ($N = 6$), two gates per qubit, and 4 possible feedthroughs between each qubit pair ($n_L = 4$).

The number of lithographic layers needed to address a number of N^2 qubits with a number of n_L possible feedthroughs between adjacent qubits is given by (see more details in appendix Sect. C.7):

$$n_{\text{lith layers}} \approx \frac{N}{2n_L + 3}. \tag{4.5.6}$$

In the example of dipole-coupled qubits within each node ($n_L \approx 4$), one could route a single gate to all qubits of a node consisting of 324 qubits (N=18) in a single lithographic layer, and 841 qubits (N=29) using a two-layer stack of gates.

In the case of qubits coupled by $\approx 2\,\mu$m-long floating gates, with two gates needed per qubit, n_L is effectively reduced from 50 to 25 and 10404 qubits ($N = 102$)can be wired using a single lithographic layer. Using a two layer stack of gates, 27225 qubits ($N = 165$) can be wired.

	dipole		floating gate	
$n_{\text{lith layers}}$	1	2	1	2
d_{NN}	200 nm		2 μm	
QB density (μm^{-2})	28		0.25	
n_L	4		50	
N_{max}	18	29	202	327
max number of QBs	324	841	40804	106 929
Node area	12 μm^2	31 μm^2	0.1 mm^2	0.4 mm^2

Table 4.1: Single lead QB numbers

Table 4.1 and 4.2 summarise the maximum number of qubits that can be routed with leads in one or two lithographic layers for the direct dipole coupling and floating-gate mediated coupling, for the case of a single lead per qubit and a pair of lead per qubit in respectively. The achievable qubits numbers are significantly higher for the floating gate implementation compare to the dipole implementation, due to the fact that the number of qubits possible in one node scales as n_L^2. However the qubit density is 100 times higher for the dipole coupled qubits since the inter-qubit separation is limited to ~ 200 nm.

	dipole		floating gate	
$n_{\text{lith layers}}$	1	2	1	2
d_{NN}	200 nm		2 μm	
QB density (μm^{-2})	28		0.25	
n_L	2		25	
N_{max}	10	17	102	165
max number of QBs	100	289	10 404	27 225
Node area	3.2 μm^2	10 μm^2	0.04 mm^2	0.11 mm^2

Table 4.2: double lead QB numbers

4.5.4 Node implementation 1: dipole coupling

We sketch a possible implementation of a node architecture for qubits coupled using the bare-dipole coupling in Fig. 4.12. The dipole-dipole coupling between two qubits is proportional to the scalar product of their respective dipole moments, see Eq. 4.5.3. The dipole moment is oriented along the axis separating the two QDs. To maximise the coupling strength between any neighbours, one favourable arrangement is to orient all dipoles (and thus qubits) out of the plane containing the qubits. This allows maximal nearest neighbour coupling between all qubits in the two dimensional surface code square lattice. Each donor QD pair forming a qubit would thus be patterned within the silicon lattice using one of two separate hydrogen lithography steps.

We propose the following manufacturing procedure for each node. Note that every node of the quantum computers could be manufactured in parallel, with all infrastructure in a given lithographic layer finalised, before manufacturing the next. After standard surface preparation of a ^{28}Si wafer (ultra high vacuum (UHV) cleaning, surface annealing, and hydrogen passivation), one would pattern a first layer of parallel Si-P control line using STM lithography. One could for example manufacture one control line for each column of qubits within each node. After standard Phosphorus incorporation, one would then encapsulate the whole chip with a layer of a few 10s of nm of ^{28}Si using state of the art molecular beam epitaxy. We call this the first encapsulation layer. The next layer would again be heat treated and passivated with hydrogen. One would then pattern the first layer containing one donor cluster per qubit. Again after phosphorus incorporation, one would then grow $\sim$ 10 nm of ^{28}Si (second encapsulation) as this is the inter-QD distance which is needed to achieve a tunnel coupling of a few GHz. One would then again prepare the surface and pattern the second qubit layer containing one donor QD per qubit, each one tunnel-coupled to a QD of the previous layer. After phosphorus incorporation, one

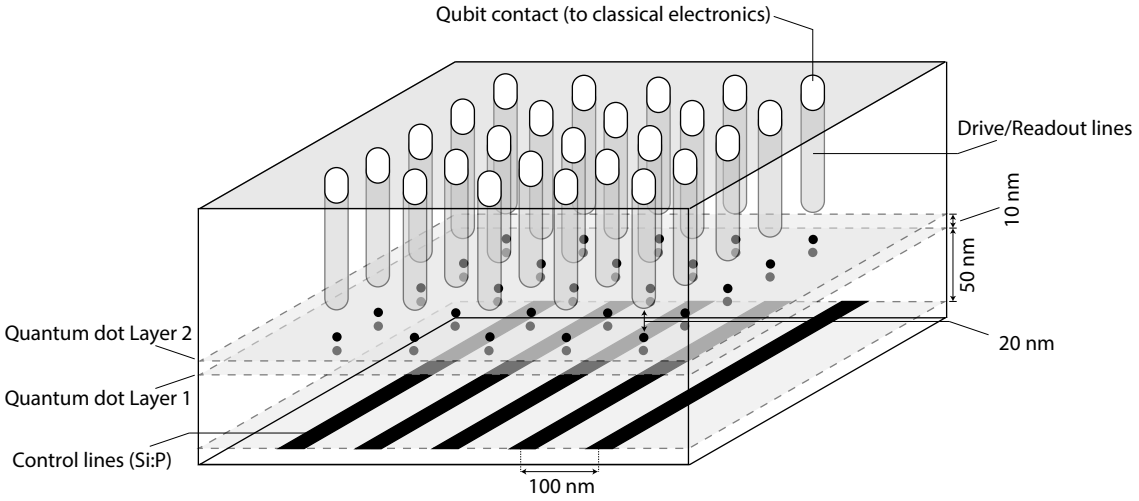

Figure 4.12: **Implementation of direct dipole coupling nodes (side view).** Vertically patterned qubits are shown by black circles on atomic layers separaeted by $\sim$ 10 nm to generate sufficiently large tunnel coupling between the QDs. Epitaxial Si:P control lines are patterned in a crystal plane $\sim$ 50 nm below the bottom qubit plane and are used to create a large global gate for arrays of qubits. Individual qubits are controlled using metallic vias as gates $\gtrsim$ 20 nm above the qubits. The qubit themselves are separated by $\sim$ 100 nm to reduce leakage between electrodes while still allowing for sufficient dipolar coupling.

would then grow 20 to 50 nm of ^{28}Si as the final encapsulation layer which finalises the STM UHV process.

After a final surface preparation, using standard lithography techniques (e.g. e-beam lithography or optical lithography), one would then pattern one or two metallic gates per qubit on the top silicon surface. As discussed in the previous section the routing of the leads from the interstitial nodes to the qubit gate may require several layers of metallic leads, separated from each other using insulating layers of high dielectric constant (for example SiO_2 or HfO_2). This is a well-known lithographic procedure within the semiconductor industry for current semiconductor circuits [59].

4.5.5 Node implementation 2: floating gates

Another possible implementation of a node architecture for qubits coupled using floating gates is sketched in Fig. 4.13 and Fig. 4.14. Qubits are represented by a pair of dots and are contained in the same lithographic plane inside a crystalline isotopically purified silicon (^{28}Si) layer.

Each nearest neighbour qubits pair is coupled via elongated metallic islands, represented by the black structures in the form of a dog bone. Electrostatic control, drive and readout of each qubit is performed via one or two gates (black rectangles). These gates are connected to metallic leads represented by white lines in both figures.

The floating gates enable spacings of up to a few micrometers between qubits allowing for multiple feedthrough of metallic leads between them. In this way, a larger number of qubits can be addressed by leads within a single lithographic layers. However the qubit density within the node is reduced by about two orders of magnitude when compared to dipole coupling (see Table 4.1 and 4.2). The "floating gates" at the outer perimeter of the node are connected to superconducting resonators (light grey lines). This allows long distance coupling of those qubits to their distant nearest neighbours in the next node(s).

Note that the floating gates and control/readout/drive gates can be manufactured either in the qubit plane, or on the silicon surface above. It is however advantageous in terms to have both patterned inside the qubit plane. Indeed this increases the capacitive coupling between the gates and the QDs, and allows for stronger qubit-qubit coupling at the same distance, qubit driving, better readout signal, and better electrostatic control. There is no downside to patterning the floating gates in the qubit plane, contrary to the control gates, which need to be contacted using vias in that case. The location of vias created by etching the silicon substrate are indicated by white circles in Fig. 4.13. A sideview of such an implementation is shown

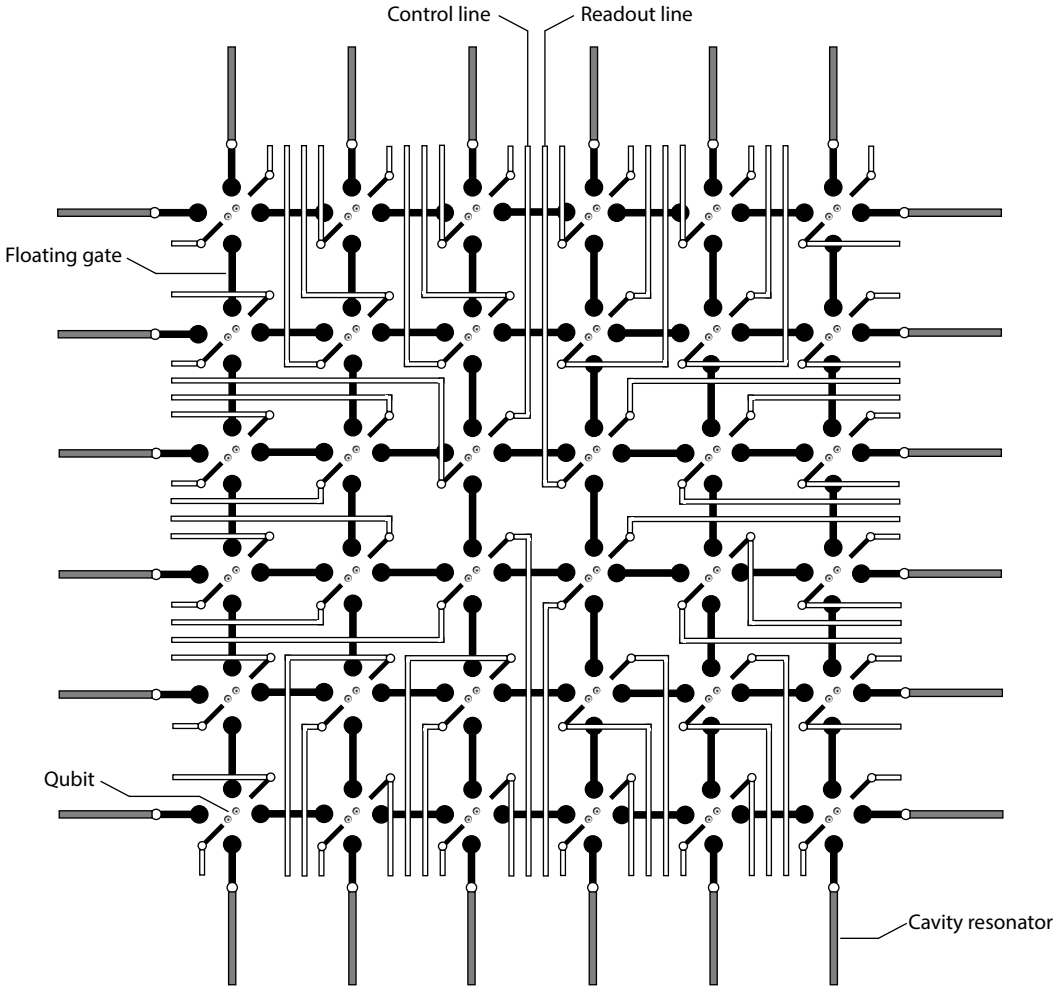

Figure 4.13: **Implementation of floating gate coupling nodes (top view).** Coupling between the qubits (pair of circles) is here achieved via in-plane SiP floating gates (black dogbone structures). Each qubit is controlled by two electrostatic gates that are contacted using etched vertical vias (white open circles), using metallic gates (white lines) patterned on the silicon surface. Superconducting resonators (grey lines) connect the edge qubits of the node to other nodes. The edge qubits are capacitively coupled to an in plane gate which is connected to the the resonator patterned on the silicon surface.

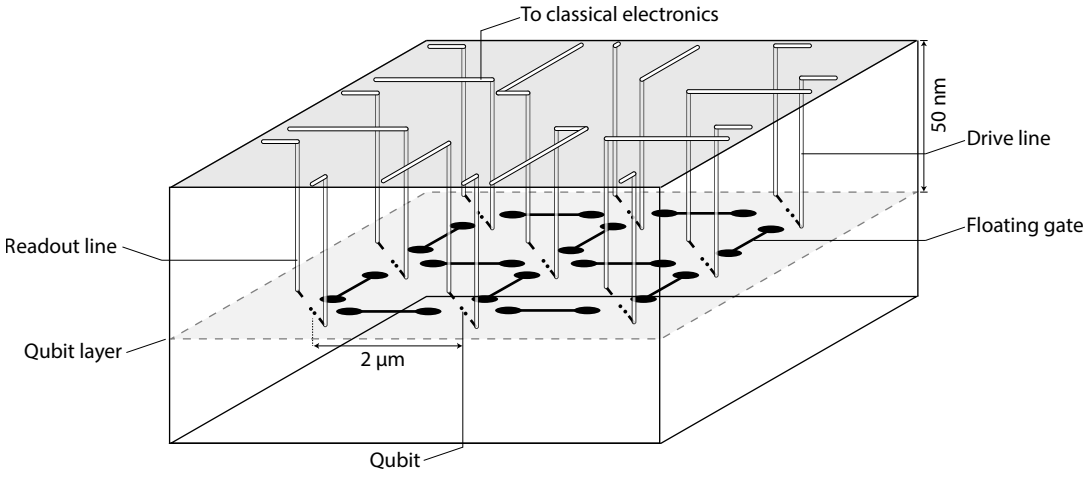

Figure 4.14: **Details of node implementation using floating gate coupling (side view).** The qubits, control gates and floating gates are all patterned in the same 2D plane. The floating gates are $\sim$ 1 μm long dramatically increasing the inter-qubit separation compared to the $\sim$ 100 nm using direct dipole coupling. The control gates are contacted using metallic vertical vias that are connected to classical control and readout electronics in between nodes.

in Fig. 4.14, where vias to the control/readout/drive gates are now represented by vertical white lines.

4.6 Conclusion

In this chapter we proposed a novel flopping-mode qubit fully based on asymmetric donor-based QDs. The qubit is based on an electron spin that can be electrically biased in such a way that the electron's wave-function is shared between two tunnel-coupled donor quantum-dots. At this biasing point the wave-function is very sensitive to electric fields and with the right value of the tunnel-coupling, the spin can become hybridised to the charge state of the QD system. This is reflected in the emergence of a large spin electric dipole moment that allows electrical driving of the spin. By minimising the hyperfine coupling of electron spin to the donor nuclear spins on one of the QDs, we show that the magnetic field gradients experienced by the spin can be engineered to allow for fast ($\sim$ ns) and high fidelity ($>$ 99%) electrical driving of the qubit. With the proper device design, the additional nuclear spins only act as a resource to facilitate qubit errors and does not significantly contribute to state leakage due to the small coupling and large detuning between the leakage states and the qubit states. Also, the qubit can be initialised and read-out

fully electrically, without the need for any additional gate or charge sensor close to the device. The large spin–charge coupling ($\sim$ 100 MHz) also allows for strong coupling of the spin to a superconducting cavity, paving the way for long distance two-qubit gates, mediated by superconducting resonators. All these characteristics make the qubit an attractive and scalable candidate for error-corrected quantum computation using the surface code. In the final section, we present initial ideas for architectures based on the flopping mode qubit described in this chapter. Further work will include error simulations for the various two-qubit gates allowable from the dipole coupling (controlled-phase, SWAP), as well as for the dispersive readout using a superconducting cavity.

In this chapter, we focused on one particular implementation of the proposed qubit that consists of a 2P-1P multi-donor quantum dot hosting three electrons. In that particular implementation the reduction of the hyperfine coupling to the 2P QD is crucial to reduce the qubit error. In this chapter we have based the values of the hyperfine couplings on tight binding simulations and one existing experimental measurements of a 2P QD. In the following chapter we experimentally investigate additional 2P QDs and show that the cancelling of the 2P hyperfine couplings relies on the orbital wavefunction being symmetric. This cancelling was observed in the existing measurement of the hyperfine couplings on a 2P donor quantum dot [36]. However, in a different device we uncovered a specific 2P configuration in which the orbital wavefunction is significantly shifted by the static electric field present in the device. This would be detrimental to low-error flopping mode operation. That particular 2P configuration would therefore need to be avoided by specific patterning strategies.

The donor configuration within the 2P donor QD containing three electrons could also have an impact on the charge state of the flopping-mode being well defined. This charge state is a linear combination of a single electron orbital in the left QD with a single electron orbital in the right QD. This description is correct as long as the single orbitals are non-degenerate. The ground state 1P orbital is known to be non-degenerate [37], and the same is expected to be the case for the third electron orbital on the 2P quantum dot [10]. However it is possible that for some donor configurations within the 2P QD, a near-degeneracy is present. This is outside the scope of this work but needs to be investigated, for example using tight-binding simulations.

[10] Private communication with Prof. Rajib Rahman

Bibliography

[1] F. N. Krauth, S. K. Gorman, Y. He, M. T. Jones, P. Macha, S. Kocsis, C. Chua, B. Voisin, S. Rogge, R. Rahman, Y. Chung, and M. Y. Simmons. Flopping-mode electric dipole spin resonance in phosphorus donor qubits in silicon. may 2021.

[2] Juha T. Muhonen, Juan P. Dehollain, Arne Laucht, Fay E. Hudson, Rachpon Kalra, Takeharu Sekiguchi, Kohei M. Itoh, David N. Jamieson, Jeffrey C. McCallum, Andrew S. Dzurak, and Andrea Morello. Storing quantum information for 30 seconds in a nanoelectronic device. *Nature Nanotechnology*, 9(12):986–991, 2014.

[3] J. T. Muhonen, A. Laucht, S. Simmons, J. P. Dehollain, R. Kalra, F. E. Hudson, S. Freer, K. M. Itoh, D. N. Jamieson, J. C. McCallum, A. S. Dzurak, and A. Morello. Quantifying the quantum gate fidelity of single-atom spin qubits in silicon by randomized benchmarking. *Journal of Physics Condensed Matter*, 27(15), 2015.

[4] R. Barends, J. Kelly, A. Megrant, A. Veitia, D. Sank, E. Jeffrey, T. C. White, J. Mutus, A. G. Fowler, B. Campbell, Y. Chen, Z. Chen, B. Chiaro, A. Dunsworth, C. Neill, P. O'Malley, P. Roushan, A. Vainsencher, J. Wenner, A. N. Korotkov, A. N. Cleland, and John M. Martinis. Superconducting quantum circuits at the surface code threshold for fault tolerance. *Nature*, 508(7497):500–503, 2014.

[5] Ensar Vahapoglu, J. P. Slack-Smith, R. C.C. Leon, W. H. Lim, F. E. Hudson, T. Day, T. Tanttu, C. H. Yang, A. Laucht, A. S. Dzurak, and J. J. Pla. Single-electron spin resonance in a nanoelectronic device using a global field. *arXiv*, 2020.

[6] C. D. Hill, E. Peretz, S. J. Hile, M. G. House, M. Fuechsle, S. Rogge, M. Y. Simmons, and L. C. L. Hollenberg. A surface code quantum computer in silicon. *Science Advances*, 1(9):e1500707–e1500707, oct 2015.

[7] F. Borjans, X. G. Croot, X. Mi, M. J. Gullans, and J. R. Petta. Resonant microwave-mediated interactions between distant electron spins. *Nature*, 577(January):195–199, 2019.

[8] Emmanuel I. Rashba. Theory of electric dipole spin resonance in quantum dots: Mean field theory with gaussian fluctuations and beyond. *Phys. Rev. B*, 78:195302, 2008.

[9] L. S. Levitov and E. I. Rashba. Dynamical spin-electric coupling in a quantum dot. *Phys. Rev. B*, 67:115324, 2003.

[10] K. C. Nowack, F. H. L. Koppens, Yu. V. Nazarov, and L. M. K. Vandersypen. Coherent control of a single electron spin with electric fields. *Science*, 318(5855):1430–1433, 2007.

[11] S. Nadj-Perge, S. M. Frolov, E. P. A. M. Bakkers, and L. P. Kouwenhoven. Spin-orbit qubit in a semiconductor nanowire. *Nature*, 468(7327):1084–1087, 2010.

[12] M. Pioro-Ladrire, Y. Tokura, T. Obata, T. Kubo, and S. Tarucha. Micromagnets for coherent control of spin-charge qubit in lateral quantum dots. *Appl. Phys. Lett.*, 90(2):024105, 2007.

[13] Yasuhiro Tokura, Wilfred G. van der Wiel, Toshiaki Obata, and Seigo Tarucha. Coherent single electron spin control in a slanting zeeman field. *Phys. Rev. Lett.*, 96:047202, 2006.

[14] Jun Yoneda, Kenta Takeda, Tomohiro Otsuka, Takashi Nakajima, Matthieu R. Delbecq, Giles Allison, Takumu Honda, Tetsuo Kodera, Shunri Oda, Yusuke Hoshi, Noritaka Usami, Kohei M. Itoh, and Seigo Tarucha. A quantum-dot spin qubit with coherence limited by charge noise and fidelity higher than 99.9%. *Nature Nanotechnology*, 13(2):102–106, 2018.

[15] X. Croot, X. Mi, S. Putz, M. Benito, F. Borjans, G. Burkard, and J. R. Petta. Flopping-mode electric dipole spin resonance. *Phys. Rev. Research*, 2:012006, Jan 2020.

[16] E. A. Laird, C. Barthel, E. I. Rashba, C. M. Marcus, M. P. Hanson, and A. C. Gossard. Hyperfine-mediated gate-driven electron spin resonance. *Phys. Rev. Lett.*, 99:246601, 2007.

[17] M. Shafiei, K. C. Nowack, C. Reichl, W. Wegscheider, and L. M. K. Vandersypen. Resolving spin-orbit- and hyperfine-mediated electric dipole spin resonance in a quantum dot. *Phys. Rev. Lett.*, 110:107601, Mar 2013.

[18] Guilherme Tosi, Fahd A Mohiyaddin, Vivien Schmitt, Stefanie Tenberg, Rajib Rahman, Gerhard Klimeck, and Andrea Morello. Silicon quantum processor with robust long-distance qubit couplings. *Nature Communications*, 8(1):450, dec 2017.

[19] K. D. Petersson, L. W. McFaul, M. D. Schroer, M. Jung, J. M. Taylor, A. A. Houck, and J. R. Petta. Circuit quantum electrodynamics with a spin qubit. *Nature*, 490(7420):380–383, 2012.

[20] Allen Kha, Robert Joynt, and Dimitrie Culcer. Do micromagnets expose spin qubits to charge and johnson noise? *Appl. Phys. Lett.*, 107(17):172101, October 2015.

[21] Xuedong Hu, Yu Xi Liu, and Franco Nori. Strong coupling of a spin qubit to a superconducting stripline cavity. *Physical Review B - Condensed Matter and Materials Physics*, 86(3):1–5, 2012.

[22] Félix Beaudoin, Dany Lachance-Quirion, W. A. Coish, and Michel Pioro-Ladrière. Coupling a single electron spin to a microwave resonator: Controlling transverse and longitudinal couplings. *Nanotechnology*, 27(46), 2016.

[23] J.M. Elzerman, R. Hanson, L.H. Willems van Beveren, B. Witkamp, L.M.K. Vandersypen, and L.P. Kouwenhoven. Single-shot read-out of an individual electron spin in a quantum dot. *Nature*, 430:431–435, 2004.

[24] D. R. McCamey, J. van Tol, G. W. Morley, and C. Boehme. Fast nuclear spin hyperpolarization of phosphorus in silicon. *Phys. Rev. Lett.*, 102:027601, 2009.

[25] M. Benito, X. Croot, C. Adelsberger, S. Putz, X. Mi, J. R. Petta, and Guido Burkard. Electric-field control and noise protection of the flopping-mode spin qubit. *Phys. Rev. B*, 100:125430, 2019.

[26] Wonjin Jang, Jehyun Kim, Min-Kyun Cho, Hwanchul Chung, Sanghyeok Park, Jaeun Eom, Vladimir Umansky, Yunchul Chung, and Dohun Kim. Robust energy-selective tunneling readout of singlet-triplet qubits under large magnetic field gradient. *npj Quantum Information*, 6(1):64, 2020.

[27] Yu Wang, Chin-Yi Chen, Gerhard Klimeck, Michelle Y. Simmons, and Rajib Rahman. All-electrical control of donor-bound electron spin qubits in silicon. *arXiv:1703.05370*, 2017.

[28] E. N. Osika, S. Monir, Y.-L. Hsueh, S. Kocsis, B. Voisin, C. Chua, S. Rogge, and R. Rahman. Spin-photon coupling for atomic qubit devices in silicon. *Unplublished*, 2021.

[29] Yu Wang, Chin Yi Chen, Gerhard Klimeck, Michelle Y. Simmons, and Rajib Rahman. Characterizing Si:P quantum dot qubits with spin resonance techniques. *Scientific Reports*, 6(August):1–9, 2016.

[30] Samuel J. Hile, Lukas Fricke, Matthew G. House, Eldad Peretz, Chin Yi Chen, Yu Wang, Matthew Broome, Samuel K. Gorman, Joris G. Keizer, Rajib Rahman, and Michelle Y. Simmons. Addressable electron spin resonance using donors and donor molecules in silicon. 4(7), 2018.

[31] Rifat Ferdous, Kok W. Chan, Menno Veldhorst, J. C.C. Hwang, C. H. Yang, Harshad Sahasrabudhe, Gerhard Klimeck, Andrea Morello, Andrew S. Dzurak, and Rajib Rahman. Interface-induced spin-orbit interaction in silicon quantum dots and prospects for scalability. *Physical Review B*, 97(24):1–5, 2018.

[32] Ludwik Kranz, Samuel Keith Gorman, Brandur Thorgrimsson, Yu He, Daniel Keith, Joris Gerhard Keizer, and Michelle Yvonne Simmons. Exploiting a Single-Crystal Environment to Minimize the Charge Noise on Qubits in Silicon. *Advanced Materials*, 32(40):1–8, 2020.

[33] Bent Weber, Yu-Ling Hsueh, Thomas F. Watson, Ruoyu Li, Alexander R. Hamilton, Lloyd C. L. Hollenberg, Rajib Rahman, and Michelle Y. Simmons. Spinorbit coupling in silicon for electrons bound to donors. *npj Quantum Information*, 4(1):61, dec 2018.

[34] F. Motzoi, J. M. Gambetta, P. Rebentrost, and F. K. Wilhelm. Simple pulses for elimination of leakage in weakly nonlinear qubits. *Phys. Rev. Lett.*, 103:110501, 2009.

[35] Tom Struck, Arne Hollmann, Floyd Schauer, Olexiy Fedorets, Andreas Schmidbauer, Kentarou Sawano, Helge Riemann, Nikolay V. Abrosimov, Łukasz Cywiński, Dominique Bougeard, and Lars R. Schreiber. Low-frequency spin qubit energy splitting noise in highly purified 28Si/SiGe. *npj Quantum Information*, 6(1):1–7, 2020.

[36] Samuel J. Hile, Lukas Fricke, Matthew G. House, Eldad Peretz, Chin Yi Chen, Yu Wang, Matthew Broome, Samuel K. Gorman, Joris G. Keizer, Rajib Rahman, and Michelle Y. Simmons. Addressable electron spin resonance using donors and donor molecules in silicon. *Science Advances*, 4(7):eaaq1459, jul 2018.

[37] Martin Fuechsle, Jill A Miwa, Suddhasatta Mahapatra, Hoon Ryu, Sunhee Lee, Oliver Warschkow, Lloyd C L Hollenberg, Gerhard Klimeck, and Michelle Y Simmons. A single-atom transistor. *Nature nanotechnology*, 7(4):242–246, 2012.

[38] Jarryd J Pla, Kuan Y Tan, Juan P Dehollain, Wee H Lim, John J L Morton, David N Jamieson, Andrew S Dzurak, and Andrea Morello. A single-atom electron spin qubit in silicon. *Nature*, 489(7417):541–545, sep 2012.

[39] Jarryd J. Pla, Kuan Y. Tan, Juan P. Dehollain, Wee H. Lim, John J. L. Morton, Floris A. Zwanenburg, David N. Jamieson, Andrew S. Dzurak, and Andrea Morello. High-fidelity readout and control of a nuclear spin qubit in silicon. *Nature*, 496(7445):334–338, apr 2013.

[40] J. R. Petta, J. M. Taylor, A. C. Johnson, A. Yacoby, M. D. Lukin, C. M. Marcus, M. P. Hanson, and A. C. Gossard. Dynamic nuclear polarization with single electron spins. *Physical Review Letters*, 100(6):1–4, 2008.

[41] M. Gullans, J. J. Krich, J. M. Taylor, H. Bluhm, B. I. Halperin, C. M. Marcus, M. Stopa, A. Yacoby, and M. D. Lukin. Dynamic nuclear polarization in double quantum dots. *Phys. Rev. Lett.*, 104:226807, 2010.

[42] M. Benito, X. Croot, C. Adelsberger, S. Putz, X. Mi, J. R. Petta, and Guido Burkard. Electric-field control and noise protection of the flopping-mode spin qubit. *Physical Review B*, 100(12):1–10, 2019.

[43] F. Motzoi, J. M. Gambetta, P. Rebentrost, and F. K. Wilhelm. Simple Pulses for Elimination of Leakage in Weakly Nonlinear Qubits. *Physical Review Letters*, 103(11):1–4, 2009.

[44] Luka Trifunovic, Oliver Dial, Mircea Trif, James R. Wootton, Rediet Abebe, Amir Yacoby, and Daniel Loss. Long-distance spin-spin coupling via floating gates. *Physical Review X*, 2(1):1–13, 2012.

[45] J. J. Viennot, M. C. Dartiailh, A. Cottet, and T. Kontos. Coherent coupling of a single spin to microwave cavity photons. *Science*, 349(6246):408–411, 2015.

[46] X. Mi, J. V. Cady, D. M. Zajac, P. W. Deelman, and J. R. Petta. Strong coupling of a single electron in silicon to a microwave photon. 355(6321):156–158, 2017.

[47] N. Samkharadze, G. Zheng, N. Kalhor, D. Brousse, A. Sammak, U. C. Mendes, A. Blais, G. Scappucci, and L. M. K. Vandersypen. Strong spin-photon coupling in silicon. *Science*, 359(6380):1123–1127, 2018.

[48] N. Samkharadze, A. Bruno, P. Scarlino, G. Zheng, D. P. DiVincenzo, L. DiCarlo, and L. M. K. Vandersypen. High-kinetic-inductance superconducting nanowire resonators for circuit qed in a magnetic field. *Phys. Rev. Applied*, 5:044004, 2016.

[49] X. Croot, X. Mi, S. Putz, M. Benito, F. Borjans, G. Burkard, and J. R. Petta. Flopping-mode electric dipole spin resonance. *Physical Review Research*, 012006:1–6, 2020.

[50] J R Petta, a C Johnson, J M Taylor, E a Laird, A Yacoby, M D Lukin, C M Marcus, M P Hanson, and a C Gossard. Coherent Manipulation of Coupled Electron Spins in Semiconductor Quantum Dots. *Science*, 309(September):2180–2184, 2005.

[51] M. A. Broome, T. F. Watson, D. Keith, S. K. Gorman, M. G. House, J. G. Keizer, S. J. Hile, W. Baker, and M. Y. Simmons. High-Fidelity Single-Shot Singlet-Triplet Readout of Precision-Placed Donors in Silicon. *Physical Review Letters*, 119(4):1–5, 2017.

[52] P. Pakkiam, A. V. Timofeev, M. G. House, M. R. Hogg, T. Kobayashi, M. Koch, S. Rogge, and M. Y. Simmons. Single-Shot Single-Gate rf Spin Readout in Silicon. *Physical Review X*, 8(4):1–5, 2018.

[53] A. West, B. Hensen, A. Jouan, T. Tanttu, C. H. Yang, A. Rossi, M. F. Gonzalez-Zalba, F. E. Hudson, A. Morello, D. J. Reilly, and A. S. Dzurak. Gate-based single-shot readout of spins in silicon. *Nature nanotechnology*, 14:437–441, 2019.

[54] Matias Urdampilleta, David J. Niegemann, Emmanuel Chanrion, Baptiste Jadot, Cameron Spence, Pierre-André André Mortemousque, Christopher Bäuerle, Louis Hutin, Benoit Bertrand, Sylvain Barraud, Romain Maurand, Marc Sanquer, Xavier Jehl, Silvano De Franceschi, Maud Vinet, Tristan Meunier, 1 Christopher Bäuerle, Louis Hutin, Benoit Bertrand, Sylvain Barraud, Romain Maurand, Marc Sanquer, Xavier Jehl, Silvano De Franceschi, Maud Vinet, and Tristan Meunier. Gate-based high fidelity spin readout in a CMOS device. *Nature Nanotechnology*, 1(8):1–6, 2019.

[55] X. Mi, M. Benito, S. Putz, D. M. Zajac, J. M. Taylor, Guido Burkard, and J. R. Petta. A coherent spin-photon interface in silicon. *Nature*, 555(7698):599–603, 2018.

[56] N. Samkharadze, G. Zheng, N. Kalhor, D. Brousse, A. Sammak, U. C. Mendes, A. Blais, G. Scappucci, and L. M.K. Vandersypen. Strong spin-photon coupling in silicon. *Science*, 359(March):1123–1127, 2018.

[57] M. Veldhorst, J. C.C. Hwang, C. H. Yang, A. W. Leenstra, B. De Ronde, J. P. Dehollain, J. T. Muhonen, F. E. Hudson, K. M. Itoh, A. Morello, and A. S. Dzurak. An addressable quantum dot qubit with fault-tolerant control-fidelity. *Nature Nanotechnology*, 9(12):981–985, 2014.

[58] L. M. K. Vandersypen, H. Bluhm, J. S. Clarke, A. S. Dzurak, R. Ishihara, A. Morello, D. J. Reilly, L. R. Schreiber, and M. Veldhorst. Interfacing spin qubits in quantum dots and donorshot, dense, and coherent. *npj Quantum Information*, 3(1):1–10, 2017.

[59] Morihiro Kada. Research and Development History of Three-Dimensional Integration Technology. *Springer International Publishing*, pages 1–23, 2015.

Chapter 5

Nuclear spin dynamics in multi-donor quantum dots

In this chapter, we benchmark the ability to engineer multi-donor quantum dots using STM Hydrogen lithography for quantum computing applications. Multi-donor quantum dots have demonstrated increased T_1 relaxation times [1, 2], addressable electron spin control using ESR [3, 4] and increased tunability of exchange-based two-qubit gates [5]. Furthermore, the additional positive charge within multi-donor quantum dots can be used to engineer the quantum dot charging energies [6], and increase the electrostatic tunability of the devices (see Sect. 5.1.3 and Sect. 5.1.1). Quantum dots formed by just two phosphorus donors are a particular point of interest because they form the basis of the electrically driven electron-nuclear spin qubit proposed in this thesis (see Chapter 4). The proposed qubit consists of a single donor (1P) and two-donor (2P) quantum dot pair. In the previous chapters, we have shown that the qubit can be protected from charge-noise induced decoherence by minimising the hyperfine coupling within the 2P donor molecule. We proposed to achieve this by controlling the electron number and the nuclear spin orientation within it. Control over the number of donors within donor quantum dots is furthermore crucial for the proposed implementation of a parity measurement between electron spin qubits on donor-quantum dots [7]. Parity measurements are the fundamental building blocks of quantum error correction using the surface code and pave a way towards large scale quantum computing (see Sect. 2.1.1).

Using two separate devices based on a novel triple-dot design and fabricated using STM hydrogen lithography we demonstrate that a high degree of control can be achieved in the engineering of 2P molecules. On a first device, we perform metrology of the configuration of a pair of two-donor quantum dots by matching their charg-

ing energies to tight binding simulation performed by collaborators in Professor Rahman's group. The metrology strongly suggest that two-donor molecules can be patterned with a precision of at least $\pm 0.25\,\mathrm{nm}$ in carefully fabricated lithographic openings using the STM tool. We then improve the readout fidelity measured on a 2P molecule in the first device from 83% to 94%, by optimising the design and fabrication of the charge sensor used to measure the electron and nuclear spins. The hyperfine interactions on the 2P molecule are then measured using microwave pulses that adiabatically invert the electron spin. The measurements reveal a previously unobserved linear Stark shift on a tightly bound donor molecule. The precise measurements of the hyperfine interaction within the 2P molecule are then used to improve the precision of the donor metrology, and pinpoint one likely configuration of the phosphorus atoms within the silicon lattice. We then perform nuclear spin readout on the 2P molecule with a fidelity of 88% and uncover previously unobserved nuclear spin dynamics in tightly bound donor molecules. The transition rates between nuclear spin states are then extracted using a hidden Markov model and confirm the presence of nuclear spin excitation through the hyperfine shock effect [8]. A finite probability of a flip-flop between antiparallel nuclear spin state is uncovered and could be related to the magnetic dipole coupling between the nuclear spin, which has not been observed previously in a single phosphorus donor-molecule.

5.1 Design of multi-donor quantum dot device

This section introduces multi-donor quantum dots device designs, which are versatile and allow for the investigation of the nuclear spin dynamics in multi-donor quantum dots. After the device design is introduced, we demonstrate measurements of a first device at milliKelvin temperatures. Based on high quality imaging of the donor quantum dots, and measurements of their charging energies at cryogenic temperatures, we determined the donor number. In particular we demonstrated that the approximate donor configuration within the dot could be determined from matching precise measurements of the quantum dot charging energies with tight-binding simulation of multi-donor quantum dots. Finally we present spin readout on one of the quantum dots with 83% fidelity. The device in this chapter was fabricated by this author and Michael Jones, with help and supervision by Dr Yousun Chung. The device was measured by this author, with help by Michael jones, Dr Yousun Chung and Sr Matthew House. The data analysis was performed by this author. The tight binding simulations were performed by Abu Mohammad Saffat-Ee Huq

from Professor Rajib Rahman's group.

5.1.1 Design and modelling of triple-dot device B016

This section first introduces the design specifications of the devices used in this chapter, before briefly summarising the optimisation process leading to the chosen device design. The devices investigated in this chapter are to contain three tunnel-coupled quantum dots, a natural progression from the well-established two-quantum-dot design [4, 9, 10]. The additional quantum dot is intended to provide important statistical information on how different donor numbers within each quantum dot affect the sensor-to-qubit tunnel rate and the interdot exchange. Each multi-donor quantum dot can potentially host an electron and a nuclear spin qubit. The device is to be designed so that the three quantum dots can be operated independently. Each electron spin qubit therefore needs to be able to be initialised, controlled and read out independently. The device will have a microwave antenna to enable independent control of the electron and nuclear spin qubits hosted on each quantum dot. Furthermore, the three quantum dots are to be patterned so that an exchange based two-qubit gate is possible between two of the three pairs of electron spin qubits (the three quantum dots therefore form a chain). These versatile design specifications are compatible with the long term goal of demonstrating a surface-code stabiliser using precision-placed donors in silicon. A stabiliser is the fundamental building block of the surface code error-correction algorithm, and relies on an ancilla qubit performing a single parity measurement (or stabiliser) on a pair of data qubit (see Sect. 2.1.1). In the following the quantum dot in the centre of the three-dot chain will be referred to as the ancilla, while the outer two quantum dots will be referred to as the data quantum dots (or qubits).

Independent operation of each of the three quantum dots rests on independent electrostatic control of the system's charge states and requires :

- the ability to define three independent qubits using three unpaired electron spins,
- a large enough gate range to access the charge states of the device necessary for initialisation and readout of the qubits and for execution of two qubit gates,
- a design to allow for high fidelity operation (initialisation, readout, single-qubit and two-qubit coupling).

This will necessitate careful design of the dot location, and coupling to each other as well as to reservoir. We only consider exchange-based two-qubit gates, the most widely studied of the gates in single-spin qubits. Also, we will use a single-electron transistor charge sensor that, to date has demonstrated the highest fidelity spin readout [11] and promises very large measurement-bandwidths when operated using radio-frequency signals [12]. For spin-readout, we will rely on spin-to-charge conversion using spin-selective tunnelling of the electron spin to a reservoir, since this method has demonstrated the highest fidelities in donor based qubits system [9].

Design of the three-dot device

Electrostatic control Full electrostatic control of the charge states on three independent quantum-dots requires at least three independent electrostatic gates [13]. We label the charge state on the three dots by $n_{\mathrm{L}}, n_{\mathrm{M}}, n_{\mathrm{R}}$, where the integers n_{L}, n_{M} and n_{R} define the charge state in the left data qubit, the (Middle-) ancilla qubit and the right data qubit. The three left, middle and right metallic gates can be placed at electrostatic voltages V_{L}, V_{M} and V_{R} respectively by dedicated voltage sources. A schematic of such a device is sketched in Fig. 5.1a, together with a single electron transistor. This design demonstrates a natural mirror symmetry present with the two data qubits being identical.

The presence of three electron-spin qubits on three donor-quantum-dots requires the system to be initialised with an unpaired electron spin on each of the three dots, corresponding to a charge state $(n_{\mathrm{L}}, n_{\mathrm{M}}, n_{\mathrm{R}})$, where the n_i are odd numbers. Without loss of generality we will use a $(1, 1, 1)$ charge region as an example. In order to perform an exchange based gate between the ancilla qubit on the middle dot and the left(right) data qubit, the wavefunction of middle dot needs to be made to overlap with the left(right) electron's wavefunction. In donor quantum-dot, this can be implemented by an electric field gradient that pushes one of the electron's wavefunction towards the other one, so that both electrons nearly occupy the same dot orbital in a singlet state. In practice, an exchange-based two-qubit gate that couples the ancilla qubit to the left and right data qubit therefore requires that the $(1, 1, 1)$ charge region is connected to the $(2, 0, 1)$ or $(0, 2, 1)$ charge states on the left, and $(1, 0, 2)$ or $(1, 2, 0)$ on the right (see Fig. 5.1b) within the device gate space. Equivalent charge states can also be found by adding any even number to any electron number in the triplet $(n_{\mathrm{L}}, n_{\mathrm{M}}, n_{\mathrm{R}})$. Figure 5.1b presents a schematic charge stability-diagram of the ground state charge state as a function of the voltage on the left, (n_{L}) and right, (n_{R}) electrostatic gates, for a typical device as sketched

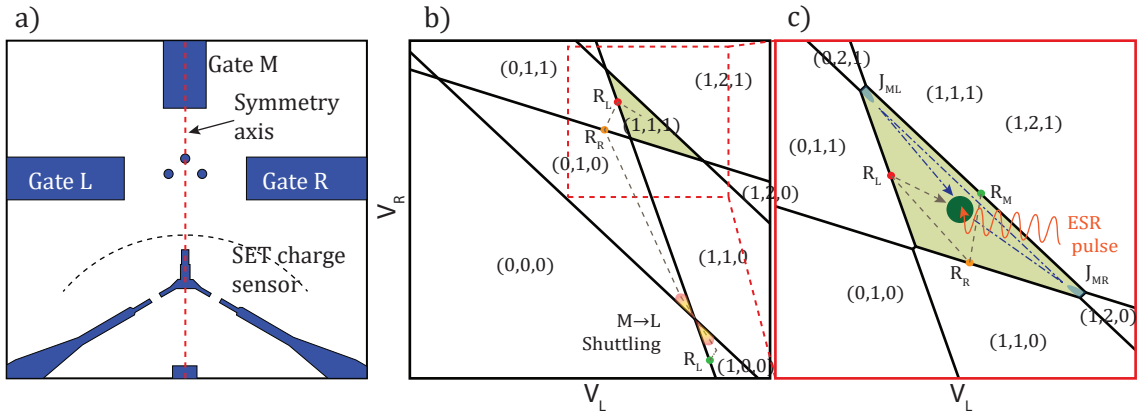

Figure 5.1: **a) Design of a triple dot exchange based spin qubit:** Schematic of three gates needed for independent electrostatic control of each dot. The centre dot is the ancilla, whilst the outer dots are the two data qubits. The single electron transistor occupies the lower half plane. The equivalence of the two outer data qubit forms a natural symmetry axes indicated by the dashed red line.
b) Schematic charge stability diagram when the middle dot is not coupled to the SET reservoir: Here we plot the charge states of the triple dot device as a function of V_L and V_R. The green triangular region corresponds to a region where all charge state on each dot are odd. When the middle dot is too far away from the SET reservoir, an electron needs to be shuttled to one of the outer dots (here the left dot). A possible trajectory through gate-space is depicted by the grey dashed line. The readout positions are labelled by coloured circles labelled R_d, where $d = L, M, R$ represents the dot which is brought in resonance with the reservoir Fermi-level during spin-readout. Accessing an anti-crossing involves a significant voltage pulse, which can be experimentally challenging and highlights the practicality of having all three dots coupled to a reservoir.
c) Stabiliser protocol when all three dots are coupled to a reservoir: In this schematic charge stability diagram all three dots are tunnel coupled to the SET reservoir. Now initialisation and readout can be performed in the same manner, as represented by the grey dashed line. Single qubit control via ESR pulsing is operated deep within the all-odd charge region, as represented by the dark green disk. The two-qubit gates can be operated at the higher and lower edges of the all-odd charge stability region (grey regions), where the exchange interaction J_{ML} and J_{MR} coupling the middle to the left and right electrons respectively. can be switched on. A possible pulse sequence is indicated by the dark blue dashed line.

in Fig. 5.1a where the middle dot is further away from the SET charge sensor and therefore not tunnel coupled. In general, applying larger voltages to the gates lead to deeper potentials at the qubit and the number of electrons in the system increase. A $(1,1,1)$ charge state, compatible with surface code operation can be seen in the centre of the diagram. The passing of boundaries between charge states corresponds to charge redistributions, either from one dot to another or between dots and an electron reservoir.

The exchange gates are operated close to the edge of the $(1,1,1)$ charge-stable region, near the neighbouring regions that contain an even singlet charge state (see coloured regions J_{ML} and J_{MR} in a closeup Fig. 5.1c of the gate map in b). To achieve an exchange-based gate, the value of the exchange coupling is set to a value of typically a few GHz by the separation of donors and by then pulsing the gate voltages to a position in proximity to this charge-state boundary. The gate timing of a few nanoseconds is calibrated to that value of exchange coupling. For high-fidelity exchange based gates it is important that the voltage pulses reach this voltage position quite precisely because the exchange coupling magnitude is very sensitive to electric field [10, 14]. In practical devices, the amplitude of such fast voltage pulses needs to be restricted to values of about 100mV to avoid rearrangements of charges within the semiconductor lattice. For practical reasons, the central $(1,1,1)$ charge-region therefore needs to be electrostatically tunable by the gates, so as to not span more than about 100 mV in gate-space. Such tuning is possible with three independent electrostatic gates, and is facilitated by maximising the coupling of the middle gate to the middle dot while minimising its coupling to the outer ones, i.e. by maximising the differential coupling of the gate to the two dot pairs (see Sect. 5.1.1).

The need for fast, high fidelity single shot electron spin readout further informs the device design. Electron-spin readout through spin-selective tunnelling requires at least one of the three quantum-dots to be tunnel-coupled to a reservoir (this reservoir can also be practically used simultaneously as a gate). Electrons trapped on different dots can then be shuttled to that reservoir-coupled dot, and read-out. It is however more useful if all three quantum-dots are tunnel-coupled to a reservoir as this allows all three dots to be read-out at the boundary of the (1,1,1) charge-stable region, and minimises the magnitude of voltage pulses (see readout positions $R_{\mathrm{L}}, R_{\mathrm{M}}$ and R_{R}) in Fig. 5.1c). If the middle-dot is not tunnel-coupled to the readout reservoir, the middle dot electron needs to be shuttled to one of the outer dots and readout out from that dot. This will require relatively large voltage pulses and is therefore not ideal due to possibility of noise activation (see full pulse sequence in

Fig. 5.1b).

Ideal donor configuration in ancilla and data qubits An exchange-based design that allows two independent two-qubit gates coupling the ancilla-qubit to both the left and right data-qubits requires the $(1,1,1)$ charge region to be connected to the $(2,0,1)$ or $(0,2,1)$ charge states on the left, and $(1,0,2)$ or $(1,2,0)$ on the right. Indeed, the exchange coupling between two donor QDs has traditionally been implemented by applying in-plane electric fields that tilt the potential landscape between the two QDs. A new approach pioneered in gate-defined quantum dot uses electrostatic barrier-gates that lower the electric potential between the two QDs instead [15]. This technique that was shown to increase the resilience of two-qubit gates to charge noise is currently under investigation in our group but is not considered in this thesis. If we consider the case where the $(1,1,1)$ charge state is connected to a $(0,2,1)$ or $(1,2,0)$ charge state for exchange coupling between the middle and the left(right) electron spin (see Fig. 5.1c) we require the middle dot chemical potential to allow for tunnelling-in of a second electron, while it requires the single electron on the outer dots to be nearly tunnelling-out. If all three donor-quantum dot were defined by single donors, we would require the difference in chemical potential to be equal to the single donor charging energy of 46 meV. Assuming typical differential gate lever-arms of 1 to 5% between the in-plane gates, voltage differences of between 1 to 5 volts would need to be applied to the gate. Experimentally, for in-plane gates separated at their closest point by $\sim$ 50 nm, voltage differences above about $\sim$ 1 V lead to a Landau Zener breakdown of the silicon semiconductor, where valence electrons can tunnel to the conduction band edge. This is undesirable as it leads to heating of the sample and the likely formation of charge traps between the gates. In practice, it would be challenging to implement the stabiliser protocol with three single donor qubits. A relatively simple solution to reduce the chemical potential difference between the inner and outer quantum dots, is to use different numbers of donors in the middle quantum dot. Larger donor dots with many electrons have demonstrated charging energies below the 46 meV (see Sect. 5.1.4) which can therefore meet the differential voltage requirement. Furthermore, the chemical potential of a desired n_{M} to $n_{\mathrm{M}}-1$ transition, is unlikely to be aligned with the n_{i} to $n_{\mathrm{i}}-1$ chemical potential of the outer dots, so in practice the chemical potential difference can be lower than the middle dot's charging energy. For our first device implementation we therefore aimed to pattern one or two donors in the outer data qubits and a 3-donor dot for the central ancilla qubit.

The number of donors patterned during STM-lithography can be controlled by

engineering the size of the hydrogen desorption site. Statistical studies of phosphorus incorporation by Füchsle [16] indicated that an opening of three dimers, has a 70% chance to yield a single donor, and a 30% chance to incorporate no donor at all (see histograms in Fig. 5.2b). This is in accordance with the theoretical understanding of phosphine dissociation and incorporation pathways [17, 18, 19]. For the outer data qubit of the parity device, an opening of 4 dimers has the advantage of a lower probability (20%) to not incorporate a donor at all (55% for a single, and 20% for two donors). This is beneficial as we typically only assess the success of the incorporation process during the first measurement in liquid helium, after a week-long cleanroom-fabrication process. It is challenging to reliably desorb precisely the desired number of dimers, so we aimed for a 4-dimer opening during device fabrication for the outer data qubit of the three-dot device. Assuming an equal probability to obtain a 3-, 4- or 5-dimer opening, this would yield a 60% chance to incorporate a single phosphorus atom, a 26% to incorporate two, and only a 14% chance not to incorporate any atom. The appropriate lithographic opening size for the 3-4P ancilla donor-dot can be estimated using the estimated 0.25 ML phosphorus donor density after incorporation of a saturation dosed bare silicon surface [17], and corresponds to 6 to 8 dimer lithographic openings.

The yield of donor incorporation using the 4-dimer lithographic opening as presented above is sufficient for the device required for this chapter, with a 70% chance that both dots incorporate one or two donors each. For devices containing more than a few dots this yield needs to be increased to obtain the exact desired donor number on each dot. Fabrication techniques which significantly increase the yield for incorporating the desired number of donor exist and have been patented by our group [20]. Most such techniques rely on the in-situ characterisation of the donor number after incorporation using the STM tip [1]. By patterning a lithographic opening that allows at most the desired donor number to incorporate, the surface can be imaged to assess if the desired number of donors has incorporated. The process can be repeated until this is the case. This strategy was employed at room temperature by Fuechsle *et al.* to pattern the first single atom transistor [22]. Fuechsle *et al.* assessed the donor number by inspecting the surface for a silicon atom that was ejected by the incorporated phosphorus atom. More precise spectroscopic techniques exist to image the incorporated phosphorus atoms itself using the STM tip. This was demonstrated on a single atom at room temperature [21] and on coupled phosphorus donors at 4 K [23]. These techniques could be used to not only assess

[1] Note that the lithographic mask remains after incorporation [21]

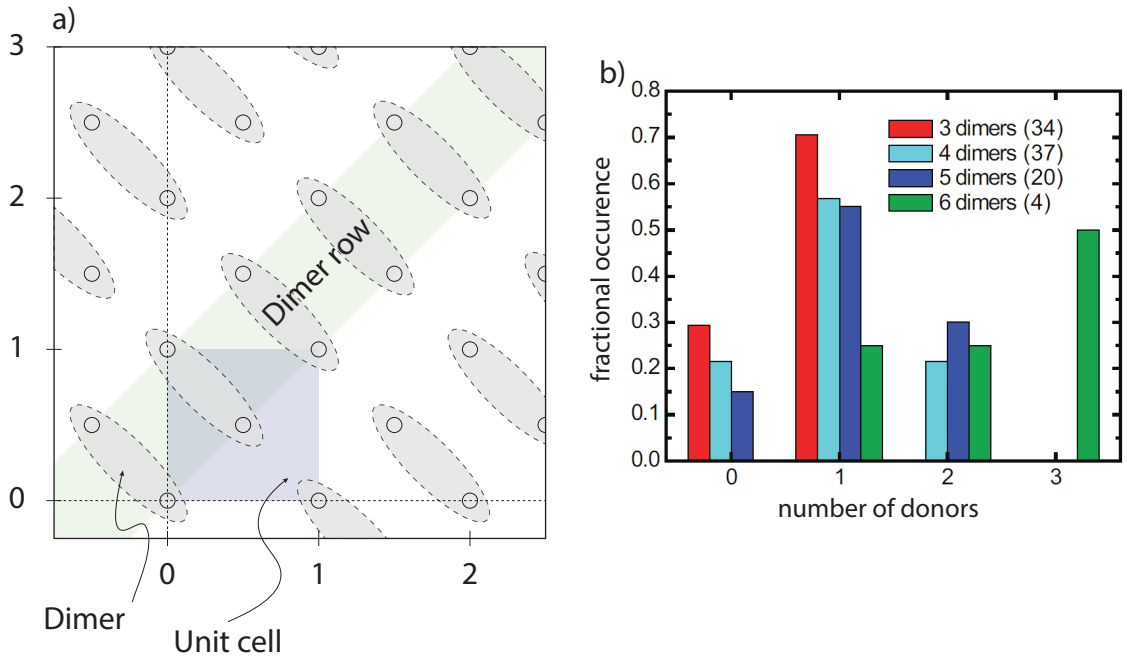

Figure 5.2: **a) Si(100) 2×1 reconstructed silicon surface.** Silicon atoms rearrange into pairs of atoms called dimers, that form dimer rows running diagonally through the unit cell. **b) Incorporation statistics of phosphorus donors in silicon as a function of the number of bare silicon dimers opened up during hydrogen-resist STM-lithography.** An opening of 4 dimers, has a 55% probability to yield a single donor, with only a 20% probability to not incorporate any donor. Figure b) adapted from ref.[16].

the number of incorporated donors but also their configuration within the silicon lattice. Importantly, recent advances in low-temperature lithography could provide higher yields [20]. Combined with techniques such feedback-controlled single hydrogen desorption [24] and voltage-pulse induced donor incorporation [25] (instead of incorporation by global heating), high yield deterministic lithography of donor quantum dot should be achievable.

The practical requirement that all three quantum dot are tunnel-coupled to a reservoir for readout of the electron spins requires all three dot-to-reservoir distances to be optimised for reliable single-shot spin readout. Experimentally, dot-reservoir distances of $\sim$ 19 – 20 nm have yielded 200 Hz tunnel-rates for the first electron on a single donor (1P) [4, 9, 26]. This is well below the achievable bandwidth ($\sim$ $1MHz$) of state-of-the-art SET charge sensors [12], so it was decided to decrease the distance between the 1P donor qubit and the SET reservoir to $\sim$ 17 nm for the first device to increase the tunnel-rate to a desired 10 kHz.

The optimal inter-dot distance required to achieve ∼GHz tunnel-coupling between the two tunnel-coupled donor quantum dot qubit was unknown at the time

this device design. Previously measured values of inter-dot tunnel-coupling ranged from 0.2 GHz to 11 GHz, for distances from 11.5 nm to 16 nm, and donor dot configurations of 2P-3P (with four electrons) and 2P-1P (with two electrons) in ref.[27] and [28] respectively. Tight-binding simulations by Wang *et al.* estimated that an inter-donor separation of $13-14$ nm would yield the desired value of tunnel-coupling for a 2P-1P system (with two electrons). A value of 13 nm was decided for the first iteration of the triple-dot.

The differential coupling of the middle gate V_M, to the inner/outer dot pairs L and R can be maximised by orienting the qubit pairs parallel to the electric field produced by the middle gate. The electric field of the middle gate near the quantum dots is oriented parallel to the the North-South axis of Fig. 5.1a due to the quantum dots being patterned near the symmetry axis of the device. The differential coupling of the middle gate to the middle dot is therefore increased by patterning the middle gate higher than the outer dots. The constraints imposed by the dot-reservoir and dot-dot distances yield a device geometry sketched in Fig. 5.3a with the three dots forming an isosceles triangle with the angle at the middle dot being 130° (23° from horizontal).

Both the SET charge sensor or the middle gate can serve as the electron reservoir (again conserving mirror symmetry). To date, donor based qubits fabricated by STM-hydrogen lithography have focused on the first approach, where the SET island serves as the electron reservoir (see design Fig. 5.4a). The SET island coupled design is attractive because it maximises the capacitive coupling between the quantum dots and the charge sensor, allowing for a single electron tunnelling event to fully switch on or off the current flowing through the single electron transistor [9, 12]. Such strong sensitivity allows for high-fidelity electron-spin readout [9, 12]. However, the current flowing through the resistive tunnel-gaps of the SET itself can lead to heating of the electrons in the charge sensor [12]. This electron heating smears the Fermi distribution of the electrons in the reservoir, and can limit the fidelity of the energy-selective spin readout, which requires a sharp Fermi distribution [29]. The limitation of the electron spin readout fidelity due to SET heating is especially problematic for more resistive SETs, which dissipate more heat for the same amount of current (and thus DC signal). This is the case for the device B016 presented in this chapter. The alternative SET island "gate-coupled" design in which each of the quantum dots are tunnel-coupled to an independent reservoir gate instead of the SET could reduce the thermal coupling between the charge sensor reservoir and the qubit. This would reduce the electron temperature and help increase the readout fidelity. Furthermore,

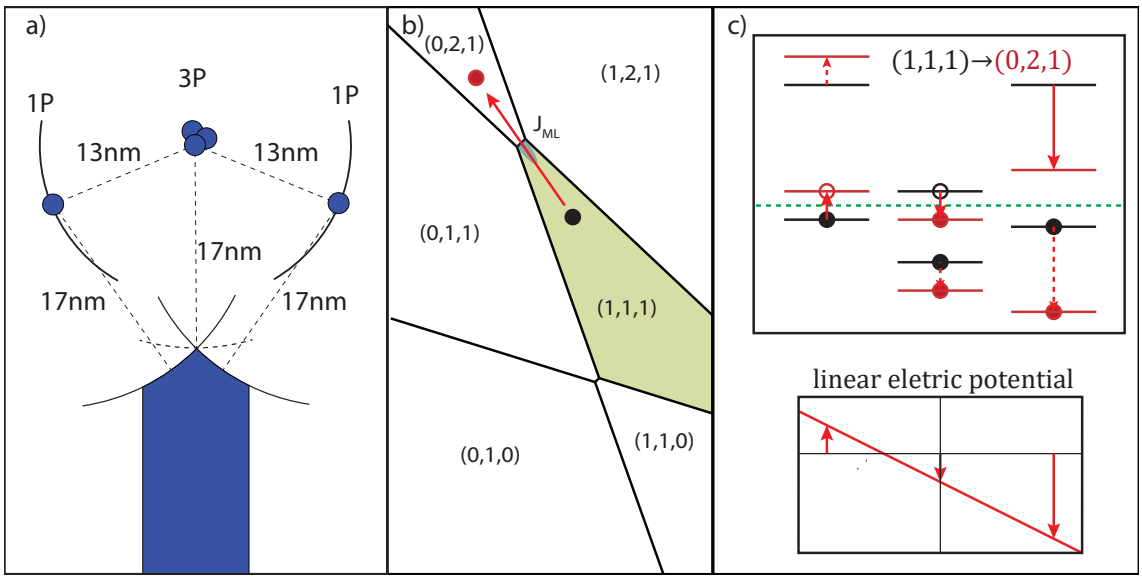

Figure 5.3: **a) Optimal SET island reservoir design of inter-dot and dot–reservoir coupling. Coupling in a triple donor qubit device.** To keep the dots all at $\sim$ 17 nm from the reservoir but ensure maximal differential coupling between the gates and the dots, we offset the outer dots and shape the SET island reservoir.
b-c) Engineering the electrochemical potential of the triple donor dot to ensure we achieve a (0,2)-(1,0) inter-dot transition for a 2-qubit gate. Accessing the (1,1,1)-(0,2,1) transition region (J_{ML}) purely via detuning potentials (c)lower), requires the middle dot electric potential to be tuned very close to the $1 \mapsto 2$ electron transition, whereas the other dots are tuned closer to the $0 \mapsto 1$ electron transition. This can be facilitated by engineering the inner dot to have different binding energies than the outer dots, as shown by the schematics of chemical potentials in **c)**.

the SET charge sensor could be operated at higher powers to increase the signal-to-noise without increasing the electron temperature and affecting the readout fidelity. Decreasing the separation of the quantum dots from the SET however also reduces the capacitive coupling between them, and the change in SET current produced by a single electron tunnelling event. This compromise between heating and capacitive coupling was investigated in detail in a separate PhD thesis by Michael Jones [7], based on the gate-coupled triple dot fabricated in this thesis. These devices were made together with Michael Jones. However, the results on electron heating on this device are presented in a separate thesis by Mr. Jones. The dependence of the electron-temperature on the power applied to the charge sensor was found to be much weaker in the gate-coupled device when compared to SET coupled ones. Simulations by Michael Jones based on this measured heating behaviour reveal that the robustness against heating largely outweigh the decrease in the signal strength (see [7]).

The two different device designs are shown in Fig. 5.4a and b respectively. The spacing and positioning of the electrodes results from optimisation of the capacitive electrode to dot coupling while respecting the heuristic constraints imposed by leakage. The devices presented in this thesis are all based on the first "SET-coupled" design of Fig. 5.4a.

5.1.2 Atomic Precision Lithography and Growth

Figure 5.5 displays a scanning tunnelling microscope (STM) image of a triple-dot device made according to the SET island reservoir coupled design. From the STM images taken after phosphine dosing, we can observe the placement accuracy of the three donor-quantum dots of ± 0.3 nm for the outer dots and with the middle quantum dot being placed 1 nm further than intended. A first estimate of the number of donors within each dot can be made from analysis of high resolution images of the dot lithographic openings, before and after phosphine dosing as shown in Fig. 5.5 c-e and f-h respectively. Here the desorption sites on the left and right dots were planned to be 4 ± 1 dimer long, on a single dimer-row with the aim of incorporating a single phosphorus donor with high probability ($\sim$ 60%). Figure 5.5c and e show the lithographic desorption patches of 4 and 3 dimers for the left and right dots respectively, on the same dimer-row, with two single hydrogen desorption dangling bond sites likely having occurred on the adjacent dimer-row for the right dot as labelled (below the main desorption site). The image of the left dot after phosphine dosing (Fig. 5.5f) shows four PH_2 species having attached to the dangling bonds of

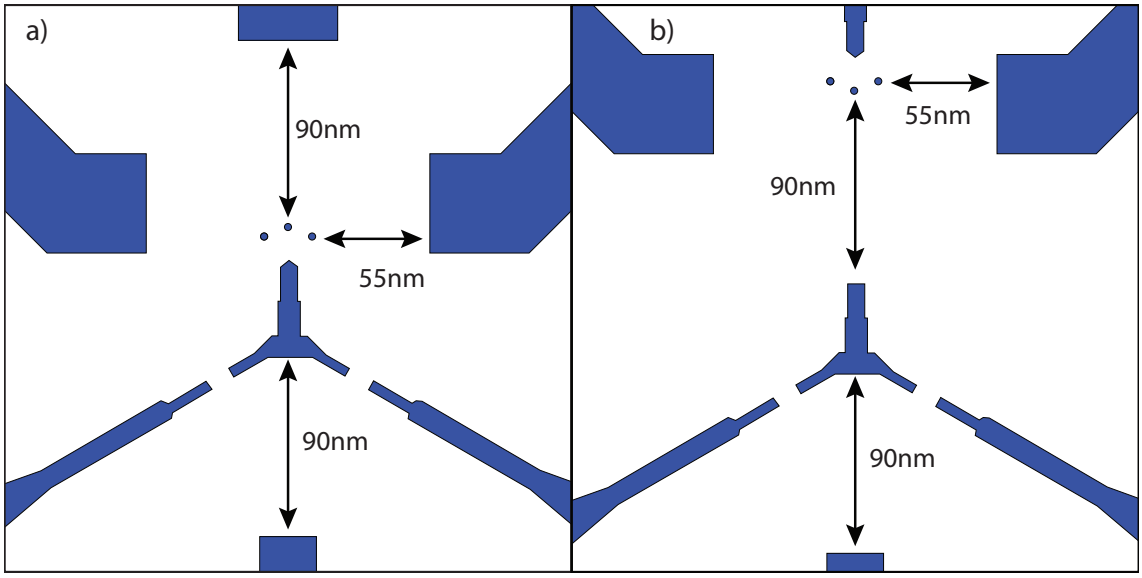

Figure 5.4: **SET versus gate coupled triple dot designs.**
a) SET coupled design made the SET island acts as the electron reservoir. The distance from the gates to the dots and other gates is limited by in plane gate leakage. The electrostatic advantage of having a bigger lever arm is balanced by the limitation of electric field due to the earlier onset of gate leakage. **b) Gate coupled design.** In this design, the middle gate acts as the electron reservoir. The gate positions are determined by electrostatics and a heuristic understanding of gate leakage ranges.

the four bare dimers in a zig-zag pattern. The absence of any dangling bonds in the four dimer patch indicates that as expected [17, 18, 19] the third hydrogen atom of each phosphine molecule has attached to the remaining silicon atom of each dimer. The image of the right dot after phosphine dosing (Fig. 5.5e) shows two similarly off-centred bright features that can also be attributed to PH_2 molecules attached on the bare dimers. Also one brighter feature that is centred on the dimer-row is visible in the right dot that can be attributed to a PH species. This PH species is one step ahead in the dissociation process of phosphine on the silicon surface. From what is known of the incorporation process of phosphine species on silicon surfaces, we expect that both dots will yield one or two donors as the device design required.

For the centre dot, the desired number of donors (3 to 4) can be achieved with a large lithographic opening of 6 to 8 dimers. A 5 dimer patch was opened, showing a few hydrogen atoms desorbed on the neighbouring dimer-row (see Fig. 5.5d). After phosphine dosing, 6 phosphine related species are visible on the surface, with two PH_2 molecules on the main dimer-row, and on having attached to the dangling bond on the neighbouring dimer (see Fig. 5.5g). Three instances of an unidentified phosphine species (labelled PH_x) have attached on the main dimer row. The features appear centred on the row, like a PH molecule, but are less bright and lower in height

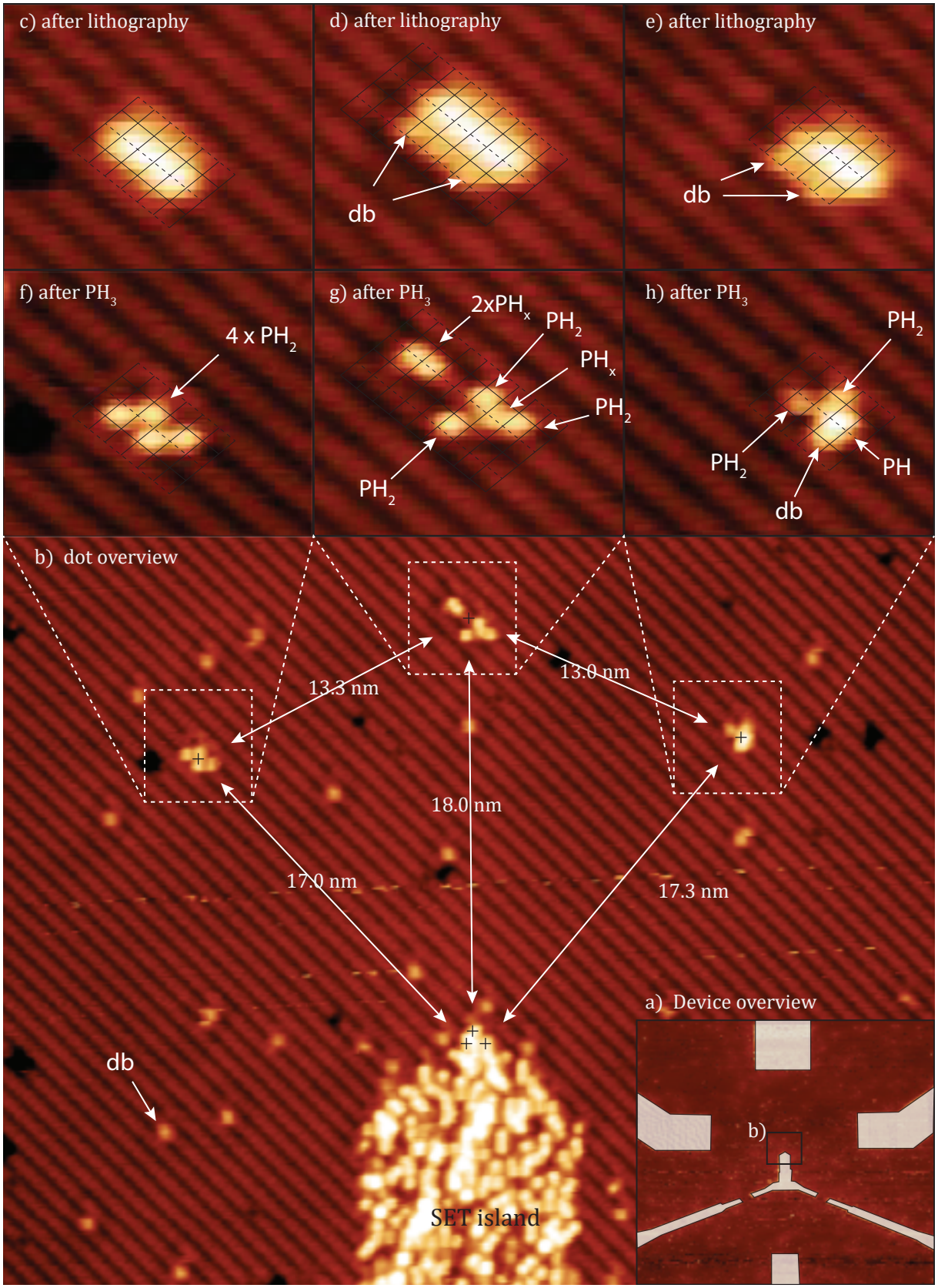

Figure 5.5: **Lithographic design and phophine dosing of a triple dot device tunnel coupled to an SET island reservoir (BO16).**
a) STM image of the hydrogen desorbed regions (highlighted by grey regions). The dots are coupled to the top of the SET island (within the black outline).
b) STM image of the black outline in a) showing the inner device region after PH_3 dosing. The tip of the SET island is visible on the bottom with the characteristic triangular shape to guarantee tunnel coupling of each dot to the reservoir, while maximising individual electrostatic control.
c-e) L, M, R dot closeups after lithography.

and resemble the size and brightness of the other PH_2 molecules. The position of the topmost PH_x species where the silicon surface was not exposed, indicates that some movement of the hydrogen and PH_x species has occurred. Due to the unknown features and complexity of the arrangements of phosphine, it is unclear how many of the 6 phosphine species are likely to incorporate in the middle-dot.

An analysis of the three different donor-quantum dot charging energies however in Sect. 5.1.4 allows us to determine the number of donors in each of the three quantum dots.

5.1.3 Electrostatic control of all three quantum dots

After cool-down of the device in a dilution-refrigerator with 50 mK base-temperature, the presence of the donor-quantum dots can be assessed by measuring the current through the SET as a function of left and right gates (see Fig. 5.6). Here we can detect charging events of each of the dots, using the single electron transistor (SET) patterned in proximity to the dots. Such charging events produce changes in the DC-current passing through the SET, under a voltage bias using the source and drain leads. These charging (or discharging) events only happen when the chemical potential of the quantum-dot is aligned with the Fermi-level of the electron-gas populating the source and drain leads of the SET (and by extension the SET island). Indeed when the chemical potential of the dot is aligned with the Fermi-level of the reservoir, an electron in the Fermi-sea at the Fermi-energy of the SET island has enough energy to move to the quantum dot. In Fig. 5.6b, the bright diagonal lines running at a slope of about -1, correspond to gate voltages at which the chemical potential of the SET island is in between the Fermi-level of the source and the drain leads, allowing for current to flow between the SET source and drain. In the darker regions of the plot the chemical potential of the SET is outside the source and the drain Fermi level, and no current flows through the SET: the SET is in Coulomb-blockade. Charging events where electrons move from the SET island to the quantum dot appear in such a gate-map as lines along which the SET-peaks are broken, due to the quantum-dot charging events shifting the SET chemical potential through capacitive coupling of the dot to the SET island. The slope of these lines are indicative of the relative capacitive coupling strength of the two gates to the quantum dot. Due to the mirror symmetry axis running from the middle gate through the middle-dot and the SET island, we expect the left and right gates to be equally coupled to the SET and the middle dot. This is reflected in Fig. 5.6b by the SET charging lines running at a slope of -1, as well as by three charging lines

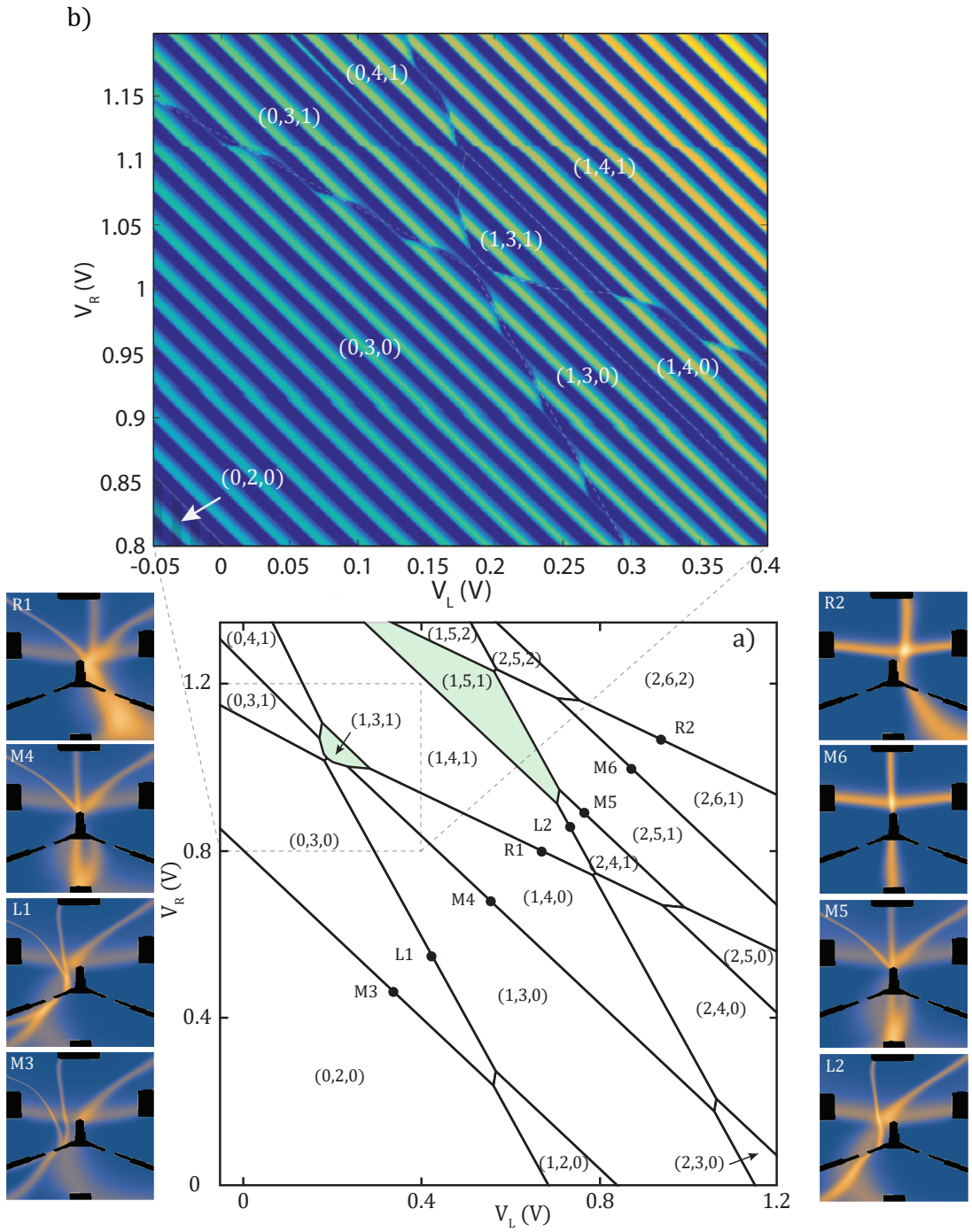

Figure 5.6: **Charge stability diagram of a triple dot B016 with.**
a) an overview schematic of the charge stability map where $V_M = 0.1V$. The black lines indicate electron charge transitions between charge stable regions. Four middle dot transitions are visible within the gate space (M1-M4), and two transitions are visible for the outer dot(L1, L2, R1, R2). The electron charge numbering is confirmed by spin and singlet triplet experiments (modulo 2 for the middle dot). The shaded green charge regions correspond to all-odd charge regions compatible with the stabiliser experiment.
a) (outer images): each colour map represents electrostatic triangulation of the charge transitions. These yellow fog maps highlight the region in the device that gives rise to the charge transition's slope in a particular gate-gate map. The intersection of the yellow regions yields the most likely location of the quantum dot charge centre in the lithographic plane. This confirms the labelling of each transition (yellow, green, blue from dots L, M, R) in the gate-gate map a).
b) gate-gate map showing the I_{SET} as a function of V_R and V_L with a closeup of the (1,3,1) charge region outlined in a).

(yellow/left dot, green/middle dot, blue/right dot) running at a similar slopes. Two other charging lines running at a more (less) negative slope, are indicative of the dot being off-centre, and more (less) capacitively coupled to the left gate, and likely correspond to the left (right) dot.

A multitude of high resolution gate maps as in Fig. 5.6b can be combined together to yield a large gate-map as sketched in Fig. 5.6a. Additional charge transitions on the dots are also detected at larger gate voltages but they all share one of the same three slopes as in (b). In total, we observe four charge transitions that can be attributed to the middle dot, and two charge transitions for each of the outer dots. This allows us to assign the total number of electrons on each dot as in the map, e.g. (0,2,0). The assignment of the transitions to the dots visible in the STM images in Fig. 5.5, can be further supported by electrostatic simulation of the device using a finite element solver[2]. The electrostatic simulation relies on the slope γ of a particular dot transition in the gate map V_{g2} (y-axis) vs V_{g1} (x-axis) being related to the ratio of the lever-arm $\alpha_{g,d}$ of the gate g to the dot d:

$$\gamma^{d}_{g_1,g_2} = -\frac{\alpha_{g_1,d}}{\alpha_{g_2,d}}. \tag{5.1.1}$$

The lever arm $\alpha_{g,d}$ of a gate g to a dot d corresponds to the change in chemical potential at the dot when the gate's voltage is increased by 1 V : $\alpha_{g,d} = \Delta\mu^{d}_{g}/\Delta V_g$. The gate lever-arm can be simulated by the finite element solver by calculating the electric potential $\phi_g(r_d)$ produced by each gate, while held at 1 V while the other are held at ground. The lever-arm $\alpha_g(r_d)$ of that gate to a quantum dot at the position r_d can then simply be estimated by the electric potential $\phi_g(r)$ at that point: $\alpha_{g,d} \approx \alpha_g(r_d) = \phi_g(r)$. In this manner, a two-dimensional map of the simulated lever-arm ratios of the two gates can be produced:

$$\gamma_{g_1,g_2}(r_d) = -\frac{\phi_{g_1}(r)}{\phi_{g_2}(r)}. \tag{5.1.2}$$

Matching this simulated ratio $\gamma_{g_1,g_2}(r_d)$ to the ratio $\gamma^{d}_{g_1,g_2}$ measured from the gate map then yields a one dimensional contour within the lithographic plane, and is depicted as yellow linear regions in the insets of Fig. 5.6a. Repeating this procedure with another independent electrostatic gate then yields another contour line. The point at which the contours intersect gives an approximate location of the quantum-dot associated with the charge transition.

[2]COMSOL

The procedure outlined above has been performed on all eight transition in Fig. 5.6b, as depicted in the outer images of Fig. 5.6b. The intersection of the contour lines for most of the transitions match the approximate location of the dots estimated from the STM images.[3]

These electrostatic simulations allow us to estimate the electron numbering for each charge transitions as shown in Fig. 5.6. These numberings are confirmed by subsequent analysis of the three dot charging energies in the next section along with information on the parity of the transitions inferred from spin-readout measurements and singlet-triplet readout measurements. Two charge stable regions exist where all the quantum dots contain an un-paired electron suitable to act as a qubit as observed in the gate-map in the $(1, 3, 1)$ region and the $(1, 5, 1)$ region. The $(1, 3, 1)$ charge stable state is delimited by two charge-stable regions ($(0, 4, 1)$ $(1, 4, 0)$) compatible with exchange-based two-qubit gates between the centre dot and the outer dots (left and right respectively). Importantly, both these charge states are accessible within the gate-space allowed by gate leakage, V$\leq$1V. The $(1, 3, 1)$ region with $V_M \sim 0.1V$ is about 100mV across such that it is compatible with realistic pulse amplitudes to conduct the exchange-based 2-qubit gates, as well as readout and initialisation of the electron spins.

Demonstrating tunability of pentagon The size of the $(1, 3, 1)$ region, which is compatible with two qubit experiments, can further be tuned by use of the middle gate. The middle gate is more strongly coupled to the middle dot than to the outer dots. This demonstrates that the device design provides enough differential coupling of the gates to the three dots to allow us to reduce the size of the region in future implementations of the device, where the all-odd charge region is too large for the amplitude of high-precision voltage pulses needed for 2-qubit gates and qubit readout. Indeed, the $(1, 3, 1)$ charge-stable, which is about 150 mV across for $V_\mathrm{M} = 0\,\mathrm{V}$ can be reduced in size until the charge region nearly vanishes at $V_\mathrm{M} = 0.3\,\mathrm{V}$, at which point a new charge-stable region $(0, 4, 0)$ appears and grows further in size for larger middle-gate voltages.

5.1.4 Estimation of donor number and configuration

The number of donors in each of the three donor-quantum dots in B016 shown in Fig. 5.5 can be pinpointed more precisely by measuring their charging energies and

[3] with exception of the transition M3, where the contour lines do not intersect at the same location.

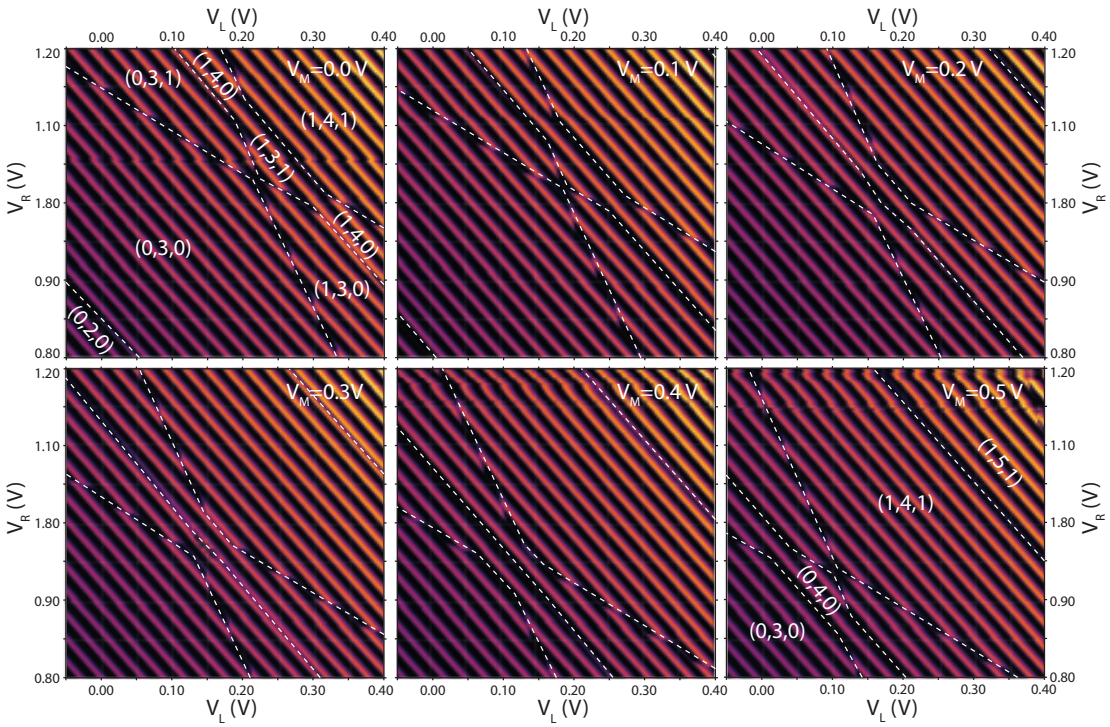

Figure 5.7: **Control of the (1,3,1) charge region size with middle gate voltage V_M.** Each plot displays a gate-gate map for the same voltage range on the left and right gate, for different middle gate voltages V_M. Note how the size of the (1,3,1) charge region can be controlled by the middle gate voltage. At $V_M = 0.3\,\mathrm{V}$, a quadruple point is formed where all three dot levels are aligned. At gate voltages above $V_M = 0.3\,\mathrm{V}$, a new charge stable region (0,4,0) appears below the anti-crossing of the L and R dot transitions.

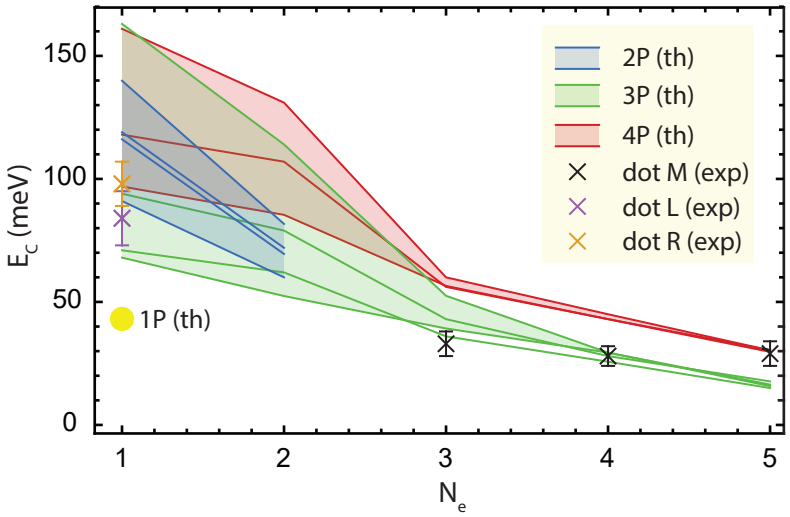

Figure 5.8: **Charging energies E_C of different donor number quantum dots as a function of the electron number.** The coloured regions show theoretical(th) values of the charging energies for 1P, 2P, 3P and 4P multi-donor quantum dots. The spread in the possible values results from the various possible donor configurations within the dot itself. Experimental(exp) values for the charging energies of device B016 are displayed by crosses. The left and right dot charging energies (purple and green circle) are compatible with simulated data for both a 2P quantum dot and a 3P quantum dot. The middle dot charging energies are more compatible with a 3P quantum dot.

comparing them to tight binding simulation performed by Saffat Huq and Rajib Rahman. The charging energy $E_c(N_e)$ of a quantum dot containing N_e electrons corresponds to the energy needed to add an additional electron to the quantum dot. The magnitude of the charging energy depends on the depth of the quantum dot's confinement potential. For small quantum dots, the addition energy decreases with the electron number N_e, as the confinement potential becoming shallower as more inner shell electrons shield the nucleus' positive charges. For donor based quantum dots containing more than one donor, the exact charging energies are also dependent on the configuration of the individual donors within the quantum dot. We can constrain the possible donor locations to those within the lithographic patches from the STM images in Fig. 5.5, yielding an uncertainty displayed by the coloured regions in Fig. 5.8 for 2P quantum dots for the left and right dots, and a 3P or 4P donor dots in the middle dot.

The charging energies of the three quantum dots are determined by measuring the gate voltages between one charge transition on a dot and the next charge transition in the gate-maps as in Fig. 5.6b. We then can compare it to the charging energy of the SET island. The charging energies obtained in this fashion are compatible with the number of donors estimated from the STM images and displayed

as crosses with error in Fig. 5.8. The outer dot charging energies of the first electron $E_c(1)$ of 84 ± 11 meV and 98 ± 9 meV for the left and right dot respectively are more than twice the value of the single donor charging energies, excluding the possibility that the outer dots are single donors as originally intended. The charging energies of both dots are compatible with both a 2P or a 3P multi-donor dot. The small lithographic patches visible in the STM images however are not compatible with the incorporation of 3 donors, so that the outer dot are likely formed by pairs of phosphorus donors (2P). The increased confinement potential created by the 2P donors (instead of 1P) will increase the confinement potential for the electrons and therefore lower the tunnel coupling. Reaching the appropriate value of the tunnel coupling is important for exchange-based gates [28]. The desired value of the tunnel coupling can however be reached by reliably patterning the 2P QDs closer to the central QD [5]. The charging energies of the middle donor quantum-dot are best fit by the simulated charging energies of a 3P multi donor dot. We note that the measurement of $E_c(5)$ is at high gate voltage where the errors are larger due to bending of the SET charging lines.

Dot	Electron number	Expected Charging Energy (meV)
R	$1 \rightarrow 2$	98±9
L	$1 \rightarrow 2$	84±11
M	$3 \rightarrow 4$	33±5
M	$4 \rightarrow 5$	28±4
M	$5 \rightarrow 6$	29±5

Table 5.1: A comparison of charging energies with uncertainty values. Here we report the charging energies for each dot as a function of both dots (left, middle, right) and electron number.

The relative locations of the donors within the 2P quantum dot qubits can be estimated by matching the measured charging energies to the values estimated from tight-binding simulations for different donor configurations. The tight binding simulations were performed by Abu Mohammad Saffat-Ee Huq from Professor Rajib Rahman's group. For both data qubits, the lithographic openings were easy to image, and restricted to less than four consecutive dimers on the same dimer-row (see STM images in Fig. 5.5, and a visualisation of the atoms within the lattice in Fig. 5.9). After the 350°C incorporation anneal, the phosphorus atoms from the PH_X absorbed species will incorporate at positions in the surface previously occupied by silicon atoms ($z = 0$ in Fig. 5.9). After incorporation however, the device

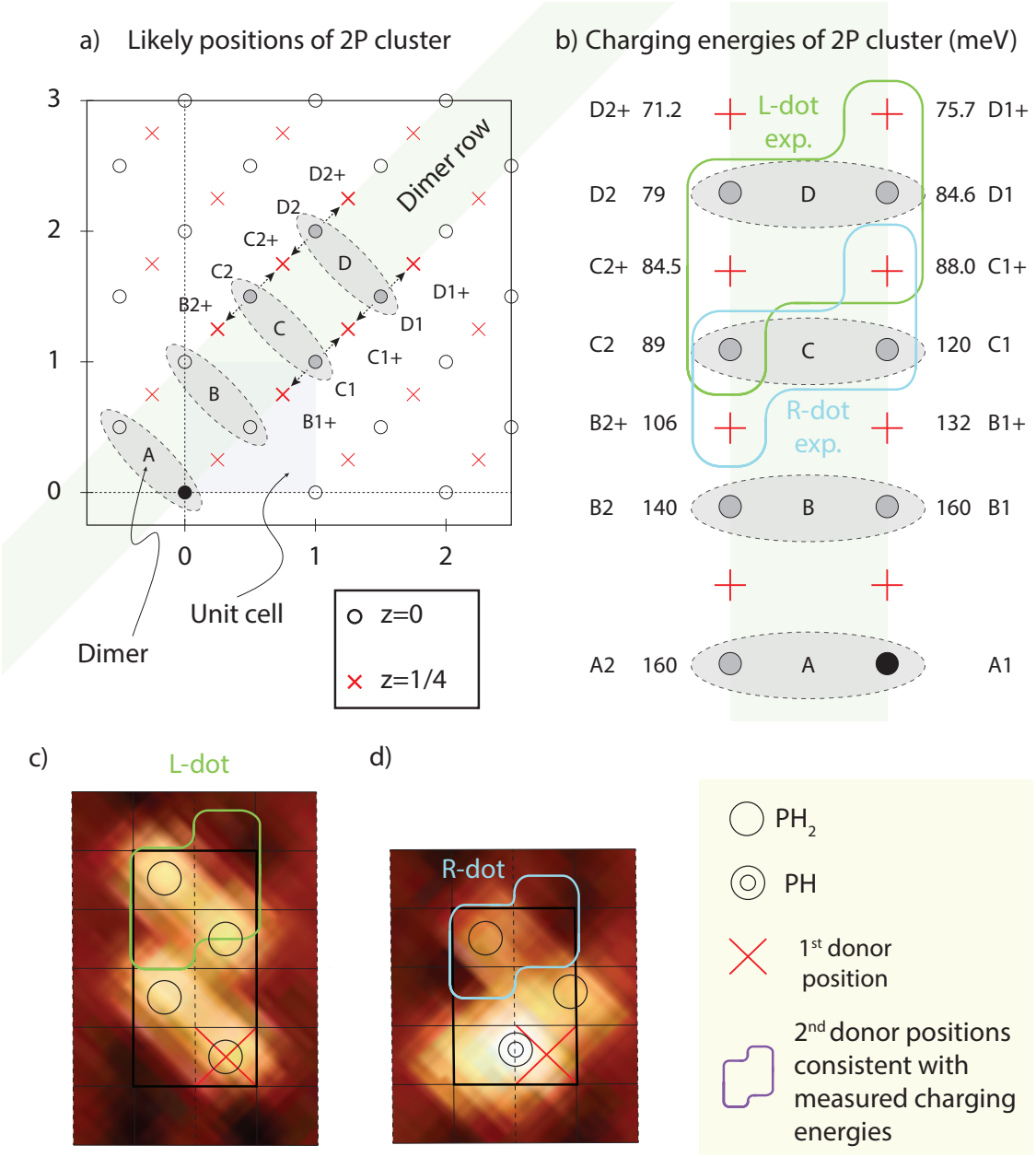

Figure 5.9: **Estimating the location of the phosphorus atoms with the left and right data qubits.**
a) A schematic of the atoms on the Si(100) 2x1 surface atom positions. Black circles represent atomic positions within the lithographic plane ($z = 0$). Red crosses indicate atomic positions one monolayer (ML) above. **b) Atomistic modelling of charging energies of a 2P quantum dot using the lithographic openings for the left dot (L-dot/green) and right dot (R-dot/blue).** Tight binding calculations of the $1 \mapsto 2$ electron charging energy, dependent on the position of the second donor (grey filled circle or red cross), from the first (black filled circle). The experimental values of the charging energies for the L and right dot on device B016 are 84 ± 11 meV and 98 ± 9 meV. These values are compatible with the second donor positions indicated by the green and blue contours respectively. **c) and d) Estimated incorporation position of the two donors,** based on the measured charging energies, overlaid over the STM image after phosphine dosing, for the left and right dot respectively. Note that we consider only one of the four equivalent positions of the first donor (red cross) at the four corner of the lithographic patch. The tight binding simulations were performed by Abu Mohammad Saffat-Ee Huq from Professor Rajib Rahman's group.

is encapsulated with epitaxial silicon at 250°C with a growth rate of 1 monolayer (ML) per minute ($\sim$ 0.135 nm/min). During encapsulation, the phosphorus donors will move from a surface location to a position in the 3D crystal. In addition, the phosphorus atoms can migrate up with the growth-front in a process called segregation. This process is however highly suppressed in our fabrication process due to the very low growth temperature chosen [30]. The probability of a phosphorus dopant from a highly delta-doped layer in silicon to segregate with our chosen growth-parameters has been estimated by McKibbin *et al.* to follow an exponential decay with a constant $l_{\text{seg}} \approx 0.81\,\text{nm} = 6\,\text{ML}$ called the segregation length [31], resulting in a 50% probability of the donor to segregate beyond 5 ML. The segregation length of dopants in lower doped regions whilst not well known, is estimated to be much smaller than that of a highly delta-doped layer. In Fig. 5.9, we display the NEMO simulated charging energies for a 2P quantum dot, with the explicit assumption that the donors have not segregated by more than one ML (1 ML = 1/4 unit cell). The left donor-quantum dot lithographic patch shown in Fig. 5.9 c showed four PH_2 molecules evenly arranged across four dimers after phosphine dosing. The measured charging energy of 84 ± 11 meV is compatible with 6 possible locations of the donors within the lithographic patch and two ML of growth (see green contour in Fig. 5.9 b). The position of the second donor is within a distance of two and three dimers from the first dimer (filled black circle) and, is consistent with the 0.25 ML coverage observed for delta-doped layers [16]. Indeed, the 0.25 ML coverage implies that one donor is incorporated for every two silicon-dimers. For the left dot, if we assume the first donor is shown by position A1 in Fig. 5.9 b, the second donor will likely incorporate within the green area shown giving charging energies of between 75.7 meV (D1+) to 89 meV (C2). Here the values of the charging energies are compatible with the experimentally measured value of 84±11 meV. The charging energy of the right dot qubit 98 ± 9 meV is larger than the one for the left dot, indicating that the two donors are indeed positioned closer to each other within the lattice. The measured charging energy is more compatible with simulated charging energies corresponding to the two donors being only two dimers apart, with a possibility of the dimers being displaced vertically by one ML. This is consistent with the scenario where the first donor is given by position A1 and the second donor will likely incorporate in the blue patch (see Fig. 5.9 d) giving charging energies between 89 meV (C2) and 106 meV (B2+).

The above atomistic study of the charging energies strongly suggests that the middle ancilla qubit is a 3P or 4P donor dot, and that the outer data qubits are 2P

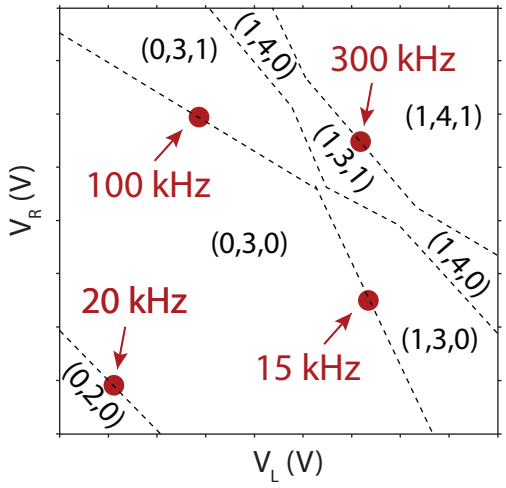

Figure 5.10: **Dot-SET tunnel rates.** At the transitions near the $(1, 3, 1)$ charge state of interest.

quantum dots. Under the assumption that donor segregation is limited to <1 ML, matching of the measured charging energies with tight binding simulations suggests that for both 2P dots the donor configurations are laterally constrained within the lithographic patches, and confirms that donor diffusion during growth at these low temperatures (250°C) is minimal.

5.1.5 Demonstration of single-shot spin readout

STM image analysis along with electrostatic device characteristics have confirmed that the device was patterned accurately according to the design specifications. Specifically we were able to engineer the (1,3,1) all-odd charge state, demonstrating independent electrostatic control over the quantum dot chemical potentials, and achieve donor numbers compatible with device specifications. To determine whether this device can now perform 2 qubit gates between each of the ancilla-data qubits, we first need to ensure we can readout each quantum dot qubit (ancilla or data). Here the different quantum dots have different distances to the SET reservoir and given the different donor number and electron number it is important to establish we have the correct tunnel rate for high fidelity readout. In the next section we will demonstrate single shot spin readout on the left quantum dot with a fidelity of 83% fidelity.

Dot-SET tunnel rates

As indicated, the tunnel-rates of the donor-bound electron spins to the SET reservoir, are critical in determining the achievable spin-readout fidelity. For slower tunnel-events more averaging is needed on the signal received from the SET. Averaging reduces the noise amplitude contained in the data, and thus increases the readout fidelity. For high performance SETs such as the one by Keith *et al.* in ref. [12], tunnel-rates of up to 1 MHz were measured with high fidelity. The tunnel rates of the left, middle and right transitions bounding the $(1, 3, 1)$ region are measured to be 15 kHz, 100 kHz and 300 kHz respectively, all below the maximal value of 1 MHz that allows for high-fidelity spin readout according to Keith *et al.*[4] A high-performance SET would thus allow high fidelity readout on all three transitions. In this respect, the distances of the dots to the reservoir in this device are close to ideal for the donor numbers and electron numbers in the device.

Single shot electron spin readout

Single shot electron spin-readout can be performed by energy-selective tunnelling of Zeeman-split spin states to a reservoir, when the dot is electrostatically tuned in such a way that the chemical potential of the more energetic up-state is above the reservoir's Fermi energy, while the chemical potential of the down-state is below it [32]. In such a configuration, if the electron spin is in a spin-down state, its chemical potential is below the Fermi-energy, and —provided the electron temperature of the Fermi-sea is low enough— there are no empty states in the Fermi-sea for it to occupy, and no tunnelling to the reservoir is possible (see Fig. 5.11d)3-5). If the electron is in the spin-up state however, its chemical potential is above the Fermi-energy, so that it has enough energy to populate an empty state in the reservoir's Fermi-sea, and the electron tunnels-out to the reservoir. Subsequently, because the dot is not occupied anymore, a spin-down electron with energy close to the Fermi-energy has sufficient energy to populate the electron spin-down state on the quantum dot. In summary, if the electron spin up was up, exactly two tunnel-events occur: the electron tunnels out from the dot, and another electron tunnel back in as seen in the 3 blips in Fig. 5.11d. If the electron spin was in the down-state, no tunnelling event occurs as sketched in panel three of Fig. 5.11d.

The electrostatic tuning of the quantum-dot's energy levels allows us to perform

[4]The two tunnel rates above 100 kHz are measured at a larger source -drain bias of 3 mV which raises the electron temperatures but is not expected to have a large influence on the tunnel-rate measurement that is performed at the centre of the Fermi-distribution.

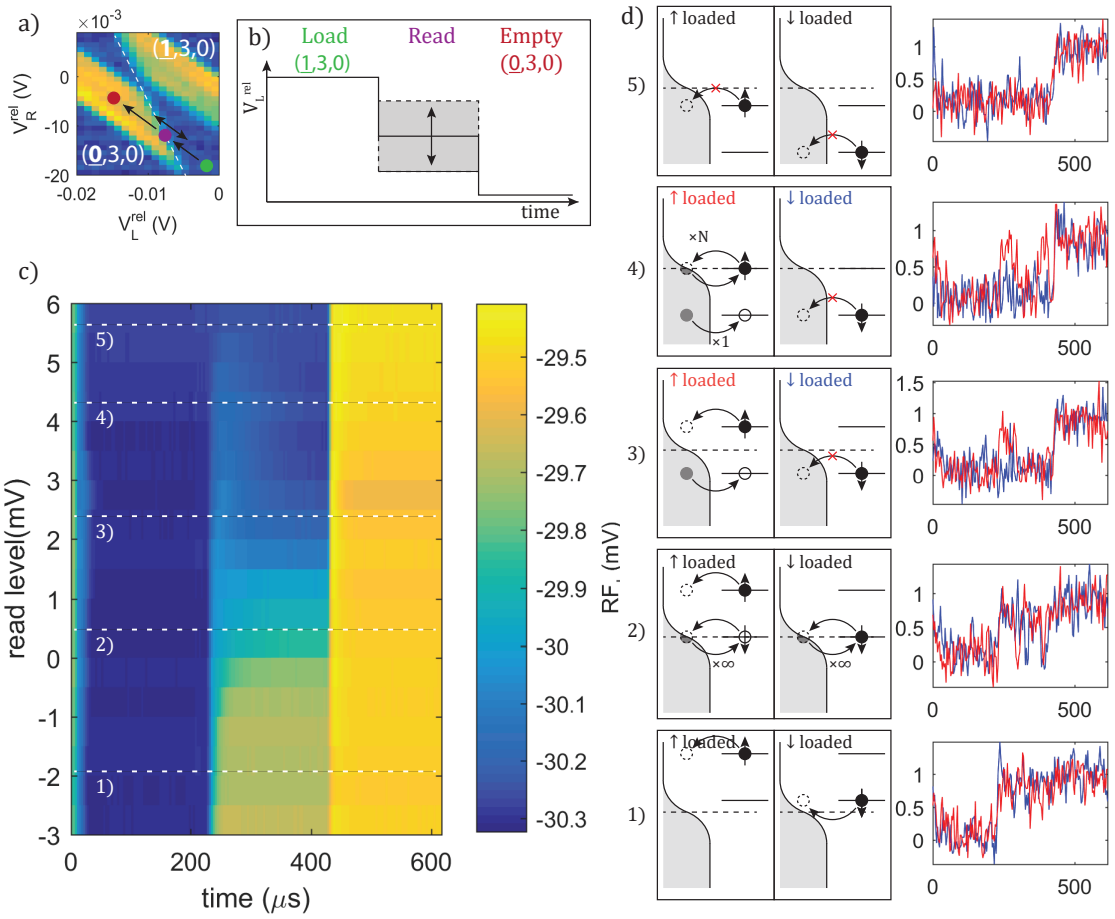

Figure 5.11: **Single shot spin readout of first electron on the left dot.**
a) Left dot SET break. This gate-gate map shows the voltage region at which spin readout is operated. The plot shows the RF in-phase quadrature signal RF_I as a function of the relative left and right gate voltage. The left donor charge transition is indicated by the white dashed line, and corresponds to the gate voltages at which one electron loads onto the left donor. **b)** Three locations in the gate map are highlighted by coloured circles, and correspond to the three levels of the spin readout pulse sequence represented schematically for the left gate voltage. The green, purple and green circles correspond to the "Load", "Read" and "Empty" stages of the pulse sequence.
c) Spin tail measurement. The RF_I signal recorded as a function of time during the duration of the three pulses described in a) and b), for different detuning positions (read levels) of the "Read" pulse, across the SET break. Each trace is an average of 10 thousand time traces, examples of which are displayed in the rightmost column of figure **d)**. The bright peak at the beginning of the read phase, for read levels from 2 to 5mV is called a spin tail, and corresponds to the situation depicted in figure(3), where the reservoir Fermi energy sits in between the Zeeman split spin levels.

an experiment called a spin-tail. We undertake this experiment at the $(0,3,0) \rightarrow (1,3,0)$ transition of the left dot, where we have a tunnel-rate of 15 kHz at the Fermi-energy (see Fig. 5.11a-c). The single shot spin readout is performed at a break in the SET charging-lines, produced by the charge transition (see closeup of the gate-gate map in Fig. 5.11a). When the gate voltages are tuned to a position on the SET peak (see red dot in Fig. 5.11a), the presence(absence) of a single electron charge on the quantum dot brings the SET in and out of Coulomb blockade completely. The SET signal level therefore allows the detection of single electron tunnelling events based on the spin state of the electron.

The spin-readout experiment consists of measuring the SET signal while executing repetitions of the following sequence. First, in the "load" phase an electron is loaded onto the quantum dot by pulsing the voltages in the $(1,3,0)$-region (green dot in Fig. 5.11a). Then, the chemical potential of the dot is brought close to the Fermi-level of the reservoir by pulsing to the vicinity of the SET break ("read" phase). Depending on the exact position of the so-called read-level, tunnelling events may occur (purple dot in Fig. 5.11a). Finally the quantum dot is emptied by pulsing into the $(0,3,0)$ charge-stable region ("empty" phase). This lowers the electrons chemical potential below the Fermi-level of the reservoir and results in any electron on the quantum dot tunnelling out to the reservoir. In the spin-tail experiment, many repetitions of this procedure are performed for each read-level position crossing the charge break from the $(0,3,0)$ charge state (negative read level) to the $(1,3,0)$ charge state (positive read level). The average of the SET signal over 10,000 time-traces is displayed in the measurement of Fig. 5.11c. In the second phase of the "read" sequence of the pulse, the SET signal changes from yellow to blue as the read position is tuned from above to below the Fermi level. The current profile describes a Fermi distribution as the density of states in the Fermi-reservoir is being sampled by the dot state. The light blue region at the beginning of the read phase that extends well into the high detuning region (in blue) is a marker of a spin-up state tunnelling out from the dot, thereby changing the charge state to (0,3,1) and putting the SET into resonance (high signal, in yellow). An electron then tunnels back in from the reservoir putting the SET back in to blockade (low signal, in blue). Additional features in the spin tail are illustrated in Fig. 5.11d.

The presence of a spin-tail confirms that the charge numbering of the left dot is odd. Otherwise no tail would be observed. We can calculate the spin readout fidelity at a position between positions 3) and 4) is 83%. The fidelity is calculated according to the process described in [29] using code provided by Samuel Gorman.

The fidelity estimation relies on the measurement of the tunnel times of spin-up and spin-down electron, together with the electrical readout parameters (e.g. signal-to-noise ratio, sampling rate, filter bandwidth). More details on the calculation can be found in Sect. 5.2.2. Unfortunately the tunnel rates of the right (300 kHz) and middle-dot (100 kHz) charge transitions surrounding the $(1, 3, 1)$ charge-stable state were too fast to allow for spin-readout with the measurement bandwidth allowed by the SET charge sensor.

5.1.6 Importance of the SET on/off ratio

Spin-readout of a donor-bound electron, through spin-selective tunnelling of the electron is reliant upon detecting tunnelling-events of electrons off and on the quantum-dots. These tunnelling events corresponds to the quantum dot gaining and losing one electron-charge, and can thus be detected by a charge sensor such as the SET patterned $\sim$ 17 nm below the three quantum dots in this triple-dot device (see Fig. 5.12a). High-fidelity spin-readout of electron spins relies on two main factors. First, the temperature of electrons within the Fermi-sea of the reservoir used for the readout must be larger than the Zeeman splitting (typically at most 1.5 T) to allow for microwave manipulations through ESR pulses. Second, the SET must display a large change in conductivity between the Coulomb-blockaded regime and the conductive regime, allowing maximum contrast in the signal measured through either DC or RF measurements. For the device investigated here, the SET island serves not only as the charge sensor but also as the electron reservoir. Therefore, good readout relies on the SET being conductive without leading to heating of the electrons within the reservoir, and an associated reduction in the fidelity of the readout.

The conductivity of the SET is related to the width of the two tunnel-gaps separating the island from the source and drain leads (see close-up STM images of the gaps in Fig. 5.12b and c). The original device specification in the STM control software was to pattern the tunnel-gaps 8 nm long, with leads 4 nm in width, leading to a 2:1 aspect ratio previously known to be associated with high conductivities. An image of the SET patterned in the device is presented in Fig. 5.12a. The image has been de-skewed by correcting for the periodicity of the crystal lattice and for drift of the STM tip during the image acquisition. The de-skewing reveals that drift of the piezoactuators of the STM was significant, and inadvertently lengthened the size of the left gap, while widening the lead-width on the right gap. This drift has resulted in sub-optimal aspect ratios of 2.36 and 1.4 for the left and right gaps respectively.

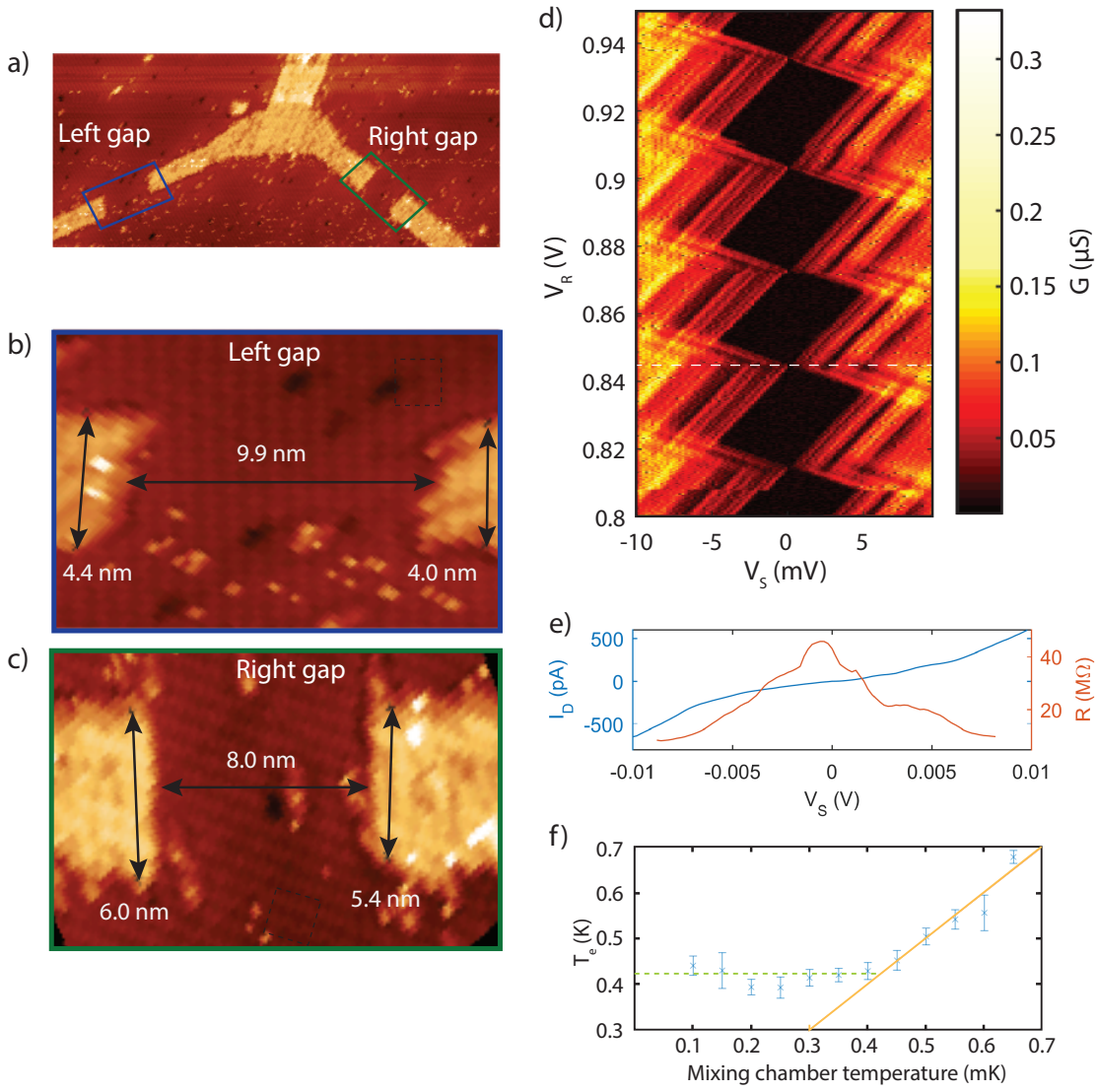

Figure 5.12: **Performance of the SET charge sensor.**
a) STM image of SET island and its associated tunnel gaps. Two tunnel-gaps are visible on the left and right, connecting the SET island to the source and drain lead. The image has been de-skewed by analysing the periodicity of the crystal lattice and correcting for drift of the STM tip during the image acquisition. The lithographic pattern is significantly distorted due to drift. **b) and c) Closeup images of the left and right tunnel gaps,** showing gaps of 4.2±2 nm x 9.9 nm and 5.7±0.3 nm x 8 nm with aspect ratio of 2.36 and 1.4 respectively.
d) Coulomb diamond measurement of the SET. SET conductance G as a function of the SD-bias V_{SD} and right gate voltage V_{R}. The black parallelograms running along the line $V_{SD} = 0$ regions indicate voltage configurations at which no current is flowing through the transistor, also called Coulomb diamonds. We can immediately see the diamonds are not symmetric and this is a sign of the asymmetric tunnel gaps either side of the SET island. The bright stripes parallel to the sides of the Coulomb diamonds are characteristic of low conductance SETs, and result from parallel conductance through excited SET charge states. **e) SET resistive of** 46 MΩ**.** A line cut of the Coulomb diamond at $V_R = 0.85$ V, where the current reaches 85 pA at 3 mV source-drain bias, with a resistance at zero bias of 46 MΩ. **f) Electron temperature measurement.** A plot of the electron temperature, T_E as a function of the mixing chamber temperature.

The size of the left gap would lead to an SET with a large zero-bias resistance of $R = 46\,\mathrm{M\Omega}$, three orders of magnitude larger than the optimal SET resistance, which is given by $2R_K = 2h/e^2 = 2 \times 25.8\,\mathrm{k\Omega} = 51.6\,\mathrm{k\Omega}$ [12], (see Fig. 5.12d and e).[5] As a consequence of this for a source-drain bias of 1 mV the current flowing through the SET only reached $\sim$ 35 pA and order of magnitude lower than ideal. The high SET resistance ($R = 46\,\mathrm{M\Omega}$) in the measured device therefore translates into significant heating of the SET, as confirmed by a measurement of the electron temperature of about 420 mK, at a source-drain bias of 1 mV (see Fig. 5.12f). The estimate of the electron temperature arises from measurements of the width of the Fermi-distribution in the reservoir, that is proportional to the electron temperature. By increasing the sample temperature, the electron temperature is identified as the sample-temperature at which the measured width of the Fermi-edge starts increasing (see Fig. 5.12f). The measured electron temperature is 8 times larger than the temperature of the mixing chamber of the dilution refrigerator at which the sample is located, and about twice that of state-of-the-art measurement on similar devices [12]. The electron temperature is however five times lower than the temperature associated with the Zeeman splitting of the spin-states at the magnetic field of 1.5 T, such that spin readout is still possible if the electron tunnel-rates are slow enough for the measurement bandwidth allowed by the SET.[6]

In summary, after analysis it was determined that the SET patterned on this first triple-dot device, was patterned with sub-optimal tunnel-gaps due to unexpected drift of the STM tip during patterning. As a result, the SET was highly resistive and limited the ability to readout all three quantum dots. The left dot did however have a low enough tunnel rate to perform single shot readout with 86% fidelity.

5.1.7 Conclusion

In this section, we introduced a triple dot device-design optimised to allow for independent control, initialisation and readout of three electron/nuclear spin qubits, as well as coupling of two of the electron spin qubit pairs using exchange-based gates. This design optimised the device geometry and the number of donors in each quantum dot to allow full electrostatic control for two qubit gates between a central ancilla qubit and two data qubits.

[5] The SET in ref. [12] has a zero-bias resistance of 100 kΩ and demonstrated large signal to noise ratios (SNR=13) for electron tunnelling, with a very large measurement bandwidth of 1 MHz.

[6] Operation of electron spin qubits at 1.5 T stem from the fact that the microwave pulses needed for ESR at such magnetic fields are bout 42 GHz at the limit of what commercially available state-of-the-art microwave generators can provide with sufficient power.)

Measurement of a first device, B016 utilising this design in a dilution refrigerator confirmed that the chosen geometry and donor numbers fulfilled the original design requirements with tunable independent electrostatic control of the charge state of three unpaired electron spins. Furthermore, the donor configurations within the two-donor quantum dots was estimated by comparing measurements of the quantum dot charging energies to recently modelled tight binding simulations. The resulting donor configurations were found to be compatible with high quality STM images of the arrangement of phosphine species adsorbed in each quantum dot before incorporation. This supports the hypothesis that sideways diffusion and segregation of phosphorus donor is negligible during growth of the silicon encapsulation layer[7].

The tunnel rates of all three unpaired electrons on the left, middle and right dots were shown to fall within the range for high fidelity spin readout. We demonstrated spin readout of the electron on the left 2P donor-quantum dot with 83% fidelity. Unexpected variations in the dimensions of the SET charge sensor due to drift in patterning in SET with the STM piezoactuators were found to limit on-off ratio of SET and prevented electron spin readout on charge transitions with a faster tunnel rate (>15 kHz) as observed on the middle and right quantum dots. The variations in the SET dimensions were attributed to drift of the STM tip during patterning and strategies to mitigate such variations are presented in Sect. 5.2.1.

5.2 Electron spin resonance on a triple-dot device

This section describes measurements of a second triple-dot device, Bron037 of similar design to that presented in Sect. 5.1. Changes in the design of the SET charge sensor were performed to improve its reliability. The design changes are shown to yield are marked improvement in the charge sensor contrast, and in the spin readout fidelity, from 83% in the previous device to 94.4% in the device presented here. Electron spin resonance by adiabatic inversion is then demonstrated and used to perform spectroscopic measurement of the hyperfine interaction of the electron with the phosphorus nuclei of the quantum-dot donors. The measured hyperfine interaction strength are used to perform metrology of the actual configuration of the donors within the quantum dot and reveal a hyperfine Stark shift larger than previously reported in phosphorus donors. The anomalously large hyperfine Stark effect is attributed to the exact orientation of the donor molecule within the silicon lattice.

The device presented in this section was fabricated by fellow PhD student Michael

[7] under the assumption of low vertical segregation.

Jones and myself, with help and supervision from Dr. Yousun Chung. The RF-readout and pulsing setup was established by this author and the ESR setup was initiated by us both with help from Dr. Pascal Macha. Electron spin resonance spectra were measured by all three of us with the tight binding simulations performed in collaboration with Md Serajum Monir from Prof Rajib Rahman's group. The results on donor metrology are presented in the thesis of Michael Jones [7] and repeated here to enable the understanding of the following section which presents nuclear spin results on the same device that are unique to this thesis.

5.2.1 STM fabrication

Limitations in the reliability of the SET charge sensor described in Sect. 5.1 were overcome by new fabrication strategies described briefly here. Drift of the STM tip during patterning was identified as the principle cause for the low conductivity of the SET described in the previous section. STM tip drift is due to hysteresis in the response of the piezoelectric actuators to the voltages used to move the tip. It typically takes tens of seconds for transient tip displacements to settle after large or fast tip movements associated with patterning of the larger structures or when imaging large areas. In particular, the low conductivity SET of Sect. 5.1 was patterned in only two lithographic steps, the second of which (blue structure in Fig. 5.13 a) is 100 nm wide but requires sub-nanometer precision lithography of the tunnel-gaps. Furthermore, the tunnel gaps in the previous design were not aligned with the underlying silicon dimers. This misalignment reduces the quality of the lithographic edges, due to the atomic nature of the lithographic mask. An improved SET fabrication strategy was developed for the device presented in this section which mitigates both effects by aligning the tunnel gaps to the silicon dimer lattice, and by separately patterning the tunnel gaps (see Fig. 5.13b). After patterning the main body of the SET island (2), a waiting period is introduced to allow for STM tip drift to settle. Each tunnel gap can then be carefully aligned to the silicon lattice and patterned. Furthermore, the lithographic patches not connected to the SET island have been shortened so that, if the dimensions of one tunnel gap are not within tolerances, the gap can be patterned again without increasing the size of the SET island significantly.

The patterning precision of the device was further improved by continually correcting distortions of the STM images due to STM-tip drift. Correcting distortions is crucial when calibrating the tunnel-gap distances and when assessing the correct dimensions of the SET patterned on the actual device. The correction process relies on transforming the image so as to match the known periodicity of the silicon-dimer

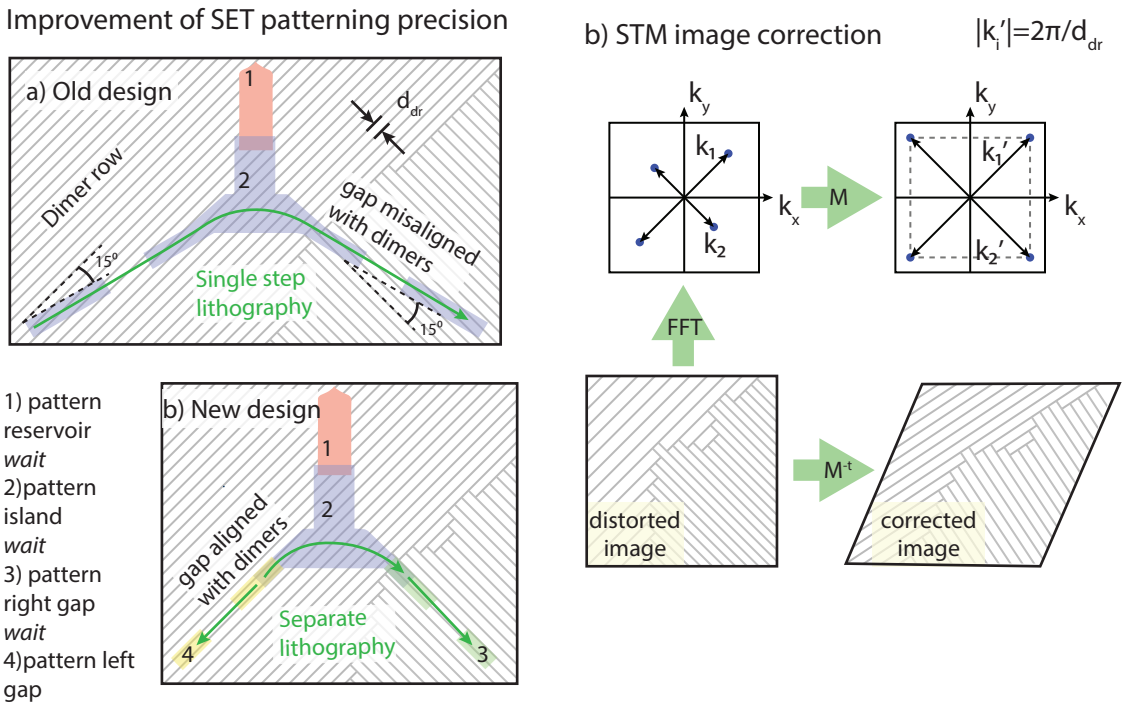

Figure 5.13: **Optimisation of SET charge sensor. a) New SET design and writing procedure.** With the previous SET design, the SET was patterned in two parts : the reservoir (1) patterned together with the quantum dots, and secondly (2), the island and the two tunnel gap. The fast movement of the SET tip during the latter phase produces drift and results in non reproducible tunnel gaps. The gaps were patterned with a 15 degree angle to the dimer rows, yielding less reproducible lithography. **b)** The new design the tunnel gaps are aligned to the crystal lattice. To minimise drift the two gaps (3 and 4) are written separately from the island (2). Any drift can be left to settle ($\sim$ 30s) before patterning the tunnel gaps. **b) STM image correction.** STM images are distorted due to STM tip drift. The images are corrected by taking a Fourier transform of the image (FFT). Four peaks become visible in the Fourier transform, corresponding to the two periodicities of the silicon dimer rows (k-vector $\pm k_1$ and $\pm k_2$). The transformation matrix M that maps the four k-vectors to a square is then calculated, so that the k vector matches the known periodicity of the 2×1-reconstructed silicon surface, with $|k| = 2\pi/d$, where $d_{\mathrm{dr}} = 0.768\,\mathrm{nm}$ is the known dimer row spacing. The STM image is then simply corrected using the transformation matrix $M^{-\mathrm{t}}$.

rows ($d_{\mathrm{dr}} = 0.768\,\mathrm{nm}$). The coordinate transformation matrix is found by taking a discrete Fourier transform of the distorted image. Four peaks in the Fourier-transformed image are identified as two pairs of distorted k vectors $\pm k_1$ and $\pm k_2$, each pair corresponding to the two perpendicular silicon dimer-row orientations. A linear transformation matrix M is then found that transforms k_1 and k_2 onto the known k-vectors $\pm k_1'$ and $\pm k_2'$, oriented along the four corners of a square, and with a norm constrained to the dimer row periodicity $|k_i'| = 2\pi/d_{\mathrm{dr}}$. The transformation is found by solving the system of equations $Mk_i = k_i'$, and usually yields a unique solution M. The coordinate transform of the STM image is then simply the transposed inverse of M : $M^{-\mathrm{t}}$.

The dimensions of the SET gap in the new design were further optimised across several devices. The trend across the devices suggests that for a lead width of about 9 dimer rows (6.9 nm), a tunnel-gap distance of 15 dimer rows (11.5 nm, aspect ratio 0.6) should yield near optimal SET resistances of $\approx 100\,\mathrm{k\Omega}$, just above two quanta of resistance ($\approx 52\,\mathrm{k\Omega}$). A full account and analysis of the SET optimisation process can be found in the PhD thesis of collaborator Michael Jones ([7]).

The improved SET fabrication techniques described above were used to fabricate device BRON037 which is the focus of the remainder of this chapter. The fabrication methods are described in Sect. 2.3. Besides changes to the SET and of the dot distances, the device design is the same as that of device B016 (or BRON016) presented in the previous section Sect. 5.1. The device consists of three quantum dots (L, M and R), tunnel-coupled to the SET charge sensor (see Fig. 5.14b). Three electrostatic gates (L, M and R) control the electrostatic potential of the three quantum dots (see Fig. 5.14b). The single electron transistor (SET) consists of a source (S) and a drain (D) contact, that are used to pass a current through the SET island. An SET gate is used to control the electrostatic potential of the SET island.

The dot-reservoir distances were increased by about 1 nm, from $17 - 18\,\mathrm{nm}$ on B016 to $18 - 19\,\mathrm{nm}$ on BRON037. This slight increase in the distance is aimed at reducing the dot-SET tunnel rates from $\approx 100\,\mathrm{kHz}$ down to $\approx 10\,\mathrm{kHz}$. This decrease in the tunnel rate will allow additional noise filtering to boost the signal-to-noise ratio of the charge sensor, but does not slow down experiments too significantly.

A closeup STM image of three donor quantum dots after phosphine dosing reveals phosphine species adsorbed to all three lithographic openings (see Fig. 5.14c). A closeup of the right donor-quantum dot, that will be in focus of the remainder of this chapter, reveals three possible PH_2 species adsorbed to the surface (green circles in Fig. 5.14d, and one PH species (green-dotted circle). As such, we would expect

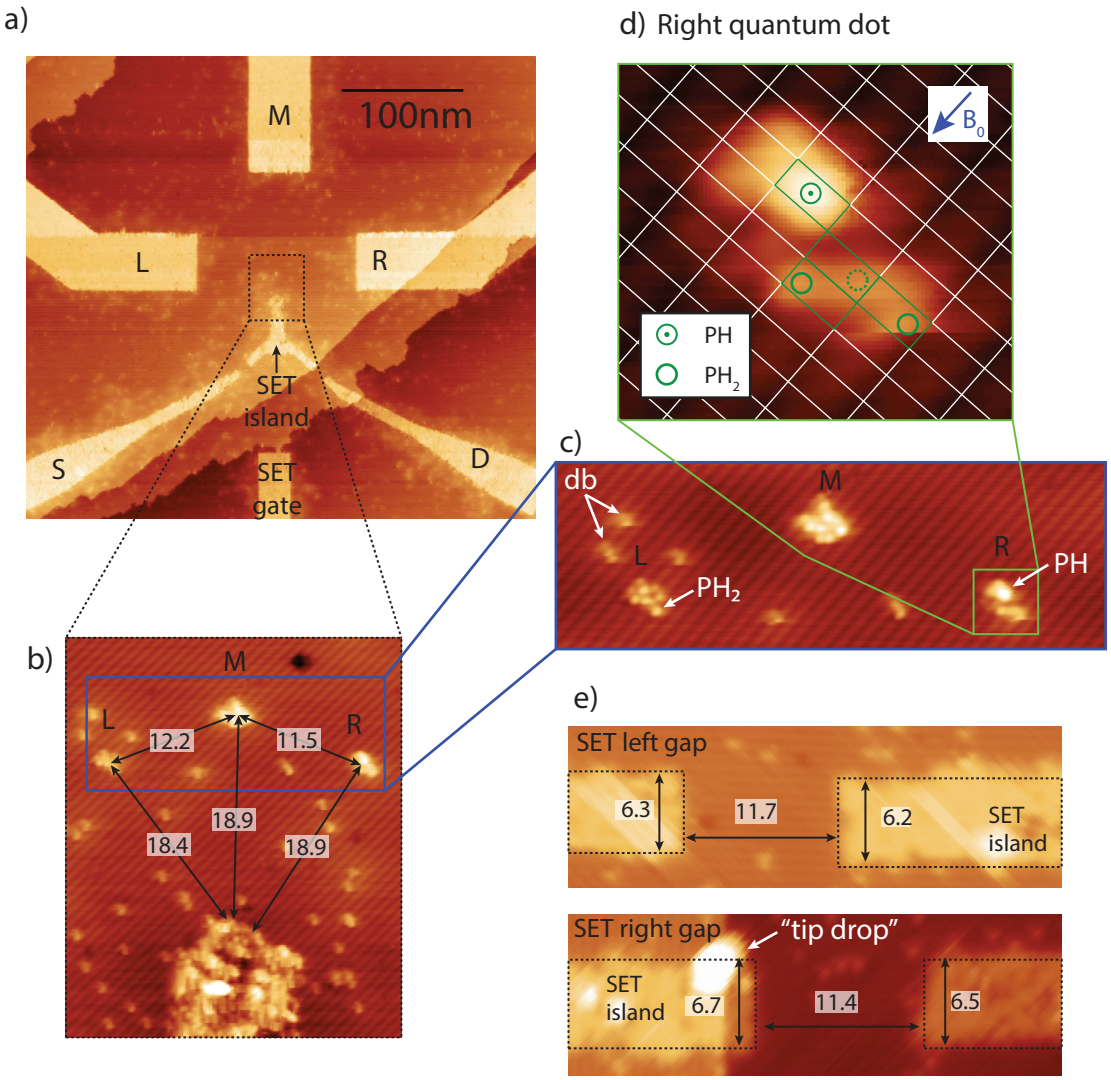

Figure 5.14: **STM images of multi donor triple dot device BRON037. a)** Overview image of the device, with electrostatic tuning gates L, M, R and the SET gate SETG, a single electron transistor consisting of a source (S) and a drain (D) lead, connected to the SET island (SET). **b)** closeup of the three patterned quantum dot (L, M and R) and distance to the electron reservoir. **c)** Closeup image of the three patterned quantum dots after phosphine dosing. PH_2 and PH species are visible in all three dots, and a silicon dangling bond is apparent (db). **d)** Closeup of the right donor quantum dot. Three PH_2 and a centred PH species are visible, on four dimers of interest marked by green rectangles. All distances are in nm.

a maximum number of 2 phosphorus donor atoms within this quantum dot. The four dimers hosting the phosphine species are highlighted as green rectangles in the figure. Closeup images of the tunnel gaps of the SET charge sensor show tunnel gap lengths of 11.7 nm and 11.4 nm for the left and right gap respectively, both within 0.2 nm of the desired length of 11.5 nm. The aspect ratio of the left(right) tunnel gap is 0.53(0.58), within 12(3) % of the desired value of 0.6 (see Fig. 5.14e).

5.2.2 Demonstration of single-shot spin readout

Device BRON037 was cooled down to sub-50 mK temperatures in a Leiden pulse-tube dilution refrigerator. The charge sensor can be operated in direct current (DC) and radio frequency (RF) mode. In both cases, a voltage bias of 500-600 µV was applied to the source and drain leads of the SET using a battery powered voltage source. The DC current flowing through the SET was amplified before digitisation by a FEMTO DLPCA-200 trans-impedance amplifier. For RF-readout, a resonant circuit on the device PCB was connected to the drain lead of the SET. The resonance frequency that is shifted by the state of the SET (Coulomb blockaded or not) is monitored using an RF signal generator ($\approx$ 240 MHz) and an IQ demodulation circuit. The demodulated quadratures of the signal are digitised using an ALAZAR ATSS9440 analog to digital converter (see Fig. 2.14). The electrostatic potential of the quantum dots is controlled using voltage sources connected to all four gates (L,M, R and SETG). Fast pulses are applied on two of the gates by an arbitrary wave form generator (see Fig. 2.15). The full experimental setup is presented in more details in Sect. 2.4. A gate-gate map of the device, in which the left and middle gate voltages are swept across a two dimensional parameter space, reveal three quantum dot transition lines (see Fig. 5.15)[8]. The transition lines appear as breaks in the regular pattern of SET charging lines (yellow lines in Fig. 5.15). The two transitions at lower gate voltages (M1 and M2 in Fig. 5.15), display the same slope, that is distinct from that of the higher transitions (R1 in Fig. 5.15). Electrostatic triangulation using the COMSOL finite element solver confirms that the first two transitions (M1 and M2) correspond to charging events on the middle dot, while the third transition (R1) correspond to the first electron charge transition on the right dot. The electrostatic triangulation relies on matching the experimentally measured ratios of gate-to-dot capacitive couplings (lever arms) to electrostatic simulations. The capacitive-coupling ratios are obtained from the measured slope of the transition lines in gate-gate maps using different pairs of electrostatic gates. For the

[8] more charge transitions appear at higher voltages.

triangulation of the right dot for example, the L-M, L-SET and SET-M gate pairs each yield a one dimensional line in the lithographic plane on which the measured capacitive coupling ratio matches the simulated one. If the transitions correspond to the same quantum dot in the lithographic plane, all lines cross in a singular point corresponding to the quantum dot position (see yellow lines crossing in the inset of Fig. 5.15).

Only two sets of transition lines triangulating to the middle and right quantum dot, respectively could be found in the available parameter space, indicating that the left lithographic patch did not incorporate any phosphorus donors. This is consistent with the PH_x species existing on different dimer rows and therefore unable to incorporate.

In the gate-gate map in Fig. 5.15 the quantum dot charging events are recorded by the SET charge sensor operated in DC mode, with a Source–Drain (SD) voltage bias of 500 µV. When the SET changes from its Coulomb-blockaded state (< 50 pA current) to its conductive state, the current contrast reaches ≈ 450 pA. This is in stark contrast with the SET charge sensor studied in Sect. 5.1, where a larger source–drain bias of 1 mV yielded only 35 pA current contrast and highlights the benefits of our new SET design.

In the remainder of this chapter, we focus on the first electron transition on the right donor quantum dot (transition R1 in Fig. 5.15). Spin readout on the right donor quantum dot is performed by applying a static magnetic field of $B_0 = 1.4$ T, in a direction parallel to the lithographic plane. The magnetic field splits the electron spin-up and spin-down states with an energy difference of $E_Z = \gamma_e B_0 h$, where $\gamma_e = 28$ GHz/T is the electron gyromagnetic ratio. The spin of the electron can be read out by adjusting the electrostatic potential of the quantum dot so that the chemical potential of the spin-up state is above the Fermi level of the electron reservoir, while that of the spin-down electron is below it [32]. With such a configuration of the chemical potentials, the spin-up electron tunnels out of the quantum dot after a characteristic time $t_{\text{out}}^{\uparrow}$ while the electron spin-down tunnels out over a much larger time scale $t_{\text{out}}^{\downarrow}$, because not enough empty states are available in the reservoir below the Fermi energy. The electron spin state can therefore be inferred from the presence or absence of a tunnelling event, as first demonstrated by Elzerman *et al.* [32]. The fidelity of the spin readout hinges on the correct detection and attribution of the tunnelling event (or non-event) to a spin spin-up (spin-down) electron. First, the correct detection of a tunnelling event (regardless of the spin state) relies on a large signal-to-noise ratio of the charge sensor, and on the resulting bandwidth of the

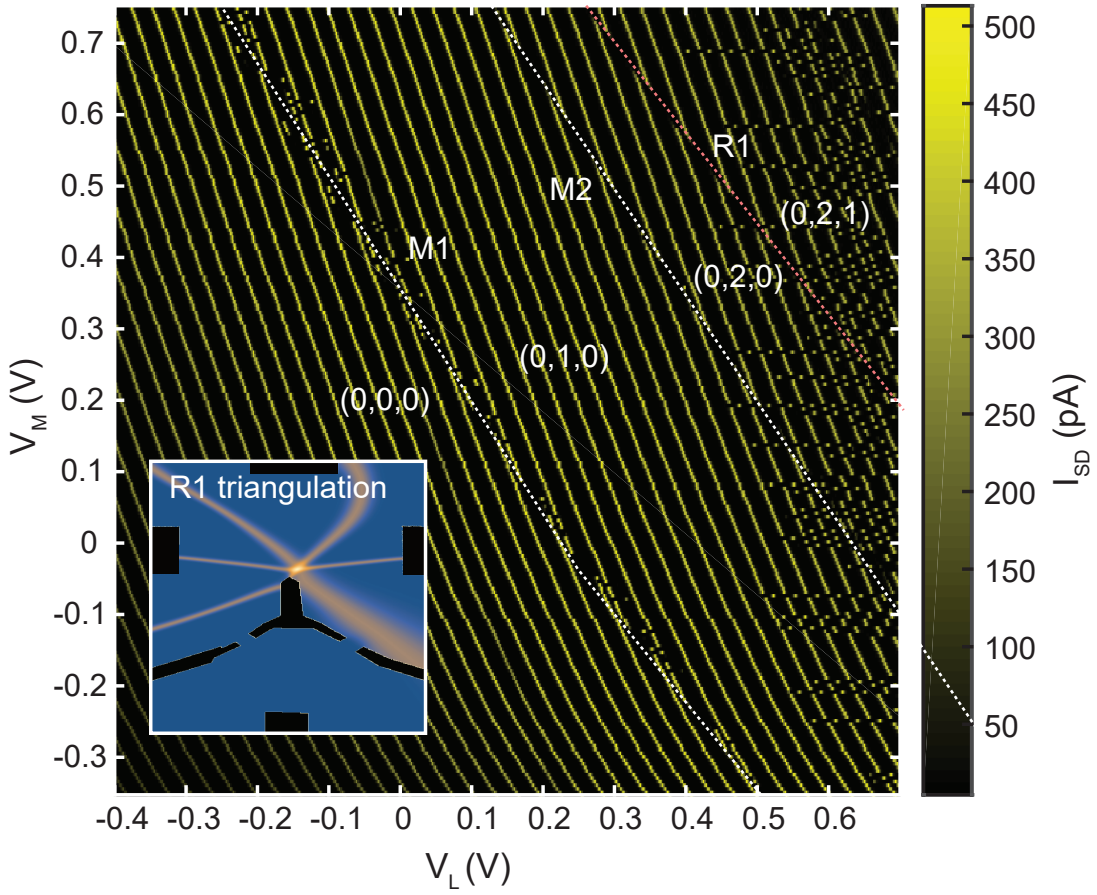

Figure 5.15: **Gate-gate map of device BRON037**. Three charge transitions are visible, two corresponding to the first two electrons populating the middle dot (M1 and M2, white dotted lines), and a third corresponding to the first electron loading event on the right donor-quantum dot (pink dotted line). This pink transition, R1 will be the focus of this chapter. **Inset:** Electrostatic triangulation of the transition R1 by matching the measured relative capacitive coupling of the left, middle and SET gate to the quantum dot and to electrostatic simulations. Each gate combination produces a one dimensional contour. The intersection of the contours matches the position of the right quantum dot obtained from STM images. With $V_{\mathrm{SET}} = 0.7\,\mathrm{V}$, $V_{\mathrm{R}} = 0\,\mathrm{V}$, $V_{\mathrm{SD}} = 0.5\,\mathrm{mV}$.

charge detector being larger than the characteristic tunnel rates of the transition. The fidelity of this tunnel-event detection can be characterised by the electrical visibility V_{EV} as proposed in [29]. Second, the correct assignment of a tunnelling event (non-event) to a spin-up (spin-down) electron, requires the characteristic time $t_{\mathrm{out}}^{\downarrow}$ it takes for spin-down electron to tunnel out to be much larger than that of the spin up electron, so that if an electron tunnels out of the dot, it can be attributed to a spin-up with a high degree of certainty. Maximising $t_{\mathrm{out}}^{\downarrow}$ without increasing $t_{\mathrm{out}}^{\uparrow}$ relies on being able to tune the spin-down state as far below the temperature-widened part of the Fermi distribution as possible while keeping the spin-up level above it. This can be achieved by increasing the Zeeman splitting E_{Z} between the spin states and reducing the electron temperature T_e in the reservoir which determines the width of the Fermi distribution. Indeed, the ratio of $t_{\mathrm{out}}^{\downarrow}/t_{\mathrm{out}}^{\uparrow}$ is equal to the Boltzmann factor $\exp\left(\frac{E_{\mathrm{Z}}}{2k_{\mathrm{B}}T_e}\right)$, where k_{B} is the Boltzmann constant [29]. The fidelity of correctly assigning a tunnelling event (or non-event) to a spin-up (spin-down) electron can is characterised by a spin-to-charge conversion visibility V_{SC} [29]. Finally, the fidelity F of the full spin readout process is characterised by $F = \frac{V_{\mathrm{SC}}+V_{\mathrm{EV}}}{2}$.

The fidelity of the readout on the right dot transition R1 in Fig. 5.15 is performed using the process detailed in [29] and the code provided by Dr. Samuel Gorman. The optimal electrostatic tuning of the chemical potential (the "read level") is found by performing an analysis on a range of read levels in a spin tail experiment (see Fig. 5.16a). We obtain a spin readout fidelity of 94.4% at a read level of −4mV (red line in Fig. 5.16a). The fidelity value is maximised by optimising the electrical visibility V_{EV} and the spin-to-charge visibility V_{SC} in a process described below.

The electrical and spin-to-charge visibility both depend on the tunnel times of the spin-up and spin-down states. The tunnel times $t_{\mathrm{out}}^{\downarrow} = 11.3\,\mathrm{ms}$ and $t_{\mathrm{out}}^{\uparrow} = 247\,\mu\mathrm{s}$ are found by fitting a bi-exponential distribution to a histogram of the tunnel-out times. When the two tunnel times are sufficiently different, the fit can be made with low uncertainties. Similarly, the characteristic time $t_{\mathrm{in}}^{\downarrow} = 52.7\,\mu\mathrm{s}$ for a spin-down electron to tunnel onto the quantum dot is found by fitting an exponential distribution to a histogram of the tunnel-in times.

The electrical visibility is first optimised by maximising the SNR of the charge detector. A SNR of 10.4 for the RF-readout is achieved by using a room temperature attenuation of the RF signal of 39 dB[9] and a source–drain bias of 600 µV at a low-pass filter bandwidth of 500 kHz[10](see Fig. 5.16c). All of the signal is shifted in one of the quadratures RF_{Q} of the RF signal by slightly tuning the RF carrier frequency.

[9]The attenuator is item 10 in Fig. 2.14
[10]The filter is item 1 in Fig. 2.14

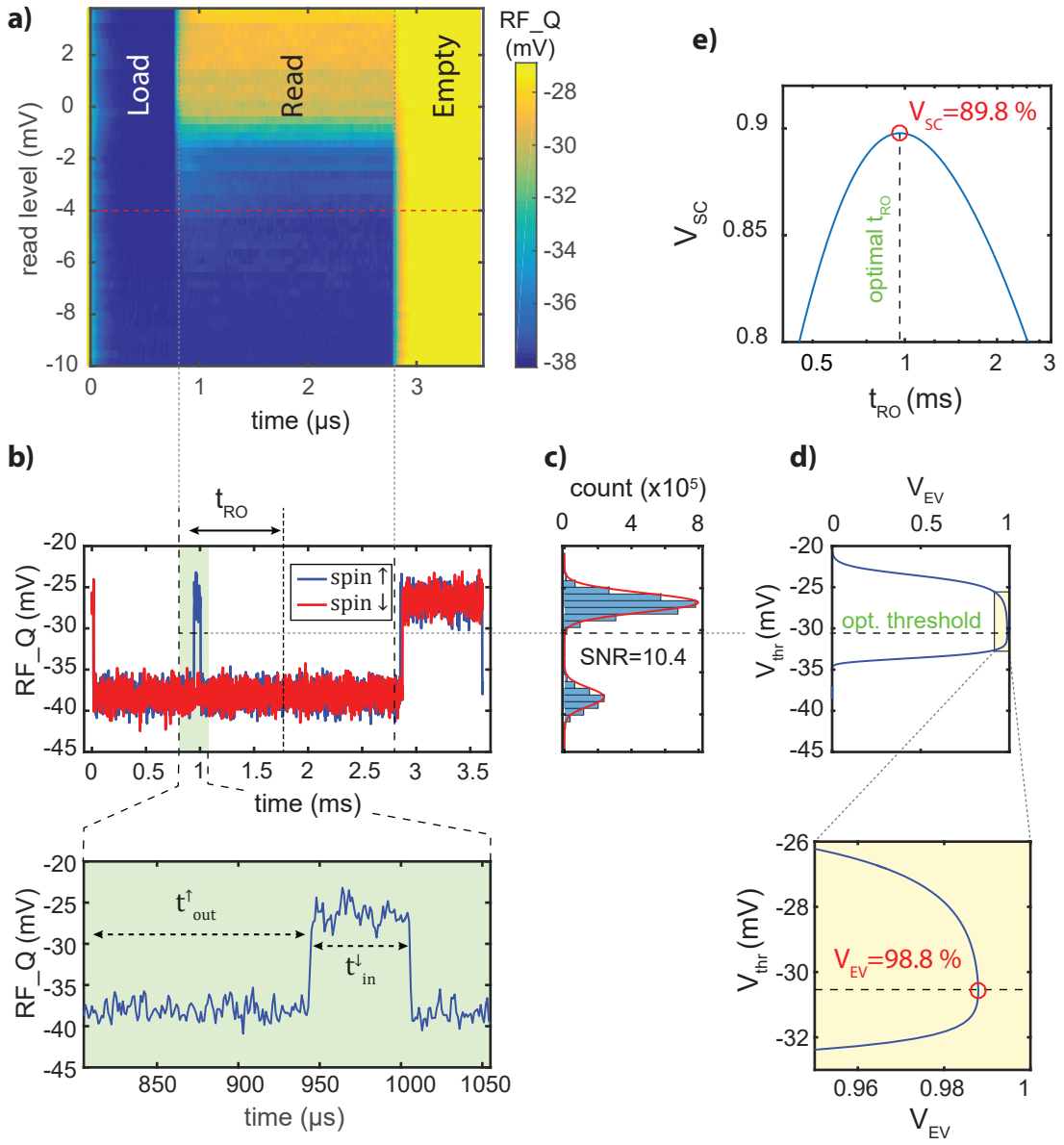

Figure 5.16: **Spin readout on transition R1. a)** Spin tail experiment. An electron is repeatedly loaded, read and emptied from the 2P molecule. Blue(yellow) regions correspond to the presence(absence) of an electron on the molecule. The pulse sequence is repeated 1000 times for read levels scanning across the Fermi edge. The optimal read level is found at $-4\,\mathrm{mV}$. **b)** Two readout traces at a read level of $-4\,\mathrm{mV}$. The blue trace corresponds to a spin $\uparrow$ tunnelling out of the quantum dot after a time $t^{\uparrow}_{\mathrm{out}}$, and a spin $\downarrow$ tunnelling back in from the reservoir after a time $t^{\downarrow}_{\mathrm{in}}$ (see inset). The red trace corresponds to a spin $\downarrow$ staying on the quantum dot throughout the read phase. **c)** Histogram of the electrical signal for all 1000 traces like in b). The high(low) level, corresponding to the absence(presence) of an electron on the quantum dot are well separated (with SNR=10.4). **d)** Electrical visibility V_{EV} as a function of the threshold voltage used to detect a tunnelling event. The maximum $V_{\mathrm{EV}} = 98.8\%$ is reached for a threshold $V_{\mathrm{thr}} = -30.5\,\mathrm{mV}$. **d)** Spin-to-charge conversion fidelity V_{SC} as a function of the tunnelling detection time-window t_{RO}. A maximum $V_{\mathrm{SC}} = 89.8\%$ is reached for $t_{\mathrm{RO}} = 0.97\,\mathrm{ms}$. Together, V_{SC} and V_{EV} yield a spin-readout fidelity $F = 94.4\%$.

Time resolved measurement of the RF quadrature RF_{Q} during electron tunnelling events, allows us to clearly distinguish tunnelling events (red trace in Fig. 5.16) from the absence of tunnelling events (blue trace in Fig. 5.16). A tunnelling event is detected by monitoring when the RF signal exceeds a detection threshold V_{thr}. The optimal threshold is found by calculating the electrical visibility across a range of threshold values (see Fig. 5.16d), and yields an optimal electrical visibility of 98.8%.

The spin-to-charge visibility is calculated based on the measured tunnel times and depends on the time t_{RO} during which tunnel events are monitored (see Fig. 5.16b and e). An optimal spin-to-charge fidelity of 89.8% was found for a readout time-window $t_{\mathrm{RO}} = 1.0\,\mathrm{ms}$ (see Fig. 5.16e). By using the optimal read-level, RF signal threshold and readout window, a total spin-readout fidelity of 94.4% was achieved. The increase in the fidelity compared to the device studied in Sect. 5.1 ($F = 83\%$), is attributed to an increase in the electrical visibility due to the higher RF signal contrast and to an increase in the spin-to-charge visibility due to the decreased electron temperature (250 mK instead of 400 mK). Both increases in the visibility are linked to the higher conductivity of the optimised SET charge sensor.

5.2.3 ESR spectrum of a 2P molecule

The electron spin on the right quantum dot can be manipulated using a magnetic field B_1, perpendicular to the static magnetic field B_0 and oscillating with a microwave drive frequency ω_d equal the instantaneous Larmor frequency ω_{L} of the electron. The oscillating magnetic field is applied using an antenna patterned above the device. The antenna is fabricated as an aluminium coplanar waveguide with a short near the location of the device. The short consists in a 1 µm long aluminium bridge, with a cross-section of $100 \times 100\,\mathrm{nm}$. This narrow cross-section results in large current densities traversing the antenna bridge when a voltage is applied to it, producing a magnetic field oriented tangentially to the bridge. The coplanar waveguide leading to the antenna bridge minimises losses of the high frequency microwave signals.

In the frame rotating with the Larmor precession of the electron, the spin is described by the two-level Hamiltonian $H = \delta\omega \cdot \sigma_z + \gamma_e B_1/2 \cdot \sigma_x$, where $\delta\omega = \omega_{\mathrm{L}} - \omega_d$ is the detuning between the Larmor and drive frequency. The electron spin can be manipulated by exactly matching the drive frequency to the instantaneous Larmor frequency of the electron, because the σ_z term vanishes, and free precession of the spin around the axis defined by the B_1 field occurs. This allows full two-axis control of the electron spin. In natural silicon, ^{29}Si isotopes with a nuclear spin 1/2

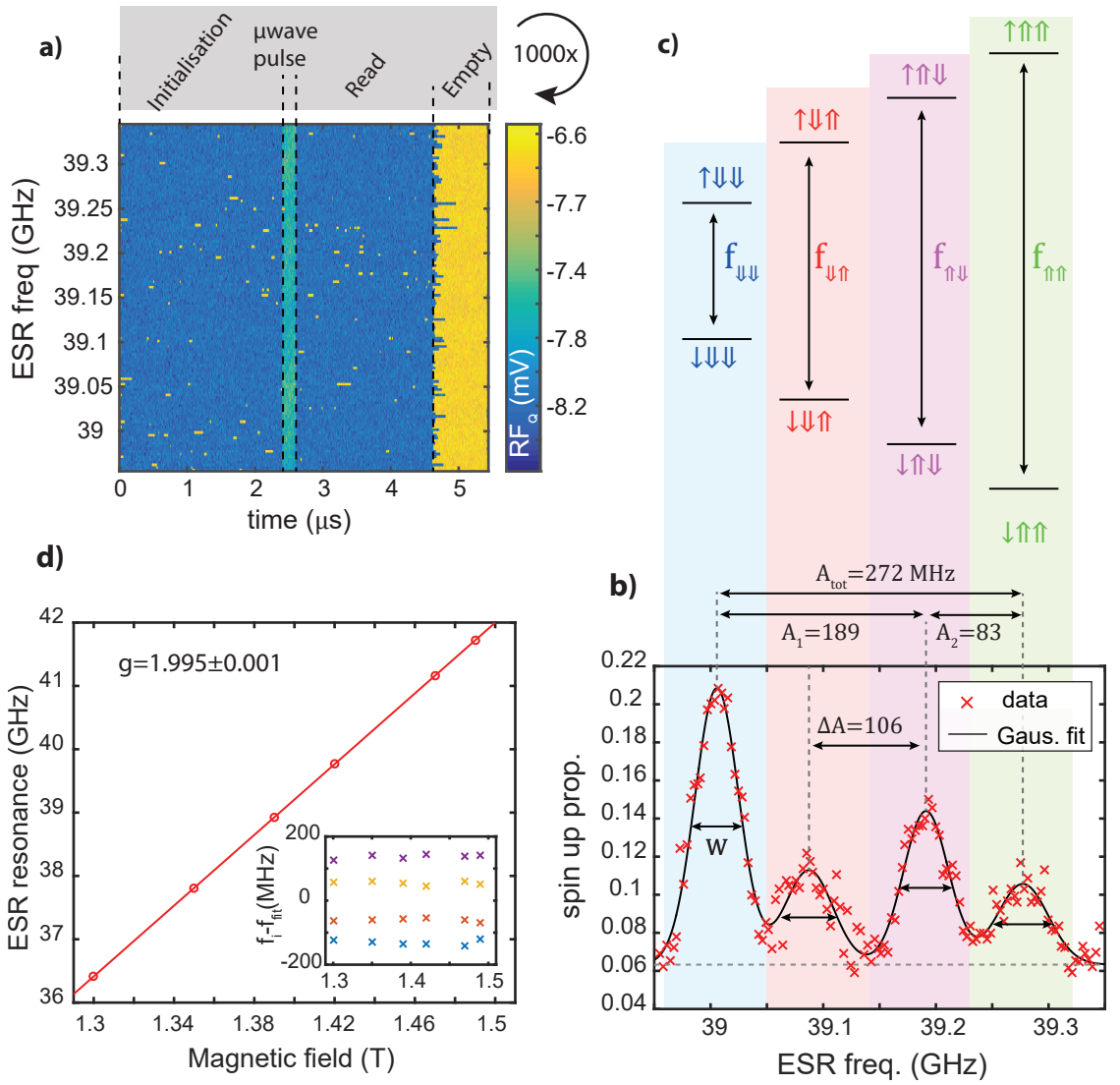

Figure 5.17: **Electron spin resonance on a 2P quantum dot. a)** The ESR spectrum is measured on the rightmost dot of the device by repeatedly loading an electron spin-down ("initialisation"), applying a microwave pulse at a frequency freq ("μwave pulse"), reading out the electron spin state ("Read") and finally unloading the electron ("Empty"). If the microwave frequency matches the Larmor frequency of the electron spin, a spin up (high RF_Q response) is recorded in the readout phase. The experiment is performed consecutively across 130 frequencies, and repeated a thousand times. Averaging the spin up counts over the entire experiment yields the ESR spectrum in **b)**. Four resonances are visible and indicate that the electron is bound to a quantum dot formed by two phosphorus donors (2P), with a hyperfine coupling of $A_1 = 189 \pm 5\,\mathrm{MHz}$ and $A_2 = 83 \pm 5\,\mathrm{MHz}$ to the first and second donor. The hyperfine difference $\Delta A = A_1 - A_2 = 106 \pm 5\,\mathrm{MHz}$ is indicative of a hyperfine Stark shift. **c)** Schematic energy level of a 2P donor quantum dot for $A_1 \neq A_2$, and $\gamma_n B < A_i < \gamma_e B$, as is observed in the spectrum in b). The four resonances can be attributed to the $\Downarrow\Downarrow$, $\Downarrow\Uparrow$, $\Uparrow\Downarrow$ and $\Uparrow\Uparrow$ nuclear spin states shifting the electron spin's resonance frequency due to the hyperfine interaction. **d)** Linear shift of the ESR resonance frequency with magnetic field. A linear fit using $g\mu_\mathrm{B}B/h$, yields a g-factor of 1.995 ± 0.001 consistent with the value measure in [4] on another 2P donor quantum dot. The peak spacing does not shift appreciably with magnetic field (see inset), consistent with a peak splitting due to the hyperfine interaction, that is independent of magnetic field.

produce a fluctuating magnetic field that shifts the instantaneous Larmor frequency of the electron in time, and render high fidelity spin control using resonant driving challenging [33, 34]. In such cases the electron spin can be flipped with higher fidelity using adiabatic inversion [35]. Adiabatic inversion can be understood by considering that the Hamiltonian H describes an energy anti-crossing with energy gap $\gamma_e B_1$ and energy detuning $\delta\omega$ (both in units of frequency). In this framework, the electron spin can be inverted by adiabatically traversing the anti-crossing. In practice this is achieved by sweeping the frequency of the microwave drive across the expected average Larmor frequency of the electron. If the rate of change in the frequency is slow enough compared to $\gamma_e B_1$, the electron spin can inverted with high fidelity [35].

We measure the electron spin resonance (ESR) spectrum of the first electron on the right dot by repeatedly attempting adiabatic inversions of the electron spin across a range of ESR frequencies centred around the expected Larmor frequency $\gamma_e B_0$ of the electron. In practice, this is performed by repeatedly performing the following sequence. First the electron is initialised in the spin-down state ("initialisation" in Fig. 5.17a), then the electron spin is flipped using adiabatic inversion ("μ-wave pulse"). The electron spin state is then read-out using the parameters described in Sect. 5.2.2 ("Read"), and finally the quantum dot is emptied of any electron ("Empty"). This pulse sequence is performed a each time for 130 frequency points across the frequency range to make sure that the instantaneous Larmor frequency of the electron is matched for every frequency sweep with high probability. The time-resolved charge sensor signal throughout such a frequency sweep is shown in Fig. 5.17a. Each frequency sweep is repeated a thousand times, and the electron spin-up proportion measured at each frequency is calculated to obtain the spectrum of Fig. 5.17b. The adiabatic spin inversion is performed with a microwave burst covering a frequency range of 40 MHz over a duration of 200 µs. The microwave burst is applied while the chemical potential of both spin states are plunged deep below the Fermi level to prevent spurious tunnelling of the electron spin.

The ESR spectrum in Fig. 5.17b displays four peaks, with the first two and the last two forming a doublets separated by a frequency $A_2 = 83 \pm 5$ MHz, and the two doublet being split by a frequency $A_1 = 189 \pm 5$ MHz. The four observed shifts in the electron Larmor frequency can be explained by the contact hyperfine interaction of the electron with two phosphorus nuclear spin, each hyperfine interaction with strength A_1 and A_2. Indeed, the hyperfine interaction term in the Hamiltonian describing an electron spin $\vec{s}$ coupled to two spin-1/2 nuclei $\vec{i_1}$ and $\vec{i_2}$ with respective hyperfine interaction strengths A_1 and A_2 is given by $A_1\vec{s}\cdot\vec{i_1} + A_2\vec{s}\cdot\vec{i_2}$.

For each of the two electron-spin states, the hyperfine term yields four energy shifts for the four possible nuclear spin configurations $\{|\Downarrow\Downarrow\rangle, |\Downarrow\Uparrow\rangle, |\Uparrow\Downarrow\rangle, |\Uparrow\Uparrow\rangle\}$ (see Fig. 5.17c). The eight states are compatible with four possible ESR transition frequencies $\{f_{\Downarrow\Downarrow}, f_{\Downarrow\Uparrow}, f_{\Uparrow\Downarrow}, f_{\Uparrow\Uparrow}\}$ that replicate the peak spacings observed in the spectrum of Fig. 5.17b. The full width at half maximum (FWHM) of each peak is $W = 49 \pm 3$MHz consistent with the frequency-sweep chirp width of 40 MHz and a peak broadening of ≈ 7 MHz measured in [33, 34]. The significant difference between the two hyperfine values A_1 and A_2 are attributed in the current section to a shift of the wavefunction due to static electric fields within the device, likely originating from band-bending near the phosphorus doped structures. The asymmetry in the ESR peak height is linked in Sect. 5.3 to the non-homogeneous occupation of the four nuclear spin states within the 2P QD. This non-homogeneous occupation of nuclear spin states is attributed to nuclear spin relaxation and excitation mechanisms, such as the hyperfine mediated coupling to phonons, the ionisation shock effect, and the magnetic dipole interaction between nuclear spins.

The ESR spectrum is acquired over a range of static magnetic fields $B_0 = 1.3 - 1.5$T, and reveals a linear trend of the average resonant frequency f, consistent with the expected trend $f = g\mu_B B_0/h$ for an electron spin, where μ_B is the Bohr magneton and h the Planck constant (see Fig. 5.17d). A least-squares fit yields an electron g-factor $g = 1.995(1)$ consistent with that measured on another 2P molecule in [4] ($g = 1.995(20)$). The ESR peak-spacing remains independent of magnetic field supporting the fact that the hyperfine interaction is the main cause of the peak splitting, $A_1 \neq A_2$ (see inset).

The contact hyperfine interaction between an electron spin and a nuclear spin is proportional to the probability density $|\Psi(r_n)|^2$ of the electron wavefunction evaluated at the position r_n of the nucleus [36]. A shift in the electron wavefunction can therefore lead to a change in the hyperfine interaction strength. In particular, such a shift can be produced by electric fields in what is called the hyperfine Stark effect. The shift of the wavefunction with an applied electric field E can be captured to first and second order by perturbation theory, leading to linear and quadratic Stark term: $A(E) = A(0)(1 + \eta_1 E + \eta_2 E^2)$[37]. When the wavefunction is symmetric along the direction of the electric field, the shift in A is constrained by symmetry to be independent of the electric field sign, and the linear Stark coefficient η_1 therefore vanishes [37]. This results in a quadratic hyperfine Stark shift that was experimentally measured on antimony [38] and phosphorus donors [39] in bulk silicon and replicated by effective mass simulations [39]. When the symmetry of the

donor system is broken along the direction of the electric field however, the effect of the electric field on the wavefunction can become dependent on its direction, and the linear Stark coefficient can become finite.

The symmetry of the single donor is for example broken in the vertical direction for ion implanted single phosphorus donors due to the vicinity of the silicon/silicon dioxide interface [37]. In such devices, an linear Stark shift was indeed demonstrated experimentally [40], with a coefficient of proportionality $\alpha_{1,\mathrm{Stark}} = A(0)\eta_1 \approx 0.34\,\mathrm{MHz/(MV/m)}$.[11] The symmetry of the single donor can also be broken by the presence of a second nearby donor, for example in a 2P molecule such as found in the device studied here. Tight binding simulations performed by Hile *et al.* in ref. [4] indeed suggest that the linear hyperfine Stark effect dominates the quadratic Start shift for 2P donor molecules when the electric field is applied parallel to the donor separation axis. This can be simply understood when considering the preferential shift of the electron wavefunction from one positively charged nucleus to the other compared to a shift away from the two positive charges of the 2P molecule. The linear Stark shift could not be resolved in the experiment of Hile *et al.* due to the predicted hyperfine shift being smaller than the ESR peak width which was broadened by the interaction with the nuclear spin bath. Indeed, the non-normalised linear Stark coefficient was predicted to be $\alpha_{1,\mathrm{Stark}} = A_0\eta_1 = 0.6\,\mathrm{MHz/(MV/M)}$ [4], and would only lead to a peak splitting of $\Delta A = 2\alpha_{1,\mathrm{Stark}}E = 5.2\,\mathrm{MHz}$ for an estimated electric field of $4.3\,\mathrm{MV/m}$, well below the chirped peak width of $28\,\mathrm{MHz}$.

The total hyperfine value A_{tot} and hyperfine Stark shift $\Delta A = A_1 - A_2$ measured in the spectrum in Fig. 5.17b can be used to estimate the exact donor configuration within the quantum dot. This was achieved by matching the experimental values to tight binding simulation (performed by Md Serajum Monir from Prof. Rajib Rahman's group). The value A_{tot} is found to be independent of electric field for the magnitudes considered here (see also [4])[12]. A_{tot} is therefore a more reliable tool for donor metrology compared with the total hyperfine Stark shift $\Delta A = A_1 - A_2$ which requires an additional estimation of the effective electric field experienced by the 2P molecule: $\Delta A = 2\alpha_{1,\mathrm{Stark}}E$. The estimation of the effective electric fields in our device is complicated by the fact that the silicon conduction-band bends near the heavily doped phosphorus structures of our gates and charge sensors [22, 41]. Band-bending leads to an effective electric field experienced by the electron and

[11] The coefficient $A(0)\eta_1$ is estimated from the measured $\frac{\partial A}{\partial V} = 0.91\,\mathrm{MHz/V}$ and the simulated $\frac{\partial E}{\partial V} = 2.62\,\mathrm{MV/m/V}$.

[12] The independence of A_{tot} can be understood by a scenario in which the weight of the electron wavefunction simply shifts from one donor to the other.

has been shown to affect the measured charging energies of a single donor [22, 41]. Whilst, tight binding simulations of conduction-band bending near a heavily-doped phosphorus lead were successful in predicting the measured charging energies of the single atom transistor [22, 41] it has not yet been performed near a finite structure such as the SET island (work in progress).

The total hyperfine interaction strength A_{tot} is simulated across two lattice vectors $a_0 = 0.54\,\text{nm}$ within the lithographic plane $Z = 0\,a_0$, and three lattice planes above : $Z = 0.25a_0$, $0.5a_0$, $0.75a_0$ (see Fig. 5.18a). In all simulated configurations, the Stark shift is mainly linear and is appropriately described by $\Delta A = 2\alpha_{1,\text{Stark}}E$.[13] The simulated total hyperfine interaction is seen to increase when the separation of the donors in the 2P molecule is decreased. This is linked to the two potential well of the donor nuclei joining together, therefore increasing the probability density $|\Psi(r_{\text{n}})|^2$ of the electron wavefunction evaluated at the position r_{n} of each nucleus. The increased probability density results in an increased contact hyperfine interaction.

All configurations that are consistent with the measured total hyperfine value have a donor separation of about 1 nm (coloured markers in Fig. 5.18a). Two configurations yield simulated total hyperfine values that fall within the confidence interval $[268, 276]\,\text{MHz}$ of the measured value. The first donor configuration, with separation vector $(1.5, 0.5, 0)a_0$ yields a total hyperfine value of 276 MHz (labelled "276" in Fig. 5.18a). The second configuration, with separation vector $(2, 1/4, 1/2)a_0$, results in a total hyperfine value of 275 MHz (labelled "275" in Fig. 5.18a). The Stark coefficient of configuration 275 however is small[14] and would require an effective electric field of $35\,\text{MV/m}$ to replicate the observed hyperfine shift $\Delta A = 106 \pm 5\,\text{MHz}$. Such a large effective electric field is well beyond the critical electric field $\epsilon_0 = 10-30\,\text{MV/m}$ measured in [42] at which the un-doped silicon becomes conductive. Such breakdown of the insulating behaviour of silicon manifests as current leakage and was not observed during operation of the device. Configuration 276 however exhibits a three times larger Stark coefficient of $2\alpha_{1,\text{Stark}} = 10.5\,\text{MHz/(MV/m)}$. This lowers the electric field magnitude required to replicate the observed hyperfine shift to $E = 10\,\text{MV/m}$. This effective electric field magnitude is within the range where current leakage is not expected to occur. However the magnitude cannot be accounted for by the simulated electric field value of $3.3\,\text{MV/m}$ found using the finite element solver COMSOL. The difference of $7.2\,\text{MV/m}$ in the electric field could be explained

[13] With the notable exception of configuration 263 where the hyperfine values are already split at zero electric field, so that $\Delta A = \alpha_0 + \alpha_{1,\text{Stark}}E$

[14] $2\alpha_{1,\text{Stark}} = 3.0\,\text{MHz/(MV/m)}$

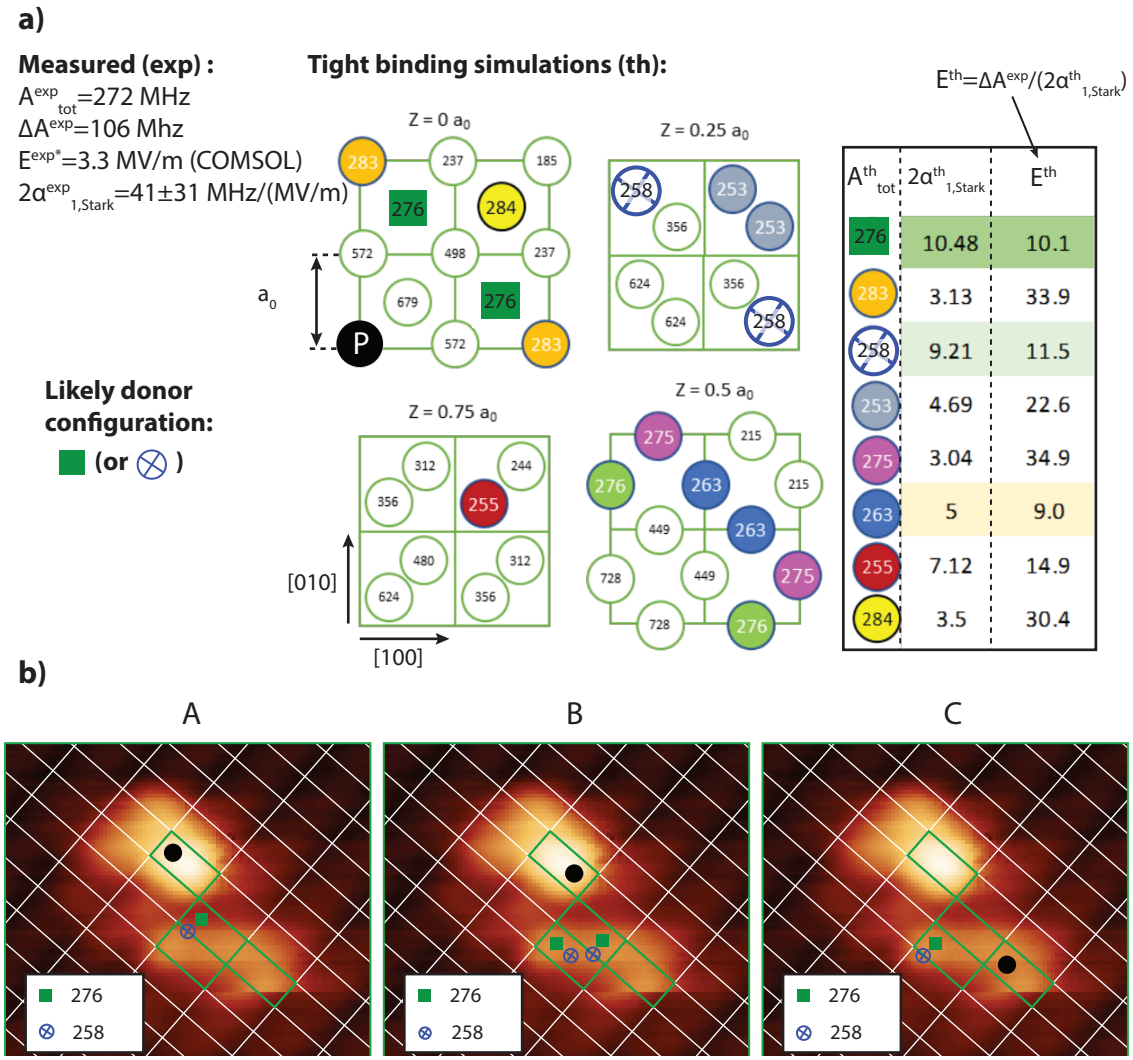

Figure 5.18: **Location of the 2 phosphorus atoms with the right 2P quantum dot. a)** The measured total hyperfine interaction $A_{\text{tot}}^{\text{exp}} = A_1 + A_2 = 272 \pm 4\,\text{MHz}$ and the hyperfine Stark shift $\Delta A^{\text{exp}} = 106 \pm 5\,\text{MHz}$ can be compared to tight binding simulations to estimate the likely relative position of the two phosphorus donors in the right quantum dot. The total hyperfine interaction strength is simulated across two lattice vectors $a_0 = 0.54\,\text{nm}$ within the lithographic plane $Z = 0\,a_0$, and the three lattice planes above ($Z = 0.25a_0$, $0.5a_0$ *and* $0.75a_0$) (simulations by Md Serajum Monir). The position of one of the two donors is fixed to the lithographic plane (black circle). The measured total hyperfine value is matched within 4 MHz by configuration 276 and 275. For the latter configuration however, the observed stark shift ΔA^{exp} would require an electric field of 35 MV/m, well above the electric field $E^{\text{exp}} = 3.3\,\text{MV/m}$ estimated from finite element simulations. Configuration 276 however would only require an electric field of 10.1 MV/m to match the observed Stark shift. The 7.2 MV/m mismatch to the simulated electric field could be explained by band bending known to occur near our heavily phosphorus-doped leads [22, 41]. Another configuration (258), also requires a similar electric field strength to match the measured hyperfine Stark shift, and is only one lattice plane above the lithographic plane. **b)** The two configuration 276 and 258 can be matched to the STM images of the quantum dot before donor incorporation. The green rectangles indicate the silicon dimers that were imaged with phosphorus adsorbates (see Fig. 5.14). The two lattice configurations 276 and 258 are compatible with 8 different configurations within the lithographic patch. Figure a) adapted from Md Serajum Monir in Prof. Rajib Rahman's group.

by conduction band bending that is known to occur near the heavily phosphorus structures[15]. An accurate simulation of the band bending in this device is under investigation.

In summary, configuration 276 not only fits the measured total hyperfine value within 4 MHz uncertainty, but also displays the largest sensitivity to electric fields. It is thus the most likely configuration of the donor molecule in the device. Another likely donor configuration is that with a separation vector $(1.75, 1/4, 1/4) * a_0$ with a total hyperfine value of 258 MHz. This configuration exhibits the second largest Stark shift $2\alpha_{1,\text{Stark}} = 9.2\,\text{MHz}/(\text{MV/m})$ and would therefore only require an effective electric field of 11.5 MV/m to match the measured Stark shift (labelled 258 and depicted as blue circles in Fig. 5.18a). The two configurations with the largest Stark coefficients are both compatible with the STM images of the phosphine adsorbates within the lithographic patches of the right quantum dot(see Fig. 5.18a).

The ESR spectrum of the 2P molecule in this work exhibits three major differences to that acquired on a 2P molecule by Hile *et al.* in [4]. First, Hile *et al.* did not measure a discernible difference $\Delta A = A_1 - A_2$ between the two hyperfine interactions (see Fig. 5.19b), yielding a two-fold degenerate central peak instead of a pair of peaks split by $\Delta A = 106$ MHz in this work (see Fig. 5.19a). Second, the sum of the hyperfine interactions $A_{\text{tot}} = A_1 + A_2$ is much larger, with a value of 524 MHz for Hile *et al.*, instead of 272 MHz in this work. Both features can be explained by differences in the donor configurations within the silicon lattice. Indeed, the large total hyperfine value observed in Hile *et al.* [4] can be explained by a reduced physical separation between the donors of the molecule. The total hyperfine value is indeed best matched by two configurations with separation vector $(1, 0, 0)a_0$ and $(1, 1, 0)a_0$ (see diamond markers in Fig. 5.19c). These two configurations are next nearest neighbours (NNN) to the configuration 276 attributed to the 2P molecule studied here. Despite the configurations being close, they display a Stark coefficient that varies by an order of magnitude. Indeed, the Stark coefficient is estimated to be $2\alpha_{1,\text{Stark}} \approx 1\,\text{MHz}/(\text{MV/m})$ for Hile *et al.* instead of $10.5\,\text{MHz}/(\text{MV/m})$ for this work (see inset of Fig. 5.19d). This large difference in the Stark coefficients, despite the vicinity of the configuration can be attributed to a difference in the crystallographic direction along which the donors have incorporated in the silicon lattice. Indeed, simulations of the Stark shift along 4 different crystallographic directions uncover a clear pattern when plotted against the donor separation, see Fig. 5.19d. Donors separated along the [100] and [120] directions display a smooth upwards trend of the

[15] the effective electric field due to band bending $10 - 20$ nm away from G1 in Fig.3 in [41] can be roughly estimated to be $\approx 5 - 10$ MV/m

hyperfine Stark coefficients. This is in contrast to donors separated along the [110] and [130] directions, where the Stark coefficient exhibits strong oscillations, within the bounds approximately set by the two smooth trends. This oscillatory behaviour with donor separation is reminiscent to that of the exchange interaction between two donor bound electrons [43, 23]. This behaviour is a possible indication of valley interference effects where the electron wavefunction shows a non-trivial oscillatory dependency on the order of single lattice sites leading to significant variation in the contact hyperfine value for small lattice displacements. The donor configuration 276 that is attributed to the donor molecule studied here lies along the crystallographic direction [130] that exhibits strong oscillations, and appears as a clear outlier for small donor separations (see inset of Fig. 5.19d). The large magnitude of the hyperfine Stark shift in the 2P molecule studied here compared to that of Hile *et al.* could therefore be attributed to a slight change in the donor configuration which brings with it a dramatic change in the valley interference effect, and thus in the measured Stark shift.

The strong dependence of the hyperfine Stark shift on the donor orientation can be used as a benefit for certain applications, for example, for EDSR [45]. Addressable nuclear magnetic resonance (NMR) on donor molecules for example requires the NMR frequencies associated with the different nuclei in the molecule to be different. In the presence of an electron, the NMR transition frequency of nucleus i is simply given by $\gamma_n B_0 \pm A_i/2$, where $\gamma_n = 17\,\mathrm{MHz/T}$ is the gyromagnetic ratio of the phosphorus nuclear spin, and the sign change accounts for the electron spin orientation. The degeneracy in the NMR transition frequencies can therefore be lifted by a hyperfine Stark shift that modifies the values of the individual hyperfine interaction strengths A_i. A different operation mode for a donor molecule is the proposal for electrically driven resonance of the electron spin shared by a 1P-2P double quantum dot (see Chapter 4). The spin rotations are driven by a flip-flop of the electron spin with the nuclear spin in the 1P quantum dot. The qubit operation error is highly dependent on the magnetic gradient produced by the two nuclear spins in the 2P quantum dot. The error can be minimised by initialising the nuclear spins in the 2P molecule in opposite directions, and can be further reduced by ensuring that the hyperfine interaction strength to the two donors in the 2P molecule cancel out by controlling the Stark shift of the donors. The qubit error can thus be minimised by reducing the Stark shift $\Delta A = A_1 - A_2 = 2\alpha_{1,\mathrm{Stark}} E$. This is best achieved by engineering the hyperfine Stark coefficient to be small, for example by patterning the two donors of the 2P molecule along the [100] direction (see STM patterning

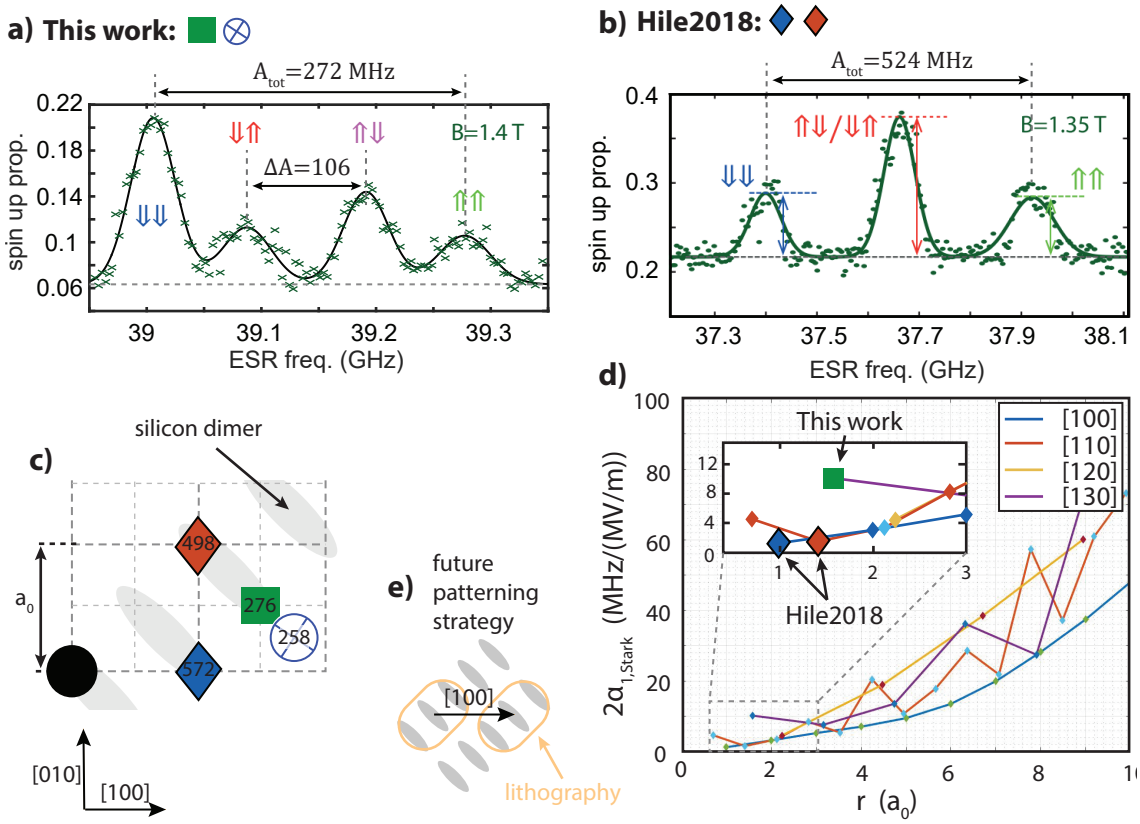

Figure 5.19: **2P Stark coefficients and donor configurations.** Stark-shifted 2P spectrum from this work **(a)** and non-Stark-shifted spectra from Hile *et al.* (Hile2018) [4] **(b)**. The splitting of the degeneracy of the central peak in a) is attributed to the linear hyperfine Stark effect. **c)** Donor configurations attributed to the 2P molecule in this work (green square, blue circle) and to the 2P molecule of Hile *et al.* (diamond markers). A shift by only one lattice site on the surface results in a near-doubling of the total hyperfine interaction. **d)** Tight binding simulation of the linear hyperfine Stark coefficient for a 2P donor molecule as a function of the donor separation, for four crystallographic directions. The hyperfine Stark coefficient displays oscillations along the [1,1,0] and [1,3,0] directions that are likely related to valley interference effects. The hyperfine Stark shift is minimised along the [1,0,0] crystallographic direction. The donor configuration 276 estimated from donor metrology (green square in the inset, and in b) corresponds to a configuration where the Stark coefficient is dramatically enhanced ($2\alpha_{1,\mathrm{Stark}} = 10.5\,\mathrm{MHz/(MV/m)}$)) compared to close-by configurations. Two such configurations (large red and blue diamond markers) were likely realised in the 2P-donor quantum dot of Hile *et al.* Indeed the hyperfine Stark shift of configuration 498 is ten times smaller ($2\alpha_{1,\mathrm{Stark}} \approx 1\,\mathrm{MHz/(MV/m)}$) than that of configuration 276 ($2\alpha_{1,\mathrm{Stark}} = 10.5\,\mathrm{MHz/(MV/m)}$). The difference in the Stark coefficients explain why the central two peaks in the ESR spectrum are split in the 2P device presented here (in **a**), while no such splitting is discernible within the peak width in the 2P device from Hile *et al.* (in **d**). **e)** Possible STM patterning strategy to minimise the Stark coefficient by increasing the chance of the donors being separated along the [100] crystallographic direction. Figure d) adapted from Md Serajum Monir in Prof. Rajib Rahman's group, and figure b) adapted from [44].

strategy in Fig. 5.19e).

A third difference in the ESR spectra measured here compared to that measured by Hile *et al.* [4] is the relative height of the ESR peaks. All four peaks in Hile *et al.* have the same magnitude (the degenerate central peak is twice the height of the outer one), while the ESR peaks measured here exhibit clear differences in their heights. The peak height can be related to differences in the nuclear spin dynamics, which is the focus of the following section Sect. 5.3.

5.2.4 Conclusion

In this section, advances in the design of the SET charge sensor were shown to yield a significant improvement of the electron spin readout fidelity on a donor quantum dot, from 83% with the previous sensor, to 94.4% with the improved sensor. Electron spin resonance using adiabatic spin inversion was then demonstrated on the first electron of the right donor quantum dots of the device. Electron spin resonance spectra revealed four peaks which can be attributed to a 2P molecule with a hyperfine interaction of the first and second nucleus to the electron of $A_1 = 189 \pm 5\,\mathrm{MHz}$ $A_1 = 83 \pm 5\,\mathrm{MHz}$ respectively. Metrology of the donor configuration within the silicon lattice was then performed by matching the measured hyperfine interaction strengths to values obtained by tight binding simulations. In particular, the total hyperfine interaction $A_{\mathrm{tot}} = A_1 + A_2 = 272 \pm 4\,\mathrm{MHz}$ was shown to be a useful metrology tool because it is independent on the electric field (to first order), and therefore does not include any fitting parameter. The measured hyperfine difference $\Delta A = A_1 - A_2 = 106 \pm 5\,\mathrm{MHz}$ allowed additional precision in the identification of the donor configuration. The difference in the hyperfine interaction strengths is attributed to a linear Stark effect that was previously observed in ion-implanted single phosphorus donors but not in 2P molecules. Together, the total hyperfine value and the hyperfine difference identify $[1.5, 0.5, 0]a_0$ from (0,0,0) as the most probable donor configurations, where a_0 is the silicon lattice constant. The measured total hyperfine interaction of this configuration falls within the uncertainty of the measured value and displays the largest Stark effect of all the compatible configurations. The chosen configuration is close to that attributed to another 2P molecule measured by Hile *et al.* in [4], for which the hyperfine Stark effect could not be observed. Tight binding simulations performed by Md Serajum Monir in collaboration with Prof. Rajib Rahman's group revealed that the hyperfine Stark effect is highly dependent on the orientation of the donors within the 2P molecule in the crystal. The orientation attributed to the 2P molecule studied here was shown

demonstrate a 10-fold enhancement of the Stark effect compared to that observed by Hile *et al.* [4], explaining the observation of the Stark shift in the ESR spectra.

5.3 Readout and dynamics of nuclear spins in a 2P molecule

5.3.1 Nuclear spin readout on a 2P molecule

Readout of the nuclear spin state of the 2P molecule studied in Sect. 5.2 is performed by measuring the instantaneous position of the electron spin resonance (ESR) transition frequency. Indeed, the ESR frequency is shifted by the hyperfine interaction of the electron with the two phosphorus nuclei in the molecule, yielding four distinct transition frequencies for each of the four nuclear spin states $\{|\Downarrow\Downarrow\rangle, |\Downarrow\Uparrow\rangle, |\Uparrow\Downarrow\rangle, |\Uparrow\Uparrow\rangle\}$. The instantaneous transition frequency of an electron on the donor molecule is measured by attempting the adiabatic inversion of an electron spin-down bound to the two donors over a range of 130 ESR frequencies encompassing the four resonant frequencies. Each electron spin adiabatic inversion attempt is performed using the following pulse sequence (see Fig. 5.20). An electron spin is loaded from the reservoir (with random spin orientation, "Load"), it is then initialised in a spin-down state by reading-out its state ("Initial./Read"). An attempt is then made at adiabatically inverting the electron spin using an ESR pulse after which the electron spin is read out and then emptied from the quantum dot. Finally, a waiting period leaves time for the microwave source to switch to the next frequency. The ESR pulse is performed using a 200 μs long ESR pulse, with a linear sweep of the microwave frequency over a range of 40 MHz centred on the probed transition frequency and using a power of -5.1 dBm at the microwave source. Each adiabatic inversion attempt requires 25.7 ms on average, most of which is spend by the microwave source switching its frequency for the next attempt. A single nuclear spin readout sequence, consisting of 130 such sequences therefore requires 3.34 s on average. The nuclear spin readout sequence is repeated 1000 times, over a period of 70 minutes, yielding 1000 instantaneous ESR spectra (see Fig. 5.21a). It is apparent from the measurement that the position of the electron resonance frequency switches between the four identified resonance frequencies over the course of the experiment. The ESR spectra of the 2P molecule are recovered when the spin-up proportion over the whole experiment is calculated at each frequency (see Fig. 5.21b). The 50 MHz width of the averaged ESR peaks arises from the 40 MHz width of the adiabatic

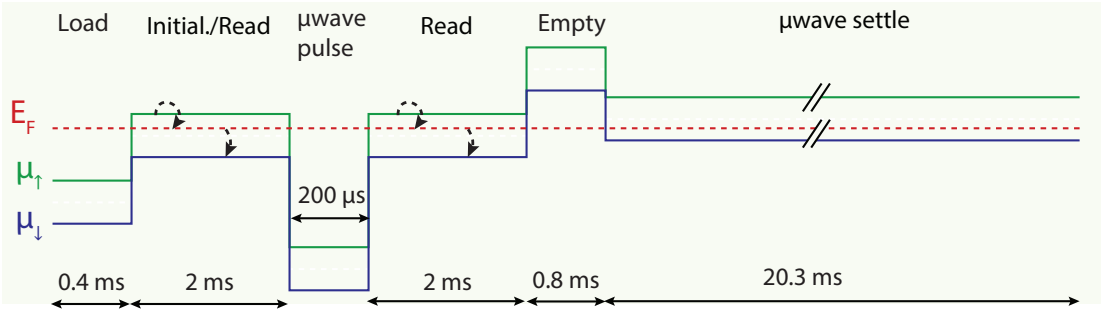

Figure 5.20: **Pulse sequence for nuclear-spin tracking** The pulse sequence performs attempts adiabatic inversion of an electron spin-down at one frequency, followed by spin readout. The pulse sequence depicted in the figure last 25.7 ms and is repeated at 130 ESR frequencies across the spectrum. Each nuclear spin measurement therefore lasts 3.34 s on average. 80% of the time is spent switching the microwave frequency between each adiabatic inversion ("μ-wave settle").

inversion frequency sweep, and from the fluctuating magnetic field produced by the ^{29}Si nuclei present in natural silicon [4, 33]. This fluctuating field could account for the slight variations in the position of the instantaneous ESR spectra in Fig. 5.21a [35].

Next we optimise and characterise the nuclear spin-readout. Four detection windows are defined around each average peak position (see Fig. 5.21a). Histograms of the spin-up count $N_\uparrow$ within each window are well described by the sum of two Poisson distributions:[16].

$$P(N_\uparrow) = (1 - a_i)P_{N_0}(N_\uparrow) + a_i P_{N_1}(N_\uparrow), \tag{5.3.1}$$

where the Poisson distribution with mean λ is $P_\lambda(N_\uparrow) = \frac{\lambda^{N_\uparrow} e^{-\lambda}}{N_\uparrow!}$, and a_i describes the relative weight of the two distributions. The fit independently yields the same pair of Poisson distributions for the four detection windows, one with an average of $N_0 = 1.95(4)$ and the second one with an average $N_1 = 7.0(3)$ (see Table 5.2). The first distribution $P_{N_0}(N_\uparrow)$ is identified as the distribution of background spin up count when no peak is in the detection window, while the second one, $P_{N_1}(N_\uparrow)$, is associated with the distribution of correct spin-up counts, when the instantaneous Larmor frequency is indeed in the detection window. On average, each detection window of $N_w = 21$ measurements therefore registers $\lambda_0 = N_0/N_w = 9.3(2)\%$ background counts when no peak is present and $\lambda_1 = N_1/N_w = 33(1)\%$ of correct spin-up counts when a peak is present. The background counts are attributed to the spin

[16]Using a window of 21 frequencies 63 MHz

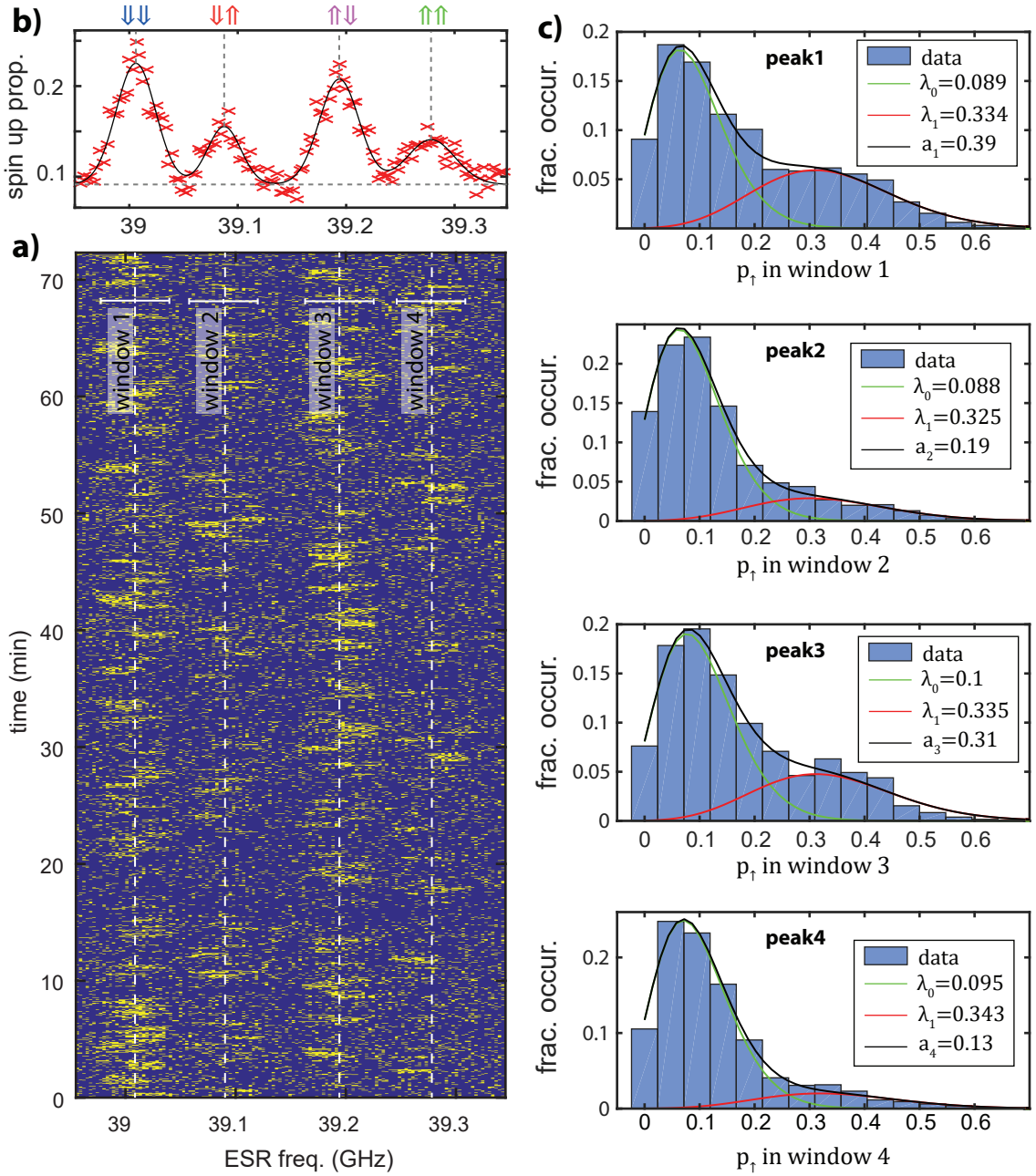

Figure 5.21: **Time-resolved ESR spectra on a 2P molecule. a)** Spin-up proportion after adiabatic inversion of an electron spin-down on the 2P molecule, as a function of ESR frequency over a duration of 70 minutes. Each instantaneous spectrum takes on average 3.4 s. The instantaneous Larmor frequency of the electron can be seen to shift in time, and is indicative of underlying time-dynamics of the spin orientation of the two phosphorus donor nuclei. **b)** Averaged over the entire duration of 70 minutes, the instantaneous spectra yield the spectrum of the 2P molecule studied previously in Sect. 5.2. **c)** Histogram of the spin up proportion in each detection window for each instantaneous spectrum. The histograms are fitted independent by the sum of two Poisson distributions. In each detection window, a first Poisson distribution describes the background spin-up counts, with an average $\lambda_0 \approx 10\%$ background counts per window. A second Poisson distribution describes the spin up proportion $\lambda_1 \approx 33\%$ in the detection window when a peak is present within the window. The relative proportion of the two Poisson distribution, describing the probability for a peak rather than the background to be observed in the window, is described by the fit parameter $p_\uparrow$. The fit parameter qualitatively reproduces the relative heights of the ESR peaks in the long-term spectrum.

readout infidelity $\approx 5\%$ and the infidelity in the adiabatic inversion. The fit parameters a_i correspond to the proportion of the total measurement time that a peak (as opposed to background detection) is detected in the window i. As expected the parameters a_i add up to 1.02(5) because a peak can only be present in one window at a time (this is not enforced by the fits). The histograms of the normalised spin up counts $p_\uparrow = N_\uparrow/N_w$ in each window is displayed in Fig. 5.21c.

Peak $i =$	1	2	3	4	weighted average
N_0	1.86(9)	1.84(6)	2.14(9)	2.00(5)	1.95(4)
N_1	7.0(4)	6.8(7)	7.0(5)	7.2(9)	7.0(3)
a_i	0.39(2)	0.19(2)	0.31(3)	0.13(2)	

Table 5.2: Fit parameters of Poisson distribution in each peak window, for a window width of 21 frequencies (63.5 MHz). The digit in parenthesis indicates the 95% confidence interval

For a given window size, the background and signal distributions $P_{N_0}(N_\uparrow) \equiv P(N_\uparrow|\text{no peak})$ and $P_{N_1}(N_\uparrow) \equiv P(N_\uparrow|\text{peak})$, allow the estimation of the peak detection fidelity within each window, when thresholding the signal with a threshold N_{th} (see Fig. 5.22a). If a spin-up count $N_\uparrow$ is recorded within the window at or above the threshold ($N_\uparrow \geq N_{\text{th}}$) at a given time, a positive peak detection is attributed to that time step. This process leads to errors if a background count is identified as a signal or if a peak is identified as background. The error in the peak detection is therefore characterised by:

$$1 - F_{\text{peak}}(N_{\text{th}}) = \frac{1}{2}\left(\sum_{N=N_{\text{th}}}^{N_{\text{w}}} P_{N_0}(N) + \sum_{N=0}^{N_{\text{th}}-1} P_{N_0}(N)\right) \tag{5.3.2}$$

We find the maximum peak detection fidelity $F_{\text{peak}} = 84.8\%$ at a window size $N_{\text{w}} = 21$ and a detection threshold $N_{\text{th}} = 4$ (see Fig. 5.22b). When applying this peak detection procedure on the measured data, it becomes apparent that on many time steps several peaks are detected at once instead of the single expected peak (see Fig. 5.22f). Only in 57% of cases is a single peak is detected, and in 28% of case two peaks are detected (see Fig. 5.22). The proportion of multiple peak detections, is very well predicted by a model based on the peak detection fidelity $F_{\text{peak}} = 84.8\%$ (red boxes in Fig. 5.22f). For example the probability to measure two peaks at a given time (when only a single peak is present) can be estimated as the probability of

- correctly detecting the peak in one window (probability F), but incorrectly

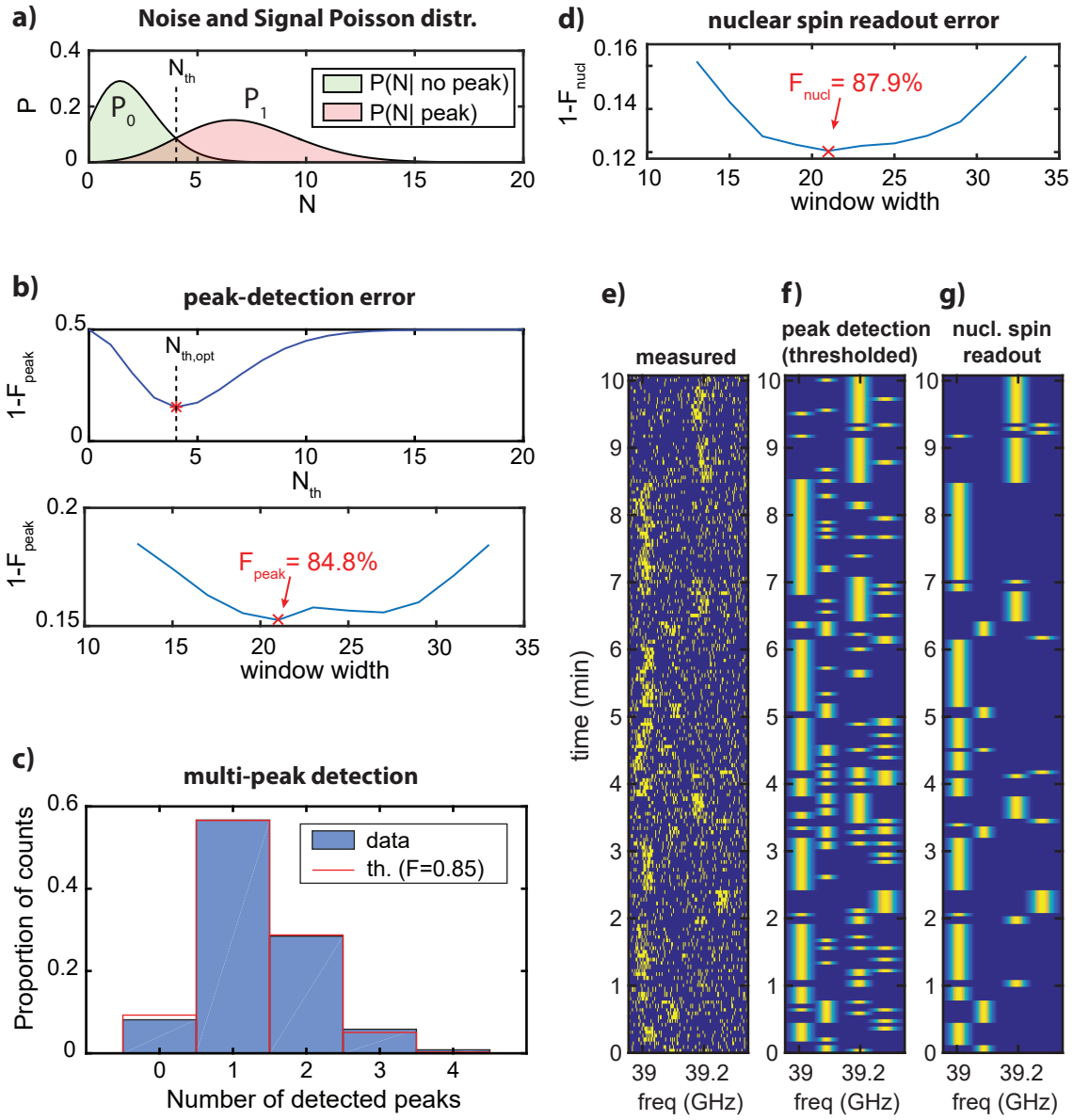

Figure 5.22: **Nuclear spin readout on a 2P molecule a)** Probability distributions of detecting a number N of spin-up electrons in the detection windows after an ESR burst, extracted form the data. If the instantaneous electron Larmor frequency is present(absent) in the window, N follows the Poisson distribution P_1 (P_0), with $\langle N \rangle = 7.0 \pm 1.3 (1.9 \pm 0.15)$ at the optimal window-width. **b)** The peak-detection within each window reaches a fidelity of 84.8% at an optimal threshold $N_{\rm th} = 4$, and a window of 21 frequencies (each corresponding to an attempted electron spin inversion and measurement). **c)** Histograms of multi-peak detection using the optimal threshold and window. In 40% of cases, more (or less) than one peak is detected. This is consistent with the estimated peak detection fidelity of 85% (theoretical prediction in red). **d)** Nuclear spin readout with 87.9% fidelity at a window width of 21 frequencies. The nuclear spin state is assigned to the detection window with most counts ("majority readout"). **e), f), g)** Nuclear-spin tracking for the first 10 minutes of the experiment. Raw data in **e**, peak detection in each window with threshold $N_{\rm th} = 4$ in **f**, and majority nuclear spin readout in **g**.

assigning a background count in another window to another peak (probability $(1-F)F^2$) yielding a probability $3F_{\mathrm{peak}}^3(1-F_{\mathrm{peak}})$

- OR, of incorrectly detecting the peak in one window (probability $1-F$), and incorrectly assigning a background count in two windows as two peaks (probability $\binom{3}{2}(1-F)^2F$), yielding a probability $\binom{3}{2}(1-F)^3F$.

The final estimation of the probability of measuring two peaks is therefore $p_{2\mathrm{peaks}} = 3F_{\mathrm{peak}}^3(1-F_{\mathrm{peak}}) + \binom{3}{2}(1-F)^3F$. The probabilities to measure 0, 1, 3 and 4 peaks can be obtained similarly. The high number of multiple peak detections, is related to the fact that there is a probability $F^4 = 52\%$ of correctly reading out the full nuclear spin states. The nuclear spin readout fidelity can be increased dramatically by utilising the fact that, while false counts due to the background occur, they rarely lead to a spin-up count that is larger than that associated with the signal. In fact, the nuclear spin state can simply be assigned to the detection window with the most count. The fidelity F_{nucl} of the resulting spin readout is just the probability of the peak producing a spin-up count N_{s} larger than any of three other background counts N_{b}:

$$F_{\mathrm{nucl}} = \sum_{N_{\mathrm{s}}=0}^{N_{\mathrm{w}}} P_{N_1}(N_{\mathrm{s}}) \left(\sum_{N_{\mathrm{b}}=0}^{N_{\mathrm{s}}-1} P_{N_0}(N_{\mathrm{b}}) \right)^3 . \tag{5.3.3}$$

This yields a nuclear spin readout fidelity $F_{\mathrm{nucl}} = 87.9\%$ at an optimal detection window size of 21 frequencies (see Fig. 5.22d). The nuclear spin assignment is shown for the first 10 minutes of the experiment in Fig. 5.22g. This is the first demonstration of nuclear spin readout on a tightly bound donor molecule in silicon.[17]

5.3.2 Extraction of the nuclear spin flip rates using a hidden Markov model

We next extract the transition rate between the four nuclear spin states. To mitigate the impact of the nuclear spin readout error, we extract the nuclear spin transition rates by fitting a discrete-time Markov model to the sequence of states estimated from the above detection procedure. We demonstrate the power of this approach by fitting the Markov model to the data of peak detection with a readout fidelity of 52%(see Fig. 5.22f, instead of the data based on the nuclear spin readout demonstrated with 88% fidelity (see Fig. 5.22g).

[17] Nuclear spin readout on two ion-implanted phosphorus donors at an estimated distance of 6 nm was very recently demonstrated by Madzik *et al.* in an ArXiv preprint [46].

Hidden Markov models

We now give a brief introduction to hidden Markov model, based on an excellent review article by Rabiner [47] of which we use the naming convention of variables. A discrete-time Markov Model is a probabilistic description of a system that changes its state (possibly back to the same state) at regular time intervals. The model describes the sequence of events as a Markov process $\mathbf{Q} = \{q_1, \ldots, q_T\}$, in which the state q_t of the system at a time t can only occupy a finite set of states S_i $(i = 1, \ldots, N)$, and for which the probability to occupy state S_j at any step t, only depends on the state q_{t-1} of the system in the previous time step (this property is referred to as memorylessness). The discrete-time Markov process is therefore fully modelled by the probabilities $a_{i,j}$ $(i, j = 1, \ldots, N)$ of the system changing from state S_i to state S_j in consecutive time steps (see Fig. 5.23a), and by the probability π_i $(i = 1, \ldots, N)$ of the initial state of the system at t=1 to be in state S_i. The evolution of the system in time is described by the probability vector $\mathbf{p}(t)$ of the system occupying any of the state S_i with probability $p_i(t)$ at each time step t. The probability vector follows the Markov equation [48]:

$$\mathbf{p}(t+1)^{\mathrm{tr}} = \mathbf{p}(t)^{\mathrm{tr}}\mathbf{A} \tag{5.3.4}$$

where $\mathbf{A} = (a_{i,j})$ is the transition probability matrix, and we use the convention of matrix multiplication from the left.

The Markov process $\mathbf{Q} = \{q_1, \ldots, q_T\}$ is called a hidden, when only probabilistic observation of the states are possible, with a discrete number of possible measurement outcomes v_k. A hidden Markov processes $\mathbf{Q} = \{q_1, \ldots, q_T\}$ can therefore only be inferred from the observation sequence $\mathbf{O} = \{O_1, \ldots, T\}$ (see Fig. 5.23b). The probabilistic measurement process, is modelled by a matrix $\mathbf{B}$ that assigns a probability $b_{j,k}$ to observing the measurement v_k when the (hidden) state of the system is S_j.

The nuclear spin state measurement data is clearly well suited to be modelled as a Markov process provided the physical processes leading to the transition events fulfil the Markovian property of memorylessness. Nuclear relaxation is one of the processes expected to lead to state transitions [8]. It is routinely modelled as a exponential process with a constant decay rate at each given time, and is therefore Markovian. The nuclear excitation processes through hyperfine shock [8] has been modelled by Pla *et al.* as a near chaotic precession of the nuclear spins in time [49], and can therefore be approximated as a Markovian process.

Given the assumption of memorylessness, the nuclear spin state experiment obtained from thresholding of the data is a hidden Markov process $\mathbf{Q} = \{q_1, \ldots, q_T |\ T =$

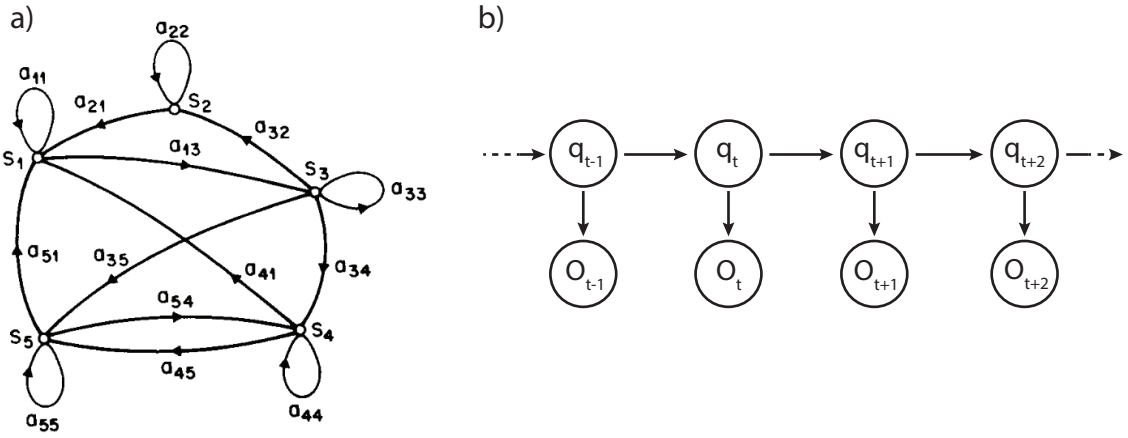

Figure 5.23: **Hidden Markov models. a)** Diagram of a 5-state discrete-time Markov model, with states S_i $(i = 1, \ldots, 5)$ and transition probabilities $a_{i,j}$ $(i, j = 1, \ldots, 5)$. **b)** Diagram of a discrete hidden Markov process. The Markov process $\mathbf{Q} = \{q_1, \ldots, q_T\}$ consists in a discrete sequence of steps q_t, at which the system can be in any of the states S_i $(i = 1, \ldots, 5)$. The state of the system at each step t is "hidden" and can only be inferred from the series of observation $\mathbf{O} = \{O_1, \ldots, O_T\}$. The state q_t of the system at each step t, depends only on the state q_{t-1} of the system in the previous step $t - 1$. Similarly, the observation of O_t of the system at step t only depends on the state q_t of the system at that step. These conditional dependences are indicated by arrows. **a** reproduced from [47].

1000}, in which the states S_i are the nuclear spin states ($S_1 = |\Downarrow\Downarrow\rangle$, $S_2 = |\Downarrow\Uparrow\rangle$, $S_3 = |\Uparrow\Downarrow\rangle$ and $S_4 = |\Uparrow\Uparrow\rangle$) and the set of measurements is the set of 16 states $(w1, w2, w3, w4) \in \{0, 1\}^4$ where $w_i = 1\,(0)$ indicates the detection (non-detection) of peak i. We encode the 4-tuples $(w1, w2, w3, w4)$ as a number $1 \leq v_i \leq 16$, using binary to decimal conversion to obtain the required dictionary v_i of observation outcomes. The observation sequence $\mathbf{O} = \{O_1, \ldots, O_T |\ T = 1000\}$, is then the encoded series of peak detection at each of the 1000 time steps during the measurement of 70 minutes. A hidden Markov model $\boldsymbol{\lambda}$ for this system consists in a transition probability matrix $\mathbf{A} = (a_{i,j})\ (\ i, j = 1, \ldots, 4)$, a measurement probability matrix $\mathbf{B} = (b_{j,k})\ (\ j = 1, \ldots, 4,\ k = 1, \ldots, 16)$ and a initial probability vector $\boldsymbol{\pi} = (\pi_i)\ (\ i = 1, \ldots, 4)$.

The optimal model $\boldsymbol{\lambda}^* = (\mathbf{A}, \mathbf{B}, \boldsymbol{\pi})$ which maximises the likelihood $p(\mathbf{O}|\boldsymbol{\lambda})$ of yielding the measured observation sequence $\mathbf{O}$ given the model $\boldsymbol{\lambda}$ is found using the Baum-Welch algorithm that converges towards a local maximum in the likelihood $p(\mathbf{O}|\boldsymbol{\lambda})$ by iteratively re-estimating the model parameters [47, 50]. The likelihood $p(\mathbf{O}|\boldsymbol{\lambda})$ is calculated using the well known inductive "forward" procedure [47]. The confidence intervals $[\lambda_m^-, \lambda_m^+]$ of each individual model parameters λ_m (e.g. $\lambda_m = a_{i,j}$, a transition probability matrix elements) are found by observing the decrease of

the maximum likelihood when the particular model parameter λ_m is constrained to a non-optimal value $\mu \neq \lambda_m^*$. The maximum likelihood of such a constrained model is $\max_{\boldsymbol{\lambda^c} \in U_c} p(\mathbf{O}|\boldsymbol{\lambda}^c)$, with the constrained model-subspace $U_c(\mu) = \{\boldsymbol{\lambda^c} \in U | \lambda_m^c = \mu\}$[48]. The constrained model parameter set $U_c(\mu)$ is nested within the non-constrained parameter set U ($U_c \subset U$), allowing a comparison of the likelihood of the two models using the likelihood ratio test:

$$\Lambda(\mathbf{O}, \mu) = \frac{\max_{\boldsymbol{\lambda^c} \in U_c(\mu)} p(\mathbf{O}|\boldsymbol{\lambda^c})}{\max_{\boldsymbol{\lambda} \in U} p(\mathbf{O}|\boldsymbol{\lambda})}. \tag{5.3.5}$$

The fact that the $-2\log(\Lambda)$ is approximately χ^2 distributed [48], allows the estimation of the intervals by finding $\lambda_m^{\pm}$ such that:

$$\Lambda(\mathbf{O}, \lambda_m^{\pm}) = \chi^2, \tag{5.3.6}$$

with $\chi^2 = 3.84$ for example for the 90% confidence intervals. In practice, we implement the constraint $\lambda_m^c = \mu$ by enforcing the constraint at each iteration of the Baum-Welch re-estimation procedure that calculates $\max_{\boldsymbol{\lambda^c} \in U_c(\mu)} p(\mathbf{O}|\boldsymbol{\lambda^c})$. Each time the re-estimated value λ_m^c is set to the value μ, physical constraints —such as the necessity of probabilities to add to one— are enforced as well.

Maximum likelihood Markov model of the 2P molecule

The Baum Welch algorithm described above yields the maximum likelihood model with the following transition probability matrix (see a diagram of the Markov model in Fig. 5.24):

$$\boldsymbol{A} = \begin{pmatrix} 86^{+3}_{-4} & 7^{+3}_{-2} & 7^{+3}_{-2} & 6 \times 10^{-5} \\ 15^{+6}_{-5} & 74^{+6}_{-8} & 7^{+5}_{-4} & 5^{+5}_{-3} \\ 8^{+3}_{-3} & 3^{+2}_{-2} & 86^{+4}_{-4} & 4^{+3}_{-2} \\ 2^{+3}_{-1} & 7^{+6}_{-4} & 8^{+6}_{-5} & 83^{+6}_{-7} \end{pmatrix} \times 10^{-2}, \tag{5.3.7}$$

where the states are numbered as $S_1 = |\Downarrow\Downarrow\rangle$, $S_2 = |\Downarrow\Uparrow\rangle$, $S_3 = |\Uparrow\Downarrow\rangle$ and $S_4 = |\Uparrow\Uparrow\rangle$, and $a_{i,j}$ gives the transition probability between S_i and S_j (from row to column). For example the transition probability from S_2 to S_1 is the matrix element $a_{2,1} = 15^{+6}_{-5} \times 10^{-2}$.[18] The diagonal elements of the matrix $\boldsymbol{A}$ represent the probability of the system to stay in its current state at each time step (82% on average), while the off-diagonal elements represent the probability of transitioning to a different

[18]The asymmetric 90% confidence interval $[x - L, x + U]$ in the value x is noted as x^{+U}_{-L}.

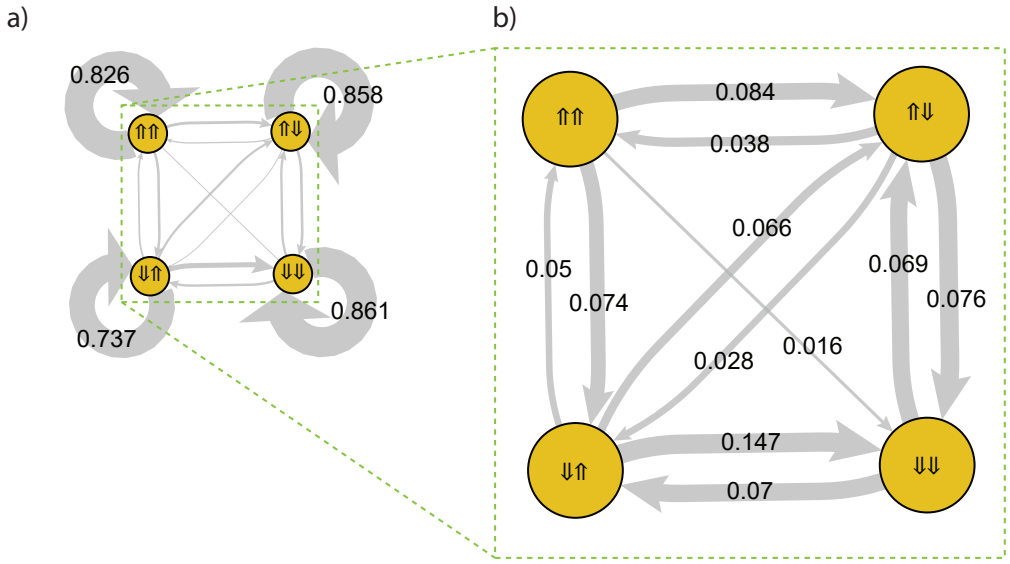

Figure 5.24: **Transition probabilities of the Markov model fitted to the nuclear spin tracking data.** The optimal Markov model maximises the likelihood of the observed nuclear spin states sequence occurring. This likelihood is estimated using the "forward-backward" algorithm [47]. This likelihood is maximised using the Baum-Welch re-estimation procedure [47, 50]. The width of the arrows in the diagrams is proportional to the magnitude of the transition probabilities. **a)** Full diagram of the Markov model. The probabilities for the system to stay in the same state (82% on average) are much larger than that of transitioning to another state (18% on average), indicating that the state lifetime is larger than the time between measurements. **b)** Closeup of the transition probabilities between distinct states. Simultaneous transitions when the nuclear spins are parallel are heavily suppressed (less than 2% probability). However, simultaneous transitions when the nuclear spins are anti-parallel (nuclear spin flip-flop) are almost as likely as single spin flips. This could be indicative of a nuclear dipole-dipole coupling.

state (18% on average). The nuclear spin lifetimes can be estimated by calculating the probability $p_i(N)$ of the system to remain in state S_i for N time steps, and to subsequently transition to another state. The probability is simply given by $p_i(N) = a_{i,i}^N(1 - a_{i,i})$ and can be rewritten as $p_{i,N} = \exp(-t/T_i)(1 - a_{i,i}) = p_i(t)$, were the discretised time (in seconds) is $t = N\Delta t$ ($\Delta t = 3.34\,\mathrm{s}$, and the lifetime of state i is $T_i = -\frac{\Delta t}{\log(a_{i,i})}$ (see also [47]). In this fashion we extract the following nuclear spin lifetimes from the Markov model:

$T_{\Downarrow\Downarrow}$	$T_{\Downarrow\Uparrow}$	$T_{\Uparrow\Downarrow}$	$T_{\Uparrow\Uparrow}$
$22^{+7}_{-5}\,\mathrm{s}$	$11^{+4}_{-3}\,\mathrm{s}$	$22^{+8}_{-5}\,\mathrm{s}$	$17^{+10}_{-6}\,\mathrm{s}$

The estimated lifetimes of the first ($\Downarrow\Downarrow$) and third state ($\Uparrow\Downarrow$) is larger than the that of the second ($\Downarrow\Uparrow$) and fourth state ($\Uparrow\Uparrow$), in the same fashion that the first and third peaks in the time averaged spectrum Fig. 5.21b are larger than the second and fourth ones. This confirms that the peak height in the ESR spectra is partly attributed to the underlying nuclear spin dynamics. However, we find that the peak heights are not exactly proportional to the lifetimes of their underlying nuclear spin state (e.g. the fourth ESR peak is smaller than the second one, but the lifetimes are not). This is likely due to variations in the adiabatic inversion efficiency that can result from limited electron spin coherence times [35].

Viterbi reconstruction of the nuclear spin dynamics of the 2P molecule

The optimal Markov model can be used to reconstruct the most likely sequence of states during the nuclear spin tracking experiment (Fig. 5.21a). The Viterbi algorithm [47, 51] is used to find the sequence of nuclear spin states $\mathbf{Q}^*$ that maximise the likelihood of leading to the measured observation sequence $\mathbf{O}$ given the optimal model $\boldsymbol{\lambda}^*$:

$$p(\mathbf{O}|\mathbf{Q}^*, \boldsymbol{\lambda}^*) = \max_{\mathbf{Q}} \left(p(\mathbf{O}|\boldsymbol{Q}^*, \boldsymbol{\lambda}) \right. \tag{5.3.8}$$

The first 10 minutes of the Viterbi reconstruction of the nuclear spin dynamics is depicted in Fig. 5.25d. The raw data of electron spin up counts (see Fig. 5.25a) was thresholded within four windows around each ESR peak, with a peak detection probability of 84% (see data in (see Fig. 5.25b). A hidden Markov model was then fitted to the thresholded data and the maximum likelihood sequence of nuclear spin states was obtained based on the model and the thresholded data (see Fig. 5.25d). The reconstructed sequence Fig. 5.25d) is similar to that obtained using the nuclear spin readout procedure in which the nuclear spin state is assigned to the detection window with most counts ("majority readout", see Fig. 5.25c). The sequence

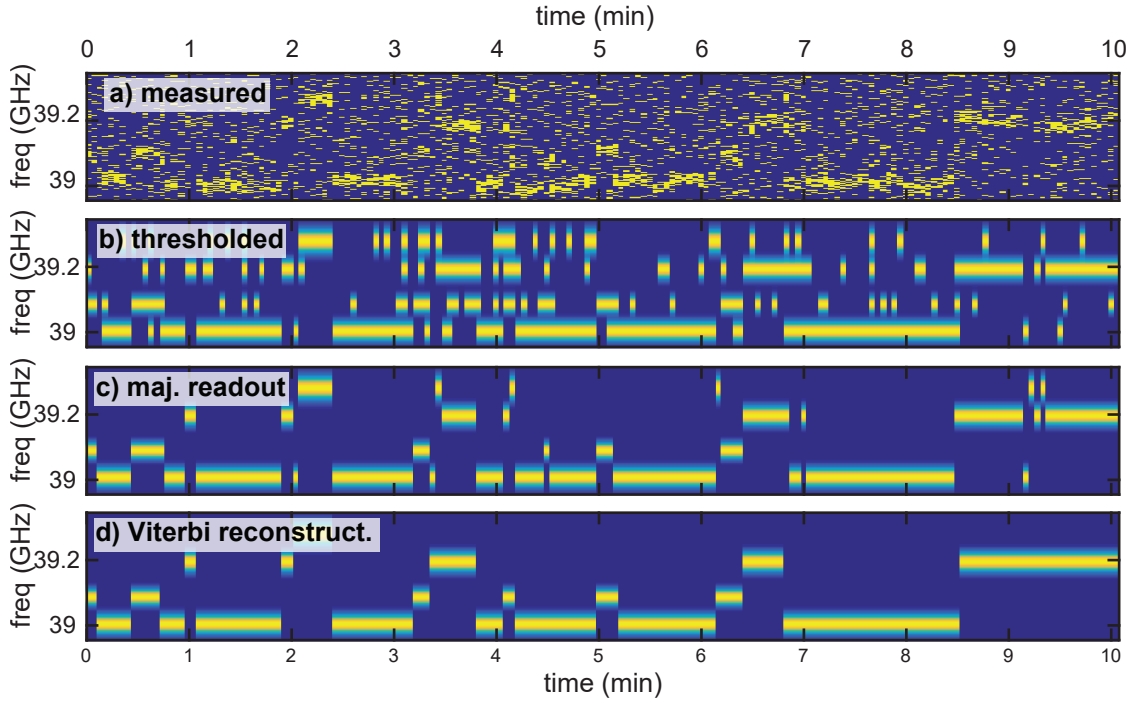

Figure 5.25: **Viterbi reconstruction of the nuclear spin dynamics.** Once the optimal hidden Markov (HMM) model is found, the most likely sequence of nuclear spin states can be reconstructed using the Viterbi algorithm [47, 51]. The Viterbi algorithm finds the sequence of states that maximises the likelihood of yielding the measured sequence of observation, given the optimal HMM. The figure shows the first 10 minutes of the measured nuclear spin dynamics. **a)** Raw data of the spin-up counts as a function of ESR frequency and time. The nuclear spin dynamics can be recognised over the background noise. **a)** Thresholded data from a. Any spin-up counts within an optimised detection window around each ESR peak that exceeds an optimised threshold is attributed to the observation of an ESR peak. The probability of correctly detecting each peak is 84%, but in only 52% of cases is the correct peak the only detection. **c)** Nuclear spin state sequence using nuclear spin readout. The nuclear spin state is attributed to the detection window that records the majority of spin-up counts ("majority readout"). The fidelity of this process is 88%. Isolated detection events lasting a single time step are likely due to the 12% error probability of the readout. **d)** Viterbi reconstruction of the most likely sequence of nuclear spin states based on the observation sequence of figure b) and the optimal Markov model fitted to the obseravtions. The reconstructed sequence is similar to that achieved using the "majority" nuclear spin readout, without many of the isolated detection events attributed to noise. The fidelity of the nuclear spin assignment of the Viterbi reconstruction is therefore expected to be higher.

reconstructed using the Markov model however does not contain the single spurious detection events visible in the sequence reconstructed using the majority nuclear spin readout. This indicates that the fidelity of the Viterbi reconstruction is likely higher than that of the "majority" nuclear spin readout. (see Sect. 5.3.1)

5.3.3 Transition rates of nuclear spin states within a 2P molecule

The transition rates between nuclear spin states in the 2P molecule can be estimated by converting the discrete-time Markov model found in the previous section and described by the transition probability matrix $\boldsymbol{A}$ to a continuous-time Markov model [48, 52]. The evolution of the system under the continuous-time Markov model is also described by a probability vector $\mathbf{p}(t)$ (with continuous time variable t), and by the continuous-time Markov equation [48]:

$$\frac{d}{dt}\mathbf{p}(t)^{\mathrm{tr}} = \mathbf{p}(t)^{\mathrm{tr}}\mathbf{M}. \tag{5.3.9}$$

The matrix $\mathbf{M}$ describes the transition rates between the states and can be estimated using the principal matrix logarithm $\mathbf{M} = \log(\mathbf{A})/\Delta t$ of the transition probability matrix $\mathbf{A}$: [48, 52]. The obtained transition rates $M_{i,j}$ between nuclear spin states i and j are summarised in the following table Table 5.4.

Start \ End	⇓⇓ (10^{-2} Hz)	⇓⇑ (10^{-2} Hz)	⇑⇓ (10^{-2} Hz)	⇑⇑ (10^{-2} Hz)
⇓⇓	$-4.8^{+0.8}_{-1.1}$	$2.6^{+0.9}_{-0.7}$	$2.3^{+0.8}_{-0.7}$	$-(0.13^{+0.18}_{-0.09})$
⇓⇑	$5.4^{1.6}_{-1.5}$	$-9.5^{+2.0}_{-3.0}$	$2.2^{+1.3}_{-1.1}$	$1.9^{+1.7}_{-1.1}$
⇑⇓	$2.6^{+0.9}_{-0.8}$	$0.89^{+0.62}_{-0.48}$	$-4.8^{+1.0}_{-1.4}$	$1.3^{0.8}_{-0.6}$
⇑⇑	$0.19^{+0.66}_{-0.26}$	$2.8^{+2.0}_{-1.4}$	$2.9^{+1.7}_{-1.5}$	$-5.9^{+1.8}_{-2.7}$

Table 5.3: Table of nuclear spin transition rates

The negative values of the diagonal elements of the transition rate matrix $\mathbf{Q}$ capture the limited lifetime of the state. In fact, we recover the nuclear spin lifetimes extracted previously by simply taking the inverse of the obtained rate (see full lifetime matrix in Appendix Table D.1). The off-diagonal elements represent the transition rates in (s^{-1}) between the nuclear spin states.

Transitions between nuclear spins correspond to either a relaxation or an excitation process. An important nuclear spin relaxation mechanism in silicon donors was first observed by Honig [53] in Arsenic donors in bulk using electron spin reso-

nance. Honig found that relaxation of the electron spin bound to the arsenic nucleus must be linked to hyperfine mediated simultaneous flips of both the electron and the nuclear spins. This effect was later observed by Feher in bulk doped phosphorus samples [54] (with relaxation times $T_x = 30(5)\,\mathrm{h}$ at $0.3(0.8)\,\mathrm{T}$) as well as single phosphorus devices [8] (with relaxation times $T_x = 65\,\mathrm{s}$ at $1.77\,\mathrm{T}$). The electron-nuclear spin flip-flops that drive both the electron and nuclear spin relaxation was attributed by Pines, Bardeen and Slichter (PBS) [55] to phonon induced variations of the hyperfine interaction between the electron and nuclear spin. In the theory of PBS, the strain induced by phonons changes the local silicon dielectric constant and effective mass. These changes modulate the amplitude of the electron wavefunction envelope and in turn modulate the contact hyperfine interaction. The theory of PBS predicts the relaxation time to be inversely proportional to the square of the static magnetic field value. This can be used to normalise relaxation rates measured at different magnetic fields.

Nuclear spin excitations, observed by Pla *et al.* in a single phosphorus donor [8] were found by the authors to be due to a sudden modification of the nuclear precession axis each time the donor is ionised or neutralised by an electron. This effect is therefore called "ionisation shock". Pla's theory was based on the observation that the transition rate $\Gamma_{\Uparrow\to\Downarrow}$ was proportional to the rate $\Gamma_{\mathrm{I/N}}$ of ionisation or neutralisation of the single donor. The sudden changes of the nuclear precession axis at each ionisation or neutralisation event is linked to sudden changes in the Hamiltonian describing the nuclear spin orientation. In the absence of the electron, the nuclear spin-up state $\Uparrow$ is an eigenstate of the system, but it is no longer so when it couples to the electrons $\downarrow$ via the hyperfine interaction. Indeed, in the presence of the hyperfine interaction the eigenstate becomes :

$$|\widetilde{\Uparrow\downarrow}\rangle = \cos(\theta/2)|\Uparrow\downarrow\rangle - \sin(\theta/2)|\Downarrow\uparrow\rangle, \tag{5.3.10}$$

where $\tan(\theta) = A/(\gamma_+ B_0))$ is the mixing angle, $\gamma_+ = \gamma_e + \gamma_n$ is the sum of the electron and nuclear gyromagnetic ratios and A the hyperfine interaction [49]. If the nuclear spin was in the $\Uparrow$-state in the absence of the electron for example, it turns into the $|\Uparrow\downarrow\rangle$ after the electron $\downarrow$ is loaded. This state then starts precessing around the new precession axis, shifted by an angle θ. The angle θ is small at the magnetic field of $1.2 - 1.8\,\mathrm{T}$ used in the experiments ($\theta \approx 2 \times 10^{-3}$), but the effect is magnified by the repeated switching of the precession axis, at random times dictated by the tunnel rates of the electron to the reservoir. Simulation by Pla *et al.* [49] revealed that the random switching lead to unpredictable trajectories of

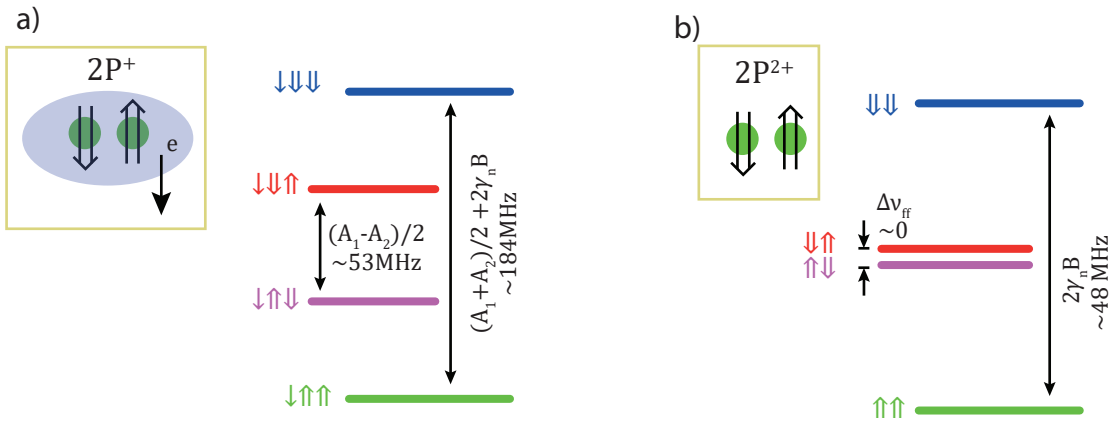

Figure 5.26: **Energy diagram of the 2P molecule with an electron spin-down ($2\mathbf{P}^{+}$) and without an electron ($2\mathbf{P}^{2+}$).**

the nuclear spin state on the nuclear spin Bloch sphere, leading to mixing of the $\Uparrow$-state with the $\Downarrow$-state. The $\Downarrow$ admixture leads to a finite probability of the nuclear spin state being projected into the $\Downarrow$-state upon measurement. The simulation of Pla *et al.* reproduced their measured transition frequencies remarkably well, and replicate the linear dependence on the ionisation/neutralisation rate $\Gamma_{\Uparrow\to\Downarrow} = p\Gamma_{\mathrm{I/N}}$, with $p = 1.91(8) \times 10^{-6}$. The coefficient $p = \Gamma_{\Uparrow\to\Downarrow}/\Gamma_{\mathrm{I/N}}$ can be interpreted as the probability of the nuclear spin flipping for each ionisation/neutralisation event. Pla *et al.* suggest that p can be related to the admixture $\sin^2(\theta/2)$ of the $\Uparrow$-state in Eq. 5.3.10. The value $\sin^2(\theta/2) \approx A^2/4(\gamma_+ B_0)^2) = 1.3 \times 10^{-}6$ indeed matches the measured value $p = 1.91(8) \times 10^{-6}$ well. This suggests that p scales as $(1/B_0)^2$, and can be used to normalise the data from experiments performed at different magnetic fields.

Before the nuclear spin transition rates of Table 5.4 measured on the 2P molecule that we investigate here can be attributed to relaxation or excitation, the ordering of the nuclear spin energy levels needs to be established, in the presence and absence of an electron spin. During the nuclear spin tracking experiment the energy levels of the nuclear spins occupy two configurations that maintain the ordering of the nuclear spin states. The energies of the nuclear spins depend on the hyperfine interaction with the electron and therefore depend on the electron spin orientation if an electron occupies the molecule. During the nuclear spin tracking experiment, the chemical potential $\mu_\uparrow$ of the electron spin-up state is maintained well above the Fermi level for 99.2% of the time (see Fig. 5.20), so that the molecule is mainly occupied by spin-down electrons. The molecule is fully emptied for only 3% of the time, but the chemical potential $\mu_\downarrow$ of the spin-down state is positioned very close to the Fermi level

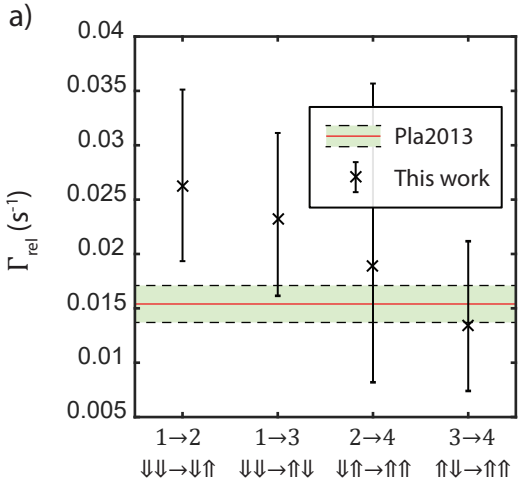

Figure 5.27: **Measured relaxation rates $\Gamma_{\Downarrow\to\Uparrow}$ on the 2P molecule, compared to that measured on a single donor, in [8] (Pla2013)**

for 79% of the pulse sequence (due to the microwave settling phase). During that time the electrons spin-down tunnels in and out of the dot repeatedly, so that the molecule spends a significant time in its fully ionised state $2P^{2+}$. These tunnelling events are studied in more detail in the appendix (see Fig. D.1). The energy diagram of the molecule in the presence and absence of a spin-down electron is depicted in Fig. 5.26a and b respectively. In the presence of an electron, the hyperfine interaction mainly determines the energy levels, with spacing on the order of 50 MHz between consecutive levels. The anti-parallel nuclear spin state are non-degenerate in the presence of an electron due to the strong Stark shift of the hyperfine values (see Sect. 5.2.3). In the absence of an electron, the energy are dictated by the nuclear Zeeman splitting only, leading to spacing of about 15 MHz between subsequent levels. However, the antiparallel nuclear spin states now become nearly degenerate, and are only split by magnetic gradients and dipolar interaction between the states. The magnetic gradient present in the fridge (0.5% variation over 1 cm), leads to a negligible energy splitting of at most 8×10^{-3} Hz due to the small 1 nm distance between the dots. The magnetic dipole-dipole interaction that can take values of up to 30 Hz, could therefore become the dominant effect and lead to hybridisation of the antiparallel states when the molecule is ionised. The ordering of the nuclear spin energy levels however remains the same in the presence or absence of the electron spin-down, in decreasing order of energy : $S_1 = |\Downarrow\Downarrow\rangle$, $S_2 = |\Downarrow\Uparrow\rangle$, $S_3 = |\Uparrow\Downarrow\rangle$ and $S_4 = |\Uparrow\Uparrow\rangle$.

The matrix element in the transition rate matrix M estimated from the Markov

model (Table 5.4) can now be assigned to relaxation and excitation events. The transition rates above the main diagonal correspond to nuclear spin relaxation (blue and cyan in Table 5.4). The single nuclear spin relaxation relaxation rates ($1.3 - 2.6 \times 10^{-2}$ Hz, in blue), are much larger than the simultaneous nuclear spin relaxation rate of $0.13^{+0.18}_{-0.09} \times 10^{-2}$ Hz (in cyan) due to the latter being an unlikely event. Three of the four measured single nuclear spin relaxation rates are in agreement with the nuclear spin relaxation value of $1.54(17) \times 10^2$ measured by Pla *et al.* on a single phosphorus donor (within uncertainties, see Fig. 5.27). The fourth relaxation rate $\Gamma_{\Downarrow\Downarrow\rightarrow\Downarrow\Uparrow} = 2.6^{+0.9}_{-0.7} \times 10^{-2}$ Hz is 70% larger than that measured on the single donor. The single spin nuclear relaxation rates measured on this 2P molecule in this work, and on the single donor of Pla *et al.* are indicative of nuclear spin-down lifetimes of 50 s. These lifetimes are four orders of magnitude smaller than that of 10 hours measured by Feher *at al.* in bulk-doped samples [54]. The reason for the decreased nuclear spin relaxation times is not understood so far. Feher *et al.* observed an alternative nuclear spin relaxation mechanism in which the nuclear and electron spin simultaneously flip ($\Downarrow\uparrow\rightarrow\Uparrow\downarrow$) [54]. This relaxation pathway cannot explain the relaxation times in our work and that of Pla, because it requires the electron to be in the spin-up states.

We now turn to the transition rates corresponding to nuclear spin excitations ($\Uparrow\rightarrow\Downarrow$). The transition rates are found below the main diagonal of the transition rate matrix $\boldsymbol{M}$ estimated from the fitted Markov model (red and orange in Table 5.4), with four values ranging from $2.6 - 5.4 \times 10^{-2}$ Hz. These values are of the same order of magnitude to the transition rate $\Gamma_{\Uparrow\rightarrow\Downarrow} = 4 \times 10^{-2} - 8 \times 10^{-3}$ Hz measured by Pla *et al.* on a single phosphorus donor [8]. In our experiment, we estimate the ionisation/neutralisation rate to be $\Gamma_{I/N} \approx 9.5$ kHz (see Fig. D.1), leading to values nuclear flip probabilities $p_{\text{exp}} = \Gamma_{\Uparrow\rightarrow\Downarrow}/\Gamma_{\text{I/N}}$ summarised in Table 5.4. In the table, we also display the values p_{exp} reported in [8] and [46], normalised to the magnetic field of 1.4 T our experiment using a $(1/B_0)^2$ dependence. The values p_{exp}, normalised for both B_0 and A, are also displayed as $\bar{p}_{\text{exp}}$.

Transition	$\Downarrow\Uparrow\rightarrow\Downarrow\Downarrow$	$\Uparrow\Downarrow\rightarrow\Downarrow\Downarrow$	$\Uparrow\Uparrow\rightarrow\Downarrow\Uparrow$	$\Uparrow\Uparrow\rightarrow\Uparrow\Downarrow$	Pla2013	Mad2021	Mad2021
p_{exp} (10^{-6} Hz)	$5.7^{+1.7}_{-1.6}$	$2.7^{+1.0}_{-0.8}$	$2.9^{+2.1}_{-1.5}$	$3.0^{+1.8}_{-1.5}$	3.0 ± 0.1	2.5	0.36
A (MHz)	91	185	185	91	114	95	9
$\bar{p}_{\text{exp}}$ (10^{-6})	9.4	1.1	1.2	4.9	3.2	3.8	61

Table 5.4: $p_{\text{exp}} = \Gamma_{\Uparrow\rightarrow\Downarrow}/\Gamma_{\text{I/N}}$ normalised to $B = 1.4$ T. $\bar{p}_{\text{exp}}$ is the value of p_{exp} normalised to $A = 117$ and $B = 1.4$ T. Pla2013 refers to [8], Mad2021 to [46].

The fully normalised flip-probabilities $\bar{p}_{\text{exp}}$ measured on our device agree within

a factor 3 with the values measured by Pla *et al.* in [8] .The ionisation shock effect is therefore the likely cause of the enhanced nuclear spin excitation rates measured in our device.

Finally, we address the transition rates that correspond to a flip-flop of the two nuclear-spin : $\Uparrow\Downarrow\leftrightarrow\Downarrow\Uparrow$. The Markov model yielded $\Gamma_{\Uparrow\Downarrow\rightarrow\Downarrow\Uparrow} = 0.89^{+0.62}_{-0.48} \times 10^{-2}\,\mathrm{Hz}$, and $\Gamma_{\Downarrow\Uparrow\rightarrow\Uparrow\Downarrow} = 2.2^{+1.3}_{-1.1} \times 10^{-2}\,\mathrm{Hz}$. The 90% uncertainty intervals do not overlap with zero, so that it is very likely that the antiparallel states are coupled by some interaction. In the following we attribute the measured flip-flop transition rate to the magnetic dipole interaction between the nuclei. First, we investigate if the measured transition rate could result from independent nuclear spin flip events that cannot be separately observed due to the limited sampling frequency of the nuclear spin measurement. In the presence of a spin-down electron, the antiparallel states $\downarrow\Uparrow\Downarrow$ and $\downarrow\Downarrow\Uparrow$ are split by 53 MHz. If we assume that the flip events are independent, a transition from one to the other would involve one excitation and one relaxation event during a single time step of the measurement. The probability of this happening over two time steps instead of one, can be estimated from the transition probability matrix A. A transition from $\Downarrow\Uparrow$ (2) to $\Uparrow\Downarrow$ (3), can occur via the state $\Downarrow\Downarrow$(1), with probability $a_{2,1} * a_{1,3}$, or the state $\Uparrow\Uparrow$ (4) with probability $a_{2,4} * a_{4,3}$. The probability of the the flip-flop transition to happen over two time-steps is therefore 1.4% and would be even less likely over a single time step. The model estimates the probability of the event happening over a single time step to be 5 times larger (7^{+5}_{-4}). Even when accounting for the confidence bound, it appears unlikely that the flip-flop process arises from two independent relaxation/excitation events occurring within the same time step.

Second, if we assume the flip-flop transition to be due to a single mechanism, it would involve a direct transverse coupling between the states. Such a coupling between the states exists in the form of the magnetic dipole-dipole interaction. The interaction between two classical magnetic dipoles, $\boldsymbol{s_1}$ and $\boldsymbol{s_2}$ separated by a distance r along the direction $\hat{\boldsymbol{r}}$ is given by :

$$\begin{aligned} D_{\mathrm{dd}} &= \frac{\mu_0}{4\pi r^3}\left(3(\boldsymbol{s_1}\cdot\hat{\boldsymbol{r}})(\boldsymbol{s_2}\cdot\hat{\boldsymbol{r}}) - \boldsymbol{s_1}\cdot\boldsymbol{s_1}\right) \\ &= \frac{\mu_0}{4\pi r^3} s_1 s_2 \left(1 - 3\cos(\theta)\right), \end{aligned} \tag{5.3.11}$$

where θ defines the angle between the donor separation axis and the global magnetic field ($\cos(\theta) = \hat{\boldsymbol{B_0}}\cdot\hat{\boldsymbol{r}}$). The angle θ allows the simplification of the expression Eq. 5.3.11 because the magnetic dipoles can be considered to be parallel to the

global magnetic field direction. Indeed, in the quantum mechanical picture the nuclear spins quantisation axis is defined by the direction of the global magnetic field.

For the magnetic dipole of the nuclei ($\gamma_n h/2$) the maximum dipole coupling strength is 30.2 Hz at two critical angles.

For the magnetic dipole interaction to lead to the observed nuclear spin flip-flops the strength of the interaction needs to be comparable or larger than the energy splitting. When an electron is neutralising the donor the splitting between the two antiparallel states $\Downarrow\Uparrow$ and $\Uparrow\Downarrow$ is 53 MHz and cannot be accounted for by the magnetic dipole interaction. However, in the absence of the electron, the energy splitting between the nuclear states is much smaller and determined only by the magnetic gradient. This gradient is small over the 1 nm separation of the dots, and leads at most to a splitting of 8×10^{-3} Hz, a value much smaller than the one of 30.2 Hz that the dipolar interaction can reach in the device. The observed flip-flop transition rates could therefore be attributed to the magnetic dipole interaction between the nuclei.

5.3.4 Conclusion

This section described the first demonstration of nuclear spin readout on a tightly bound donor molecule, with a fidelity of 88%. We then use a hidden Markov model to extract the transition rates between the nuclear spin states of the donor molecule consisting of two phosphorus donors separated by $\approx$ 0.9 nm. Using the optimal Markov model we reconstruct the most likely nuclear spin state sequence. The transition rates obtained from the Markov model indicate that the nuclear spin relaxation rates are of similar magnitude as that measured in ion-implanted single donor [8]. This is consistent with a relaxation process dominated by hyperfine mediated nuclear-electron spin flip-flops, and could indicate that additional noise sources present in ion-implanted devices due to the proximity of electrostatic gates do not play a role in nuclear spin relaxation. This needs to be confirmed by further measurement such as magnetic field dependencies that are know to differ for different relaxation mechanisms [56]. The transition rates of the $\Uparrow\rightarrow\Downarrow$ that correspond to nuclear spin excitation could be attributed to the hyperfine shock effect, also observed in single donor devices. Finally, non-zero transition rates between the antiparallel nuclear spin states were identified as a possible manifestation of a magnetic dipole interaction between the two nuclear spins in the molecule. Further measurements of the transition rates could provide further evidence that the dipole interaction

is indeed responsible for the observed flip-flop transition. In particular, we expect the flip-flop transition rate to increase with the time the molecule spends in the fully ionised state, because only then are the nuclear spin sensitive to the dipolar interaction. Unfortunately the antenna of the device was damaged shortly after the nuclear spin tracking experiment (likely due to an electrostatic discharge (ESD) that occurred during work on the microwave setup) [7], and such an experiments could not be carried out. To avoid damage of the antenna due to ESD, extreme care has to be taken when connecting/disconnecting instruments to the coaxial cables leading to the antenna, by grounding oneself and manually checking that the pulse amplitudes are limited. Damage to the antenna can still occur despite these precautions, as was the case for the device studied in this chapter. An alternative strategy to limit the risk of ESD damage to the antenna is to increase the cross-sectional area of the antenna bridge [57]. This reduces the electric current densities associated with an ESD discharge and can avoid damage to the metal. However, this also reduces the current densities during ESR operation of the antenna, and accordingly reduces the amplitude of the microwave magnetic field used to drive electron spin transitions. Madzik [57] increased the cross-section of the antenna bridge from $\approx 50 \times 40\,\mathrm{nm}^2$ to $\approx 100 \times 100\,\mathrm{nm}^2$ as is the case in our devices and found that this solved the issues with antenna damage due to ESD. It is therefore unclear if increasing the bridge cross-section is the appropriate strategy to avoid the damage that happened in our device.

5.4 Conclusion

In this chapter, measurement on two three-dot devices fabricated using STM hydrogen lithography were used to assess the feasibility of engineering multi-donor quantum dots. A particular focus was placed on two-donor quantum dots ("2P molecules") that are at the core of the electrically driven donor qubit proposed in Chapter 4. We presented measurements on three such 2P donor molecules.

First we estimated the donor configurations on two such donor molecules to demonstrate a placement precision of $\pm 0.25\,\mathrm{nm}$. The precise placement of the donors hinges on the defining a precise lithographic opening in the hydrogen resist, to constrain the number of donors that will incorporate within it, and the spacing between them. The electron spin readout fidelity of 83% measured on one 2P molecule of this device is increased to 94% on a 2P molecule in a second device, by optimising the design and fabrication of the charge sensor. Precise spectroscopic measurements

of the hyperfine coupling within that molecule is then performed using adiabatic electron spin inversion. The measurements uncover a strong linear Stark shift not observed on previous tightly bound donor molecules [4]. The spectroscopic measurements improve the precision of the donor metrology and allow to pinpoint the likely spatial configuration of the donors within the silicon lattice.

We then achieve the first demonstration of nuclear spin readout on a tightly bound donor molecule, with a fidelity of 88%. Using nuclear spin readout we track the nuclear spin states over time. The Markov model is used to reconstruct the most likely nuclear spin sequence and extract the transition rates between nuclear spin states. The Markov model uncovers nuclear spin dynamics within the molecule on the time scale of 30 seconds. Individual excitation of the nuclear spin states are consistent with the hyperfine shock mechanism measured by Pla *et al.* on single phosphorus donors [8]. The individual relaxation rates measured on the 2P molecule are in agreement with those measurements by Pla *et al.* on the single donor. The Markov model also reveals a finite, previously unreported transition probability between the two antiparallel nuclear spin states of a single donor-molecule. These transition events correspond to flip-flops of the nuclear spins and are attributed to the dipolar interaction between the nuclear spins, that can become relevant when the donor molecule is fully ionised.

Finally, the measurement of the nuclear spin dynamics on the 2P donor molecule presented in this chapter gives experimental support to the electrically-driven donor-based qubit proposed in Chapter 4. Indeed, nuclear spins produce the magnetic gradients that drive the qubit and couple it to charge noise. In order to provide reliable driving and protection from charge noise it is therefore essential for the nuclear spins to remain stable in time. The long nuclear spin lifetimes (10 to 20 seconds) measured in this chapter on a 2P donor molecule indicate that the nuclear spins are stable enough for the particular implementation of the qubit focused on in Chapter 4, which uses a 2P donor molecule to protect the qubit from charge noise. Indeed, the measured nuclear spin lifetimes would allow for tens of millions of qubit operations before the nuclear spins flip.

Bibliography

[1] Yu Ling Hsueh, Holger Büch, Yaohua Tan, Yu Wang, Lloyd C.L. Hollenberg, Gerhard Klimeck, Michelle Y. Simmons, and Rajib Rahman. Spin-lattice relaxation times of single donors and donor clusters in silicon. *Physical Review Letters*, 113(24):1–5, 2014.

[2] Thomas F. Watson, Bent Weber, Yu Ling Hsueh, Lloyd C.L. Hollenberg, Rajib Rahman, and Michelle Y. Simmons. Atomically engineered electron spin lifetimes of 30 s in silicon. *Science Advances*, 3(3):1–7, 2017.

[3] H. Büch, S. Mahapatra, R. Rahman, A. Morello, and M. Y. Simmons. Spin readout and addressability of phosphorus-donor clusters in silicon. *Nature Communications*, 4:ncomms3017, jun 2013.

[4] Samuel J. Hile, Lukas Fricke, Matthew G. House, Eldad Peretz, Chin Yi Chen, Yu Wang, Matthew Broome, Samuel K. Gorman, Joris G. Keizer, Rajib Rahman, and Michelle Y. Simmons. Addressable electron spin resonance using donors and donor molecules in silicon. *Science Advances*, 4(7):eaaq1459, jul 2018.

[5] Yu Wang, Archana Tankasala, Lloyd C L Hollenberg, Gerhard Klimeck, Michelle Y Simmons, and Rajib Rahman. Highly tunable exchange in donor qubits in silicon. *npj Quantum Information*, 2(1):16008, nov 2016.

[6] Bent Weber, Y H Matthias Tan, Suddhasatta Mahapatra, Thomas F Watson, Hoon Ryu, Rajib Rahman, Lloyd C L Hollenberg, Gerhard Klimeck, and Michelle Y Simmons. Spin blockade and exchange in Coulomb-confined silicon double quantum dots. *Nature nanotechnology*, 9(6):430–5, 2014.

[7] Michael T Jones. *Design and implementation of parity error detection in donor qubits in silicon*. Phd. thesis, University of New South Wales, 2021.

[8] Jarryd J. Pla, Kuan Y. Tan, Juan P. Dehollain, Wee H. Lim, John J. L. Morton, Floris A. Zwanenburg, David N. Jamieson, Andrew S. Dzurak, and Andrea Morello. High-fidelity readout and control of a nuclear spin qubit in silicon. *Nature*, 496(7445):334–338, apr 2013.

[9] T. F. Watson, B. Weber, M. G. House, H. Büch, and M. Y. Simmons. High-Fidelity Rapid Initialization and Read-Out of an Electron Spin via the Single Donor D Charge State T. *Physical Review Letters*, 115(16):166806, oct 2015.

[10] Y. He, S. K. Gorman, D. Keith, L. Kranz, J. G. Keizer, and M. Y. Simmons. A two-qubit gate between phosphorus donor electrons in silicon. *Nature*, 571(7765):371–375, 2019.

[11] Patrick Harvey-Collard, Benjamin D'Anjou, Martin Rudolph, N. Tobias Jacobson, Jason Dominguez, Gregory A.Ten Eyck, Joel R. Wendt, Tammy Pluym, Michael P. Lilly, William A. Coish, Michel Pioro-Ladrière, and Malcolm S. Carroll. High-Fidelity Single-Shot Readout for a Spin Qubit via an Enhanced Latching Mechanism. *Physical Review X*, 8(2):1–11, 2018.

[12] D. Keith, M. G. House, M. B. Donnelly, T. F. Watson, B. Weber, and M. Y. Simmons. Single-Shot Spin Readout in Semiconductors Near the Shot-Noise Sensitivity Limit. *Physical Review X*, 9(4):41003, 2019.

[13] Thomas Ihn. *Semiconductor nanostructures*. Oxford University Press, 2010.

[14] Yu E. Wang, Archana Tankasala, Lloyd C. L. Hollenberg, Gerhard Klimeck, Michelle Y. Simmons, and Rajib Rahman. Engineering inter-qubit exchange coupling between donor bound electrons in silicon. *arXiv*, pages 1–7, 2015.

[15] Frederico Martins, Filip K Malinowski, Peter D Nissen, Edwin Barnes, Saeed Fallahi, Geoffrey C Gardner, Michael J Manfra, Charles M Marcus, and Ferdinand Kuemmeth. Noise Suppression Using Symmetric Exchange Gates in Spin Qubits. *Physical Review Letters*, 116801(March):1–5, 2016.

[16] Martin Fuechsle. *Precision Few-Electron Silicon Quantum Dots*. PhD thesis, UNSW, 2011.

[17] H. F. Wilson, O. Warschkow, N. A. Marks, N. J. Curson, S. R. Schofield, T. C.G. Reusch, M. W. Radny, P. V. Smith, D. R. McKenzie, and M. Y. Simmons. Thermal dissociation and desorption of P H3 on Si(001): A reinterpretation

of spectroscopic data. *Physical Review B - Condensed Matter and Materials Physics*, 74(19):1–10, 2006.

[18] O. Warschkow, H. F. Wilson, N. A. Marks, S. R. Schofield, N. J. Curson, P. V. Smith, M. W. Radny, D. R. McKenzie, and M. Y. Simmons. Phosphine adsorption and dissociation on the Si(001) surface: An ab initio survey of structures. *Physical Review B - Condensed Matter and Materials Physics*, 72(12):1–15, 2005.

[19] H. F. Wilson, O. Warschkow, N. A. Marks, S. R. Schofield, N. J. Curson, P. V. Smith, M. W. Radny, D. R. McKenzie, and M. Y. Simmons. Phosphine dissociation on the Si(001) surface. *Physical Review Letters*, 93(22):2–5, 2004.

[20] Michelle Simmons and Joris Keizer. Method for selective incorporation of dopant atoms in a semiconductive surface, U.S. Patent US11227768B2, 18th of January 2022.

[21] Thilo C G Reusch, Marian W. Radny, Phillip V. Smith, Oliver Warschkow, Nigel A. Marks, Neil J. Curson, David R. McKenzie, and Michelle Y. Simmons. Single Phosphorus Atoms in Si(001): Doping-Induced Charge Transfer into Isolated Si Dangling Bonds. *The Journal of Physical Chemistry C*, 111(17):6428–6433, may 2007.

[22] Martin Fuechsle, Jill A Miwa, Suddhasatta Mahapatra, Hoon Ryu, Sunhee Lee, Oliver Warschkow, Lloyd C L Hollenberg, Gerhard Klimeck, and Michelle Y Simmons. A single-atom transistor. *Nature nanotechnology*, 7(4):242–246, 2012.

[23] B. Voisin, J. Bocquel, A. Tankasala, M. Usman, J. Salfi, R. Rahman, M. Y. Simmons, L. C.L. Hollenberg, and S. Rogge. Valley interference and spin exchange at the atomic scale in silicon. *Nature Communications*, 11(1):1–11, 2020.

[24] Morten Moller, Samuel P Jarvis, Laurent Guérinet, Peter Sharp, Richard Woolley, Philipp Rahe, and Philip Moriarty. Automated extraction of single H atoms with STM: tip state dependency. *Nanotechnology*, 28(7):075302, feb 2017.

[25] Qin Liu, Yanhua Lei, Xiji Shao, Fangfei Ming, Hu Xu, Kedong Wang, and Xudong Xiao. Controllable dissociations of PH 3 molecules on Si(001). *Nanotechnology*, 27(13):135704, apr 2016.

[26] M. A. Broome, T. F. Watson, D. Keith, S. K. Gorman, M. G. House, J. G. Keizer, S. J. Hile, W. Baker, and M. Y. Simmons. High-Fidelity Single-Shot

Singlet-Triplet Readout of Precision-Placed Donors in Silicon. *Physical Review Letters*, 119(4):046802, jul 2017.

[27] M. G. House, T. Kobayashi, B. Weber, S. J. Hile, T. F. Watson, J. van der Heijden, S. Rogge, and M. Y. Simmons. Radio frequency measurements of tunnel couplings and singlettriplet spin states in Si:P quantum dots. *Nature Communications*, 6:8848, nov 2015.

[28] M. A. Broome, S. K. Gorman, M. G. House, S. J. Hile, J. G. Keizer, D. Keith, C. D. Hill, T. F. Watson, W. J. Baker, L. C. L. Hollenberg, and M. Y. Simmons. Two-electron spin correlations in precision placed donors in silicon. *Nature Communications*, 9(1):980, dec 2018.

[29] D. Keith, S. K. Gorman, L. Kranz, Y. He, J. G. Keizer, M. A. Broome, and M. Y. Simmons. Benchmarking high fidelity single-shot readout of semiconductor qubits. *New Journal of Physics*, 21(6), 2019.

[30] Sarah R. McKibbin, Warrick R. Clarke, and Michelle Y. Simmons. Investigating the surface quality and confinement of Si:P δ -layers at different growth temperatures. *Physica E: Low-Dimensional Systems and Nanostructures*, 42(4):1180–1183, 2010.

[31] S. R. McKibbin. *Towards Three Dimensional All-Epitaxial Silicon Architectures Patterned By Scanning Tunnelling Microscopy*. Phd. thesis, University of New South Wales, 2012.

[32] J.M. Elzerman, R. Hanson, L.H. Willems van Beveren, B. Witkamp, L.M.K. Vandersypen, and L.P. Kouwenhoven. Single-shot read-out of an individual electron spin in a quantum dot. *Nature*, 430:431–435, 2004.

[33] Jarryd J Pla, Kuan Y Tan, Juan P Dehollain, Wee H Lim, John J L Morton, David N Jamieson, Andrew S Dzurak, and Andrea Morello. A single-atom electron spin qubit in silicon. *Nature*, 489(7417):541–545, sep 2012.

[34] Lukas Fricke, Samuel James Hile, Prasanna Pakkiam, and Michelle Y. Simmons. To be published. 2021.

[35] Arne Laucht, Rachpon Kalra, Juha T. Muhonen, Juan P. Dehollain, Fahd A. Mohiyaddin, Fay Hudson, Jeffrey C. McCallum, David N. Jamieson, Andrew S. Dzurak, and Andrea Morello. High-fidelity adiabatic inversion of a 31P electron spin qubit in natural silicon. *Applied Physics Letters*, 104(9), 2014.

[36] B. E. Kane. A silicon-based nuclear spin quantum computer. *Nature*, 393(6681):133–137, may 1998.

[37] Rajib Rahman, Cameron J. Wellard, Forrest R. Bradbury, Marta Prada, Jared H. Cole, Gerhard Klimeck, and Lloyd C.L. Hollenberg. High precision quantum control of single donor spins in silicon. *Physical Review Letters*, 99(3):3–6, 2007.

[38] F. R. Bradbury, Alexei M. Tyryshkin, Guillaume Sabouret, Jeff Bokor, Thomas Schenkel, and S. A. Lyon. Stark tuning of donor electron spins in silicon. *AIP Conference Proceedings*, 893(May 2007):1093–1094, 2007.

[39] Giuseppe Pica, Gary Wolfowicz, Matias Urdampilleta, Mike L.W. Thewalt, Helge Riemann, Nikolai V. Abrosimov, Peter Becker, Hans Joachim Pohl, John J.L. Morton, R. N. Bhatt, S. A. Lyon, and Brendon W. Lovett. Hyperfine Stark effect of shallow donors in silicon. *Physical Review B - Condensed Matter and Materials Physics*, 2014.

[40] Arne Laucht, Juha T. Muhonen, Fahd A. Mohiyaddin, Rachpon Kalra, Juan P. Dehollain, Solomon Freer, Fay E. Hudson, Menno Veldhorst, Rajib Rahman, Gerhard Klimeck, Kohei M. Itoh, David N. Jamieson, Jeffrey C. McCallum, Andrew S. Dzurak, and Andrea Morello. Electrically controlling single-spin qubits in a continuous microwave field. *Science Advances*, 2015.

[41] Hoon Ryu, Sunhee Lee, Martin Fuechsle, Jill A. Miwa, Suddhasatta Mahapatra, Lloyd C. L. Hollenberg, Michelle Y. Simmons, and Gerhard Klimeck. A Tight-Binding Study of Single-Atom Transistors. *Small*, 11(3):374–381, jan 2015.

[42] Bent Weber. *Towards Scalable Planar Donor-Based Silicon Quantum Computing Architectures*. Phd. thesis, University of New South Wales, 2013.

[43] J. Salfi, J. A. Mol, R. Rahman, G. Klimeck, M. Y. Simmons, L. C.L. Hollenberg, and S. Rogge. Spatially resolving valley quantum interference of a donor in silicon. *Nature Materials*, 13(6):605–610, 2014.

[44] Samuel James Hile. *Spin Control and Coherence in Scalable Phosphorus Donor Qubits by*. Phd. thesis, University of New South Wales, 2017.

[45] Guilherme Tosi, Fahd A Mohiyaddin, Vivien Schmitt, Stefanie Tenberg, Rajib Rahman, Gerhard Klimeck, and Andrea Morello. Silicon quantum processor

with robust long-distance qubit couplings. *Nature Communications*, 8(1):450, dec 2017.

[46] Mateusz T. Madzik, Serwan Asaad, Akram Youssry, Benjamin Joecker, Kenneth M. Rudinger, Erik Nielsen, Kevin C. Young, Timothy J. Proctor, Andrew D. Baczewski, Arne Laucht, Vivien Schmitt, Fay E. Hudson, Kohei M. Itoh, Alexander M. Jakob, Brett C. Johnson, David N. Jamieson, Andrew S. Dzurak, Christopher Ferrie, Robin Blume-Kohout, and Andrea Morello. Precision tomography of a three-qubit electron-nuclear quantum processor in silicon. *arXiv*, 2021.

[47] L.R. Rabiner. A tutorial on hidden Markov models and selected applications in speech recognition. *Proceedings of the IEEE*, 77(2):257–286, aug 1989.

[48] Matthew Gregory House. *Lateral Quantum Dots for Quantum Information Processing*. Phd. thesis, University of California, Los Angeles, 2012.

[49] Jarryd James Pla. *Single Atom Spin Qubits in Silicon*. PhD thesis, University of New South Wales, 2013.

[50] Leonard E. Baum and George Sell. Growth transformations for functions on manifolds. *Pacific Journal of Mathematics*, 27(2):211–227, nov 1968.

[51] A. Viterbi. Error bounds for convolutional codes and an asymptotically optimum decoding algorithm. *IEEE Transactions on Information Theory*, 13(2):260–269, apr 1967.

[52] Robert B. Israel, Jeffrey S. Rosenthal, and Jason Z. Wei. Finding generators for Markov chains via empirical transition matrices, with applications to credit ratings. *Mathematical Finance*, 11(2):245–265, 2001.

[53] A. Honig. Polarization of arsenic nuclei in a silicon semiconductor. *Phys. Rev.*, 96:234–235, Oct 1954.

[54] G. Feher and E. A. Gere. Electron spin resonance experiments on donors in silicon. II. Electron spin relaxation effects. *Physical Review*, 114(5):1245–1256, 1959.

[55] David Pines, John Bardeen, and Charles P. Slichter. Nuclear polarization and impurity-state spin relaxation processes in silicon. *Physical Review*, 106(3):489–498, 1957.

[56] Stefanie B. Tenberg, Serwan Asaad, Mateusz T. Madzik, Mark A. I. Johnson, Benjamin Joecker, Arne Laucht, Fay E. Hudson, Kohei M. Itoh, A. Malwin Jakob, Brett C. Johnson, David N. Jamieson, Jeffrey C. McCallum, Andrew S. Dzurak, Robert Joynt, and Andrea Morello. Electron spin relaxation of single phosphorus donors in metal-oxide-semiconductor nanoscale devices. *Phys. Rev. B*, 99:205306, May 2019.

[57] Mateusz Tomasz Madzik. *Two-qubit gates with ion-implanted phosphorus donors in silicon.* Phd. thesis, University of New South Wales, 2020.

Chapter 6

Conclusion

Electron spins bound to phosphorus donors in silicon have demonstrated all of the basic requirements for a large-scale quantum computer, initialisation, single and two-qubit gates, and measurements [1, 2, 3, 4, 5, 6]. However, scaling up to the millions of qubits required for a fault-tolerant universal quantum computer requires the careful design and optimisation of qubit parameters that are not immediately obvious from small-scale quantum devices. In this thesis, we have investigated different techniques to aid in the scalability of phosphorus donor electron spin qubits in silicon. For a large-scale quantum computing architecture long-distance coupling is a crucial requirement to allow for the integration of the classical control electronics required to operate the quantum computer [7]. Such long range coupling is not easily achieved using single spin qubits. To this end, we have proposed a new fast, high-fidelity, qubit that can be strongly coupled to superconducting microwave cavities, allowing for this critical long-distance coupling. The qubit is based on a pair of donor-based quantum dots and relies on engineering the hyperfine interaction of the electron with the donors in the system. We showed that the hyperfine interaction necessary for such a qubit can be readily measured and characterised using ESR and examined the nuclear spin dynamics associated with the donor system. These results put the demonstration of a low error-rate donor-based flopping-mode qubit that can readily coupled to microwave cavities for long-distance inter-qubit coupling within reach.

6.1 Summary of results presented in this thesis

In **Chapter 3**, we theoretically analysed the performance of the general class of qubits known as flopping-mode EDSR qubits [8, 9, 10, 11, 12] when a single electron is delocalised across a double quantum in a gradient magnetic field. We showed

how the qubit gate time can be controlled by the strength of the perpendicular magnetic field gradient and that the longitudinal magnetic field gradient gives rise to second-order charge noise sweet-spots previously reported in [11, 13]. However, unlike previous work on charge noise sweet-spots we find that the second-order sweet spot, while increasing the dephasing time due to noise in the qubit energy, lowers the overall fidelity of single qubit gates. Therefore, we propose that to obtain the optimal qubit performance the longitudinal magnetic field gradient should be minimised (lower dephasing rates) and the perpendicular magnetic field gradient should be maximised (fast qubit operations). Through a detailed theoretical analysis of qubit driving and errors we showed that single-qubit gate errors below 10^{-3}—well below the 2D surface-code error threshold are feasible in current device architectures. Throughout the chapter we showed that complicated error channels involving dephasing, relaxation, and leakage can be readily explained by a series of analytical expressions, greatly simplifying the required calculations and allows for a more intuitive picture of the optimisation of the qubit. The results presented will allow for the design and optimisation of flopping-mode qubits in quantum dot and donor systems, which, was the focus on the next chapter.

In **Chapter 4** we theoretically propose and analyse a flopping-mode qubit based on phosphorus donor quantum dots in silicon. The qubit was defined between a two-donor quantum dot (2P) and a single donor (1P) where the hyperfine interaction is used to electrically drive flip-flop transitions between the electron and the 1P nuclear spin. We use the theoretical error model in the previous chapter to estimate the qubit performance while including additional leakage states due to the nuclear spin states of the phosphorus donors. The longitudinal effective magnetic field gradient in this flopping-mode qubit arises from the hyperfine interaction of the two donors on the 2P quantum dot. We show that the longitudinal magnetic field gradient can be minimised through electron shielding (operating with two closed shell electrons on the 2P) and initialising the nuclear spins into antiparallel nuclear spin states to cancel the total hyperfine interaction felt by the electron spin. We then showed that using the optimised magnetic field gradients the qubit can be operated with an error rate of 2×10^{-4} at a magnetic field of ~ 0.2 T. Crucially, the qubit maintains an error rate below 10^{-3} over a wide range of magnetic fields ($0.1 - 0.6\,\mathrm{T}$) and tunnel couplings ($\sim 1 - 20\,\mathrm{GHz}$). We then showed that the qubit can theoretically reach the strong-coupling regime to a superconducting microwave cavity with a cooperativity, $C = 130 \gg 1$. The robustness to fabrication tolerances in terms of tunnelling coupling and magnetic fields will be crucial when considering scaling such a qubit

to a large quantum computer. Indeed, using the excellent donor-based flopping-mode qubit we proposed a 2D surface-code quantum computing architecture where the qubit can be coupled either via direct charge-dipoles or floating gate structures. The architecture utilises only 2 gates per qubit in nodes with qubit densities 28 μm^{-2} (0.25 μm^{-2}) for the dipole coupling (floating gate coupling) meaning that thousands of qubits could potentially fit on a single silicon chip. Inter-node coupling can be achieved by superconducting microwave cavities over the millimetre length-scale to allow for the classical control electronics required for measurement and control of the qubits.

Lastly, in Chapter 5, we investigated the feasibility of engineering small donor molecules using STM hydrogen lithography. We designed and optimised a three-dot device to allow for independent operation of three donor qubits and coupling of two of the three qubit pairs. The device design is compatible with the long term goal of running a small fragment of the surface-code error-correction algorithm with independent electrostatic control, initialisation, and measurement of three donor-based quantum dots [14]. Using this new device design, we demonstrated a high degree of control over the fabrication of small donor molecules. On a first device with two 2P molecules, the donor configurations were estimated for each of the quantum dots by comparing measurements of the quantum dot charging energies to recently modelled tight binding simulations and matched the lithographic areas imaged during STM fabrication. This donor metrology indicates that a precision of $\approx \pm 0.25\,\text{nm}$ can be achieved for 2P molecules by defining the lithographic mask with atomic precision. We demonstrated single-shot spin readout of the electron on the left 2P donor-quantum dot with 83% fidelity, which was limited by the signal-to-noise ratio of the SET and prevented electron spin readout on charge transitions with a faster tunnel rate ($> 15\,\text{kHz}$). The sub-optimal on-off ratio of the SET was caused by variations in the tunnel gap dimensions of the SET caused by drift of the STM tip during patterning. We then demonstrated strategies to mitigate such lithographic variations and in a subsequent device the optimised SET yielded a significant improvement of the electron spin readout fidelity to 94.4% on another donor quantum dot. Electron spin resonance using adiabatic spin inversion was then demonstrated on the first electron of the quantum dot. The ESR spectra revealed four spin inversion peaks which we attributed to a 2P molecule with a hyperfine interaction of the first and second nucleus to the electron of $A_1 = 189 \pm 5\,\text{MHz}$ and $A_2 = 83 \pm 5\,\text{MHz}$, respectively. The difference in the hyperfine interaction of each phosphorus nuclear spin was attributed to a linear Stark effect of larger magnitude

than that observed in an ion-implanted single phosphorus donors (with a linear Stark coefficient of $\alpha_{2P} = 5.05$ MHz/MV/m compared to $\alpha_{1P} = 0.34$ MHz/MV/m measured in a single donor device [15]). Using the total hyperfine value and the difference between A_1 and A_2 we identified $[1.5, 0.5, 0]a_0$ as the most probable donor configuration, where a_0 is the silicon lattice constant, which was consistent with the lithographic region defined during STM fabrication. Finally, we demonstrated nuclear spin readout on the 2P molecule with a fidelity of 88%. This is the first demonstration of nuclear spin readout on a tightly bound donor molecule and was used to track the state of the nuclear spin in real-time. A hidden Markov model was used to reconstruct the sequence of nuclear spin states over time and to extract the nuclear spin lifetimes. The optimal Markov model yielded nuclear spin lifetimes ranging from 11^{+4}_{-3} s to 22^{+8}_{-5} s of the four nuclear spin states. The measured relaxation rates of $1.3 - 2.6 \times 10^{-2}$ Hz are in agreement with the value of $1.54(17) \times 10^{-2}$ measured by Pla *et al.* on a single phosphorus donor [16]. The nuclear excitation rates extracted from the Markov model ($2.6 - 5.4 \times 10^{-2}$ Hz) were attributed to the ionisation-shock mechanism identified by Pla *et al.* on single donors [16]. Finally the observed transition rates between the antiparallel nuclear spin state $\Uparrow\Downarrow \rightarrow \Downarrow\Uparrow$ was attributed to the first experimental observation of the dipole coupling between nuclear spins of a donor molecule.

6.2 Future work

In this thesis we investigated the feasibility of electrically driving a donor-based electron spin qubit fabricated using STM hydrogen lithography.

Chapters 3 and 4 theoretically demonstrated that a flopping-mode EDSR qubit is feasible using a 1P-2P quantum dot pair in an all-epitaxial silicon device. Chapter 5 demonstrated that the precise manufacturing of the 2P quantum dot is possible, and previous work [17] demonstrated that the single donor can also be manufactured using precision STM lithography. The natural stepping stone would therefore be to fabricate a dedicated device with at least one 1P-2P quantum dot pair. The three quantum dot design with a 1P-2P-1P configuration would be a already proven device design that would be suitable for demonstrating the flopping-mode qubit. Demonstration of electrical driving in the regime where the charge qubit energy is much larger than that of the spin qubit should be the first goal, that is, the tunnel coupling is much larger than the Zeeman energy. This could be simplified by operating the spin qubit at low magnetic field ($B = 0.2 - 1$ T) and by measuring

the spin state with Pauli blockade [18], and by manufacturing a device with large tunnel coupling t_c, such that $2t_c > \gamma_e B$.

In Chapter 5, the flip-flop transition rates between the nuclear spin states was attributed to the dipolar coupling. The dipolar coupling could be further explored in two ways. First, the uncertainty bounds in the calculated transition frequencies could be simply lowered by using the "majority" peak identification of the nuclear spin readout instead of the single peak detection procedure. Additionally, the uncertainty bounds could be further reduced by using a continuous-time hidden Markov model (instead of a discrete-time model), and using a model that describes the measurement with continuous variables. Using a continuous-time Markov model will allow for better time resolution of the transition rates and therefore a better estimate of the dipolar coupling strength. Secondly, the measured flip-flop transition rate should be matched to time-domain simulations, modelling the continuous switching on and off of the dipolar interaction. This modelling will allow for a direct comparison to the experimentally measured nuclear spin probabilities and will directly confirm the effect of the dipolar coupling on the nuclear spin dynamics.

Finally, the nuclear spin readout fidelity of 88% demonstrated in Chapter 5 could be dramatically increased by improving the ESR setup to avoid the waiting time required for the microwave source switches frequency (80% of the measurement time is spent waiting). This can be circumvented by implementing IQ modulation of the microwave signal such that the mixed microwave can be swept in real-time and not require switching of the internal microwave generator.

Bibliography

[1] H. Büch, S. Mahapatra, R. Rahman, A. Morello, and M. Y. Simmons. Spin readout and addressability of phosphorus-donor clusters in silicon. *Nature Communications*, 4:ncomms3017, jun 2013.

[2] Lukas Fricke, Samuel James Hile, Prasanna Pakkiam, and Michelle Y. Simmons. To be published. 2021.

[3] Y. He, S. K. Gorman, D. Keith, L. Kranz, J. G. Keizer, and M. Y. Simmons. A two-qubit gate between phosphorus donor electrons in silicon. *Nature*, 571(7765):371–375, 2019.

[4] Andrea Morello, Jarryd J Pla, Floris a Zwanenburg, Kok W Chan, Kuan Y Tan, Hans Huebl, Mikko Möttönen, Christopher D Nugroho, Changyi Yang, Jessica a van Donkelaar, Andrew D C Alves, David N Jamieson, Christopher C Escott, Lloyd C L Hollenberg, Robert G Clark, and Andrew S Dzurak. Single-shot readout of an electron spin in silicon. *Nature*, 467(7316):687–91, 2010.

[5] Jarryd J Pla, Kuan Y Tan, Juan P Dehollain, Wee H Lim, John J L Morton, David N Jamieson, Andrew S Dzurak, and Andrea Morello. A single-atom electron spin qubit in silicon. *Nature*, 489(7417):541–545, sep 2012.

[6] Mateusz T. Madzik, Arne Laucht, Fay E. Hudson, Alexander M. Jakob, Brett C. Johnson, David N. Jamieson, Kohei M. Itoh, Andrew S. Dzurak, and Andrea Morello. Conditional quantum operation of two exchange-coupled single-donor spin qubits in a MOS-compatible silicon device. *Nature Communications*, 12(1):1–8, 2021.

[7] L. M. K. Vandersypen, H. Bluhm, J. S. Clarke, A. S. Dzurak, R. Ishihara, A. Morello, D. J. Reilly, L. R. Schreiber, and M. Veldhorst. Interfacing spin qubits in quantum dots and donorshot, dense, and coherent. *npj Quantum Information*, 3(1):1–10, 2017.

[8] Xuedong Hu, Yu Xi Liu, and Franco Nori. Strong coupling of a spin qubit to a superconducting stripline cavity. *Physical Review B - Condensed Matter and Materials Physics*, 86(3):1–5, 2012.

[9] J. J. Viennot, M. C. Dartiailh, A. Cottet, and T. Kontos. Coherent coupling of a single spin to microwave cavity photons. *Science*, 349(6246):408–411, 2015.

[10] Félix Beaudoin, Dany Lachance-Quirion, W. A. Coish, and Michel Pioro-Ladrière. Coupling a single electron spin to a microwave resonator: Controlling transverse and longitudinal couplings. *Nanotechnology*, 27(46), 2016.

[11] Guilherme Tosi, Fahd A Mohiyaddin, Vivien Schmitt, Stefanie Tenberg, Rajib Rahman, Gerhard Klimeck, and Andrea Morello. Silicon quantum processor with robust long-distance qubit couplings. *Nature Communications*, 8(1):450, dec 2017.

[12] X. Croot, X. Mi, S. Putz, M. Benito, F. Borjans, G. Burkard, and J. R. Petta. Flopping-mode electric dipole spin resonance. 1:1–6, 2019.

[13] M. Benito, X. Croot, C. Adelsberger, S. Putz, X. Mi, J. R. Petta, and Guido Burkard. Electric-field control and noise protection of the flopping-mode spin qubit. *Physical Review B*, 100(12):1–10, 2019.

[14] Michael T Jones. *Design and implementation of parity error detection in donor qubits in silicon*. Phd. thesis, University of New South Wales, 2021.

[15] Arne Laucht, Rachpon Kalra, Juha T. Muhonen, Juan P. Dehollain, Fahd A. Mohiyaddin, Fay Hudson, Jeffrey C. McCallum, David N. Jamieson, Andrew S. Dzurak, and Andrea Morello. High-fidelity adiabatic inversion of a 31P electron spin qubit in natural silicon. *Applied Physics Letters*, 104(9), 2014.

[16] Jarryd J. Pla, Kuan Y. Tan, Juan P. Dehollain, Wee H. Lim, John J. L. Morton, Floris A. Zwanenburg, David N. Jamieson, Andrew S. Dzurak, and Andrea Morello. High-fidelity readout and control of a nuclear spin qubit in silicon. *Nature*, 496(7445):334–338, apr 2013.

[17] Martin Fuechsle, Jill A Miwa, Suddhasatta Mahapatra, Hoon Ryu, Sunhee Lee, Oliver Warschkow, Lloyd C L Hollenberg, Gerhard Klimeck, and Michelle Y Simmons. A single-atom transistor. *Nature nanotechnology*, 7(4):242–246, 2012.

[18] M. A. Broome, T. F. Watson, D. Keith, S. K. Gorman, M. G. House, J. G. Keizer, S. J. Hile, W. Baker, and M. Y. Simmons. High-Fidelity Single-Shot Singlet-Triplet Readout of Precision-Placed Donors in Silicon. *Physical Review Letters*, 119(4):1–5, 2017.

Appendix A

Chapter 2 appendix

A.1 Surface code estimations

The number of qubits and operation time needed to factorise a N-bit number using a quantum computer running the surface code (as displayed in Fig. 2.3 and Table 2.2) is obtained following calculation in ref. [1].

The number of physical qubits needed to define as single computational logical qubit can be obtained using equations (10) and (11) in ref. [1]. The logical qubit error P_L is well approximated by $P_L \approx 0.03\,(p/p_{\text{th}})^{d_e}$ where d_e is the error dimension $d_e = (d+1)/2$ defined using the surface code distance d. The number of physical qubit n_q can be expressed as a function of the surface code distance: $n_q = (2d-1)^2$. Using all three equations, we find that the number of physical qubit, each with an error rate p, below the error correction threshold p_{th}, needed to encode a single logical qubit with error P_L is given by:

$$n_q \approx \left(4\frac{\ln(0.03/P_L)}{\ln(p_{\text{th}}/p)}\right)^2. \tag{A.1.1}$$

The time of execution of Shor's algorithm for an N-bit number is given in appendix M of ref. [1] to be equal to $120N^3 t_M$ for one specific implementation of the algorithm optimised for low number of logical qubits needed. This is the formula used in Table 2.2.

Note that the algorithm that we chose needs only $2N$ computational logical qubits, but but the completion time of the algorithm scales as N^3 [1, 2, 3, 4], whereas other algorithms need much more computational logical qubits (scaling as $\mathrm{O}(N^3)$), but operate much faster ($\mathrm{O}(\log^3 N)$).

Appendix B

Chapter 3 appendix

B.1 Full second order effective flopping mode Hamiltonian

A Schrieffer-Wolff transformation on the full flopping mode Hamiltonian, allows a demonstration of the natural symmetry in the matrix and the estimation of the leakage couplings.

The full matrix including the lowest excited charge states becomes as follows in the systems's eigen-basis $\left\{\widetilde{|\uparrow -\rangle}, \widetilde{|\downarrow -\rangle}, \widetilde{|\uparrow +\rangle}, \widetilde{|\downarrow +\rangle}\right\}$:

$$H_{rl} = \begin{pmatrix} 0 & \Omega_r & \Omega_l^{13}(\epsilon) & \Omega_l^{14} \\ \Omega_r & \tilde{\Omega}_s(\epsilon) & \Omega_l^{23} & \Omega_l^{13}(-\epsilon) \\ \Omega_l^{13}(\epsilon) & \Omega_l^{23} & \tilde{\Omega} & \Omega_r \\ \Omega_l^{14} & \Omega_l^{13}(-\epsilon) & \Omega_r & \tilde{\Omega} + \tilde{\Omega}_s(-\epsilon) \end{pmatrix}, \tag{B.1.1}$$

where we used a different global energy shift, the qubit splitting $\tilde{\Omega}_s$ and Rabi frequency Ω_r are as defined in Eqs. 3.2.19 and 3.2.20 and we defined the modified charge qubit energy $\tilde{\Omega}$, and the additional coupling terms Ω_l^{13}, Ω_l^{14} and Ω_l^{23} are leakage couplings:

$$\tilde{\Omega} = \Omega - \frac{\epsilon}{\Omega}\Delta\Omega_z + \frac{t^2}{2\Omega^3}\Delta\Omega_z^2 + \frac{t^2}{2\Omega\left(\Omega^2 - \Omega_s^2\right)}\Delta\Omega_x^2 \tag{B.1.2}$$

$$\Omega_l^{13}(\pm\epsilon) = \frac{2t}{\Omega}\left(1 \pm \frac{\epsilon}{\Omega^2}\Delta\Omega_z\right)\cdot\epsilon_d \tag{B.1.3}$$

$$\Omega_l^{23} = -\epsilon\frac{t_c\Delta\Omega_x(\Omega^2 + \Omega\Omega_s - \Omega_s^2)}{\Omega^3\Omega_s(\Omega - \Omega_s)}\cdot\epsilon_d \tag{B.1.4}$$

$$\Omega_l^{14} = -\epsilon\frac{t_c\Delta\Omega_x(\Omega^2 - \Omega\Omega_s - \Omega_s^2)}{\Omega^3\Omega_s(\Omega + \Omega_s)}\cdot\epsilon_d \tag{B.1.5}$$

As expected, the charge qubit splitting $\tilde{\Omega}$ is equal to the bare charge qubit splitting Ω to zeroth order in the energy gradients $\Delta\Omega$, and the coupling element is also equal to the bare charge qubit coupling element $\frac{2t}{\Omega}\epsilon_d$ to zeroth order.

At low spin-charge detunings, when $\Omega_s \to \Omega$, we find the following asymptotic expressions for the leakage couplings Ω_l^{23} and Ω_l^{14} that involve both a charge transition and a spin transition:

$$\Omega_l^{23} \xrightarrow[\Omega_s\to\Omega]{} -h\frac{2\epsilon}{\Omega}\cdot\epsilon_d \tag{B.1.6}$$

$$\Omega_l^{14} \xrightarrow[\Omega_s\to\Omega]{} -h\frac{\epsilon\Delta}{\Omega^2}\cdot\epsilon_d \tag{B.1.7}$$

Both transition matrix element are vanishingly small[1] when the qubit is operated at small electric detuning $\epsilon << \Omega$, especially compared to the direct charge transition coupling element $\Omega_l^{13} =: \Omega_l$ that is approaches the value $\Omega_l^{13} \approx \epsilon_d$ in that regime. This reflects the fact that direct charge transitions are a lot more probable then the two indirect ones involving both a charge and spin transition.

In summary, the analysis of the matrix element of the effective Hamiltonian motivates the use of the following simplified effective Hamiltonian of the following form:

$$H_{rl} = \begin{pmatrix} 0 & \Omega_r & \Omega_l & 0 \\ \Omega_r & \tilde{\Omega}_s & 0 & \Omega_l \\ \Omega_l & 0 & \tilde{\Omega} & \Omega_r \\ 0 & \Omega_l & \Omega_r & \tilde{\Omega} + \tilde{\Omega}_s \end{pmatrix}, \tag{B.1.8}$$

[1] Physically, the hybridisation factor h is bound by one due to the normalisation condition of the wavefunction $|h|^2 \leq 1$

In our numerical error modelling Sect. 3.3, we numerically compute the flopping mode Hamiltonian, under the only assumption that the indirect leakage coupling vanish, as in the above matrix.

B.2 Rotating frame approximation for the flopping mode qubit

In Sect. B.1 we derived through an analysis of the matrix elements of the effective flopping mode Hamiltonian that the flopping mode qubit can be accurately described by the effective Hamiltonian of the following form (see Eq. B.1.1):

$$H_{\text{fm}} = \begin{pmatrix} 0 & \Omega_r & \Omega_l & 0 \\ \Omega_r & \tilde{\Omega}_s & 0 & \Omega_l \\ \Omega_l & 0 & \tilde{\Omega} & \Omega_r \\ 0 & \Omega_l & \Omega_r & \tilde{\Omega} + \tilde{\Omega}_s \end{pmatrix}, \tag{B.2.1}$$

Where $\tilde{\Omega}_s$ is the flopping mode qubit energy splitting (splitting between hybridised spin states), Ω_r is the flopping mode qubit Rabi frequency (Rabi frequency that drives flips of the hybridised spin) and Ω_l is the dominant leakage coupling corresponding to a charge excitation without spin flip, between the states separated by the hybridised charge qubit splitting $\tilde{\Omega}$. Not that all coupling terms are proportional to the electric detuning drive amplitude $\epsilon_d(t)$ reflecting the fact that these coupling terms all emerge from coupling of the states to the drive electric field.

To understand the dynamics of the system when it is driven, it is useful to go into a rotating frame that precesses with the frequency associated with the one or two qubit splitting. In that way, the dynamics associated with the drive can be separated from the natural Larmor precession of the qubit(s). For a four level system like the one we are considering, this can be achieved with the following unitary transformation $U(t) = \exp(-\imath R\omega_f t)$, where the generator matrix R is given by:

$$R = \cdot \begin{pmatrix} 1 & 0 & 0 & 0 \\ 0 & 1 & 0 & 0 \\ 0 & 0 & 1 & 0 \\ 0 & 0 & 0 & -1 \end{pmatrix}$$

Let us now transform the Hamiltonian H_{fm} , assuming the electric field is driven with a drive frequency ω_d:

$$\Omega_r(t) = \Omega_r \cos(\omega_d t) \tag{B.2.2}$$

$$\Omega_l(t) = \Omega_l \cos(\omega_d t) \tag{B.2.3}$$

The transformed Hamiltonian in the rotating frame consists in a first term originating from the transformation being time dependent, and a second canonical change of coordinates:

$$H_{\text{fm}}^{\text{RF}} = \omega_f R + U(t) \cdot H_{\text{fm}} \cdot U(-t) \tag{B.2.4}$$

$$= \begin{pmatrix} 0 & \exp(-\imath\omega_f t)\Omega_r(t) & \exp(-\imath\omega_f t)\Omega_l(t) & 0 \\ \exp(\imath\omega_f t)\Omega_r(t) & \tilde{\Omega}_s - \omega_f & 0 & \exp(-\imath\omega_f t)\Omega_l(t) \\ \exp(\imath\omega_f t)\Omega_l(t) & 0 & \tilde{\Omega} - \omega_f & \exp(-\imath\omega_f t)\Omega_r(t) \\ 0 & \exp(\imath\omega_f t)\Omega_l(t) & \exp(\imath\omega_f t)\Omega_r(t) & \tilde{\Omega} + \tilde{\Omega}_s - 2\omega_f \end{pmatrix} + \omega_f \mathbb{1} \tag{B.2.5}$$

Here we can subtract the global energy shift $\omega_f \mathbb{1}$.

By rotating the frame with the driving frequency ($\omega_f \mapsto \omega_d$), we can expand the off diagonal driving terms, into a stationary term and two terms rotating with twice the drive frequency ω_d

$$\exp(\pm\imath\omega_f t)\Omega_{r/l}(t) \mapsto \frac{1}{2}\left(\Omega_{r/l} + \Omega_{r/l}\cos(2\omega_d t) \pm \imath\Omega_{r/l}\sin(2\omega_d t)\right). \tag{B.2.6}$$

If the driving strengths $\Omega_{r/l}$, are much smaller then the driving frequency ω_d, the terms oscillating with twice the drive frequency average out over a Rabi rotation of much slower frequency $\Omega_{r/l}$, and the off diagonal terms simplify to $\frac{\Omega_{r/l}}{2}$. This is called the rotating wave approximation (RWA), and yields the following Hamiltonian in the rotating frame:

$$H_{\text{fm}}^{RF} = \begin{pmatrix} 0 & \Omega_r/2 & \Omega_l/2 & 0 \\ \Omega_r/2 & \tilde{\Omega}_s - \omega_d & 0 & \Omega_l/2 \\ \Omega_l/2 & 0 & \tilde{\Omega} - \omega_d & \Omega_r/2 \\ 0 & \Omega_l/2 & \Omega_r/2 & \tilde{\Omega} + \tilde{\Omega}_s - 2\omega_d \end{pmatrix}, \tag{B.2.7}$$

When the electric field is driven at the frequency corresponding to the flopping mode qubit splitting ($\omega_d = \tilde{\Omega}_s$), the Hamiltonian transforms into two 2-level systems

corresponding to the ground charge state spin system (the flopping mode qubit) and its excited charge state counterpart, that are separated by the energy gap $\Delta = \tilde{\Omega} - \tilde{\Omega}_s$ and coupled via the leakage couplings Ω_l:

$$H_{\mathrm{fm}}^{RF} = \begin{pmatrix} 0 & \Omega_r/2 & \Omega_l/2 & 0 \\ \Omega_r/2 & 0 & 0 & \Omega_l/2 \\ \Omega_l/2 & 0 & \Delta & \Omega_r/2 \\ 0 & \Omega_l/2 & \Omega_r/2 & \Delta \end{pmatrix}, \tag{B.2.8}$$

The coupling Ω_l between the two subsystems corresponds to charge leakage and is studied in detail in Sect. 3.3.2, using time evolutions of Hamiltonians of the form Eq. B.2.8.

B.3 Variance of a noisy variable with given PSD

For a given time dependent noise parameter $x(t)$, sampled as $x_n = x(n\Delta t)$ at intervals Δt, over a time $T = N\Delta t$, the power spectral density of the signal at the angular frequency ω is defined as :

$$S(\omega) = \Delta t^2/T \left| \sum_{n=1}^{N} x_n e^{-\imath\omega n\Delta t} \right|. \tag{B.3.1}$$

The PSD can be written in terms of the DFT coefficients X_k:

$$X_k = \sum_{k=1}^{N} x_n e^{-\imath 2\pi kn/N}. \tag{B.3.2}$$

We use $\omega(k) = 2\pi/Tk = \Delta\omega k$, and get:

$$S(\omega(k)) = T/N^2 |X_k|^2 \tag{B.3.3}$$

The variance of the discrete variable x (with zero expectation value, without loss of generality), when sampled over the time interval $I = [\Delta t, T]$ can be approximated

by :

$$\begin{aligned} \mathrm{var}(x) = \langle |x|^2 \rangle_I - \langle x \rangle_I^2 &\approx \frac{1}{N} \sum_{n=1}^{N} |x_n|^2 \\ &\underset{Par.th.}{=} \frac{1}{N} \frac{1}{N} \sum_{k=1}^{N} |X_k|^2 = \frac{1}{T} \sum_{k=1}^{N} S(\omega(k)) \end{aligned} \tag{B.3.4}$$

Where we used Parseval's theorem for DFTs to relate the samples x_n to the DFT coefficients X_k. We can write the last sum as a Riemann integral in the limit $N \to \infty$:

$$\mathrm{var}(x) \approx \frac{1}{2\pi} \sum_{k=1}^{N} S(\omega(k)) \Delta\omega \approx \frac{1}{2\pi} \int_{2\pi/T}^{2\pi/\Delta t} S(\omega) d\omega = \int_{f_T}^{f_{\Delta t}} S(f) df. \tag{B.3.5}$$

We have here approximated the variance of the random variable when sampled over a time T, in discrete time steps Δt, by the integral of the PSD over the corresponding frequency range $[f_T, f_{\Delta t}]$, where $f_T = 1/T$ and $f_{\Delta t} = 1/\Delta t$. For a white noise power spectrum, the variance of the parameter will essentially be proportional to the length of the measurement.

For a white noise power spectrum, the variance of the parameter will essentially be proportional to the length of the measurement. In the case of the two noise sources we are considering, we can use the $f^{-\alpha}$ PSD dependance to get an estimate of the variance of the noise parameter when sampled similarly:

$$\mathrm{var}(x) \approx \int_{f_T}^{f_{\Delta t}} f_{1\mathrm{Hz}} \cdot f^{-\alpha} df = \frac{f_{1\mathrm{Hz}}}{1-\alpha} \left(\frac{1}{f_{\Delta t}^{\alpha-1}} - \frac{1}{f_T^{\alpha-1}} \right) \approx \frac{f_{1\mathrm{Hz}}}{\alpha - 1} T^{\alpha-1}, \tag{B.3.6}$$

Were the last step assumes (as in most measurement), that $f_T \gg f_{\Delta t}$, and we have assumed $\alpha > 1$. Thus the variance of the noise parameter when sampled during a time interval T grows as $T^{\alpha-1}$. If $\alpha = 1$, the integral simplifies to :

$$\mathrm{var}(x) \approx f_{1\mathrm{Hz}} \ln(T/\Delta t) \approx f_{1\mathrm{Hz}} \ln(T). \tag{B.3.7}$$

Thus, for pure $1/f$ noise, the noise variance grows logarithmically with the length T of the measurement.

B.4 Analytical error with only x-noise source

Let us now investigate how the dephasing error of a single qubit gate can be calculated within the frame of the quasi-static approximation. A general qubit Hamiltonian H, tuned in to resonance to perform an x gate (e.g. in the rotating frame or tuned physically), under the presence of noise $\delta\Omega_1$ and δE on the x and z axes respectively, has the form (in angular frequency units) :

$$H/\hbar = \delta E\sigma_z + (\Omega_1 + \delta\Omega_1)\sigma_x, \tag{B.4.1}$$

This is the case for the reduced flopping mode Hamiltonian H_r derived in equ. 3.2.18, when transformed in a rotating frame.

The time evolution associated with the above Hamiltonian can be seen as an imperfect rotation around the x-axis of the Bloch sphere, with angular Rabi frequency $2\Omega_1$:

$$U(t) = \exp\left(-\imath Ht/\hbar\right) \approx \exp\left(-\imath 2\pi\nu_1 t\sigma_x\right), \tag{B.4.2}$$

Where $\nu_1 = \Omega_1/2\pi$. Let us consider an arbitrary unitary gate operation U_x, subject to a noisy parameter x, that we model as a random variable following a normal PDF with a variance calculated form a PSD as outlined above. We define the charge dephasing error of the $\Pi/2$ gate to be the deviation of the expectation value of the noisy unitary evolution projected onto the ideal unitary evolution U_{id} of the initial state $\Psi_{i,x}$ [5], averaged over the charge noise detuning PDF $P(\delta\epsilon)$ and over all startstates in the qubit subspace.

$$\begin{aligned}
\text{error} &= 1 - E\left(\left|\langle\Psi_{i,x}|U_x^\dagger U_{\mathrm{id}}|\Psi_{i,x}\rangle\right|^2\right) && \text{(B.4.3)}\\
&\approx 1 - E\left(\left|\langle\Psi_{i,\mathrm{id}}|U_x^\dagger U_{\mathrm{id}}|\Psi_{i,\mathrm{id}}\rangle\right|^2\right) && \text{(B.4.4)}\\
&= 1 - E\left(\left|\langle\Psi_{f,x}|\Psi_{f,\mathrm{id}}\rangle\right|^2\right). && \text{(B.4.5)}
\end{aligned}$$

For computational simplicity, we have here neglected the variation in the initial state due to noise. As motivated previously, we are interested in estimating the π rotation error form the qubit ground state $|\downarrow\tilde{-}\rangle'$ (abbreviated as $|\downarrow\rangle$) to the qubit excited state $|\uparrow\tilde{-}\rangle'$ (abbreviated as $|\uparrow\rangle$):

$$\begin{aligned}
\text{error} &= 1 - E\left(\left|\langle\Psi_{f,x}|\uparrow\rangle\right|^2\right) && \text{(B.4.6)}\\
&= 1 - E\left(p_\uparrow(x)\right). && \text{(B.4.7)}
\end{aligned}$$

We have here reduced the error calculation of the π x-gate to an estimation of the expectation value of the spin up probability $p_\uparrow(x)$. Under the typical time evolution of an x-gate as outlined in equ. B.4.2, $p_\uparrow$ follows the Rabi formula [6]:

$$p_\uparrow(\delta E, \delta\nu_1, t) = \frac{\nu_1 + \delta\nu_1}{\sqrt{(\nu_1 + \delta\nu_1)^2 + \delta E^2}} \sin^2\left(2\pi t\sqrt{(\nu_1^2 + \delta\nu_1)^2 + \delta E^2}\right). \tag{B.4.8}$$

Without any noise, the spin up probability describes a pure $\sin^2$ oscillation, with frequency $2\nu_1$, and according period $1/(2\nu_1)$. A π gate is achieved at time $t_\pi = 1/(4\nu_1)$.

Again, for simplicity, we assume that the operator of the qubit will use this π gate time also in the presence of noise. The average Rabi frequency will actually be slightly higher in the presence of noise, as the actual frequency for each shot is the sum of squares $2\sqrt{(\nu_1^2 + \delta\nu_1)^2 + \delta E^2}$ which does not always average to $2\nu_1$, even for symmetric distributions of δE. However, for small noise values t_π is close to the optimal π gate time.

In the presence of only transverse x-noise $\delta\nu_1$, the π gate error in equ. B.4.7 can be calculated analytically:

$$\begin{aligned}
\text{error} &= 1 - E\left(p_\uparrow(0, \delta\nu_1, t_\pi)\right) && \text{(B.4.9)}\\
&= 1 - \int_{-\infty}^{+\infty} P(\delta\nu_1) p_\uparrow(0, \delta\nu_1, t_\pi)\, \mathrm{d}\nu_1 && \text{(B.4.10)}\\
&= 1 - \int_{-\infty}^{+\infty} \frac{1}{\sqrt{2\pi\sigma_{\nu_1}^2}} \exp\left(-\frac{\delta\nu_1^2}{2\sigma_{\nu_1}^2}\right) \sin^2\left(\frac{\pi}{2}\frac{\nu_1 + \delta\nu_1}{\nu_1}\right) \mathrm{d}\nu_1 && \text{(B.4.11)}\\
&= \frac{1}{2}\left(1 - \exp\left(-\frac{\pi^2\sigma_{\nu_1}^2}{2\nu_1^2}\right)\right) && \text{(B.4.12)}\\
&= \frac{1}{2}\left(1 - \exp\left(-\frac{\pi^2\sigma_{\nu_1}^2}{2\nu_1^2}\right)\right) && \text{(B.4.13)}\\
&= \frac{1}{2}\left(1 - \exp\left(-2(2\pi\sigma_{\nu_1} t_\pi)^2\right)\right) && \text{(B.4.14)}\\
& && \text{(B.4.15)}
\end{aligned}$$

This shows that the dephasing error due to a noisy Rabi frequency decays like a Gaussian with the noise standard deviation and the gate time. For very fast gates, or very small noise values, the error approaches, zero, whereas it asymptotically decays to 1/2 for slow gates and high noise values. In the low error regime $\sigma_{\nu_1} \ll \nu_1$,

the error can be approximated to third order to :

$$\text{error} = \left(\frac{\pi}{2}\right)^2 \left(\frac{\sigma_{\nu_1}}{\nu_1}\right)^2 + \mathrm{O}\left(\frac{\sigma_{\nu_1}}{\nu_1}\right)^4 \tag{B.4.16}$$

The error formula Eq. B.4.11 can be related to the Q factor $Q = \frac{2\nu_1}{\sigma_{\nu_1}}$:

$$\text{error} = \frac{1}{2}\left(1 - \exp\left(-2\left(\frac{\pi}{Q}\right)^2\right)\right) \tag{B.4.17}$$

B.5 T1 error decomposition

The decomposition of the error rests on the splitting of the excited state proportion $\sum_k \left|\langle\Psi(t)|\Psi_k^+\rangle\right|^2$ in the equation above. The latter can be bound by introducing the identity in the spin-charge eigenbasis $\{|i\rangle,\, i = 0, \ldots, 3\}$:

$$\sum_k \left|\langle\Psi(t)|\Psi_k^+\rangle\right|^2 = \sum_k \left|\sum_{i=0}^{3} \langle\Psi(t)|i\rangle\langle i|\Psi_k^+\rangle\right|^2 \tag{B.5.1}$$

$$\approx \sum_k \left|\sum_{i=1}^{3} \langle\Psi(t)|i\rangle\langle i|\Psi_k^+\rangle\right|^2 \tag{B.5.2}$$

$$< |\langle\Psi(t)|1\rangle|^2 \sum_k \left|\langle 1|\Psi_k^+\rangle\right|^2 \tag{B.5.3}$$

$$+ \sum_k \left|\sum_{i=2}^{3} \langle\Psi(t)|i\rangle\langle i|\Psi_k^+\rangle\right|^2 \tag{B.5.4}$$

In the second step (B.5.2) we used the fact that the overlap $\langle 0|\Psi_k^+\rangle$ of the ground qubit state $|0\rangle$ with any of the two excited charge states can be neglected, and in the following one we used the triangular inequality.

The last term (B.5.4) can be simplified by approximating $\langle i|\Psi_k^+\rangle \approx 1$ for the two excited charge states $k = 2, 3$. We then we get a decomposition of the wavefunction overlap into the overlap O_i and O_d, corresponding to the idle T1 error and drive T1 error respectively:

$$\sum_k \left|\langle\Psi(t)|\Psi_k^+\rangle\right|^2 < |\langle\Psi(t)|1\rangle|^2 \sum_k \left|\langle 1|\Psi_k^+\rangle\right|^2 \tag{B.5.5}$$

$$+ \sum_{i=2}^{3} |\langle\Psi(t)|i\rangle|^2 =: O_i(t) \cdot O_{1,+} + O_d(t), \tag{B.5.6}$$

Where we defined $O_{1,+} = \sum_k \left|\langle 1|\Psi_k^+\rangle\right|^2$ to be the charge hybridization proportion of the qubit $|1\rangle$ state.

Appendix C

Chapter 4 appendix

C.1 Equivalence of flopping-mode qubits

C.1.1 Flip-flop Hamiltonian

Let us now consider a flip-flop qubit, as described in [7], where the left orbital occupies a MOS dot, and the right orbital occupies the unpaired D_0 state of a single phosphorus donor, in which case the electron spin and the nuclear spin are coupled via the hyperfine interaction A_R. We assume the static magnetic field B_z to be static across both dots, but take into account that the electron gyromagnetic ratio $\gamma_e^{L/R}$ differs between the MOS dot and the donor so that a difference in the gyromagnetic ratio arises: $\Delta\gamma = \gamma^L - \gamma^R$. The Hilbert space of this system is here twice as large as the one corresponding to the general Hamiltonian of Eq. 3.2.1 due to the extra nuclear spin degree of freedom: $\mathscr{H} = \mathscr{H}_n \otimes \mathscr{H}_e \otimes \mathscr{H}_c$.

The full Hamiltonian H_f in the basis $|\Uparrow / \Downarrow\rangle \otimes |\uparrow / \downarrow\rangle \otimes |L/R\rangle$ is given by:

$$
\begin{aligned}
H_f =& \bar{\gamma_e} B \cdot \mathbb{1} \otimes \sigma_z/2 \otimes \mathbb{1} - \gamma_n B_z \cdot \sigma_z/2 \otimes \mathbb{1} \otimes \mathbb{1} + \mathbb{1} \otimes \mathbb{1} \otimes (\epsilon\sigma_z + t\sigma_x) && \text{(C.1.1)}\\
&+ \delta\gamma_z B_z \cdot \mathbb{1} \otimes \sigma_z/2 \otimes (\mathbb{1}/2 + \sigma_z/2) && \text{(C.1.2)}\\
&- \delta\gamma_z B_z \cdot \mathbb{1} \otimes \sigma_z/2 \otimes (\mathbb{1}/2 - \sigma_z/2) && \text{(C.1.3)}\\
&+ A_R \left(\sigma_i/2 \otimes \sigma_i/2\right) \otimes (\mathbb{1}/2 - \sigma_z/2)\,. && \text{(C.1.4)}
\end{aligned}
$$

We have here defined the average electron gyromagnetic ratio as $\bar{\gamma} = \left(\gamma^L + \gamma^R\right)/2$, $\delta\gamma_z = \Delta\gamma_z/2$, and have used the Einstein summation notation for the hyperfine interaction term. From this Hamiltonian it can be seen that only the hyperfine interaction mixes the nuclear and electron spin states. Because this Heisenberg-type interaction only couples the electron-nuclear singlet states one can split the nuclear-

and electron-spin Hilbert space into a direct sum of non-interacting subspaces with respect to H, corresponding to the total spin states -1, 0 and 1:

$$\mathscr{H}_n \otimes \mathscr{H}_e = \mathscr{H}_{-1} \oplus \mathscr{H}_0 \oplus \mathscr{H}_1, \tag{C.1.5}$$

where

$$\mathscr{H}_{-1} = \mathrm{Span}\left(\{|\Downarrow\downarrow\rangle\}\right), \tag{C.1.6}$$
$$\mathscr{H}_1 = \mathrm{Span}\left(\{|\Uparrow\uparrow\rangle\}\right), \tag{C.1.7}$$
$$\mathscr{H}_0 = \mathrm{Span}\left(\{|\Uparrow\downarrow\rangle, |\Downarrow\uparrow\rangle\}\right) \tag{C.1.8}$$

The fact that those subspaces are invariant under H_f simply reflects total spin conservation in this system that we assume closed for now (electron–phonon interaction for example would allow spin relaxation and thus violate spin conservation within our restricted system). The subspaces $\mathscr{H}_{\pm 1}$ are one dimensional, and thus of no interest regarding application for quantum computing. We can reduce H_f to the space $\mathscr{H}_0$, by using the following transformations:

$$\sigma_i \otimes \sigma_i \mapsto -\mathbb{1} + 2\sigma_x \tag{C.1.9}$$
$$\mathbb{1} \otimes \sigma_z \mapsto +\sigma_z \tag{C.1.10}$$
$$\sigma_z \otimes \mathbb{1} \mapsto -\sigma_z\,. \tag{C.1.11}$$

By applying these transformation to H_f, we can reduce it to a Hamiltonian H_r acting purely on the reduced total Hilbert space $\mathscr{H}_r = \mathscr{H}_0 \otimes \mathscr{H}_c$:

$$H_r = \left[\left(\frac{\bar{\gamma_e} + \gamma_n}{2}\right) B_z \sigma_z + \frac{A_R}{4}\right] \otimes \mathbb{1} \tag{C.1.12}$$
$$+ \mathbb{1} \otimes \left[\left(\epsilon + \frac{A_R}{8}\right)\sigma_z + t\sigma_x\right] \tag{C.1.13}$$
$$+ \left[\frac{\Delta\gamma_z}{4} B_z \sigma_z - \frac{A_R}{4}\sigma_x\right] \otimes \sigma_z\,, \tag{C.1.14}$$

where we subtracted a global energy shift $\propto \mathbb{1} \otimes \mathbb{1}$.

The first summand above (Eq. C.1.12) can be diagonalised, and this will finally transform H_r into the form of the general flopping-mode Hamiltonian in equ. 3.2.1,

with its different parameters defined as follows:

$$\Omega_z = \sqrt{(\gamma^+ B_z)^2 + \left(\frac{A_R}{2}\right)^2}, \tag{C.1.15}$$

$$\gamma^+ = \bar{\gamma_e} + \gamma_n, \tag{C.1.16}$$

$$\tilde{\epsilon} = \epsilon + \frac{A_R}{8}, \tag{C.1.17}$$

$$\Delta\Omega_z = \Delta\gamma_z B_z \cos(\theta_B) - A_R \sin(\theta_B), \tag{C.1.18}$$

$$\Delta\Omega_x = A_R \cos(\theta_B) + \Delta\gamma_z B_z \sin(\theta_B). \tag{C.1.19}$$

Here, the angle θ corresponds to a very small rotation of the qubit quantisation axis due the x-component of the hyperfine interaction:

$$\cos(\theta_B) = \frac{\gamma^+ B_z}{\Omega_z} \approx 1, \tag{C.1.20}$$

$$\sin(\theta_B) = \frac{A_R/2}{\Omega_z} \approx 0. \tag{C.1.21}$$

The pseudo-spin basis is here defined as:

$$\tilde{\uparrow}/\tilde{\downarrow} = \frac{1}{\sqrt{2}}\left(\mp\sqrt{1 \pm \cos(\theta_B)}, \mp\sqrt{1 \mp \cos(\theta_B)}\right),$$

here expressed in the explicit combined nuclear and electron spin basis $\{|\Downarrow\uparrow\rangle = |\Downarrow\rangle \otimes |\uparrow\rangle, \Uparrow\downarrow = |\Uparrow\rangle \otimes |\downarrow\rangle\}$.

The transverse energy difference, that will drive transitions between the two pseudo-spin states, also called the flip-flop states $\Downarrow\uparrow$ and $\Uparrow\downarrow$, is here purely produced by the hyperfine interaction with the right nuclear spin A_R, whereas the longitudinal gradient is purely determined by the electronic g-factor difference.

C.1.2 All-epitaxial flopping-mode hamiltonian

We now consider the epitaxial flopping-mode qubit, comprising N-phosphorus donors, with N_L donors defining the left donor orbital, and one donor ($N_R = 1$) defining the right electron orbital. This differs from the flip-flop implementation, only in that the MOS dot is replaced by a phosphorus-donor cluster. For reasonably small cluster sizes, the electron-shell filling is trivial and an unpaired electron is present if the total electron number on the system is odd. The left and right orbitals used in the following correspond to the orbitals of that unpaired electron. We will see in chapter 4.2.1 that a higher electron number can reduce qubit errors.

We will now show that the full Hamiltonian describing this double-donor quantum-dot system can be reduced to a four-dimensional flopping-mode Hamiltonian as in Eq. 3.2.1, describing a pseudo-spin state corresponding to the combined electron-nuclear spin state of the phosphorus atoms, such that the electron flip-flops with the single nuclear spin $N_R = 1$ on the right dot while all other N_L nuclear spins on the left dot stay fixed. This generalised Hamiltonian accurately describes the flopping-mode operation of the system but fails to capture leakage into nuclear spin states.

The full Hamiltonian of the double quantum dot system with a total of $N = N_L + N_R$ nuclear spins can be written in the product basis $\left(\bigotimes_{k=1}^{N} |\Uparrow^k / \Downarrow^k\rangle\right) \otimes |\Uparrow / \Downarrow\rangle \otimes |\uparrow / \downarrow\rangle \otimes |L/R\rangle$: of the combined nuclear and electron spin as well as charge Hilbert spaces $\mathscr{H}_n$, $\mathscr{H}_s$ and $\mathscr{H}_c$, respectively:

$$H = \gamma_e \boldsymbol{B}\cdot\boldsymbol{s} - \gamma_n \boldsymbol{B}\cdot\sum_{k=1}^{N}\boldsymbol{i}^k + (\epsilon\tau_z + t_c\tau_x) + \sum_{k=1}^{N_L} A_{L,k}(\boldsymbol{i}^k\cdot\boldsymbol{s})\,(\mathbb{1}+\tau_z)\,/2 + A_R\left(\boldsymbol{i}^N\cdot\boldsymbol{s}\right)(\mathbb{1}-\tau_z)\,/2. \quad \text{(C.1.22)}$$

Here we have defined the spin-vector operators $\boldsymbol{s}$ and $\boldsymbol{i}^k$, of the electron and the k-th donor nucleus respectively, τ_i are the Pauli operators acting on the charge subspace $\mathscr{H}_c$, $\boldsymbol{B} = (0, 0, B_0)$ is the external static magnetic field, $A_{L,k}$ is the kth contact hyperfine strength for the left quantum dot and A_R is the hyperfine term for the right donor. For convenience we have defined the right donor nuclear spin to be the Nth nuclear-spin operator.

The only coupling terms within the nuclear and electron spin subspace $\mathscr{H}_n \otimes \mathscr{H}_s$ are due to the hyperfine interaction. The full Hilbert space (electron, nuclear, and charge) can be decomposed into a direct sum of H-invariant subspaces according to their total spin polarisation m (electron and nuclear spin),

$$\mathscr{H} = \bigoplus_{m=-(N+1)/2}^{(N+1)/2} \mathscr{H}_m^{N+1} = \bigoplus_{m=-(N+1)/2}^{(N+1)/2} \mathscr{H}_{s,m}^{N+1} \otimes \mathscr{H}_c. \quad \text{(C.1.23)}$$

The electron spin introduces the extra state (summation is over N nuclear spins and 1 electron spin). The decomposition of the spin subspaces into $\mathscr{H}_{s,m}^{N+1}$ is carried over to the charge subspace. Due to spin conservation, the charge part of the Hamiltonian only connects states with the same subspace $\mathscr{H}_m^{N+1}$ of total spin m and as a result

simply doubles the size of the Hilbert space. The decomposition is optimal as there exists no smaller invariant subspace within each $\mathscr{H}_m^{N_s}$ (a simple proof can be found in Appendix C.2).

The dimensions of each invariant subspace hosting a number N_s of spins (nuclear and electron)[1] are given by the binomial coefficients:

$$\dim(\mathscr{H}_{s,m}^{N_s}) = \binom{N_s}{m + N_s/2}.$$

Table C.1 lists the dimensions of the invariant subspaces $\mathscr{H}_m^{N+1}$ of same spin polarisation m, for different donor numbers N. Any of the invariant subspaces in

Table C.1: Dimensions of the invariant spin and charge subspaces of same spin polarisation m with a single electron spin and N donors.

	m										
N	$-5/2$	-2	$-3/2$	-1	$-1/2$	0	$1/2$	1	$3/2$	2	$5/2$
1	0	0	0	2	0	4	0	2	0	0	0
2	0	0	2	0	6	0	6	0	2	0	0
3	0	2	0	8	0	12	0	8	0	2	0
4	2	0	10	0	20	0	20	0	10	0	2

Table C.1 offer the possibility of a flip-flop transition with the right nuclear spin except the two two-dimensional spaces $\mathscr{H}_{\pm(N+1)/2}^{N+1}$ that correspond to full polarisation of the electron and nuclear spins. The $N = 1$ system (a single nuclear spin in the right quantum dot) corresponds to the quantum dot-donor (flip-flop) qubit and is the only case where one of subspace is four-dimensional and directly corresponds to a flopping-mode EDSR qubit. For all other values of N the subspaces are larger than four-dimensional since the electron spin can flip-flop with more than one nuclear spin. In the donor–donor implementation ($N = 3$, 2 nuclei on the left quantum dot and 1 on the right quantum dot) there are therefore 5 invariant subspaces with spin polarisation $m = -2$, -1, 0, 1, 2 and respective dimensions 2, 8, 12, 8, 2. The $m = \pm 2$ subspaces correspond to all the spins being parallel: $|\Downarrow\Downarrow\Downarrow\downarrow\rangle$ and $|\Uparrow\Uparrow\Uparrow\uparrow\rangle$, respectively and cannot be used for EDSR since there is no electron-nuclear flip-flop transition. If the system reaches either of these states then NMR or dynamic nuclear polarisation would be needed to flip one of the nuclear spins into the opposite spin state. The $m = 0$ subspace is especially promising for quantum computing applications as the spectator nuclear spins on the left quantum dot can be initialised within that subspace in such a way as to minimise the effective longitudinal magnetic-field

[1] in the 2p1P case, $N_s = N + 1$.

gradient as will be discussed extensively in Chapter 4.

The Hamiltonian H can be reduced further, by treating the coupling to the N_L nuclear spins perturbatively to first order in their hyperfine coupling strength. If the subspaces are non-degenerate, it is possible to fully remain within the qubit subspace by performing an appropriate state initialisation and by driving adiabatically at the frequency defined by the qubit splitting. The individual dipole moments and energy gaps all determine how fast a transition can be driven adiabatically, without leaking into the other states. For superconducting qubit, elaborate pulses sequences have reduced leakage to non-qubit subspaces while allowing for fast driving, and thus minimising of the influence of dephasing and relaxation errors. In Sect. 3.3 we will model the leakage out of the qubit subspace, using adiabatic pulse shapes that reduce the associated errors.

The Hamiltonian in Eq. C.1.22 can be approximated by a first-order Schrieffer–Wolff transform. Effectively, we restrict the Hamiltonian to the four-dimensional subspace spanned by the spin states $|N_L\rangle \otimes |\Downarrow\rangle \otimes |\uparrow\rangle$ and $|N_L\rangle \otimes |\Uparrow\rangle \otimes |\downarrow\rangle$, and the two orbital charge states $|L\rangle$ and $|R\rangle$. The state $|N_L\rangle$ corresponds to the nuclear spin configuration of all N_L nuclear spins in the left dot. Numerically, we find that this approximation very accurately describes the system provided the system is not operated at a point where nuclear spin states hybridise. The Schrieffer–Wolff transform performs the following transformations on the Hamiltonian:

$$\boldsymbol{i}^k \cdot \boldsymbol{s} \mapsto \begin{cases} \frac{1}{4}\left(-\mathbb{1} + 2\sigma_x\right) & \text{if } k = N \\ \langle \boldsymbol{i}_z^k \rangle \sigma_z/2 & \text{if } k < N, \end{cases} \tag{C.1.24}$$

where now σ_i is defined in the new four-state basis. The nuclear Zeeman terms become:

$$\boldsymbol{i}_z^k \mapsto \begin{cases} -\sigma_z/2 & \text{if } k = N \\ \langle \boldsymbol{i}_z^k \rangle \mathbb{1} & \text{if } k < N. \end{cases} \tag{C.1.25}$$

The first order Schrieffer–Wolff transformation essentially selects the matrix elements of the multidimensional matrices $\boldsymbol{i}^k \cdot \boldsymbol{s}$ and $\boldsymbol{i}_z^k$ that correspond to the last two dimensions of the Hilbert space (right nuclear spin state and electron spin state).

After performing the transformation and subtracting global energy shifts, we

get:

$$H_E = \left[\frac{1}{2}\left(\left(\gamma_e+\gamma_n\right)B_z + M_n\right)\sigma_z + \frac{A_R}{4}\sigma_x\right] + \left[\left(\epsilon + \frac{A_R}{8}\right)\tau_z + t_c\tau_x\right] + \frac{1}{4}\left(2M_n\sigma_z - A_R\sigma_x\right)\tau_z, \quad \text{(C.1.26)}$$

where we capture the influence of the effective magnetic field produced from the spectator nuclear spins as the averaged hyperfine interaction $M_n = \sum_{k=1}^{N_L} A_{L,k}\langle \boldsymbol{i}_z^k\rangle/2$.

We can diagonalise the spin-like terms (σ_i) in Eq. C.1.26, which results in a small rotation of the quantisation axis due to the nuclear-spin Zeeman and hyperfine terms. Afterwards, we finally recover the Hamiltonian of the form described in Eq. 3.2.1, with the following parameters:

$$\Omega_z = \sqrt{\Omega_s^2 + \left(\frac{A_R}{2}\right)^2}, \quad \text{(C.1.27)}$$

$$\text{with } \Omega_s = \left(\gamma_e+\gamma_n\right)B_0 + M_n + \frac{\delta\Omega^{(2)}}{2}, \quad \text{(C.1.28)}$$

$$\epsilon_A = \epsilon + \frac{A_R}{8} + \frac{\delta\Omega^{(2)}}{4}, \quad \text{(C.1.29)}$$

$$\Delta\Omega_z = \left(2M_n - \delta\Omega^{(2)}\right)\cos(\theta) - A_R\sin(\theta), \quad \text{(C.1.30)}$$

$$\Delta\Omega_x = A_R\cos(\theta) + \left(2M_n - \delta\Omega^{(2)}\right)\sin(\theta). \quad \text{(C.1.31)}$$

The correction term $\delta\Omega^{(2)} = O\left(\frac{A_L^2}{(\gamma_e+\gamma_n)B_0}\right)$ arises from the higher-order terms of the Schrieffer-Wolff trasnformation which we neglect for the following analysis since they only have a small effect on the Hamiltonian parameters. Very close to nuclear-spin level-crossings, some even higher order effects describing nuclear-spin-state hybridisation via the electron hyperfine interaction become relevant, but can safely be neglected by staying clear of the levels crossings during driving of the qubit, and can be traversed diabatically when initialising the qubit.

The angle θ in Eqs. C.1.30 and C.1.31 corresponds to a very small rotation of the qubit quantisation axis due to the perpendicular component of the hyperfine interaction:

$$\cos(\theta) = \frac{\Omega_s}{\Omega_z} \approx 1, \quad \text{(C.1.32)}$$

$$\sin(\theta) = \frac{A_R/2}{\Omega_z} \approx 0. \quad \text{(C.1.33)}$$

Finally, the new spin basis is defined as:

$$\tilde{\uparrow}/\tilde{\downarrow} = \frac{1}{\sqrt{2}}\left(\mp\sqrt{1 \pm \cos(\theta)}, \mp\sqrt{1 \mp \cos(\theta)}\right),$$

expressed in the combined basis of nuclear and electron spins $\{|N_L\rangle \otimes |\Downarrow\uparrow\rangle, |N_L\rangle \otimes |\Uparrow\downarrow\rangle\}$.

Similarly to the quantum flip-flop qubit, the coupling between the qubit states is purely determined by the hyperfine coupling to the nuclear spin that the electron spin flip-flops with (A_R). However, $\Delta\Omega_z$ is determined by the averaged hyperfine interaction M_n of the electron with the nuclear spins in the left quantum dot, which are not involved in the qubit dynamics, and that we therefore call the spectator nuclear spins. In Chapter 4 we will describe how we can engineer this averaged hyperfine interaction M_n in order to minimise $\Delta\Omega_z$ and in turn increase the dephasing time of the qubit.

Summary

In summary we have shown that three proposals for qubits based on an electron spin qubit shared by two quantum dot are mathematically equivalent and can be described by the general Hamiltonian of Eq. 3.2.1. In the QD–QD proposal the electron is shared between two gate defined quantum dots, and a transverse and spurious longitudinal magnetic field is produced by an in-chip micromagnet. For the QD–donor proposal, one of the two quantum dots is replaced by a single phosphorus donor, and in the donor–donor implementation both quantum dots are defined using phosphorus donor clusters. The latter two proposals involve the presence of nuclear spins from the donor clusters which increases the dimensionality of the system. However, both systems reduce to a four-dimensional subspace, as depicted in Fig. C.1 a). They can be described by the same Hamiltonian as the QD-QD proposal, with longitudinal and transverse energy terms not originating from longitudinal and transverse magnetic fields. In the QD-donor case (flip-flop qubit), the longitudinal energy difference $\Delta\Omega_z$ results from a difference in the electron g-factor on the gate-defined quantum dot and the donor quantum dot respectively, while the transverse-energy difference $\Delta\Omega_x$ results from the hyperfine interaction of the electron spin with the donor nucleus. In the donor–donor case, the transverse coupling similarly originates from the hyperfine interaction of the electron spin with one of the nuclei of the donors (the one the spin slip-flops with when electrically driven), while the longitudinal energy difference originated from the hyperfine interaction of

the electron spin with all the other nuclei, that do not participate in the electrically driven electron–nuclear-spin flip-flops. The different origins of the longitudinal and transverse energy differences are summarised in Fig. C.1 b).

a)

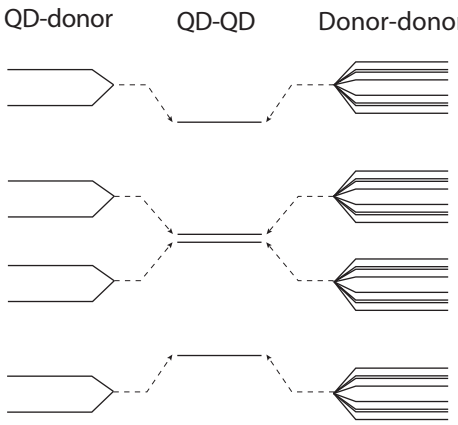

b)

Implementation	QD - Donor	QD - QD	Donor - Donor
Coupling mech.	Hyperfine	Grad. magn. field	Hyperfine
$\Delta\Omega_{\perp}$	100 MHz	100 - 800 MHz	100 MHz
$\Delta\Omega_{\parallel}$ mech.	Spin-orbit	Grad. magn. field	Hyperfine
$\Delta\Omega_{\parallel}$	25 - 80 MHz	10 - 100 MHz	0 - 50 MHz
Refs	Tosi	Croot, Benito	This work

Figure C.1: **Three different systems reduced to a four level system. a):** Schematic representation of the energy levels of the three flopping-mode implementations discussed in this section. The QD–donor and donor–donor implementations (left and right), display a hyperfine structure, but can be reduced to the a four level system, as in the QD–QD implementation (in the middle). **b):** Comparison of the longitudinal and transverse gradients and of mechanisms for different flopping-mode qubit proposals.

C.2 Irreducible nuclear spin subspaces

The space of spin with magnetic quantum number m is spanned by any combinations of spin containing a number $N_{\uparrow}$ of spin ups and $N_{\downarrow}$ of spin downs (electron and nuclear spins), such that:

$$\begin{aligned} \left(N_{\uparrow} - N_{\downarrow}\right)/2 &= m \\ N_{\uparrow} + N_{\downarrow} &= N_s. \end{aligned} \tag{C.2.1}$$

This fully determines the value of $N_{\uparrow}$ and $N_{\downarrow}$, as well as the dimensionality of

$\mathscr{H}_m^{N_s}$:

$$\dim(\mathscr{H}_m^{N_s}) = \binom{N_s}{N_\uparrow} = \binom{N_s}{(N_s+2m)/2} = \binom{N_s}{m+N_s/2}.$$

We will now show that any two spin state I and J satisfying the conditions C.2.1 can be transformed into each other by a series of nuclear-electron spin flip-flops $f_i = P_{i,N_s}$, corresponding to the permutation of the nuclear spin $i = 1, .., N_s - 1$ and the electron spin (the N_sth spin). Note that any permutation of spins can be constructed from these flip-flop transformations:

$$P_{i,j} = f_i \circ f_j, \qquad \text{if } i,j < N_s \tag{C.2.2}$$

$$P_{i,j} = f_i, \qquad \text{if } j = N_s \tag{C.2.3}$$

Let us now define the trivial state $K \in \mathscr{H}_m^{N_s}$, consisting of $N_\uparrow$ up spins and $N_\downarrow$ down spins. Both the states I and J can be transformed into this trivial state by permuting any spin pair $(\downarrow, \uparrow)$. In that way a series of permutation, and thus of flip-flops is found that transforms I into J. This proves that $\mathscr{H}_m^{N_s}$ cannot be decomposed further.

C.3 Energies and couplings for the 2P1P all epitaxial qubit

In this section we will provide a detailed overview of all the qubit energy states in the zero spin polarisation subspace of the 2P1P flopping mode qubit. We will also provide a detailed analysis of the coupling strength of the two qubit states to all of the other states in that subspace, some of which could become a pathway for state leakage

Each of those branches is further split according to the nuclear spin configuration resulting in the same total spin magnetisation m (including electron spin). For the 2p1p system in a zero spin magnetisation state, every branch contains three nuclear spin configuration.

We visualise the influence of the electric field on the electron and nuclear spin states of a 2p1p system in figure C.2 a). We have subtracted the bare charge electric Field dependency $\pm(\sqrt{\epsilon^2+t^2}-t)$ from the ground/excited charge state branches.

The ground/excited state branch is displayed in the two lower/higher plots in the figure. The spin down/up branches are further subdivided into separate plots. Each subplot thus displays the three nuclear possible nuclear spin configuration of

same magnetisation $m = 0$, for electron and charge states $|\downarrow \tilde{-}\rangle$, $|\uparrow \tilde{-}\rangle$,$|\downarrow \tilde{+}\rangle$ and$|\uparrow \tilde{+}\rangle$, from bottom to top in ascending energy.

In figure C.2 a), we have chosen a hyperfine coupling A_L of 30 MHz to the left dot (with a splitting of 10 MHz). For clarity, these hyperfine values are chosen larger then what could be achieved in a real device, in order to better separate the states. The hyperfine coupling to the right dot is chosen to be the standard bulk hyperfine value of 117 MHz.

The detuning dependency visible after having subtracted the charge state dependency is closely related to the bare hyperfine dependency $A_L^i(\epsilon)$ and $A_R(\epsilon)$, where the right hyperfine value is large at $\epsilon \gg 0$ (when the electron is primarily located on the right dot), and vanishes at $\epsilon \ll 0$. The two closely spaced levels correspond to the two nearly degenerate left dot nuclear spin state $|\Downarrow\Uparrow\rangle$ and $|\Downarrow\Uparrow\rangle$.

The proposed qubit is primarily encoded by the spin state in the charge ground state. Thus, any of the three states in the lowest branch can be chosen as the qubit ground state. In chapter 4 we show that it is advantageous to choose a nuclear spin state that is connected via nuclear-electron spin flip-flop to a state in the electron spin up branch (charge ground), such that the nuclear spin participating in the flip flop has a strong hyperfine coupling with the electron spin, and such that the magnetisation of the nuclear spins not involved in the flip-flop (the spectator nuclear spins) have near zero magnetization.

Given the chosen values of hyperfine coupling, we would choose the qubit ground to be $|g(\epsilon)\rangle \approx |\Downarrow\Uparrow\Uparrow\downarrow \tilde{-}\rangle$ (in black). Indeed it is connected the the electron spin up branch by a flip-flop with the right nuclear spin (with strongest hyperfine coupling) $|e(\epsilon)\rangle \approx |\Downarrow\Uparrow\Downarrow\uparrow \tilde{-}\rangle$)(in red). The two nuclear spin in the left dot stay in the state $|\Downarrow\Uparrow\rangle$ across both qubit states, and can thus be viewed as being spectators to any dynamics driven between the qubit states. The hyperfine interaction to both nuclear spin cancels out to the difference ΔA_L which is usually very small in a 2P system. This is the longitudinal magnetic gradient that will be experienced by the qubit. As we will show in a later section, driving errors can be reduced by reducing this gradient. The qubit ground end excited states can be seen to be close in energy to their near degenerate states $|\Uparrow\Downarrow\Uparrow\downarrow \tilde{-}\rangle$ and $|\Uparrow\Downarrow\Downarrow\uparrow \tilde{-}\rangle$ respectively.

The tunnel coupling is chosen to be 6.0 GHz and the magnetic field is chosen to be 0.4 T, so that the states in the third and fourth branch are close in energy and hybridize. The spin states of otherwise purely ground charge state character $|\tilde{-}(\epsilon)\rangle$ in the third branch ($|\uparrow -\rangle$) acquire a proportion of excited charge state character $|\tilde{+}(\epsilon)\rangle$. As we will see in more detail in the next section, the amount hybridization

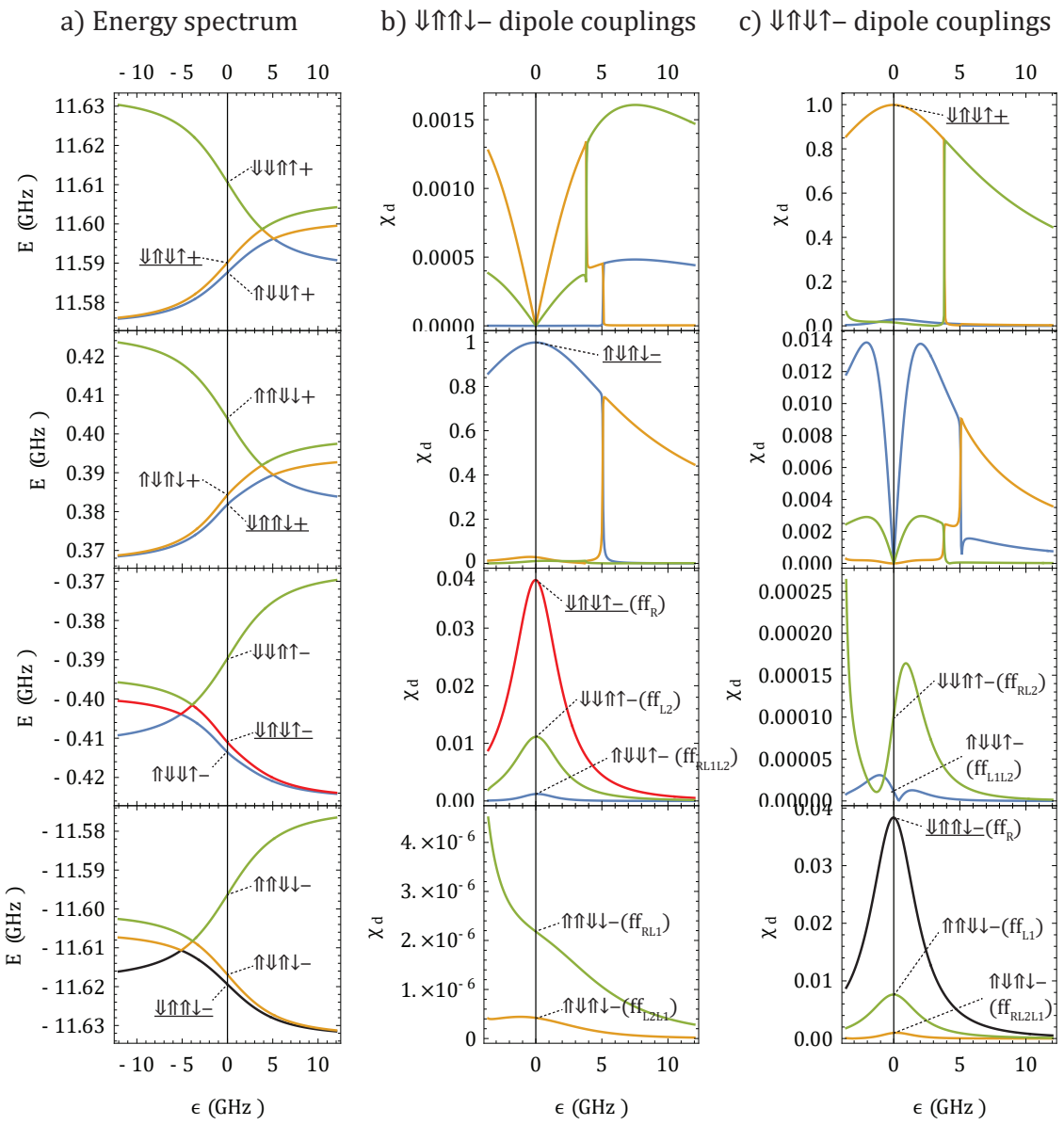

Figure C.2: **Eigenstate energies E and their electric dipole couplings** χ_d The system parameters are $B = 0.4\,\mathrm{T}$, $t = 6.0\,\mathrm{GHz}$, $\Delta A_L = 10\,\mathrm{MHz}$, $A_L = 30\,\mathrm{MHz}$, $A_R = 117\,\mathrm{MHz}$. We chose well separated hyperfine values for clarity. In the proposed qubit, we will privilege smaller values of ΔA_L. **a): Schematics of the Eigenstates Energies** E The electric field dependency of the bare charge qubit has been subtracted for clarity. The qubit ground and excited state are depicted in black and red respectively (first and 5th eigenenergy at $\epsilon = 0$). **b, c: Ground/excited state dipole coupling coefficient** The dipole coupling coefficient between the two qubit states is depicted in red and black. The dipole coupling coefficient for the pure charge transitions reach unity at $\epsilon = 0$ (Third and fourth frame from the bottom, for the ground/excited state respectively.)

is proportional to the energy difference between the two states. It is thus most pronounced around zero detuning. The increase hybridization of eigenstates also results in significantly increased electric coupling between the qubit states, close to zero detuning.

Electric coupling between eigenstates is provided by the electric field driving E_d. Without any hybridization, the electric field can only drive the charge state, and the coupling element is proportional the product of the charge dipole moment with the drive electric field $\chi_d \frac{ed}{\hbar} \cdot E_d$. The dipole coefficient χ describes the attenuation of the dipole moment when moving away from the zero detuning point: $\chi_d = \frac{t}{\Omega_c}$. It reaches unity at zero detuning. There is no dipole moment associated with any two states in the ground charge state branch.

With increasing hybridisation however, a dipole moment arises between states in the respective ground state branches. This is related to the electron $\uparrow$ state acquiring an excited charge character. We have plotted the dipole coefficient χ_d between the qubit ground/excited state and all other states in figure C.2 b) and c) respectively. The purely charge dipole coupling (peaking at 1 at $\epsilon = 0$ can be seen in the third and fourth subplot from the bottom, for the ground and excited state respectively. Due to the proximity in energy between the $|\uparrow \tilde{-}\rangle$ and $|\downarrow \tilde{+}\rangle$ branch for the chosen magnetic field value, the hyperfine mediated coupling between spin and charge states become energetically favourable. A second order interaction between flip-flopped $\downarrow$ and $\uparrow$ arises. It is mediated by a virtual simultaneous electron-nuclear spin flip flop and direct charge transition, as well as a simple charge transition. Such a second order coupling occurs between the ground state and the excited state (red and black in b) and c) respectively) and corresponds to a flip-flop of the electron spin with the right nuclear spin, which we label $\text{ff}_{\uparrow R}$. The coupling approaches 4% of the bare charge qubit coupling at zero detuning ($\chi_d \approx 0.04$). Note a similar second order coupling $\text{ff}_{\uparrow L2}$ arises between the ground state and the state $\Downarrow\Downarrow\Uparrow \tilde{-}$, this time mediated by a flip-flop with the second left nuclear spin (L2), that was in its $\Uparrow$ configuration, and thus could flip-flop with the electron spin (Green line below the red line). This coupling strength is however reduced by a factor 4 to about 1% of the bare charge qubit coupling, primarily due to the 4 fold reduction in the hyperfine coupling of the nuclear spin involved in the flip-flop ($A_{L2} \approx 30\,\text{MHz}$ instead of $A_R = 117\,\text{MHz}$). The same analysis is valid for the coupling of the excited qubit state, to the ground state ($\text{ff}_{\downarrow R}$) and to the state $\Uparrow\Uparrow\Downarrow\downarrow \tilde{-}$ (ff_{L1}).

We have so far mentioned two first order electric transitions (namely pure charge transitions), followed in magnitude by four possible second order flip-flop transition,

involving flip-flop with a single nuclear spin ($\mathrm{ff}_{\uparrow R}$, $\mathrm{ff}_{\downarrow R}$, $\mathrm{ff}_{\downarrow L1}$ and $\mathrm{ff}_{\uparrow L2}$. Coupling between the two qubit states to other, not directly flip-flopped states, are only possible through 4th and 6th order processes, and are therefore quiet weak. The ground state $\Downarrow\Uparrow\Uparrow\downarrow$ for example can be seen in figure C.2 b) to be weakly coupled to the state $\Uparrow\Uparrow\Downarrow\downarrow$. No direct coupling between those two states exists, and therefor the two states are only via higher order processes to the target state. One such coupling arises via second order virtual transition to the state to the state $\Downarrow\Uparrow\Downarrow\uparrow$ (which is a flip flop $\mathrm{ff}_{\uparrow R}$ with the right nuclear spin), followed by another second order transition to the target state (which is a flip-flop $\mathrm{ff}_{\downarrow L1}$). The resulting fourth order process can be notated as $\mathrm{ff}_{RL1} \equiv \mathrm{ff}_{\downarrow L1} \circ \mathrm{ff}_{\uparrow R}$, and is very weak $\chi_d < 3 \times 10^{-6}$ at $\epsilon \approx 0$. This coupling ff_{RL_1} is stronger then the coupling $\mathrm{ff}_{L2L1} \equiv \mathrm{ff}_{\downarrow L1} \circ \mathrm{ff}_{\uparrow L2}$, due to the fact that the first virtual transition $\mathrm{ff}_{\uparrow L2}$ is a factor 4 weaker then the coupling $\mathrm{ff}_{\uparrow R}$. All such fourth order transitions, corresponding to two virtual flip-flops with different nuclear spins, are at least two orders of magnitude lower then single flip-flops. They have been annotated within the two lower branches, in figure C.2 b). We have also annotated 6th order transition within the two $|-\rangle$ branches, corresponding to three consecutive virtual flip flops. For example $\mathrm{ff}_{\uparrow RL1L2} \equiv \mathrm{ff}_{\uparrow L2} \circ \mathrm{ff}_{\downarrow L1} \circ \mathrm{ff}_{\uparrow R} \equiv \mathrm{ff}_{\uparrow R} \circ \mathrm{ff}_{\downarrow L1} \circ \mathrm{ff}_{\uparrow L2}$, where now two main pathways for the virtual transitions are possible (involving the same three second order processes, in a different order).

Higher order couplings of the qubit states to the excited charge state branches are present as well. It is noteworthy that the higher order couplings between the qubit states in the $\downarrow -$ and $\uparrow -$ branches and the branches $\uparrow +$ and $\downarrow +$, respectively, is highly suppressed at $\epsilon = 0$, irrespective of the amounts of nuclear spin flips involved in the transition.

Note that all dipole couplings reach a maximum at $\epsilon = 0$, and asymptotically fall down to zero for positive and negative detuning values. This is a manifestation of the increased bare charge dipole coupling coinciding with an increased hybridization between spin and charge closer to zero detuning linked to the proximity in energy of the spin and charge state around zero detuning.

In summary we have shown that electric coupling of the qubit states to all states in the same magnetisation subspace are present. However they significantly differ in order and magnitude. The dominant coupling sources are first order direct charge transitions and second order, single flip-flop transitions. In the following we will neglect all other higher order couplings. We show in chapter 4, that when adiabatically the qubit transition ff_R, the direct charge transition is limiting the adiabaticity, and not the other possible (spurious) flip-flop transition $\mathrm{ff}_{\uparrow L2}$ and $\mathrm{ff}_{\downarrow L1}$.

Despite the direct transition being much further away in energy (detuned by $\approx 0.8\,\mathrm{GHz}$ in our example, as opposed to only $\approx 50\,\mathrm{MHz}$ for the other spurious flip-flop transition), the direct charge coupling is overwhelmingly larger then the spurious coupling $\chi_d = 1$ instead of $\chi_d \approx 10 \times 10^{-3}$. This motivates a second simplification restricting the same-magnetisation subspace even further to the four dimensional space spanned by the two qubit states and their corresponding excited charge states.

C.4 Rotating frame approximation for all epitaxial flopping mode qubit

The rotating wave approximation (RWA) transforming the Hamiltonian describing the three separate four level leakage systems can be performed in a way analogous to that found for the flopping mode qubit in Sect. B.2 using different generator matrices R to perform the unitary coordinate transformation into the rotating frame. In Fig. C.3 we summarise the process for the three systems, using an energy diagram of each system, the Hamiltonian describing the system, the generator matrix R that allows transformation of the Hamiltonian into the rotating frame (using the RWA), from top to bottom respectively.

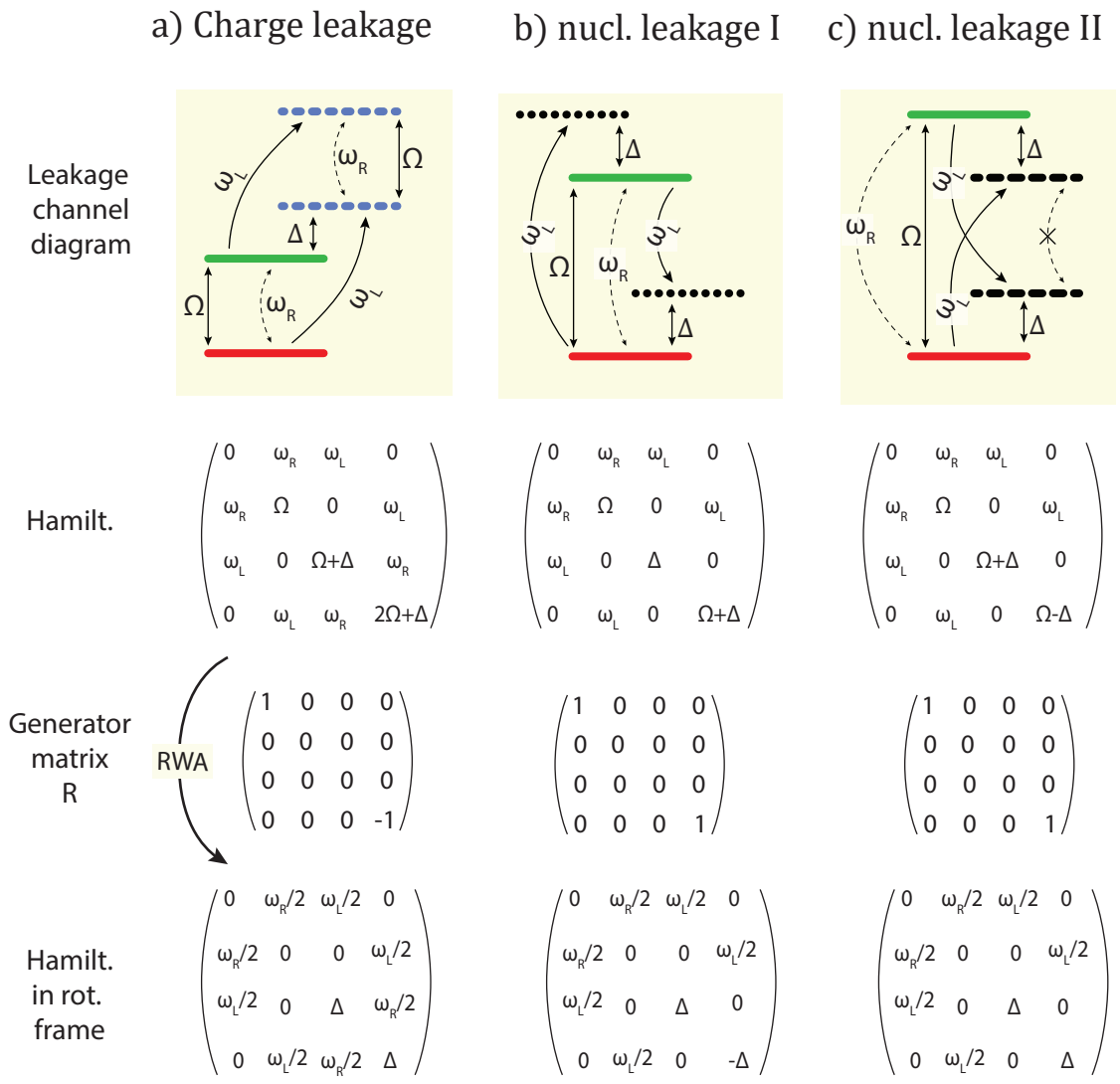

Figure C.3: **Rotating wave approximation for the three leakage channels of the 2P1P all-epitaxial flopping mode qubit,** for the charge leakage pathway and the two nuclear spin leakage pathways in **a)**, **b)** and **c)** respectively.

C.5 Charge limited adiabatic orbital state transfer

It can be advantageous to perform flopping mode qubit operations in either of the two orbital regimes (hybridised "two dot regime", or pure spin "single dot" regime). This requires being able to transfer the orbital state in a reversible manner. We have shown in Sect. 4.4.1, that for the particular 2P1P implementation studied in detail in Chapter 4, the speed of that transfer is limited by pure charge excitation, and the additional nuclear spin states can be neglected.

In such a system, when operating with two passive electron on the 2P donor cluster, the average hyperfine coupling of the electron to the left nuclei is reduced to about $\bar{A_L} = 10\,\mathrm{MHz}$ due to shielding from the inner shell electrons and the hyperfine coupling to the right nucleus would be close to the bare 1P coupling: $A_R = 117\,\mathrm{MHz}$. The spectator hyperfine difference ΔA_L in the hyperfine coupling of the electron to the two nuclei in the left dot determines how closely the two state $|\Uparrow\Downarrow\rangle$ and $|\Downarrow\Uparrow\rangle$ are to being fully degenerate. In order to minimise charge dephasing, this difference has to be engineered as close to zero as possible. In a realistic device, we expect the difference to be close to $1\,\mathrm{MHz}$, due to minor hyperfine Stark shift differences.

The energy diagram of this system is represented in figure C.4 d) for $\Delta A_L = 1\,\mathrm{MHz}$. Again, we have subtracted the bare charge qubit electric Field dependency $\pm(\sqrt{\epsilon^2 + t^2} - t)$ from the ground/excited charge state branches in order to only visualise the influence of the electric field on the electron and nuclear spin states. The ground/excited state branch is displayed in the two lower/higher plots in the figure and are split by the charge qubit splitting $\Omega_C = 2(\sqrt{\epsilon^2 + t^2})$. The spin down/up branches are further subdivided into separate plots. Each subplot thus displays the three nuclear possible nuclear spin configuration of same magnetisation, for electron and charge states $|\downarrow \tilde{-}\rangle$, $|\uparrow \tilde{-}\rangle$,$|\downarrow \tilde{+}\rangle$ and$|\uparrow \tilde{+}\rangle$, from bottom to top in ascending energy. The qubit ground and excited state ($|g(\epsilon)\rangle \approx |\Downarrow\Uparrow\Uparrow\downarrow \tilde{-}\rangle$ and $|e(\epsilon)\rangle \approx |\Downarrow\Uparrow\Downarrow\uparrow \tilde{-}\rangle$) energies (in black), are very close in energy to their near degenerate states $|\Uparrow\Downarrow\Uparrow\downarrow \tilde{-}\rangle$ and $|\Uparrow\Downarrow\Downarrow\uparrow \tilde{-}\rangle$ respectively.

As previously described (figure C.2), for high detuning values ϵ, the eigenstates asymptotically approach the single dot regime, where the ground charge state $|\tilde{-}(\epsilon)\rangle$ is the right dot orbital $|R\rangle$, the spins are not hybridised to charge, and no higher order coupling between the degenerate state is present. When approaching $\epsilon = 0$, the right dot orbital state hybridises into an antisymmetric superposition with the other dot orbital. At the same time a higher order coupling weakly couples the

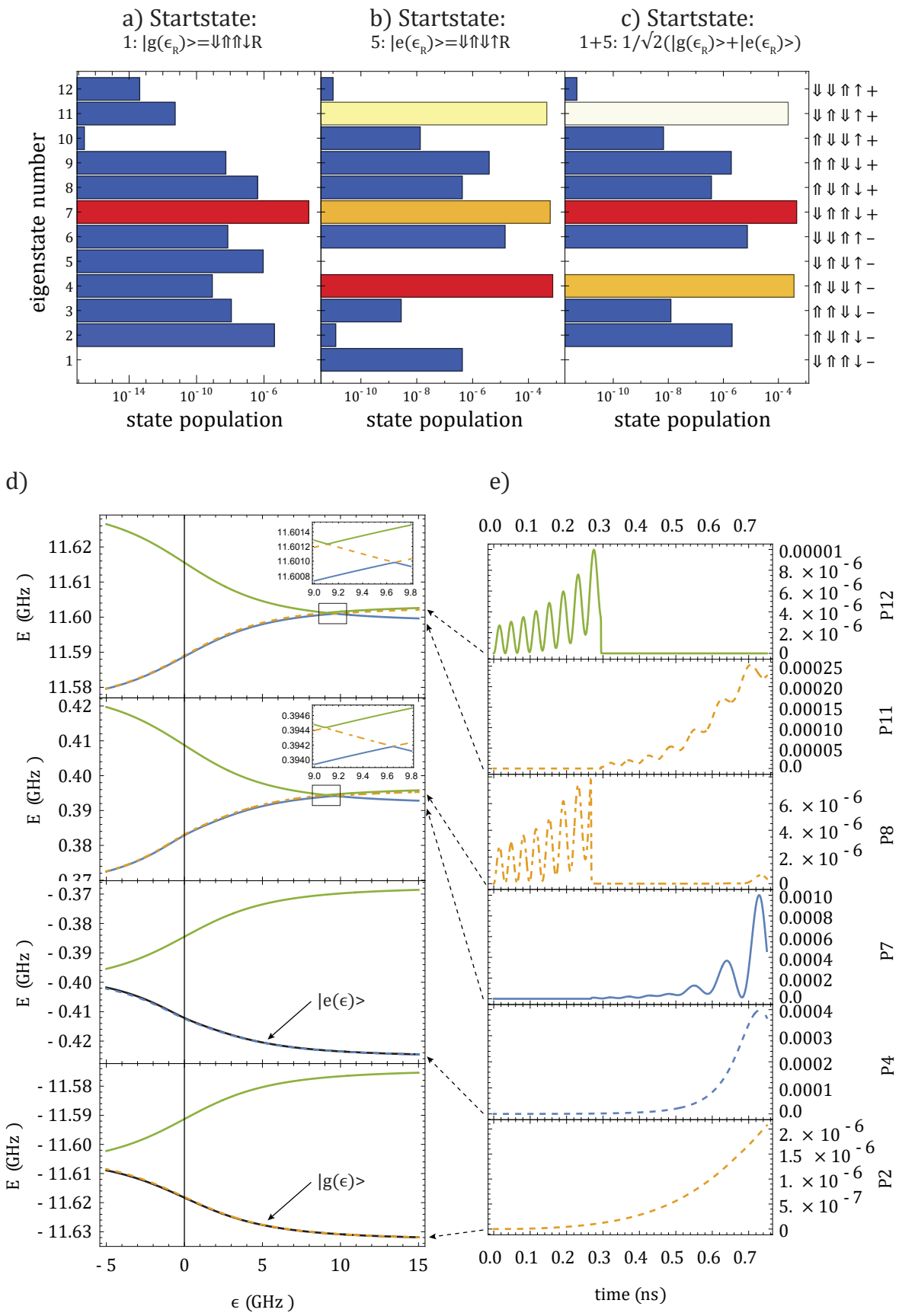

Figure C.4: **Adiabatic transfer of a spin state from the right orbital $|R\rangle$ to the antisymmetric orbital superposition $|-\rangle$.** We used a 0.75 ns linear ramp from $\epsilon = 15$ to 0 GHz (ramp speed=20GHz/ns). The system parameters are $B = 0.4\,\mathrm{T}$, $t = 6.0\,\mathrm{GHz}$, $\Delta A_L = 1\,\mathrm{MHz}$, $A_L = 10\,\mathrm{MHz}$, $A_R = 117\,\mathrm{MHz}$. **a, b, c:** Population of the final state in the leakage eigenstates after the adiabatic ramp for an initial state at $\epsilon = 15\,\mathrm{GHz}$ consisting of the qubit ground state, the excited state, and an equal superposition of the two respectively. **d: Eigen states energies.** For clarity, the ϵ dependency of the bare

degenerate states in the electron spin up branch.

In figure C.4 a-c), we simulate a 0.75 ns transfer between the single dot regime (at $\epsilon = 15\,GHz$) and the two dot regime at $\epsilon = 0$, for the ground qubit state $|g(\epsilon = 15\,\text{GHz})\rangle \approx |\Downarrow\Uparrow\Uparrow\downarrow R\rangle$, the excited qubit state $|e(\epsilon = 15\,\text{GHz})\rangle \approx |\Downarrow\Uparrow\Downarrow\uparrow R\rangle$, and an equal superposition of the latter:

$$\frac{1}{\sqrt{2}}\left(|g(\epsilon = 15\,\text{GHz})\rangle + |e(\epsilon = 15\,\text{GHz})\rangle\right).$$

In all three plots we show a histogram of the population of the final state (at $\epsilon(t = 0.75\,\text{ns})$) in each of the other eigenstates. In all cases less then 0.1% of the state leaks to other states during the transfer. The transfer of the ground state in a) shows that direct charge excitation (4.5×10^{-4}) to state 7 is the primary source of leakage, two orders of magnitudes higher then the next biggest leakage to the near degenerate state 2 (4.1×10^{-6}). The transfer of the qubit excited state in b) also predominantly leaks the excited charge states associated not only with the excited qubit state (6.0×10^{-4}) to state7) but also with the ground qubit state (4.5×10^{-4} to state 11). Leakage to the corresponding degenerate spin state 4, is now more pronounced then for the ground state (7.4×10^{-4} from $|e\rangle$ state 4 instead of 4.1×10^{-6} of $|g\rangle$ to state2). This is the result of a weak coupling of the qubit spin up state with its degenerate spin state, that arises due to their respective coupling to charge. The transfer of the qubit superposition state shows similar predominant leakage to those three states (leading by almost two orders of magnitude again).

Note that the respective amount of leakage to the degenerate state (4) as compared to the excited charge states (7 and 11) decrease exponentially with increasing splitting δA_L, so that for $\delta A_L > 1\,\text{MHz}$, leakage to the nuclear spin degenerate state is negligible.

In figure C.4 e), we show the time dependence of the leakage during transfer of the qubit superposition state considered in c). We plot the proportion of the time evolved state $\Psi(\epsilon(t))$ in the instantaneous eigenstates at $\epsilon(t)$. Only proportion in states of interest discussed above are shown. Non adiabatic passing of the crossing between state 7 and 8, as well as 11 and 12 in the excited charge state branches are visible.

In summary, we have shown that for a realistic 2p1p device configuration, subnanosecond orbital state transfer is possible. For degeneracies as low as 1 MHz they are limited by direct charge excitation. We have also shown that when the orbital state transfer passes through a degeneracy point where nuclear spin energy levels cross, the crossing is passed diabatically at the transfer speed demonstrated here.

This highlights that nuclear spin crossing need not be considered for the orbital state transfer..

C.6 Calculation of the spin-cavity coupling and the qubit dephasing time

We investigate the qubit-cavity coupling characteristic, which is shown in the Fig. 4.9 of the main text. Strong coupling of a cavity to a qubit can be achieved if the qubit-cavity coupling strength, g_{sc} is larger then the dephasing rate γ of the qubit as well as the decay rate κ of the cavity. The coupling strength, g_{sc} can be calculated as the product of the qubit electric dipole transition matrix element χ_{01} and the electric field amplitude produced by the cavity at the location of the qubit. Following the cavity simulation of Osika *et al.* [8], we use detuning amplitudes of about $\epsilon_c = 100\,\mathrm{MHz}$, and a cavity decay rate $\kappa = 1\,\mathrm{MHz}$. The detuning amplitude corresponds to zero point voltage fluctuations of the cavity of the order of $0.4\,\mu\mathrm{V}$ for quantum dots separated by about 10 nm, or equivalently to cavity electric fields of about 10V/m. We calculate the transition matrix element χ_{01} numerically and estimate the qubit dephasing rate, $\gamma = 1/T_2^*$ by converting the average qubit error using the formula,

$$T_2^* \approx 2\sqrt{2}\sqrt{\frac{t_{\pi/2}^2}{\mathrm{Log}\left(\frac{1}{1-2\,\mathrm{error}}\right)}}. \tag{C.6.1}$$

The dephasing rate is then calculated as a function of magnetic field strength and tunnel coupling, while the cavity detuning amplitude ϵ_c and the cavity decay rate κ are assumed to be constant across the parameter range investigated in Fig. 4.9.

C.7 Qubit routing and lithographic layers

Without loss of generality, let us consider the case where we need only one gate per qubit. The number of feedthroughs that can be conveniently pass through one of the edges of the first perimeter of the node is given by $(N-2)n_L$. Let us group the qubits in concentric perimeters, where the first perimeter are the qubits at the very outside of the node, and the last one are the qubit(s) at the very centre of the node. There are a number $P = \lceil N/2 \rceil$ concentric perimeters in the square of $N \times N$ qubits. Fully routing a number n_{P1} of perimeters can be expressed as:

$$(N-2)n_L \geq \sum_{i=2}^{n_{P1}} N-(2i-1) \tag{C.7.1}$$

$$\geq -n_{P1}^2 + Nn_{P1} - (N-1). \tag{C.7.2}$$

For $N \leq 2(2n_L+1)$, no root exists, and the condition is always satisfied. This means that one can route all the qubits of the node in a single layer, using the leads fed through through the outer perimeter. For example for a single possible feedthrough between adjacent qubits($n_L = 1$), one can route up to 36 qubits in a single layer ($N = 6$).

For $N > 2(2n_L+1)$ one can only route the outer n_{P1} perimeter given by:

$$n_{P1} = \left\lfloor \frac{1}{2}\left(N - \sqrt{N-2}\sqrt{N-2(2n_L+1)}\right)\right\rfloor. \tag{C.7.3}$$

The next square of $N_2 = N - ((2n_{P1})+1)$ qubits will need to be routed in a similar manner, but in another lithographic plane separated by a dielectric material.

By using the above procedure recursively, we find that the number of lithographic layers needed to address a number of N^2 qubits with a number of n_L possible feedthroughs between adjacent qubits is given by:

$$n_{\text{lith layers}} \approx \frac{N}{2n_L+3}. \tag{C.7.4}$$

Appendix D

Chapter 5 appendix

D.1 Ionisation/Neutralisation rate during nuclear spin dynamics experiment

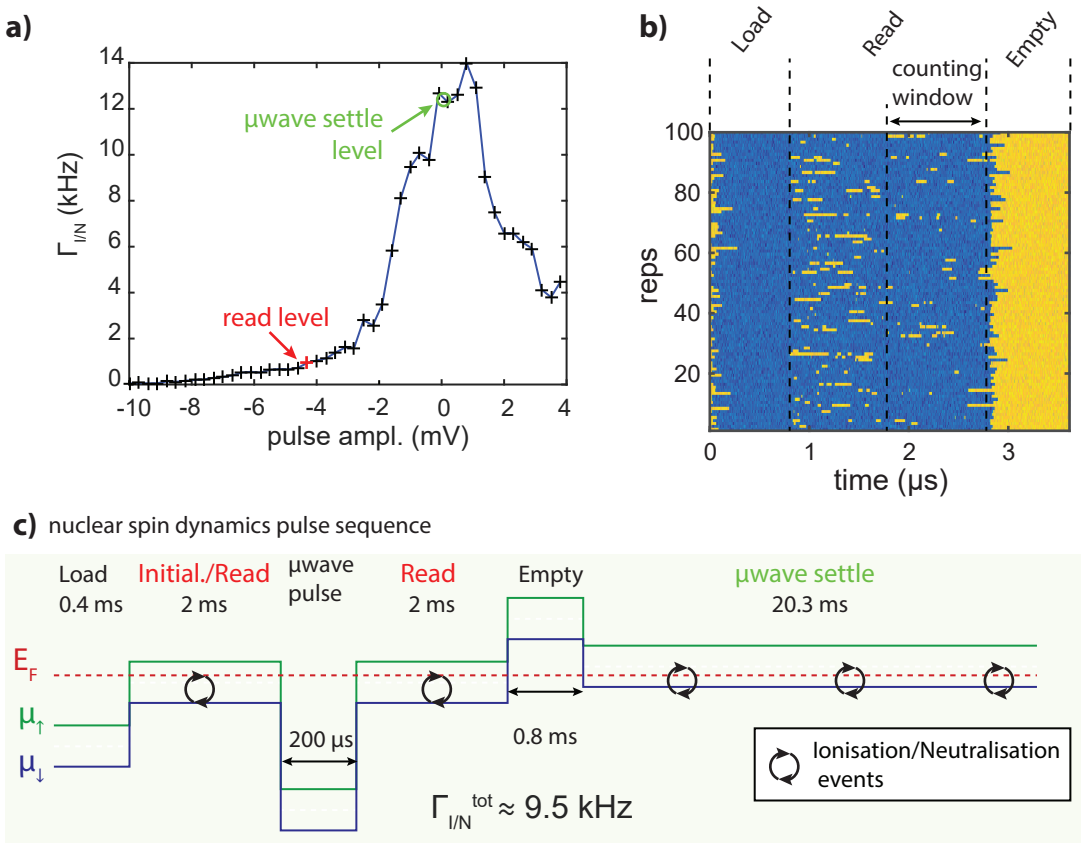

Figure D.1: **Estimation of ionisation/neutralisation rate $\Gamma_{I/N}$ of the 2P molecule. a) and b)** Measurement of $\Gamma_{I/N}$ during the spin tail experiment of Fig. 5.16. The ionisation events are detected within a counting window in the second half of the "read" sequence (see at a read level of $-4.3\,\mathrm{mV}$ in b)), to avoid counting spin ↑-out events which do not occur in the microwave settle phase at a pulse amplitude of 0. The resulting rate $\Gamma_{I/N}$ is calculated as a function of the pulse amplitude in a). $\Gamma_{I/N}$ is maximal at a pulse amplitude of 0, reaching values of 12 kHz. **c)** $\Gamma_{I/N}$ during the first read phase in the nuclear spin dynamics experiment (at a read level of 4.3mV). The average rate $\Gamma_{I/N} = 0.5\,\mathrm{kHz}$ is consistent with that calculated during the spin-tail experiment in a) and b), where $\Gamma_{I/N} = 1\,\mathrm{kHz}$.

D.2 Nuclear spin transition lifetime

The transition lifetimes are estimated from just taking the inverse of the elements of the transition rate matrix Q of the Markov model (see Table 5.4):

Start \ End	$\Downarrow\Downarrow$	$\Downarrow\Uparrow$	$\Uparrow\Downarrow$	$\Uparrow\Uparrow$
$\Downarrow\Downarrow$	21^{+4}_{-4}	38^{+14}_{-9}	43^{+19}_{-11}	NaN
$\Downarrow\Uparrow$	18^{+7}_{-4}	11^{+3}_{-3}	46^{+44}_{-17}	53^{+69}_{-25}
$\Uparrow\Downarrow$	39^{+17}_{-10}	112^{+133}_{-46}	21^{+6}_{-5}	75^{+61}_{-27}
$\Uparrow\Uparrow$	520^{+NaN}_{-402}	36^{+38}_{-15}	35^{+36}_{-13}	17^{+8}_{-5}

Table D.1: Table of state lifetimes (diagonal) and transition times (off-diagonal)

Bibliography

[1] Austin G. Fowler, Matteo Mariantoni, John M. Martinis, and Andrew N. Cleland. Surface codes: Towards practical large-scale quantum computation. *Physical Review A*, 86(3):032324, sep 2012.

[2] Stephane Beauregard. Circuit for Shor's algorithm using 2n+3 qubits. *Quantum Information and Computation*, 3(2):175–185, 2003.

[3] Pijush Kumar Koley and Srimanta Pal. Comments on "Quantum networks for elementary arithmetic operations". *Neural, Parallel and Scientific Computations*, 20(1):11–16, 2012.

[4] Steven A. Cuccaro, Thomas G. Draper, Samuel A. Kutin, and David Petrie Moulton. A new quantum ripple-carry addition circuit. *ArXiv*, pages 1–9, 2008.

[5] Guilherme Tosi, Fahd A. Mohiyaddin, Stefanie Tenberg, Arne Laucht, and Andrea Morello. Robust electric dipole transition at microwave frequencies for nuclear spin qubits in silicon. *arXiv*, jun 2017.

[6] Jarryd J Pla, Kuan Y Tan, Juan P Dehollain, Wee H Lim, John J L Morton, David N Jamieson, Andrew S Dzurak, and Andrea Morello. A single-atom electron spin qubit in silicon. *Nature*, 489(7417):541–545, sep 2012.

[7] Guilherme Tosi, Fahd A Mohiyaddin, Vivien Schmitt, Stefanie Tenberg, Rajib Rahman, Gerhard Klimeck, and Andrea Morello. Silicon quantum processor with robust long-distance qubit couplings. *Nature Communications*, 8(1):450, dec 2017.

[8] E. N. Osika, S. Monir, Y.-L. Hsueh, S. Kocsis, B. Voisin, C. Chua, S. Rogge, and R. Rahman. Spin-photon coupling for atomic qubit devices in silicon. *Unplublished*, 2021.